

2014

## Multiscale Estimation of Inertial Effects for Frac-Pack Completed Gas Reservoirs

Sultan Anbar

*Louisiana State University and Agricultural and Mechanical College*

Follow this and additional works at: [https://digitalcommons.lsu.edu/gradschool\\_dissertations](https://digitalcommons.lsu.edu/gradschool_dissertations)



Part of the [Petroleum Engineering Commons](#)

---

### Recommended Citation

Anbar, Sultan, "Multiscale Estimation of Inertial Effects for Frac-Pack Completed Gas Reservoirs" (2014).  
*LSU Doctoral Dissertations*. 1715.

[https://digitalcommons.lsu.edu/gradschool\\_dissertations/1715](https://digitalcommons.lsu.edu/gradschool_dissertations/1715)

This Dissertation is brought to you for free and open access by the Graduate School at LSU Digital Commons. It has been accepted for inclusion in LSU Doctoral Dissertations by an authorized graduate school editor of LSU Digital Commons. For more information, please contact [gradetd@lsu.edu](mailto:gradetd@lsu.edu).

MULTISCALE ESTIMATION OF INERTIAL EFFECTS FOR FRAC-PACK COMPLETED  
GAS RESERVOIRS

A Dissertation

Submitted to the Graduate Faculty of the  
Louisiana State University and  
Agricultural and Mechanical College  
in partial fulfillment of the  
requirements for the degree of  
Doctor of Philosophy

in

The Department of Petroleum Engineering

by  
Sultan Anbar  
B.S., METU University, 2007  
M.S., METU, 2009  
December 2014

*for my family and friends who were there to support me*

## ACKNOWLEDGEMENTS

I take great joy from acknowledging and giving thanks to my family, friends, and colleagues who provided for their support and assistance throughout this journey.

I am also grateful for each member of my faculty committee. I am grateful for the guidance that I have received from Dr. Christopher White on core scale analysis, from Dr. Karsten E. Thompson on network modeling, from Dr. Mayank Tyagi on LBM and reservoir modeling simulations, and from Dr. Richard Hughes on Matlab and CMG integration. I am very thankful to Dr. Clinton S Willson and Dr. Stephen O. Sears for their constructive comments. Also, I am very grateful to Dr. Huiming Bao voluntariness to join my faculty committee.

I would to thank Dr. Mileva Radonjic for her invitation that initiated my graduate studies at LSU. I would like to acknowledge Dr. Lee Yan for his support on packing algorithm and issues related to HPC resources. I am grateful to Dr. Sait Ahmet Binselam for his financial contribution and technical help in setting up the personal-supercomputer and providing encouragement. Also, I am thankful to Mr. George Ohrberg for providing technical support related to computer hardware and software. I would like to thank Dr. Paul Kemp for providing encouragement and study environment for me.

Funding received to complete my dissertation research came from YOK and Shell Oil Company. This work would not have been possible without these financial supports in the form of scholarship and graduate assistantships, respectively. I gratefully acknowledge experimental data provided by Schlumberger.

I thank my parents, sisters and brother for their encouragement and support to pursue this journey. I am also grateful for my friends, who were supportive, especially when I felt discouraged.



## TABLE OF CONTENTS

ACKNOWLEDGEMENTS .....	iii
LIST OF TABLES .....	vi
LIST OF FIGURES .....	ix
ABSTRACT.....	xxii
CHAPTER 1: INTRODUCTION .....	1
CHAPTER 2: LITERATURE REVIEW .....	10
2.1 Non-Darcy Flow .....	10
2.2 Slip Flow .....	12
2.3 Flow Regimes .....	14
2.4 Non-Darcy Flow Criteria .....	16
2.5 Non-Darcy Coefficient Observations .....	18
2.5.1 Theoretical Non-Darcy Coefficient Correlations .....	19
2.5.2 Experimental Analysis of Non-Darcy Coefficient .....	20
2.5.3 Non-Darcy Coefficient Estimation from Field Data .....	28
2.5.4 Non-Darcy Coefficient Estimation from Network Modeling .....	29
2.6 Non-Darcy Flow Simulations .....	33
CHAPTER 3: STATEMENT OF THE PROBLEM.....	39
CHAPTER 4: OBJECTIVES.....	45
CHAPTER 5: CORE-SCALE ANALYSIS.....	47
5.1 Optimization for Steady State Flow Lab Experiment.....	47
5.2 Pulse Decay Experiment Analysis .....	61
5.3 Pulse Decay Simulation Algorithm and Validation .....	77
5.4 Sensitivity Analysis of Pulse-Decay Experiment .....	84
5.5 Pulse-Decay Experiment Duration Estimation .....	87
CHAPTER 6: PORE-SCALE ANALYSIS .....	110
6.1 Lattice Boltzmann Method and Network Modeling .....	110
6.2 Packing Algorithm Reproducibility Validation .....	115
6.3 Representative Elementary Volume of Gravel Packs .....	121
6.4 Lattice Boltzmann Method and Network Modeling Comparison.....	123
6.4.2 Resolution and Model Specific Parameters Effect on Flow Properties Estimation .....	125
6.4.3 Grain Shape and Packing Effect.....	137
6.5 Permeability and Non-Darcy Coefficient Correlation Development.....	148
6.5.1 Design of Experiment for Gravel Packs.....	148
6.5.2 Non-Darcy Coefficient and Tortuosity Calculations from LBM Simulations .....	152
6.5.3 Flow Parameters Comparison with Literature Data.....	155

6.5.4	Non-Darcy coefficient and Permeability Correlations Development .....	167
6.5.5	Compaction Effect on Flow Properties .....	203
6.6	Sand Migration Effect on Flow Properties .....	212
CHAPTER 7: RESERVOIR-SCALE ANALYSIS .....		230
7.1	Simulation Algorithm for Single Phase Flow with Sand Migration.....	230
7.2	Reservoir Simulation Algorithm Validation .....	240
7.3	Parametric Study of Sand Migration.....	255
7.3.1.	Initial Movable Sand Concentration Effect on Sand Production .....	261
7.3.2.	Critical Velocity Effect on Sand Production.....	267
7.3.3.	Flow Rate Effect on Sand Production .....	272
7.3.4.	Pore Throat Plugging Rate Constant Effect on Sand Production.....	278
7.3.5.	Pore Surface Retention Rate Constant Effect on Sand Production.....	283
7.3.6.	Pore Surface Entrainment Rate Constant Effect on Sand Production.....	286
7.4	Fracture Effect on Sand Migration .....	291
7.4.1	Fracture Half-Length Effect on Sand Production .....	299
7.4.2	Fracture Width Effect on Sand Production .....	302
7.4.3	Fracture Permeability Effect on Sand Production.....	305
CHAPTER 8: RESULTS AND DISCUSSIONS .....		309
CHAPTER 9: CONCLUSION .....		318
REFERENCES .....		321
VITA.....		329

## LIST OF TABLES

Table 3.1	Input Data Used in the 1-D Single Phase Simulations .....	41
Table 5.1	Pressure Measurement Error Effect on Flow Parameters Estimation .....	51
Table 5.2	Flow Rate Measurement Error Effect on Flow Parameters Estimation .....	53
Table 5.3	Experiment Condition and Core properties .....	55
Table 5.4	Optimization Results of Steady State Lab Experiment .....	56
Table 5.5	Bootstrap Results of Steady State Lab Experiment.....	60
Table 5.6	Core Properties and Lab Experiment Conditions .....	64
Table 5.7	Input Parameters of Pulse-Decay Simulation.....	83
Table 5.8	Base Case Simulation Input Parameters.....	84
Table 5.9	Sensitivity Parameters and Their Ranges .....	85
Table 5.10	Hamersley Design Variables and Their Ranges for Pulse Decay Experiments with 2 Tanks .....	89
Table 5.11	Correlation Coefficients of Design Variables for Pulse Decay Experiments with 2 Tanks .....	89
Table 5.12	Summary of Fit Statistics for Experiment Duration (2 Tanks) .....	91
Table 5.13	Parameter Estimates of Experiment Duration Equation (2 Tanks) .....	92
Table 5.14	Hamersley Design Variables and Their Ranges for Pulse Decay Experiments with 1 Tank.....	97
Table 5.15	Correlation Coefficients of Design Variables for Pulse Decay Experiments with 1 Tank.....	97
Table 5.16	Summary of Fit Statistics for Experiment Duration (1 Tank).....	99
Table 5.17	Parameter Estimates of Experiment Duration Equation (1 Tank).....	99
Table 5.18	Summary of Fit Statistics for Experiment Duration (1 Tank) for 2 Groups .....	103
Table 5.19	Parameter Estimates of Experiment Duration Equation (1 Tank) for Group 1 .....	103

Table 5.20	Parameter Estimates of Experiment Duration Equation (1 Tank) for Group 2 .....	104
Table 5.21	2C Core Pulse Decay Experiment Parameters used in Monte Carlo Simulation.....	107
Table 6.1	Packing Simulation Runs .....	116
Table 6.2	Anova Table for Voxel Separation of 0.9430 .....	120
Table 6.3	p values for Semi-variance Comparison .....	120
Table 6.4	Network Results of Random Pack.....	122
Table 6.5	Domain Resolution of Heterogeneous Pack.....	127
Table 6.6	Domain Resolution of Cubic Pack .....	134
Table 6.7	Normal Distribution Fit Parameters and Sorting Calculation .....	151
Table 6.8	Fit Summary of $\beta = f(k, \phi)$ .....	171
Table 6.9	Parameters Estimate of $\beta = f(k, \phi)$ .....	172
Table 6.10	Fit Summary of $\beta = f(k, \tau)$ .....	173
Table 6.11	Parameters Estimate of $\beta = f(k, \tau)$ .....	173
Table 6.12	Fit Summary of $\beta = f(k, \phi, \tau)$ .....	175
Table 6.13	Parameters Estimate of $\beta = f(k, \phi, \tau)$ .....	176
Table 6.14	Fit Summary of $\beta = f(k, \phi, \tau, SSA)$ .....	177
Table 6.15	Parameters Estimate of $\beta = f(k, \phi, \tau, SSA)$ .....	179
Table 6.16	Non-Darcy Coefficient Correlations of Gravel Packs.....	180
Table 6.17	Permeability Correlations of Gravel Packs .....	181
Table 6.18	Decision Criteria for Different Discrepancy Functions.....	185
Table 6.19	Standardized Regression Weights between Observed Petrophysical Variables.....	195
Table 6.20	Squared Multiple Correlations of Predicted Observed Petrophysical Variables.....	196
Table 6.21	Correlations between Error Terms .....	196

Table 6.22	Regression Weights between Observed Petrophysical Variables .....	197
Table 6.23	Variances of Exogenous Variables.....	198
Table 6.24	Covariance between Error Terms .....	198
Table 6.25	Direct, Indirect and Total Effects .....	198
Table 6.26	Chi-square Statistics of Path Model .....	199
Table 6.27	HOELTER Critical N .....	199
Table 6.28	Standardized Residual Covariances of Path Model.....	200
Table 6.29	Fit Statistics Based on Model Parsimony .....	201
Table 6.30	Fit Statistics Based on Model Comparison .....	201
Table 6.31	Sand Migration Domains and Sand Particle Range .....	214
Table 7.1	Gas Composition used in Reservoir Simulation (W. J. Lee & Wattenbarger, 1996) .....	242
Table 7.2	Input Data for Sand-Gravel with G-S Ratio of 7.5.....	243
Table 7.3	Input Data for Sand-Gravel with G-S Ratio of 6.3.....	244
Table 7.4	2D Reservoir Simulation Input Parameters .....	256
Table 7.5	2D Frac-pack Completed Reservoir Simulation Input Parameters .....	293

## LIST OF FIGURES

Figure 1.1	Work Flow of the Study .....	9
Figure 2.1	Nonlinear Flow of Air through Sand (Adopted from Katz, 1959) .....	12
Figure 2.2	Friction Factor Plot (Adopted from Cornell and Katz, 1953) .....	13
Figure 2.3	Observed Permeability Change with Reciprocal Mean Pressure (Adopted from Klinkenberg, 1941) .....	14
Figure 2.4	Flow regimes in porous media (Adopted from Basak, 1977) .....	16
Figure 3.1	Non-Darcy Coefficient (Beta Factor) Comparison for Core#9 (Adopted from Amao, 2007) .....	40
Figure 3.2	Flow Rate Change with Inlet Pressure for 1-D Single Phase Steady-State Simulations .....	41
Figure 3.3	Klinkenberg Analysis without non-Darcy Effects Correction for Synthetic Data .....	43
Figure 3.4	Forchheimer Analysis without Slippage Effect Correction for Synthetic Data.....	43
Figure 3.5	Impairment Effect on Non-Darcy Coefficient (Chukwudozie, 2011).....	44
Figure 5.1	Synthetic Case – Forchheimer (left) and Klinkenberg (right) Plots obtained Optimization Algorithm Results.....	50
Figure 5.2	Pressure Measurement Error Effect on Flow Parameters Estimation .....	52
Figure 5.3	Pressure Measurement Error Effect on Mean Flow Parameters Estimation.....	53
Figure 5.4	Flow Rate Measurement Error Effect on Flow Parameters Estimation .....	54
Figure 5.5	Pressure Measurement Error Effect on Mean Flow Parameters Estimation.....	54
Figure 5.6	Steady State Lab Measurements.....	55
Figure 5.7	Forchheimer and Klinkenberg Plots obtained from Optimization Method for Steady-State Lab Measurements.....	55
Figure 5.8	Comparison of Lab Flow Rate Measurement and Flow Rate Calculation .....	56
Figure 5.9	Flow Parameters Estimate from Jackknifing Method .....	57

Figure 5.10	Outlier Detection with Distance Methods .....	58
Figure 5.11	Flow Parameters Estimation from Bootstrap for Steady-State Lab Measurements .....	58
Figure 5.12	Comparison of Lab Flow Rate Measurement and Flow Rate Calculation after Jackknife .....	60
Figure 5.13	Pulse Decay Experiment Setup (S.C. Jones, 1997) .....	62
Figure 5.14	Upstream Tank Pressure Change with Time – 2C Core Data (left), 3C Core Data (right).....	64
Figure 5.15	Jones Approximation Plot for 2C Core Data (left) and 3C Core Data (right).....	65
Figure 5.16	Jones Method –Flow Rate Comparison for 2C Core Data (left) and 3C Core Data (right).....	65
Figure 5.17	Bootstrap Sampling - Permeability, Klinkenberg Coefficient and Forchheimer Coefficient for 2C Core Data .....	67
Figure 5.18	Bootstrap Sampling - Permeability, Klinkenberg Coefficient and Forchheimer Coefficient for 3C Core Data .....	67
Figure 5.19	Error Analysis of Pulse-Decay Simulation of 2C Core.....	68
Figure 5.20	Error Analysis of Pulse Decay Simulation of 3C Core .....	68
Figure 5.21	Non-Darcy Effect of 2C Core Experiment .....	69
Figure 5.22	Non-Darcy Effect of 3C Core Experiment .....	70
Figure 5.23	Flow Rate Along the 2C Core (left) and 3C Core (right).....	70
Figure 5.24	Kaczmarek Method - Inlet Pressure Comparison with for the 2C Core (left) and 3C Core (right).....	71
Figure 5.25	Kaczmarek Method –Flow Rate Comparison for 2C Core Data (left) and 3C Core Data (right).....	72
Figure 5.26	Kaczmarek Method –Error Analysis of Pulse Decay Simulation of 2C Core .....	73
Figure 5.27	Kaczmarek Method –Error Analysis of Pulse Decay Simulation of 3C Core .....	73
Figure 5.28	Experiment Time Duration Effect on Permeability Estimation .....	74

Figure 5.29	Experiment Time Duration Effect on Klinkenberg Coefficient Estimation.....	75
Figure 5.30	Experiment Time Duration Effect on Non-Darcy Coefficient Estimation.....	76
Figure 5.31	Flow Parameter Estimation Effect on Cumulative Gas Production .....	76
Figure 5.32	Pulse-Decay Simulation Algorithm.....	80
Figure 5.33	Contour Plot of Pressure from Pulse Decay Simulation .....	82
Figure 5.34	Pressure Comparison Obtained from Simulation and from Inverse Laplace Transformation of Eqn.5.46.....	83
Figure 5.35	Core Diameter Effect on Pulse-Decay Experiment Duration.....	85
Figure 5.36	Permeability Effect on Pulse-Decay Experiment Duration.....	86
Figure 5.37	Upstream Tank Volume Effect on Pulse-Decay Experiment Duration.....	86
Figure 5.38	Pulse-Decay Experiment Duration Sensitivity Analysis Results .....	87
Figure 5.39	Generated and Observed Klinkenberg Coefficient Comparison .....	90
Figure 5.40	Generated and Observed Forchheimer Coefficient Comparison.....	90
Figure 5.41	Actual by Predicted Plot of Pulse-Decay Experiment (2 Tanks) Duration .....	92
Figure 5.42	Leverage Plot of Pulse Decay Experiment Duration Design Variables (2 Tanks) .....	93
Figure 5.43	Residual vs. Predicted Plot of Experiment Duration (2 Tanks) .....	95
Figure 5.44	Residual Distribution of Experiment Duration (2 Tanks) .....	95
Figure 5.45	Profiler Plot of Simulation Time Design Variables .....	96
Figure 5.46	Actual by Predicted Plot of Pulse-Decay Experiment (1 Tank) Duration.....	98
Figure 5.47	Residual vs. Predicted Plot of Experiment Duration (1 Tank) .....	99
Figure 5.48	Discriminant analysis of Residual vs. Predicted Experiment Duration (1 Tank).....	100
Figure 5.49	Scatter Plot of Residual vs. Design Variables (1 Tank) .....	101
Figure 5.50	Scatter Plot of Residual vs. Permeability (1 Tank) .....	102
Figure 5.51	Actual by Predicted Plot of Pulse-Decay Experiment (1 Tank) Duration for 2 Groups.....	103



Figure 5.52	Residual vs. Predicted Plot of Experiment Duration (1 Tank) for 2 Groups .....	104
Figure 5.53	Residual Distribution of Experiment Duration (1 Tank) for 2 Groups .....	105
Figure 5.54	Leverage Plot of Pulse Decay Experiment Duration Design Variables (1 Tank) for Group 1.....	105
Figure 5.55	Leverage Plot of Pulse Decay Experiment Duration Design Variables (1 Tank) for Group 2.....	106
Figure 5.56	Pulse-Decay Experiment Duration Estimation from Developed Correlation with Monte Carlo Simulation.....	108
Figure 5.57	Inverse Prediction of 2C Core Permeability by using Developed Correlation.....	109
Figure 6.1	Lattice Structure, and Velocity Distribution and Histogram View (Sukop & Thorne, 2007) .....	112
Figure 6.2	Maximum Ball Algorithm (Silin, Jin, & Patzek, 2003) .....	115
Figure 6.3	Grain Size Distribution and Packing Formation for Packing Algorithm Verification.....	117
Figure 6.4	Voxel Image of Layer 150 for Run1 through Run4 .....	118
Figure 6.5	Extended Semi-variogram for Voxelized Packing Formation of Run1 .....	119
Figure 6.6	Semivariance Comparison for Voxel Separation of 0.9430 .....	119
Figure 6.7	Swanson Point of Capillary Pressure of Packing Domain Run01.....	121
Figure 6.8	Heterogeneous Pack used in Representative Elementary Volume Study .....	123
Figure 6.9	Subdomains of Heterogeneous Pack .....	124
Figure 6.10	Representative Elementary Volume of Heterogeneous Pack for Porosity and Permeability .....	125
Figure 6.11	Image Resolution Effect on Particle Surface Representation.....	126
Figure 6.12	Resolution Effect on Porosity.....	128
Figure 6.13	Resolution and Relaxation Time Effect on Permeability Estimation from BGK.....	129
Figure 6.14	Resolution and Relaxation Time Effect on Permeability Estimation from MRT .....	129

Figure 6.15	Comparison of Resolution Effect on Permeability Estimation from BGK and MRT.....	130
Figure 6.16	Comparison of Resolution Effect on Permeability Estimation from LBM and Network Model.....	130
Figure 6.17	Resolution Effect on Pore Number and Average Coordination Number .....	131
Figure 6.18	Resolution Effect on Pore Number and Average Throat Length .....	132
Figure 6.19	Resolution Effect on Network Structure Constructed with Touching Merge Condition.....	132
Figure 6.20	Resolution Effect on Capillary Pressure calculated from Network Modeling.....	133
Figure 6.21	Resolution Effect on Network Model for Cubic Pack.....	135
Figure 6.22	Permeability Calculated from Network Modeling for Cubic Pack .....	136
Figure 6.23	Permeability Calculated from LBM for Cubic Pack .....	137
Figure 6.24	Extended Domain of Cubic Pack .....	138
Figure 6.25	Cubic Pack Permeability and Tortuosity Change from LBM with Domain Extension .....	139
Figure 6.26	Cubic Pack Pore Structure Change with Domain Extension.....	140
Figure 6.27	Comparison of Cubic Pack Permeability Calculated from LBM and Network with Domain Extension .....	141
Figure 6.28	Extended Domain of Heterogeneous Pack .....	141
Figure 6.29	Heterogeneous Pack Permeability and Tortuosity Change from LBM with Domain Extension .....	142
Figure 6.30	Pore Structure Change of Heterogeneous Pack with Domain Extension .....	143
Figure 6.31	Pore Structure Change of Heterogeneous Pack in x, y and z directions with Domain Extension .....	144
Figure 6.32	Stream Lines of Domain with Aspect Ratio 3.0.....	145
Figure 6.33	Comparison of Heterogeneous Pack Permeability Calculated from LBM and Network with Domain Extension .....	146
Figure 6.34	Resolution Effect on Specific Surface Area of Cubic Pack .....	147

Figure 6.35	Specific Surface Change with Domain Extension.....	147
Figure 6.36	Cumulative Probability Distribution of 24 Proppant Samples Found From Literature.....	149
Figure 6.37	Normal Cumulative Probability Distribution Fits of 24 Samples .....	150
Figure 6.38	Comparison of Mean, Standard Deviation and Sorting Calculated for Gravel Packs .....	150
Figure 6.39	Hamersley Design of Experiment for Gravel Packs.....	152
Figure 6.40	Permeability Change with Reynold Number.....	153
Figure 6.41	Permeability Change Comparison of Heterogeneous and Cubic Packs .....	153
Figure 6.42	Forchheimer Plot for non-Darcy Coefficient and Permeability .....	154
Figure 6.43	Tortuosity Change with Reynold Number .....	155
Figure 6.44	Velocity Field Change with Tortuosity .....	156
Figure 6.45	Comparison of Permeability Calculated from LBM and Network Model .....	157
Figure 6.46	Comparison of Non-Darcy Coefficient with Theoretically Develop Correlations .....	158
Figure 6.47	Comparison of Non-Darcy Coefficient with Theoretically Develop Correlations .....	159
Figure 6.48	Comparison of Non-Darcy Coefficients with Geertsma Correlation .....	159
Figure 6.49	Comparison of Non-Darcy Coefficients with Jones Correlations .....	160
Figure 6.50	Comparison of Permeabilities from LBM with Low Pressure Difference Method and Forchheimer Equation .....	161
Figure 6.51	Comparison of Permeability with Berg Correlation.....	162
Figure 6.52	Comparison of Permeability with Kozeny Correlations .....	163
Figure 6.53	Tortuosity Comparison with Logarithmic Formula .....	164
Figure 6.54	Tortuosity Comparison with Analytic Equation by Matyka et al. (2009).....	164
Figure 6.55	Tortuosity Porosity Relation – Archie Law.....	165
Figure 6.56	Specific Surface Area Comparison with Minkowski Functional .....	166

Figure 6.57	Swanson Point Relation with Porosity and Mean Grain Size .....	167
Figure 6.58	Swanson Point Correlation for Gravel Packs .....	168
Figure 6.59	Scatter Plot of Flow Parameters and Network Parameters for Gravel Packs.....	170
Figure 6.60	Actual by Predicted Plot of Non-Darcy Coefficient for $\beta = f(k, \phi)$ .....	171
Figure 6.61	Leverage Plots of Correlation Parameters for $\beta = f(k, \phi)$ .....	171
Figure 6.62	Residual by Predicted Plot for $\beta = f(k, \phi)$ .....	172
Figure 6.63	Actual by Predicted Plot of Non-Darcy Coefficient for $\beta = f(k, \tau)$ .....	173
Figure 6.64	Leverage Plots of Correlation Parameters for $\beta = f(k, \tau)$ .....	174
Figure 6.65	Residual by Predicted Plot for $\beta = f(k, \tau)$ .....	174
Figure 6.66	Actual by Predicted Plot of Non-Darcy Coefficient for $\beta = f(k, \phi, \tau)$ .....	175
Figure 6.67	Leverage Plots of Correlation Parameters for $\beta = f(k, \phi, \tau)$ .....	176
Figure 6.68	Residual by Predicted Plot for $\beta = f(k, \phi, \tau)$ .....	177
Figure 6.69	Actual by Predicted Plot of Non-Darcy Coefficient for $\beta =$ $f(k, \phi, \tau, SSA)$ .....	178
Figure 6.70	Leverage Plots of Correlation Parameters for $\beta = f(k, \phi, \tau, SSA)$ .....	178
Figure 6.71	Residual by Predicted Plot for $\beta = f(k, \phi, \tau, SSA)$ .....	179
Figure 6.72	Path Model Analysis of Petrophysical Properties and Design Variables Notation .....	194
Figure 6.73	Path Model Analysis of Petrophysical Properties and Design Variables .....	196
Figure 6.74	Sample Data File used in the Data Imputation .....	202
Figure 6.75	Actual by Predicted Data Comparison of Petrophysical Parameters .....	203
Figure 6.76	Grain Expansion of Heterogeneous Domain .....	204
Figure 6.77	Compaction Effect on Porosity and Permeability .....	205
Figure 6.78	Kozeny-Carman Relation of Porosity and Permeability .....	205
Figure 6.79	Compaction Effect on Network Parameters .....	207

Figure 6.80	Compaction Effect on Network Model .....	208
Figure 6.81	Compaction Effect on Forchheimer Plot.....	209
Figure 6.82	Permeability Comparison of Low Body Force Method and Low Pressure Difference Method.....	209
Figure 6.83	Non-Darcy Coefficient Change with Permeability Change due to Compaction.....	210
Figure 6.84	Kozeny-Carman Relation of Permeability and Non-Darcy Coefficient.....	211
Figure 6.85	Comparison of Non-Darcy Coefficients Calculated from LBM and Estimated from Correlation .....	211
Figure 6.86	Gravel Pack Generation for Pore Scale Analysis of Sand Migration.....	213
Figure 6.87	Sand Particle Location for 1% Pore Volume Plugging .....	214
Figure 6.88	Edge Trimming Effect on Gravel Size Distribution.....	215
Figure 6.89	Sand Particle Distributions .....	216
Figure 6.90	Sand Particle Location in the Domain F10.....	217
Figure 6.91	Permeability Comparison of Low Body Force Method and Low Pressure Difference Method.....	218
Figure 6.92	Forchheimer Plot for Periodic Domains with 1 Layer and 5 Layers.....	219
Figure 6.93	Velocity Field Comparison of Low Body Force Method and Low Pressure Difference Method .....	220
Figure 6.94	Velocity Comparison of Low Body Force Method and Low Pressure Difference Method.....	221
Figure 6.95	Kozeny-Carman Relation of Porosity and Permeability .....	223
Figure 6.96	Non-Darcy Coefficient of Domain F00.....	223
Figure 6.97	Non-Darcy Coefficient Change with Permeability .....	224
Figure 6.98	Kozeny-Carman Relation of Porosity and Non-Darcy Coefficient.....	225
Figure 6.99	Kozeny-Carman Relation of Permeability and Non-Darcy Coefficient.....	226
Figure 6.100	Non-Darcy Coefficient Comparison.....	227
Figure 6.101	Kozeny-Carman Relation of Sand Concentration and Permeability .....	228

Figure 6.102	Kozeny-Carman Relation of Sand Concentration and Non-Darcy Coefficient .....	229
Figure 7.1	Material Balance Plot of Volumetric Dry Gas Reservoir .....	241
Figure 7.2	Sand Migration Experiment Set-Up .....	243
Figure 7.3	Sand Concentration along the Core for Gravel-Sand Ratio of 7.5 .....	245
Figure 7.4	Porosity along the Core after Experiment for Gravel-Sand Ratio of 7.5 .....	246
Figure 7.5	Permeability along the Core after Experiment for Sand-Gravel Ratio of 7.5 .....	246
Figure 7.6	Cumulative Sand Production for Sand-Gravel Ratio of 7.5 .....	247
Figure 7.7	Sand Concentration along the Core for Sand-Gravel Ratio of 6.3 .....	248
Figure 7.8	Porosity along the Core after Experiment for Sand-Gravel Ratio of 6.3 .....	249
Figure 7.9	Permeability along the Core after Experiment for Sand-Gravel Ratio of 6.3 .....	249
Figure 7.10	Cumulative Sand Production for Sand-Gravel Ratio of 6.3 .....	250
Figure 7.11	Sensitivity Analysis of Surface Retention Rate Coefficient.....	250
Figure 7.12	Sensitivity Analysis of Surface Entrainment Rate Coefficient .....	251
Figure 7.13	Sensitivity Analysis of Initial Mobile Sand Concentration.....	251
Figure 7.14	Sensitivity Analysis of Critical Velocity .....	252
Figure 7.15	Sensitivity Analysis of Inlet Velocity.....	253
Figure 7.16	Sand Pack and Gravel Pack Permeabilities Effect on Pressure.....	254
Figure 7.17	Sand Pack and Gravel Pack Permeability along the Core .....	254
Figure 7.18	Sand Pack and Gravel Pack Non-Darcy Coefficient along the Core .....	255
Figure 7.19	Sand Migration Effect on Wellblock Pressure and Reservoir Pressure Profile after 100 days Production .....	256
Figure 7.20	Porosity Profile after 100 days Production.....	258
Figure 7.21	Permeability Profile after 100 days Production.....	258
Figure 7.22	Non-Darcy Coefficient Profile after 100 days Production .....	259

Figure 7.23	Pore Surface Sand Concentration Profile after 100 days Production.....	259
Figure 7.24	Sand Concentration in Gas Phase Profile after 100 days Production.....	260
Figure 7.25	Sand Production Change with Time .....	260
Figure 7.26	Pore Throat Sand Concentration Profile after 100 days Production .....	261
Figure 7.27	Wellblock Pressure Change with Initial Movable Sand Concentration .....	262
Figure 7.28	Wellblock Sand Concentration Change with Initial Movable Sand Concentration .....	263
Figure 7.29	Sand Production Change with Initial Movable Sand Concentration.....	263
Figure 7.30	Pore Surface Sand Concentration Profile after 100 days Production with Initial Movable Sand Concentration.....	264
Figure 7.31	Sand Concentration Profile Change after 100 days Production with Initial Movable Sand Concentration.....	264
Figure 7.32	Pore Throat Sand Concentration Profile Change after 100 days Production with Initial Movable Sand Concentration .....	265
Figure 7.33	Permeability Profile Change after 100 days Production with Initial Movable Sand Concentration .....	265
Figure 7.34	Non-Darcy Coefficient Profile Change after 100 days Production with Initial Movable Sand Concentration.....	266
Figure 7.35	Porosity Profile Change after 100 days Production with Initial Movable Sand Concentration .....	266
Figure 7.36	Wellblock Pressure Change with Critical Velocity .....	267
Figure 7.37	Wellblock Sand Concentration Change with Critical Velocity.....	268
Figure 7.38	Sand Production Change with Critical Velocity .....	268
Figure 7.39	Pore Surface Sand Concentration Profile after 100 days Production with Critical Velocity .....	269
Figure 7.40	Sand Concentration Profile Change after 100 days Production with Critical Velocity .....	270
Figure 7.41	Pore Throat Sand Concentration Profile Change after 100 days Production with Critical Velocity.....	270

Figure 7.42	Permeability Profile Change after 100 days Production with Critical Velocity .....	271
Figure 7.43	Non-Darcy Coefficient Profile Change after 100 days Production with Critical Velocity .....	271
Figure 7.44	Porosity Profile Change after 100 days Production with Critical Velocity.....	272
Figure 7.45	Wellblock Pressure Change with Flow Rate .....	273
Figure 7.46	Wellblock Sand Concentration Change with Flow Rate .....	274
Figure 7.47	Sand Production Change with Flow Rate.....	274
Figure 7.48	Sand Concentration Profile Change after 100 days Production with Flow Rate.....	275
Figure 7.49	Pore Throat Sand Concentration Profile Change after 100 days Production with Flow Rate .....	275
Figure 7.50	Permeability Profile Change after 100 days Production with Flow Rate.....	276
Figure 7.51	Non-Darcy Coefficient Profile Change after 100 days Production with Flow Rate.....	276
Figure 7.52	Pore Surface Sand Concentration Profile after 100 days Production with Flow Rate.....	277
Figure 7.53	Porosity Profile Change after 100 days Production with Flow Rate.....	277
Figure 7.54	Wellblock Pressure Change with Pore Throat Plugging Constant.....	278
Figure 7.55	Wellblock Sand Concentration Change with Pore Throat Plugging Constant.....	279
Figure 7.56	Sand Production Change with Pore Throat Plugging Constant.....	279
Figure 7.57	Sand Concentration Profile Change after 100 days Production with Pore Throat Plugging Constant.....	280
Figure 7.58	Pore Surface Sand Concentration Profile after 100 days Production with Pore Throat Plugging Constant .....	281
Figure 7.59	Pore Throat Sand Concentration Profile Change after 100 days Production with Pore Throat Plugging Constant.....	281
Figure 7.60	Permeability Profile Change after 100 days Production with Pore Throat Plugging Constant .....	282



Figure 7.61	Non-Darcy Coefficient Profile Change after 100 days Production with Pore Throat Plugging Constant .....	282
Figure 7.62	Porosity Profile Change after 100 days Production with Pore Throat Plugging Constant .....	283
Figure 7.63	Wellblock Sand Concentration Change with Pore Surface Retention Rate Constant .....	284
Figure 7.64	Sand Production Change with Pore Surface Retention Rate Constant.....	284
Figure 7.65	Sand Concentration Profile after 100 days Production with Pore Surface Retention Rate Constant .....	285
Figure 7.66	Pore Surface Sand Concentration Profile after 100 days Production with Pore Surface Retention Rate Constant .....	285
Figure 7.67	Wellblock Pressure Change with Pore Surface Entrainment Rate Constant .....	286
Figure 7.68	Wellblock Sand Concentration Change with Pore Surface Entrainment Rate Constant.....	287
Figure 7.69	Sand Production Change with Pore Surface Entrainment Rate Constant .....	287
Figure 7.70	Sand Concentration Profile after 100 days Production with Pore Surface Entrainment Rate Constant.....	288
Figure 7.71	Pore Surface Sand Concentration Profile after 100 days Production with Pore Surface Entrainment Rate Constant .....	288
Figure 7.72	Pore Throat Sand Concentration Profile Change after 100 days Production with Pore Surface Entrainment Rate Constant.....	289
Figure 7.73	Permeability Profile Change after 100 days Production with Pore Surface Entrainment Rate Constant .....	290
Figure 7.74	Non-Darcy Coefficient Profile Change after 100 days Production with Pore Surface Entrainment Rate Constant .....	290
Figure 7.75	Porosity Profile Change after 100 days Production with Pore Surface Entrainment Rate Constant.....	291
Figure 7.76	Rock Index of Frac-pack Completed Reservoir .....	292
Figure 7.77	Frac-pack Completion Effect on Wellblock Pressure .....	293
Figure 7.78	Pressure Profile of Frac-pack Completed Reservoir after 100 days Production.....	294

Figure 7.79	Frac-pack Completion Effect on Sand Production Change.....	295
Figure 7.80	Frac-Pack Completion Effect on Sand Concentration in Gas Phase .....	295
Figure 7.81	Frac-Pack Completion Effect on Pore Surface Sand Concentration .....	296
Figure 7.82	Frac-Pack Completion Effect on Pore Throat Sand Concentration.....	296
Figure 7.83	Frac-Pack Completion Effect on Porosity .....	297
Figure 7.84	Frac-Pack Completion Effect on Permeability .....	298
Figure 7.85	Frac-Pack Completion Effect on Non-Darcy Coefficient .....	298
Figure 7.86	Velocity Field of Frac-Pack Completed Reservoir .....	299
Figure 7.87	Wellblock Pressure Change with Fracture Half-Length .....	300
Figure 7.88	Wellblock Sand Concentration Change with Fracture Half-Length .....	300
Figure 7.89	Sand Production Change with Fracture Half-Length .....	301
Figure 7.90	Cumulative Sand Production after 100 days Change with Fracture Half Length.....	302
Figure 7.91	Wellblock Pressure Change with Fracture Width .....	303
Figure 7.92	Wellblock Sand Concentration Change with Fracture Width .....	303
Figure 7.93	Sand Production Change with Fracture Width.....	304
Figure 7.94	Cumulative Sand Production after 100 days Change with Fracture Width.....	305
Figure 7.95	Wellblock Pressure Change with Fracture Permeability .....	306
Figure 7.96	Wellblock Sand Concentration Change with Fracture Permeability.....	306
Figure 7.97	Sand Production Change with Fracture Permeability .....	307
Figure 7.98	Cumulative Sand Production after 100 days Change with Fracture Permeability.....	308

## ABSTRACT

Accurate estimation of production from frac-pack completed gas wells requires reliable estimation of flow properties from reservoir rocks and proppants. This study is composed of three parts: core-scale, pore-scale and reservoir-scale analyses of this problem. In the core-scale analysis, simultaneous estimation of permeability, non-Darcy, and Klinkenberg coefficients of reservoir rock is conducted from steady-state and pulse-decay experiments. Confidence intervals of the estimated parameters are determined from the Bootstrap method. The duration of pulse-decay experiments has a large impact on confidence intervals; therefore, correlations are developed to estimate the experimental duration for both 1-tank and 2-tank set-ups from the core properties and design parameters.

In the pore-scale analysis, the Lattice Boltzmann method (LBM) and network modeling are used to calculate proppant flow properties. For reliable simulation, resolution- and relaxation-time effects on LBM simulation are investigated; resolution and network-structure effects for network modeling are investigated. It is found that the minimum particle diameter should be represented with 30 voxels for reliable estimations. Statistically significant permeability and non-Darcy coefficient correlations are developed by using other calculated petrophysical properties and network model parameters. A new approach, path analysis, is applied to petrophysical properties to show the relationship between them. Compaction and sand-migration effects on porosity, permeability and the non-Darcy coefficient are investigated. Trends in permeability and the non-Darcy coefficient as a function of porosity and sand concentration are found. Pore-scale simulations indicate that non-Darcy coefficients obtained from correlations always underestimate the inertial effects.

A reservoir simulator is developed using the finite difference method by integrating the continuity and sand-migration equations, and by using the compaction and sand-migration

correlations developed from pore-scale simulations. A parametric study is conducted for the rate constants for sand migration equations, critical velocity, flow rate, and initial movable sand concentration, to investigate their effects on sand production, reservoir flow properties, and pressure profile near the wellbore. While pore-throat plugging has a large impact on the pressure profile and reservoir flow properties, it causes an insignificant decrease in sand production. In addition, a sensitivity analysis is conducted for fracture dimensions and fracture conductivity to investigate their effects on sand production. Sand production does not decrease linearly with sensitivity parameters; therefore, designing fractures with moderate half-length, width, and conductivity is recommended.

## CHAPTER 1: INTRODUCTION

Henry Darcy (1856) found his famous equation while working on flow characteristics of sand filters used to filter public water in the city of Dijon in France. He observed a linear relationship between flow rate and pressure difference. The Darcy equation is analogous to Fourier's law for heat conduction, Ohm's law for electricity or Fick's law for diffusion. Even though the Darcy equation is a phenomenologically derived constitutive equation, Hubbert (1956) derived the Darcy equation from the Navier-Stokes equation via homogenization. Darcy's law is only valid for viscous flow; usually, most groundwater flow is slow and falls into this category.

Forchheimer (1901) noticed deviations from Darcy flow and attributed this deviation to turbulence in the fluid flow. He proposed a second order equation as a function of velocity from an experimental data fit. Cornell and Katz (1953) modified the second term as a product of  $\beta$  and density so that for low velocities, the equation converges to the Darcy equation. This equation is called the Forchheimer equation in literature.

The coefficient  $\beta$  and the reason for the deviation from Darcy equation has been investigated for decades. The first investigation was conducted by Fancher et al. (1933). They used the Reynolds number and friction factor to fit the data; therefore, early papers refer to  $\beta$  as the turbulence coefficient (Cornell & Katz, 1953; Tek, Coats, & Katz, 1962). However; Bear (1972) clarified the difference between flow equations for the pipes and the porous media and he explained that flow transition is sharp in pipe flow and occurs at high Reynold numbers. On the other hand, in porous media, there is a transition zone and a nonlinear relation between flow rate and pressure gradient occurs about Reynolds number unity. Comparing with the flow equation, there is no linear term in the pipe flow equation. Many researchers also agreed that the flow

deviation does not result from turbulence (e.g. Bear, 1972; Geertsma, 1974; H. Ma & Ruth, 1993) but rather it is caused by inertial effects due to diverging-converging flow paths. However, there is no common term for  $\beta$ . Many researchers give different name based on their preferences. For example,  $\beta$  is called turbulence factor (Cornell & Katz, 1953; Tek et al., 1962), inertial resistance coefficient (Al-Rumhy & Kalam, 1993; Geertsma, 1974), velocity coefficient (Firoozabadi & Katz, 1979), non-Darcy coefficient (Civan & Evans, 1991; X. Liu, Civan, & Evans, 1995), Forchheimer coefficient (Ruth & Ma, 1992) and inertial coefficient (Huiping Ma & Ruth, 1997), among various other names. In this study  $\beta$  is called the non-Darcy coefficient.

Flow regimes for pipes flow are well established. If the Reynolds number is greater than approximately 2100, the expected flow regime will be turbulent; otherwise, flow regime will be laminar. On the other hand, the flow regimes in porous media are different from pipes flow due to complex structure of the pore space. There are mainly two classifications of flow regimes. Basak (1977) classified the flow into three regimes. For very low velocities, slip flow exists and the increase in velocity is larger than increase in the pressure gradient. He named this region the pre-Darcy zone. With increasing flow rate, the flow will be laminar and the velocity increase is directly proportional to the pressure gradient. In this regime, the Darcy equation can be applied and it is called the Darcy zone. Further increases in velocity leads to increases in inertial effects. This leads to velocity increases that are less than the increase in pressure gradient. This flow regime is called the post-Darcy zone. Dyybs and Edwards (1984) used laser anemometry and a visualization technique to investigate the flow regimes and defined four flow zones with the intervals based on Reynold number. Reynold number up to 1, the flow is laminar and the region is in the Darcy flow regime. For Reynolds numbers from 1-10 to 150, flow is still laminar and flow velocity, pressure gradient trend is not linear anymore, and this regime is called inertial

flow. For Reynold numbers between 150 and 300, unsteady state characteristics appear and the flow regime is called unsteady laminar flow. For Reynolds numbers greater than 300, flow is turbulent, like in turbulent flow in pipes, and flow is dominated by eddies.

The transition between Darcy to non-Darcy flow is summarized by Zeng and Grigg (2003). There are mainly two types of criteria is used in the literature: Reynolds number and Forchheimer number. A Reynolds number criterion was started with the Chilton and Colburn (1931) study. After that many researchers investigated the critical Reynold number (e.g. Ergun, 1952; Fancher et al., 1933; H. Ma & Ruth, 1993); however their observations were very different with the transition changing between 1 and 100. This implies that there is no magic number to classify the flow type. In addition, the main problem in Reynolds number definition is characteristic lengths. For pipe flow or flow in unconsolidated media, characteristic lengths are well defined; pipe diameter and mean particle diameter. However, the structure of consolidated media is too complicated for a clear definition of characteristic length. Due to the disadvantages of Reynolds number, the second criterion, the Forchheimer number, was proposed by Ma and Ruth (1993). With this criterion, the characteristic length is defined as a product of permeability and non-Darcy coefficient. The studies conducted for Forchheimer number also indicates that there is no clear value for flow transition between Darcy to non-Darcy flow; the critical Forchheimer number changes between 0.005 and 0.2. Therefore, some authors suggest some factor based on the ratio of pressure decrease caused by viscous forces and pressure decrease due to inertial effects under which inertial effects can be ignored (Belhaj, Agha, Nouri, Butt, & Islam, 2003; Zeng & Grigg, 2003). Since these factors depend on inertial effects, accurate estimation of non-Darcy coefficient is important.

Inertial flows cannot be neglected for gas flow, gas condensate reservoirs, near wellbore flows (especially at the perforations). Therefore, the non-Darcy coefficient is investigated every decade. Many researchers were developed non-Darcy correlations from theory, core lab experiments, field data and network modeling. Porous media can be modeled with parallel and series bundles of capillaries. Non-Darcy correlations were derived through comparison of theoretical flow equations with the Forchheimer equation (Li & Engler, 2001, 2002). However, non-Darcy coefficients estimated from these correlations are different than the one obtained from lab measurements. The main reasons for this difference results from the complicated pore structure. This implies that reservoir rock properties should be determined from lab measurement.

Many experimental studies were conducted to estimate non-Darcy coefficients from petrophysical properties such as permeability, porosity and tortuosity (e.g. Geertsma, 1974; S.C. Jones, 1987; Tek et al., 1962). Some researchers thought non-Darcy coefficients depend on the fluid properties and overburden pressure (e.g. Avila & Evans, 1986; Evans, Hudson, & Greenlee, 1987). Most of the correlations are not consistent in terms of units. Therefore, some researchers developed dimensionally consistent correlations from dimensional analysis (Avila & Evans, 1986; Evans et al., 1987; Geertsma, 1974). However, they are not sufficient to estimate the non-Darcy coefficient. There are only few studies to investigate non-Darcy flow at the pore scale with network modeling (Cooper, Wang, & Mohanty, 1999; Thauvin & Mohanty, 1998). They investigated how the pore and throat radius and the connectivity of pores affect inertial effects. They also investigated the impact of compaction and sand deposition by changing the network parameters.



Inertial effects become more significant for two-phase flow. Experimental studies indicate that the non-Darcy coefficient increases up to an order of magnitude compared to single phase flow (Gewers & Nichol, 1969; Wong, 1970). The main causes of the increase in inertial effects are the decrease in the relative permeability of gas. Some researchers suggest the use of non-Darcy coefficient correlations developed for single phase flow provided that effective gas permeability and void volume occupied by gas should be used instead of single phase permeability and pore volume (Avila & Evans, 1986; Coles & Hartman, 1998; Frederick Jr. & Graves, 1994; Geertsma, 1974). The other estimation method relates relative non-Darcy coefficient with relative permeability (X. Liu et al., 1995a). Heterogeneity has a great effect on inertial effects. Therefore, the non-Darcy coefficient obtained from lab experiment can be different than the one obtained from well-test analysis. Most of the correlations include porosity and permeability as a predictive petrophysical parameter; however, two core samples with similar porosity and permeability can show different inertial characteristics due to different pore structure. This characteristic is apparent especially for carbonate samples since their pore structures are complicated due to precipitation and dissolution. Therefore, for non-Darcy coefficient estimation for heterogeneous reservoirs, specific surface area should be considered as a required petrophysical parameter.

Some researchers have proposed that the field is more heterogeneous compared with cores; therefore, non-Darcy coefficient should be determined from field tests. They defend this point by the inconsistency between non-Darcy coefficient obtained from lab measurements and the ones obtained from well tests (Morrison & Dugan, 1991; Pascal & Quillian, 1980). On the other hand, some researchers are against this idea and they used both lab measurement and well test data to develop a correlation (Noman, Shrimanker, & Archer, 1985).

If the formation is layered, a small high-permeability layer in the direction of flow leads to a decrease in inertial effects and increases the well productivity. For modeling of such reservoirs, estimating inertial effects from a correlation using average permeability may cause underestimation of production. The effective permeability should be determined to estimate the effective non-Darcy coefficient. The trend between single phase permeability and non-Darcy coefficient can be used to estimate effective non-Darcy coefficient from effective permeability.

Reservoir pressure decreases with production and this results in changes in effective pressure. This leads to porosity and permeability decreases and an increase in inertial effects. Pore-scale studies about compaction clearly show that a decrease in pore volume leads to a significant increase in the non-Darcy coefficient (Thauvin & Mohanty, 1998). Some experimental studies indicate that overburden pressure has significant effects on inertial effects (Avila & Evans, 1986). Some researches claimed that including effective stress in non-Darcy correlations is unnecessary if the non-Darcy correlation includes both porosity and effective permeability (Frederick Jr. & Graves, 1994).

Accurate estimation of non-Darcy coefficient effects on well productivity estimation is investigated with reservoir simulations. For low permeability reservoirs, high rate gas flows and gas condensate reservoirs, inertial effects cannot be ignored. Even though inertial effects are considered near-wellbore phenomena, inertial effects cannot be neglected away from the wellbore if the reservoir is tight. The pressure drop due to inertial effects can be significant even for flow rates less than 1MMscf/D if reservoir permeability and porosity are small. Ignoring inertial effects in well test data can cause misestimation of reservoir and fracture properties. For single-phase flow, permeability estimation is higher than the actual values. If the reservoir is fractured, higher estimation of permeability leads to lower estimation of fracture length and its

conductivity. On the other hand, for two-phase flow, both permeability and fracture estimation is uncertain if inertial effects are ignored.

In this study, inertial effects for frac-pack completed gas reservoirs are investigated closely. Accurate estimation of well productivity of frac-pack completed gas reservoirs, the reservoir and fracture permeabilities and non-Darcy coefficients, and compaction and sand migration effect on them should be known. Therefore, this study consists of three main parts: core-scale analysis, pore-scale analysis and reservoir-scale analysis (Figure 1.1). This dissertation is organized into eight chapters.

In the Literature Review, flow regimes, non-Darcy flows and non-Darcy flow criteria are explained in detail. Non-Darcy correlations developed from theoretical derivations, lab experiments, field data, and numerical studies are given in historical order. Important observations about multi-phase flow and heterogeneity effects are given. To emphasize the inertial effects for well productivity estimation, some studies are given as examples.

In the Problem Statement Chapter, the reason why there are so many correlations are available in the literature is discussed and some misinterpretation of lab experiments are illustrated with example to emphasize the importance of this study. Misuse of correlations in the case of compaction and sand migration are given.

In Objectives, based on the stated problems, for correct estimation of production from high-rate frac-pack completed gas reservoirs, the methodology is given. For reliable estimation of production, flow properties of the reservoir and proppants used in the fracture, and compaction and sand migration effects on the flow properties should be modeled accurately. Therefore, the objectives of this study are divided into five steps given in Chapter 5 through Chapter 7.

In Chapter 5, core-scale analyses are conducted to estimate reservoir flow properties; permeability, Klinkenberg coefficient and non-Darcy coefficient. A new optimization approach for steady-state lab-experiment interpretation is given for simultaneous estimation of flow properties. The effect of measurement errors on the estimation process is discussed. The methodology for pulse decay experiments and statistical analysis techniques are illustrated for reliable estimation of flow properties. The effects of the experimental duration on the estimation of flow parameters confidence intervals and production are given. A sensitivity analysis is conducted for the duration of pulse-decay experiments and development of correlations to estimate the experiment duration is given in this chapter.

In Chapter 6, pore-scale analyses are conducted by using two numerical methods, Lattice Boltzmann Method (LBM) and Network modeling, to estimate the flow properties of gravel packs. LBM is investigated for grid resolution and relaxation time; Network modeling is investigated for pore resolution and pore merging conditions to determine which conditions reliable estimations are done from these methods. Due to the domain-size limitations of LBM, representative elementary volume sizes of gravel packs are investigated. By creating a database systematically, some correlations are developed for permeability and non-Darcy coefficient. A new approach, path analysis, is used to correlate petrophysical variables and it is used for missing data estimation. Pore-scale analyses are used for studying compaction effects on permeability and the non-Darcy coefficient. Changes in pore structure with compaction is investigated with Network modeling. Similarly, the effect of sand migration on permeability and non-Darcy coefficient is found and correlations are developed for use in reservoir simulations. In addition to the comparison of pore-scale results for compaction and sand migration, some misuse of non-Darcy correlations is illustrated.

In Chapter 7, to integrate the findings from core-scale and pore-scale analyses, a 2-D reservoir simulator is developed using a finite difference algorithm. This simulator is validated with core experiment data found from the literature. A parametric study is conducted to estimate the effect of the sand migration rate equation constant on production. Some simulations are presented to show how fracture properties affect the sand production.

In Chapter 8, the findings from core-scale, pore-scale and reservoir-scale analyses are given and discussed. Some recommendations are given for further improvement of this study. In the Conclusions, the most important points of this study are summarized.

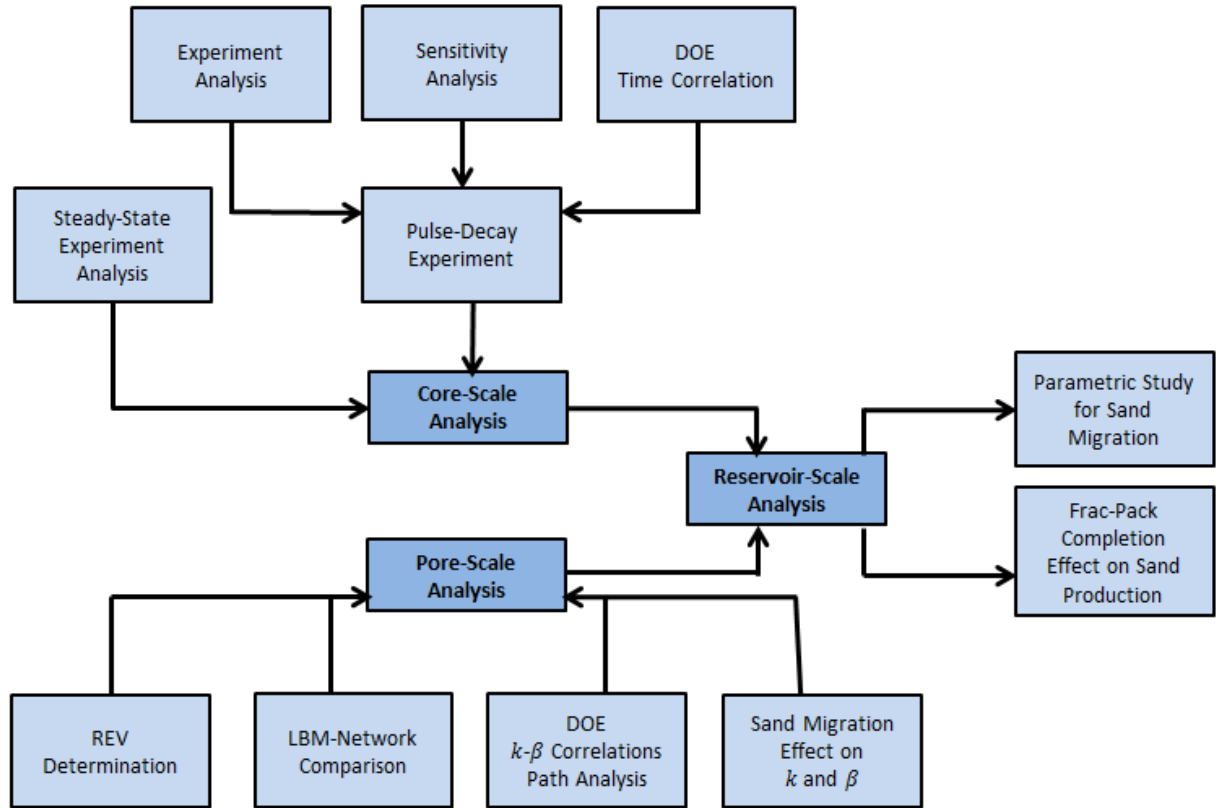


Figure 1.1 Work Flow of the Study

## CHAPTER 2: LITERATURE REVIEW

Henry Darcy (1856) conducted water flow experiments through sand beds and observed that the flow rate,  $q$  is directly proportional to the potential difference,  $\Delta h$ , and flow area,  $A$ , of the filter sand with a thickness,  $L$ .

$$q = -\frac{KA \Delta h}{L} \quad (2.1)$$

$K$  in this relation represents the hydraulic conductivity and it can be expressed as  $k/\mu$  where  $k$  is permeability of the porous medium and  $\mu$  is viscosity of the flowing fluid. The Darcy equation can be written in the form of a partial differential equation as;

$$-\frac{dP}{dx} = \frac{\mu}{k} u \quad (2.2)$$

Darcy equation states that pressure gradient,  $-dP/dx$ , is linearly related with velocity,  $u$ .

Hubbert (1956) derived the Darcy equation from the Navier-Stokes equation with the assumptions of laminar and viscous flow and negligible inertial terms and he stated that Darcy law is valid for liquids and gases at high pressure.

### 2.1 Non-Darcy Flow

Forchheimer (1901) discovered that Darcy flow did not accurately describe the pressure drop if the flow rate was high, and the deviation of pressure drop was related to the flow rate. To account for this non-Darcy part, he proposed an equation (Eqn.2.3) by fitting the pressure gradient to velocity obtained from experimental data. Later, a third order equation (Eqn.2.4) was derived in order to fit very high flow rate experiments (Ezeudembah & Dranchuk, 1982). In these equation, the coefficients,  $a$ ,  $b$  and  $c$ , are constants.

$$-\frac{dP}{dx} = au + bu^2 \quad (2.3)$$

$$-\frac{dP}{dx} = au + bu^2 + cu^3 \quad (2.4)$$

Another equation proposed to express the non-linearity between measured pressure data and Darcy equation is power law model (Eqn.2.5). The power  $n$  is between 1 and 2.

$$-\frac{dP}{dx} = au^n \quad (2.5)$$

Cornell and Katz (1953) reformulated Eqn.2.3 by replacing the constant term  $a$  as the product of fluid density and  $\beta$  (Eqn.2.6). This equation implies that Darcy's equation is still valid and the additional pressure drop is accounted for. The factor  $\beta$  is called the turbulence factor (Cornell & Katz, 1953; Tek et al., 1962), inertial resistance coefficient (Al-Rumhy & Kalam, 1993; Geertsma, 1974), velocity coefficient (Firoozabadi & Katz, 1979), non-Darcy coefficient (Civan & Evans, 1991; X. Liu et al., 1995), Forchheimer coefficient (Ruth & Ma, 1992) and inertial coefficient (Huiping Ma & Ruth, 1997), among various other names. Eqn.2.6 equation turns into Darcy equation for low flow rates.

$$-\frac{dP}{dx} = \frac{\mu}{k}u + \beta\rho u^2 \quad (2.6)$$

The non-linearity can be identified with the flow rate vs. pressure drop as indicated in Figure 2.1. For high flow rates, pressure drop is higher than what is expected from Darcy's equation. Therefore, permeability prediction from the experiments conducted in that region will be lower than the actual if inertial effects are ignored.

Fancher et al.(1933) correlated the pressure drops by using the friction factor and Reynolds number (Figure 2.2). Based on the fit, Katz et al. (1959) explained the excessive pressure drop based on turbulence. Therefore,  $\beta$  was known as turbulent factor. Bear (1972) systematically expressed the difference between turbulent flow and non-Darcy flow. He indicated that there is no linear term in turbulent flow and the flow transition is sharp at higher

Reynolds number for flow in conduits. Geertsma (1974) related the deviation of Darcy's equation with the acceleration and de-acceleration of fluid in the pore space. Ruth and Ma (1993) attributed this excessive pressure drop to inertial effects.

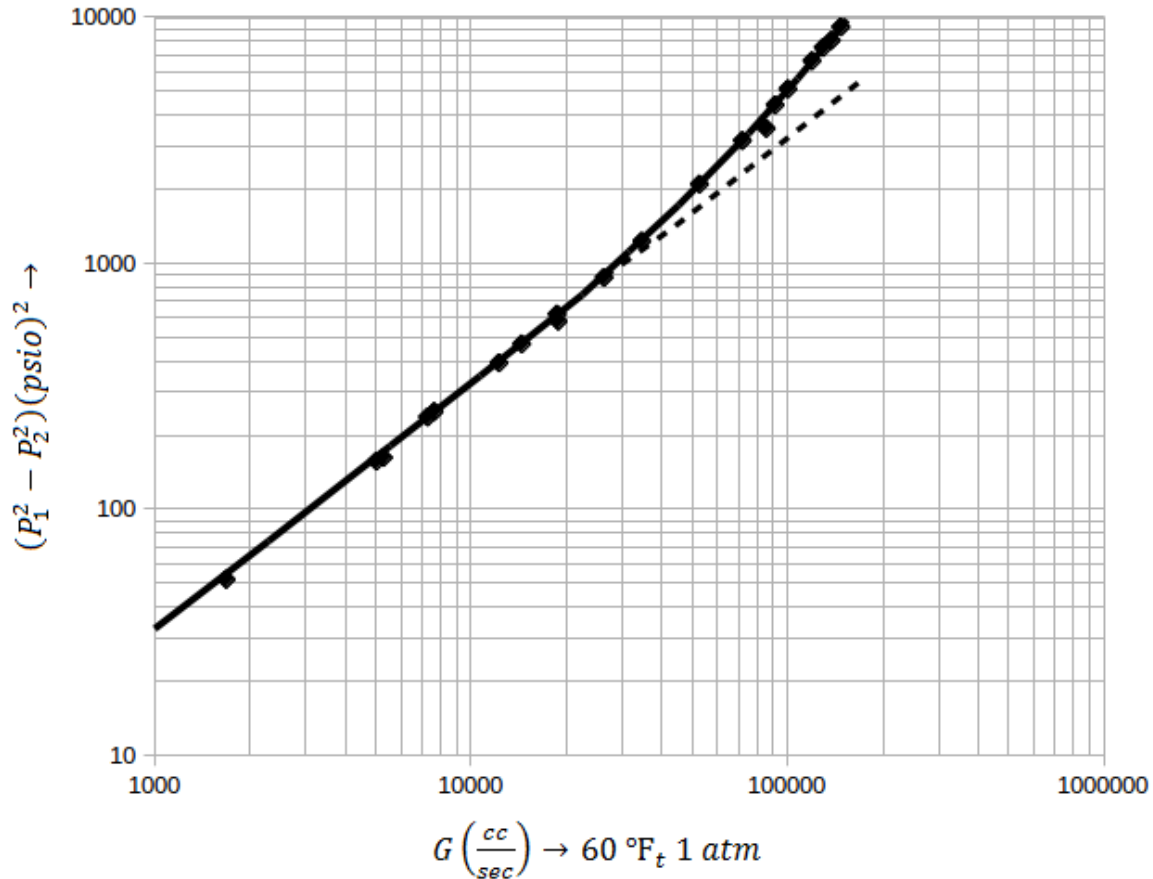


Figure 2.1 Nonlinear Flow of Air through Sand (Adopted from Katz, 1959)

## 2.2 Slip Flow

Another type of non-Darcy flow is slip flow. Muskat (1937) recognized a large discrepancy between air permeability and water permeability. Klinkenberg (1941) noted a similar discrepancy from experiments conducted with flowing fluids hydrogen, nitrogen and carbon dioxide (Figure 2.3). He observed that the mean free path of gas,  $\lambda$ , was directly proportional with the mean pressure,  $P_m$  in pore capillary system.



$$\frac{4c\lambda}{r} = \frac{b}{P_{av}} \quad (2.7)$$

In this equation,  $r$  is pore capillary radius.  $c$  is constant and  $b$  is called Klinkenberg coefficient or gas slippage factor. For low pressures, the mean free path increases; therefore slippage effect.

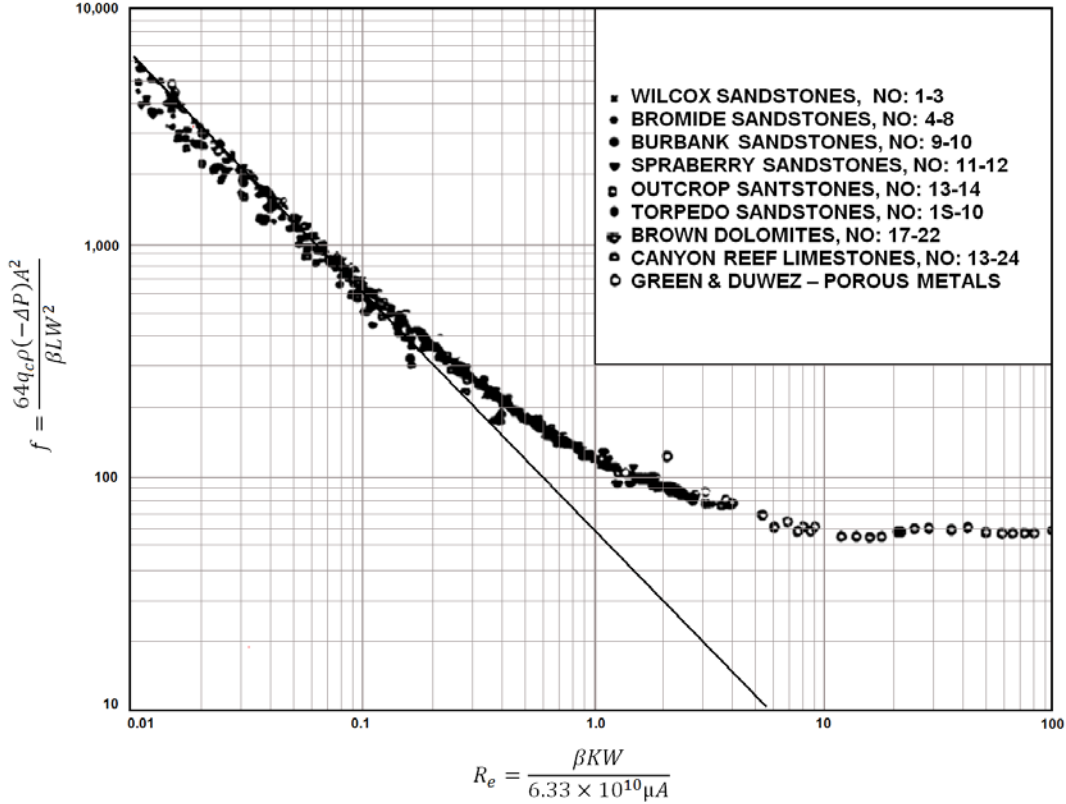


Figure 2.2 Friction Factor Plot (Adopted from Cornell and Katz, 1953)

He combined the Poiseuille's law with Darcy equation and derived the following equation.

$$k_g = k \left( 1 + \frac{4c\lambda}{r} \right) \quad (2.8)$$

Here,  $k_g$  and  $k$  are observed gas permeability and liquid (intrinsic) permeability, respectively.

Combining the Eqn.2.7 with Eqn.2.8, the Klinkenberg equation is written as;

$$k_g = k \left( 1 + \frac{b}{P_{av}} \right) \quad (2.9)$$

Slippage effects depend on both gas type and pore-space structure of the medium (Figure 2.3). Klinkenberg claimed that if the pore radius is close to the mean free path of gas, interaction between gas molecules and walls leads to gas molecules moves forward in flow direction which leads to decrease in viscous drag and increase in apparent permeability.

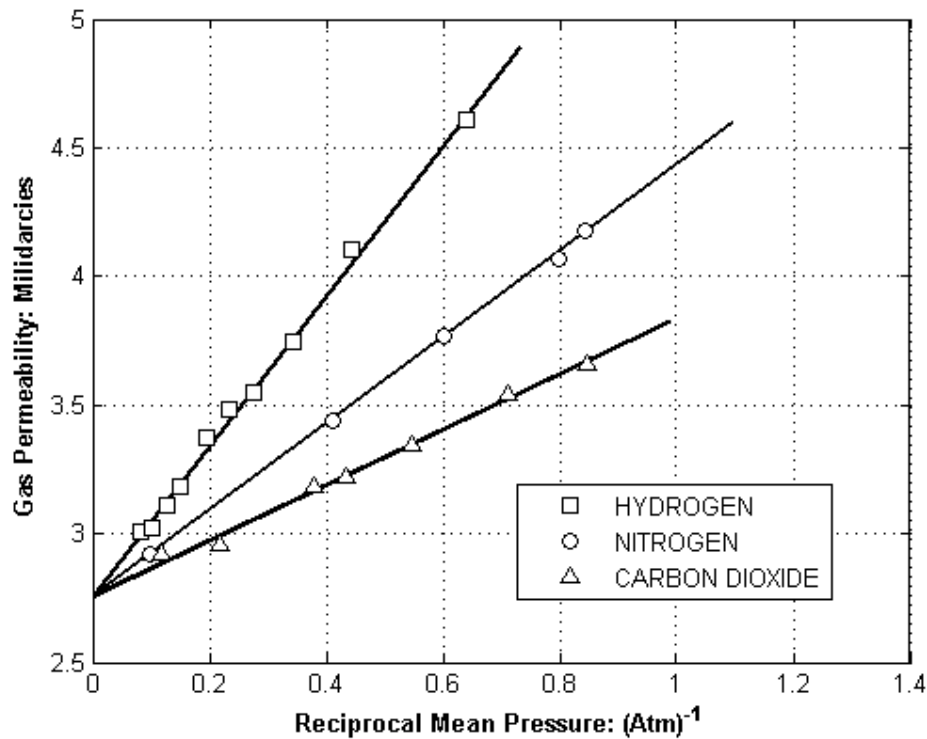


Figure 2.3 Observed Permeability Change with Reciprocal Mean Pressure (Adopted from Klinkenberg, 1941)

## 2.3 Flow Regimes

For pipes and conduit flow, the flow regimes are well established and can be determined based on the Reynold number. If Reynold number is less than 2100, then flow is laminar; otherwise, flow is turbulent. However, in porous media there is no well-established criteria for flow regimes. Researchers have tried to formulate expressions for flow regimes where inertial terms are not negligible.

Dybbs and Edwards (1984) conducted water flow experiments in bundles of rods and classified the flow regimes into four groups using laser anemometry and visualization techniques. These regimes are:

- Darcy (Creeping Flow) Regime: This flow regime is dominated by viscous forces. The velocity profile depends on local geometry. This flow regime exists until the Reynolds number is close to unity.
- Inertial Flow Regime: As the Reynolds number becomes greater than one, inertial effects appear outside the boundary layers. Even though flow is still laminar, the relationship between pressure drop and velocity deviates from linearity. This flow regime starts at Reynolds numbers between 1 and 10 and persists until Reynolds numbers up to 150.
- Unsteady Laminar Flow Regime: This flow regime exists at Reynolds number between 150 and about 300. This regime is characterized by the occurrence of waves and the flow shows unsteady characteristics.
- Turbulent Flow Regime: If Reynolds number is greater than 300, the flow is dominated by eddies like with turbulent flow in pipes.

Basak (1977) divided the flow regimes into 3 zones with observations (Figure 2.4).

- Pre-Darcy Zone: Increase in flow rate is more compared to increase in pressure gradient.
- Darcy Zone: The flow rate is directly proportional with the pressure gradient. Flow is laminar and Darcy's equation is applied in that regime.
- Post-Darcy Zone: The increase in flow rate is less than proportional to pressure gradient.

In reservoir flow, the observed flow regimes are Darcy Zone and early Post-Darcy Zone (Forchheimer).

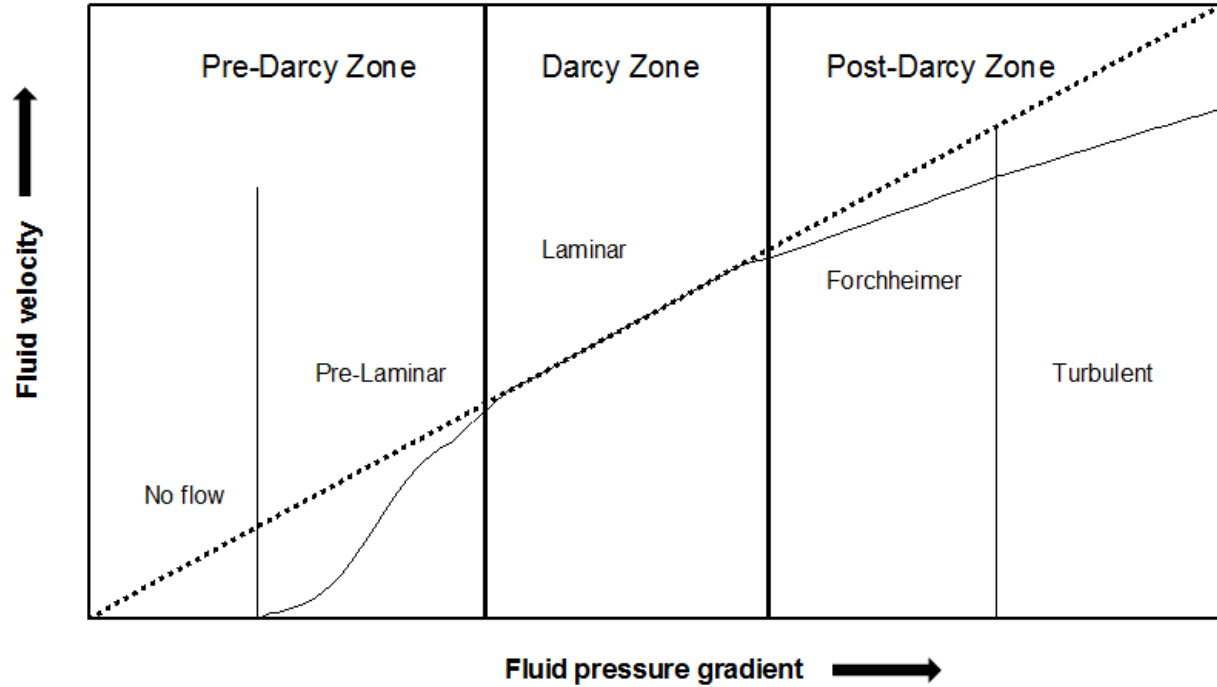


Figure 2.4 Flow regimes in porous media (Adopted from Basak, 1977)

## 2.4 Non-Darcy Flow Criteria

Some criteria for transition from Darcy flow to Post-Darcy flow are specified. The first criterion used in the literature is Reynold number (Eqn.2.10).  $\rho$ ,  $D_p$ ,  $v$  and  $\mu$  are fluid density, velocity, the mean particle diameter and fluid viscosity, respectively. The limitation of this criterion is that there is no specific number to define the transition between Darcy and non-Darcy flow. For laminar flow, Reynold number is less than one. The transition can occur for Reynolds numbers between 1 and 10. The Reynolds number criterion is generally applied in columns of packed particles in which characteristic length,  $D_p$ , can easily be identified. There are many different observations about the critical Reynolds numbers at which the transition between Darcy and non-Darcy occurs.

Chilton and Colburn (1931) conducted flow experiment on packed particles and reported the critical Reynolds number changed between 40 and 80. Fancher et al. (1933) observed that

non-Darcy flow occurs at a critical Reynold number between 10 and 1000 for unconsolidated media, or between 0.4 and 3 for loosely consolidated media. Ergun (1952) modified the Reynolds number proposed by Chilton and Colburn by adding porosity (Eqn. 2.11). He conducted gas flow experiments through packed particles and observed that non-Darcy flow started at modified Reynolds number between 3 and 10.

$$Re = \frac{\rho D_p u}{\mu} \quad (2.10)$$

$$Re = \frac{\rho D_p u}{\mu} \frac{1}{1 - \phi} \quad (2.11)$$

Due to the difficulty in determination of characteristic length of consolidated porous media, another criterion, Forchheimer number is proposed (Eqn. 2.12) (H. Ma & Ruth, 1993). It is the ratio of pressure drop due to non-Darcy effects to viscous effects. For this criterion, the characteristic length is defined as the product of permeability and non-Darcy coefficient. Green and Duwez (1951) conducted gas flow experiment for different porous metal and they observed the critical Forchheimer number between 0.1 and 0.2. However, they referred the term as Reynolds number. Ma and Ruth (1993) used non-Darcy flow simulation using a diverging-converging model and they defined Reynold number by using pore-throat diameter (Eqn.2.13). They observed that the critical Reynolds changes between 3 and 10, and the critical Forchheimer number changes between 0.005 and 0.02. Andrade et al. (1998) modelled non-Darcy flow for distorted media and found that the critical Forchheimer number is between 0.01 and 0.1. Thauvin and Mohanty (1998) simulated porous media with network modeling and noted that critical Reynolds number is 0.11. Based on these observations the range of critical Reynold number and Forchheimer numbers are large: between 1 and 100 and between 0.005 and 0.2, respectively.

$$F_o = \frac{k\beta\rho u}{\mu} \quad (2.12)$$

$$Re = \frac{\rho D_t u}{\mu} \quad (2.13)$$

Belhaj et al. (2003) noticed that the point where pressure trend estimated from Darcy equation and the one estimated from non-Darcy equation deviation depends on fluid and rock properties and flow characteristics. With dimensional analysis, they developed the dimensionless group  $Be$  (same with Forchheimer number) and they specified critical pressure drop ratio (Eqn.2.14) as 5% and the corresponding  $Be$  is 0.0526.

$$Pressure\ Drop\ Ratio = \frac{1}{1 + Be} \quad (2.14)$$

Because the critical value at which non-Darcy terms become significant is unclear, Zeng et al. (2003) suggested new non-Darcy effect criteria,  $E$  based on the Forchheimer number. This is simply ratio of pressure drop due to non-Darcy effects to the total pressure drop (Eqn.2.15). Specifying the limit of  $E$  under which pressure drop can be ignored, the critical Forchheimer number can be determined.

$$E = \frac{F_o}{1 + F_o} \quad (2.15)$$

## 2.5 Non-Darcy Coefficient Observations

Forchheimer equation is the most common model used in the literature. The second term of Eqn.2.6 become significant as the flow rate increases; therefore inertial effects cannot be neglected gas reservoirs, gas condensate reservoirs or high potential wells, hydraulically fractured gas reservoirs, near wellbore especially at the perforation.

Similar to permeability, non-Darcy coefficient is a rock property depending on pore structure of the media. Therefore, it depends on rock parameters such as porosity and tortuosity. Katz (1959) is the first researcher who determined the non-Darcy coefficient from core

experiments. After Katz, many studies were conducted and non-Darcy coefficient correlations were developed from theory, lab experiments, field data and network simulations.

### 2.5.1 Theoretical Non-Darcy Coefficient Correlations

Bird et al. (1965) derived a non-Darcy coefficient by comparing the Ergun equation (Eqn.2.16) with the Forchheimer equation (Eqn.2.17).

$$\frac{\Delta P}{\Delta L} = \frac{150\mu u (1 - \phi)^2}{D_p^2 \phi^2} + \frac{1.75\rho u^2 (1 - \phi)}{D_p \phi^2} \quad (2.16)$$

$$\beta = \frac{0.0117 D_p}{k (1 - \phi)} \quad (2.17)$$

Porous media can be modeled with bundles of capillaries of uniform diameter. Two types of arrangement are used: serial and parallel. Li et al. (2001) compared flow equations derived for parallel (Irmay, 1958) and series models (Scheidegger, 1974) and derived Forchheimer coefficients (Eqn.2.18 and Eqn.2.19).

$$\beta = \frac{c}{k^{0.5} \phi^{1.5}} \quad (2.18)$$

$$\beta = \frac{c''\tau}{k\phi} \quad (2.19)$$

In this equation,  $c$  and  $c''$  are constants related to pore size distribution.

Li and Engler (2002) proposed a semi-theoretical non-Darcy coefficient equation by using non-Darcy correlations developed for two extreme pore arrangements: parallel and serial models (Eqn.2.20). In this equations  $c_1(\tau, \delta)$  is the parameter related with medium tortuosity,  $\tau$ , and pore size distribution,  $\delta$ . The coefficients  $c_2$  and  $c_3$  are constants related with permeability heterogeneity and pore geometry and their sum is equal to 1. They developed a one-phase 2-D simulator to investigate non-Darcy effects and they validated the simulator with analytical equations given by Katz et al. (1959). To validate the correlation they proposed, they conducted flow experiments using  $N_2$  as flowing fluid and compared with the simulation results. They

found that the proposed semi-theoretical correlation could better estimate the inertial effects in all directions compared with the correlations developed from the parallel and serial models

$$\beta = \frac{c_1(\tau, \delta)}{k^{0.5+0.5c_2}\phi^{1+0.5c_3}} \quad (2.20)$$

### 2.5.2 Experimental Analysis of Non-Darcy Coefficient

The pore structure is much more complicated to represent with capillaries; therefore, many experimental studies were conducted to derive non-Darcy coefficient correlations. Although they are different, they all depend on petrophysical properties such as permeability, porosity and tortuosity. In this part, all non-Darcy correlations developed from experimental measurements of single-phase or multi-phase flow and experimental observations are given in historical order..

The first study was conducted by Cornell and Katz (1953). They investigated gas flow through consolidated sandstone, limestone, and dolomite samples. They measured permeability, porosity and resistivity factor of these samples and proposed a relation (Eqn.2.21).

$$\beta = \frac{32 F^{3/2}}{k_2 D_E X^{1/2}} \quad (2.21)$$

$F$ ,  $k_2$ ,  $D_E$ ,  $X$  are electrical resistivity factor, dimensionless geometrical factor, effective diameter of porous structure and porosity, respectively.

After that Tek et al. (1962) revised the study of Cornel and Katz and (1953). They observed that  $F$  is approximately  $4/\phi$  and  $k_2$  is related with porosity and permeability. They expressed the non-Darcy coefficient in a simpler form (Eqn.2.22).

$$\beta = \frac{5.5 \times 10^9}{k^{5/4} \phi^{3/4}} \quad (2.22)$$

Gewers et al. (1969) studied the non-Darcy coefficient for microvugular carbonate cores and the effect of liquid saturation on the non-Darcy coefficient. He observed that although the



same non-Darcy coefficient-permeability trends were observed, measured non-Darcy coefficients were higher by about an order of magnitude compared to those estimated from data in the literature, perhaps due to the heterogeneity. He made flow experiments for different water saturation and observed that the non-Darcy coefficient decreased between 0 and 10% liquid saturation and then rapidly increased.

Wong (1970) studied the effect of liquid saturation on the non-Darcy coefficient and he observed similar trend of water saturation and non-Darcy coefficient change with Gewers et al. (1969). He observed increases in non-Darcy coefficient by a factor 8 with the increase in liquid saturation from 40% to 70%. He explained this decrease as a result of streamlining of the pores by the liquid. After this effect, he explained the increase of the non-Darcy coefficient as caused by a decrease in gas effective permeability. He claimed that for two-phase flow, the non-Darcy coefficient could be obtained from correlations developed for dry cores provided that gas effective permeability is used instead of rock permeability.

Geertsma (1974) found the following dimensionally consistent relation from linear regression by using the experiment data of Green and Duwez (1951) and Cornell and Katz (1953) in addition to his experiments.

$$\frac{\beta}{\sqrt{1/k}} \phi^{5.5} = 0.005 \quad (2.23)$$

Geertsma also pointed out that this correlation could be updated for multiphase flow considering the gas effective permeability,  $k_e(k \times k_r)$  and void volume occupied by gas ( $\phi(1 - S_w)$ ).

$$\beta = 0.005 \frac{1}{\phi^{5.5} k^{0.5}} \left( \frac{1}{(1 - S_w)^{5.5} k_r^{0.5}} \right) \quad (2.24)$$

In these equations,  $k$  and  $\beta$  are in mD and 1/cm, respectively.

Avila et al. (1986) studied the temperature and overburden stress effect on the non-Darcy coefficient. They conducted the experiment over a temperature range of 70 to 200 °F and overburden pressure of 1000 to 4000 psia by using consolidated sandstone and permeability, porosity and the non-Darcy coefficient were recorded. They observed that the non-Darcy coefficient increased as temperature increased and the change in non-Darcy coefficient with overburden stress was negligible. In addition, they investigated immobile water saturation between saturations of 0 to 30% on the non-Darcy coefficient and observed that the non-Darcy coefficient increased with an increase in water saturation. They performed dimensional analysis by considering the both rock and fluid properties and developed the following correlation.

$$\beta = 13.387 \left[ \frac{\left( \frac{\sqrt{\rho k \sigma}}{\mu} \right)^{-0.7865}}{\phi(1 - S_w)\sqrt{k}} \right] \quad (2.25)$$

In this equation,  $\rho$  and  $\mu$  are fluid density and viscosity, and  $\sigma$  is overburden pressure, respectively.

Jones (1987) conducted flow experiments using consolidated cores of 355 sandstone cores and 29 limestone cores from different reservoirs. Based on these measurements, two correlations were put forward using regression (Eqn.2.26 and Eqn.2.27). Jones developed two more correlations (Eqn.2.28 and Eqn.2.29) based on Geertsma (1974) equation.

$$\beta = \frac{6.15 \times 10^{10}}{k^{1.55}} \quad (2.26)$$

$$\beta = \frac{1.88 \times 10^{10}}{k^{1.47} \phi^{0.53}} \quad (2.27)$$

$$\beta = \frac{3.13 \times 10^{12}}{k^{1.78} \phi^{1.78}} \quad (2.28)$$

$$\beta = \frac{1.27 \times 10^5}{k^{0.52} \phi^{5.68}} \quad (2.29)$$

Evans et al. (1987) measured the non-Darcy coefficient for Berea sandstone cores for dry conditions and different immobile saturations. They used dimensionless variables derived from Geertsma and developed the following correlation using linear regression.

$$\beta = \frac{5.123 \times 10^{-5}}{\phi} \left[ \frac{1}{(1 - S_w) \sqrt{k_g}} \right]^{1.839} \quad (2.30)$$

Also, they used the data by Geertsma (1974), and Cornell and Katz (1953) to estimate the non-Darcy coefficient with this correlation and Geertsma's correlation and they indicated that the prediction of the non-Darcy coefficient was better with this new correlation except in low permeability core samples. Evans et al. (1987) developed a dimensionally consistent correlation (Eqn.2.31) to estimate non-Darcy coefficients using rock and fluid properties. This correlation is similar to one developed by Avila et al. (1986).

$$\beta = 13.387 \frac{\left( \frac{\sqrt{\rho_g k_g \sigma}}{\mu_g} \right)^{-0.787}}{\phi (1 - S_{wr}) \sqrt{k_g}} \quad (2.31)$$

Here,  $\rho_g$ ,  $k_g$ ,  $\sigma$ ,  $\mu_g$  are gas density, gas effective permeability, effective stress and gas viscosity, respective, in units of lbm/ft<sup>3</sup>, darcy, psi, and cp, respectively.

Morrison and Dugan (1991) noted that estimation of the non-Darcy coefficient should be field specific. They measured the non-Darcy coefficient of samples taken from three facies of the Sherwood reservoir: channel sands, sheetflood deposit and aeolian sand. They also separated the samples based on the clay content. They indicated that the facies and diagenetic group had little effect on measured non-Darcy coefficients. They developed a correlation by combining all measured data (Eqn.2.32). In Eqn.2.32, permeability and non-Darcy are in units of mD and 1/ft, respectively.

$$\beta = \frac{1.56 \times 10^{11}}{k^{1.84}} \quad (2.32)$$

Frederick et al. (1994) conducted experiments for varying overburden stress and immobile liquid saturation and developed four correlations for non-Darcy coefficient estimation.

$$\beta = \frac{1.98 \times 10^{11}}{k_e^{1.64}} \quad (2.33)$$

$$\beta = \frac{7.89 \times 10^{10}}{k_e^{1.60} [\phi(1 - S_w)]^{0.404}} \quad (2.34)$$

$$\beta = \frac{2.11 \times 10^{10}}{k_e^{1.55} [\phi(1 - S_w)]} \quad (2.35)$$

$$\beta = \frac{1}{[\phi(1 - S_w)]^2} e^{45 - \sqrt{407 + 81 \ln\left(\frac{k_e}{\phi(1 - S_w)}\right)}} \quad (2.36)$$

Here,  $k_e$  is effective permeability, and  $k_e$  and  $\beta$  are in units of mD and 1/ft. In their correlations development, they neglected the overburden stress since stress directly influenced the porosity and permeability.

Liu et al. (1995) used the porosity, permeability, tortuosity and non-Darcy coefficient data by Cornell and Katz (1953). They plotted all data against the Geertsma (1974) correlation and showed that the Geertsma correlation was not adequate even if it is dimensionally consistent. Therefore, they modified the Geertsma's correlation to fit the experiment data (Eqn.2.37).

$$\beta = \frac{20.6}{\phi^{4.62} \sqrt{k}} \quad (2.37)$$

The fit was improved compared to Geertsma's correlation and they considered tortuosity factor for further improvement. They proposed the following correlation.

$$\beta = \frac{8.91 \times 10^6 \tau}{\phi k} \quad (2.38)$$

In these equations,  $\beta$  and  $k$  are in units of 1/ft and mD. To estimate the non-Darcy coefficient in multi-phase flow, they used the relative non-Darcy coefficient,  $\beta_{rl}$ , of phase  $l$  (Eqn.2.39).

$$\beta_{rl} = \frac{\beta}{\beta_l} \quad (2.39)$$

They pointed out (Eqn.2.40) that the relative non-Darcy coefficient could be easily obtained if relative permeability and non-Darcy coefficient of single phase were known.

$$\beta_{rl} = k_{rl} \quad (2.40)$$

They also emphasized that effective stress should not be included since it affects the permeability, porosity and tortuosity. In short, effective stress has no direct effect but rather an indirect effect on the non-Darcy coefficient.

Coles et al. (1998) made experimental studies on dry core samples and core samples with different immobile liquid saturations to estimate the non-Darcy coefficient. In their experiments, they used solidified paraffin wax to mimic immobile condensate phase. They compared the estimated non-Darcy coefficients for dry cores with data by Jones et al. (1987) to indicate that while some data followed the same trend with the literature data, some did not which may lead to significant errors. They derived correlations (Eqn.2.41 and Eqn.2.42) using the dry core experimental results.

$$\beta = 1.07 \times 10^{12} \frac{\phi^{0.449}}{k^{1.88}} \quad (2.41)$$

$$\beta = 2.49 \times 10^{11} \frac{\phi^{0.537}}{k^{1.79}} \quad (2.42)$$

In these correlations,  $\beta$  and  $k$  are in units of 1/ft and mD, respectively. They pointed out that these correlations could be used for immobile liquid saturation cases provided that effective porosity and permeability should be used instead of absolute porosity and permeability. They showed that for different immobile liquid saturation, non-Darcy coefficient and permeability

trends were similar, but plots were much more steep. In the case of immobile liquid saturation, the non-Darcy coefficient could be calculated following correlation which was valid saturation of 0 – 0.5 and gave almost perfect fits for saturations less than 0.20.

$$\beta(S_w) = \beta_{dry} e^{6.265 S_w} \quad (2.43)$$

Lombard et al. (1999) indicated that high pressure decrease near the wellbore leads to increases in condensate saturation and high velocities. Both increases in gas condensate saturation and velocity lead to increase in inertial effects. He conducted experiments with dry cores and cores with irreducible water saturation and different condensate saturations. He stated that observed non-Darcy coefficients trends were consistent with literature data. For example, he found that non-Darcy coefficients were higher for consolidated media than for unconsolidated media. The non-Darcy coefficient was more significant for low permeability media and increased with water saturation. They compared the Non-Darcy coefficient measurements for dry cores with the literature data and found that the ones calculated from the Geertsma correlation underestimated inertial effects. He calculated the equivalent pore radius and found a good linear relation between the non-Darcy coefficient and equivalent pore radius.

Cooper et al. (1999) studied the non-Darcy effect on anisotropic and layered medium by conducting experiments and constructing macroscopic and microscopic models. They measured permeability, non-Darcy coefficient and tortuosity in both flow directions for different Berea sandstone and carbonates cores. For macroscopic models, they proposed the effective non-Darcy coefficients for parallel,  $\bar{\beta}_{eff}$ , and perpendicular,  $\hat{\beta}_{eff}$ , arrangement of layers given in Eqn.2.44 and Eqn.2.46, respectively. In Eqn.2.44,  $w_i$  is mass flow rate and is found iteratively. For effective non-Darcy coefficient calculation, layer permeabilities measured from experiment were used and effective permeabilities for parallel and perpendicular models were calculated from

Eqn.2.45 and Eqn.2.47, respectively. They noticed that the calculated effective non-Darcy coefficient changes with effective permeability and showed a similar trend with intrinsic non-Darcy coefficient and permeability of each layer.

$$\bar{\beta}_{eff} = \left[ \frac{w_i A}{w A_i} \left( \frac{\mu}{k_i} + \beta_i \frac{w_i}{A_i} \right) - \frac{\mu}{\bar{k}_{eff}} \right] \frac{A}{w} \quad (2.44)$$

$$\bar{k}_{eff} = \frac{\sum k_i L_i}{\sum L_i} \quad (2.45)$$

$$\hat{\beta}_{eff} = \frac{\sum \beta_i L_i}{\sum L_i} \quad (2.46)$$

$$\hat{k}_{eff} = \frac{\sum L_i}{\sum L_i / k_i} \quad (2.47)$$

They investigated the effect of water saturation on inertial effects and they found that the non-Darcy coefficient increased with water saturation. They observed an order of magnitude increase in non-Darcy coefficient for perpendicular core, and for parallel core, non-Darcy coefficient did not change because high permeability layers in perpendicular cores led to lower water saturations. For carbonate cores, they observed that non-Darcy coefficient almost did not change since the carbonate cores used in the experiments were very homogenous.

Khaniaminjan and Goudarzi (2008) conducted flow experiments using sand beads with different grain sizes changing from 0.192 mm to 1.0 mm. They measured the pressure decrease and found that it was consistent with the pressure decreases calculated from Kozeny-Carman equation. In experiments, they measured the porosity, permeability and non-Darcy coefficients and developed two correlations to estimate non-Darcy coefficient.

$$\beta = \frac{17.2 \times 10^{10}}{k^{1.76}} \quad (2.48)$$

$$\beta = \frac{4.8 \times 10^{11}}{k^{1.8} \phi^{-0.48}} \quad (2.49)$$

### 2.5.3 Non-Darcy Coefficient Estimation from Field Data

Pascal et al. (1980) obtained non-Darcy coefficients from single-point, variable flow drawdown tests of shallow low permeability and developed the following correlation.

$$\beta = \frac{4.8 \times 10^{12}}{k^{1.176}} \quad (2.50)$$

Here,  $\beta$  and  $k$  are in units of 1/m and mD, respectively.

Noman et al. (1985) estimated the non-Darcy coefficient from reservoir porosity, permeability and gas saturation by using a multi-rate pressure test analysis conducted for 105 sandstone gas wells and 24 sets of experimental core data. They used linear and multiple regression and proposed the following correlations.

$$\log \beta = 2.4388 \log \left( \frac{k}{\phi S_g} \right)^{-0.5} - 2.4071 \quad (2.51)$$

$$\log \beta = -1.0609 \log k + 11.0485 \quad (2.52)$$

$$\log \beta = -1.0805 \log(k \exp(-0.03S)) + 11.0756 \quad (2.53)$$

$$\log \beta = -1.0356 \log(k\phi) + 10.1544 \quad (2.54)$$

$$\log \phi = -0.0233 \log \beta - 0.6068 \quad (2.55)$$

$$\log \left( \frac{\beta}{\sqrt{k}} \right) = -30.0799 \log \phi - 21.7707 \quad (2.56)$$

$$\log \left( \frac{\beta}{\sqrt{k}} \right) = -13.4639 \log(\phi S_g) - 10.7036 \quad (2.57)$$

$$\beta = \frac{4.7543 \times 10^{10}}{k^{0.9212} (\phi S_g)^{0.2429}} \quad (2.58)$$

$$\beta = \frac{1.3633 \times 10^{10}}{(k \exp(-0.19 S))^{0.8804} (\phi S_g)^{0.7770}} \quad (2.59)$$

In these correlations,  $S$  and  $S_g$  are skin and gas saturation respectively. Units of  $k$  and  $\beta$  are in mD and  $\text{ft}^{-1}$ . Also, Noman et al. (1985) compared the non-Darcy coefficients measured with the



ones calculated from Geertsma's correlation, and they showed the discrepancy between them. The inaccuracy of the Geertsma correlation was attributed to an insufficient porosity range (0.07 – 0.23) for the measurements.

Narayanaswamy et al. (1999) used well test data conducted in 12 different wells in a carbonate gas condensate reservoir; they calculated non-Darcy coefficients and compared with the lab data of carbonate cores by Gewers and Nichols (1969), Geertsma (1974), Jones (1972) and Frederick and Graves (1994). They found significant differences between the non-Darcy coefficient obtained from well testing and the ones from lab experiments especially for high-permeability regions. They explained the difference with heterogeneity of carbonate reservoirs. They modified the non-Darcy correlations developed by Bird (1965) by replacing the particle diameter with specific surface area so that reservoir heterogeneity could be taken into account.

$$\beta = \frac{0.07}{ka_v(1 - \phi)} \quad (2.60)$$

Khaniaminjan and Goudarzi (2008) used field data and developed a correlation (Eqn.2.61). In these equations, non-Darcy coefficient and permeability are in 1/ft and mD, respectively.

$$\beta = \frac{9 \times 10^9}{k^{-6/7} \phi^{-8/7}} \quad (2.61)$$

#### 2.5.4 Non-Darcy Coefficient Estimation from Network Modeling

Thauvin and Mohanty (1998) used network modeling to estimate porous medium morphology effect on flow properties. To define the pore network, they used a regular cubic pack arrangement with connectivity of six. They defined converging-diverging pore segments with spheres and cylinders for pores located at the lattice nodes and pore throats. Pore and pore throat sizes were determined based on the random number generated based on a specified distribution. They calculated the pressure drop caused by viscous forces, bending of flow at the

pore body, and expansion and contraction as suggested by Bird et al. (1965). With this methodology, they investigated the pore morphology effect on flow properties. They observed that an increase in pore throat diameter led to a decrease in non-Darcy coefficient and increase in permeability. Pore throat radius had little effect on porosity and tortuosity. Porosity slightly increased and tortuosity slightly decreased with the increase in pore throat diameter.

They observed that the pore radius increase led to porosity increase and a slight decrease in non-Darcy coefficient; however, this had no effect on permeability and tortuosity. They observed that the most significant parameter affecting the flow properties was average coordination number. The non-Darcy coefficient increased sharply and the permeability and tortuosity decreased with a decrease in average coordination number. The effect of decreasing average coordination number on porosity was less compared with how it affected flow properties. Porosity slightly decreased with the decrease in average coordination number. They created a database of flow parameters calculated from all network parameters and developed some non-Darcy coefficient correlations given below.

$$\beta = 1.55 \times 10^4 \frac{\tau^{3.35}}{k^{0.98} \phi^{0.29}} \quad (2.62)$$

$$\beta = \frac{2.5 \times 10^5}{k} \quad (2.63)$$

$$\beta = \frac{3.1 \times 10^4 \tau^3}{k} \quad (2.64)$$

In these correlations, permeability and non-Darcy coefficient units are Darcy and 1/cm, respectively.

Thauvin and Mohanty (1998) also investigated the compaction effect by reducing the all pore and pore throat radii with a multiplication of constant factors. With compaction, the non-Darcy coefficient increased sharply due to increasing velocities. Similarly, permeability and

porosity decreased sharply due to decreases in pore throats radii. Even though the non-Darcy coefficient, permeability, and porosity were significantly affected by compaction, compaction had little effect on tortuosity. For compaction, the non-Darcy coefficient change can be estimated from porosity with the correlation given below.

$$\beta = 7.2 \times 10^3 \phi^{2.316} \quad (2.65)$$

They investigated the deposition effect by reducing the pore and pore throat radii with constant thickness to simulate particle deposition even though natural deposition reduces the pore size in a more complex way. They observed that decreasing the pore and pore-throat radii led to increases in velocity. The ratios of pore radius to adjacent pore throat radius increase due to constant thickness reduction of the pore and pore throat radii. These led to decrease in porosity, permeability and increases in non-Darcy coefficient and tortuosity. Changes in non-Darcy coefficient due to deposition can be estimated from permeability with the following correlation.

$$\beta = \frac{2.8 \times 10^5}{k^{1.14}} \quad (2.66)$$

Cooper et al. (1999) investigated carbonate samples with microscopic models by using network modeling. They calculated the pressure drop similar to the study of Thauvin and Mohanty (1998). They conducted the network simulations in three directions to estimate the non-Darcy coefficient, permeability and tortuosity tensors. They found that carbonate cores were anisotropic since  $k_{xx} \neq k_{zz}$  and  $\beta_{xx} \neq \beta_{zz}$ . They noticed that the tensor product of permeability and non-Darcy coefficient,  $\bar{\bar{C}}$  was not as anisotropic compared with the permeability and non-Darcy coefficient tensors.

They used to same network model used for carbonate samples and investigated anisotropy effects on flow properties by reducing the pore throat radii in the z direction with a

multiplication factor between 0.25 and 1. Decreasing the multiplication factor up to 0.25 led to increases in non-Darcy coefficient and tortuosity and decreases in permeability in  $z$  direction up to a factor of 610, 2 and 200, respectively. The change of flow parameters in  $x$  and  $y$  directions were negligible compared with in the  $z$  direction. They noticed that the product of permeability and non-Darcy coefficient change with tortuosity were similar in each direction and their relation is given as in Eqn.2.67. In this equation, the index  $ii$  represents the direction and  $C$  is given in cm. In addition, they found a correlation by using step-wise regression to estimate the non-Darcy coefficient (Eqn.2.68). In this correlation,  $k$  and  $\beta$  are in  $\text{cm}^2$  and cm units, respectively.

$$\bar{C}_{ii} = 10^{-3.16} \tau_{ii}^{1.43} \quad (2.67)$$

$$\beta = \frac{\tau^{1.943}}{10^{3.25} k^{1.023}} \quad (2.68)$$

Balhoff and Wheeler (2009) used network modeling to generate a modified Delaunay tessellation (MDT) algorithm to calculate the permeability and non-Darcy coefficient of computer generated packs and sandstones samples digitized from microtomography. First, they used a duct geometry and they calculated the pressure drop for different diameters, lengths and aspect ratios from Navier-Stokes equation with FEM and an empirical equation was developed to calculate pressure considering the linear term (viscous term) and nonlinear term (inertial term) (Eqn.2.69). In this equation,  $g_{ij}$  is the hydraulic conductance between pore throats connecting pores  $i$  and  $j$ .  $\mu$ ,  $P$  and  $q$  are fluid viscosity, pressure and flow rate, respectively.  $b_{ij}$  and  $c_{ij}$  are constants that depend on throat properties: its length, radius and aspect ratio. With the constraint of summation of  $q_{ij}$  equals to 0, the equation was solved.

$$(P_i - P_j) = \frac{\mu}{g_{ij}} q_{ij} + \mu b_{ij} q_{ij} \log \left[ 1 + \left( c_{ij} \frac{\rho q_{ij}}{\mu} \right)^3 \right] \quad (2.69)$$

The non-Darcy coefficient for a computer generated pack and real sandstone sample was estimated by calculating permeability for different pressure differences and fitting the results with the Forchheimer equation. They found that the permeability calculated from Forchheimer equation gave a slightly different result than when calculated from the Darcy equation, but the error was small and could be ignored. However, they found that the deviation was high for high velocities, in which the trend become concave down reaching a minimum plateau suggested by Barree and Convey (2004).

They used the experimental data found from the literature (Kim, 1985) and constructed a network model of sphere packs with specific grain-size distribution used in the experiment. They calculated the non-Darcy coefficient and found that the calculated permeability and non-Darcy coefficient were close to experimental values (within 20% error range). Unlike numerical analysis, they could not observe the deviation at high flow rates in experiments. They concluded that the Forchheimer equation was valid over limited range of velocities.

## **2.6 Non-Darcy Flow Simulations**

With the development of computational methods, many researchers have solved numerical equations with finite difference methods. In this part of the dissertation, some examples are given to emphasize inertial effects especially for frac-pack completed gas reservoirs.

Narayanaswamy et al. (1999) investigated the effects of heterogeneity on the effective non-Darcy coefficient. They show that using average permeability for the non-Darcy coefficient caused underestimation by up to two orders of magnitude. They noticed that a small fraction of high permeability layers could lead to lower estimation of effective non-Darcy coefficients if average permeability was used in the estimation. They suggested Eqn.2.70 to calculate the

effective non-Darcy coefficient for reservoir simulation. In this equation,  $A_i$  and  $A_t$  are the cross-sectional area of layer  $i$  and total cross-sectional area, respectively.

$$\beta_{eff} = \frac{1}{A_t} \sum \beta_i A_i \quad (2.70)$$

They conducted single-well radial simulations to investigate the effect of heterogeneity and they observed that the productivity index decreased from 180 MSCF/D/psi to 150 MSCF/D/psi with an increase in the Dykstra-Parsons coefficient from 0 to 0.8 due to an increase in effective non-Darcy coefficient. They also conducted reservoir simulations and found that most of the rate-dependent skin in gas wells resulted of non-Darcy flow and small part was related to decreases in gas relative permeability due to condensate drop out.

Even though many authors assume that non-Darcy flow is related with high flow rates and near-well bore phenomena, Armenta and Wojtanowicz (2003) indicated the importance of non-Darcy effects away from the wellbore with reservoir simulation even for low flow rates. They did sensitivity analysis for permeability, porosity and flow rates, and calculated the pressure drop due to non-Darcy effects from an analytical equation. They observed that for lower permeability and porosity, non-Darcy effects were significant. For reservoirs with permeability and porosity of 100 mD and 0.01, inertial effects for flow rate of 5.5 MMscf/day caused half of the pressure drop. To support their observations from sensitivity analysis, they used Brar and Aziz (1978) multi-rate well test data and calculated that the pressure drop resulted from inertial effects changing between 30% and 70%.

They also used a commercial simulator to estimate the gas recovery and they observed that for volumetric reservoir the ultimate recovery was not change with inertial effects; however, the recovery time increased with inertial effects. For a water drive gas reservoir, the recovery

depended on inertial effects. They observed that the recovery decreased from 61% to 42.9% when inertial effects were included due to early well load up.

Alvarez et al. (2002) studied well-test techniques to evaluate pressure transient tests of hydraulically fractured gas wells to illustrate the importance of inertial effects on reservoir permeability, fracture half-length and fracture conductivity estimation. They used reservoir simulator to generate pressure drawdown and build-up data for both Darcy flow and non-Darcy flow and analyzed synthetic data with well-testing techniques. They conducted simulations for different fracture half-lengths and fracture conductivities and they observed that bottom-hole pressures obtained from Darcy simulations were significantly higher especially at early times. From well test analysis, they obtained the same permeabilities and fracture properties used in the simulations. However, for the non-Darcy simulations permeabilities were higher than the simulation input by about 50%. On the other hand, fracture lengths and fracture conductivities were significantly lower than the actual values especially for the well test conducted for high flow rates. For example, estimated permeability, fracture half-length and fracture conductivity from well test for flow rate 4 MMscf/D were 0.153 mD, 103.7 ft and 26.57 mD-ft, respectively, while simulation inputs were 0.1 mD, 660 ft and 100 mD-ft. A similar sensitivity analysis was conducted for two-phase flow. The estimated parameters changed with water saturation; however, there was no trend with estimation parameters and water saturation. For example, estimated permeabilities were 0.085 mD and 0.109 mD for the flow rates 2 MMscf/D and 4 MMscf/D, respectively. The estimated fracture half-lengths were always greater than the simulation input. After sensitivity analysis, they conducted reservoir simulations to see the impact of misestimation of parameters on reserve estimation. They conducted simulations for

input parameters used in well test simulations and parameters obtained from well test analysis and observed that recovery could be misestimated up to 25%.

Belhaj et al. (2003) developed a Forchheimer diffusivity equation (Eqn.2.71) for single phase flow for numerical investigation of inertial effects. They developed a simulator by using the finite difference method and conducted several simulations by using different non-Darcy correlations from literature (Coles & Hartman, 1998; S.C. Jones, 1987; Li & Engler, 2001). The estimated pressure gradients for specific flow rates changed significantly with the non-Darcy coefficient estimated from different correlations. This emphasizes the importance of accurate estimation of the non-Darcy coefficient. They suggested that for correct estimation of pressure gradients, the non-Darcy coefficient should be experimentally determined or it should be estimated from well tests.

$$\frac{\partial^2 P}{\partial x^2} + \frac{\partial^2 P}{\partial y^2} = c \left( \frac{\mu}{k} + 2\beta\rho v \right) \left( \phi \frac{\partial P}{\partial t} + v \left[ \frac{\partial P}{\partial x} + \frac{\partial P}{\partial y} \right] \right) \quad (2.71)$$

They conducted experiments using synthetic sandstone samples and calculated the non-Darcy coefficients from the Forchheimer equation. Using the calculated coefficient, they validated the proposed diffusivity equation. Also, to show the importance of accurate estimation of the non-Darcy coefficient, they used the Jones correlation (1987) to calculate the pressure drop. For the same core experiments, the estimated pressure drops were less than the measured ones.

Lolon et al. (2004) investigated the non-Darcy flow effect for high rate, frac-pack completed gas reservoirs with sensitivity analysis for gas rate, fracture conductivity, fracture half length, reservoir permeability, non-Darcy coefficient of proppant, irreducible water saturation, gel damage in order to show the importance of modeling the entire system to accurately estimate the well productivity. For their simulations, they used the Forchheimer equation and the non-



Darcy coefficient for the reservoir was estimated from Geertsma (1974) and Frederick and Graves (1994) for single-phase and two-phase flows, respectively. In their work, they calculated pressure drops in the reservoir due to viscous forces and inertial effects and the pressure drop in the fracture due to viscous forces and inertial effects, separately, to compare them.

For single-phase flow, the pressure drop due to viscous forces was more in the reservoir and fracture compared in the perforation. However, the pressure drops in the reservoir, fracture and perforation due to viscous forces were negligible compared the pressure drops due inertial effects. The majority of the pressure drop was observed in the perforations. Fracture length significantly affected the pressure drop in the reservoir. For example, they observed that an increase in fracture length from 12 to 50 ft led to decrease in pressure drop due to the inertial effects in the fracture from 1620 to 498 psi for a flow rate of 4 MMscf/D/ft. Sensitivity analysis of fracture conductivity indicated that the increase in fracture conductivity led to a decrease in pressure drop. For example, they observed that an increase in dimensionless fracture conductivity from 0.001 to 0.1 led to a decrease in pressure drop in the fracture due inertial effects from 498 to 121 psia for the same flow rate. Compared to the pressure drop in the fracture due to inertial effects, pressure drop in the reservoir due to inertial effects was only significant for the moderate or low permeability reservoirs.

They also investigated the effect of flow rate on pressure drop and found that below 0.4 MMscf/D/ft, only pressure drop in the fracture due to inertial effects could be considered; however, above this flow rate, pressure drop in the reservoir due to inertial effects should be taken into account. They investigated the non-Darcy coefficient for proppants in the fracture with sensitivity analysis by decreasing the non-Darcy coefficient calculated from Frederick and Graves correlation up to 10% of original value. They observed that the decrease in non-Darcy

coefficient for proppants highly affected the pressure drop especially for low-permeability reservoirs. For example, the decrease in non-Darcy coefficient up to 10% of the original value led to a decrease in pressure drop in the fracture from about 650 to 180 psi for the flow rate 100 MMscf/D for the reservoir with 15 mD permeability. They also investigated the effect of water saturation on non-Darcy pressure drop. They found that increases in mobile water saturation led to increases in non-Darcy pressure drop especially for low permeability reservoir.

Mohan et al. (2006) studied non-Darcy flow effects for hydraulically fractured gas-condensate reservoirs to study grid refinement and inertial effects on recovery estimation. They investigated the effect of fracture length and fracture conductivity on the productivity in addition to inertial effects by using the compositional reservoir simulator. They used the Geertsma correlation (1974) to estimate the non-Darcy coefficient. In the first attempt, they ignored the inertial effect and they observed that frac-pack completion for tight gas reservoir led to an increase in productivity index up to 9 times compared to the reservoir without fractures. They observed that the increase in production or decrease in pressure led to a condensate band around the well. The condensate band was circular if the well was not fractured; in the case of the fracture, the condensate band was elongated along the fracture due to bilinear flow. They observed that the estimated productivity could be three times higher than the real one if inertial effects were ignored and the increase in fracture conductivity or fracture length led to a productivity index increase.

### CHAPTER 3: STATEMENT OF THE PROBLEM

Accurate production estimation of frac-pack completed gas reservoirs depends on correct estimation of flow properties of both the reservoir and proppants used in frac-pack completions. In addition, the effects of compaction and sand migration on flow properties should be known and quantifiable. In this part, some deficiencies of non-Darcy correlations and flow-property estimation from lab experiments are explained. Problems associated with the misuse of Kozeny-Carman and non-Darcy correlations are also illustrated.

There are many correlations to estimate the non-Darcy coefficient in the literature. Two questions that arise from the literature review are why there are so many correlations and whether these correlations are reliable. Amao (2007) conducted core experiments and determined the permeability and porosity of a set of cores. Then he compared the non-Darcy coefficients calculated from well-known correlations. Figure 3.1 gives the calculated non-Darcy coefficient from these correlations (Table 7.1 from his thesis) for a sandstone core with porosity and permeability 0.18 and 6.18 mD.

Based on this comparison, the estimated non-Darcy coefficients from correlations are very different. To better assess this problem, understanding of the derivation of these correlations is necessary. They were derived by taking of the logarithm of the petrophysical properties and doing linear regression (Eqn.3.1).

$$\log\beta = a_0 + a_1\log k + a_2\log\phi + a_3\log\tau + \dots \quad (3.1)$$

The main assumption of the linear regression is that all explanatory variables should be independent. For the petrophysical properties used in the equations, this assumption does not hold because petrophysical properties are highly correlated, creating a multicollinearity problem. Therefore, the  $a_i$  coefficients in front of the petrophysical properties change from data set to data set. This indicates that these correlations are not reliable and interpretable.

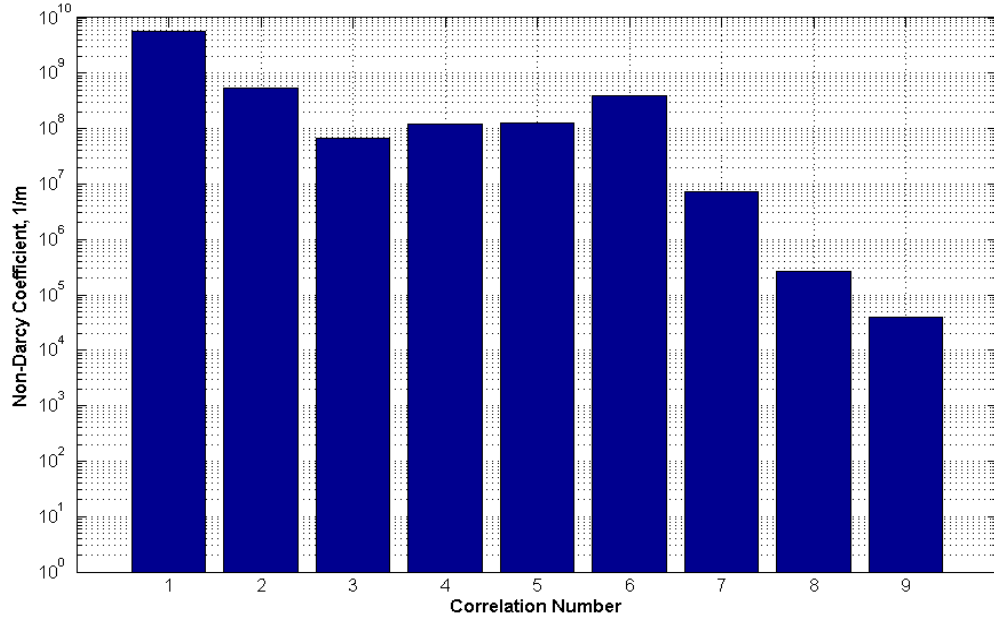


Figure 3.1 Non-Darcy Coefficient (Beta Factor) Comparison for Core#9 (Adopted from Amao, 2007)

The second problem is misestimation of permeability, Klinkenberg coefficient, and non-Darcy coefficient determination from steady-state lab experiments. In the lab measurement analysis, inertial effects in Klinkenberg Analysis and slippage effect in Forchheimer Analysis are ignored. Neglecting these effects may cause errors and misestimation of the predicted parameters. To demonstrate this error, 1-D single-phase simulations are conducted for a synthetic core (Table 3.1) with constant outlet pressure equal to 0.20 MPa, and used for prediction of the relevant parameters (see below). Figure 3.2 gives the steady-state flow rate change as a function of inlet pressure.

For gas flow, mass flow rate,  $q_m$ , is used instead of velocity, and gas properties are calculated at core mean pressures. The Forchheimer equation is written as,

$$\frac{\bar{\rho}A}{\bar{\mu}q_mL}(P_o - P_L) = \frac{1}{k} + \beta \frac{q_m}{A\bar{\mu}} \quad (3.2)$$

Plotting groups for a linear plot are:  $x$  axis =  $\frac{q_m}{A\bar{\mu}}$  and  $y$  axis =  $\frac{\bar{\rho}A}{\bar{\mu}q_mL}(P_o - P_L)$ . From the Forchheimer plot, core permeability and non-Darcy coefficient are obtained from the intercept ( $1/k$ ) and slope ( $\beta$ ), respectively.

Table 3.1 Input Data Used in the 1-D Single Phase Simulations

Gas	N <sub>2</sub>
Temperature, $T$ (°F)	70
Core Length, $L$ (cm)	4.2
Core Diameter, $D$ (cm)	3.8
Porosity, $\phi$ (fraction)	0.25
Permeability, $k$ (mD)	500
Klinkenberg Coefficient, $b$ (MPa)	0.08
Non-Darcy Coefficient, $\beta$ (1/m)	$1.77 \times 10^7$

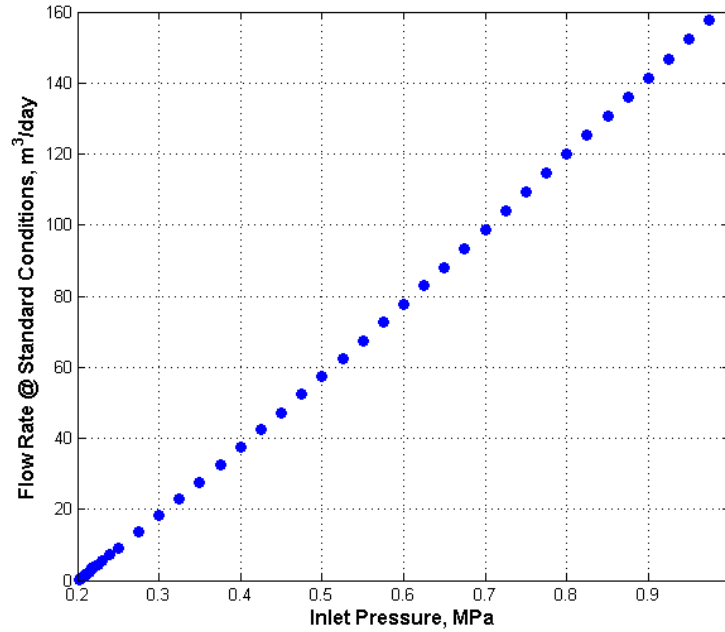


Figure 3.2 Flow Rate Change with Inlet Pressure for 1-D Single Phase Steady-State Simulations

For the Klinkenberg equation, plotting groups are:  $x$  axis =  $1/P_{av}$  and  $y$  axis =  $k_g$ . From the Klinkenberg plot, permeability and the Klinkenberg coefficient are obtained from the intercept ( $k$ ) and slope( $k \times b$ ), respectively.

$$k_g = k \left( 1 + \frac{b}{P_{av}} \right) \quad (3.3)$$

Figure 3.3 and Figure 3.4 give the Klinkenberg and Forchheimer plots for synthetic data, respectively. In these plots, the blue points and blue lines give the plotting variables and linear fits. For the Klinkenberg plot, the calculated permeability and Klinkenberg coefficient are 62 mD and 2.06 MPa, respectively. The calculated permeability is 88% lower than the simulation input permeability, 500 mD. The calculated Klinkenberg coefficient is  $2.5 \times 10^3$  % higher than the simulation input Klinkenberg coefficient, 0.08 MPa. For Forchheimer plot, the calculated permeability and non-Darcy coefficient are 684 mD and  $2.10 \times 10^7$  1 / m, respectively. The calculated permeability is 37% higher than the simulation input permeability, 500 mD. The calculated non-Darcy coefficient is 19% higher than the simulation input non-Darcy coefficient,  $1.77 \times 10^7$  1 / m. In these plots, the red lines give actual trends calculated from simulation inputs. The actual trends are different from trend obtained from the plotting variables. These are the most common errors in the literature. This analysis demonstrates the importance of the simultaneous estimation of permeability, Klinkenberg coefficient and non-Darcy coefficient.

Production can lead to compaction due to a decrease in pore pressure. Compaction causes a pore volume reduction, decrease in permeability, and increase in inertial effects. The permeability reduction can be estimated from the porosity decrease using the Kozeny-Carman relation. The change in non-Darcy coefficient due to permeability reduction with compaction is estimated from correlation(s) based on porosity and permeability. Using these correlations as if the resulting porosity and permeability are initial properties of reservoir may lead underestimation of inertial effects. There is no study available in the literature about how inertial effects change with compaction; therefore, the compaction effect on permeability and the non-Darcy coefficient should be investigated.

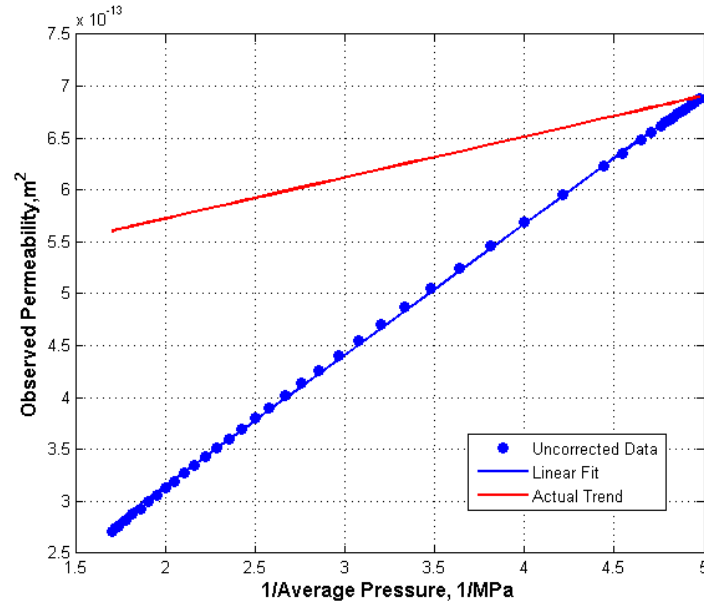


Figure 3.3 Klinkenberg Analysis without non-Darcy Effects Correction for Synthetic Data

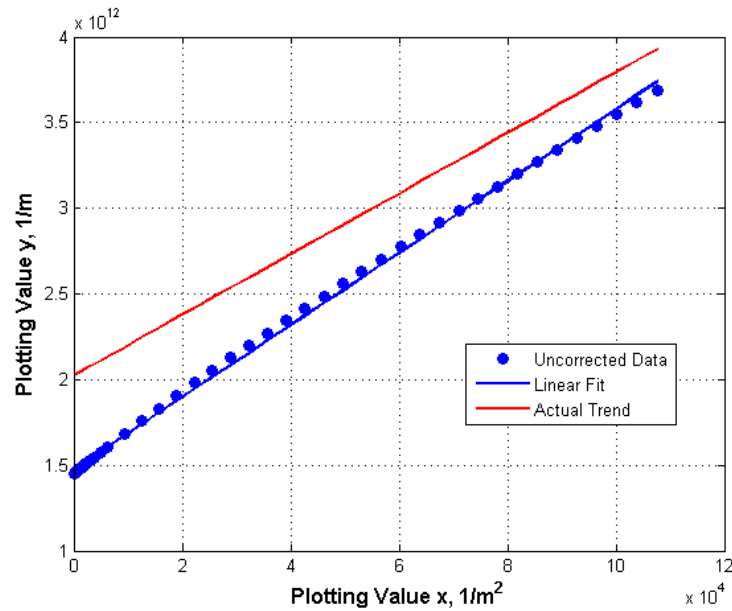


Figure 3.4 Forchheimer Analysis without Slippage Effect Correction for Synthetic Data

High flow rates during production can lead to sand migration in loosely or unconsolidated reservoirs. Sands attached to rock surface can release, migrate and plug at pore constraints or redeposit to the pore surface. There is no realistic study available about how the non-Darcy coefficient changes with permeability impairment due to sand migration. The

roughness effect on flow properties was investigated by Chukwudozie (2011). He conducted LBM simulations for a body centered cubic pack with different protrusions to calculate permeability and non-Darcy coefficient. A porosity decrease from 0.3206 to 0.3039 (5% decrease) led to a permeability decrease from 11.70 to 8.53 Darcy (27.09%) and the non-Darcy coefficient increased from  $75.5 \times 10^3$  to  $370 \times 10^3$  1/m (390.07%). The Kozeny-Carman exponent for porosity and permeability is higher (5.97) than what is commonly given in the literature as three (Figure 3.5). Correlations significantly underestimate the non-Darcy coefficient. Using the Kozeny-Carman correlation to estimate the permeability or non-Darcy correlation leads to misestimation of production. Therefore, the effect of sand migration on permeability impairment and non-Darcy flow should be investigated for accurate estimation of well productivity.

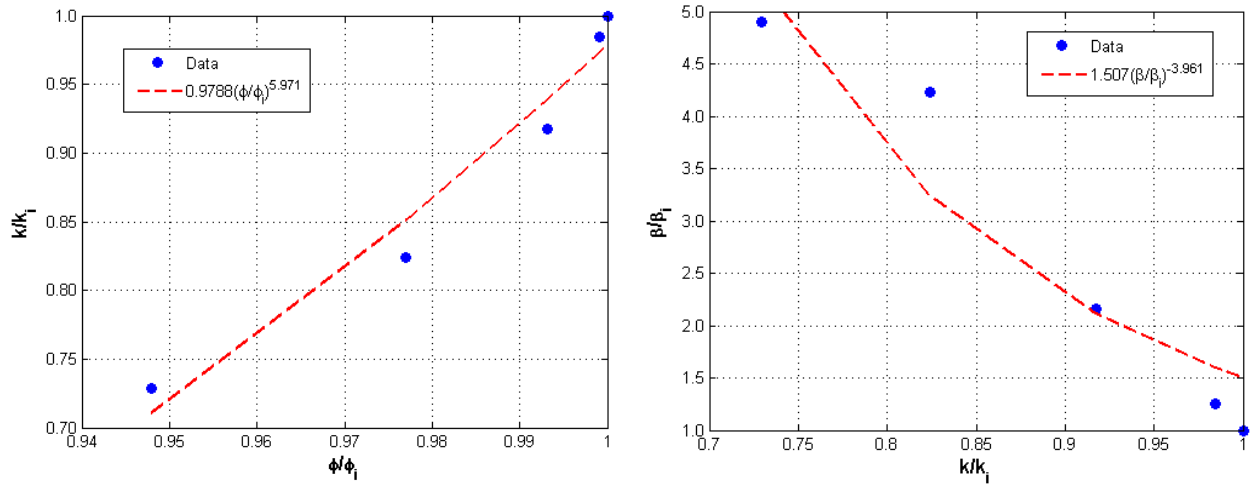


Figure 3.5 Impairment Effect on Non-Darcy Coefficient (Chukwudozie, 2011)



## CHAPTER 4: OBJECTIVES

The objective of the project is to improve methods for predicting the productivity of frac-pack completed gas wells using first-principles analysis and modeling techniques. Since this overall problem involves different physical processes, experiments, and/or modeling techniques for different parts of the reservoir, a number of methods are employed to address this problem:

- *Analysis of core-scale experiments:* To improve estimation of reservoir properties, data from both steady-state and pulse-decay experiments are analyzed using statistics, and the effect of measurement error on the estimation of reservoir properties is investigated. The results give improved methods for interpreting experimental data for estimation of permeability, the Klinkenberg coefficient, and the Forchheimer coefficient.

- *Pore-scale simulation of inertial and Darcy flow:* To better understand the flow within the gravel or proppant pack, fundamental pore-scale simulations are performed. First, an analysis is performed to determine the appropriate domain size needed for these simulations, using the most heterogeneous packing that is expected. Lattice Boltzmann modeling and network modeling are performed to obtain reliable estimation of flow parameters and pore structure. Subsequently, many different computer-simulated gravel packs are created using a Hamersley design. For each packing, network modeling is used to determine permeability, capillary pressure curves, and a variety of parameters describing pore structure. Lattice Boltzmann modeling is then used to determine permeability, non-Darcy coefficient, and tortuosity.

- *Development of correlations:* To develop macroscopic correlations for the gravel and proppant packs, ranges of particle-size distribution and porosity in gravel packs are determined from literature. Properties obtained from pore-scale flow modeling are used to develop correlations for permeability and the Forchheimer coefficient. A new method, structural equation

modeling (SEM), is used to find statistically significant relationships between petrophysical properties. These results can be used for hypothesis testing and missing data estimation.

- *Sand production and formation damage:* To account for the potentially significant impact of formation damage due to sand production, fundamental simulations are performed on the computer-simulated packings. A network model of particle injection is run to determine locations of pore-throat plugging during sand production. Lattice Boltzmann simulations are then run on the resulting structures (damaged by the injected sand) to quantify the impact on both permeability and non-Darcy coefficients. Correlations are developed to quantify the change in permeability and non-Darcy coefficient caused by pore-throat plugging.

- *Reservoir Simulation:* To integrate this information into a model that improves prediction of production from frac-packed gas wells, reservoir simulations are performed. For future deliverability estimation, reservoir simulations are conducted while considering the permeability, porosity and non-Darcy coefficient changes caused by compaction and sand migration. A sand-migration phenomenon is investigated using a parametric study. Finally, sensitivity analysis is conducted to find the optimum frac-pack completion strategies.

## CHAPTER 5: CORE-SCALE ANALYSIS

Reservoir rock pore-structure is too complicated to specify its flow properties only one correlation. Therefore, there are many non-Darcy correlations in the literature. This implies that the flow properties should be estimated from lab experiments. In this chapter, steady-state experiment and pulse-decay experiment analyses techniques are discussed.

### 5.1 Optimization for Steady State Flow Lab Experiment

Neglecting the inertial effect in Klinkenberg analysis or ignoring slippage effect in Forchheimer analysis may lead to misestimation of permeability, non-Darcy coefficient and Klinkenberg coefficient. Simultaneous estimation of flow properties is required to obtain accurate flow properties estimations. For simultaneous estimation of permeability, Klinkenberg coefficient and non-Darcy coefficient, optimization algorithm is developed. In this algorithm, Forchheimer equation is corrected for slippage effect and Klinkenberg equation is corrected for inertial effects.

Forchheimer Equation is given as,

$$-\frac{dP}{dx} = \frac{\mu}{k_g} u + \beta \rho u^2 \quad (5.1)$$

Because the velocity of gas,  $u$  is not constant due to high compressibility of gas, velocity is written in terms of mass flow rate,  $q_m$ .

$$u = \frac{q_m}{\rho A} \quad (5.2)$$

Then the Forchheimer Equation becomes,

$$-\frac{dP}{dx} = \frac{\mu}{k_g} \frac{q_m}{\rho A} + \beta \frac{q_m^2}{\rho A^2} \quad (5.3)$$

Integrating the Eqn.5.3 by calculating the gas properties at average core pressure and arranging the terms leads to;

$$\frac{\bar{\rho}A}{\bar{\mu}q_mL}(P_o - P_L) = \frac{1}{k_g} + \beta \frac{q_m}{A\bar{\mu}} \quad (5.4)$$

Plotting groups are:  $x$  axis =  $\frac{q_m}{A\bar{\mu}} \left(1 + \frac{b}{p_{av}}\right)$  and  $y$  axis =  $\frac{\bar{\rho}A}{\mu q_m L} (P_o - P_L) \left(1 + \frac{b}{p_{av}}\right)$ . By using the plotting groups, core permeability and non-Darcy coefficient are obtained from intercept ( $= 1/k$ ) and slope ( $\beta$ ), respectively.

The Klinkenberg Equation is given as;

$$k_g = k \left(1 + \frac{b}{P_{av}}\right) \quad (5.5)$$

Because the experiments are conducted at high flow rates, the permeability should be modified to remove inertial effects.

$$k_g = \frac{1}{\left(\frac{(P_o - P_L)}{L} \frac{\bar{\rho}A}{\bar{\mu}q_m} - \beta \frac{q_m}{\bar{\mu}A}\right)} \quad (5.6)$$

Plotting groups are:  $x$  axis =  $1/P_{av}$  and  $y$  axis =  $k_g$ . By using the plotting groups, core permeability and Klinkenberg coefficient are obtained from intercept ( $k$ ) and slope ( $= k \times b$ ), respectively.

To estimate permeability and non-Darcy coefficient from Forchheimer equation, Klinkenberg coefficient should be known. Similarly, to estimate permeability and Klinkenberg coefficient from Klinkenberg equation, non-Darcy coefficient should be known. The problem is that there are three unknowns: permeability, Klinkenberg coefficient and non-Darcy coefficient; however, there are two equations: Forchheimer and Klinkenberg. For simultaneous estimation, the Klinkenberg coefficient is firstly estimated and permeability and non-Darcy coefficient are

calculated from Forchheimer equation. Then by using the calculated non-Darcy coefficient, permeability and Klinkenberg coefficient are calculated from Klinkenberg equation. These calculations can be done iteratively. If the objective minimization function is defined such that it considers the differences of Klinkenberg coefficient estimated,  $b_{est}$ , and calculated from Klinkenberg analysis,  $b_{cal}$ , differences of permeability calculated from Klinkenberg,  $k_{klin}$ , and Forchheimer,  $k_{forch}$ , analyses, coefficient determination of Klinkenberg,  $R_{klin}^2$ , and Forchheimer,  $R_{forch}^2$ , plots and differences of outlet pressures measured from lab experiments,  $p_L(obs)$ , and calculated from integration of Forchheimer equation,  $p_L(cal)$ . The problem turns out to be a simple root finding problem.

$$f_{min} = \text{abs}\left(\frac{b_{est} - b_{cal}}{b_{est}}\right) + \text{abs}\left(\frac{k_{forch} - k_{klin}}{k_{forch}}\right) + \text{abs}(1 - R_{klin}^2) + \text{abs}(1 - R_{forch}^2) + \sum \text{abs}\left(\frac{p_L(obs) - p_L(cal)}{p_L(obs)}\right) \quad (5.7)$$

Matlab fminbnd (Mathworks) function is used to estimate the Klinkenberg coefficient which minimizes the objective function (Eqn.5.7). This function uses the golden search ratio and parabolic interpolation to find the minimum of the defined function. The optimization algorithm is verified by using the steady-state synthetic data used in the statement of the problem (Figure 3.2). Figure 5.1 gives the Klinkenberg and Forchheimer plots obtained from optimization algorithm. Calculated permeability, Klinkenberg coefficient and non-Darcy coefficient are same with the simulation parameters: 500 mD, 0.08 MPa and  $1.77 \times 10^7$  1/m, respectively. Since there is no error in the data, confidence intervals (red lines) coincide with regression lines (green lines).

No measurements are perfect; measurement errors are inevitable. Therefore, measurement error effect on Forchheimer and Klinkenberg analyses should be investigated. For

pressure measurements, percent errors are added to inlet pressures and optimization algorithm is used to calculate flow parameters. Since there is no idea about the error, random number is generated from uniform distribution within specified percent intervals (e.g. the first interval is  $\pm 0.1$  %). Since errors are random, the estimated flow parameters are different each time. Therefore, 1000 error added samples are prepared, and permeability, Klinkenberg coefficient and non-Darcy coefficient are estimated from optimization algorithm for each sample to figure out their variations.

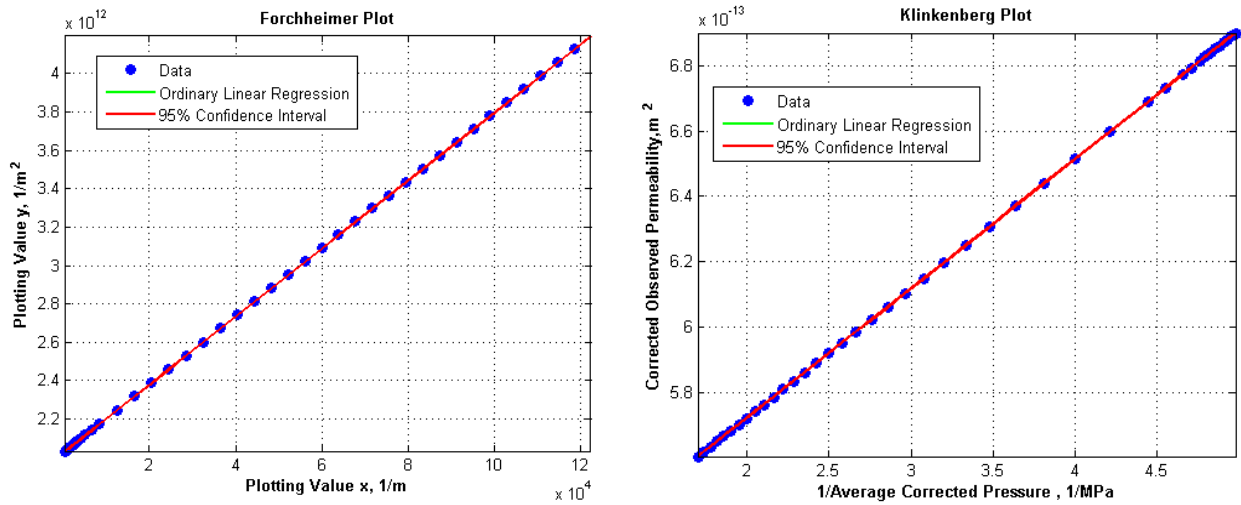


Figure 5.1 Synthetic Case – Forchheimer (left) and Klinkenberg (right) Plots obtained Optimization Algorithm Results

Normal distribution of calculated flow parameters are given in the Figure 5.2. Up to  $\pm 0.3\%$  error interval, the mean estimated permeability, Klinkenberg coefficient and non-Darcy coefficient are similar to simulation input parameters, 500 mD, 0.08 MPa and  $1.7701 \times 10^7$  1/m, respectively; however, the standard deviation increases which makes the estimation more uncertain (Table 5.1). Standard deviation of permeability, Klinkenberg coefficient and non-Darcy coefficient increase from 11.4 mD, 0.0075 MPa and  $2.1786 \times 10^5$  1/m to 32.9 mD, 0.0222 MPa and  $6.3722 \times 10^5$  1/m, respectively. Increase in error more than  $\pm 0.3\%$  leads to higher estimation of Klinkenberg coefficient and lower estimation of permeability and non-Darcy

coefficient. Figure 5.3 gives the percent difference between actual and mean estimated parameters. Pressure error has much more effect on estimated Klinkenberg coefficient. The difference increases up to 40%, 9% and 5% for Klinkenberg coefficient, permeability and non-Darcy coefficient with a pressure error interval  $\pm 0.5\%$ . Generally, the pressure gauge has an accuracy of about 0.25%. This error has almost no effect on mean estimation; but it leads to increase in estimation standard deviation.

Table 5.1 Pressure Measurement Error Effect on Flow Parameters Estimation

Error	Klinkenberg Coefficient (MPa)		Non-Darcy Coefficient (1/m)		Permeability (mD) from Klinkenberg Analysis		Permeability (mD) from Forchheimer Analysis	
	Mean	Std	Mean	Std	Mean	Std	Mean	Std
0.1%	0.0812	0.0075	$1.7701 \times 10^7$	$2.1786 \times 10^5$	498.41	11.42	498.41	11.42
0.2%	0.0821	0.0151	$1.7682 \times 10^7$	$4.3744 \times 10^5$	497.80	22.87	497.80	22.87
0.3%	0.0841	0.0222	$1.7634 \times 10^7$	$6.3722 \times 10^5$	495.88	32.94	495.83	32.89
0.4%	0.0931	0.0249	$1.7384 \times 10^7$	$6.9417 \times 10^5$	483.33	34.30	482.90	34.10
0.5%	0.1114	0.0277	$1.6885 \times 10^7$	$7.3951 \times 10^5$	459.26	34.10	458.11	34.14

Similar measurement error effect is investigated for flow rates. Uniformly distributed random number is generated with specified percent intervals (e.g. the first interval is  $\pm 0.1\%$ ), and 1000 samples are prepared. Permeability, Klinkenberg coefficient and non-Darcy coefficient are estimated from optimization algorithm for each sample. Figure 5.4 gives the normal distribution of estimated parameters for flow rate errors up to  $\pm 0.5\%$ . Unlike effect of pressure measurement error, flow rate error has a great effect on mean parameter estimation; on the other hand, the standard deviation of estimated parameters has little affected with flow rate measurement errors (Table 5.2). While estimated permeability and non-Darcy coefficient decrease with flow rate errors, Klinkenberg coefficient increases. Figure 5.5 gives the absolute percent difference between simulation flow parameters and mean flow parameters obtained from optimization algorithm. Compared with pressure error effect on flow parameters, flow rate error

has much more effect on mean estimated parameters. For example, change of Klinkenberg coefficients are 40% and 90% for  $\pm 0.5\%$  pressure and flow rate errors, respectively. Generally, accuracy of flow meters is more, about 1%.

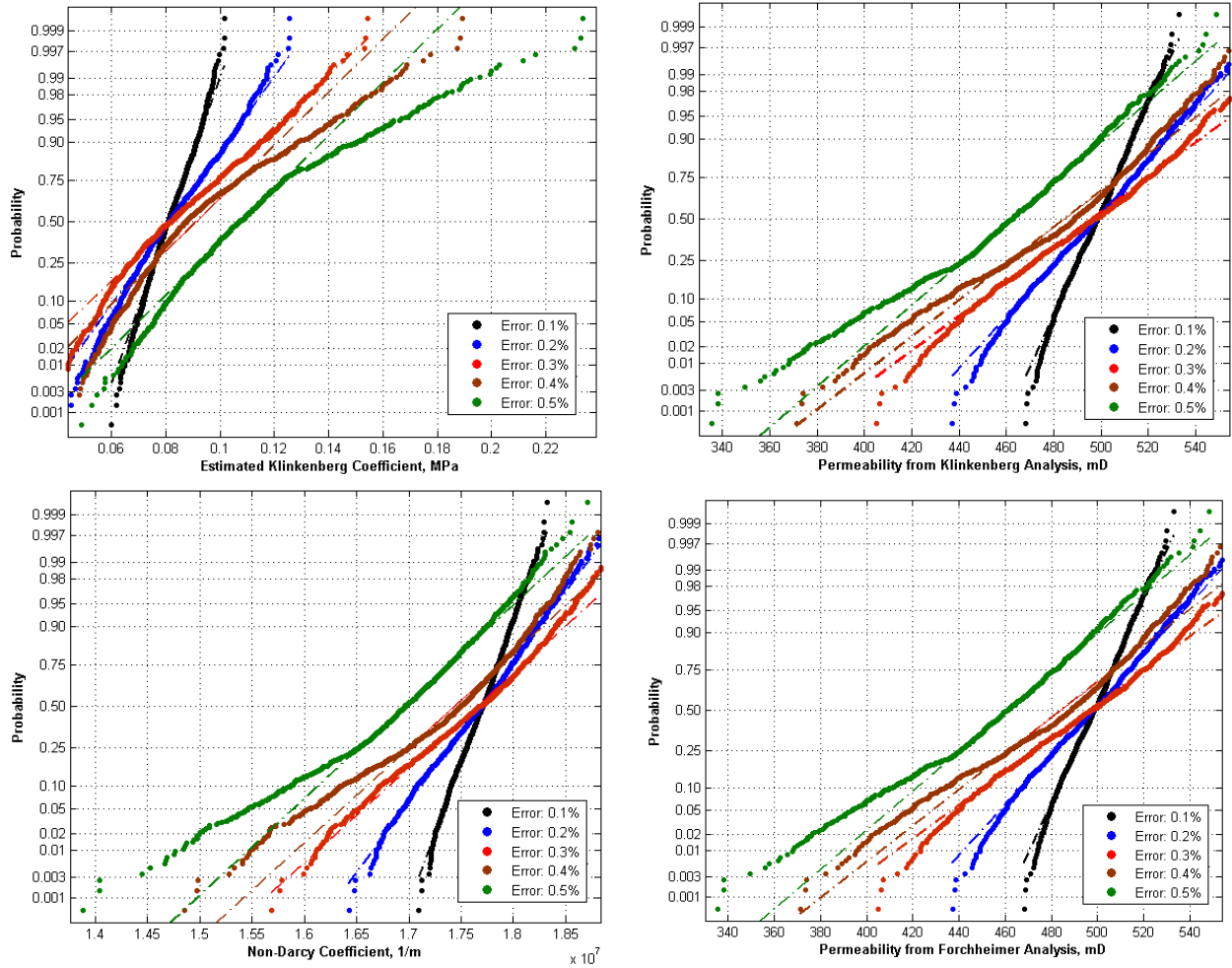


Figure 5.2 Pressure Measurement Error Effect on Flow Parameters Estimation

The methodology is tested with lab experiment provided by Exxon-Mobil. The core data and lab measurements are given in Table 5.3 and Figure 5.6, respectively. Each experiment point is numbered for further analysis.  $N_2$  was used in the experiment and  $N_2$  properties are calculated from correlations (Lemmon & Jacobsen, 2004; Span, Lemmon, Jacobsen, & Wagner, 1998). Figure 5.7 shows Forchheimer and Klinkenberg plots obtained from optimization algorithm. Estimated permeabilities from both Klinkenberg and Forchheimer analyses are similar, 548 mD



and 541.3 mD, respectively; however, the confidence interval of permeability obtained from Klinkenberg analysis (506 mD – 590 mD) is large due to scattered points, which can be resulted from measurement errors (Table 5.4). Estimated Klinkenberg coefficient and the one obtained from Klinkenberg plot are similar; 0.0827 MPa 0.0791 MPa, respectively. Using the optimization results, the flow rates are calculated from 1-D single-phase simulations. Figure 5.8 gives the cross plot of measured and calculated flow rates, and corresponding percent errors. Even though flow rates measured and calculated match, flow rates measurement errors are as high as 8% especially for low flow rates, which is one of the steady-state measurement disadvantage.

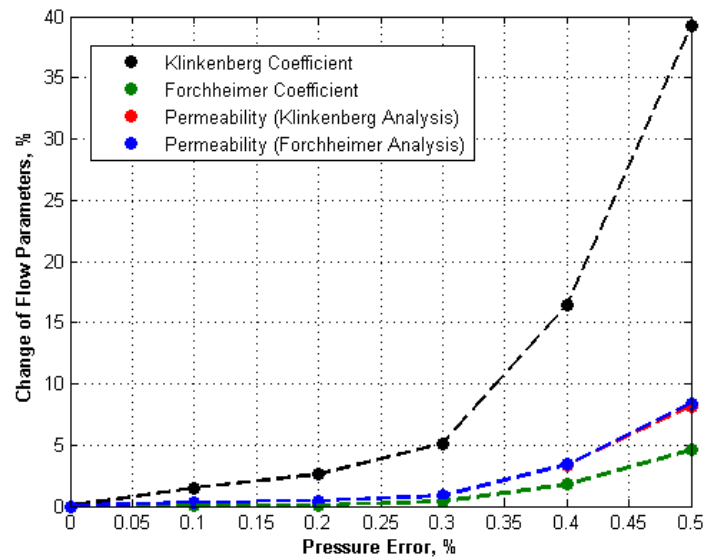


Figure 5.3 Pressure Measurement Error Effect on Mean Flow Parameters Estimation

Table 5.2 Flow Rate Measurement Error Effect on Flow Parameters Estimation

Error	Klinkenberg Coefficient (MPa)		Non-Darcy Coefficient (1/m)		Permeability (mD) from Klinkenberg Analysis		Permeability (mD) from Forchheimer Analysis	
	Mean	Std	Mean	Std	Mean	Std	Mean	Std
0.1%	0.0844	$2.0827 \times 10^{-16}$	$1.7608 \times 10^7$	$2.3379 \times 10^4$	493.51	0.45	493.34	0.33
0.2%	0.0880	$5.4150 \times 10^{-16}$	$1.7506 \times 10^7$	$4.6755 \times 10^4$	488.34	0.90	487.99	0.65
0.3%	0.1152	$2.8603 \times 10^{-15}$	$1.6756 \times 10^7$	$7.0097 \times 10^4$	452.13	1.23	450.64	0.88
0.4%	0.1325	$2.2771 \times 10^{-15}$	$1.6305 \times 10^7$	$9.3437 \times 10^4$	431.69	1.56	429.60	1.11
0.5%	0.1509	$1.3885 \times 10^{-15}$	$1.5844 \times 10^7$	$1.1677 \times 10^5$	411.79	1.85	409.18	1.30

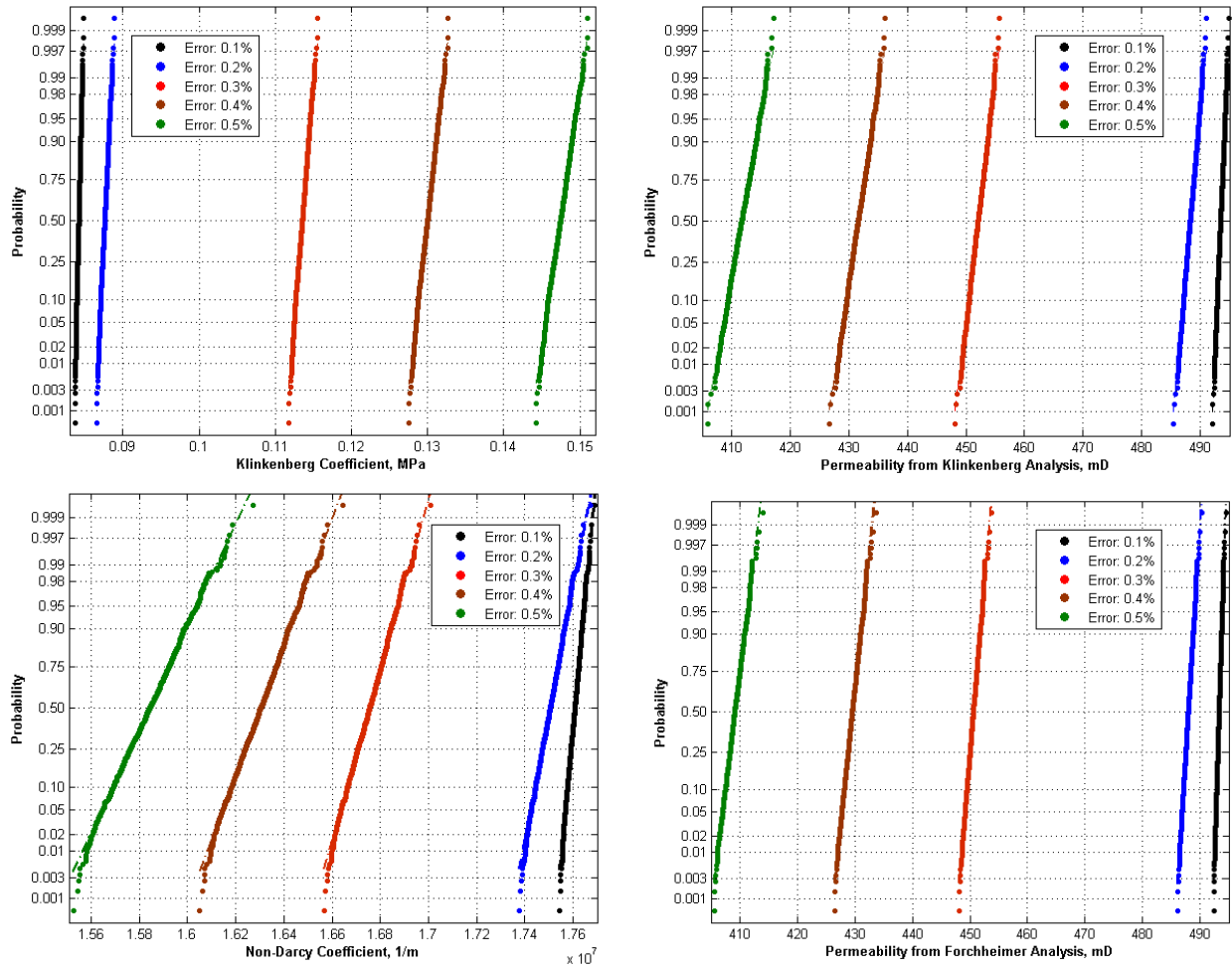


Figure 5.4 Flow Rate Measurement Error Effect on Flow Parameters Estimation

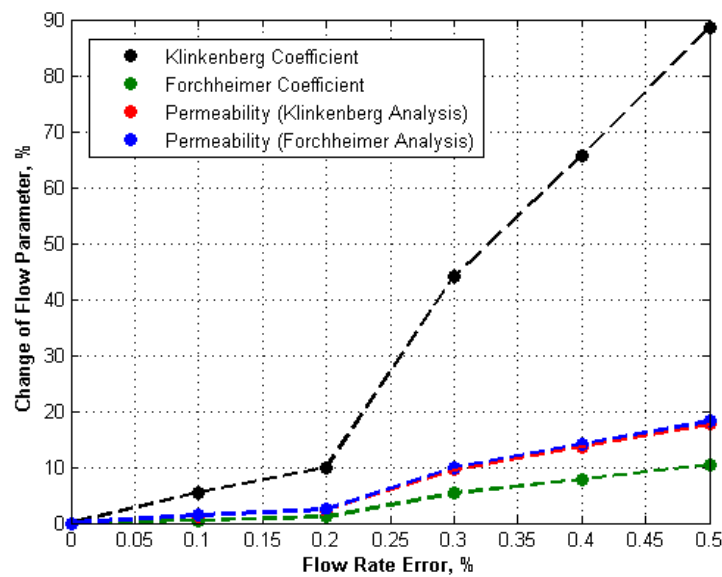


Figure 5.5 Pressure Measurement Error Effect on Mean Flow Parameters Estimation

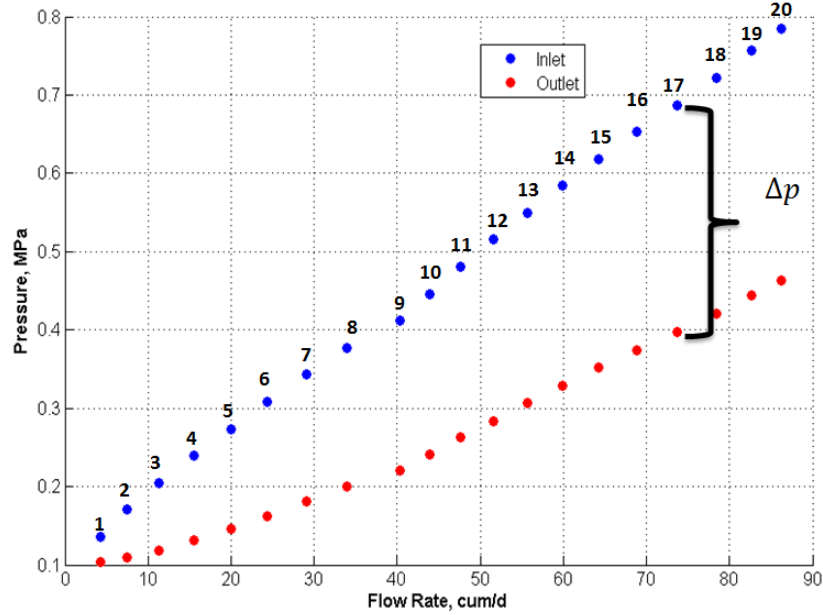


Figure 5.6 Steady State Lab Measurements

Table 5.3 Experiment Condition and Core properties

Gas	N <sub>2</sub>
Temperature, T (°F)	72
Core Length, L (cm)	4.168
Core Diameter, D (cm)	3.7
Porosity, $\phi$ (fraction)	0.267
Confining Pressure (MPa)	34.6

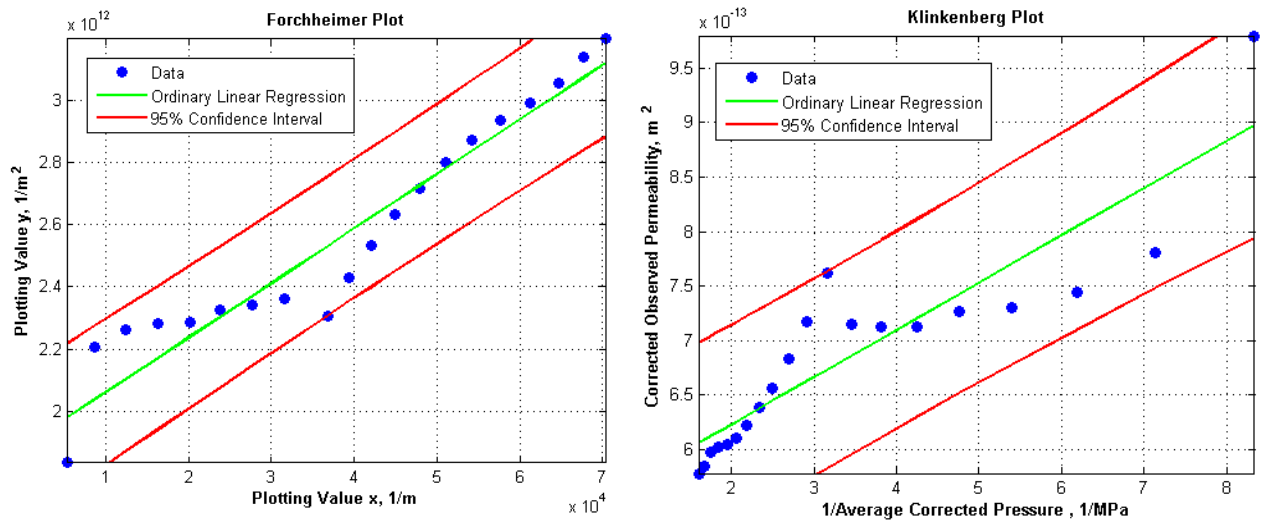


Figure 5.7 Forchheimer and Klinkenberg Plots obtained from Optimization Method for Steady-State Lab Measurements

Table 5.4 Optimization Results of Steady State Lab Experiment

Klinkenberg Coefficient (MPa)		$8.27 \times 10^{-2}$	
Forchheimer Analysis	Estimated	95% Lower Confidence Interval	95% Upper Confidence Interval
Permeability (mD)	541.3	512.1	574.1
Forchheimer Coefficient (1/m)	$1.77 \times 10^7$	$1.53 \times 10^7$	$2.02 \times 10^7$
Klinkenberg Analysis	Estimated	95% Lower Confidence Interval	95% Upper Confidence Interval
Permeability (mD)	548.0	506.0	590.0
Klinkenberg Coefficient (MPa)	$7.91 \times 10^{-2}$	$5.99 \times 10^{-2}$	$9.83 \times 10^{-2}$

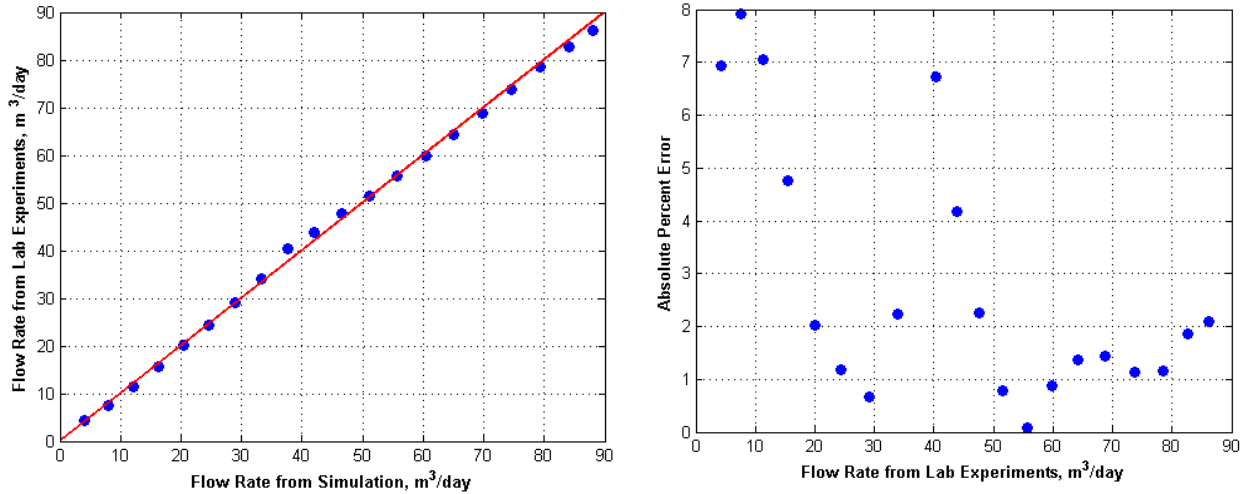


Figure 5.8 Comparison of Lab Flow Rate Measurement and Flow Rate Calculation

Since measurement errors are inevitable, the each measurement point effect on the analysis is investigated with Jackknifing method. In this method, each time one measurement point is removed and the permeability, Klinkenberg coefficient and non-Darcy coefficient are estimated from optimization algorithm. Figure 5.9 gives the scatter plots of all estimated parameters from optimization and red circles give the 95% confidence intervals. The points outside the confidence intervals; 1, 8, and 9, are the measurement points which may contain high measurement errors since removing these points highly effect the estimation. Even though second experiment point inside the confidence intervals, it is removed from further analysis since

it is far from the point clouds. Points suspected to be outliers are confirmed with distance calculations,  $T^2$  and Jackknife distance.  $T^2$  is simple square of the Mahalanobis Distance (MD) (Eqn.5.8). In the MD equation,  $\bar{X}$  and  $S$  are estimated mean and covariance matrix of data. The upper control limit (UCL) (Eqn.5.9) is used to detect outlier, which is shown as blue dashed lines in Figure 5.10. In the UCL calculation,  $N$  and  $p$  are number of observations and variables.  $B$  is beta distribution and  $B_{\left[\alpha, \frac{p}{2}, \frac{n-p-1}{2}\right]}$  is the upper  $\alpha$  quantile (0.05) of  $B_{\left[\frac{p}{2}, \frac{n-p-1}{2}\right]}$ . Since the outlier data distort the estimated mean and covariance matrix, the alternative distance calculation, Jackknife distance, is also checked. In this distance calculation, the observation point is removed from mean and covariance matrix calculation. As the shown in distance plots, the point 1, 8, 9 are outliers.

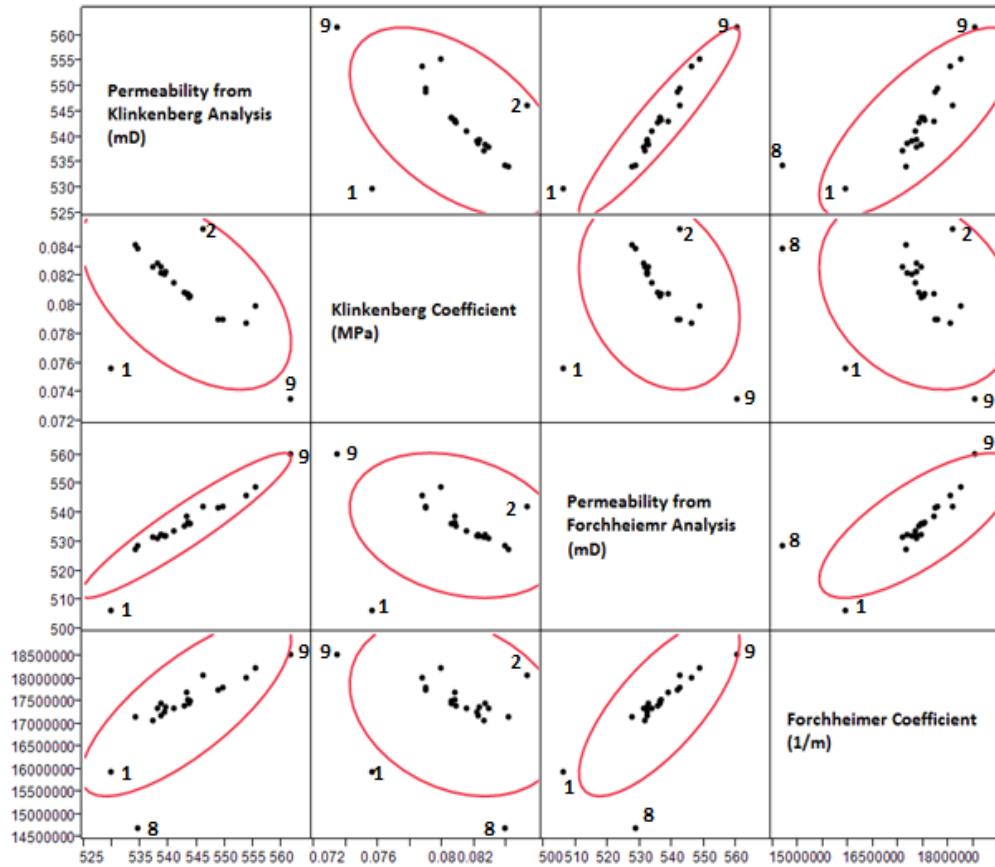


Figure 5.9 Flow Parameters Estimate from Jackknifing Method

$$MD = \sqrt{(X - \bar{X})' S^{-1} (X - \bar{X})} \quad (5.8)$$

$$UCL = \frac{(N - 1)^2}{N} B \left[ \alpha, \frac{p}{2}, \frac{n-p-1}{2} \right] \quad (5.9)$$

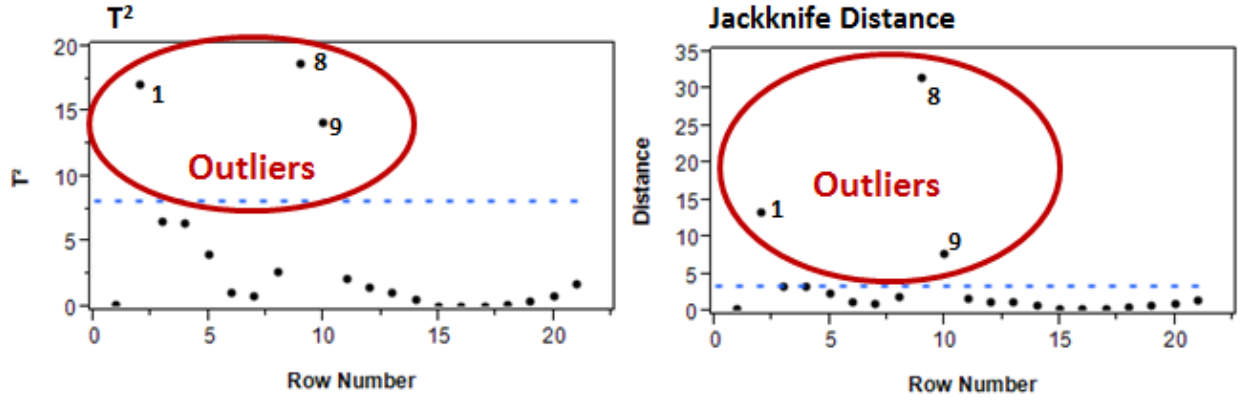


Figure 5.10 Outlier Detection with Distance Methods

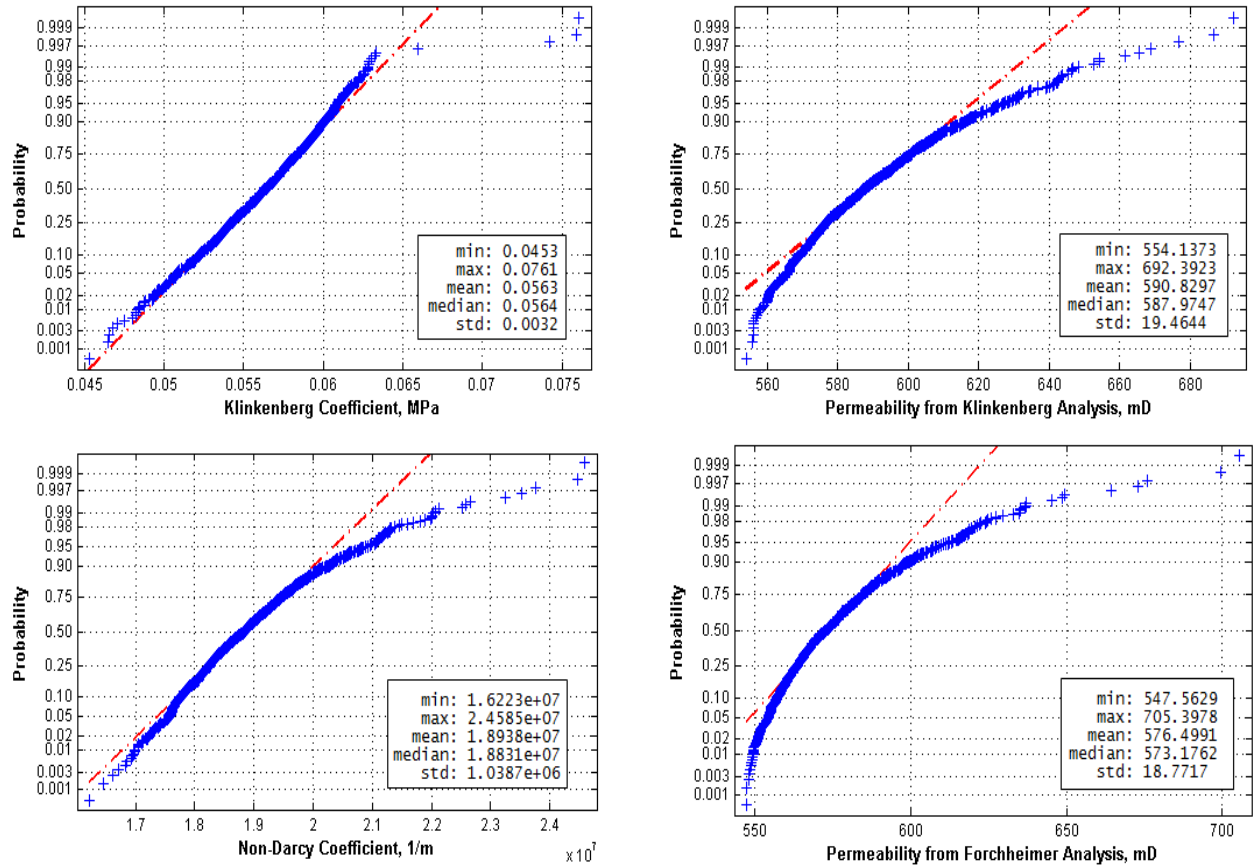


Figure 5.11 Flow Parameters Estimation from Bootstrap for Steady-State Lab Measurements

Lab measurements considered as outliers (1, 2, 8 and 9) are removed. 1000 bootstrap samples are prepared and for each sample permeability, Klinkenberg coefficient and non-Darcy coefficients are obtained from optimization algorithm. Figure 5.11 gives the distribution of Klinkenberg coefficient and permeability obtained from Klinkenberg analysis, and permeability and non-Darcy coefficient obtained from Forchheimer analysis. In this figure, red lines give the normal distribution calculated from 25 and 75 quantiles. Upper and lower quantiles of flow parameters are highly deviates from normality, which indicates that there are still some measurements contain high errors in the analysis. Estimated permeability, Klinkenberg coefficient and non-Darcy coefficient are little different from the ones obtained from optimization with all data. Estimated mean Klinkenberg coefficient obtained from bootstrap is lower, 0.0563 MPa, than the one obtained from optimization with all data, 0.0791 MPa. However, mean permeability obtained from bootstrap is higher, 590.8 mD and 576.5 mD from Klinkenberg and Forchheimer analyses, than the ones obtained from optimization with all data, 541.3 mD and 548.0 mD from Klinkenberg and Forchheimer analyses. Similar to permeability, mean estimated non-Darcy coefficient from bootstrap is higher,  $1.89 \times 10^7$  1/m, than the one obtained from optimization with all data,  $1.77 \times 10^7$  1/m. Generally, confidence interval obtained from bootstrap is larger since this method also considers the all extreme cases. However, flow parameters confidence intervals from bootstrap are generally lower than the confidence intervals from optimization with all data because all possible outlier (measurement with high error) are removed from the analysis (Table 5.5).

Figure 5.12 gives the comparison of the measured flow rates with the ones calculated from 1-D single-phase simulations with mean permeability, Klinkenberg coefficient and non-Darcy coefficient obtained from bootstrap: 583.7 mD, 0.0563 MPa and  $1.89 \times 10^7$  1/m,

respectively. In this figure, the red dots give the previous flow rate errors obtained from optimization with all data. For the first lab measurement, the error is very high, about 12.8%; this measurement is pointed as outlier in Jackknife analysis and should be removed from the analysis. Compared with previous errors, calculated low flow rates and high flow rates measurements are improved. However, the errors between 30 and 55 m<sup>3</sup>/day are still higher.

Table 5.5 Bootstrap Results of Steady State Lab Experiment

Forchheimer Analysis	Estimated	95% Lower Confidence Interval	95% Upper Confidence Interval
Permeability (mD)	576.5	539.7	613.3
Forchheimer Coefficient (1/m)	$1.89 \times 10^7$	$1.69 \times 10^7$	$2.10 \times 10^7$
Klinkenberg Analysis	Estimated	95% Lower Confidence Interval	95% Upper Confidence Interval
Permeability (mD)	590.8	552.7	629.0
Klinkenberg Coefficient (MPa)	$5.63 \times 10^{-2}$	$5.00 \times 10^{-2}$	$6.26 \times 10^{-2}$

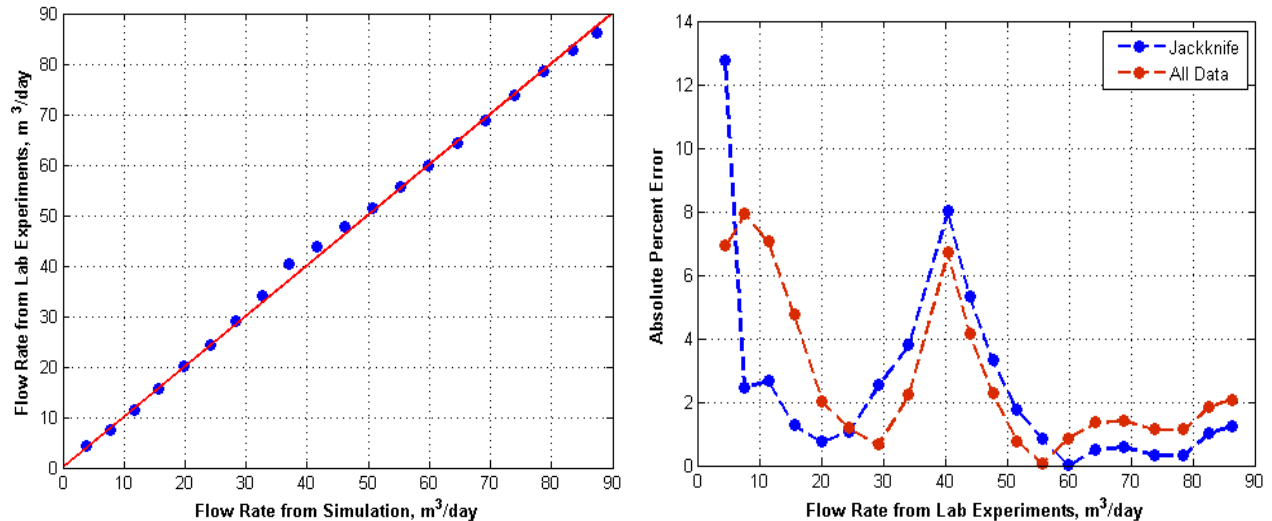


Figure 5.12 Comparison of Lab Flow Rate Measurement and Flow Rate Calculation after Jackknife

In steady-state lab experiments both pressure and flow rates are measured. Pressure errors are generally low and these errors has almost no effect on the mean estimation of the flow parameters, but estimation the confidence interval of the flow parameters. On the other hand,



flow rate errors have significant effect on the estimation process. Therefore, single steady-state analysis may not be reliable. The suggested methodology in steady-state lab experiment is detection of measurements with high errors (outliers) with Jackknife and removal of them from the analysis; and determination of the mean flow parameters and their confidence intervals with bootstrap by using optimization algorithm.

## **5.2 Pulse Decay Experiment Analysis**

For determination of core permeability, Klinkenberg coefficient and non-Darcy coefficient, steady-state experiments are conducted. There are two main disadvantages of steady-state measurements. The first one is that both pressure and flow rates should be recorded for estimation process. Generally, flow rates measurements contain high errors. These errors may result in misleading estimation. In addition, for low-permeability cores, it takes a long time to reach steady-state. For example, for 1  $\mu\text{D}$  core, steady-state stabilization may require a day. There are more than one measurements are required for steady-state lab analysis. Therefore, steady-state flow experiments are time consuming. Brace et al. (1968) suggested a pulse-decay method in which only pressure pulses are recorded; this method is more practical and very short.

Figure 5.13 gives the conventional pulse-decay experimental set-up. The core is placed in the core holder, and confining pressure is applied to prevent flow between the core and core holder. The inlet of the core is attached to the upstream tank, and the outlet of the core may be attached downstream tank or may be open to the atmosphere. Before the experiment, valves 1 and 2 are open, and the system pressure is increased to downstream tank pressure; after the system reaches equilibrium, valves 1 and 2 are closed, and the upstream tank pressure is increased. Then, valve 1 is opened, and upstream and downstream tank pressures are recorded until pressure difference between two tank decreases to 50% - 80% of the initial pressure difference.

After Brace et al. (1968), many study were conducted and analytical solutions were developed. There are many papers in the literature about the how pulse-decay experiment should be conducted and interpreted. Kamath et al. (1992) summarized previous pulse-decay methods and specifies the intervals and conditions at which pulse-decay methods are valid.

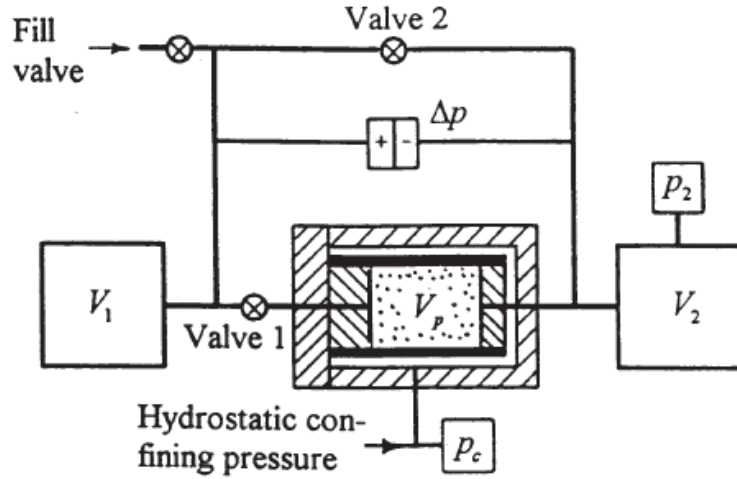


Figure 5.13 Pulse Decay Experiment Setup (S.C. Jones, 1997)

Jones (1972) developed the following analytical equation for the non-Darcy flow by using the Forchheimer equation. The equation he proposed is similar to Forchheimer equation.

$$\frac{P_g}{L} = \frac{\mu u_m}{k} + \beta \rho_{avg} u_{avg}^2 \quad (5.10)$$

Jones approximated the upstream tank pressure,  $P_u$  as ,

$$P_u = P_g = \sqrt{P_1 P_2} \quad (5.11)$$

$P_1$  and  $P_2$  are upstream tank pressures at time  $t_1$  and  $t_2$ .  $u_m$  and  $u_{avg}$  are both mean velocity at the core and given in Eqn.5.12 and Eqn.5.13, respectively;  $u_m$  is corrected for Klinkenberg effect.

$$u_m = \frac{u_0 (P_g + P_a)}{1/2 (P_g + 2P_a + 2b)} \quad (5.12)$$

$$u_{avg} = \frac{u_0(P_g + P_a)}{1/2(P_g + 2P_a)} \quad (5.13)$$

$u_0$  is defined as;

$$u_0 = \frac{y_c P_g}{A(P_g + P)} \quad (5.14)$$

The non-constant volumetric flow rate,  $y_c$  is defined as,

$$y_c = \frac{V_u}{t_2 - t_1} \ln \frac{P_1}{P_2} (1 + \delta G(c)) \quad (5.15)$$

$\delta$  and  $G(c)$  are correction factors for unsteady state flow given in Eqn.5.16 and Eqn.5.17, respectively.

$$\delta = \frac{2\phi AL}{3V_u} \quad (5.16)$$

$$G(c) = \frac{1}{5}(c + 1)(8c^2 - 4c + 3) - \frac{8}{5}(c + 1)^{1/2}c^{1/5} \quad (5.17)$$

$$c = \frac{(2(P_a + b))^2}{4p_g(P_g + 2(P_a + b))} \quad (5.18)$$

From Eqn.5.10, the plotting groups are defined as:  $x$  axis =  $\rho_{avg} u_{avg}^2 / \mu u_m$  and  $y$  axis =  $P_g / \mu u_m L$ . Permeability and non-Darcy coefficient can be calculated from intercept ( $1/k$ ) and slope ( $\beta$ ) of the plot, respectively. To calculate  $u_m$ , Klinkenberg coefficient should be known. It can be estimated from trial and error procedure or it can be calculated iteratively. In this study, Klinkenberg coefficient is estimated by maximizing the coefficient of determination of the plot of Eqn.5.10.

Table 5.6 gives the lab experiment conditions and experiment results for 2 core samples - 2C (Dolomite) and 3C (Castlegate Sandstone) cores - taken from Schlumberger. Figure 5.14 gives the pressure change with time during the experiments. Figure 5.15 gives the plot of Eqn.5.10 for 2C and 3C cores data. For 2C data, Jones approximation is good, linear fit is almost

perfect. However, for 3C data, scattered plot is obtained from this approximation. This may indicate the measurement errors. Permeability, Klinkenberg coefficient and non-Darcy coefficient are 79 mD, 0.0271 MPa,  $3.70 \times 10^{10}$  1/m and 1419 mD,  $5.573 \times 10^{-5}$  MPa and  $6.81 \times 10^8$  1/m for 2C and 3C cores, respectively. Permeability of cores calculated from Jones method are close to measured values; however, calculated Klinkenberg coefficients are different from recorded values and calculated Forchheimer coefficients are more two orders of magnitude than recorded values.

Table 5.6 Core Properties and Lab Experiment Conditions

	2C Core	3C Core
Gas	He	He
Core Diameter, D(cm)	3.768	3.617
Core Length, L(cm)	2.528	2.712
Porosity, $\phi$ (fraction)	0.216	0.260
Permeability, k(mD)	78	1369
Klinkenberg Coefficient, b(MPa)	0.01062	0.00193
Non-Darcy Coefficient, $\beta$ (1/m)	$3.74 \times 10^8$	$6.28 \times 10^6$
Upstream Tank Volume, $V_u$ (cc)	1885	1885
Initial Tank Pressure, $P_u^0$ (MPa)	1.34	0.58
Atmospheric Pressure, $P_a$ (MPa)	0.1015	0.1015
Temperature, T(°F)	68.9	68.9
Total Simulation Time, t(sec)	114.8	10.1

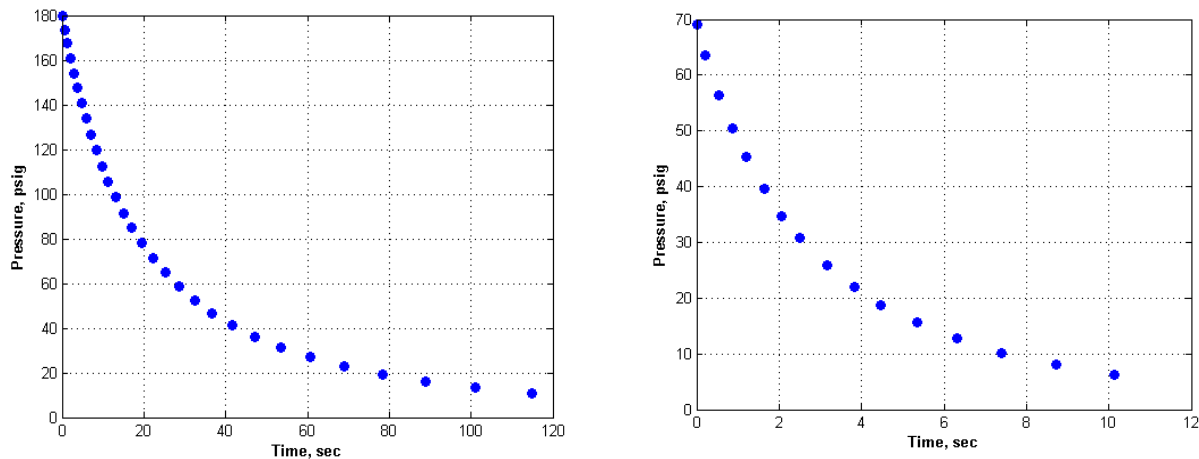


Figure 5.14 Upstream Tank Pressure Change with Time – 2C Core Data (left), 3C Core Data (right)

By using Jones method results, pulse-decay simulations are conducted by imposing the measured upstream tank pressures as a boundary condition. Flow rate out of the tank and flow rate at the core inlet are calculated at standard condition and they are compared (Figure 5.16). Even though Klinkenberg coefficients and non-Darcy coefficients are different, flow rate out of the tank and flow rate at the core inlet are similar for both data sets.

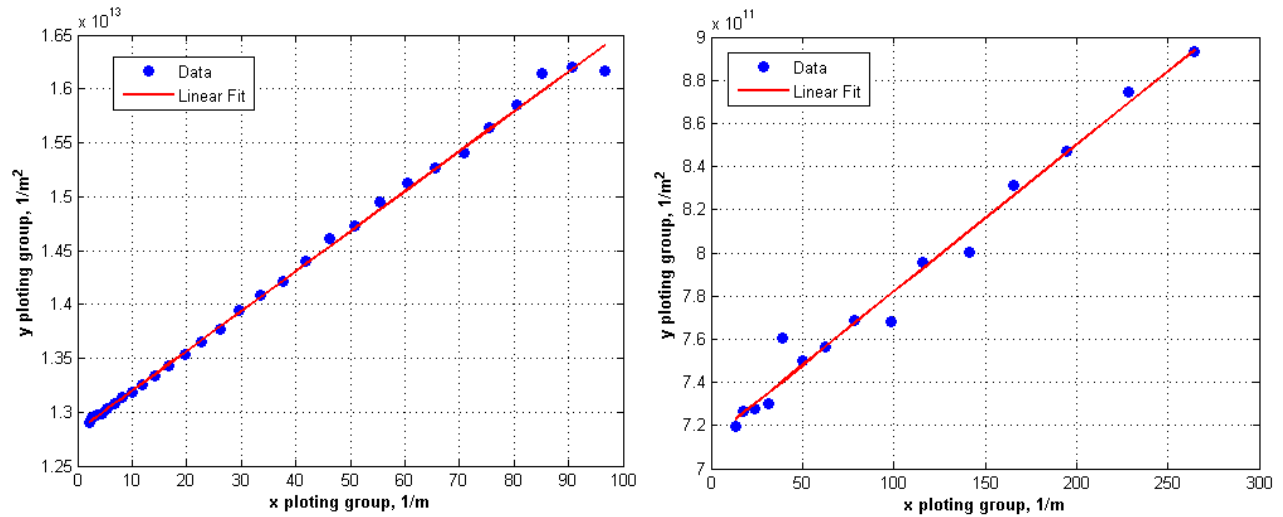


Figure 5.15 Jones Approximation Plot for 2C Core Data (left) and 3C Core Data (right)

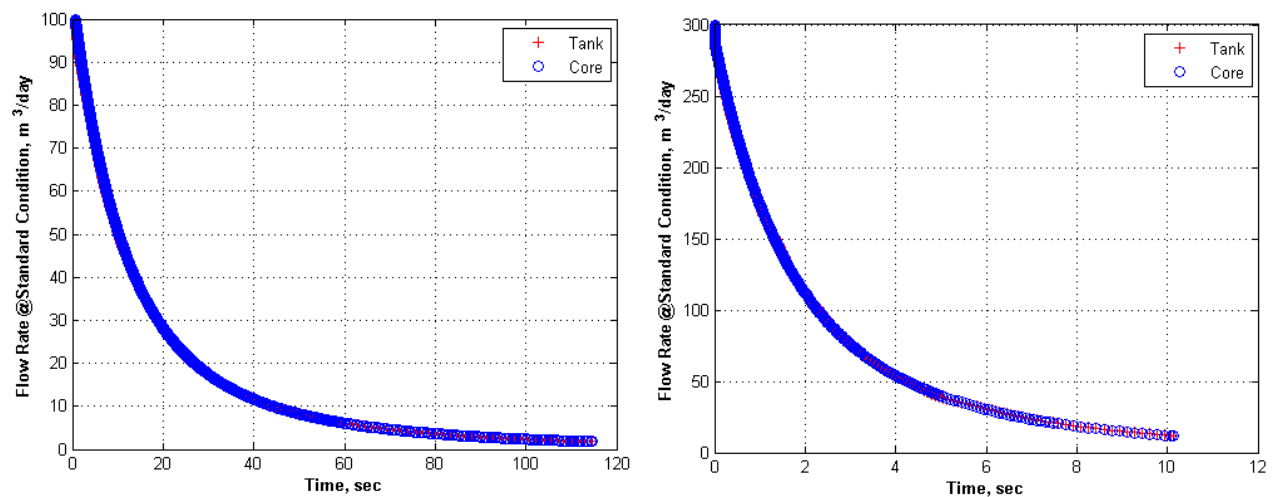


Figure 5.16 Jones Method –Flow Rate Comparison for 2C Core Data (left) and 3C Core Data (right)

Bootstrap sampling method is used to find the confidence interval of calculated flow properties. 1000 samples are prepared for 2C and 3C cores data and then permeability, Klinkenberg coefficient and non-Darcy coefficient are calculated for each sample. Figure 5.17 and Figure 5.18 give the results for 2C and 3C data. In these figures, red circles give 95% confidence ellipses. For 2C core data, estimated mean permeability, Klinkenberg coefficient and non-Darcy coefficient are 78.96 mD, 0.0272 MPa and  $3.72 \times 10^{10}$  1/m, respectively. For 3C core data, estimated mean permeability, Klinkenberg coefficient and non-Darcy coefficient are 1419.20 mD,  $2.80 \times 10^{-5}$  MPa and  $6.82 \times 10^8$  1/m, respectively.

Bootstrap gives much more reliable interval for parameter estimation. For 2C core data, permeability, Klinkenberg coefficient and non-Darcy coefficient intervals are 77.5 mD – 80 mD, 0.024 MPa – 0.032 MPa and  $3.45 \times 10^{10}$  1/m –  $3.95 \times 10^{10}$  1/m, respectively. However, for 3C data, most of the Klinkenberg coefficients are close to 0. This indicates that objective function cannot be minimized. The problem about 3C core data is experiment duration is too short. Even if 3C core has high permeability, initial tank pressure is much more lower, 0.476 MPa; therefore experiments only lasts 10.1 sec. Comparison of these two samples indicates the importance of the experiment duration; as experiment time decreases, error effect on estimation process increases.

Jones method is not give a unique solution because of measurement errors. Therefore; for each sample, pulse decay simulation is conducted and the difference between simulated pressure and observed pressure is calculated. Figure 5.19 and Figure 5.20 give the mean percent error plots for 2C and 3C cores, respectively. For 2C core the minimum and maximum mean errors are about 0.205% and 0.337%, respectively. Even though most of the estimated Klinkenberg coefficients are close to 0 for 3C core, simulated pressures are very consistent with

the observed pressures; the minimum and maximum mean errors are about 0.074% and 0.393%, respectively. The low errors can be results of negligible inertial effects during the pulse-decay experiments.

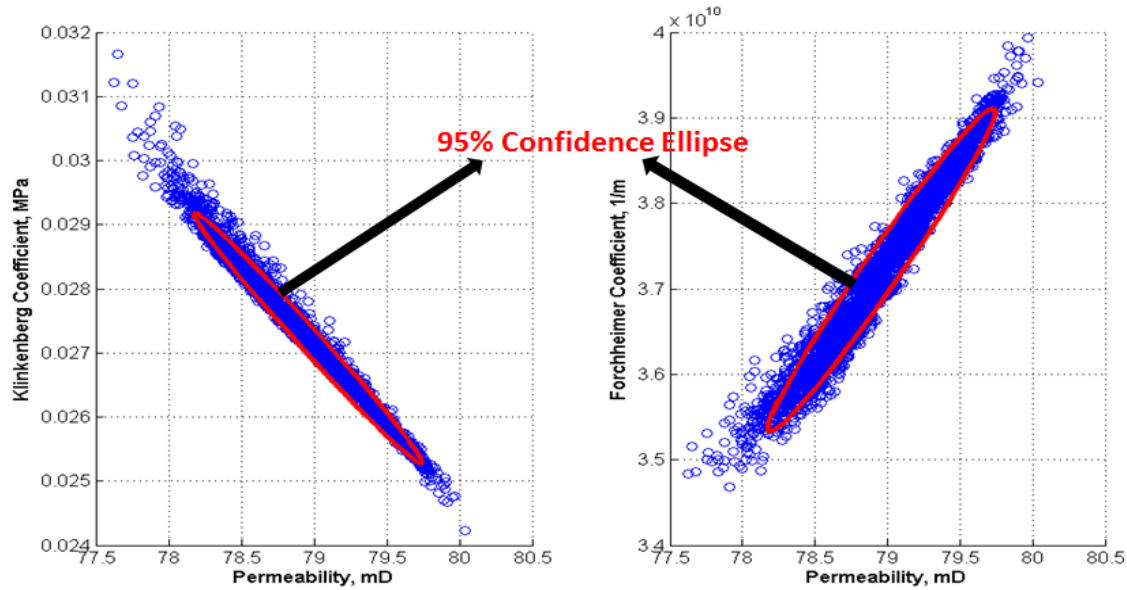


Figure 5.17 Bootstrap Sampling - Permeability, Klinkenberg Coefficient and Forchheimer Coefficient for 2C Core Data

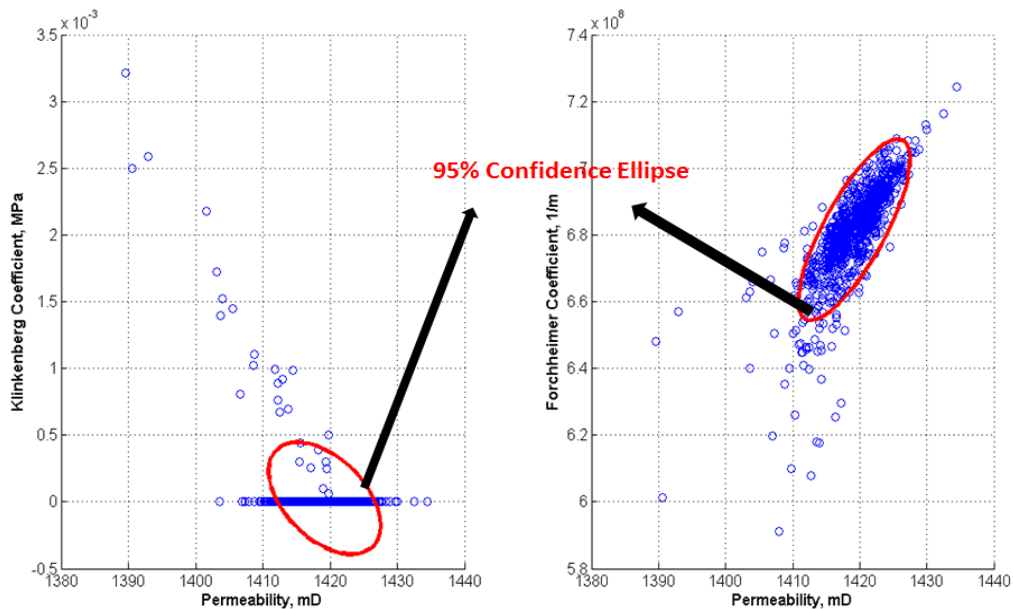


Figure 5.18 Bootstrap Sampling - Permeability, Klinkenberg Coefficient and Forchheimer Coefficient for 3C Core Data

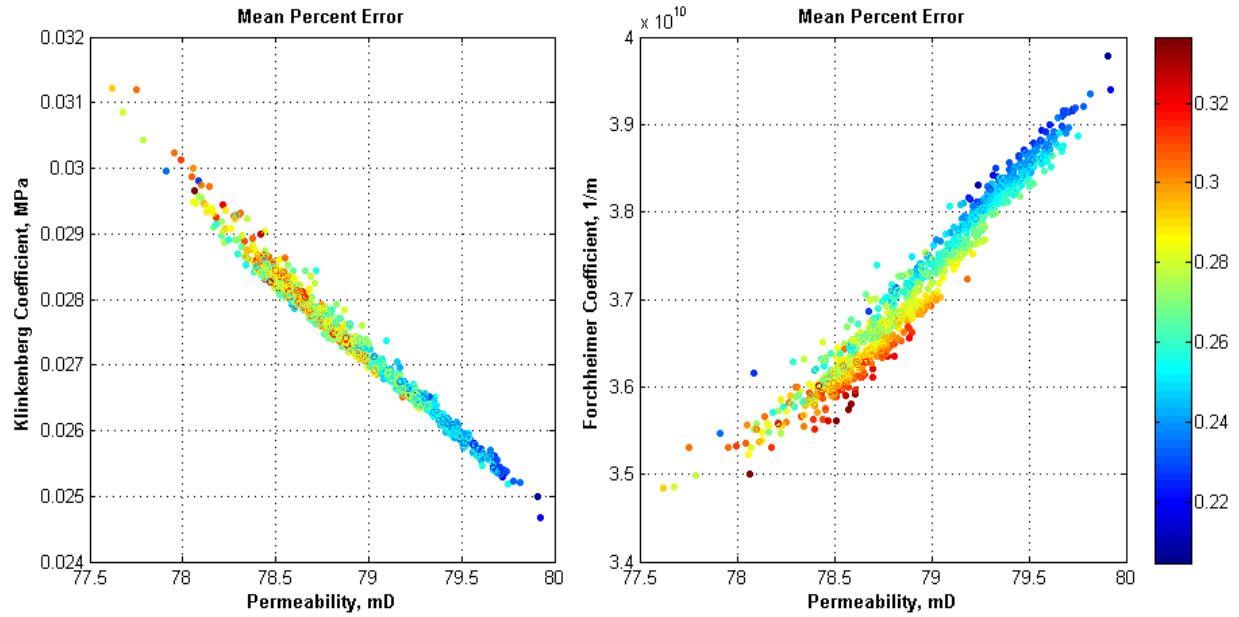


Figure 5.19 Error Analysis of Pulse-Decay Simulation of 2C Core

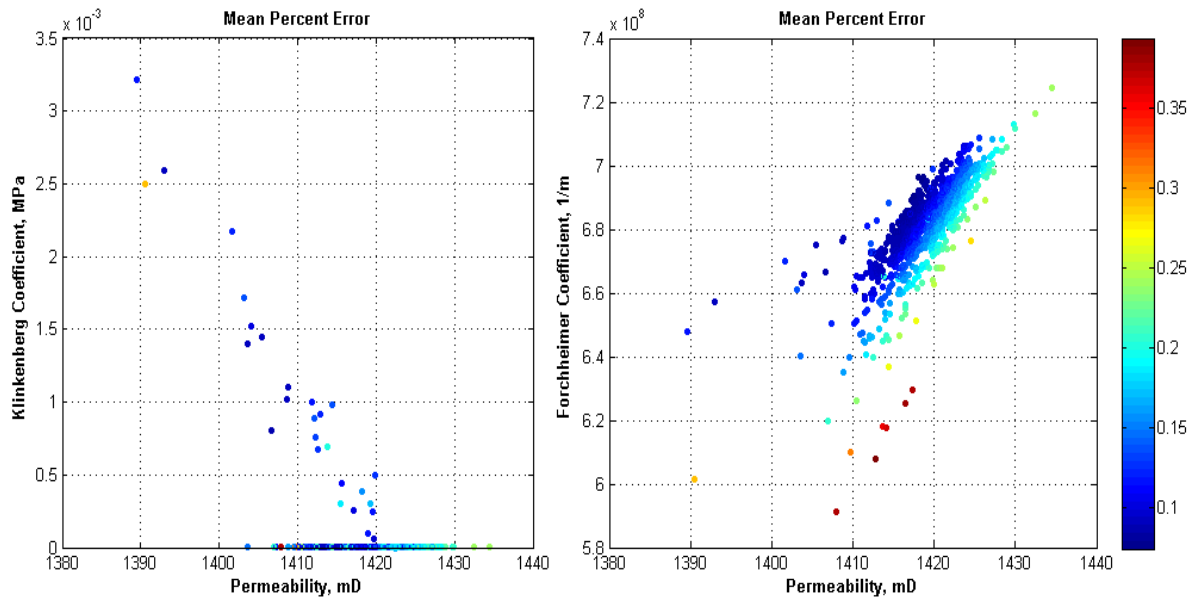


Figure 5.20 Error Analysis of Pulse Decay Simulation of 3C Core

To see how inertial effects are changed during the experiment, Forchheimer number is calculated at different core location (Eqn.5.19) and non-Darcy effect, ratio of pressure gradient caused by inertial effect to total pressure gradient, is calculated (Eqn.5.20) (Zeng & Grigg, 2003). Non-Darcy effect simply indicates the error fraction if inertial effects are neglected.



Figure 5.21 and Figure 5.22 give the non-Darcy effect plot for 2C and 3C core experiments, respectively. For both experiment, non-Darcy effects are significant at the core inlet at early time of the experiments due to high flow rates and decrease with time as flow rates decrease due to the decrease in pressure difference (Figure 5.23). At the outlet, non-Darcy effects increase as the flow rates increase then decrease. The point where all lines of non-Darcy effects meets indicates that flow rate is almost constant along the core. For 2C core experiment, up to 10 seconds, neglecting inertial effects leads to more than 10% error in pressure gradient. On the other hand, for 3C core, only up to 2 seconds, neglecting the inertial effects lead to more than 10% error in pressure gradient.

$$F_o = \frac{k\beta\rho u}{\mu} \quad (5.19)$$

$$E = \frac{F_o}{(1 + F_o)} \quad (5.20)$$

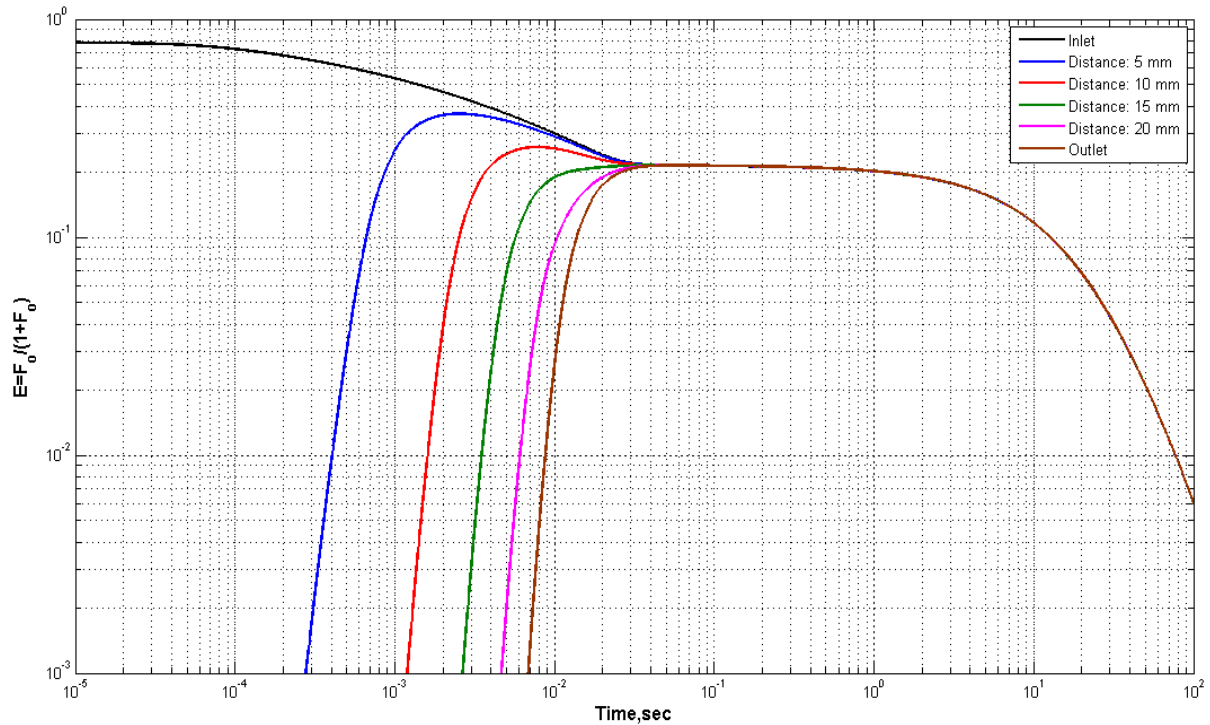


Figure 5.21 Non-Darcy Effect of 2C Core Experiment

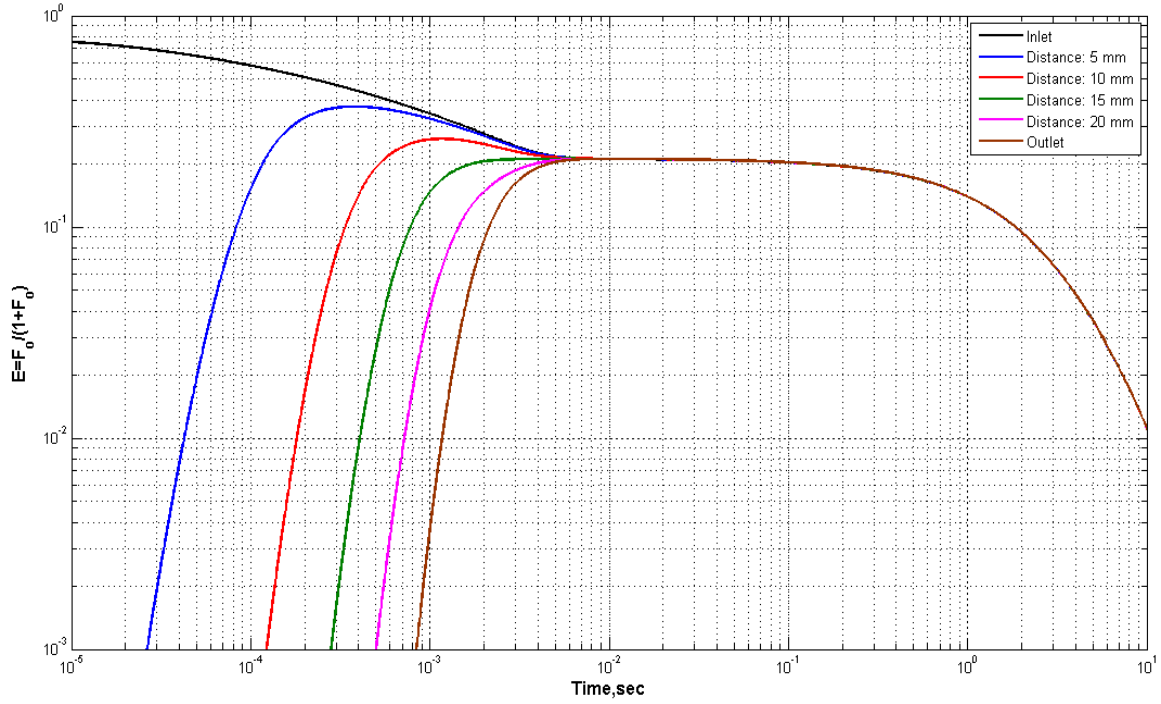


Figure 5.22 Non-Darcy Effect of 3C Core Experiment

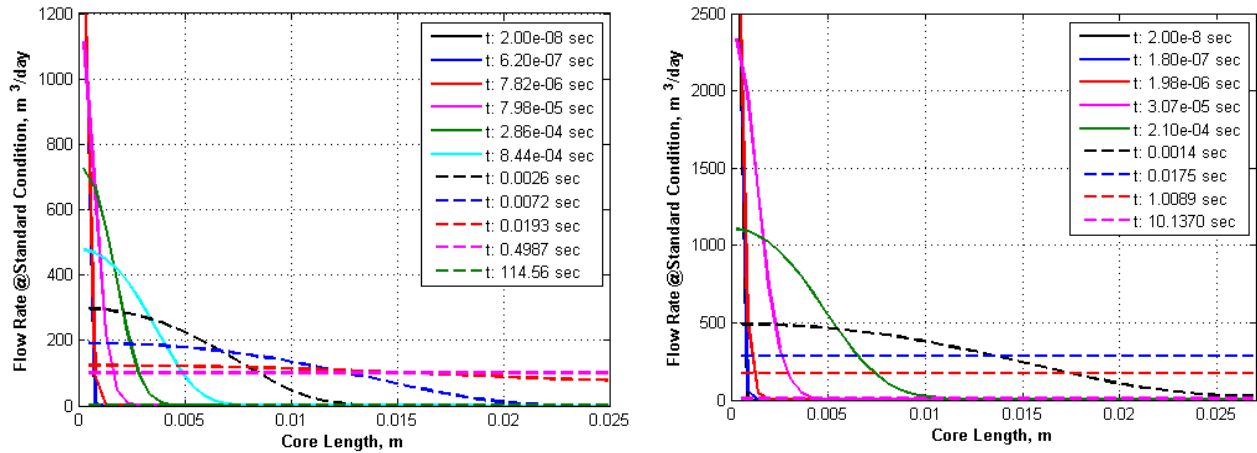


Figure 5.23 Flow Rate Along the 2C Core (left) and 3C Core (right)

To emphasize the inertial effects importance, permeability and Klinkenberg coefficient are estimated from Kaczmarek method. Kaczmarek (2008) derived the analytical solutions for pulse decay experiments with the following assumptions:

1. Gas flux is constant along the sample.
2. Non-Darcy effects are negligible.

3. Gas is ideal.
4. Porosity and permeability change is negligible during the pulse decay experiment.

For single reservoir test, the upstream pressure,  $P_u$ , at the upstream tank,  $V_u$ , is calculated as;

$$P_u = \frac{(2b + P_a) \frac{(P_u^0 - P_a)}{(P_u^0 + 2b + P_a)} + P_a \exp\left(\frac{Ak_l}{\mu LV_u} (b + P_a)t\right)}{\exp\left(\frac{Ak_l}{\mu LV_u} (b + P_a)t\right) - \frac{(P_u^0 - P_a)}{(P_u^0 + 2b + P_a)}} \quad (5.21)$$

$P_u^0$  and  $P_a$  are initial tank pressure and atmospheric pressure, respectively. Pressure along the core is given as;

$$P(x, P_u) = -b + \sqrt{(P_a + b)^2 + \frac{1}{L} [P_u(P_u + 2b) - P_a(P_a + 2b)]x} \quad (5.22)$$

$x$  is the distance from the outlet of the core. Figure 5.24 gives the comparison of the inlet pressure calculated from Eqn.5.22 and measured during experiments for 2C and 3C cores. For both experiments, calculated pressures perfectly match with the experiment data. Estimated permeability and Klinkenberg coefficient for 2C and 3C cores are 59.02 mD and 984.65 mD, and 0.1064 MPa and 0.0626 MPa, respectively.

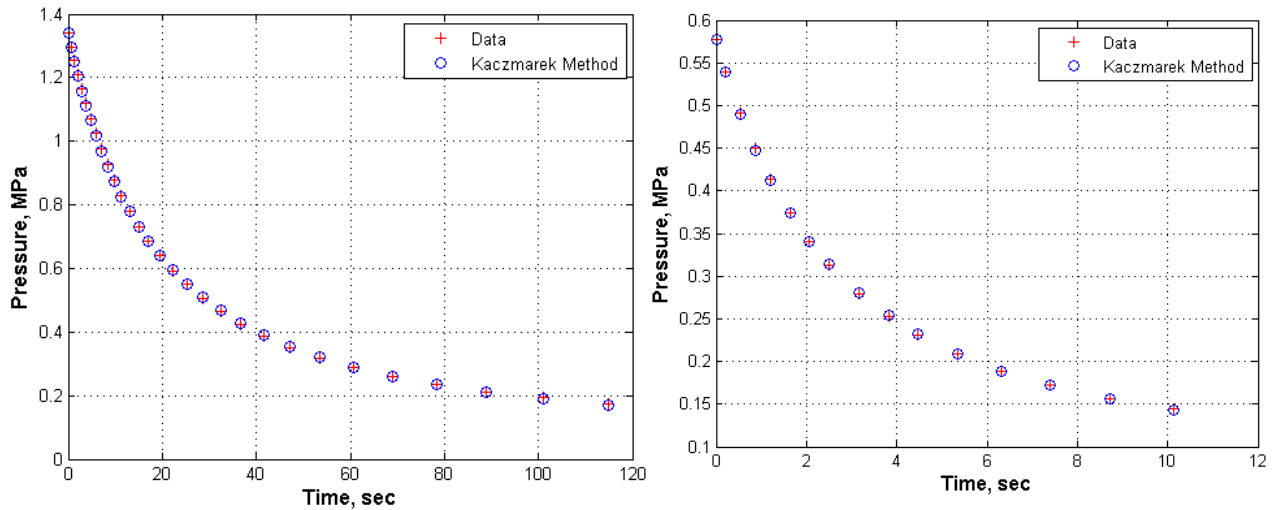


Figure 5.24 Kaczmarek Method - Inlet Pressure Comparison with for the 2C Core (left) and 3C Core (right)

To confirm the estimated parameters, pulse decay simulations are conducted with neglecting the inertial effects ( $\beta = 0$  1/m). Figure 5.25 gives the comparison of the flow rate out of the tank and the flow rate at core inlet for 2C and 3C cores. There are differences between flow rates at early times where inertial effects are not negligible due to high flow rates. To find the estimation confidence intervals, 1000 bootstrap samples are prepared and permeability and Klinkenberg coefficient are found from Kaczmarek method. For each sample, pulse-decay simulation is conducted and the difference between measured inlet pressure and simulated inlet pressure are calculated. Figure 5.26 and Figure 5.27 give the mean percent error between the pressures for 2C and 3C core, respectively. For 2C core, neglecting the inertial effect leads to high errors, the minimum and maximum mean errors are 6.6% and 7.8%, respectively. For 3C core, errors are lower; the minimum and maximum mean errors are 0.35% and 0.8%, respectively. This indicates that inertial effects are not significant for 3C core experiment; this may reason for parameters cannot be estimated from Jones method.

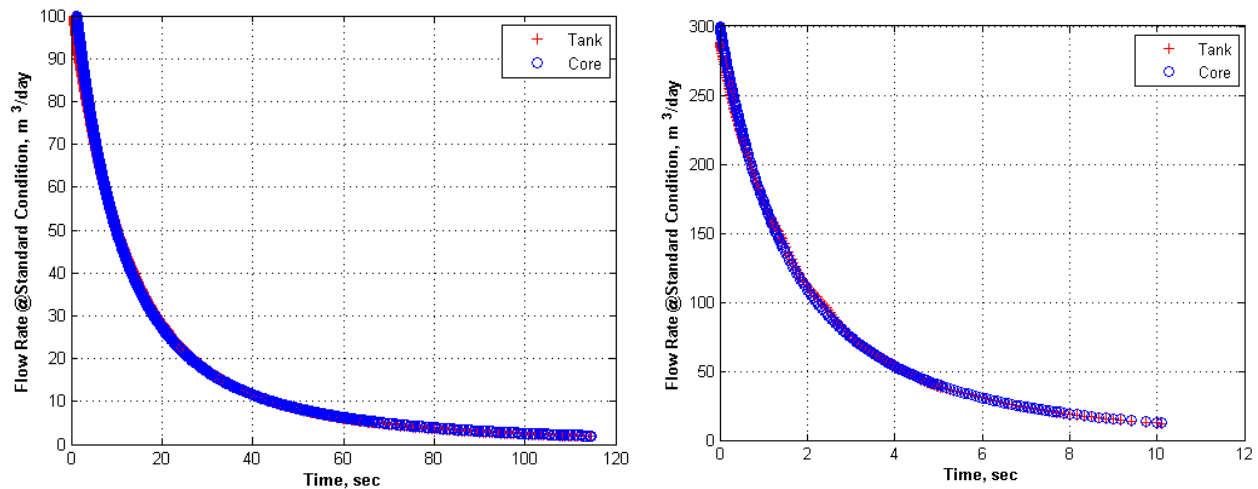


Figure 5.25 Kaczmarek Method –Flow Rate Comparison for 2C Core Data (left) and 3C Core Data (right)

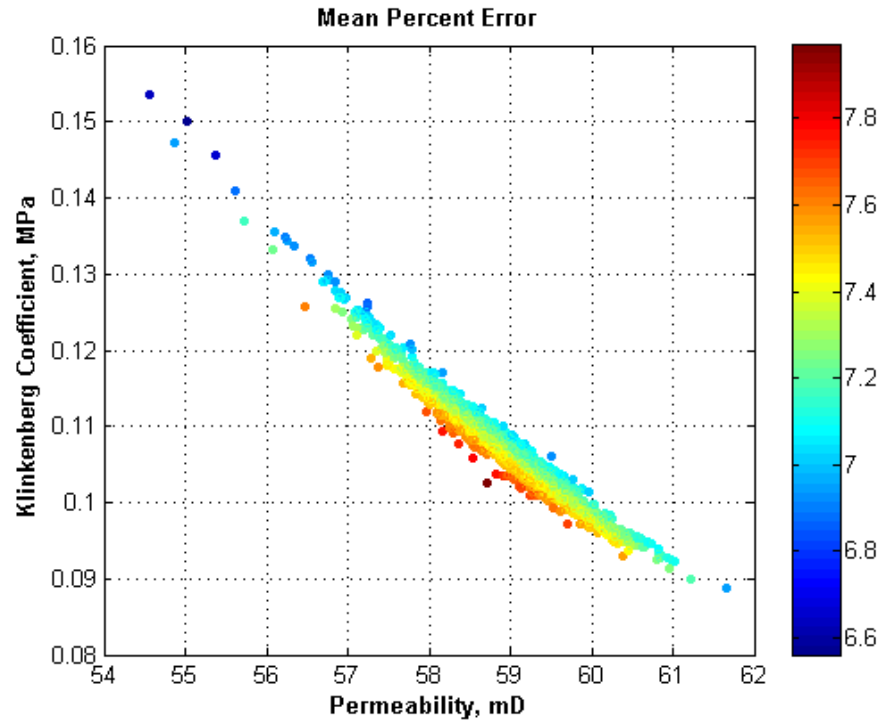


Figure 5.26 Kaczmarek Method –Error Analysis of Pulse Decay Simulation of 2C Core

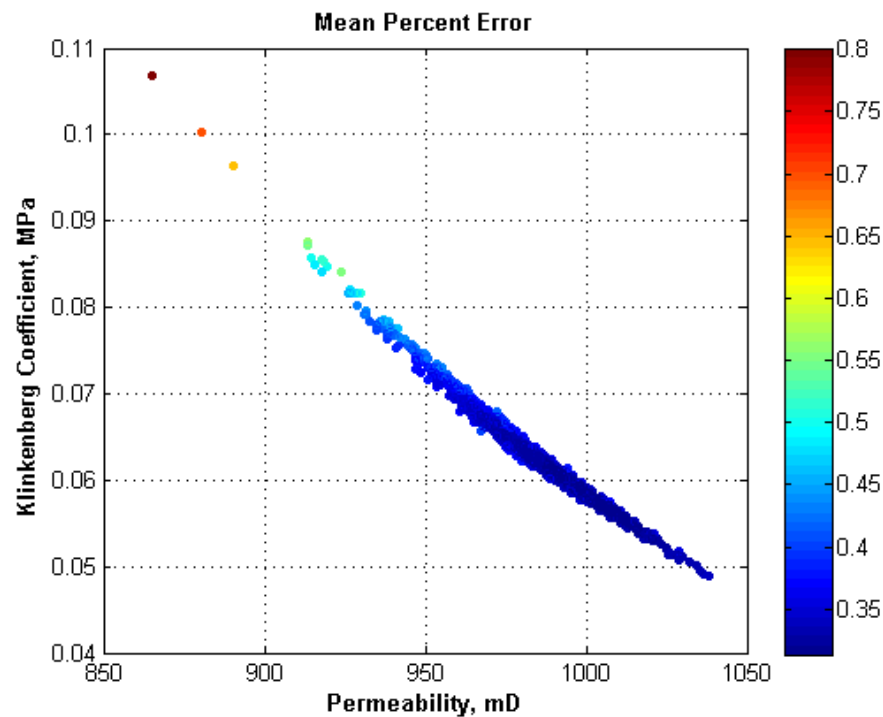


Figure 5.27 Kaczmarek Method –Error Analysis of Pulse Decay Simulation of 3C Core

It is proposed that the main difference between two experiments is experiment duration. To estimate the time effect on the parameter estimate, 2C core experiment data is used. Each time at the end of the data is removed and 1000 bootstrap sample is prepared and for each sample flow parameters are estimated with Jones method. Figure 5.28, Figure 5.29 and Figure 5.30 gives the permeability, Klinkenberg coefficient and non-Darcy coefficient estimation change with experiment duration. In these figures, the blue '+' sign gives the calculated flow parameter from bootstrap samples and red lines give the standard deviations. As experiment duration decreases, the confidence intervals of the estimated flow parameters increase. Before 36.73 sec, the estimated Klinkenberg coefficients decrease, they are close to zero and both estimated permeability and Forchheimer coefficient increase.

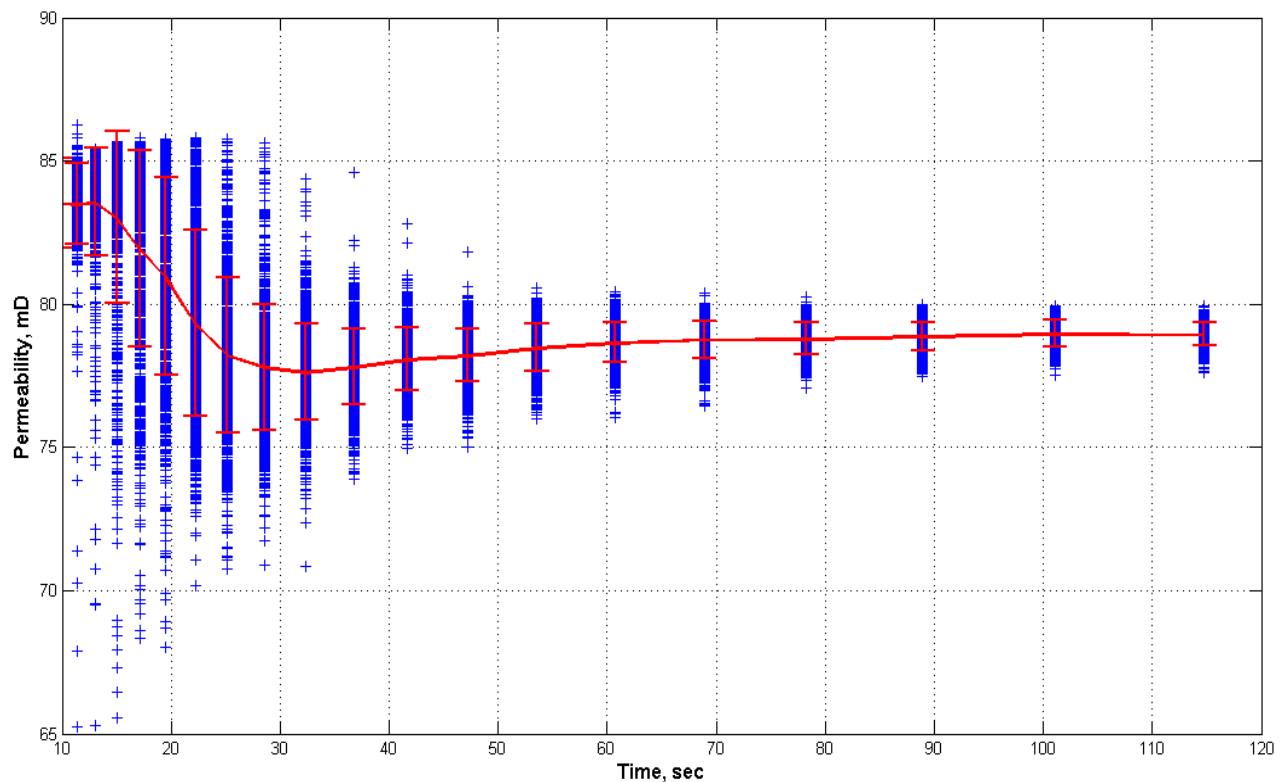


Figure 5.28 Experiment Time Duration Effect on Permeability Estimation

For accurate estimation of well deliverability, correct estimation of flow parameters are necessary. Flow parameters estimation effect on production is investigated with reservoir

simulations. For each estimation, reservoir simulations are conducted by using compositional simulator GEM (CMG, 2013) and cumulative productions are compared for 10 years production (Figure 5.31). Reservoir length is 2000 m in  $x$  and  $y$  directions. Grid numbers in  $x$  and  $y$  directions are 65 and refined grids are used near the wellbore. The wellblock is located at the center and its dimension is 0.5 m. Reservoir porosity and irreducible water saturation are 0.25 and 0.2, respectively. Initial reservoir pressure is 35 MPa. For production constrain, maximum production rate and minimum flowing bottom pressure are chosen as  $0.5 \times 10^6 \text{ m}^3/\text{day}$  and 5 MPa, respectively. As experiment duration decreases, the flow properties estimation intervals increase, so does the production estimation interval. The shortest experiment duration, the maximum and minimum production estimations are  $1.80 \times 10^8 \text{ m}^3$  and  $1.62 \times 10^8 \text{ m}^3$ , respectively. The difference is about  $1.83 \times 10^7 \text{ m}^3/\text{m}$ .

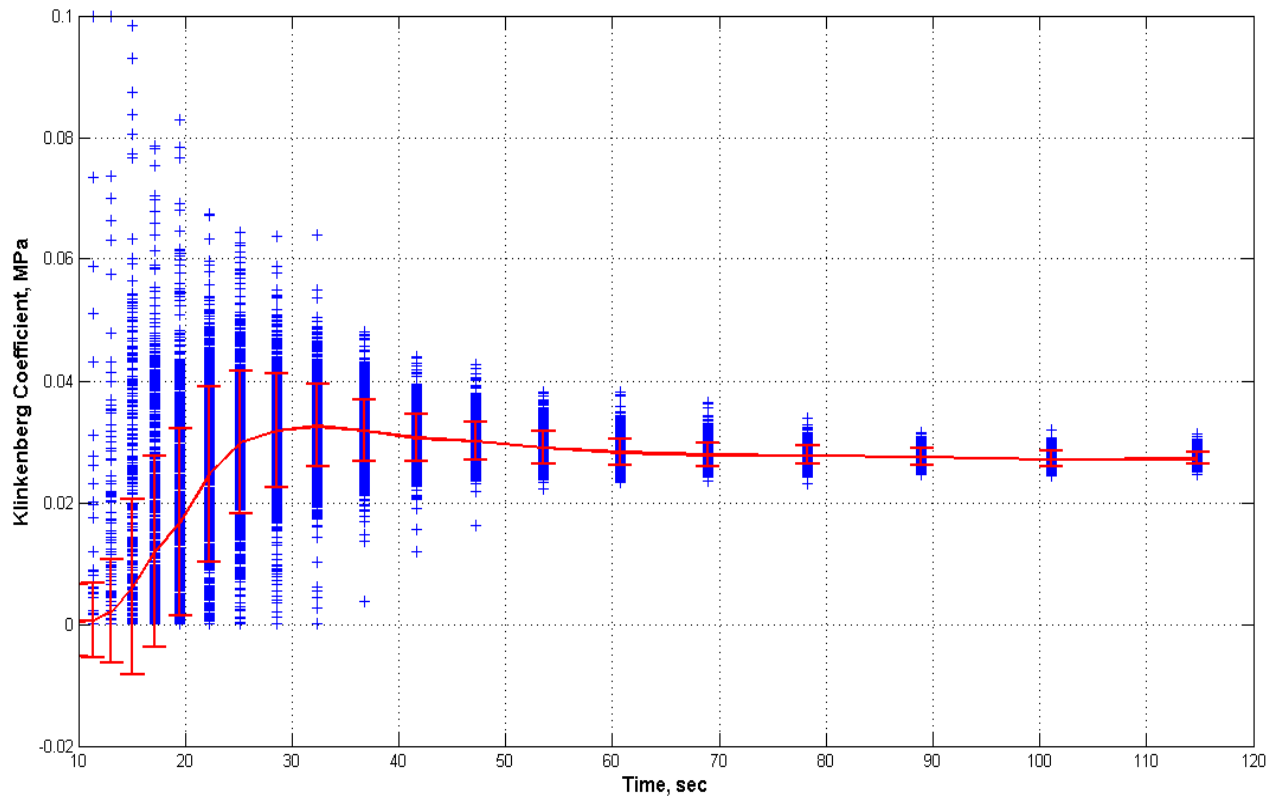


Figure 5.29 Experiment Time Duration Effect on Klinkenberg Coefficient Estimation

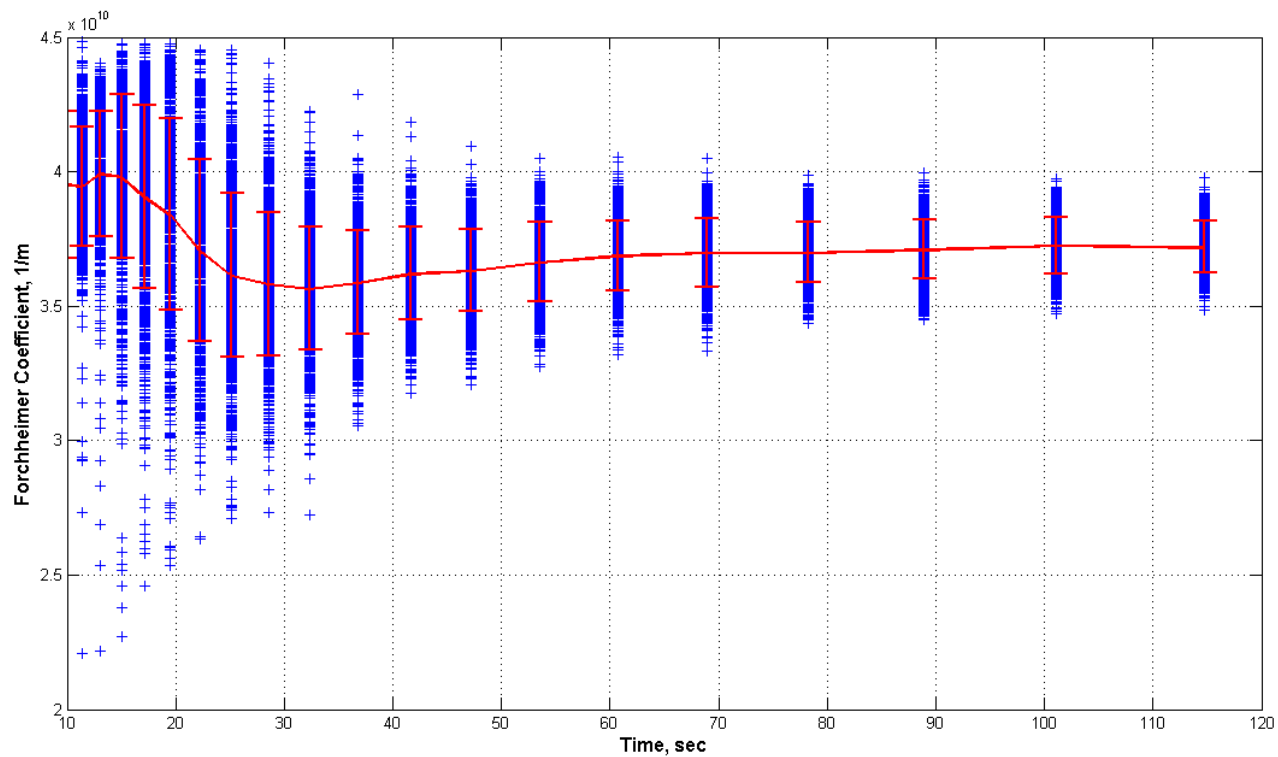


Figure 5.30 Experiment Time Duration Effect on Non-Darcy Coefficient Estimation

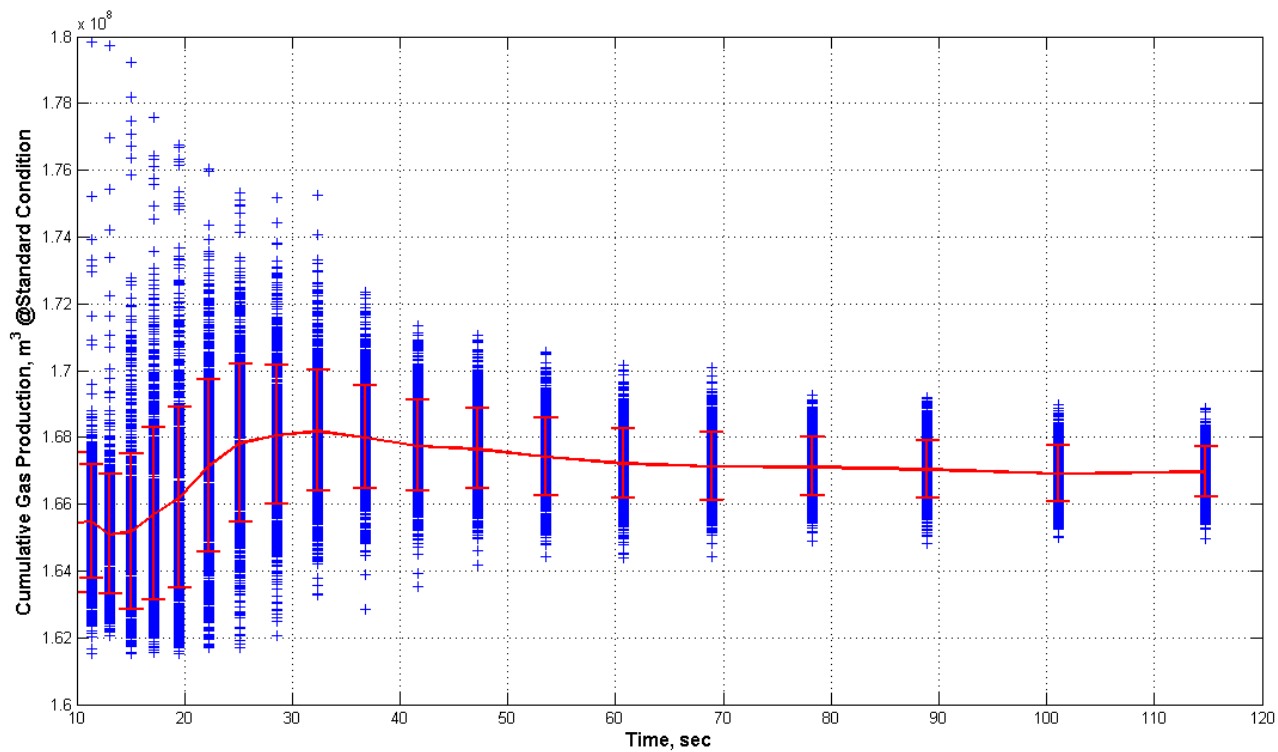


Figure 5.31 Flow Parameter Estimation Effect on Cumulative Gas Production



### 5.3 Pulse Decay Simulation Algorithm and Validation

Permeability, Klinkenberg coefficient and non-Darcy coefficient can be estimated from pulse-decay experiments with Jones method. To validate the flow parameters estimated from pulse-decay experiments, the simulator is developed and it is validated with analytical equation. Non-Darcy flow is modelled with Eqn.5.23 (Li, Svec, Engler, & Grigg, 2001).

$$\nabla \left[ \delta \frac{k_{ap}}{B\mu} \nabla P \right] + \frac{q}{V_b \rho_{sc}} = \frac{\phi c}{B} \frac{\partial P}{\partial t} \quad (5.23)$$

$\delta$  is controlling parameter including the inertial effects. Velocity,  $u$ , is calculated from modified Darcy equation. In this equation  $k_{ap}$  is apparent permeability including the slippage effects.

$$\delta = \frac{1}{1 + \frac{\beta \rho k_{ap}}{\mu} |u|} \quad (5.24)$$

$$u = -\delta \frac{k_{ap}}{\mu} \frac{\partial P}{\partial x} \quad (5.25)$$

$$k_{ap} = k \left( 1 + \frac{b}{P_{av}} \right) \quad (5.26)$$

$B_g$  is formation volume factor and it is defined as;

$$B_g = \frac{\rho_{sc}}{\rho} \quad (5.27)$$

Multiplying both side of Eqn.5.23 with density at standard condition,  $\rho_{sc}$ , and bulk volume,  $V_b(\Delta x \Delta y \Delta z)$ , and using Eqn.5.27, Eqn.5.23 becomes,

$$\nabla \left[ \delta \frac{\rho k_{ap}}{\mu} V_b \nabla P \right] + q = \rho \phi c V_b \frac{\partial P}{\partial t} \quad (5.28)$$

To model the flow more precise, point distributed grid system is used for discretization. In this method, points are placed on the boundaries of the reservoir and reservoir interior and block boundaries are placed at the midpoint of two adjacent points. Central difference approximation is used for spatial derivatives.

$$\begin{aligned}
& \left( \nabla \left[ \delta \frac{\rho k_{ap}}{\mu} V_b \nabla P \right] \right)_i \\
&= \frac{1}{\Delta x} \left[ \left( \delta \frac{\rho k_{ap}}{\mu} A_x \right)_{i+\frac{1}{2}} (P_{i+1} - P_i) - \left( \delta \frac{\rho k_{ap}}{\mu} A_x \right)_{i-\frac{1}{2}} (P_i - P_{i-1}) \right]
\end{aligned} \tag{5.29}$$

Controlling parameter and velocity terms are discretized as;

$$\delta_{i\pm\frac{1}{2}} = \frac{1}{1 + \beta \left( \frac{\rho k_{ap}}{\mu} \right)_{i\pm\frac{1}{2}} |u|_{i\pm\frac{1}{2}}} \tag{5.30}$$

$$u_{i+\frac{1}{2}} = -\delta_{i+\frac{1}{2}} \left( \frac{k_{ap}}{\mu} \right)_{i+\frac{1}{2}} \left( \frac{P_{i+1} - P_i}{\Delta x} \right) \tag{5.31}$$

$$u_{i-\frac{1}{2}} = -\delta_{i-\frac{1}{2}} \left( \frac{k_{ap}}{\mu} \right)_{i-\frac{1}{2}} \left( \frac{P_i - P_{i-1}}{\Delta x} \right) \tag{5.32}$$

For fluid density,  $\rho$ , and viscosity,  $\mu$ , at the boundaries arithmetic average is used.

Backward difference approximation is used for time derivative.

$$\frac{\partial P}{\partial t} = \frac{P^{n+1} - P^n}{\Delta t} \tag{5.33}$$

$n + 1$  and  $n$  are new and old time steps, respectively. Using space and time derivatives,

Eqn.5.23 becomes,

$$\begin{aligned}
& \left( \delta \frac{\rho k \left( 1 + \frac{b}{P_{av}} \right)}{\mu \Delta x} A_x \right)_{i+\frac{1}{2}} (P_{i+1} - P_i) - \left( \delta \frac{\rho k \left( 1 + \frac{b}{P_{av}} \right)}{\mu \Delta x} A_x \right)_{i-\frac{1}{2}} (P_i - P_{i-1}) \\
&= -q_i + (\rho \phi c V_b)_i \frac{P^{n+1} - P^n}{\Delta t}
\end{aligned} \tag{5.34}$$

Transmissibility and central term are defined as,

$$T_{i\pm\frac{1}{2}} = \left( \delta \frac{\rho k \left( 1 + \frac{b}{P_{av}} \right)}{\mu \Delta x} A_x \right)_{i\pm\frac{1}{2}} \tag{5.35}$$

$$Tc_i = \frac{(\rho\phi cV_b)_i}{\Delta t} \quad (5.36)$$

For implicit solution, Eqn.5.23 is written in a compact form as;

$$\begin{aligned} T_{i+\frac{1}{2}}^{(v+1)} \left( P_{i+1}^{(v+1)} - P_i^{(v+1)} \right) - T_{i-\frac{1}{2}}^{(v)} \left( P_i^{(v+1)} - P_{i-1}^{(v+1)} \right) \\ = -q_i + Tc_i^{(v+1)} \left( P_i^{(v+1)} - P_i^n \right) \end{aligned} \quad (5.37)$$

$v + 1$  and  $v$  are new and old iteration steps, respectively. Pressure terms are separated so that system of equations can be written for each grid point.

$$\begin{aligned} P_{i+1}^{(v+1)} \left( T_{i+\frac{1}{2}}^{(v)} \right) + P_i^{(v+1)} \left( -T_{i+\frac{1}{2}}^{(v)} - T_{i-\frac{1}{2}}^{(v)} - Tc_i^{(v)} \right) + P_{i-1}^{(v+1)} \left( T_{i-\frac{1}{2}}^{(v)} \right) \\ = -q_i - Tc_i^{(v+1)} P_i^n \end{aligned} \quad (5.38)$$

Pressures are known for the first and last points (Dirichlet boundary condition). Figure 5.32 shows the calculation procedure. First, pressure is assumed, previous time step pressure, and the fluid properties; viscosity, density and compressibility, are calculated so that controlling parameter,  $\delta$ , is calculated. Velocity,  $u$ , and  $\delta$  are calculated until the difference between previous and current  $\delta$  difference is less than specified tolerance. After  $\delta$  convergence, fluid properties are recalculated. Later, transmissibility and pressure are calculated until the pressure difference between previous and current iteration is less than specified tolerance for pressure.

To confirm the developed pulse-decay simulation, the analytical solution proposed by Chen et al. (1984) is used. They proposed the solution for pulse-decay experiments for the case where pore volume is negligible, and the upstream tank pressure,  $P_u$ , is constant. They solved the diffusion equation (Eqn.5.39) for stated initial (Eqn.5.43) and boundary conditions (Eqn.5.44- Eqn.5.45). To use Eqn.5.39, Klinkenberg effects and non-Darcy effects should be negligible.

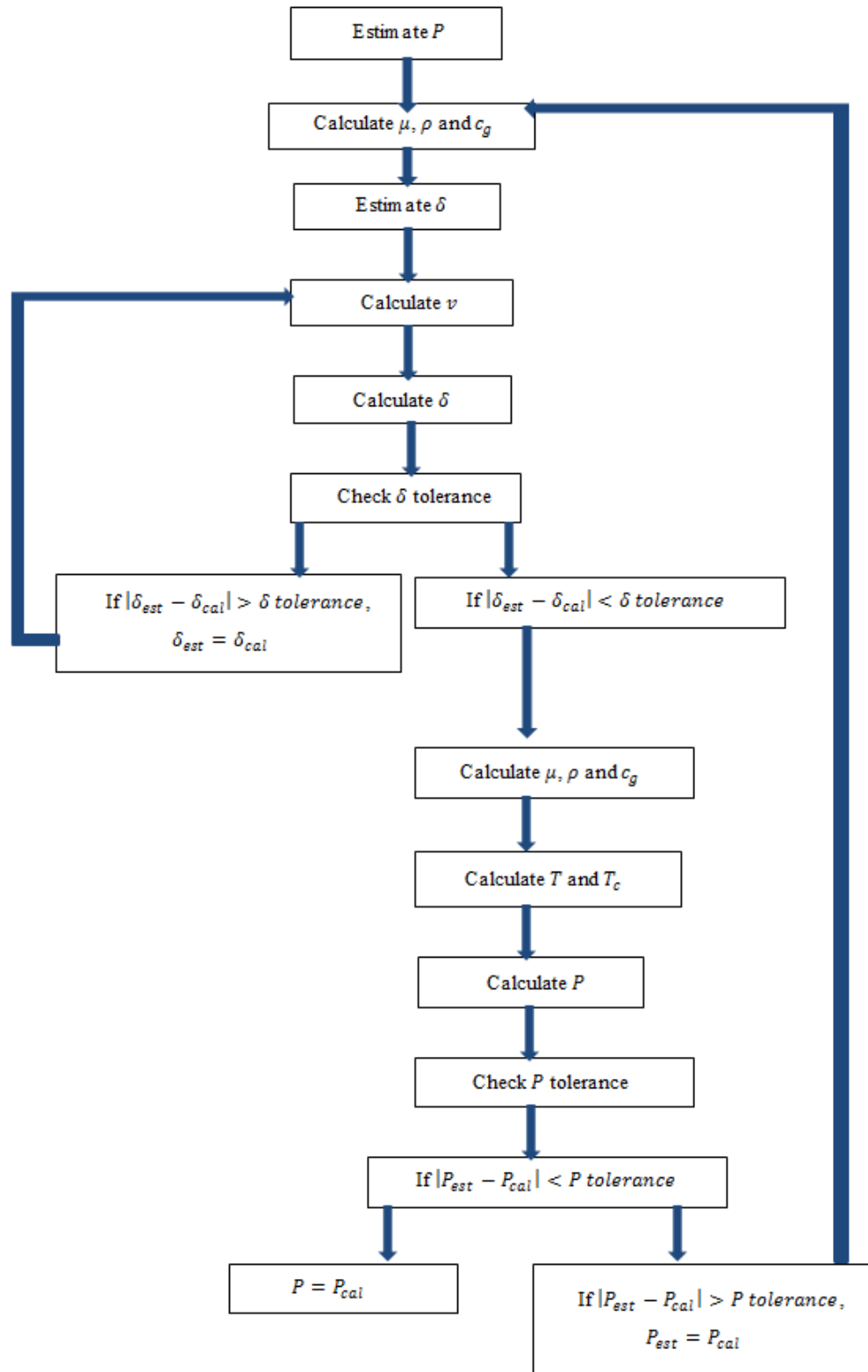


Figure 5.32 Pulse-Decay Simulation Algorithm

$$\frac{\partial^2 P_D}{\partial x_D^2} = \frac{\partial P_D}{\partial t_D} \quad (5.39)$$

Dimensionless pressure,  $P_D$ , dimensionless length,  $x_D$ , and dimensionless time,  $t_D$  are defined as,

$$P_D(x_D, t_D) = \frac{P_u - P(x, t)}{P_u - P_d^0} \quad (5.40)$$

$$x_D = \frac{x}{L} \quad (5.41)$$

$$t_D = \frac{kt}{\phi \mu c L^2} \quad (5.42)$$

$P_d^0$  is initial downstream tank pressure. Initial and boundary conditions are defined as;

$$P_D(x_D, 0) = 1 \quad (5.43)$$

$$P_D(0, t_D) = 0 \quad (5.44)$$

$$\frac{\partial}{\partial t_D} P_D(1, t_D) = -\gamma \frac{\partial}{\partial x_D} P_D(1, t_D) \quad (5.45)$$

$\gamma$  is defined as ratio of pore volume to downstream tank volume,  $V_d$ .

$$\gamma = \frac{\phi AL}{V_d} \quad (5.46)$$

The solution of diffusion equation in Laplace space is given as,

$$\bar{P}_D = \frac{1}{s} \left\{ 1 - \frac{\exp[\sqrt{s}(1 - x_D)] - \left(\frac{\sqrt{s}-\gamma}{\sqrt{s}+\gamma}\right) \exp[-\sqrt{s}(1 - x_D)]}{\exp(q) - \left(\frac{\sqrt{s}-\gamma}{\sqrt{s}+\gamma}\right) \exp(-q)} \right\} \quad (5.47)$$

Table 5.7 gives the simulation input parameters used for validation of pulse-decay simulation algorithm study. Klinkenberg coefficient and non-Darcy coefficient are estimated from Jones correlations (1972). Upstream and downstream pressures are chosen high to prevent

the slippage effects and the pressure difference between these two tanks is small to prevent the inertial effects.

Figure 5.33 gives the pressure change (MPa) along the core with time. Downstream tank pressure increases with time while upstream tank pressure is almost constant. Numerical Laplace transformation is used to calculate pressure distribution from Eqn.5.47. The trapezoidal approximation of the Bromwich integral is used for inverse Laplace transformation (de Hoog, Knight, & Stokes, 1982). Figure 5.34 gives the comparison of pressures obtained from simulation (squares) and calculated from Eqn.5.47 (solid line) at different core locations. The match between simulated and calculated pressures confirms that simulation algorithm is correct, and it can be used for further studies.

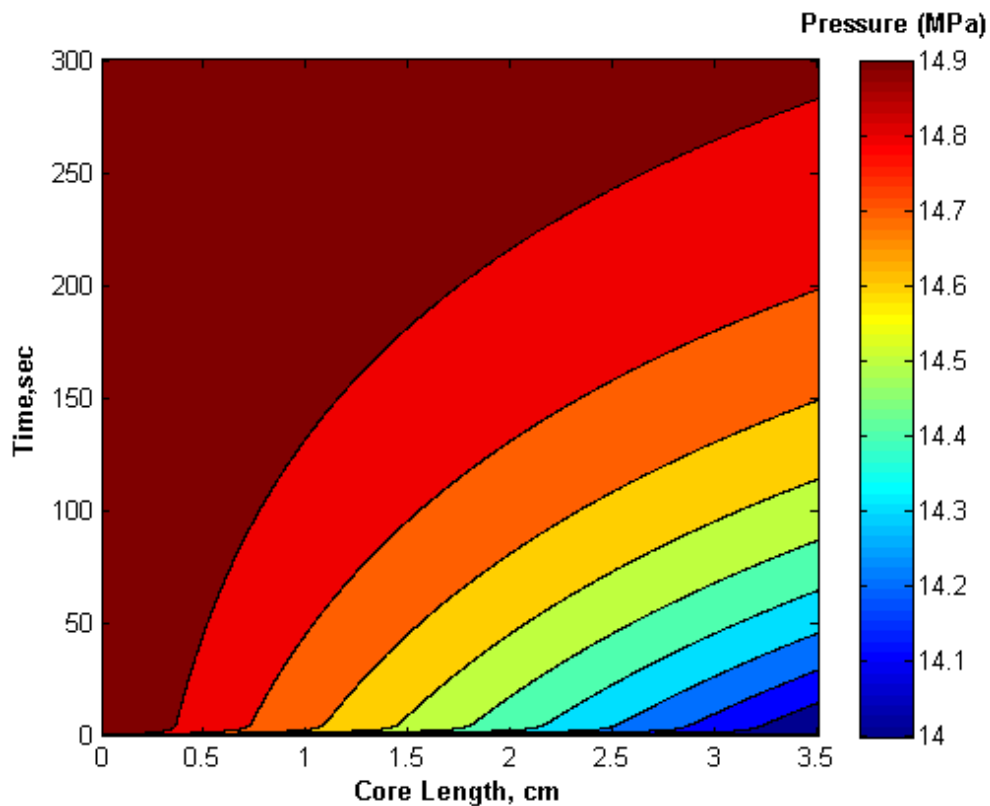


Figure 5.33 Contour Plot of Pressure from Pulse Decay Simulation

Table 5.7 Input Parameters of Pulse-Decay Simulation

Gas	He
Core Diameter, D(cm)	1.5
Core Length, L(cm)	3.5
Porosity, $\phi$ (fraction)	0.05
Permeability, k(mD)	0.01
Klinkenberg Coefficient, b(MPa)	0.6567
Non-Darcy Coefficient, $\beta$ (1/m)	$2.54 \times 10^{14}$
Upstream Tank Volume, $V_u$ (cc)	2000
Downstream Tank Volume, $V_d$ (cc)	5
Initial Upstream Tank Pressure, $P_u^0$ (MPa)	15
Initial Downstream Tank Pressure, $P_d^0$ (MPa)	14
Temperature, T( $^{\circ}$ F)	60
Atmospheric Pressure, $P_{sc}$ (MPa)	0.1014
Total Simulation Time, t(sec)	300

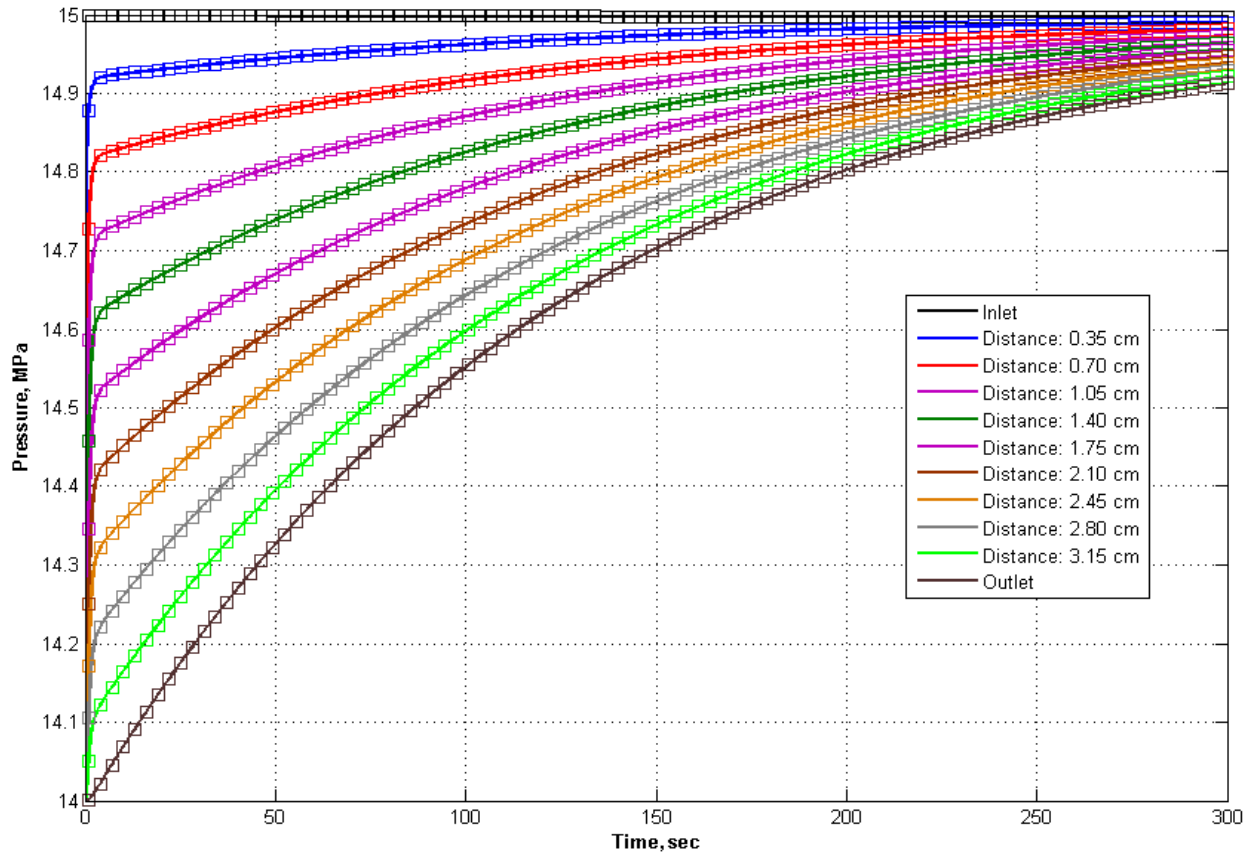


Figure 5.34 Pressure Comparison Obtained from Simulation and from Inverse Laplace Transformation of Eqn.5.46

#### 5.4 Sensitivity Analysis of Pulse-Decay Experiment

2C and 3C core pulse-decay experiments analyses indicate that for correct estimation of permeability, Klinkenberg coefficient and non-Darcy coefficient, experiment duration should be long enough to avoid measurement errors effects. Sensitivity analysis is conducted to see the how core properties and experiment design affect the experiment duration. Table 5.8 gives the simulation input parameters used in the base case. Based on this case, each variable is changed at a time while the remaining variables are kept constant. Table 5.9 gives the variables used in sensitivity analysis and their ranges. Simulation runs are conducted for He. Klinkenberg coefficient,  $b$ , and Forchheimer coefficient,  $\beta$ , are calculated from Jones correlations (1972). Simulations are conducted until the pressure difference between the upstream and downstream tanks,  $\Delta P$ , reduces to 99% of the initial pressure difference.

Table 5.8 Base Case Simulation Input Parameters

Gas	He
Core Diameter, D (cm)	4.0
Core Length, L (cm)	3.0
Porosity, $\phi$ (fraction)	0.1
Permeability, k (mD)	100.0
Klinkenberg Coefficient, b (MPa)	0.0194699
Non-Darcy Coefficient, $\beta$ (1/m)	$1.603 \times 10^8$
Upstream Tank Volume, $V_u$ (cc)	500
Downstream Tank Volume, $V_d$ (cc)	250
Initial Upstream Tank Pressure, $P_u^0$ (MPa)	0.7
Initial Downstream Tank Pressure, $P_d^0$ (MPa)	0.3
Atmospheric Pressure, $P_{sc}$ (MPa)	0.1014
Temperature, T (°F)	60

Figure 5.35 through Figure 5.37 are some examples how the upstream and downstream tank pressures change with time for different core diameters, permeabilities and upstream tank pressures. Change in core properties; e.g., core diameter and permeability, lead to change the



time at which pressure difference is less than 0.01% of initial difference; however, the final pressures of upstream and downstream tanks do not change. On the other hand; change of experiment set-up; e.g. upstream tank volume, has effect on final tanks pressures.

Table 5.9 Sensitivity Parameters and Their Ranges

Variables	Lower Range	Upper Range
Core Diameter, D(cm)	2.5	8
Core Length, L(cm)	2.5	8
Porosity, $\phi$ (fraction)	0.01	0.4
Permeability, k(mD)	0.001	2000
Upstream Tank Volume, $V_u$ (cc)	100	3000
Downstream Tank Volume, $V_d$ (cc)	5	3000
Initial Upstream Tank Pressure, $P_u^0$ (MPa)	0.35	20
Initial Downstream Tank Pressure, $P_d^0$ (MPa)( $P_u^0 = 19$ MPa)	0.5	18
Upstream Tank Pressure, $P_u^0$ (MPa)( $\Delta P = P_u^0 - P_d^0 = 1$ MPa)	2	20

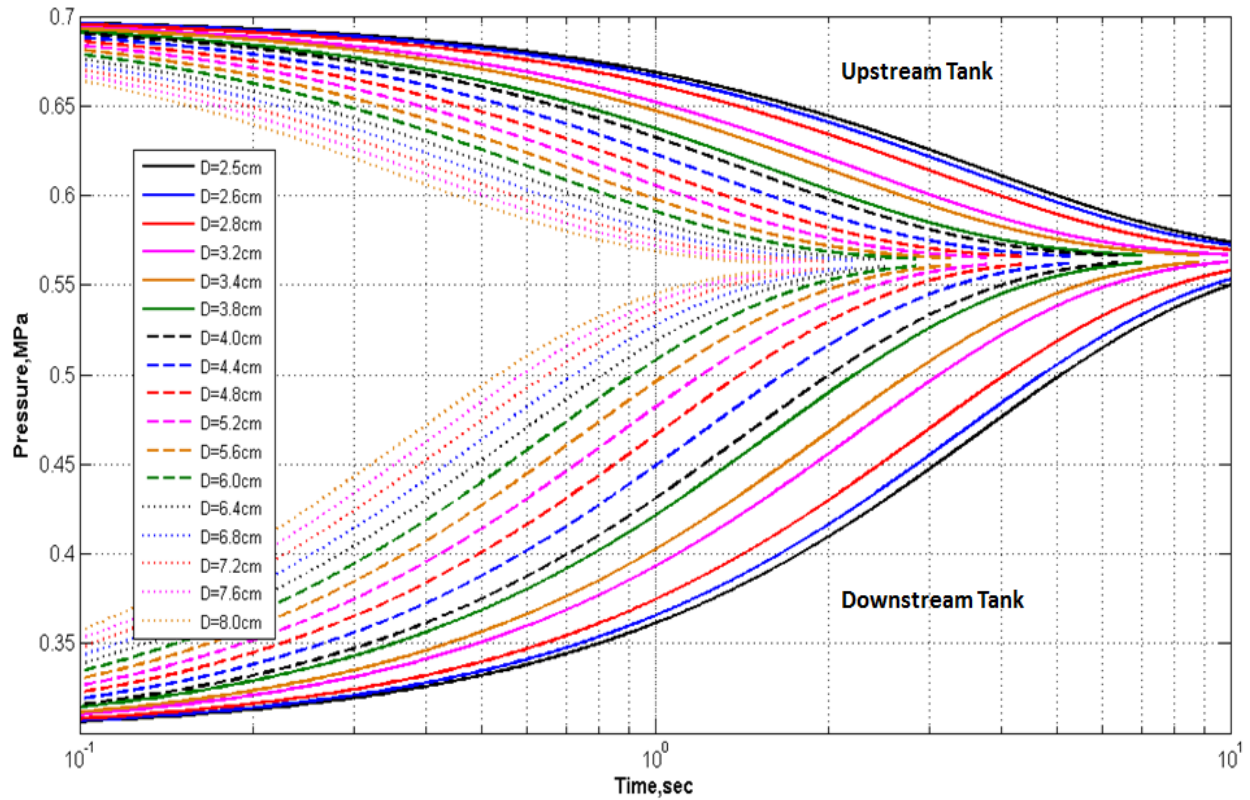


Figure 5.35 Core Diameter Effect on Pulse-Decay Experiment Duration

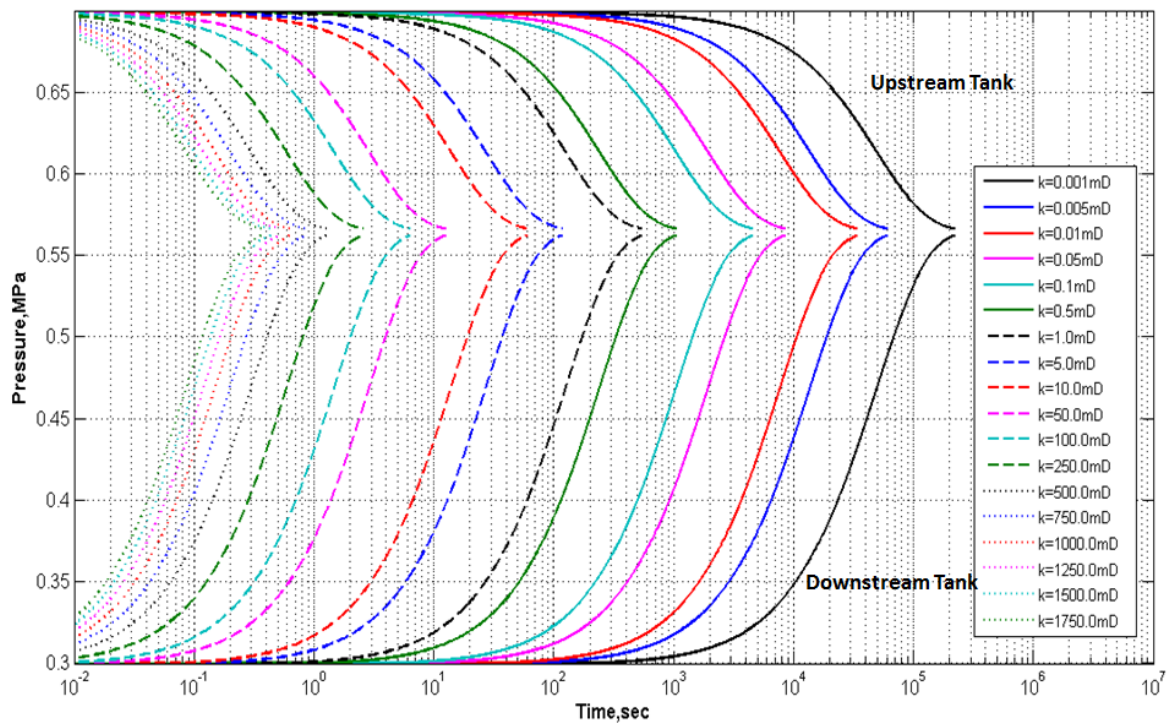


Figure 5.36 Permeability Effect on Pulse-Decay Experiment Duration

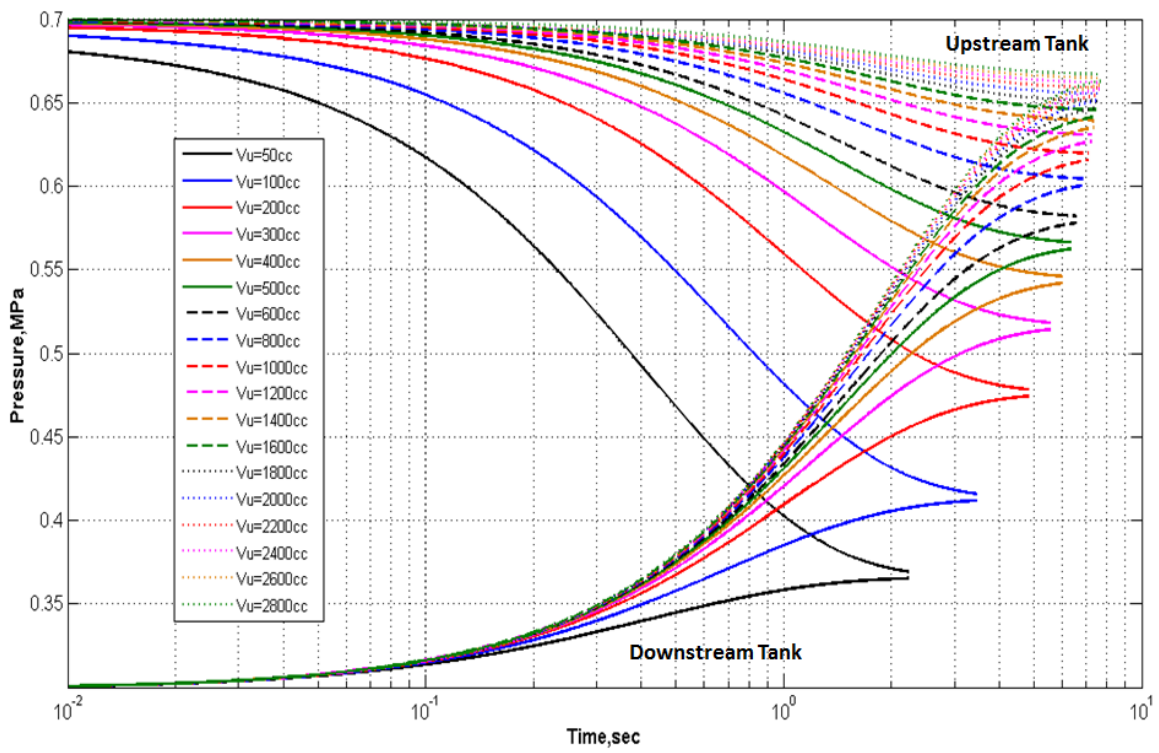


Figure 5.37 Upstream Tank Volume Effect on Pulse-Decay Experiment Duration

Figure 5.38 summarizes the sensitivity analysis results as a whole. Increase in core diameter, permeability, upstream and downstream tank pressures lead to decrease in experiment duration while increase in core length, porosity, upstream and downstream tank volumes lead to increase in experiment duration. If the pressure difference between upstream and downstream pressures is constant, increase in upstream pressure leads to decrease in experiment duration. Based on this analysis, the most and least sensitive parameters are permeability and porosity of the core.

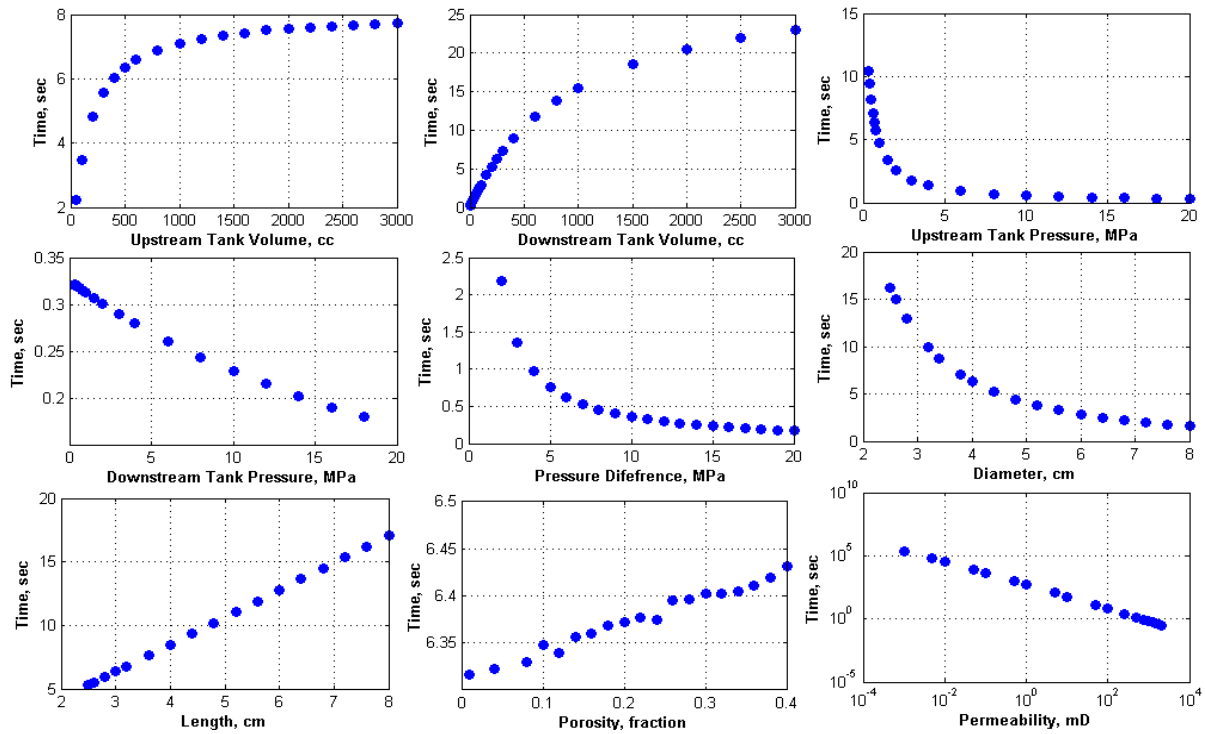


Figure 5.38 Pulse-Decay Experiment Duration Sensitivity Analysis Results

## 5.5 Pulse-Decay Experiment Duration Estimation

Sensitivity analysis shows the smooth change of the pulse-decay experiment duration with each experiment set-up variables such as upstream and downstream tanks volume and pressures, and core properties such as porosity and permeability, and core dimensions; its length

and diameter. This indicates that if taking the logarithm of the parameters and experiment duration, then the trends become linear.

To develop a correlation in order to estimate pulse-decay experiment duration, Hamersley design is used to prepare 300 simulations based on the variables given in Table 5.10. Generally, the upstream tank volume,  $V_u$  is greater than the downstream tank volume,  $V_d$ ; therefore, the ratio of downstream tank volume to the upstream tank volume is specified,  $V_r$  ( $V_d/V_u$ ) instead of the downstream tank volume. To ensure that the upstream tank pressure,  $P_u$  is greater than the downstream tank pressure,  $P_d$ , pressure difference between tanks,  $\Delta P$  is specified instead of the upstream tank pressure. Logarithm of permeability is sampled in order to better quantify the lower permeability ranges. Pulse-decay simulations in sensitivity analysis are conducted until the pressure difference between tanks drop the 99% of the initial pressure difference. In lab experiments, pulse-decay experiments are conducted until the pressure difference between the tanks decreases to about 80% of the initial pressure difference. The pressure decrease range is chosen between 60% and 90%.

In sensitivity analysis, non-Darcy coefficient and Klinkenberg coefficient are calculated from Jones' correlations. Jones data are obtained with digitization and standard errors of log-log plot of permeability and Klinkenberg coefficient, and permeability and non-Darcy coefficient are calculated, 0.2102 and 0.6209, respectively. Random variations are added to the calculated Klinkenberg coefficients and non-Darcy coefficients between standard deviations of -1.96 and 1.96 (95% confidence intervals) to simulate real experiment data (Figure 5.39 and Figure 5.40). All variables are independent except permeability and porosity. Initially, permeability and porosity are assumed to be independent that causes the simulation of some unrealistic cases such as a core with high porosity and low permeability, or, with low porosity and high permeability.

This assumption is required to develop a correlation with linear regression, because the main assumption of linear regression is that all explanatory variables should be independent that means there are no colinearity problems. Table 5.11 gives the correlation coefficients of variables used in the design. The design points cover the whole range of intervals and correlation coefficients are close to 0 that indicates that design is orthogonal; each variable is independent, and they can be used for correlation development.

Table 5.10 Hamersley Design Variables and Their Ranges for Pulse Decay Experiments with 2 Tanks

Variables	Lower Range	Upper Range
Upstream Tank Volume, $V_u$ (cc)	100	3000
Tank Volume Ratio, $V_r$ ( $V_d/V_u$ )	0.05	1
Initial Downstream Tank Pressure, $P_d$ (MPa)	0.15	18
Initial Tanks Pressure Difference, $\Delta P$ ( $P_u - P_d$ , MPa)	0.1	10
Core Diameter, $D$ (cm)	2.5	8
Core Length, $L$ (cm)	2.5	8
Porosity, $\phi$ (fraction)	0.01	0.35
Permeability, $k$ (mD)	0.001	2000
Pressure Difference Decrease, $P_{dec}$ (%)	60	90
Standard Deviation of Klinkenberg Coefficient	-1.96	1.96
Standard Deviation of non-Darcy Coefficient	-1.96	1.96

Table 5.11 Correlation Coefficients of Design Variables for Pulse Decay Experiments with 2 Tanks

	$V_u$ (cc)	$V_r$	$P_d$ (MPa)	$\Delta P$ (MPa)	$D$ (cm)	$L$ (cm)	$\phi$ (frac)	$\log_{10}k$ (mD)	$P_{dec}$ (%)
$V_u$ (cc)	1.0000	0.0056	0.0085	0.0199	0.0449	0.0119	0.0403	0.0601	0.0734
$V_r$	0.0056	1.0000	-0.0043	-0.0041	-0.0072	-0.0132	-0.0115	0.0034	-0.0205
$P_d$ (MPa)	0.0085	-0.0043	1.0000	-0.0085	-0.0099	0.0040	-0.0161	-0.0211	-0.0183
$\Delta P$ (MPa)	0.0199	-0.0041	-0.0085	1.0000	-0.0060	-0.0043	-0.0144	-0.0144	-0.0046
$D$ (cm)	0.0449	-0.0072	-0.0099	-0.0060	1.0000	-0.0232	-0.0043	-0.0086	0.0036
$L$ (cm)	0.0119	-0.0132	0.0040	-0.0043	-0.0232	1.0000	0.0132	-0.0162	-0.0012
$\phi$ (frac)	0.0403	-0.0115	-0.0161	-0.0144	-0.0043	0.0132	1.0000	0.0074	0.0222
$\log_{10}k$ (mD)	0.0601	0.0034	-0.0211	-0.0144	-0.0086	-0.0162	0.0074	1.0000	-0.0560
$P_{dec}$ (%)	0.0734	-0.0205	-0.0183	-0.0046	0.0036	-0.0012	0.0222	-0.0560	1.0000

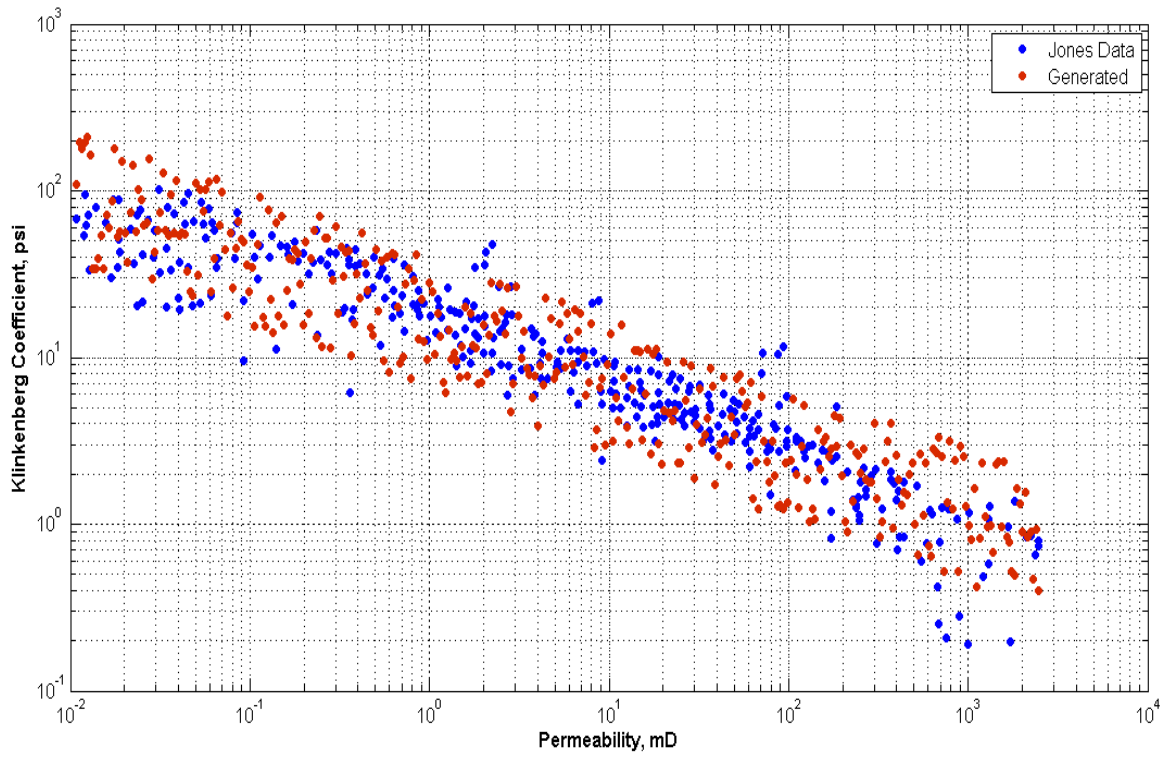


Figure 5.39 Generated and Observed Klinkenberg Coefficient Comparison

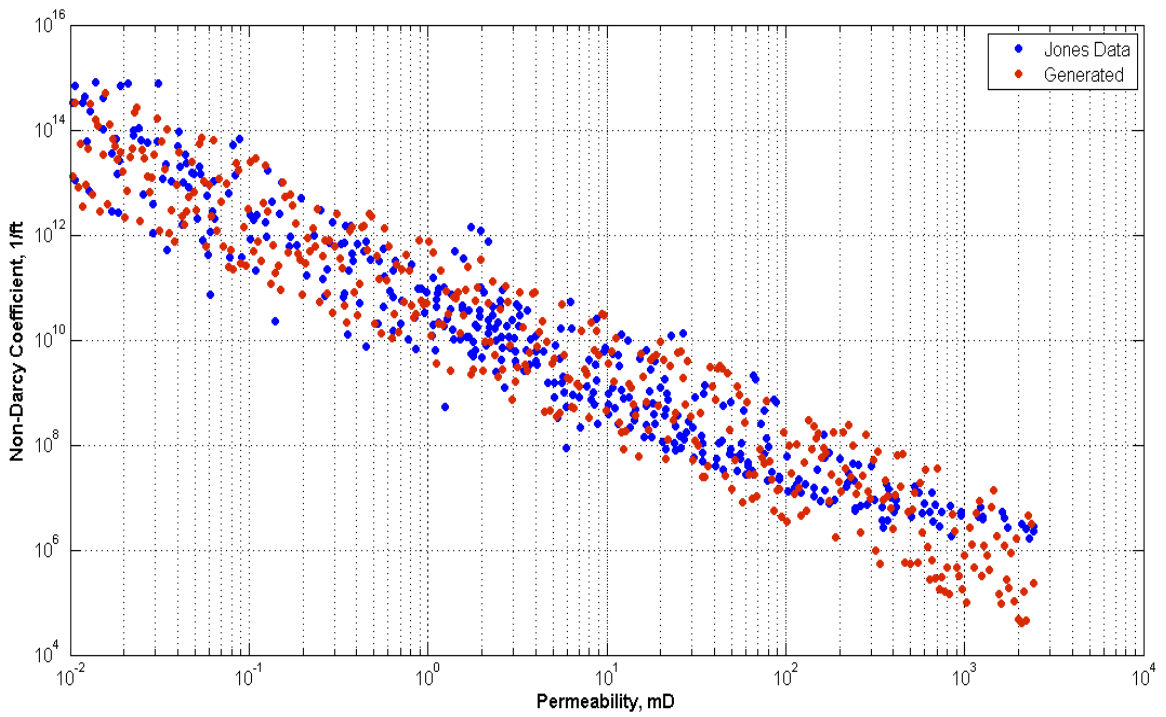


Figure 5.40 Generated and Observed Forchheimer Coefficient Comparison

By using the logarithm of the design variables (except calculated Klinkenberg coefficient and non-Darcy coefficient) and the experiment duration obtained from pulse-decay simulations, the correlation is developed with linear regression for experiment duration by using JMP (SAS, 2014). Klinkenberg coefficient and non-Darcy coefficient are calculated from Jones' correlation based on permeability; therefore, these three parameters are highly correlated (Figure 5.39 and Figure 5.40). Due to colinearity problem, only permeability is used for experiment duration correlation development. Figure 5.41 gives the experiment durations cross plot. In this figure, predicted and actual represent the experiment duration obtained from developed correlation (Eqn.5.48) and the ones obtained from pulse-decay simulations, respectively. The red solid line is the 45° line in order to evaluate the goodness of fit. The red dashed lines give the 95% confidence interval. The points lie on the 45° line and confidence interval is narrow that indicates the good estimation of experiment duration. Table 5.12 gives the summary of fit statistics. According to statistics, the fit is good because the coefficient of determination,  $R^2$ , is high, 0.9976 and adjusted  $R^2$ , 0.9975, is close to the  $R^2$  and RMSE is low, 0.0916, compared with mean response, 1.2636.

$$t(sec) = \frac{10^{-3.7811} V_u^{0.9834} V_r^{0.7441} L^{0.9364} \phi^{0.0042} P_{dec}^{1.9832}}{P_d^{0.5810} \Delta P^{0.1640} D^{2.0058} k^{0.9788}} \quad (5.48)$$

Table 5.12 Summary of Fit Statistics for Experiment Duration (2 Tanks)

Coefficient of Determination, $R^2$	0.9976
Adjusted $R^2$	0.9975
Root Mean Square Error, RMSE	0.0916
Mean of Response	1.2636

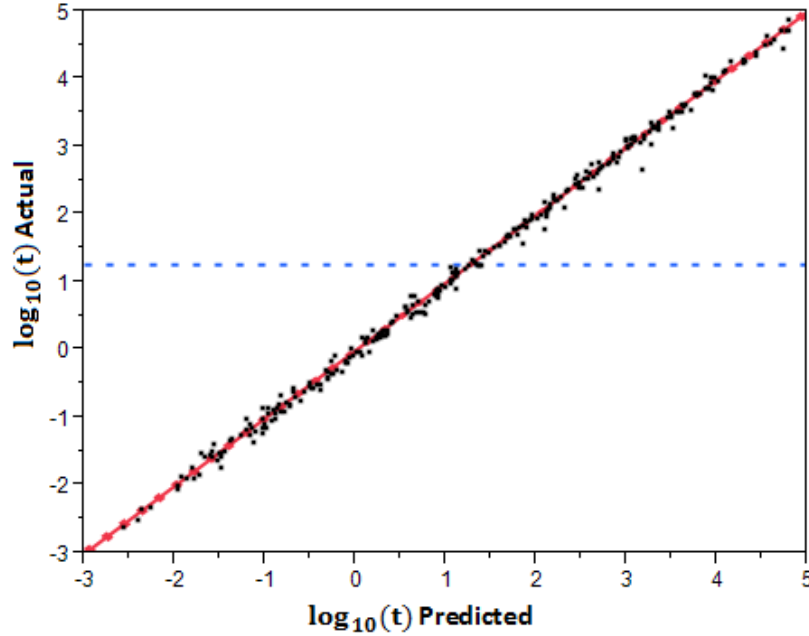


Figure 5.41 Actual by Predicted Plot of Pulse-Decay Experiment (2 Tanks) Duration

Table 5.13 Parameter Estimates of Experiment Duration Equation (2 Tanks)

Term	Estimate	Std. Error	t Ratio	Prob> t	Lower 95% CI	Upper 95% CI
Intercept	-3.7811	0.2050	-18.44	<0.0001	-4.1846	-3.3776
$\log_{10}(V_u)$	0.9834	0.0162	60.67	<0.0001	0.9515	1.0153
$\log_{10}(V_r)$	0.7441	0.0172	43.38	<0.0001	0.7103	0.7779
$\log_{10}(P_d)$	-0.5810	0.0135	-43.17	<0.0001	-0.6074	-0.5545
$\log_{10}(\Delta P)$	-0.1640	0.0135	-12.17	<0.0001	-0.1905	-0.1375
$\log_{10}(D)$	-2.0058	0.0376	-53.30	<0.0001	-2.0798	-1.9317
$\log_{10}(L)$	0.9364	0.0373	25.10	<0.0001	0.8630	1.0098
$\log_{10}(\emptyset)$	0.0042	0.0153	0.28	0.7816	-0.0258	0.0343
$\log_{10}(k)$	-0.9788	0.0029	-332.0	<0.0001	-0.9846	-0.9730
$\log_{10}(P_{dec})$	1.9832	0.1061	18.68	<0.0001	1.7743	2.1921

Figure 5.42 gives the Leverage plots of the design variables used in the correlation. This plot gives the errors with and without the variable effect in the model. The distance between the points to the fit line (red line) give the error when the variable is in the model, and the distance between the points and horizontal line (blue line) give the error when the variable is removed from the model. According to this plot, porosity has almost no effect on the pulse-decay



experiment duration. This can be confirmed from  $t$  statistics and  $p$  value given in Table 5.13. For a significant variable, absolute  $t$  value should be greater than 2 and  $p$  value should be less than 0.05. For porosity,  $t$  statistics and  $p$  values are 0.28 and 0.7806, respectively. Porosity variable can be excluded from correlation given in Eqn.5.48 so that the independence of porosity and permeability assumption would be obsolete.

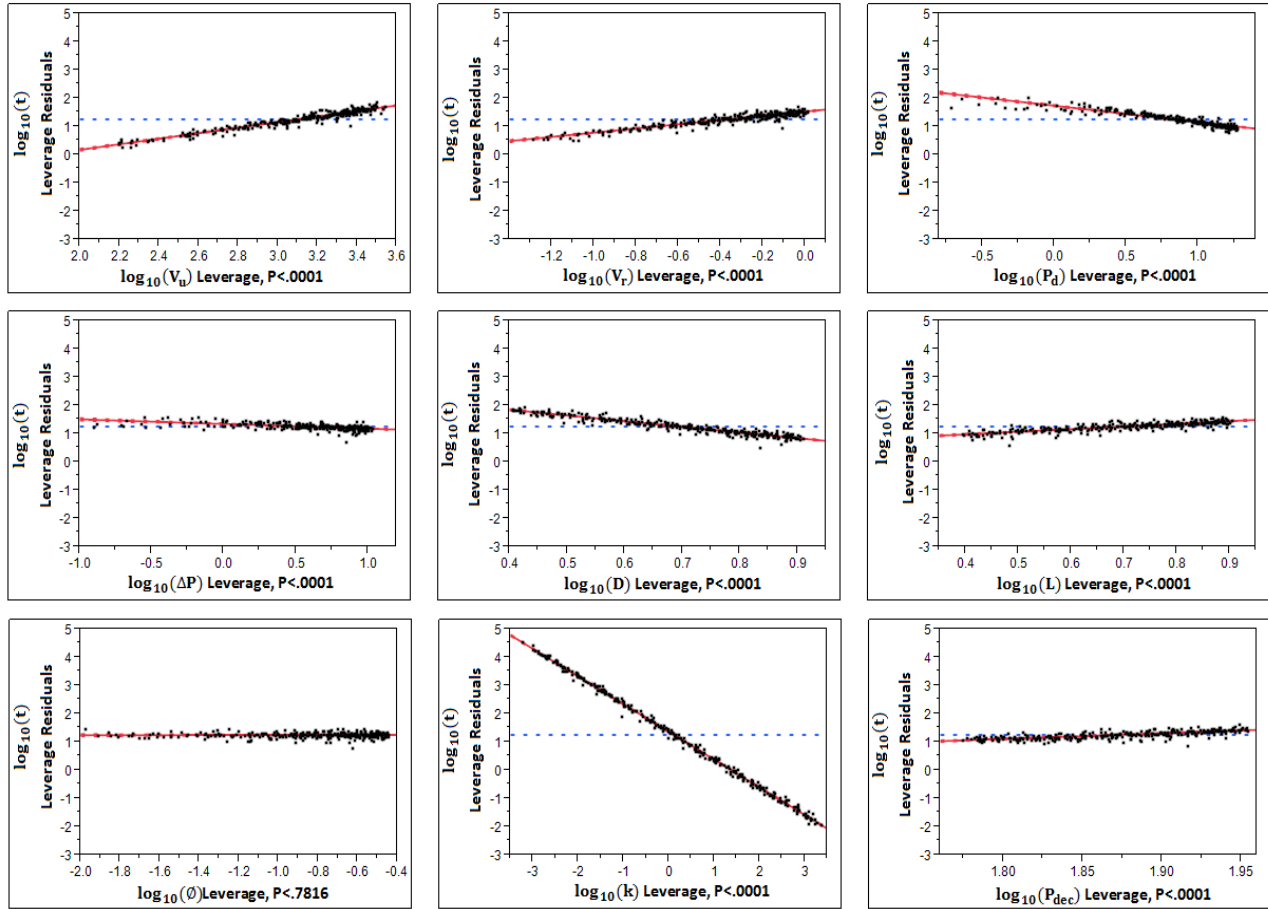


Figure 5.42 Leverage Plot of Pulse Decay Experiment Duration Design Variables (2 Tanks)

Figure 5.43 gives the logarithm of experiment duration residual vs. logarithm of the experiment duration predicted from a developed correlation. The residuals do not depend on experiment duration prediction that means they are randomly distributed. One of the basic assumptions of linear regression is that the residuals should be normally distributed with mean 0.

Figure 5.44 gives the residual analysis of the pulse-decay experiment duration. Lower part of the plot gives the residuals histogram, and upper part of the plot gives the normal quantile plot. In the upper plot, the scales inside and outside of the plot give the normal quantile and z scores, respectively. In this plot, points show the residuals and the red solid line gives the theoretical distribution of normal plot for specified mean and standard deviation,  $7.0 \times 10^{-16}$  and 0.09, respectively. The area between two red dashed lines gives the 95% confidence interval. Based on this figure, residual distribution is close to the normal distribution with mean about 0.

Figure 5.45 gives the prediction profiler of variables. In this figure,  $x$  axis gives the logarithm of variables, and their current values are indicated by red numbers.  $y$  axis gives the corresponding logarithm of the pulse-decay experiment duration, and red time indicates the pulse-decay duration corresponding current values of the variables. The numbers given in the parenthesis on  $y$  axis give the 95% confidence interval corresponding current experiment duration. For this specific case, the estimated pulse-decay experiment duration is about 13.60 sec ( $10^{1.1336}$ ) with confidence interval of (12.78 – 14.47 sec). In this figure, black lines give the changes of experiment duration if the variable is changed while the other variables remain constant. Based on Figure 5.45, the most sensitive variable is permeability, and the experiment duration increases as the permeability decreases. As stated before, porosity has no effect on the experiment duration. Increase in upstream tank volume,  $V_u$ , ratio of downstream tank volume to upstream tank volume,  $V_r$ , and core length,  $L$ , lead to increase in experiment duration while increase in downstream tank pressure,  $P_d$ , initial pressure difference between upstream and downstream tanks,  $\Delta P$ , and core diameter,  $D$ , lead to decrease in experiment duration.

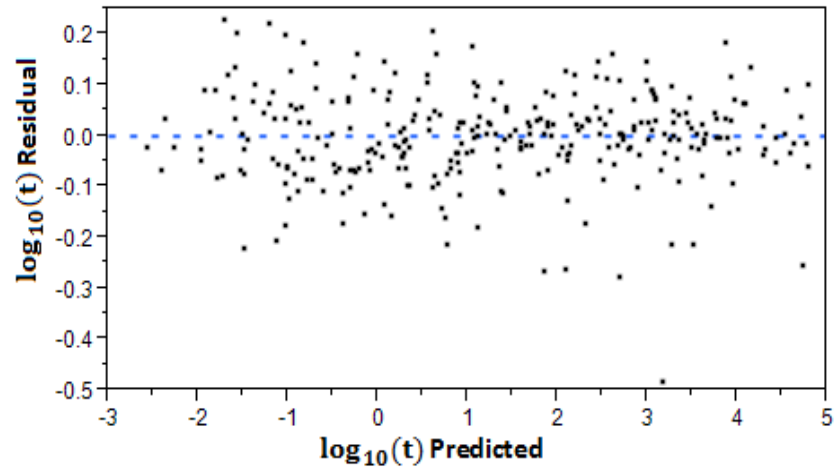


Figure 5.43 Residual vs. Predicted Plot of Experiment Duration (2 Tanks)

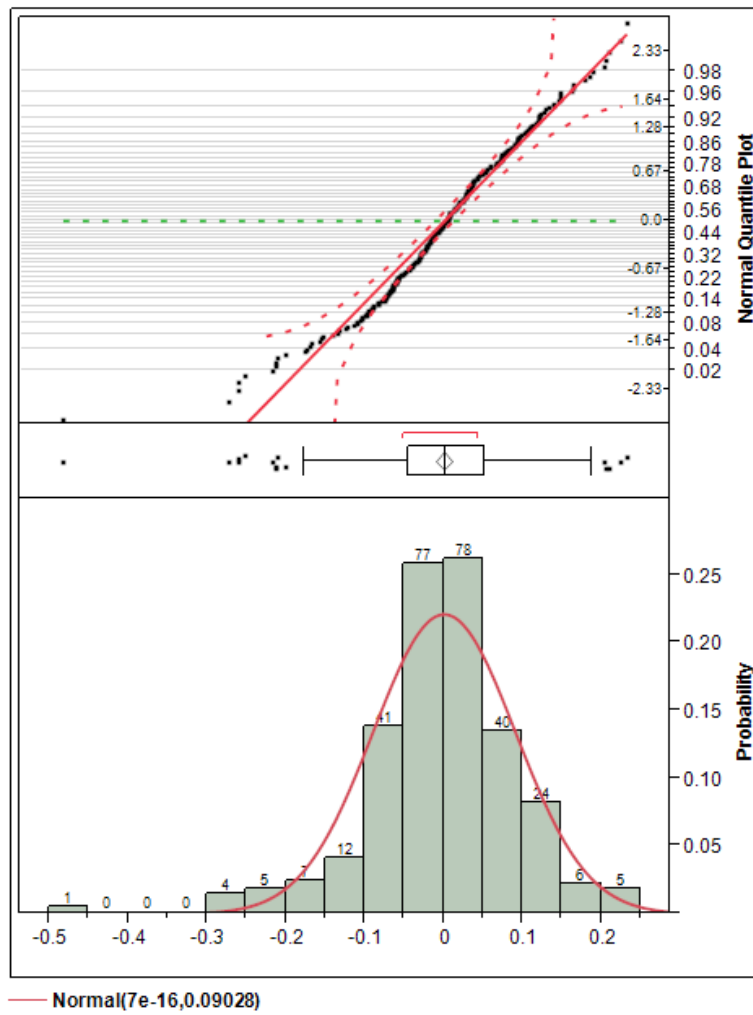


Figure 5.44 Residual Distribution of Experiment Duration (2 Tanks)

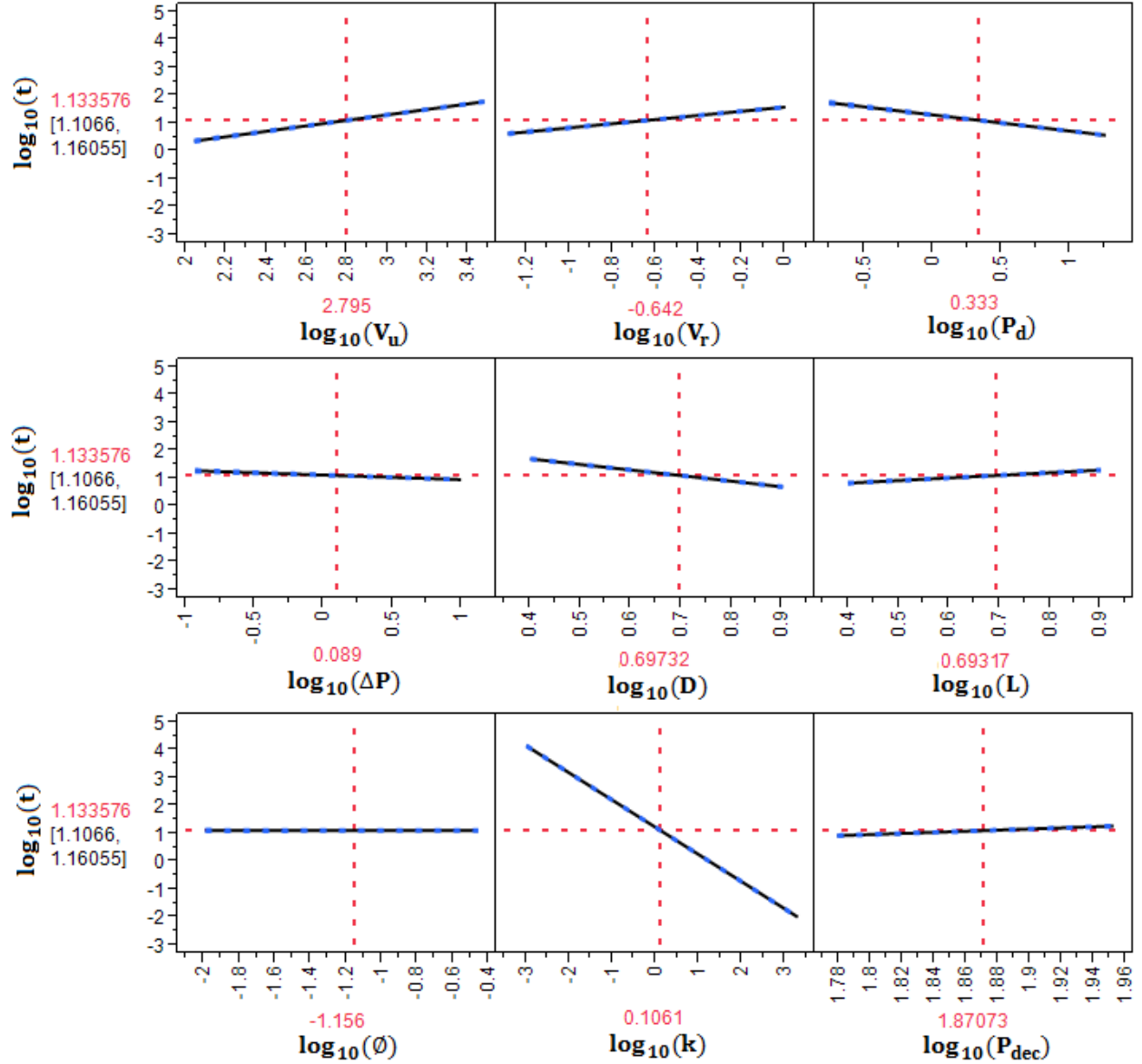


Figure 5.45 Profiler Plot of Simulation Time Design Variables

Similar study is conducted for the pulse-decay experiments in which core outlet is open to the atmosphere. For 1 tank pulse-decay experiment, the design variables are upstream tank volume and its pressure, core properties; its length, diameter, porosity and permeability (Table 5.14). Again, pressure difference is specified instead of upstream tank pressure since for low upstream tank pressures, pressure decrease specification leads to final upstream pressures less than atmospheric pressure. Logarithm of the permeability is sampled in order to better quantify

the lower permeability range. 300 cases are prepared with Hammersley design with the variable and their ranges given in the Table 5.14. The pulse-decay simulations are conducted until the difference between upstream tank pressure and atmospheric pressure decreases to 60% - 90% of the initial difference. The design is cover the whole ranges of variables and the correlation between variables are close 0 (Table 5.15).

Table 5.14 Hamersley Design Variables and Their Ranges for Pulse Decay Experiments with 1 Tank

Variables	Lower Range	Upper Range
Upstream Tank Volume, $V_u$ (cc)	5	3000
Initial Tank Pressure Difference, $\Delta P$ ( $P_u - P_{atm}$ , MPa)	0.1	10
Core Diameter, $D$ (cm)	2.5	8
Core Length, $L$ (cm)	2.5	8
Porosity, $\phi$ (fraction)	0.01	0.35
Permeability, $k$ (mD)	0.001	2000
Pressure Difference Decrease, $P_{dec}$ (%)	60	90
Standard Deviation of Klinkenberg Coefficient	-1.96	1.96
Standard Deviation of non-Darcy Coefficient	-1.96	1.96

Table 5.15 Correlation Coefficients of Design Variables for Pulse Decay Experiments with 1 Tank

	$V_u$ (cc)	$\Delta P$ (MPa)	$D$ (cm)	$L$ (cm)	$\phi$ (frac)	$\log_{10}k$ (mD)	$P_{dec}$ (%)
$V_u$ (cc)	1.0000	0.0056	0.0085	0.0199	0.0449	0.0119	0.0734
$\Delta P$ (MPa)	0.0056	1.0000	-0.0043	-0.0041	-0.0072	-0.0132	-0.0205
$D$ (cm)	0.0085	-0.0043	1.0000	-0.0085	-0.0099	0.0040	-0.0183
$L$ (cm)	0.0199	-0.0041	-0.0085	1.0000	-0.0060	-0.0043	-0.0046
$\phi$ (frac)	0.0449	-0.0072	-0.0099	-0.0060	1.0000	-0.0232	0.0036
$k$ (mD)	0.0119	-0.0132	0.0040	-0.0043	-0.0232	1.0000	-0.0012
$P_{dec}$ (%)	0.0734	-0.0205	-0.0183	-0.0046	0.0036	-0.0012	1.0000

After pulse-decay experiment simulations, the pulse-decay experiment duration correlation is developed with linear regression by using the base 10 logarithm of design variables and experiment durations obtained from pulse-decay simulations. Similar to previous analysis,

Klinkenberg coefficients and non-Darcy coefficients are not used in the correlation development due to high correlation between them and permeability. Figure 5.46 gives the cross plot of experiment duration obtained from developed correlation (predicted) (Eqn.5.49) and the ones obtained from pulse-decay simulations (actual). Even though the points are more scattered compared with 2 tanks actual vs. predicted plot, the coefficient of determination is high (Table 5.16) and all variables effect are similar to 2 tanks case (Table 5.17). Increase in upstream tank volume,  $V_u$ , core length,  $L$ , and porosity,  $\phi$ , and the percent decrease in pressure difference,  $P_{dec}$ , lead to increase in pulse-decay experiment duration. On the other hand, increase in difference between upstream tank pressure and atmospheric pressure,  $\Delta P$ , core diameter,  $D$ , and permeability,  $k$ , lead to decrease in pulse-decay experiment duration. Porosity effect on pulse-decay experiment duration is insignificant based on the  $t$  statistics, 0.60, and  $p$  value, 0.5517 (Table 5.17).

$$t(sec) = \frac{10^{-5.4358} V_u^{0.9790} L^{0.9610} \phi^{0.0112} P_{dec}^{3.3458}}{\Delta P^{0.6051} D^{1.9479} k^{0.9345}} \quad (5.49)$$

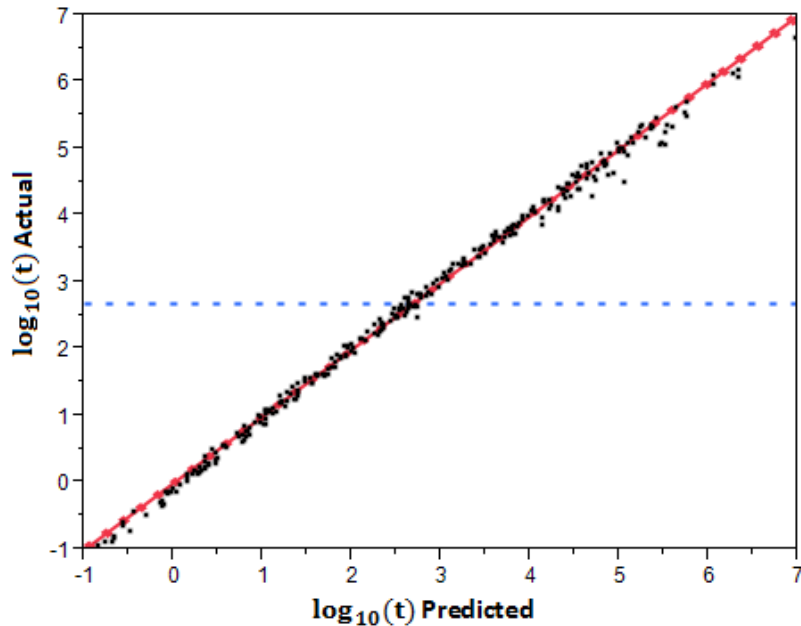


Figure 5.46 Actual by Predicted Plot of Pulse-Decay Experiment (1 Tank) Duration

Table 5.16 Summary of Fit Statistics for Experiment Duration (1 Tank)

Coefficient of Determination, $R^2$	0.9962
Adjusted $R^2$	0.9961
Root Mean Square Error, RMSE	0.1112
Mean of Response	2.6851

Even though fit statistics is good and all variable except porosity are significant, the fit is not acceptable based on the residual by predicted plot of experiment duration (Figure 5.47). There are three observed trends in the residuals; for lower experiment duration, residuals increase with increase in predicted values (1); for middle experiment durations, residuals are not related with predicted values (2); and for high experiment duration, residuals decrease with increase in predicted values (3).

Table 5.17 Parameter Estimates of Experiment Duration Equation (1 Tank)

Term	Estimate	Std. Error	t Ratio	Prob> t	Lower 95% CI	Upper 95% CI
Intercept	-5.4358	0.2465	-22.05	<0.0001	-5.9209	-4.9506
$\log_{10}(V_u)$	0.9790	0.0158	61.93	<0.0001	0.9479	1.0102
$\log_{10}(\Delta P)$	-0.6051	0.0166	-36.39	<0.0001	-0.6378	-0.5724
$\log_{10}(D)$	-1.9479	0.0455	-42.85	<0.0001	-2.0374	-1.8584
$\log_{10}(L)$	0.9610	0.0453	21.20	<0.0001	0.8718	1.0503
$\log_{10}(\emptyset)$	0.0112	0.0188	0.60	0.5517	-0.0258	0.0482
$\log_{10}(k)$	-0.9345	0.0035	-263.8	<0.0001	-0.9415	-0.9275
$\log_{10}(P_{dec})$	3.3458	0.1286	26.01	<0.0001	3.0926	3.5989

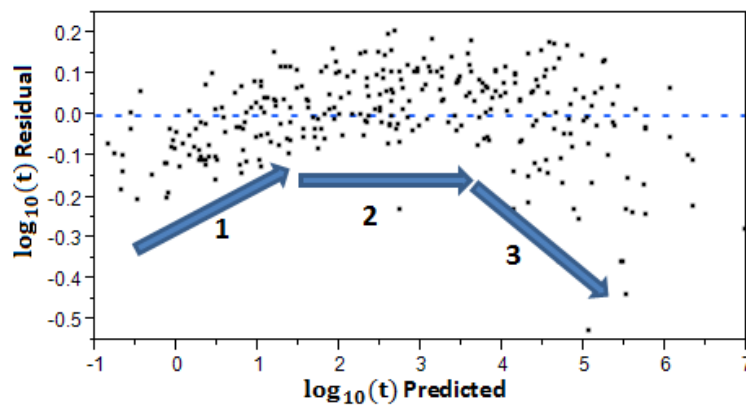


Figure 5.47 Residual vs. Predicted Plot of Experiment Duration (1 Tank)

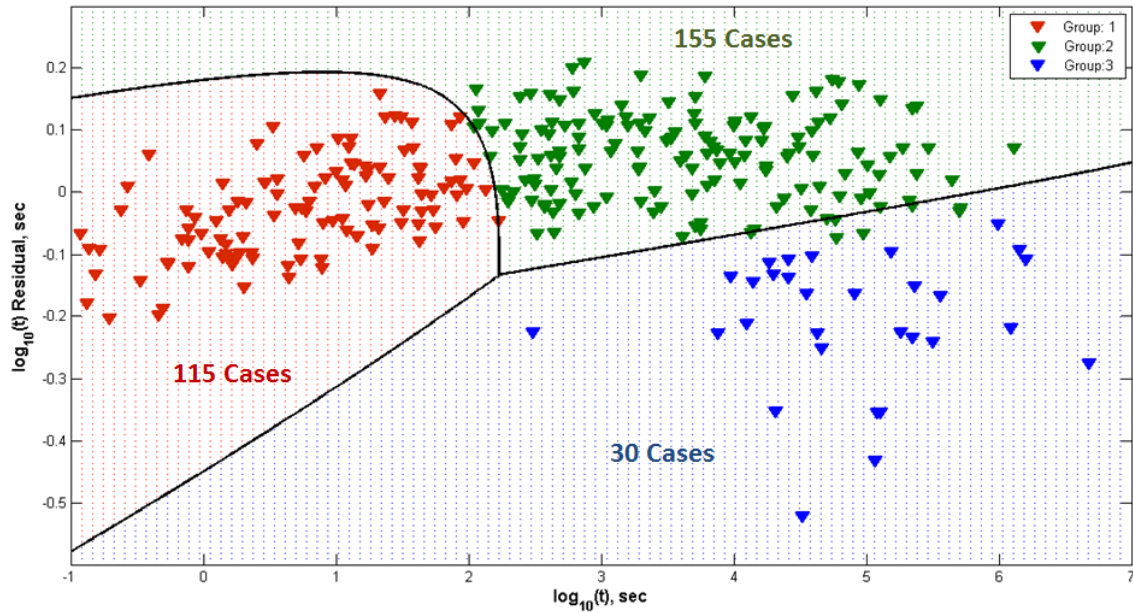


Figure 5.48 Discriminant analysis of Residual vs. Predicted Experiment Duration (1 Tank)

Based on the specified trends (correlations) of residual vs. predicted experiment duration, the design dataset is separated into three groups by using SPSS Amos (Arbuckle, 2008). By using the separated data as training groups, the boundaries between the groups are determined. Figure 5.48 gives the three groups and the solid lines between the groups show the group boundaries. Group 3 contains small number of cases, 30, compared with the number of cases of Group 1 and Group 2, 115 and 155, respectively. In addition, there are some misclassification of cases between Group 2 and Group 3.

Even though the grouping is not perfect due to unavailable of training data, these groups can be used to figure out the which design variable leads to trend in the residuals of experiment duration. Figure 5.49 gives the residuals vs. design variables plot in terms of groups. The main factor creates the trend in the residual of experiment duration is permeability. The permeability range is high for the experiment duration of 1 tank set-up. Figure 5.50 gives the permeability vs. residual experiment durations. There is a significant overlap between Group 1 and Group 2 (black circle). Therefore, the base 10 logarithm of permeability cut-off point is determined as -



0.5 (0.316 mD) so that some part of Group 2 and Group 1, and the other part of Group 2 and Group 3 are merged. This time there is only one case is misclassified indicated with purple circle. Determining base 10 logarithm of permeability is more useful for the group classification than the correlation between experiment duration and residual of experiment duration because it is impossible to get the residuals without simulation.

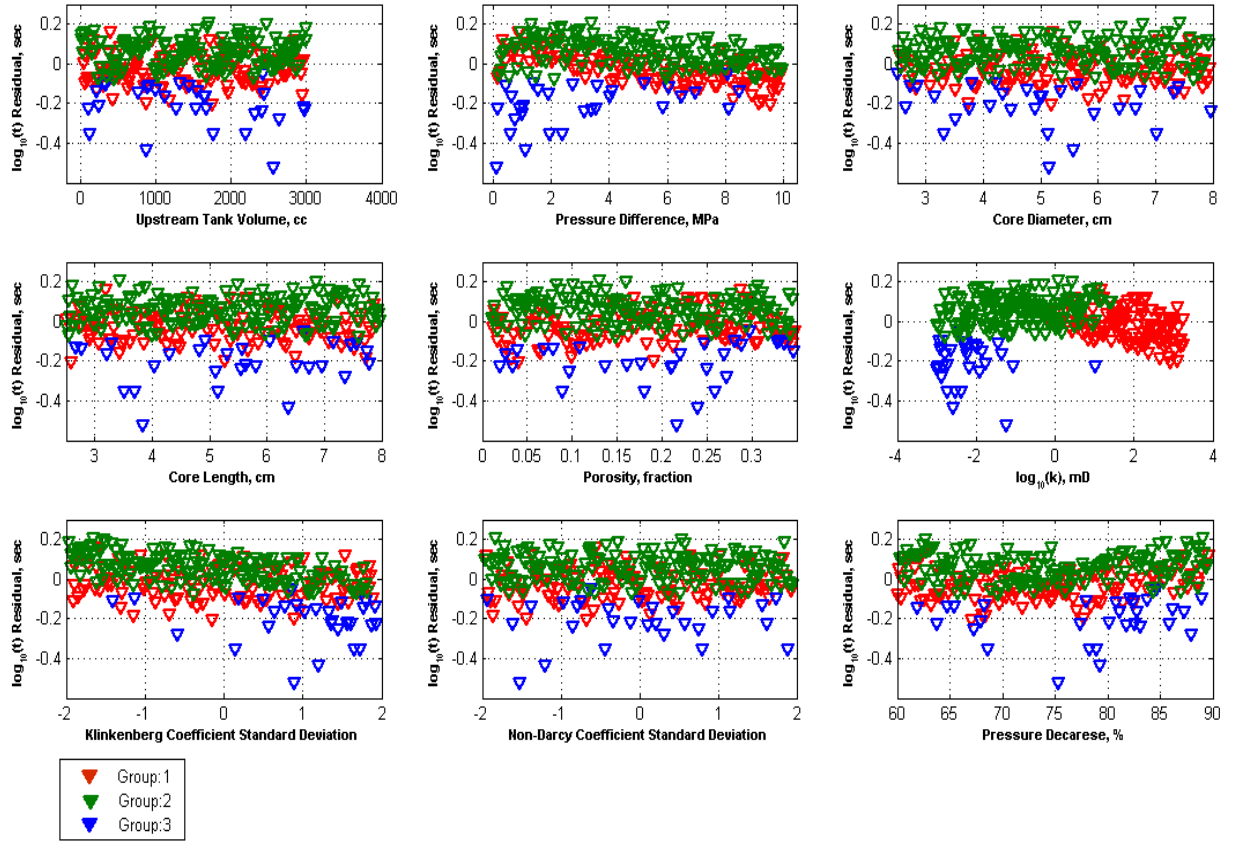


Figure 5.49 Scatter Plot of Residual vs. Design Variables (1 Tank)

Based on the two groups indicated in Figure 5.50, the pulse-decay experiment duration correlation is developed for each group from linear regression. Figure 5.51 gives the cross-plot of experiment duration obtained from correlations (predicted) (Eqn.5.50 and Eqn.5.51 for Group 1 and Group 2, respectively) and the ones obtained from pulse-decay simulations (actual). Considering the fit statistics (Table 5.18), both fits are acceptable and Group 2 fit statistics are

better. Comparing Group 1 estimates (Table 5.19) with and Group 2 estimates confidence intervals (Table 5.20) indicates that powers of intercept, pressure difference, permeability and pressure decrease are different. In addition, porosity is insignificant for Group 1 ( $p>0.05$ ), on the other hand, for Group 2 (low permeability cases), porosity is significant. This can be explained that for low permeability cores, the increase in porosity leads to delay in pulse-decay experiment duration since the pore volume is filled slowly. For both groups, there are no trends in residual vs. predicted experiment durations (Figure 5.52) and both experiment duration residuals are normally distributed (Figure 5.53). For Group 1, there is no outlier in the residuals; however, for Group 2, one point (misclassified point) is outlier. For leverage plots, there is nothing unusual (Figure 5.54 and Figure 5.55). For Group 1 the points are more scattered; therefore, the confidence intervals (standard deviation of estimation) is higher.

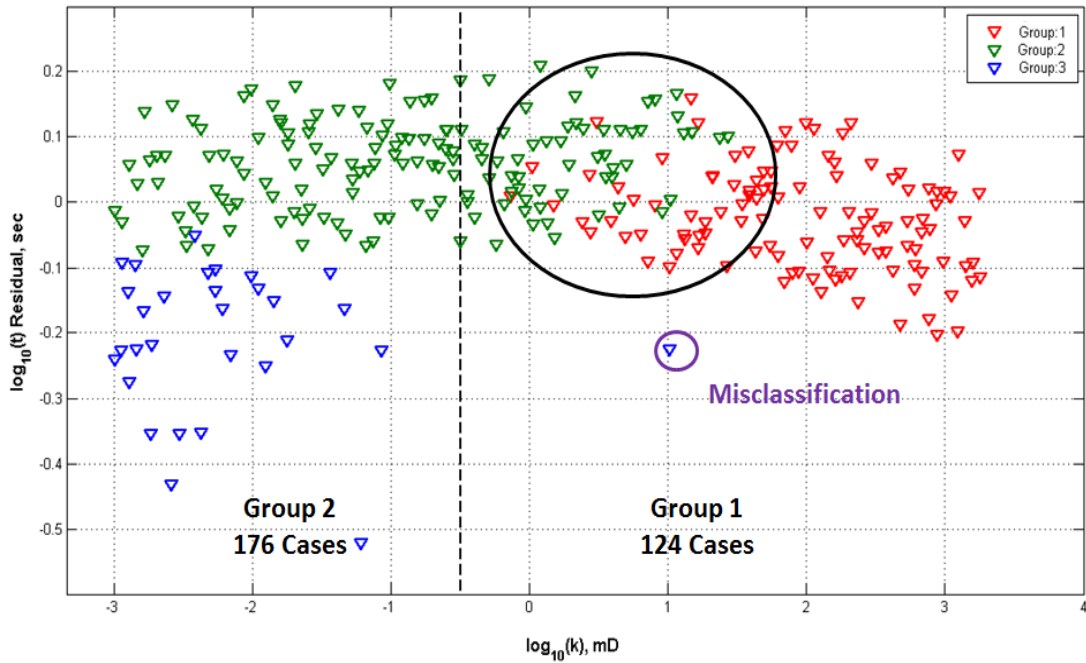


Figure 5.50 Scatter Plot of Residual vs. Permeability (1 Tank)

$$t(sec) = \frac{10^{-4.2857} V_u^{0.9759} L^{0.9759} \phi^{0.0159} P_{dec}^{2.7598}}{\Delta P^{0.4560} D^{1.9623} k^{0.8575}} \quad (5.50)$$

$$t(sec) = \frac{10^{-6.0874} V_u^{0.9929} L^{0.9685} \phi^{0.0307} P_{dec}^{3.7517}}{\Delta P^{0.6954} D^{1.9860} k^{0.9737}} \quad (5.51)$$

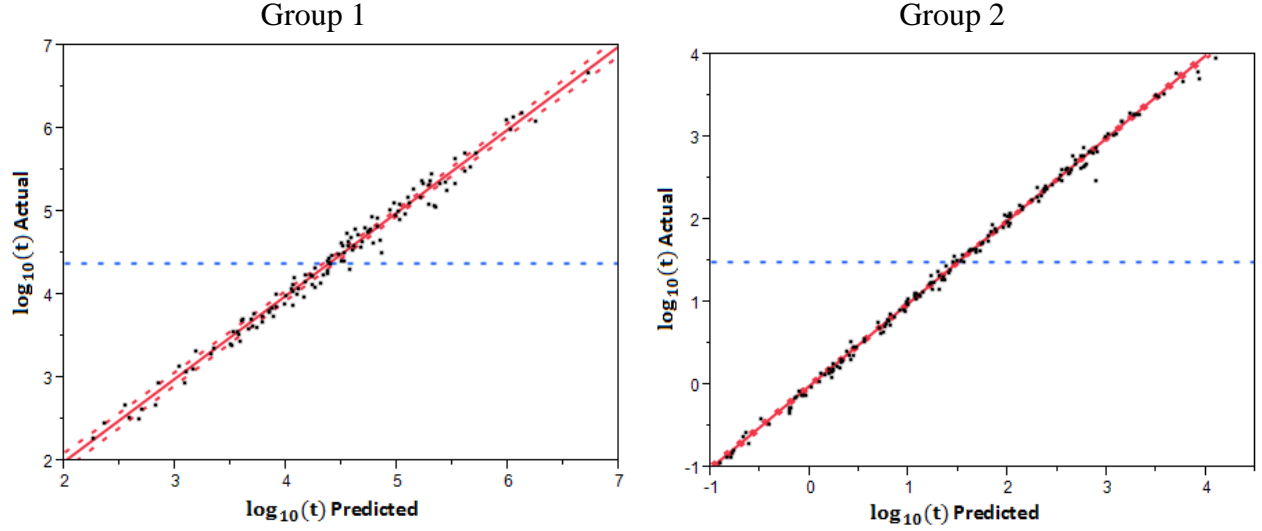


Figure 5.51 Actual by Predicted Plot of Pulse-Decay Experiment (1 Tank) Duration for 2 Groups

Table 5.18 Summary of Fit Statistics for Experiment Duration (1 Tank) for 2 Groups

Group 1		Group 2	
Coefficient of Determination, $R^2$	0.9850	Coefficient of Determination, $R^2$	0.9971
Adjusted $R^2$	0.9841	Adjusted $R^2$	0.9970
Root Mean Square Error, RMSE	0.1111	Root Mean Square Error, RMSE	0.0654
Mean of Response	4.3833	Mean of Response	1.4886

Table 5.19 Parameter Estimates of Experiment Duration Equation (1 Tank) for Group 1

Term	Estimate	Std. Error	t Ratio	Prob> t	Lower 95% CI	Upper 95% CI
Intercept	-4.2857	0.4081	-10.50	<0.0001	-5.0939	-3.4774
$\log_{10}(V_u)$	0.9759	0.0221	44.08	<0.0001	0.9320	1.0197
$\log_{10}(\Delta P)$	-0.4560	0.0266	-17.13	<0.0001	-0.5087	-0.4033
$\log_{10}(D)$	-1.9623	0.0710	-27.64	<0.0001	-2.1030	-1.8217
$\log_{10}(L)$	0.9759	0.0711	13.72	<0.0001	0.8350	1.1168
$\log_{10}(\phi)$	0.0159	0.0310	0.51	0.6095	-0.0455	0.0773
$\log_{10}(k)$	-0.8575	0.0136	-62.86	<0.0001	-0.8845	-0.8305
$\log_{10}(P_{dec})$	2.7598	0.2074	13.31	<0.0001	2.3491	3.1706

Table 5.20 Parameter Estimates of Experiment Duration Equation (1 Tank) for Group 2

Term	Estimate	Std. Error	t Ratio	Prob> t	Lower 95% CI	Upper 95% CI
Intercept	-6.0874	0.1897	-32.09	<0.0001	-6.4619	-5.7128
$\log(V_u)$	0.9929	0.0133	74.68	<0.0001	0.9667	1.0192
$\log(\Delta P)$	-0.6954	0.0126	-55.38	<0.0001	-0.7202	-0.6706
$\log(D)$	-1.9860	0.0351	-56.53	<0.0001	-2.0554	-1.9166
$\log(L)$	0.9685	0.0348	27.87	<0.0001	0.8999	1.0371
$\log(\phi)$	0.0307	0.0144	2.13	0.0347	0.0022	0.0592
$\log(k)$	-0.9738	0.0046	-212.7	<0.0001	-0.9828	-0.9647
$\log(P_{dec})$	3.7517	0.1005	37.34	<0.0001	3.5533	3.9500

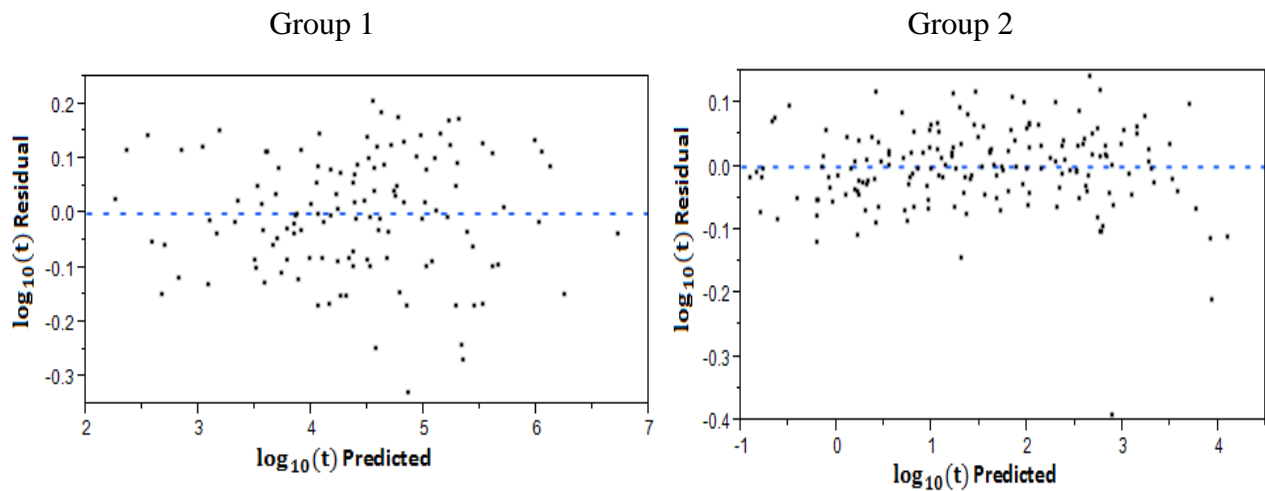


Figure 5.52 Residual vs. Predicted Plot of Experiment Duration (1 Tank) for 2 Groups

Pulse-decay experiment analysis indicates that for reliable estimation of permeability, Klinkenberg coefficient and non-Darcy coefficient from Jones method, experiment duration should be long enough so that measurement error effect on estimations is less. If there is an idea about permeability range, these correlations can be used to estimate the pulse-decay experiment duration. In addition, these correlations give a rough estimation of permeability by using experiment design parameters and experiment duration. There is only one reliable pulse-decay experiment in hand, 2C core data. With this data, the developed correlation is used to estimate pulse-decay experiment duration and permeability with inverse prediction to illustrate the methodology.

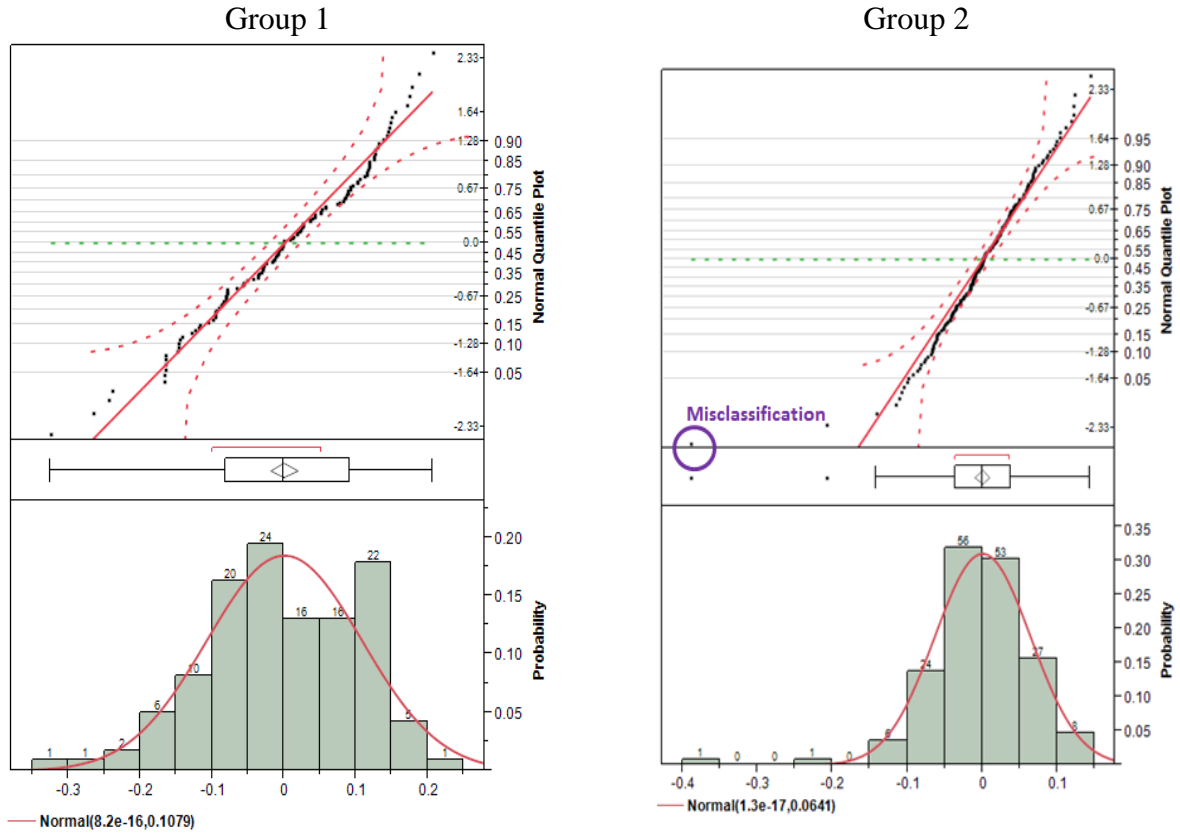


Figure 5.53 Residual Distribution of Experiment Duration (1 Tank) for 2 Groups

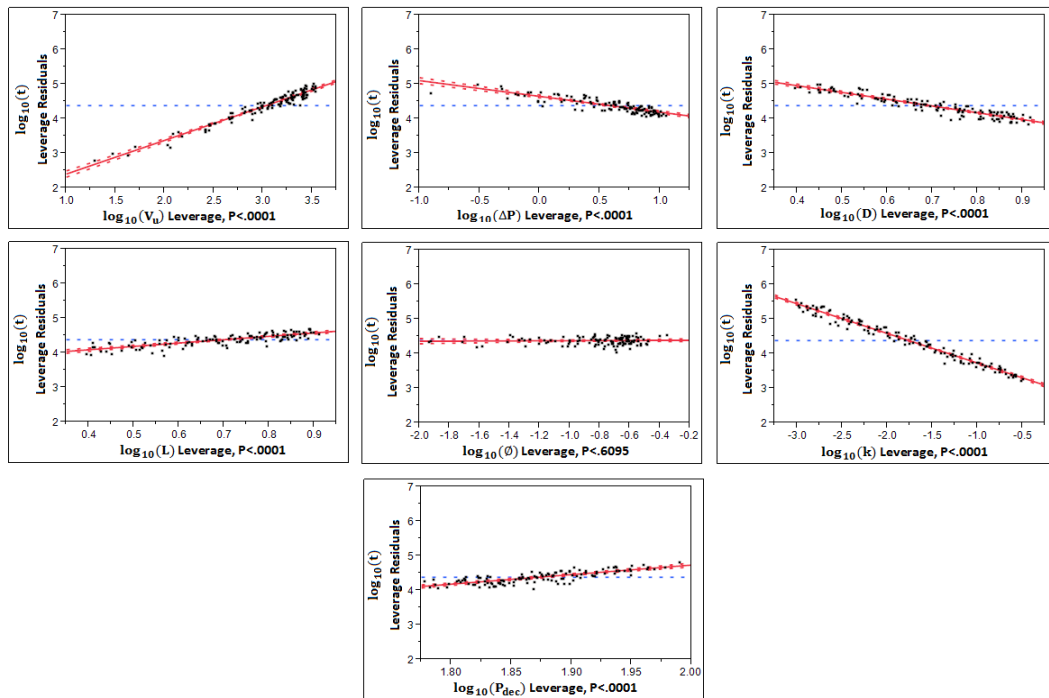


Figure 5.54 Leverage Plot of Pulse Decay Experiment Duration Design Variables (1 Tank) for Group 1

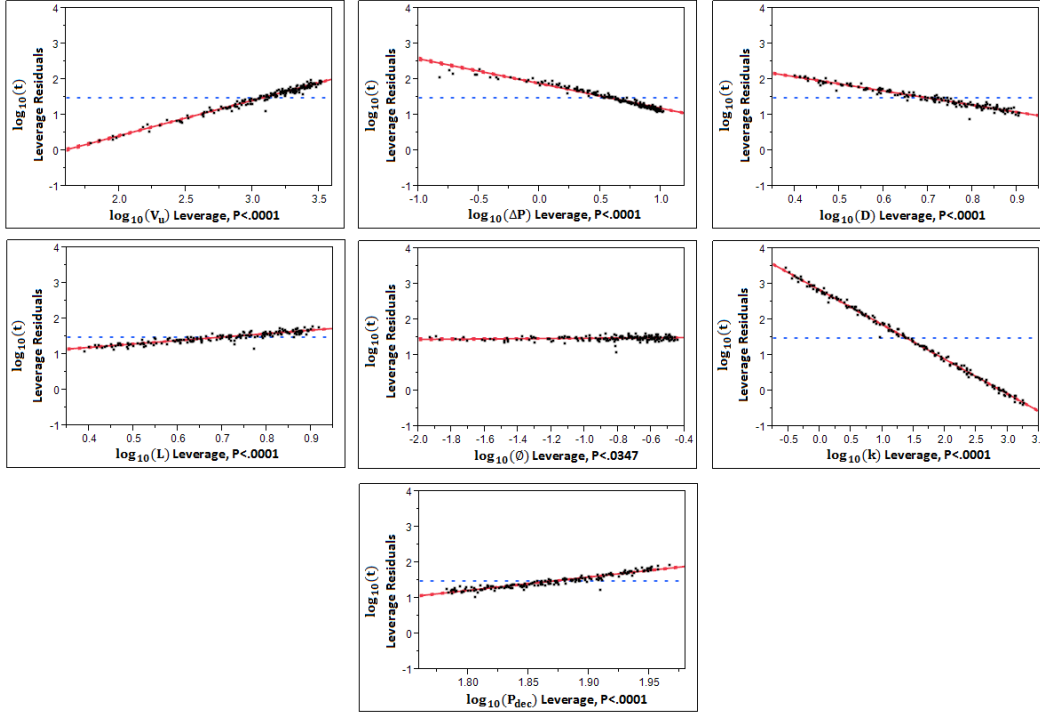


Figure 5.55 Leverage Plot of Pulse Decay Experiment Duration Design Variables (1 Tank) for Group 2

Monte Carlo simulation is used to validate the correlations by estimating the experiment duration. 2C core experiment was conducted with 1 tank set-up and core permeability is high; therefore, Eqn.5.50 is used. Table 5.21 gives the variables and their distributions used in the Monte Carlo simulation. There is no information available how the measurement is done. Therefore, for upstream tank volume, core diameter and core length intervals are determined based on last significant digit of measurements and their distributions are chosen as uniform. For example, upstream tank volume is given as 1885.341 cc; therefore its interval is chosen as [1885.340 – 1885.342]. The interval of upstream tank pressure error is determined based on assumed pressure gage error. Pressure gage error is chosen as  $\pm 0.25\%$ . The given upstream gage pressure is 1.2327 MPa; therefore the interval is  $1.2327 \times (1 \pm 0.0025)$  MPa. Similarly, the pressure decrease is determined both initial and final tank pressure errors. The final pressure is chosen as 0.2172 MPa. Therefore, the pressure decrease range is [82.36%-82.54%]. Permeability is

estimated from Jones' Method by using bootstrap sampling method and it is normally distributed with mean and standard deviation of 78.9508 mD and 0.3926 mD, respectively. 10000 samples are used to find the distribution of experiment duration. Figure 5.56 gives the lognormal distribution of experiment duration with median value of 60.74 sec and the histogram of experiment duration estimated from Monte Carlo simulation. In the histogram plot, the red line gives the real experiment duration, 53.52 sec, and magenta lines give 95% confidence interval [36.61 – 99.81 sec] obtained from Monte Carlo. The real experiment duration is close to median experiment duration value and it is between 95% confidence interval.

Table 5.21 2C Core Pulse Decay Experiment Parameters used in Monte Carlo Simulation

Variables	Distribution
Upstream Tank Volume, $V_u$ (cc)	Uniform(1885.340, 1885.342)
Initial Tank Pressure Difference, $\Delta P$ ( $P_u - P_{atm}$ , MPa)	Uniform(1.234601, 1.240794)
Core Diameter, $D$ (cm)	Uniform(3.767, 3.769)
Core Length, $L$ (cm)	Uniform(2.527, 2.529)
Porosity, $\phi$ (fraction)	Uniform(0.20539, 0.22701)
Permeability, $k$ (mD)	Normal(78.9508, 0.3926)
Pressure Difference Decrease, $P_{dec}$ (%)	Uniform(82.36246, 82.53796)

For permeability estimation of 2C core from the developed correlation (Eqn.5.50) with inverse prediction, the measurements are assumed to be perfect. Permeability of 2C core is estimated by using each point between about 17 sec and 78 sec in which the difference between upstream tank pressure and atmospheric pressure decreases between 60% and 90% of initial pressure difference. Figure 5.57 gives the estimated permeabilities with experiment duration points. In this figure, the black dots give the estimated mean permeability by using corresponding experiment duration and pressure decrease at that experiment duration and blue vertical lines give the %95 confidence intervals calculated by using the standard deviation (standard error) of permeability power. Permeability calculated from Jones' method is indicated

as a red line. Order of estimated mean permeability from correlation is consisted with the one obtained from Jones' analysis.

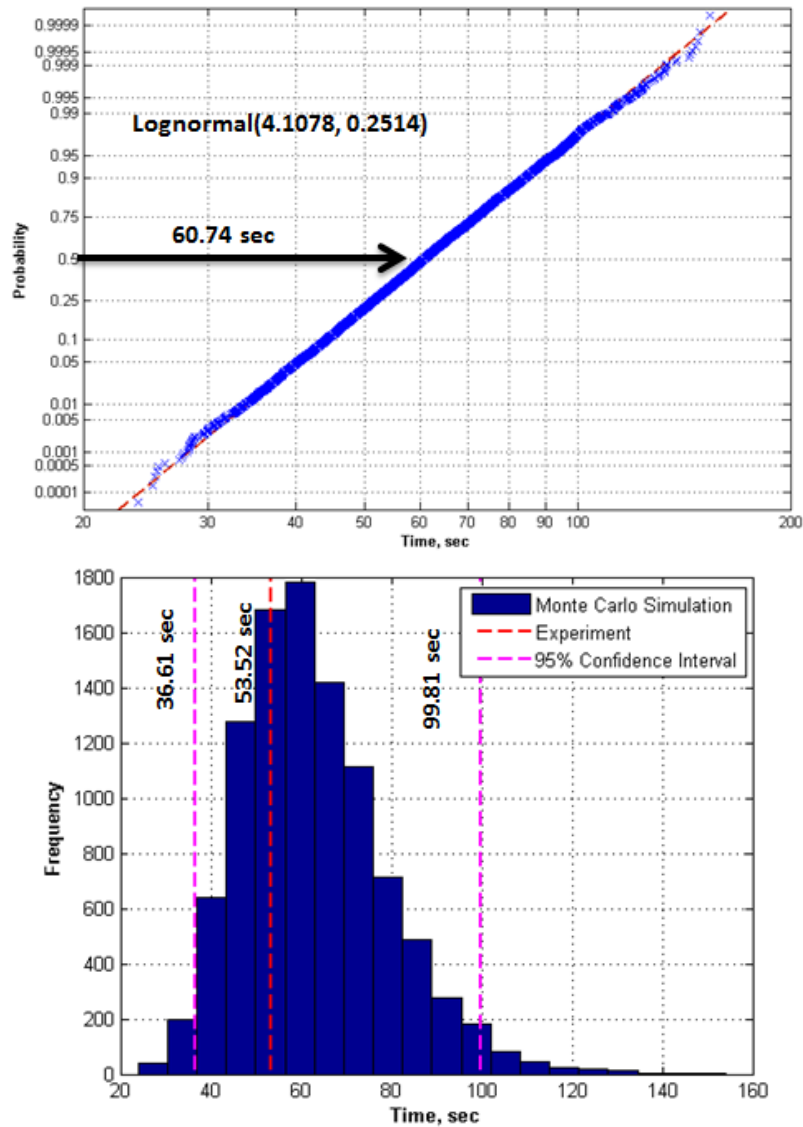


Figure 5.56 Pulse-Decay Experiment Duration Estimation from Developed Correlation with Monte Carlo Simulation

Pulse-decay experiment duration is important for reliable estimation of permeability, Klinkenberg coefficient and non-Darcy coefficient. In this part of study, experiment duration time for the 1 tank and 2 tank pulse-decay experiment set-up are developed by using the experiment conditions and core properties. These correlations give an idea about the how long



pulse-decay experiments last for the specified experiment set-up and experiment conditions. Since in these correlations Klinkenberg coefficient and non-Darcy coefficient are ignored to prevent multicollinearity problem, estimated time intervals and permeability interval obtained from inverse prediction is large. The main question left for the pulse-decay experiment is: what is the necessary pulse-decay experiment duration for reliable estimation of permeability, Klinkenberg coefficient and non-Darcy coefficient? To answer this question, pulse-decay experiments are necessary for cores with different permeability. This part of the study is left as a future work of this research.

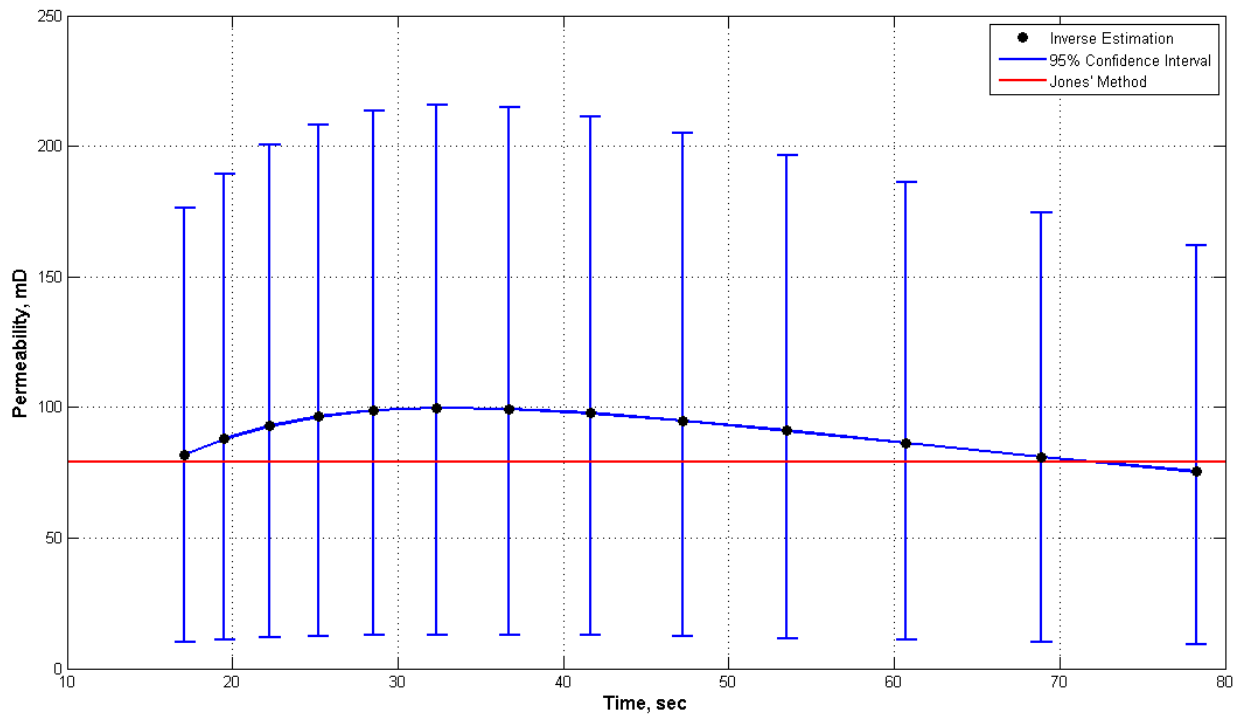


Figure 5.57 Inverse Prediction of 2C Core Permeability by using Developed Correlation

## CHAPTER 6: PORE-SCALE ANALYSIS

Fluid dynamics can be modeled in three different scales: microscopic, mesoscopic and macroscopic scales. At all scales, the main concept governing modeling is conservation of mass, momentum and energy. At microscopic scales, atoms and molecules are considered, and fluid dynamics can be modeled with the Hamilton equation. At the macroscopic scale, fluid acts as a continuum and fluid dynamics is modeled from the Navier-Stokes equations. The mesoscopic scale is the connection between these two extremes. At this scale, fluid is considered as fictitious particles and translates on a fixed mesh. Lattice gas and lattice Boltzmann are examples of techniques that can be used for fluid dynamics.

In pore-scale analysis of porous media, rock properties are estimated with two different approaches: lattice Boltzmann Method (LBM) and network modeling. In this chapter, after brief introduction to these methods, the packing algorithm used to construct the packing domain is checked. Then two approaches are compared with respect to resolution effects and grain shape or pore-shape effects. The database containing rock properties and pore structure properties is constructed with LBM and network modeling simulations and correlations are developed for non-Darcy coefficient and permeability. Path analysis is conducted for better estimation of flow properties and missing data estimation is conducted. As a final part of pore-scale analysis, compaction and sand migration effects on permeability and non-Darcy coefficient are investigated and some correlations are developed for reservoir simulator.

### 6.1 Lattice Boltzmann Method and Network Modeling

The Boltzmann equation gives time evaluation of the particle distribution function,  $f$  in phase space in which coordinates are given by position,  $x$  and momentum vectors,  $e$ .

$$f(x + e\Delta t, e, t + \Delta t) = f(x, e, t) - \Omega(f)\Delta t \quad (6.1)$$

$\Omega(f)$  is the collision function defining the rate of change of the distribution function. In the limit  $\Delta t \rightarrow 0$ , the Boltzmann equation can be written as;

$$\mathcal{D}_t f = \Omega(f) \quad (6.2)$$

$\mathcal{D}_t$  is total derivative and defined as  $\mathcal{D}_t = \partial_t + \mathbf{e} \cdot \nabla$ . Macroscopic quantities such as density,  $\rho$ , velocity,  $u$  and specific internal energy,  $\epsilon$ , can be calculated from integration of the distribution function moment over velocity space.

$$\rho(x, t) = \int f(x, \mathbf{e}, t) d\mathbf{e} \quad (6.3)$$

$$u(x, t) = \frac{1}{\rho} \int \mathbf{e} \cdot f(x, \mathbf{e}, t) d\mathbf{e} \quad (6.4)$$

$$\epsilon(x, t) = \frac{1}{2\rho} \int (\mathbf{e} - \mathbf{u})^2 \cdot f(x, \mathbf{e}, t) d\mathbf{e} \quad (6.5)$$

The Boltzmann equation is difficult to solve. The lattice Boltzmann method (LBM) is a simplified form of Boltzmann equation obtained by discretizing time and space.

$$f_a(\mathbf{x} + \mathbf{e}_a \Delta t, t + \Delta t) - f_a(\mathbf{x}, t) = \Omega(f) \quad (6.6)$$

In this method, particles are placed on nodes of the lattice and variation in velocity directions and magnitudes and particle mass are reduced to a specific number of directions (Figure 6.1). Microscopic velocities are equivalent to momenta since particle mass is uniform (1 mass unit,  $m_u$ ). In LBM, fundamental length and time units are the lattice unit (lu) and lattice time step (ts). The LBM scheme proposed by Qian et al (1992) is based on the dimensions and the number of velocity directions. For example, the 2-dimensional and 9-velocity (D2Q9) scheme is shown in Figure 6.1. The velocity of  $\mathbf{e}_0$  is 0, and it represent the particle at rest. The velocity magnitude of  $\mathbf{e}_1$  through  $\mathbf{e}_4$  is 1 lu/ts and velocity magnitude  $\mathbf{e}_5$  through  $\mathbf{e}_8$  is  $\sqrt{2}$  lu/ts. Single particle distribution,  $f$  is represented with histogram and each bin gives the direction-

specific fluid densities,  $f_\alpha$ . With histogram representation, the integral equations describing macroscopic quantities (Eqn.6.3 through Eqn.6.5) turn into summation as;

$$\rho(x, t) = \sum_{\alpha=0}^8 f_\alpha \quad (6.7)$$

$$u(x, t) = \frac{1}{\rho} \sum_{\alpha=0}^8 f_\alpha e_\alpha \quad (6.8)$$

$$\epsilon(x, t) = \frac{1}{2\rho} \sum_{\alpha=0}^8 (e_\alpha - u)^2 \cdot f_\alpha \quad (6.9)$$

Bhatnagar, Gross and Krook (1954) simplified the collision term in Eqn.6.6 considering that collisions tends to relax the distribution functions into equilibrium.

$$\Omega(f) = -\frac{f_\alpha - f_\alpha^{eq}}{\tau} \quad (6.10)$$

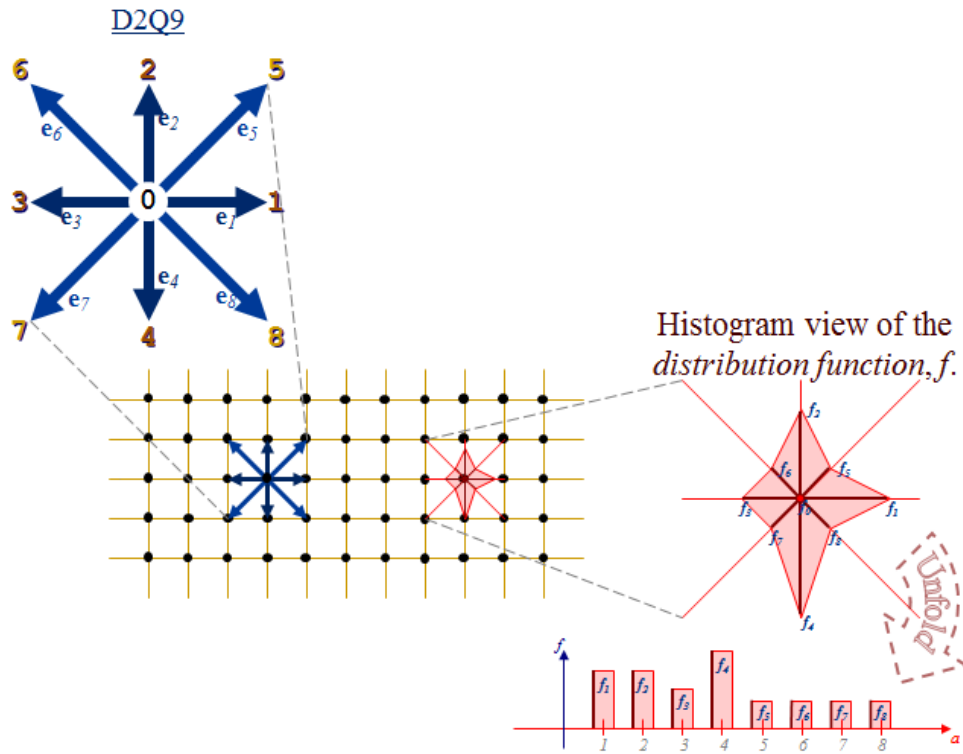


Figure 6.1 Lattice Structure, and Velocity Distribution and Histogram View (Sukop & Thorne, 2007)

$\tau$  and  $f_\alpha^{eq}$  are relaxation time and equilibrium distribution function, respectively. Single relaxation time LBM is called BGK. To make LBM more stable, a multi-relaxation time, MRT, was developed by D'Humieres et al. (2002). In this model, distribution function relaxes independently for each direction.

$$\Omega(f) = S(f_\alpha - f_\alpha^{eq}) \quad (6.11)$$

$S$  is the collision matrix and the eigenvalues of  $S$ , the inverse of relaxation times, are all between 0 and 2 to maintain linear stability. BGK is special case of MRT in which all relaxation times are equal,  $S = \tau^{-1}I$ , where  $I$  is identity matrix.

Equilibrium distribution function for the D2Q9 is

$$f_\alpha^{eq}(x) = w_\alpha \rho(x) \left[ 1 + 3 \frac{\mathbf{e}_\alpha \cdot \mathbf{u}}{c^2} + \frac{9}{2} \frac{(\mathbf{e}_\alpha \cdot \mathbf{u})^2}{c^4} - \frac{3}{2} \frac{u^2}{c^2} \right] \quad (6.12)$$

$c$  is basic speed on 1 lu/ts and  $w_\alpha$  is weights which is 4/9 for rest particle, 1/9 for  $e_1$  through  $e_4$  and 1/36 for  $e_5$  through  $e_8$  for D2Q9 lattice structure.

Fluid kinematic viscosity is calculated using relaxation and lattice sound speed as;

$$\nu = c_s \left( \tau - \frac{1}{2} \right) \quad (6.13)$$

$c_s$  is speed velocity,  $1/\sqrt{3}$  and viscosity unit is  $\text{lu}^2/\text{ts}$ .

Pressure is related to fluid density by the equation state.

$$P(x, t) = c_s^2 \rho(x, t) \quad (6.14)$$

LBM units can be converted to geophysical units with mapping functions;  $L_o$ ,  $T_o$  and  $M_o$  for length, time and mass; respectively (Llewellyn, 2010). Length mapping  $L_o$  is the resolution of the simulation. Mass mapping is calculated from density,  $\rho$ . Density has dimension of  $[M][L]^{-3}$ ,

$$\rho = \frac{M_o}{L_o^3} \rho_l \quad (6.15)$$

$\rho_l$  is lattice density. Time mapping  $T_o$  is calculated from kinematic viscosity,  $\nu$ . Viscosity has dimension of  $[L]^2[T]^{-1}$ ,

$$\nu = \frac{L_o^2}{T_o} \nu_l \quad (6.16)$$

$\nu_l$  is lattice viscosity. With finding mapping functions, lattice velocity,  $u_l$  and pressure,  $P_l$  can be converted to physical velocity,  $u$ , and pressure,  $P$ , as ;

$$u = \frac{L_o^2}{T_o} u_l \quad (6.17)$$

$$P = \frac{L_o^2}{T_o^2} P_l \rho \quad (6.18)$$

The other method to estimate permeability is network modeling. Network modeling divides the pore structure into pores and pore throats. The major algorithms to extract networks from 3D image of real or synthetic porous media are multi-orientation scanning method, the medial axis based method, the maximum ball method, and Voronoi diagram method (Dong, 2007). In the multi-orientation scanning method, multi-oriented plates scanning pores channels to detect pore bodies and pore throats. Pore throats are detected with overlapping plates; however, the algorithm has difficulty in finding the pore bodies. In the medial axis based method, the pore space is converted to the medial axis by a thinning algorithm or burning algorithm. The pore space is eroded starting from the grain surface until different burn numbers end up in a voxel. Local maximums along the medial axis are where the pores are located. Pore throats are located at local minima. Even though the medial axis method preserves the topology, it has a difficulty to identify the pores because of sensitivity of the algorithm to noise in digitalized images. The Voronoi diagram based algorithms use grain centers to extract pore networks using Voronoi diagram.

In the maximal ball algorithm, each voxel in the pore space is searched to locate the largest inscribed spheres, which just touch the grain surface. Then, the spheres enclosed in the other spheres are removed. The remaining are maximum balls which define the pore bodies. The smallest pores between the maximum balls are defined as pore throats (Figure 6.2).

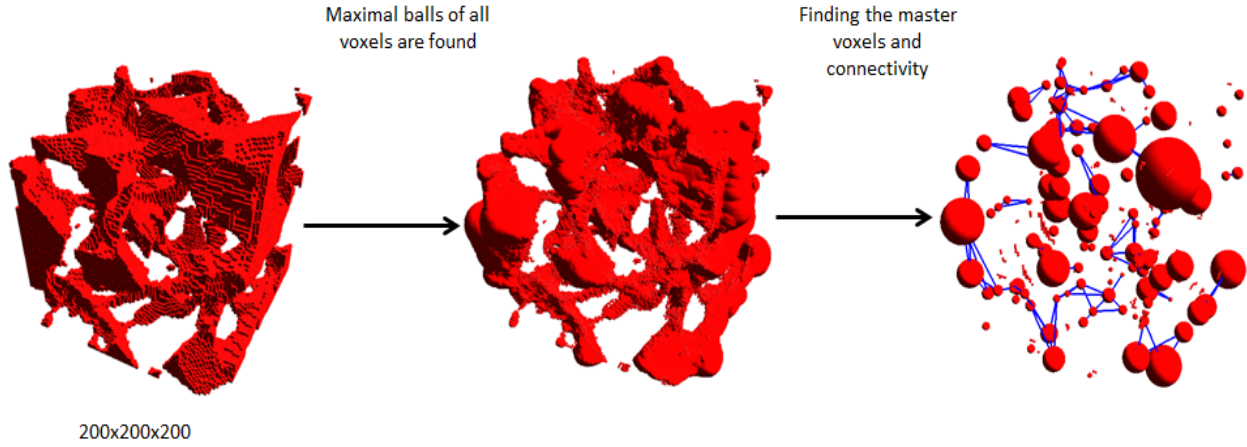


Figure 6.2 Maximum Ball Algorithm (Silin, Jin, & Patzek, 2003)

After pore and pore throat identification, steady-state flow of an incompressible fluid is modeled using mass conservation for each pore body, described as;

$$\sum q_{ij} = 0 \quad (6.19)$$

$q_{ij}$  is flow rate between pores  $i$  and  $j$ . Flow rate is given as,

$$q_{i,j} = \frac{g_{i,j}}{\mu} (P_j - P_i) \quad (6.20)$$

$g_{i,j}$  is hydraulic conductivity. The resulting system of linear equations for the pore pressures is solved so that pressure distribution is obtained and permeability is calculated from the Darcy equation.

## 6.2 Packing Algorithm Reproducibility Validation

For lattice Boltzmann simulations and network modeling, computer generated packs are used. The packing domains are constructed with an algorithm written by Dr. Le Yan. To check

the repeatability of the packing structure, ten packing domains were prepared with same target inputs and the spatial variability of the packing domains were compared with extended variograms. For packing domains, porosity, mean particle diameter and domain size are chosen as 0.5, 0.448 mm and 5.149 mm, respectively. Figure 6.3 gives the grain size distribution used in packing domain generation and packed domains of Run1. Table 6.1 gives the porosity, mean particle size, particle number, min and max particle sizes and their ratios obtained from each run. Even though target mean particle size is obtained, there are small differences between pack porosity and target porosity, 0.5. The other variables, particle number and min/max particle sizes are similar for each run.

Table 6.1 Packing Simulation Runs

Run	Porosity (fraction)	Mean Particle Size (mm)	Particle Number	Min Particle (mm)	Max Particle (mm)	Max/Min
1	0.518	0.448	1212	0.1539	0.4061	2.639
2	0.519	0.448	1210	0.1539	0.4057	2.636
3	0.519	0.448	1211	0.1539	0.4061	2.639
4	0.519	0.448	1212	0.1539	0.4061	2.639
5	0.519	0.448	1213	0.1539	0.4061	2.639
6	0.518	0.448	1213	0.1539	0.4061	2.639
7	0.518	0.448	1216	0.1539	0.4026	2.616
8	0.517	0.448	1217	0.1539	0.4061	2.639
9	0.518	0.448	1214	0.1539	0.4055	2.635
10	0.518	0.448	1212	0.1539	0.4061	2.639

After packing, each packed domain is voxelized into 343x343x343 voxels. Figure 6.4 gives voxel image of Run1 through Run4 at the 150<sup>th</sup> layer. White and black colors represent the grain and pore voxels respectively. Grain locations change in each run because the algorithm is based on Monte-Carlo algorithm. For the variogram calculations, 40 voxels at the edges are trimmed and the remaining domain is subdivided into subdomains with 50 voxels edge size. There is no overlap between the subdomains, and the total number of subdomain is 125. For each



subdomain, an omnidirectional semi-variogram is calculated using the Matlab toolbox mGstat. Figure 6.5 gives the box plot of the calculated semi-variogram of packed formation obtained from Run1. In this figure, the red lines in the boxes give the median of the semivariance, and lower and upper edges of boxes give the 25 and 75 percentiles of the semivariance, respectively. Lower and upper parts of the boxes sizes are almost similar which indicates that calculated semi-variograms are not skewed. The lines above and below the boxes give the 1.5 times of the interquartile range. Data outside these lines are considered outliers. The sill value, 0.26, is close to  $\phi(1 - \phi)$ , 0.25.

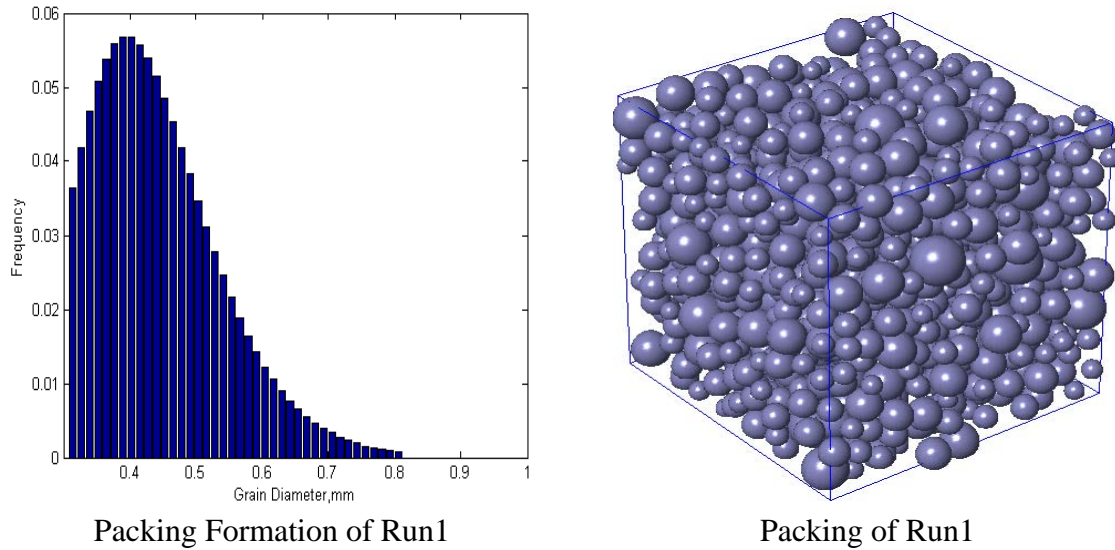
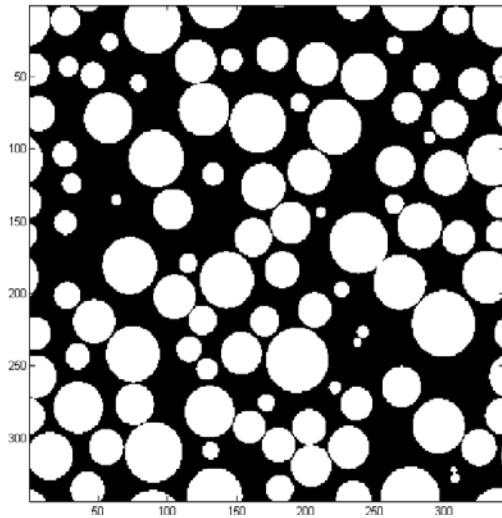


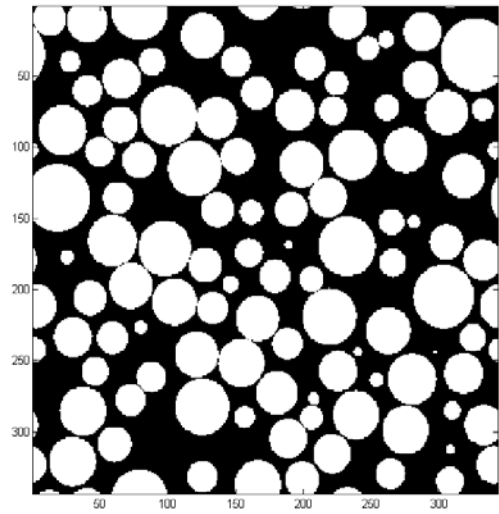
Figure 6.3 Grain Size Distribution and Packing Formation for Packing Algorithm Verification

Anova (Analysis of variance) is conducted for each point of voxel separation to test whether the all runs give the similar semi-variance mean or not. Figure 6.6 gives the box plot of semivariance for the first voxel separation point (0.9430). Both the median and, first and third quartile ranges are similar for 10 runs. Table 6.2 gives the Anova results for the first voxel separation point. In this table, ‘Source’, ‘SS’, ‘df’, ‘MS’, ‘F’ and ‘Prob>F’ give the source of variability, sum of squares of each source, mean square of each source, F statistics and the  $p$

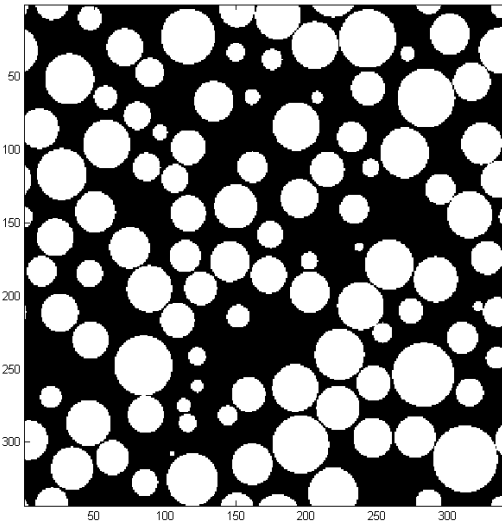
value corresponding to F statistics. The  $p$  value is greater than the significance level, 0.05. This indicates that all runs give similar semivariance mean. Table 6.3 gives  $p$  values for all voxel separation and all of them greater than 0.05. This indicates that packing algorithm generates similar packs with the same inputs.



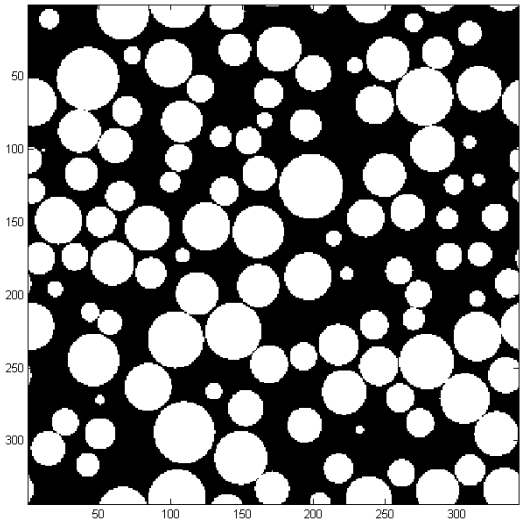
a) Voxel Image of Run1



b) Voxel Image of Run2



c) Voxel Image of Run3



d) Voxel Image of Run4

Figure 6.4 Voxel Image of Layer 150 for Run1 through Run4

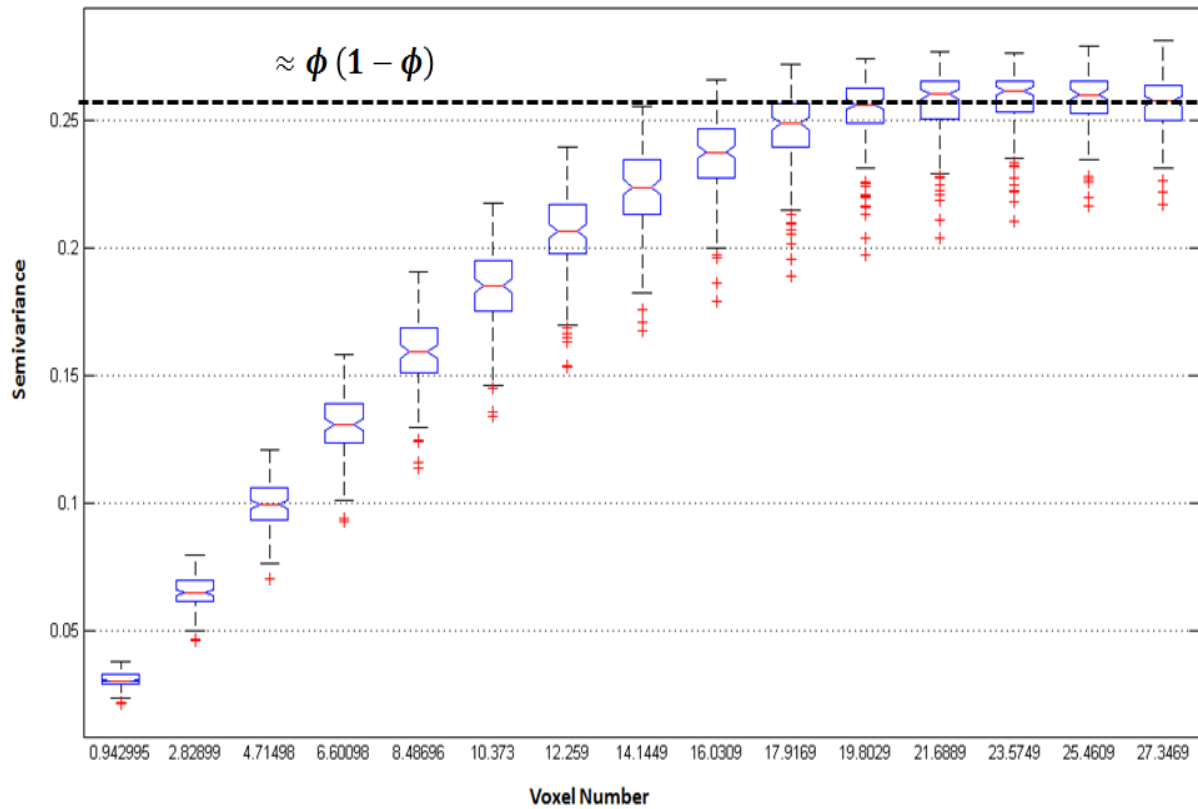


Figure 6.5 Extended Semi-variogram for Voxelized Packing Formation of Run1

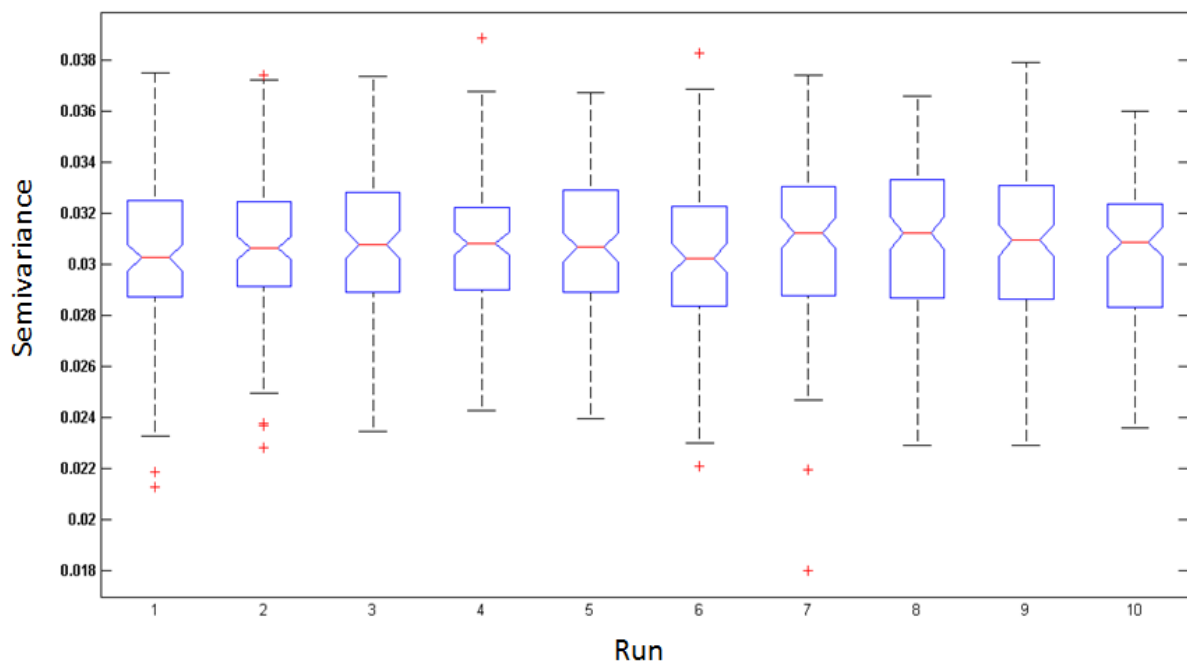


Figure 6.6 Semivariance Comparison for Voxel Separation of 0.9430

Table 6.2 Anova Table for Voxel Separation of 0.9430

Voxel Separation	'Source'	'SS'	'df'	'MS'	'F'	'Prob>F'
0.943	'Columns'	4.44E-05	9	4.93E-06	0.579758	0.814583
	'Error'	0.010553	1240	8.51E-06	[]	[]
	'Total'	0.010597	1249	[]	[]	[]

Table 6.3 p values for Semi-variance Comparison

Voxel Separation	'Prob>F'
0.943	0.814583
2.829	0.862132
4.715	0.895205
6.601	0.916491
8.487	0.928131
10.373	0.939762
12.259	0.953248
14.145	0.966038
16.031	0.972879
17.917	0.971862
19.803	0.958317
21.689	0.925107
23.575	0.882198
25.461	0.861835
27.347	0.861835

Extended variogram indicates that the spatial variability of each pack is similar. To confirm that the domains with similar spatial variability have similar macroscopic flow properties, network parameters are investigated. The permeability and capillary pressure of each domain are calculated from network modeling. For capillary calculation, wetting and non-wetting phases are chosen as air and mercury. Air and mercury densities are  $0.0013 \text{ g/cm}^3$  and  $13.534 \text{ g/cm}^3$ , respectively. The interfacial tension between air and mercury is  $486.0 \text{ dynes/cm}$ . The Swanson point, where the  $45^\circ$  tangent line intercepts with the log-log plot of mercury saturation according to bulk volume vs. capillary pressure, is found. Figure 6.7 gives the

Swanson Point plot for Run1. In this plot, the blue circles, green line, and red point give the calculated capillary pressures, 45° line and Swanson point, respectively. Calculated Swanson points are very close for each run. Table 6.4 gives the network results: coordination number (the number of pore throat connected to the pore), average throat length and permeability, and Swanson point. All results are similar. This indicates that even though the spatial locations of particles are different (Figure 6.4), flow properties are similar due to similar spatial variability of packing domains.

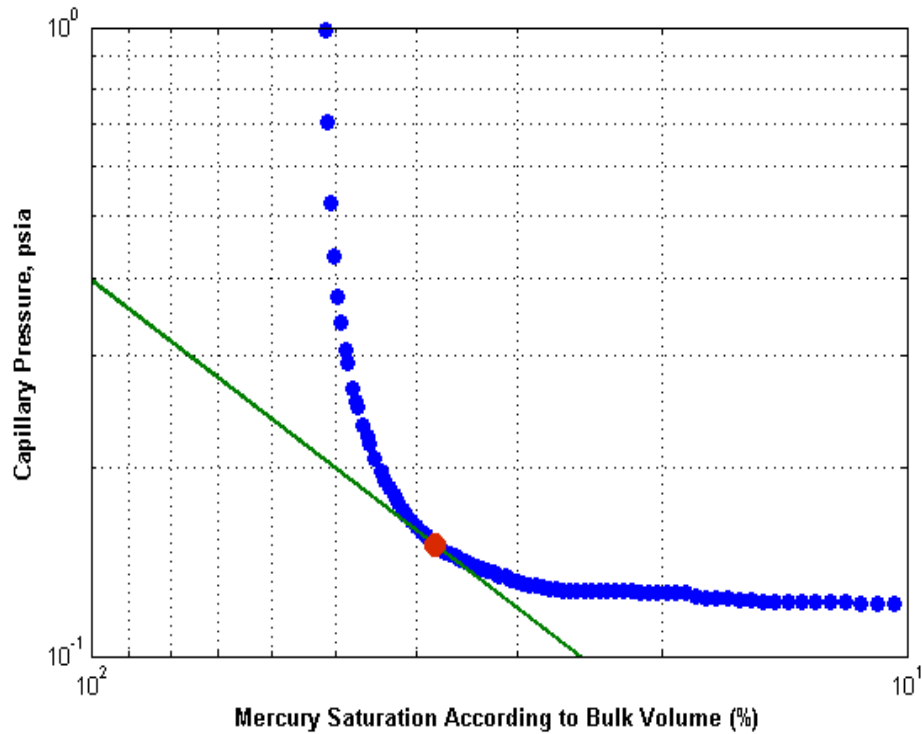


Figure 6.7 Swanson Point of Capillary Pressure of Packing Domain Run01

### 6.3 Representative Elementary Volume of Gravel Packs

For LBM simulations, the domain should be voxelized with higher resolutions so that boundaries between the grain particles and pore space smooth. Due to high resolution, the domain used in LBM simulation is limited. Therefore, the representative domain for gravel packs should be determined to obtain reliable porosity and permeability. Packing is constructed with

highest standard deviation of base 2 logarithm of grain size equal to 0.5. The domain size is 9 mm and contains 334 particles; minimum and maximum particles sizes are 0.6568 mm and 2.6434 mm, respectively (Figure 6.8).

Table 6.4 Network Results of Random Pack

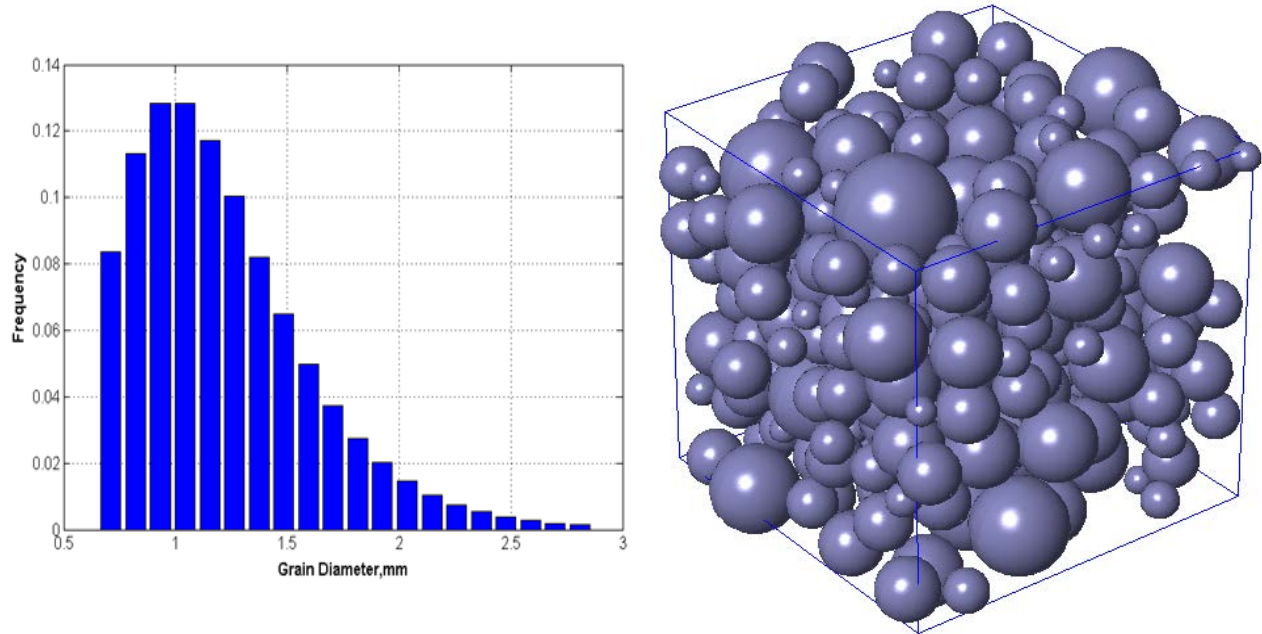
Run	Coordination Number			Average throat length (cm)	Permeability (mD)	$S_{wn}$ (%)	$P_c$ (psia)	$S_{wn}/P_c$
	min	max	average					
1	0	32	8.54	0.054916	1177.2	37.82	0.1508	250.85
2	0	44	8.65	0.055309	1217	37.91	0.1516	250
3	0	42	8.55	0.056277	1192.9	37.84	0.1506	251.22
4	0	34	8.57	0.055596	1210.1	37.82	0.1511	250.21
5	0	35	8.45	0.055377	1213.1	37.72	0.1506	250.5
6	0	41	8.48	0.054811	1163.7	37.77	0.1522	248.18
7	0	37	8.34	0.055891	1168.7	37.48	0.1516	247.31
8	0	33	8.4	0.056335	1169.9	37.89	0.153	247.59
9	0	35	8.45	0.055266	1198.8	37.64	0.1497	251.39
10	0	45	8.55	0.055785	1174.7	37.75	0.1506	250.62

For the discretized packings, voxel resolution is chosen as 0.015 mm in which domain side and minimum particle diameter are represented with 600 voxels and 44 voxels. Starting with 50 voxels per side inside the pack (0.75 mm), the domain is extended to 600 voxels per side with an increment of 50 voxels.

Figure 6.9 gives images from subdomain samples. In these figures, particles and pore space are indicated with red and blue voxels, respectively. The green voxels are boundaries between grains and pore-space where LBM bounce back conditions are applied. For each domain, porosity is calculated by counting the pore voxels and permeability is calculated with Bhatnagar-Gross-Krook (BGK) method with  $\omega$  (1/relaxation time) of 1.0 (Figure 6.10) by using open source codes PALABOS (Parallel Lattice Boltzmann Solver). The source codes are

available at web address [www.lbmmethod.org/palabos](http://www.lbmmethod.org/palabos). All LBM simulations are conducted on Louisiana High Performance Computing (HPC) resources.

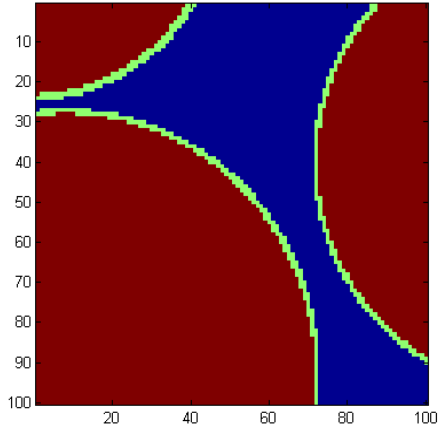
For small domains, both porosity and permeability fluctuate in similar trends and fluctuations decrease with the increase in domain size, and both porosity and permeability approach the true values. For gravel packs, the representative elementary volume (REV) of porosity and permeability are same. For this most heterogeneous pack, REV contains 400 voxels per side (6 mm).



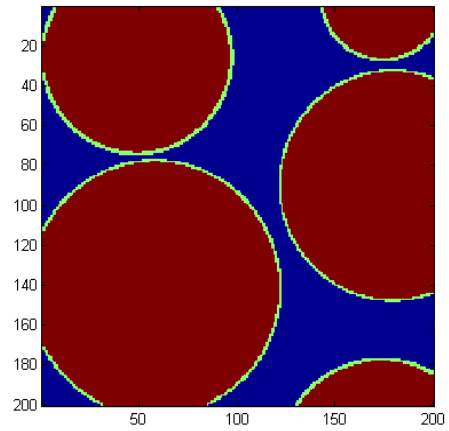
a) Grain Size Distribution  
b) Heterogenous Pack  
Figure 6.8 Heterogeneous Pack used in Representative Elementary Volume Study

#### 6.4 Lattice Boltzmann Method and Network Modeling Comparison

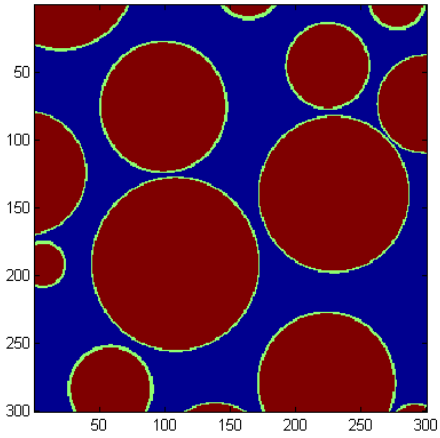
To obtain reliable estimation of flow properties, two methods, LBM and Network Modeling, are closely investigated based on resolution and model specific parameters such as relaxation time (LBM) and pore merging (network modeling). In addition, the effects of grain shape and grain packing are examined by extending the domain in the z direction.



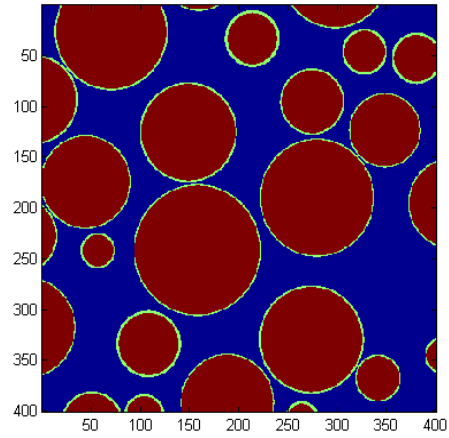
a) Domain Size: 100 voxels (1.5 mm)



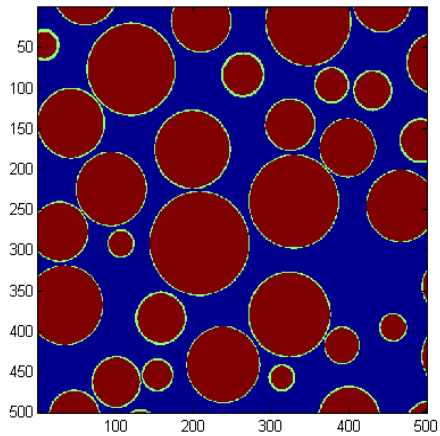
b) Domain Size: 200 voxels (3.0 mm)



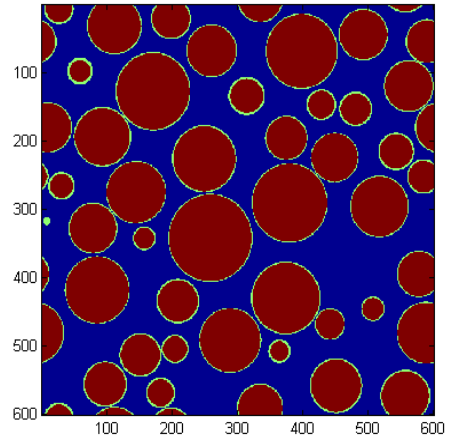
c) Domain Size: 300 voxels (4.5 mm)



d) Domain Size: 400 voxels (6.0 mm)



e) Domain Size: 500 voxels (7.5 mm)



f) Domain Size: 600 voxels (9.0 mm)

Figure 6.9 Subdomains of Heterogeneous Pack



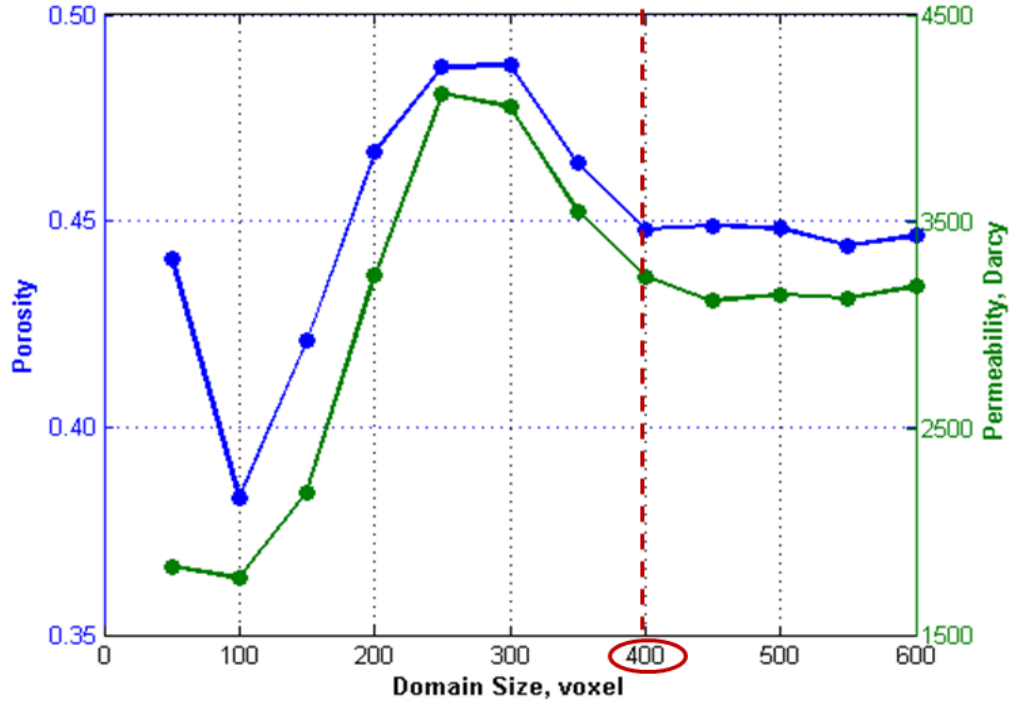


Figure 6.10 Representative Elementary Volume of Heterogeneous Pack for Porosity and Permeability

#### 6.4.2 Resolution and Model Specific Parameters Effect on Flow Properties Estimation

LBM results depend on the resolution and boundary effect due to the bounce-back rule, in which particles meeting the wall nodes reversed. To investigate these effects, the domain used in Representative Elementary Volume (REV) determination is voxelized with different resolutions in which minimum particle diameter is represented with between 10 and 44 voxels (Table 6.5). For lowest and highest resolutions, voxel sizes are 0.066 mm and 0.015 mm, and the cubic domain sides are represented with 136 and 600 voxels, respectively. As the voxel size decreases, the grains are represented with more voxels and grains boundaries become more smooth (Figure 6.11).

Porosity calculated from voxelized images are similar and close to real porosity, 0.446 (Figure 6.12). This indicates that porosity is almost not affected by voxel resolution. Permeabilities are calculated for different  $\omega$  (1/relaxation time) between 0.6 and 1.5 from BGK (Figure 6.13)

and MRT (Figure 6.14) methods. For both methods, calculated permeabilities strongly depend on resolution and relaxation time. For the largest voxel size, 0.066 mm (136 voxels per domain size), calculated permeability using the BGK method changes from  $2.81 \times 10^3$  Darcy ( $\omega$ : 1.5) and  $4.15 \times 10^3$  Darcy ( $\omega$ : 0.6). For smallest voxel size, 0.015 mm (600 voxels per domain size), calculated permeability using the BGK method changes from  $3.37 \times 10^3$  Darcy ( $\omega$ : 1.5) and  $3.17 \times 10^3$  Darcy ( $\omega$ : 0.6). The difference between calculated permeabilities decreases as voxel size decreases. For example, the calculated permeability differences are  $1.34 \times 10^3$  Darcy and 194 Darcy for voxel sizes of 0.066 mm and 0.015 mm, respectively. For  $\omega$  1.1, the calculated permeability seems to be independent of resolution; however this is the compensation of grid and image resolution errors about this artifact is explained more detailed by Borujeni (2013).

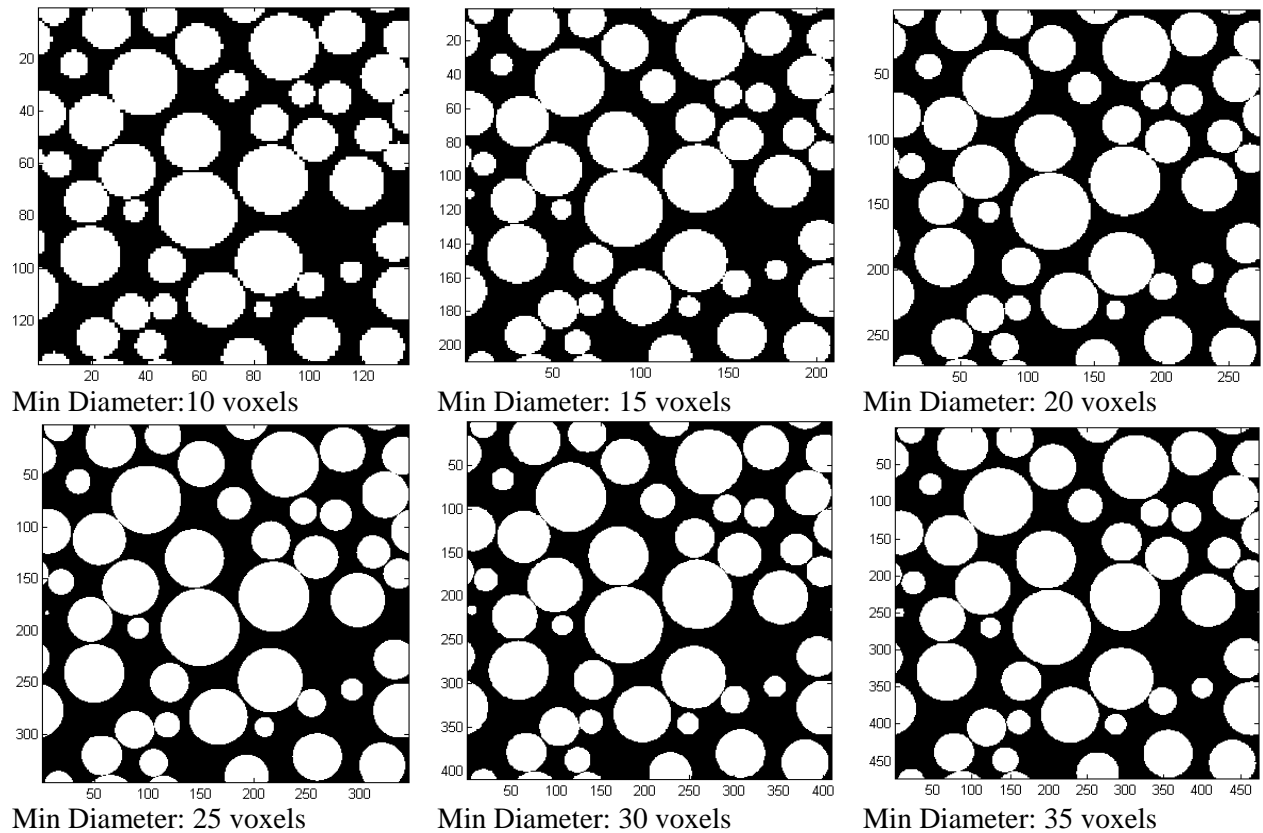


Figure 6.11 Image Resolution Effect on Particle Surface Representation

Similar to the BGK method, for the largest voxel size, 0.066 mm, permeability from MRT method changes from  $2.99 \times 10^3$  Darcy ( $\omega$ : 1.5) and  $2.66 \times 10^3$  Darcy ( $\omega$ : 0.6). For smallest voxel size, 0.015mm, calculated permeability from MRT method changes from  $3.21 \times 10^3$  Darcy ( $\omega$ : 1.5) and  $3.15 \times 10^3$  Darcy ( $\omega$ : 0.6). Calculated permeability differences are 329 Darcy and 66 Darcy for voxel sizes of 0.066 mm and 0.015 mm, respectively. Differences between calculated permeabilities from MRT methods are less compared to the ones from BGK methods. In BGK method calculated permeabilities approaches true value with voxel size decrease; on the other hand, in MRT method calculated permeabilities increases and approaches to true value with voxel size decrease. As resolution increases, differences between calculated permeability for different relaxation time decrease. For both methods, for reliable permeability estimation, minimum particle diameter should be represented with 30 voxels. Figure 6.15 gives the comparison of BGK and MRT for different relaxation times at different resolutions. As the resolution increases, the difference between calculated permeabilities from both methods decreases and calculated permeability has a weaker dependence on relaxation time.

Table 6.5 Domain Resolution of Heterogeneous Pack

Resolution (mm)	Min D Voxel	Domain Voxel per Side
0.066	10	136
0.043	15	209
0.033	20	273
0.026	25	346
0.022	30	409
0.019	35	474
0.016	44	563
0.015	44	600

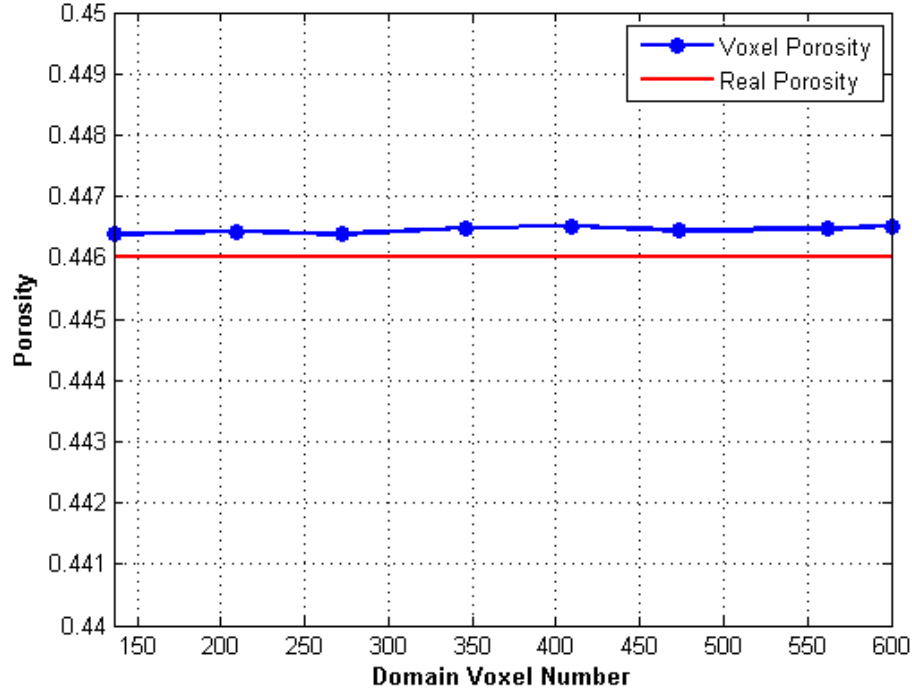


Figure 6.12 Resolution Effect on Porosity

The permeability for each domain is calculated from network modeling for two different pore merging criteria: overlapping and touching. Figure 6.16 gives the comparison of permeability calculated from network modeling and LBM. Unlike LBM, permeabilities calculated from network modeling fluctuate with resolution but calculated permeability does not depend on resolution. The minimum and maximum permeability calculated from network modeling are  $3.48 \times 10^3$  Darcy and  $3.60 \times 10^3$  Darcy for the overlap merge condition, and  $3.21 \times 10^3$  Darcy and  $3.45 \times 10^3$  Darcy for the touching merge condition. Permeability predictions from network modeling with overlap merge condition are always higher than the ones from network modeling with the touching merge condition. The permeability calculated from network modeling with touching merge condition is close the one calculated from LBM. The network modeling is an approximation of the true permeability. Even though the calculated permeability is independent of resolution, the fluctuations are as high as the difference between permeability calculated from LBM for low resolution; 117 Darcy and 248 Darcy for overlapping and touching

merge conditions, respectively. However, network modeling gives an idea about the pore and pore-throat distribution and connectivity of pores.

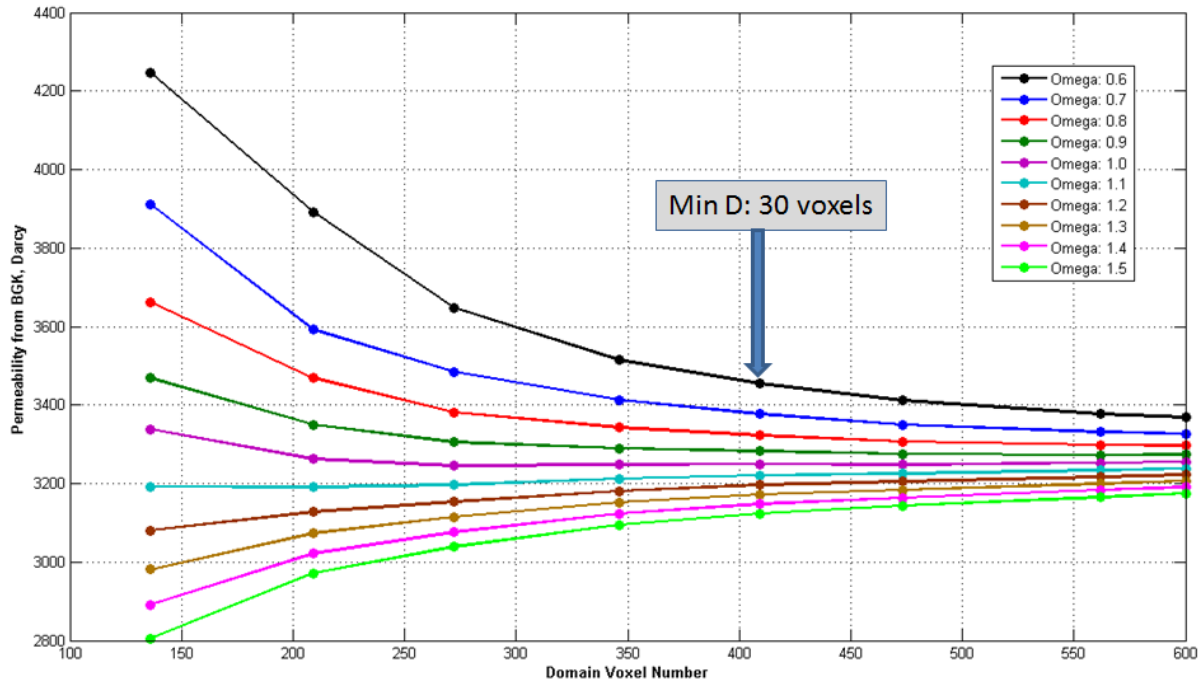


Figure 6.13 Resolution and Relaxation Time Effect on Permeability Estimation from BGK

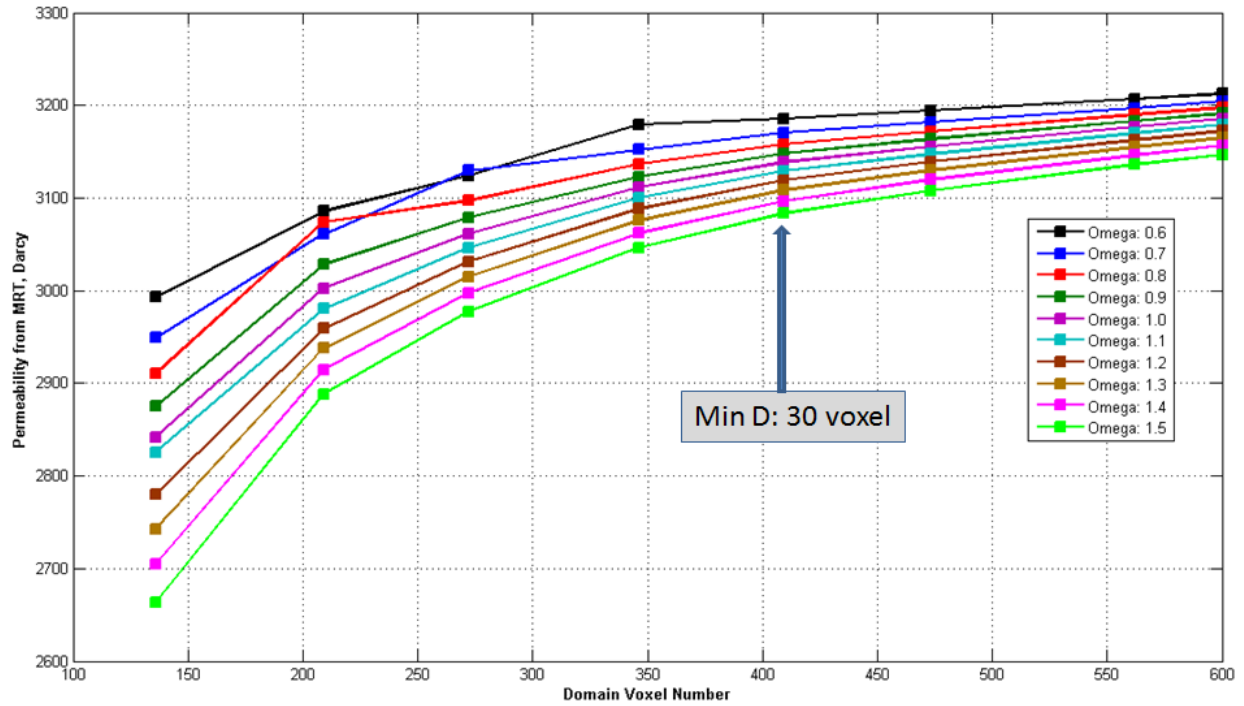


Figure 6.14 Resolution and Relaxation Time Effect on Permeability Estimation from MRT

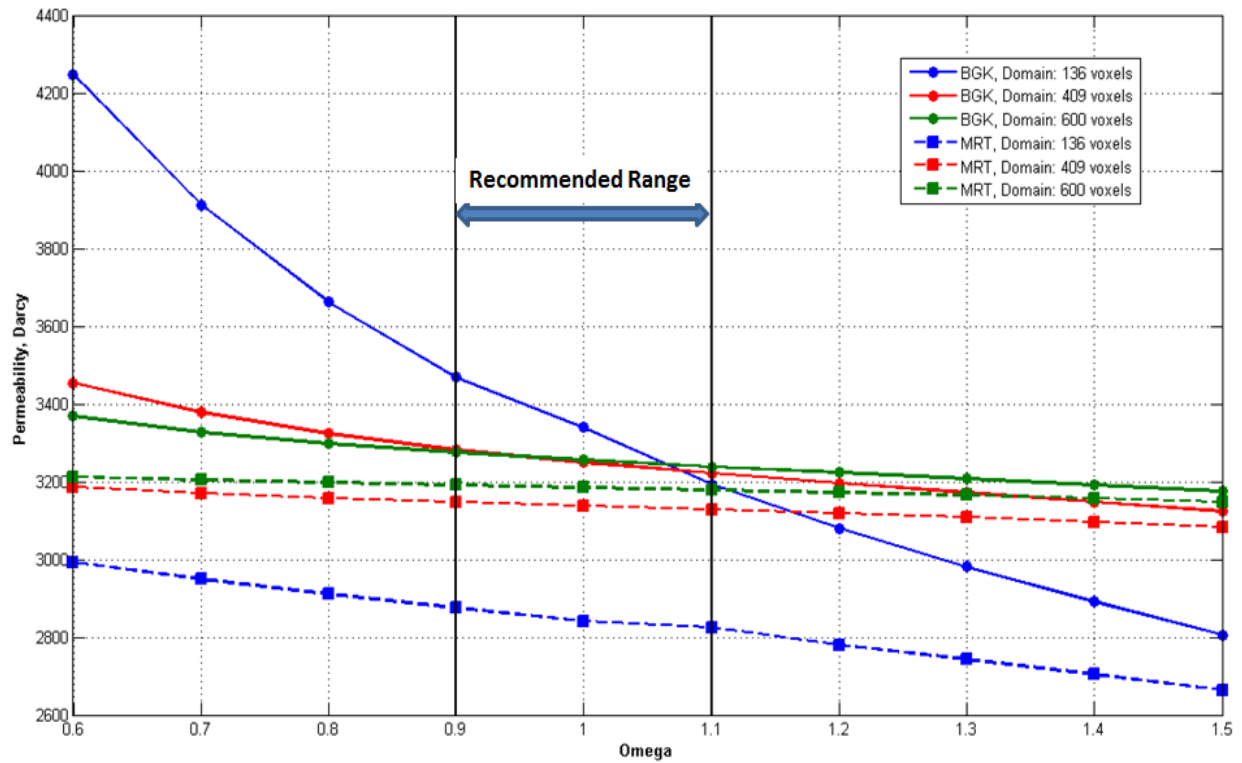


Figure 6.15 Comparison of Resolution Effect on Permeability Estimation from BGK and MRT

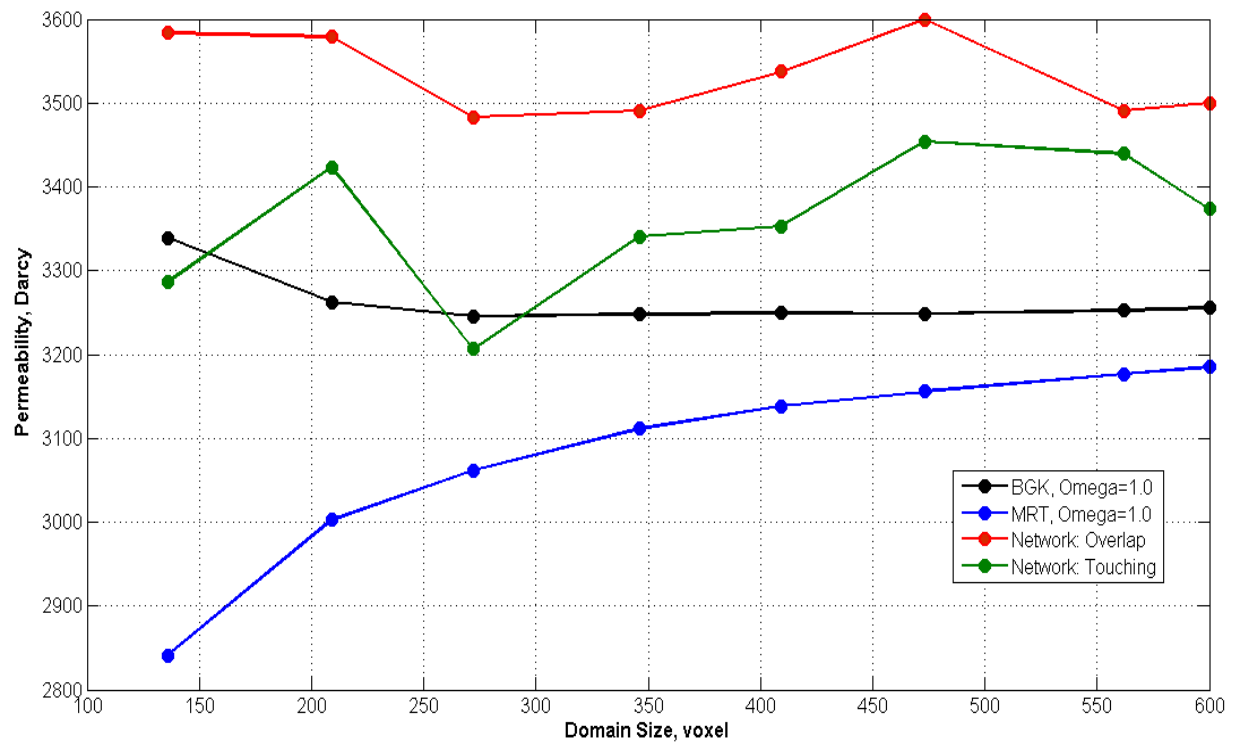


Figure 6.16 Comparison of Resolution Effect on Permeability Estimation from LBM and Network Model

The effect of resolution on network parameters including pore number, average coordination number (the number of pore throat connected to the pore) and average throat length are given in Figure 6.17 and Figure 6.18 for both merging conditions. With increasing voxel number per domain size or decrease in voxel size, the number of pore number increases, and average coordination number and average throat length decrease for both merging conditions.

Figure 6.19 shows the network models constructed with the touching merge condition for the resolutions in which minimum particle are represented with 10 voxels and 44 voxels. In these figures, blue spheres give the pores found with maximum ball algorithm and red and green cylinders depict the throats connecting two pores and the ones open to the domain boundaries, respectively. Close examination of pore networks at different resolution indicates that new pores whose sizes are close to throat diameter appear as resolution increases (indicated with red circles in Figure 6.19) which explains the decrease in average coordination number and throat length.

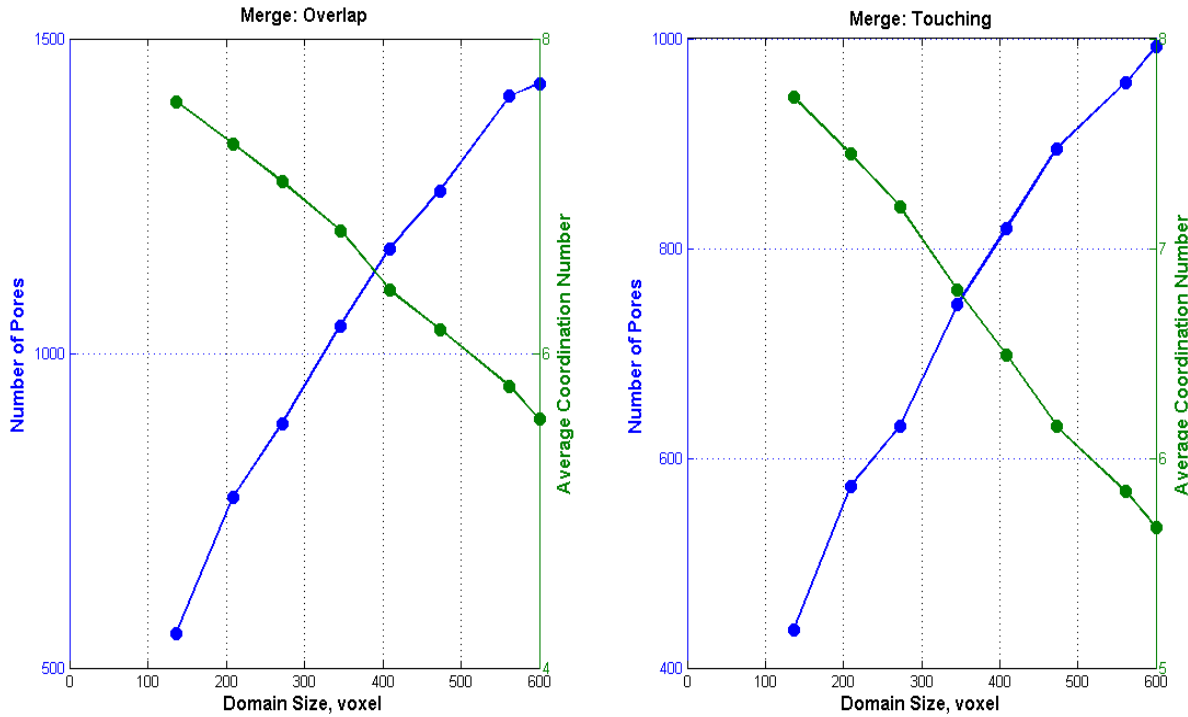


Figure 6.17 Resolution Effect on Pore Number and Average Coordination Number

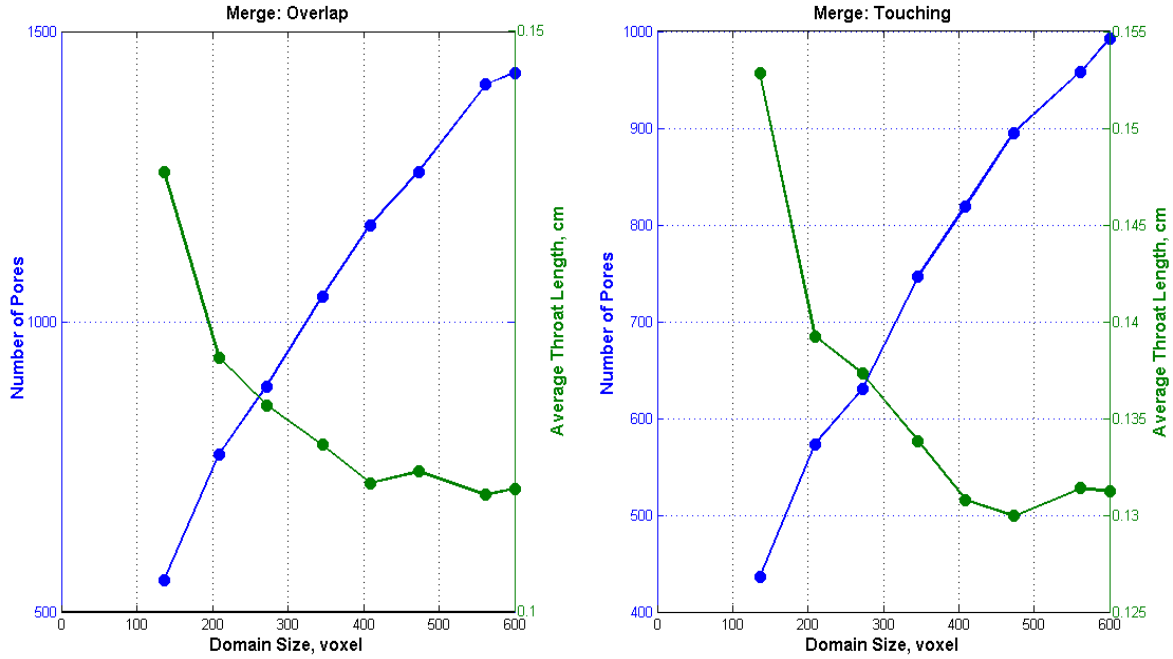


Figure 6.18 Resolution Effect on Pore Number and Average Throat Length

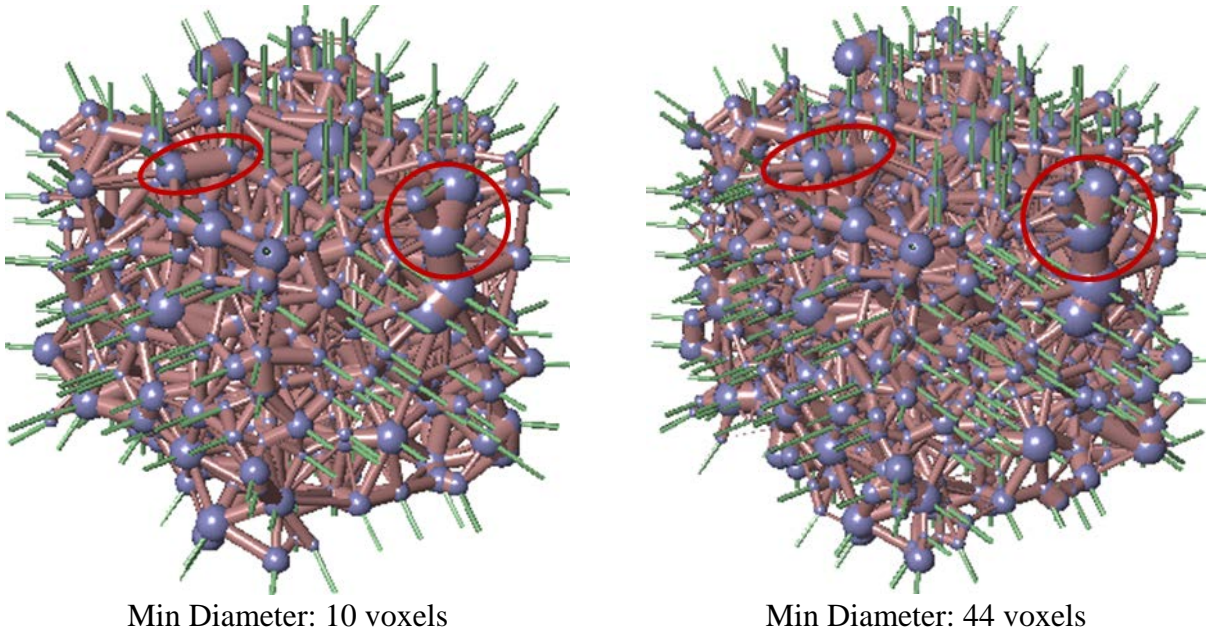


Figure 6.19 Resolution Effect on Network Structure Constructed with Touching Merge Condition

Capillary pressure functions are calculated from network modeling at all resolutions (Figure 6.20). Although the network structure changes with resolution, capillary pressure is



almost not affected. This indicates that for all resolutions, the main structure of pore space is captured with network modeling.

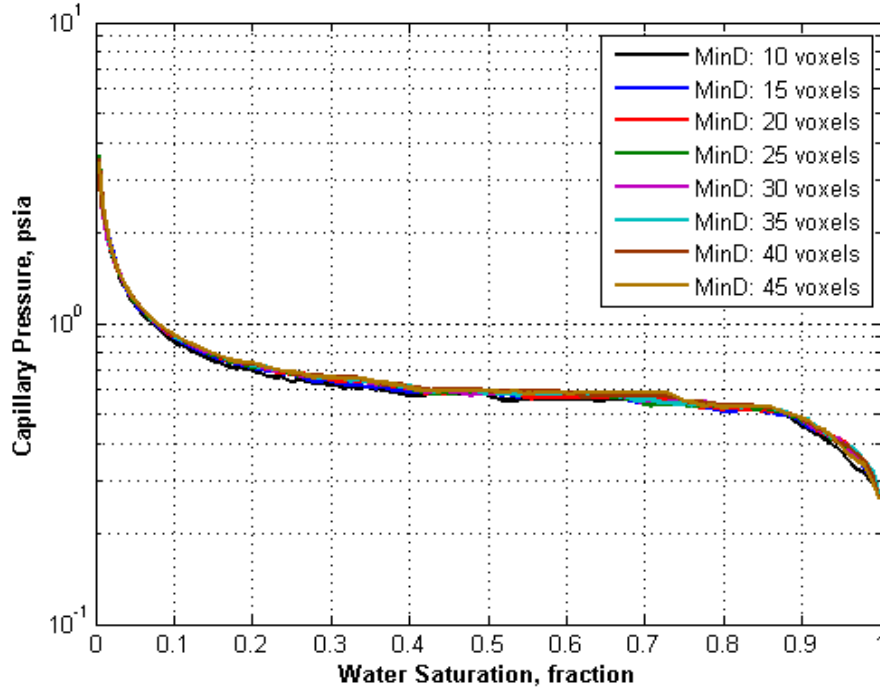


Figure 6.20 Resolution Effect on Capillary Pressure calculated from Network Modeling

To investigate the resolution effect on network model in detail, body centered cubic pack with 512 particles is used. The pack domain size and particle radius are 14 mm and 1 mm, respectively. Packing porosity calculated from voxelized image is 0.476. The domain is voxelized with a resolution between 0.060 mm and 0.025 mm so that particle diameter is represented with more than 30 voxels (Table 6.6).

For each resolution, a pore network model is constructed. Figure 6.21 gives three networks constructed from voxelized images with resolutions of 0.060 mm, 0.035 mm and 0.025 mm. If the resolution is 0.025 mm, the particle diameter is resolved completely and there is only one pore size (0.7345 mm), and one throat size (0.4188 mm) and the correct coordination number (coordination number of interior pores), 6 (Figure 6.21). However, if resolution cannot represent the whole particle diameter, (e.g. resolution of 0.035 mm and 0.060 mm), pore sizes

change and unrealistic throats are appears. If unrepresentative fraction of particle diameter left is large, the pore and throat sizes and coordination number increases. For example, for resolution 0.035 mm and 0.060 mm, the unrepresented particles diameters are 0.005 and 0.02 mm, respectively. Therefore; the change of the network parameters are large for the network constructed with voxel image with 0.060 mm. Pore diameter changes from 0.7147 mm to 0.7354 mm and 0.7055 mm and 0.7418 mm for resolution of 0.035 mm and 0.060 mm, respectively. For both resolutions, two size of throat radius appear. Throat radiuses are 0.035 mm and 0.4256 mm for resolution of 0.035 mm, and 0.06 mm and 0.4327 mm for resolution of 0.06 mm. The smaller throat radius sizes are same with the resolutions and they appear due to incomplete resolution of particle diameter. The lengths of throats connected to the nearest pores are similar, 1.9871 mm and 1.98 mm, respectively. The throats appear due to incomplete resolution of particle diameter diagonally extend and connect the pore with the farthest neighbor. Their sizes are 2.8383 mm and 2.8426 mm for resolutions of 0.035 mm and 0.060 mm, respectively. Due to the unrealistic throats, the corrected coordination number increases up to 12 and 8 for resolutions of 0.035 mm and 0.060 mm, respectively.

Table 6.6 Domain Resolution of Cubic Pack

Resolution (mm)	Min D Voxel	Domain Voxel per Side
0.060	33	233
0.055	36	255
0.050	40	280
0.045	44	311
0.040	50	350
0.035	57	400
0.030	67	467
0.025	80	560

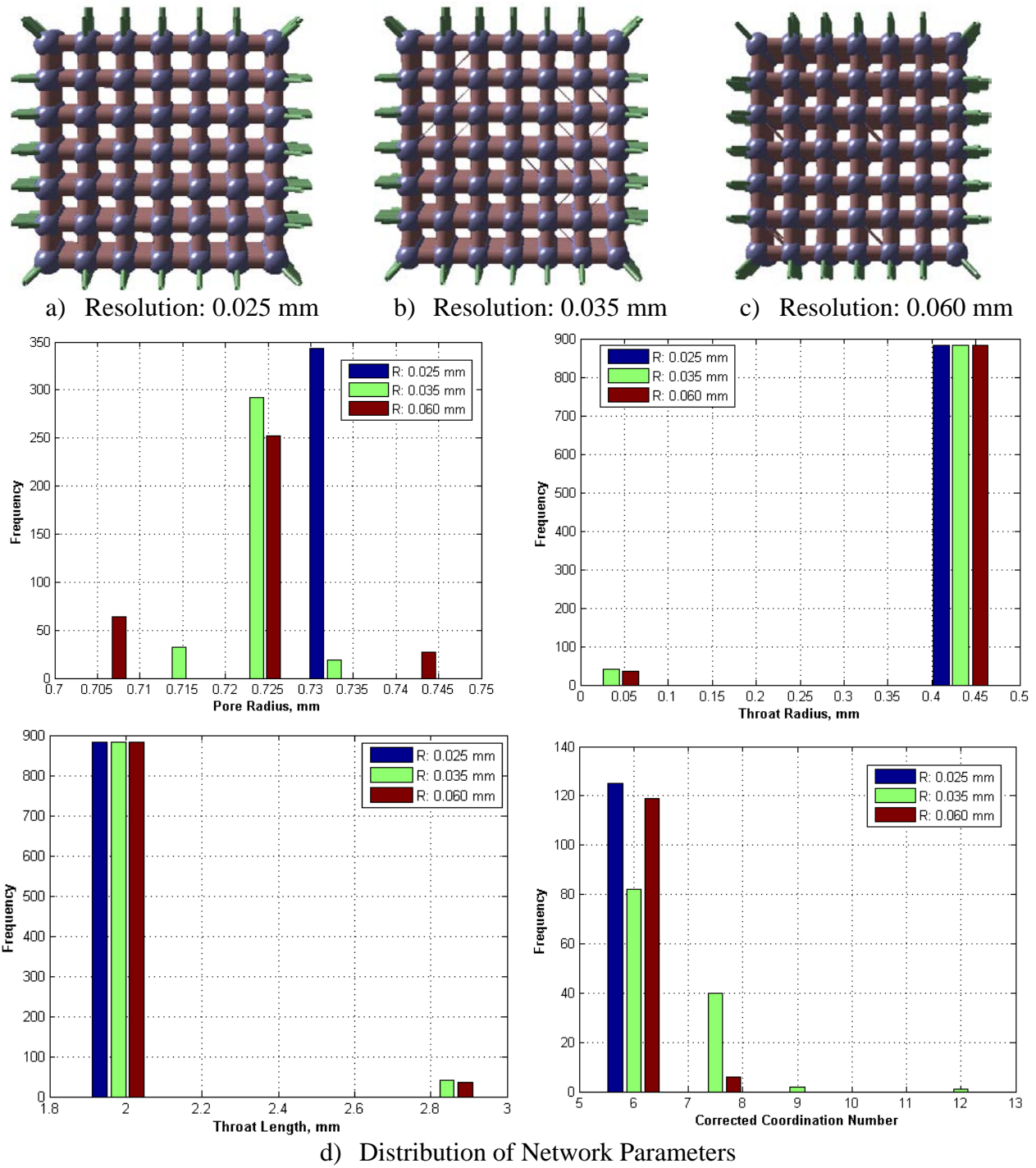


Figure 6.21 Resolution Effect on Network Model for Cubic Pack

For each resolution, permeability is calculated from network modeling. Similar to the heterogeneous domains, the calculated permeabilities from network modeling fluctuate with resolution. The calculated permeability changes from  $1.20 \times 10^4$  Darcy to  $1.27 \times 10^4$  Darcy. The

fluctuation decreases as voxel size decreases. For the resolutions for the particle diameters completely represented, 0.050 mm, 0.040 mm and 0.025 mm (indicated with red rectangles in Figure 6.22), permeability increases with decrease in voxel size due to increase in throat radius. Assuming the permeability calculated for lowest voxel size is true permeability,  $1.26 \times 10^4$  Darcy, the maximum permeability difference is only 4.95%. In addition, permeability is calculated from LBM with omega of 1.0. The calculated permeability changes from  $1.0 \times 10^4$  Darcy and  $1.03 \times 10^4$  Darcy. Similarly, the calculated permeability for lowest voxel size is true permeability,  $1.02 \times 10^4$  Darcy, the maximum percent difference is only 1.60%. Compared to resolution effects of heterogeneous packings, the change in permeability is small since the particle diameter is represented more than 30 voxels.

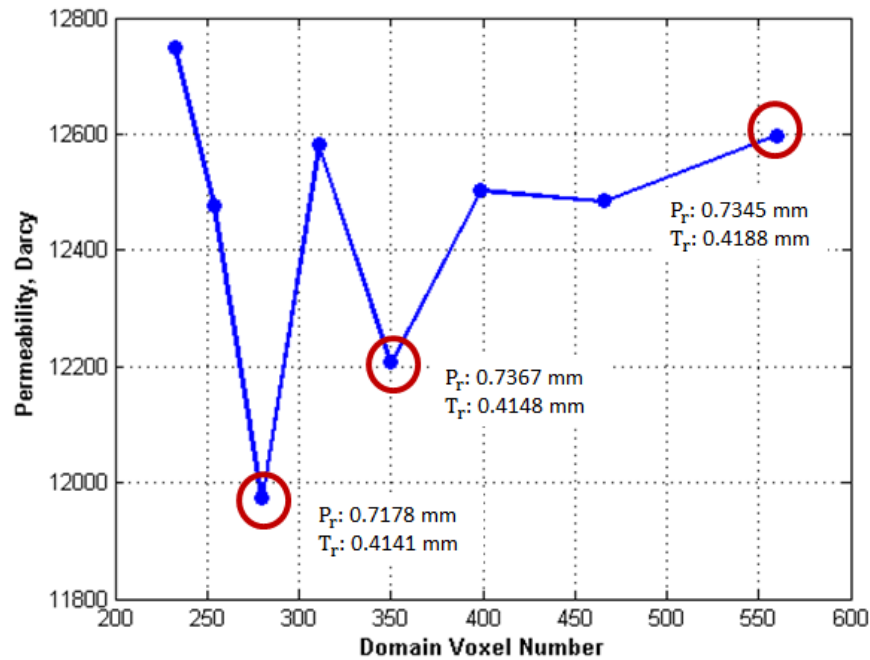


Figure 6.22 Permeability Calculated from Network Modeling for Cubic Pack

Incomplete resolved particle effect for LBM simulations is insignificant. 3 points indicated in Figure 6.23 gives calculated permeabilities for the resolution of 0.025 mm, 0.030 mm and 0.035 mm, respectively. For resolution of 0.030 mm and 0.035 mm, the unrepresented

particle diameter is 0.02 mm and 0.005 mm, respectively. This unsolved particles lead to decrease in contact area (Point 2) and pore space between touching particles (Point 3). This leads to small increase in permeability.

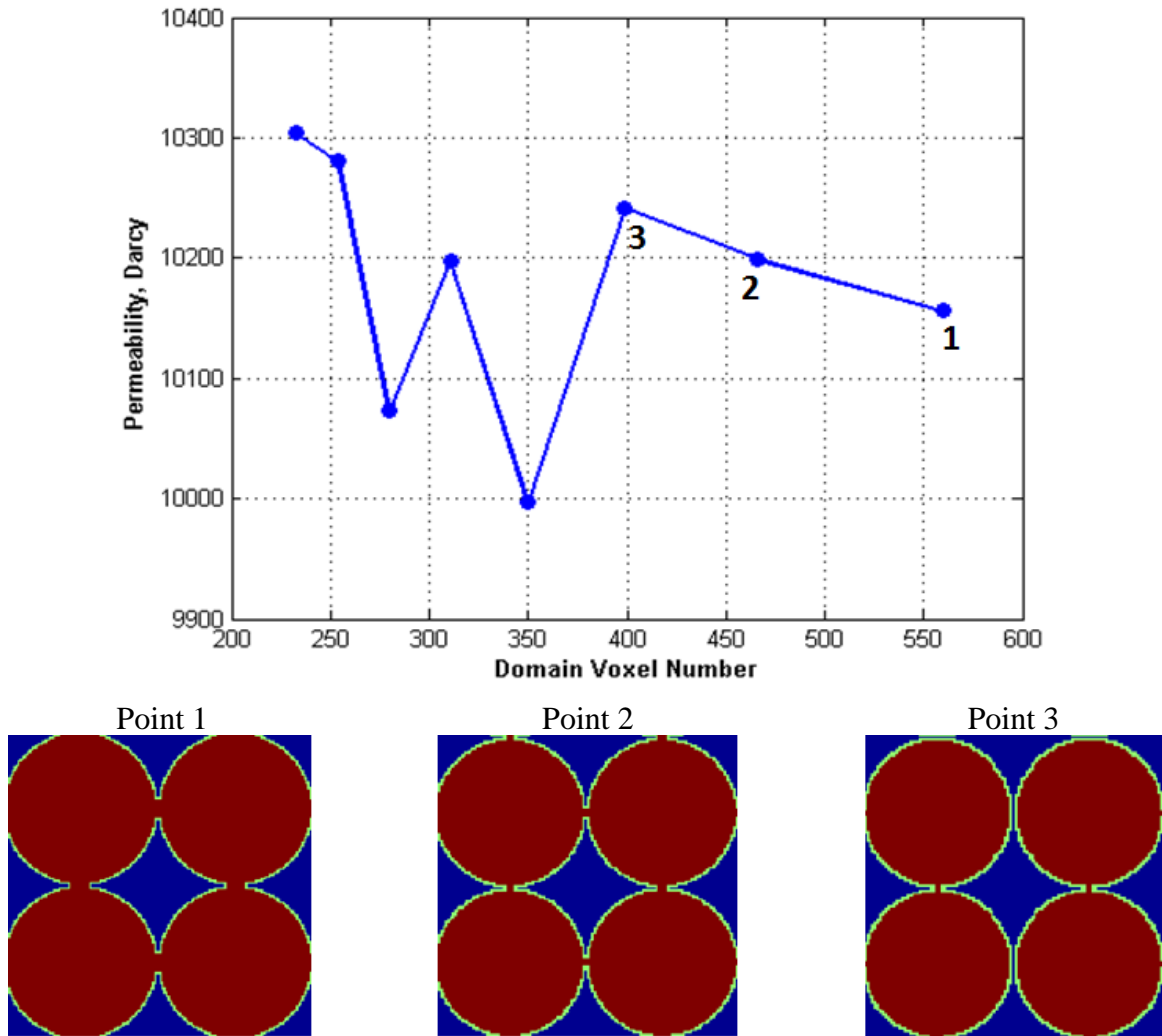


Figure 6.23 Permeability Calculated from LBM for Cubic Pack

#### 6.4.3 Grain Shape and Packing Effect

In order to investigate the grain shape effect, a regular cubic pack with 512 particles is used. The domain is voxelized by 560x560x560 in which particle diameter is represented with 80 voxels (resolution of 0.025 mm). The cubic pack is stretched along the z direction (Figure 6.24) with different aspect ratios up to 3.0. The porosity remains same for each stretched domain.

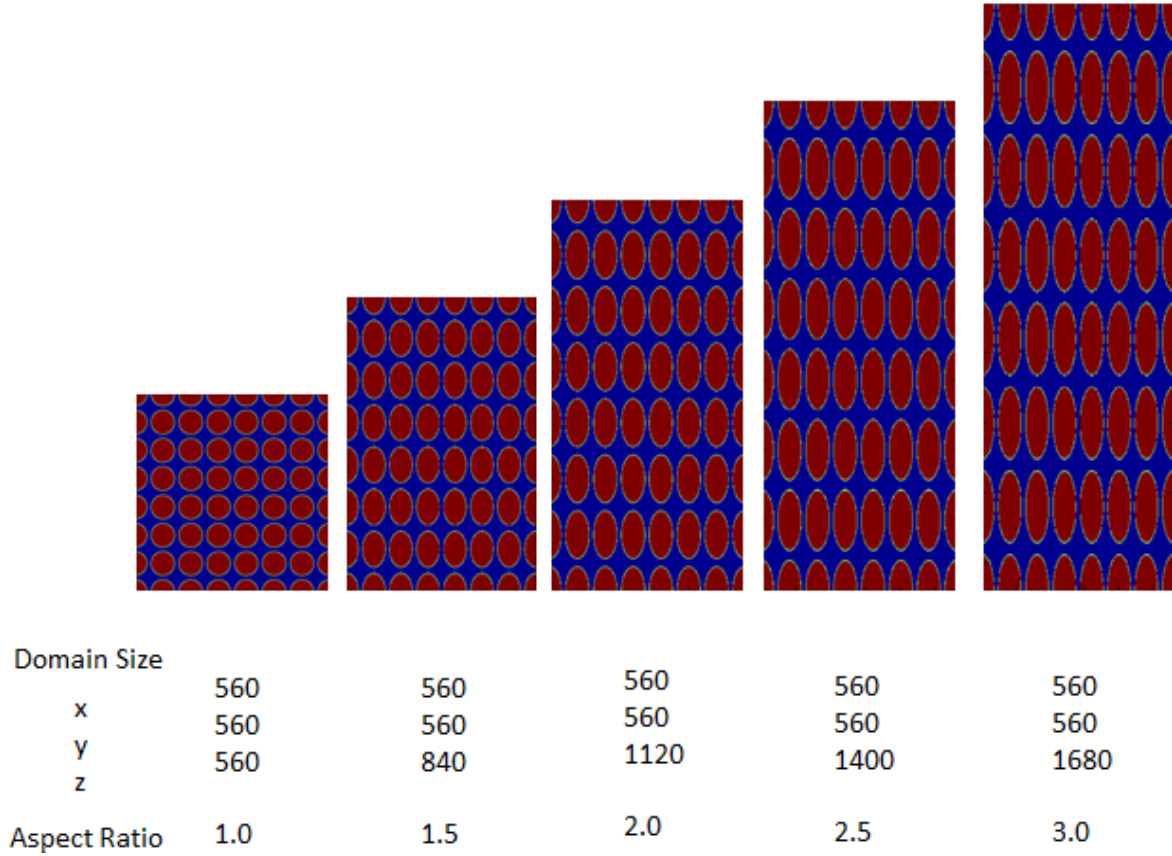


Figure 6.24 Extended Domain of Cubic Pack

Figure 6.25 shows the calculated permeability and tortuosity in  $x$ ,  $y$  and  $z$  directions, calculated from LBM. For tortuosity calculations, volume averaged velocities are used (Nabovati & Sousa, 2009); detailed explanation of tortuosity calculation is given in the correlation development part of this thesis. Permeabilities in  $x$  and  $y$  directions are the same for each extended domain. Permeability in  $x$  and  $y$  directions increase from  $1.02 \times 10^4$  Darcy to  $2.07 \times 10^4$  Darcy with an increase in aspect ratio from 1.0 to 3.0. Even though tortuosity decreases more in the  $z$  direction, the permeability increases in the  $z$  direction is less compared to  $x$  and  $y$  directions. Permeability in the  $z$  direction increases from  $1.02 \times 10^4$  Darcy to  $1.18 \times 10^4$  Darcy with an increase in aspect ratio from 1.0 to 3.0. Network modeling is used to compare the change in pore structure (Figure 6.26). Since the pore is symmetric, the number of pores and pore throats

do not change for the extended domain. Pore radius increases from 0.7345 mm to 0.9888 mm. This explains the increase in permeability in all directions. While pore throat radius in  $z$  direction does not change, 0.4188 mm, the pore throat length increases from 2 mm to 6 mm. On the other hand, the pore throat radius in  $x$  and  $y$  directions increase from 0.4188 mm to 0.6368 mm while pore throat length does not change, 2 mm. Overall, the pore throat aspect ratio (ratio of pore throat diameter to its length) decreases in the  $z$  direction, while the pore throat aspect ratio in the  $x$  and  $y$  directions increases. This explains the large increase in permeability in these directions.

Figure 6.27 gives the permeability changes in  $x$ ,  $y$  and  $z$  directions calculated from LBM and network modeling. Permeability estimation for cubic pack from network modeling,  $1.26 \times 10^4$  Darcy, is higher than the ones calculated from LBM,  $1.02 \times 10^4$  Darcy. Although permeability trends with domain extension are similar, there is a significant difference between the permeabilities calculated from LBM and network modeling in the  $z$  direction. Permeability difference increases up to  $1.08 \times 10^4$  Darcy. This indicates that if the symmetric pore is elongated, the use of LBM for permeability estimation is more reliable than network modeling.

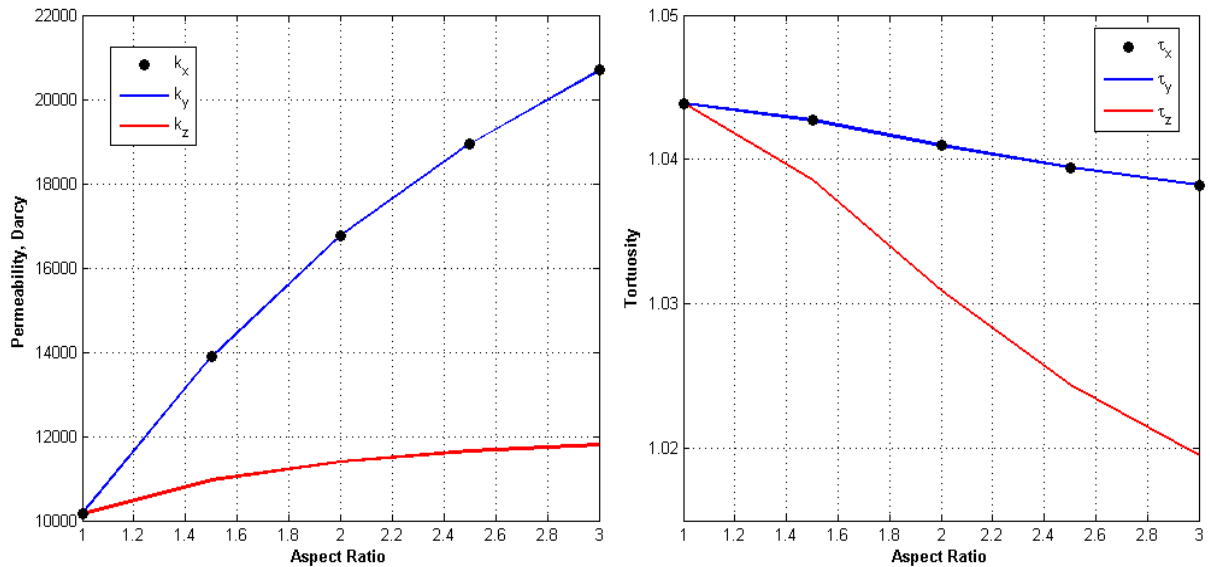


Figure 6.25 Cubic Pack Permeability and Tortuosity Change from LBM with Domain Extension

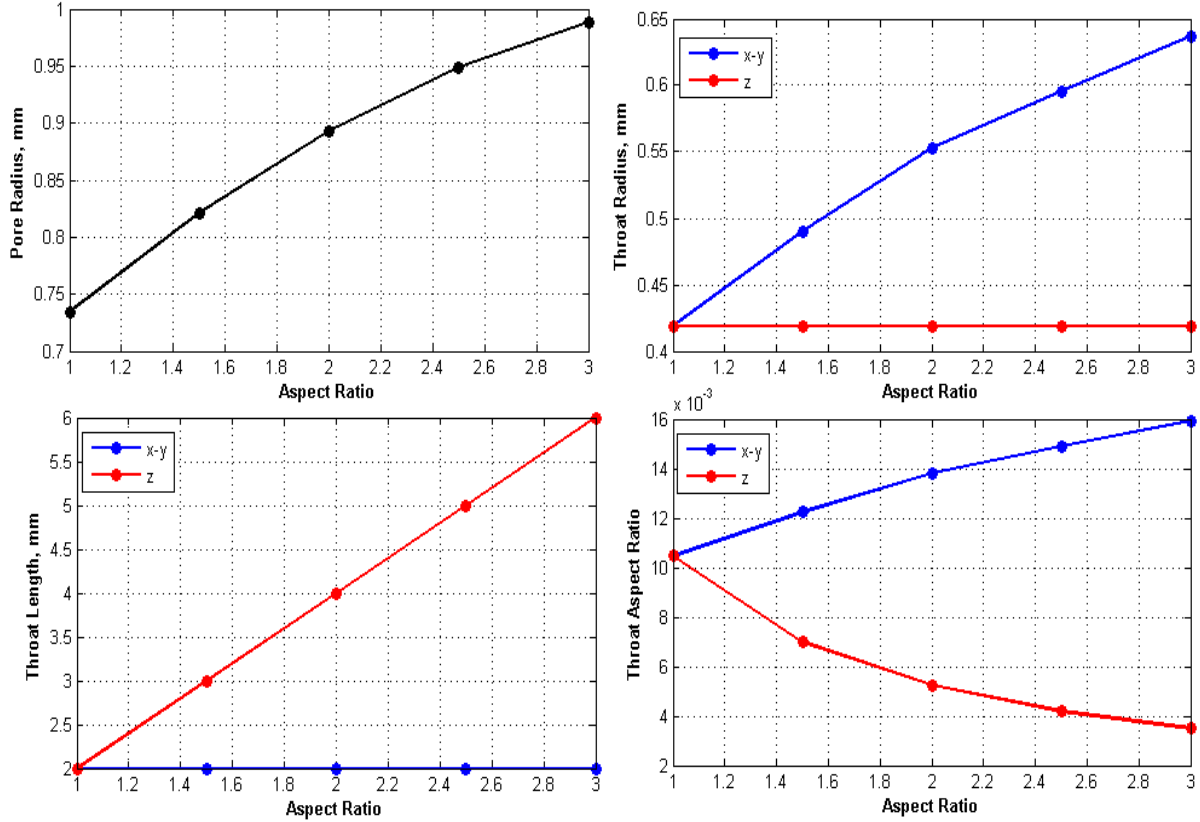


Figure 6.26 Cubic Pack Pore Structure Change with Domain Extension

A similar extension is applied to the heterogeneous domain (Figure 6.28). The domain is voxelized at  $600 \times 600 \times 600$  (resolution of 0.015 mm), corresponding to minimum particle diameter represented with 44 voxels. Permeability and tortuosity are calculated using LBM (Figure 6.29). The permeability for the original domain in  $x$ ,  $y$  and  $z$  directions are close,  $3.23 \times 10^3$  Darcy,  $3.32 \times 10^3$  Darcy and  $3.33 \times 10^3$  Darcy respectively. The domain is almost isotropic. With domain extension, the permeability increases in all directions; however, the increase in permeability in the  $z$  direction is more significant (up to  $7.99 \times 10^3$  Darcy), compared to  $x$  direction (up to  $3.90 \times 10^3$  Darcy) and  $y$  direction (up to  $3.71 \times 10^3$  Darcy). Initial tortuosities in all directions are also the same, with a value of 1.47. While tortuosity in the  $x$  and  $y$  directions increase to 1.79 and 1.85, tortuosity in  $z$  direction decreases to 1.19. The notable increase in permeability in the  $z$  direction resulted from a decrease in tortuosity in that direction.



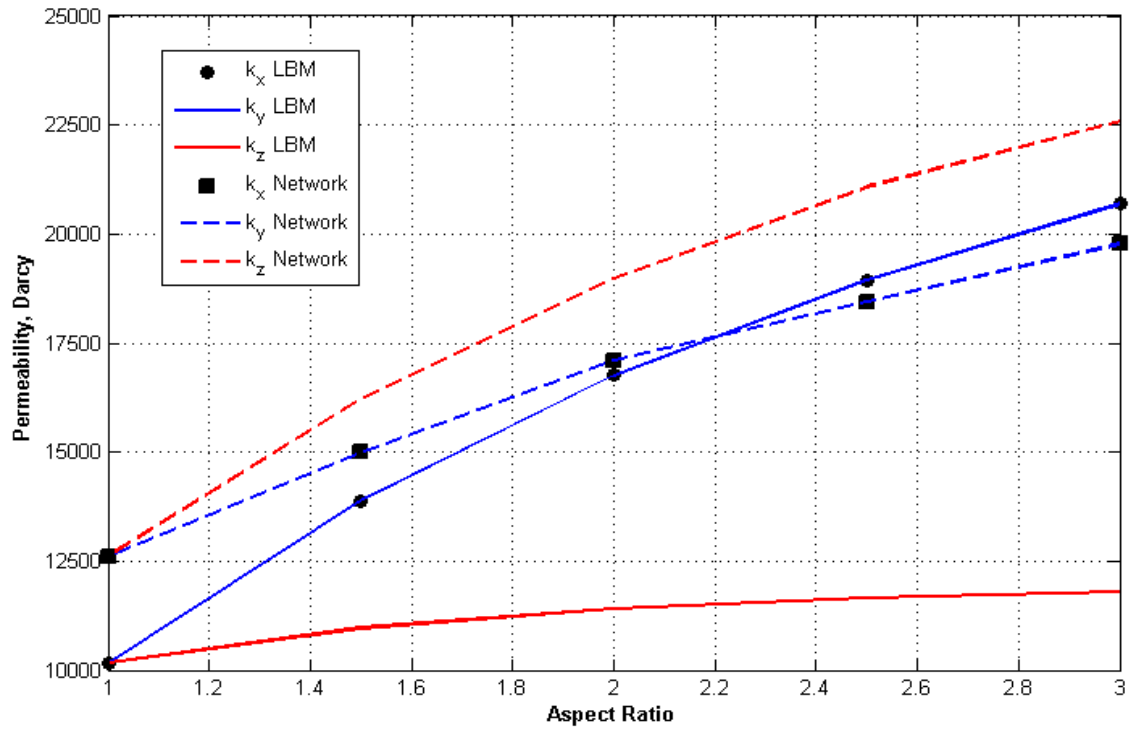


Figure 6.27 Comparison of Cubic Pack Permeability Calculated from LBM and Network with Domain Extension

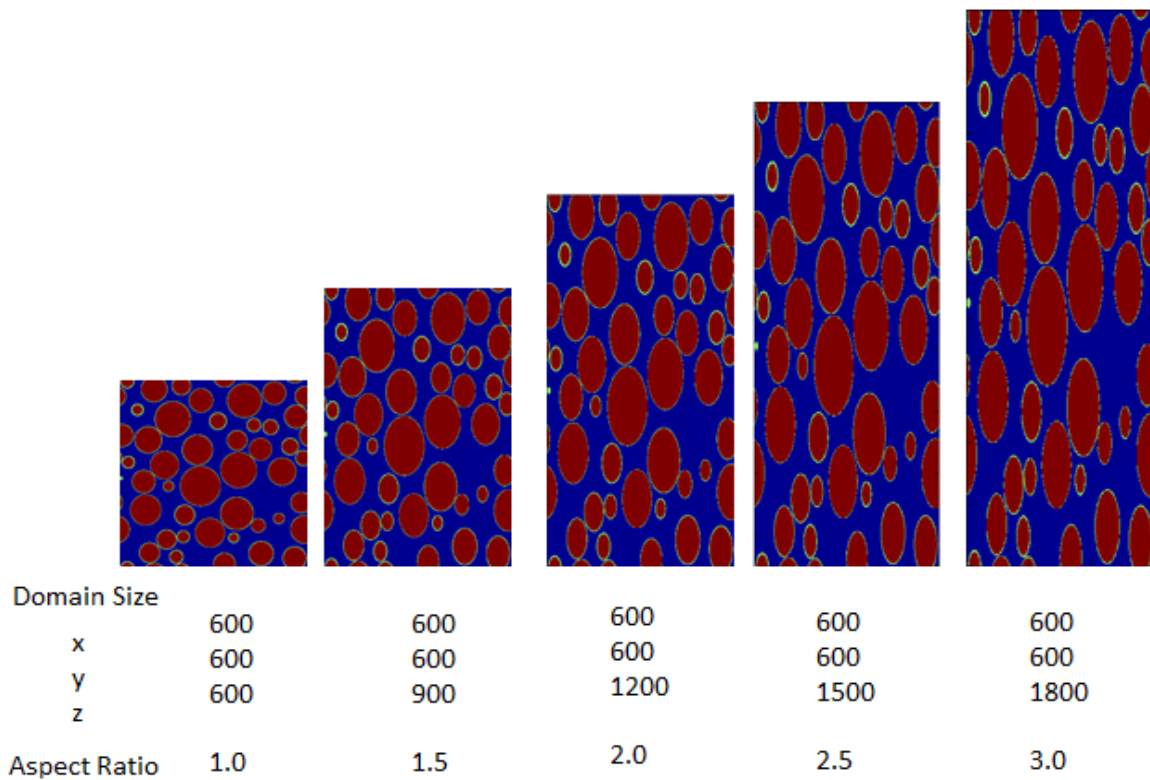


Figure 6.28 Extended Domain of Heterogeneous Pack

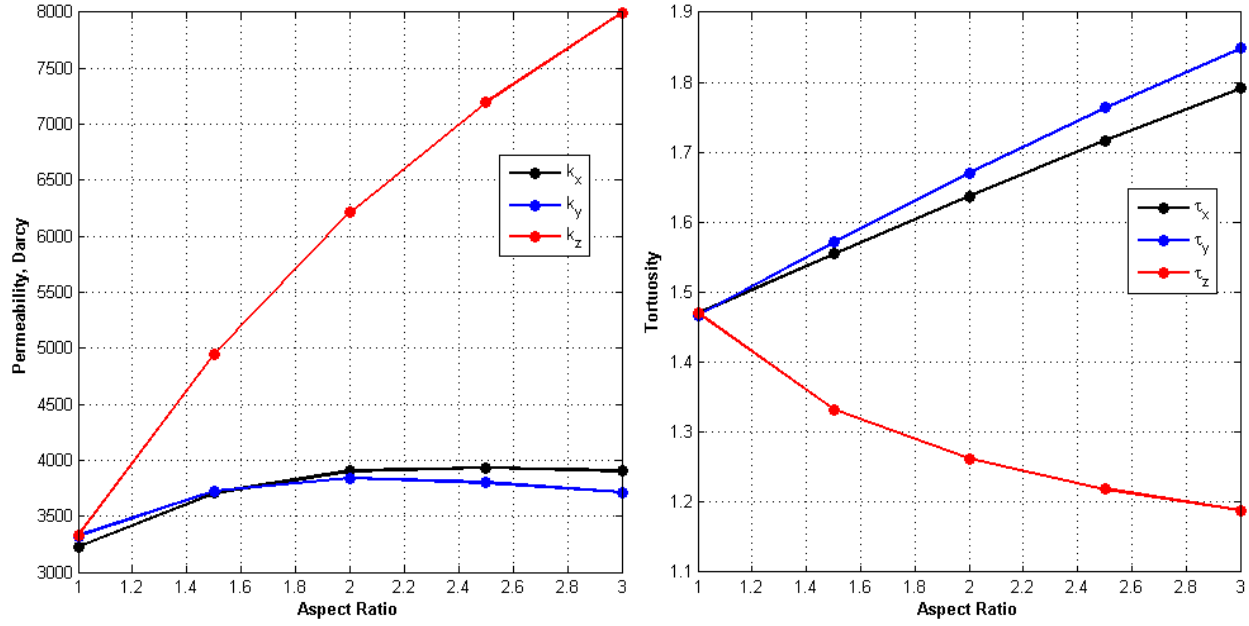


Figure 6.29 Heterogeneous Pack Permeability and Tortuosity Change from LBM with Domain Extension

The change in network parameters with domain extension is investigated to determine the reasons for permeability and tortuosity change. Unlike the body-centered cubic pack, extension causes a change in the number of pores and pore throats; therefore, their cumulative probability plots are given instead of their histograms (Figure 6.30). As the aspect ratio increases, pore and pore throat radii get larger, comparing the median values, the pore radius increases from 0.23 mm to 0.27 mm (%17.78 increase) and the pore throat radius increases from 0.14 mm to 0.16 mm (%17.65 increase).

The change in throat length is larger compared to pore and throat radius since the domain extension is only in one direction. Throat lengths change from 1.24 mm to 1.73 mm (39.20% increase). The increase in pore number with domain extension leads to decrease in coordination number. While pore number increase from 858 to 1155, average coordination number decreases from 3.52 to 2.22 (36.96% decrease). The changes in throat properties are not same in each direction since the domain is extended in the  $z$  direction (Figure 6.31). The lengths of pore

throats in  $z$  direction increases more compared to the  $x$  and  $y$  directions. On the other hand, the pore throat radius is less affected by direction. Even though the throat lengths increase in  $z$  direction, permeability increases more and tortuosity decreases in that direction. This indicates that the change of permeability and tortuosity are not only related to pore throats length and radius. Flow path has a larger effect on the permeability and tortuosity. The separation of flow path increases more as the grain elongation increases in  $x$  and  $y$  directions. On the other hand, in  $z$  direction, flow separation does not change (Figure 6.32).

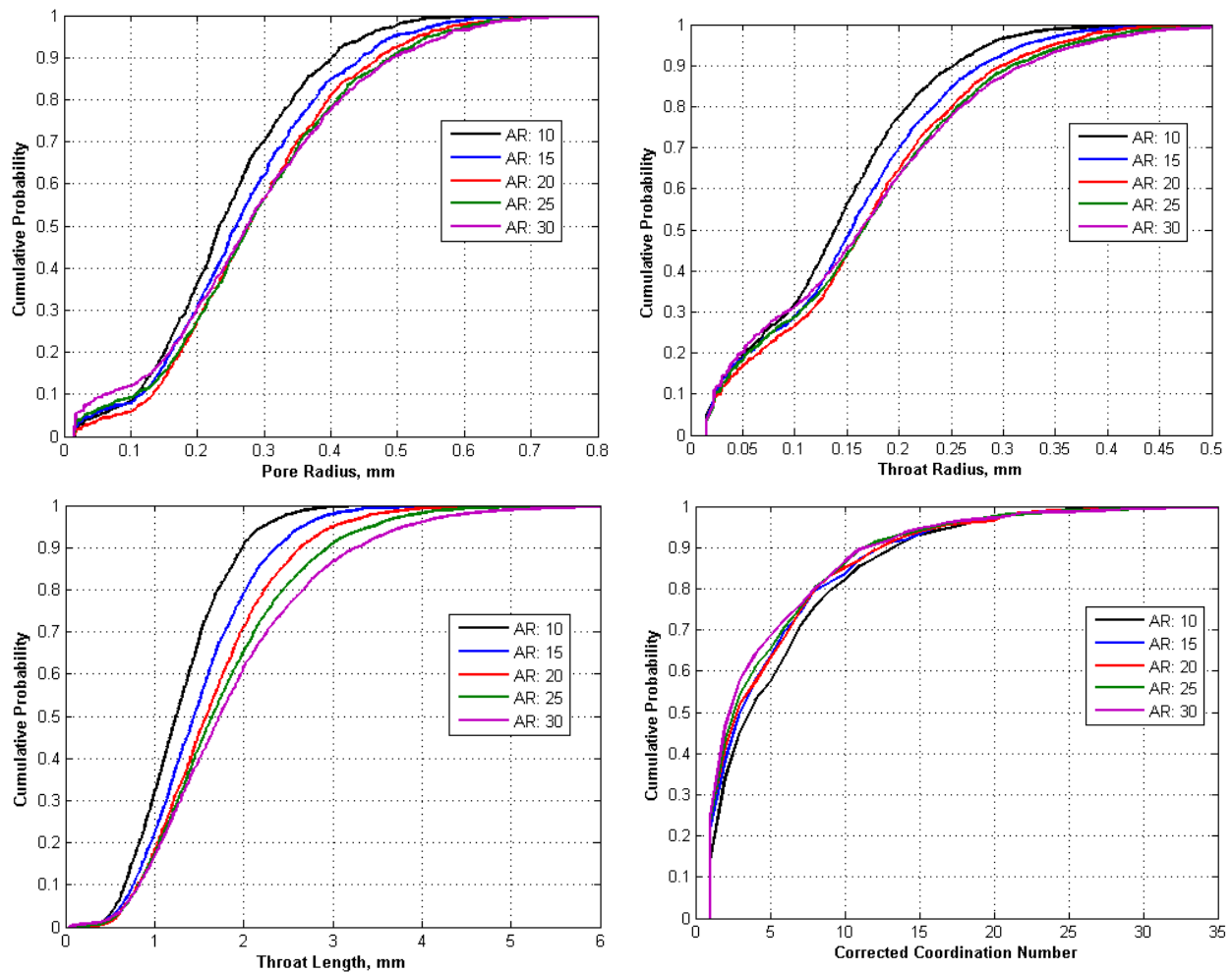


Figure 6.30 Pore Structure Change of Heterogeneous Pack with Domain Extension

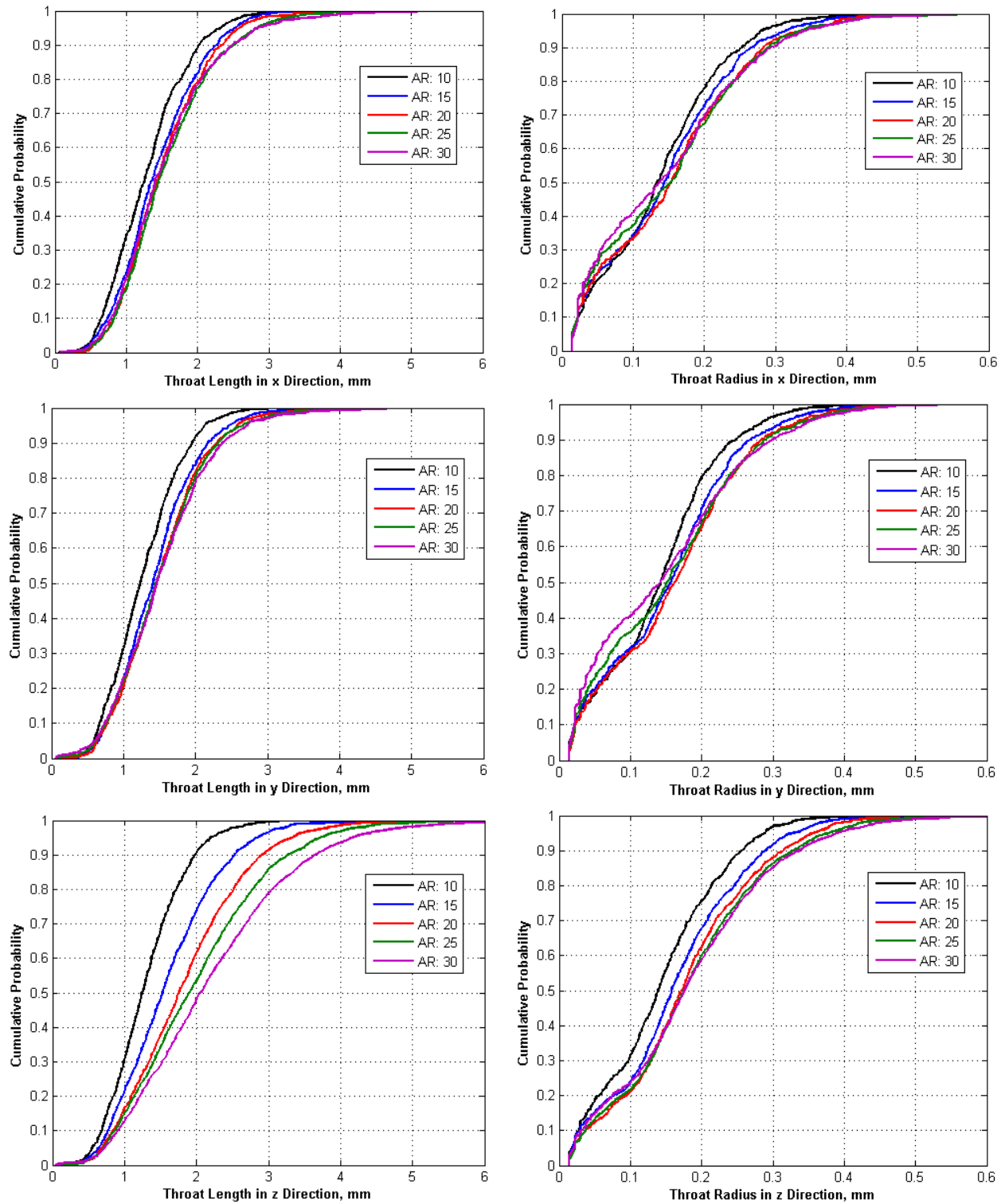


Figure 6.31 Pore Structure Change of Heterogeneous Pack in x, y and z directions with Domain Extension

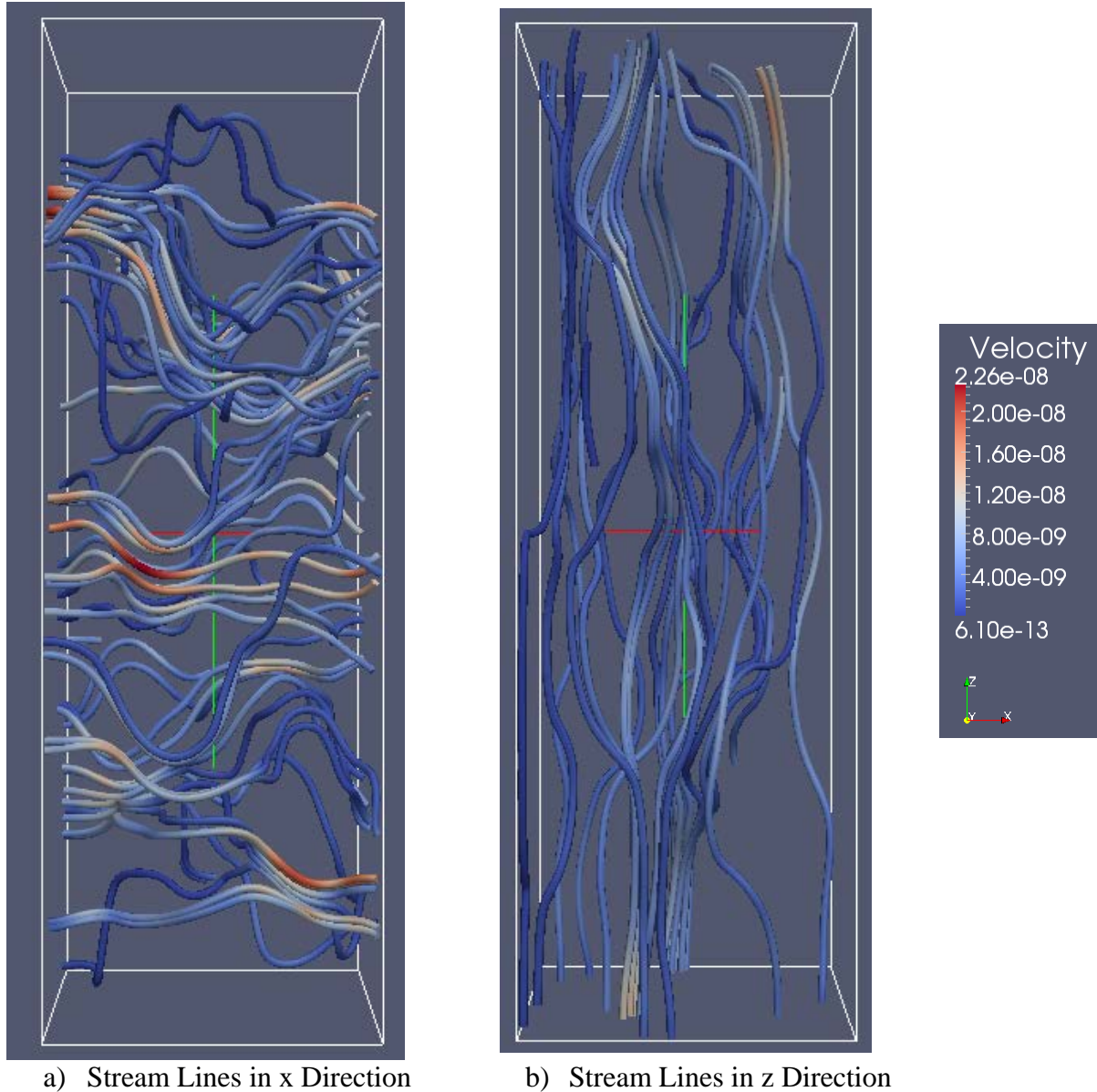


Figure 6.32 Stream Lines of Domain with Aspect Ratio 3.0

Comparing the permeability calculated from LBM and network modeling (Figure 6.33), the difference in permeability from two methods are smaller compared to the cubic pack: the maximum permeability difference is  $1.77 \times 10^3$  Darcy in z direction for aspect ratio 3. In the cubic pack, the pores are symmetric; therefore, the number of pores and pore throat do not change with domain extension and the pore space representation deviates from reality with increasing aspect ratio. On the other hand, in the heterogeneous domain, the pores and pore throats are rearranged;

therefore, the difference between permeability calculated from LBM and the one calculated from Network model is less.

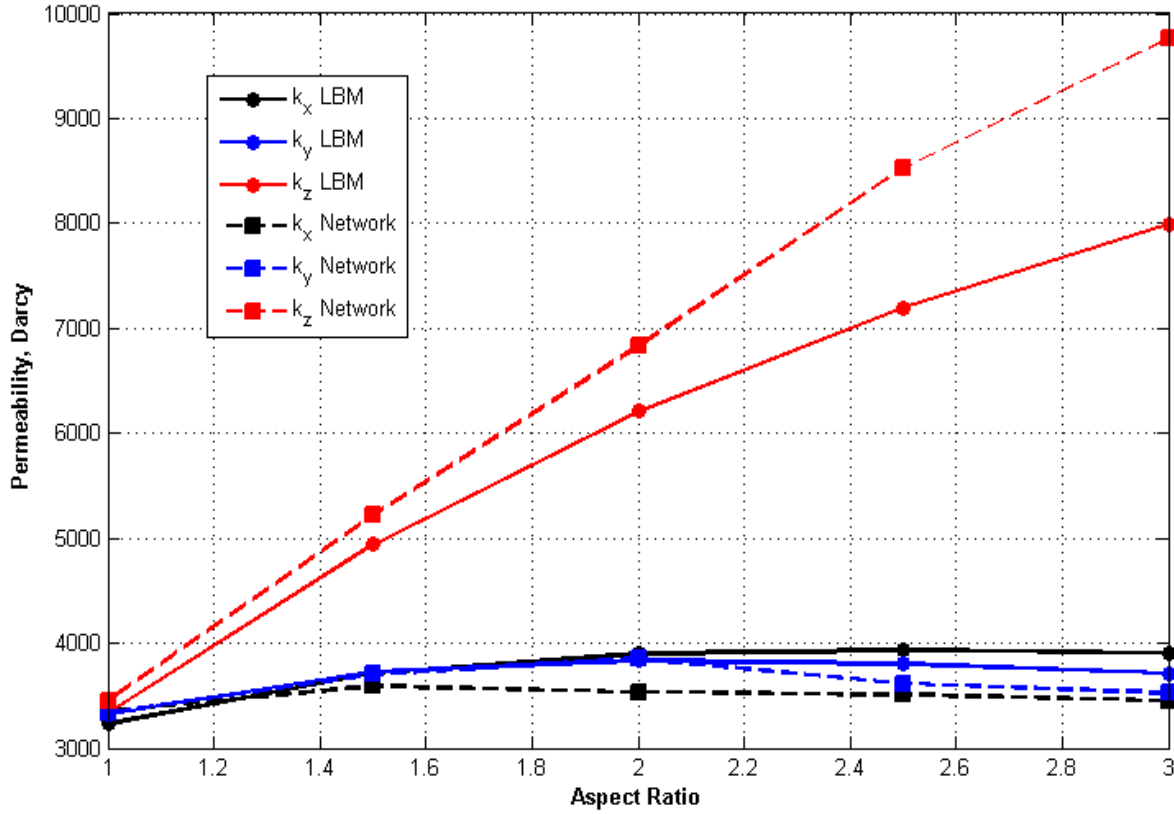


Figure 6.33 Comparison of Heterogeneous Pack Permeability Calculated from LBM and Network with Domain Extension

Specific surface areas of the cubic pack for different resolutions are calculated from voxel image with face search between pore voxel and solid voxel (Figure 6.34). Specific surface area is almost not sensitive to resolution, changing between 2.25 1/mm and 2.32 1/mm. However, the actual specific surface area is 1.571 1/mm. Considering the 2-dimensional case, a circle circumference calculated from voxel image is 4 times a grain diameter. For 3-dimensional case, a specific surface area calculated from voxel image is approximately 6 times a cross sectional area. Therefore, the ratio of the specific surface area calculated from voxel image to the actual specific surface area is approximately 1.5. The adjusted specific surface area is 1.533

1/mm, which is close to the actual specific area. For the cubic and heterogeneous packs, permeability increase in all directions with aspect ratio can also be explained with decrease in the specific surface area (Figure 6.35).

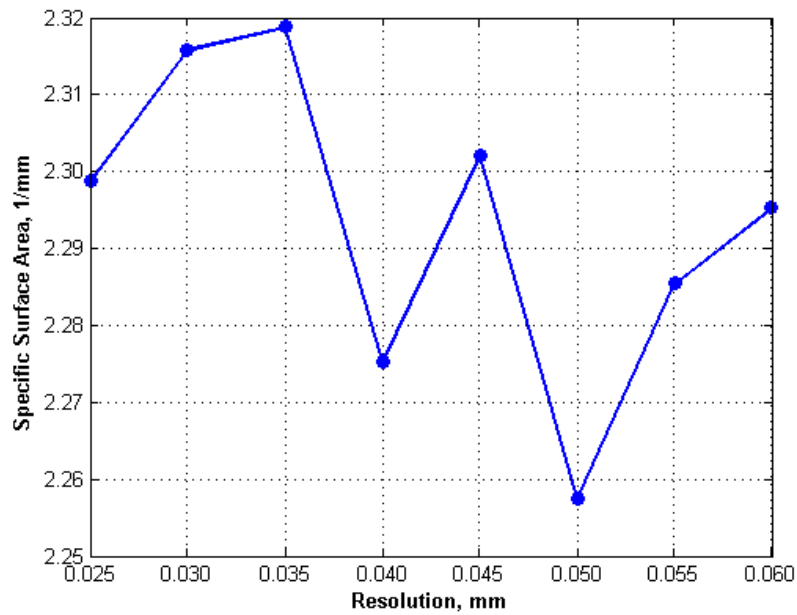


Figure 6.34 Resolution Effect on Specific Surface Area of Cubic Pack

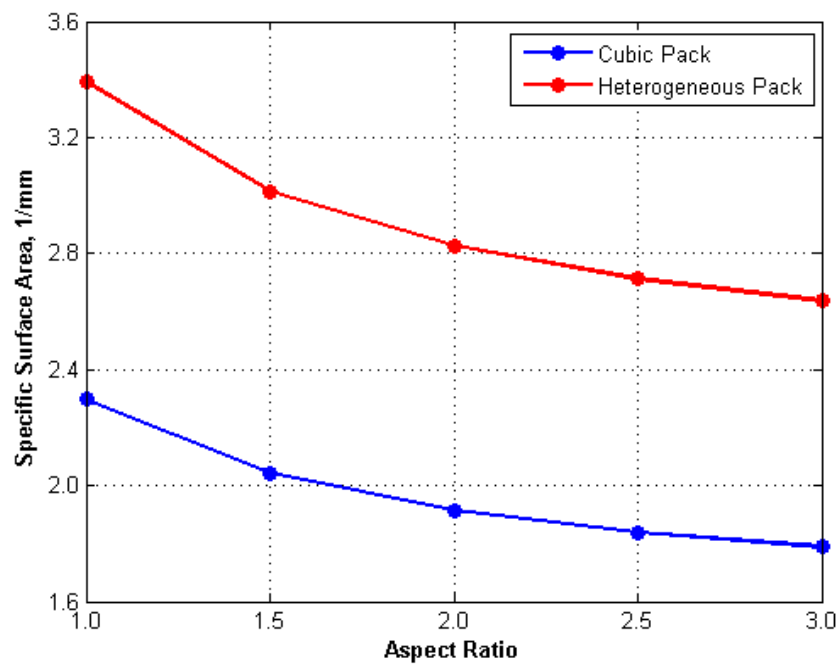


Figure 6.35 Specific Surface Change with Domain Extension

## 6.5 Permeability and Non-Darcy Coefficient Correlation Development

Proppant, a granular material, is used to keep the hydraulic fracture open. Proppant flow properties are hard to estimate from lab experiments due to its high porosity and permeability. A long length gravel pack is required for the necessary pressure drop during the experiment. In this part of the study, some correlations are developed by using flow properties: permeability, tortuosity and non-Darcy coefficient obtained from LBM and pore structure: pore radius and throat radius and length and coordination number obtained from network modeling.

### 6.5.1 Design of Experiment for Gravel Packs

To develop permeability and non-Darcy coefficient correlations for gravel packs, all possible packs need to be considered. The range of packing input parameters: mean grain size, standard deviation of gravel size distribution and porosity should be known. 24 proppant data sets are found in the literature and web pages (Hampton & Heuvelhorst, 1990; Hampton, Smith, & Shank, 1991; Torrest, 1974; Web1, N.d.) to estimate the proppant size distribution and relations between distribution parameters. Figure 6.36 gives the cumulative probability distribution (cdf) of grain size obtained from sieve analysis. The volume distribution of base 2 logarithm of grain size ( $\varphi = \log_2(d)$ ) is normal (Eqn.6.21).

$$f(x; \mu, \sigma^2) = \frac{1}{\sigma\sqrt{2\pi}} e^{-\frac{1}{2}\left(\frac{x-\mu}{\sigma}\right)^2} \quad (6.21)$$

To find the normal distribution parameters, mean ( $\mu$ ) and standard deviation ( $\sigma$ ), the difference between measured cdf and calculated cdf is minimized with Matlab `fminsearch` function. Figure 6.37 gives the normal distribution fits for all samples. All calculated parameters are given in Table 6.7.



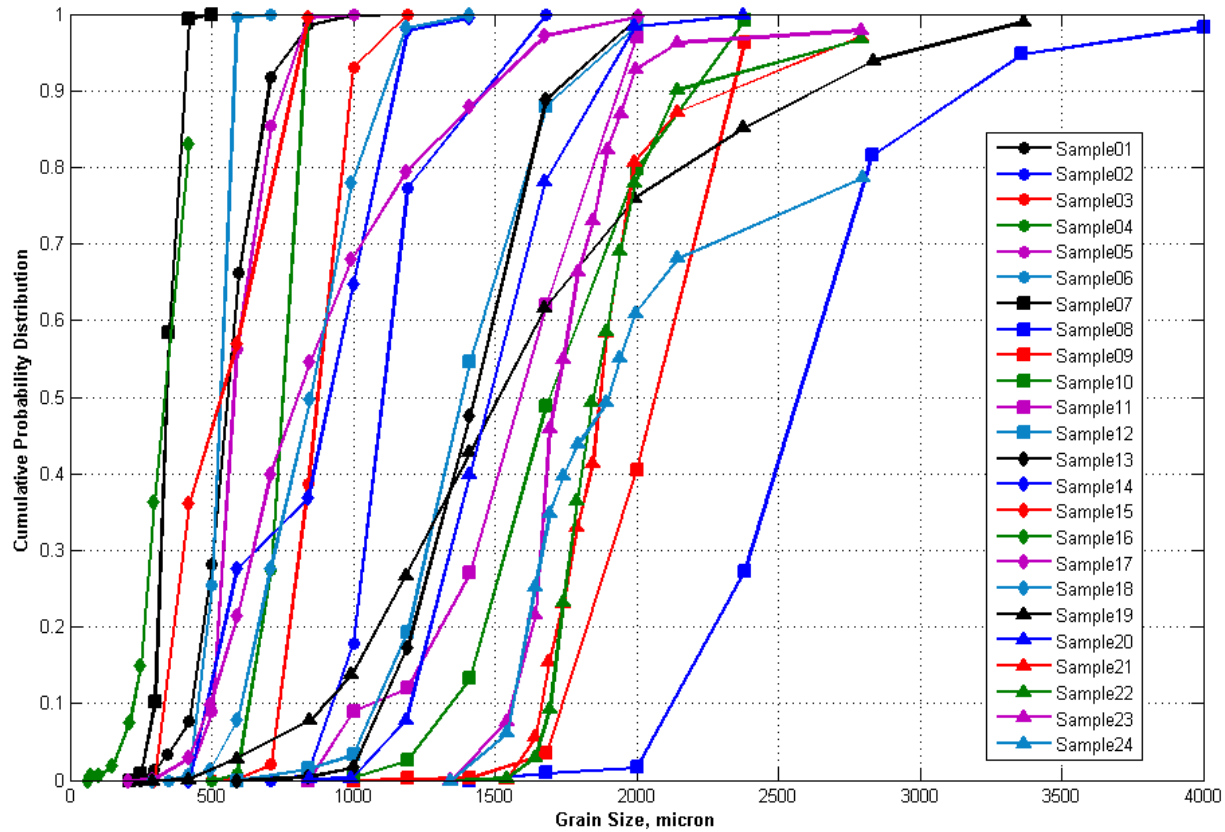


Figure 6.36 Cumulative Probability Distribution of 24 Proppant Samples Found From Literature

Based on the comparison plot of the mean grain size and the ratio of mean to the standard deviation of base 2 logarithm of grain size distribution, there is no trend in the normal distribution parameters (Figure 6.38). The mean grain size range is between 326 and 2252 micron which is in the range of coarse to medium grain size. A sorting is calculated from 25-quantile and 75-quantile grain sizes with Eqn.6.22. The relation between the sorting and the standard deviation is given in Eqn.6.23 (Figure 6.38). The coefficient of determination,  $R^2$ , is 0.99. The sorting range is between 1.035 and 1.323 which is in the range of extremely well sorted to well sorted.

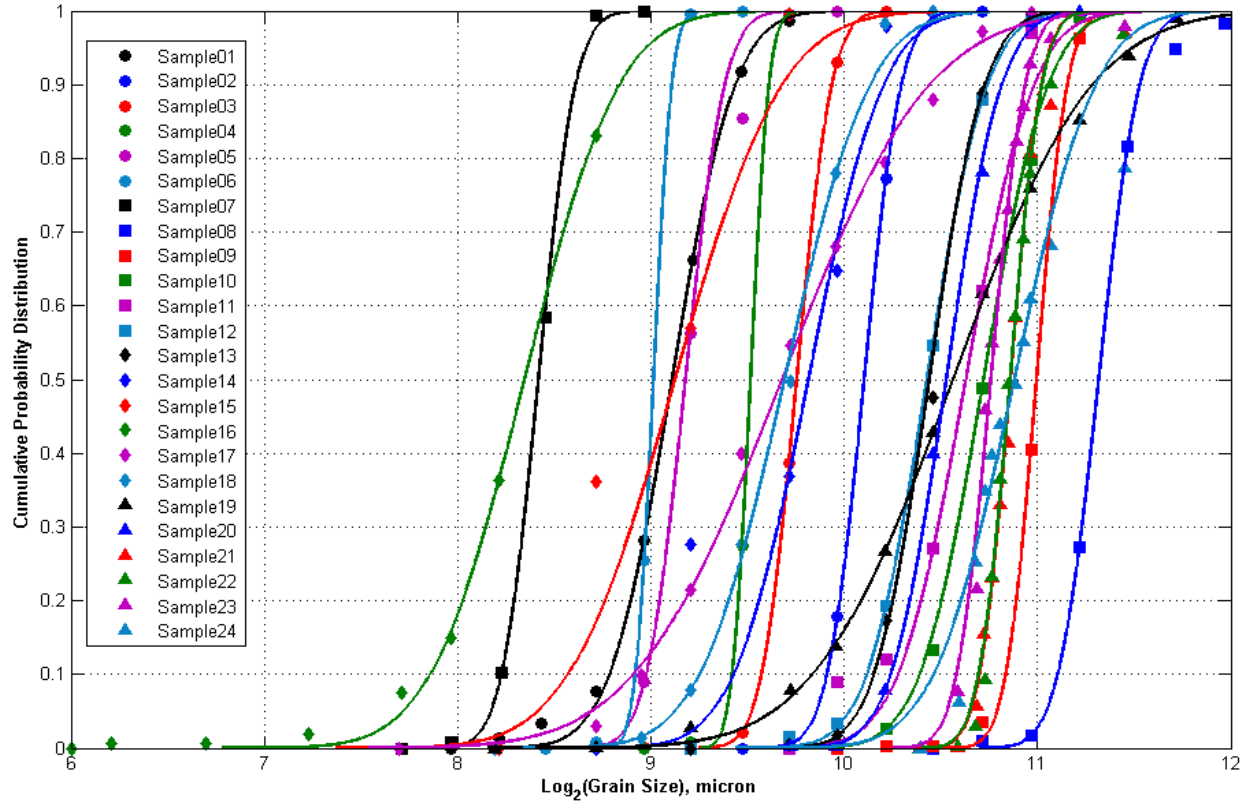
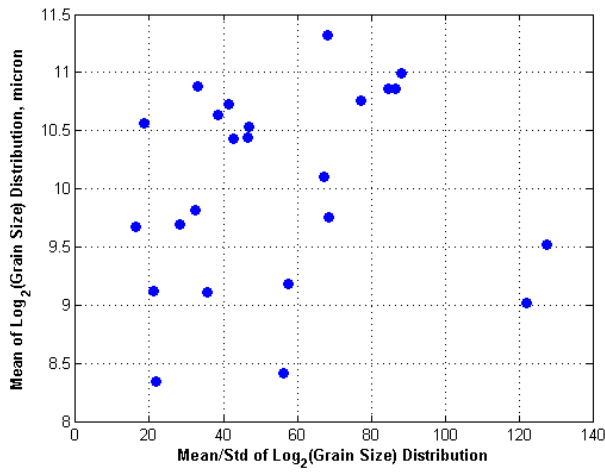
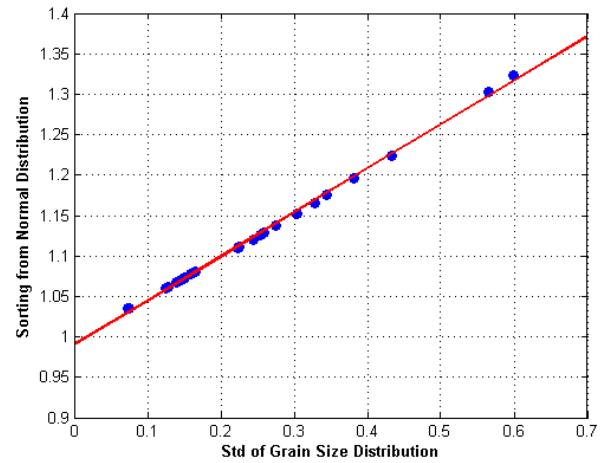


Figure 6.37 Normal Cumulative Probability Distribution Fits of 24 Samples



a) Mean and Standard Deviation Comparison of Normal Distribution



b) Standard Deviation and Sorting Comparison

Figure 6.38 Comparison of Mean, Standard Deviation and Sorting Calculated for Gravel Packs

$$S_o = \left( \frac{d_{75}}{d_{25}} \right)^{\frac{1}{2}} \quad (6.22)$$

$$S_o = 0.99 + 0.54 \times \sigma \quad (6.23)$$

Table 6.7 Normal Distribution Fit Parameters and Sorting Calculation

Sample Number	Mean, $\mu$	Std, $\sigma$	Mean/Std, $\mu/\sigma$	Mean Particle, micron	$\varphi_{25}$	$\varphi_{75}$	$d_{25}$	$d_{75}$	Sorting, $S_o$
1	9.111	0.254	35.804	552.850	8.939	9.282	490.841	622.693	1.126
2	10.104	0.150	67.165	1100.624	10.003	10.206	1025.873	1180.821	1.073
3	9.755	0.142	68.682	864.076	9.659	9.851	808.562	923.400	1.069
4	9.516	0.075	127.434	732.313	9.466	9.567	707.187	758.331	1.036
5	9.180	0.159	57.709	579.946	9.072	9.287	538.381	624.720	1.077
6	9.014	0.074	122.093	517.144	8.965	9.064	499.597	535.306	1.035
7	8.419	0.150	56.244	342.274	8.318	8.520	319.139	367.085	1.072
8	11.318	0.166	68.154	2552.310	11.206	11.430	2361.657	2758.356	1.081
9	10.996	0.125	88.310	2042.148	10.912	11.080	1926.662	2164.556	1.060
10	10.722	0.259	41.322	1689.316	10.547	10.897	1496.322	1907.201	1.129
11	10.630	0.275	38.622	1584.866	10.445	10.816	1393.504	1802.507	1.137
12	10.429	0.244	42.793	1378.302	10.264	10.593	1229.882	1544.633	1.121
13	10.441	0.224	46.602	1389.861	10.290	10.592	1251.647	1543.338	1.110
14	9.816	0.303	32.343	901.238	9.611	10.020	782.020	1038.630	1.152
15	9.126	0.433	21.084	558.538	8.834	9.417	456.219	683.804	1.224
16	8.347	0.382	21.842	325.667	8.089	8.605	272.383	389.375	1.196
17	9.677	0.599	16.168	818.656	9.273	10.081	618.838	1082.995	1.323
18	9.692	0.345	28.095	827.374	9.460	9.925	704.134	972.183	1.175
19	10.562	0.566	18.676	1511.431	10.180	10.943	1160.279	1968.859	1.303
20	10.529	0.224	46.942	1477.227	10.377	10.680	1330.168	1640.544	1.111
21	10.861	0.126	86.540	1859.904	10.776	10.946	1753.913	1972.299	1.060
22	10.860	0.128	84.698	1858.014	10.773	10.946	1749.911	1972.795	1.062
23	10.760	0.139	77.329	1733.584	10.666	10.853	1624.403	1850.105	1.067
24	10.881	0.328	33.164	1885.940	10.660	11.102	1617.744	2198.599	1.166

Based on the proppant size distribution, the mean and the sorting range are chosen as 0.30-2.50 mm and 0.1-0.5, respectively. Porosity range is chosen as 0.38-0.48 based on the experimental study conducted by Beard et al. (1973). To cover the all possible packings, Hammersley Design is used to prepare 100 packs (Figure 6.40).

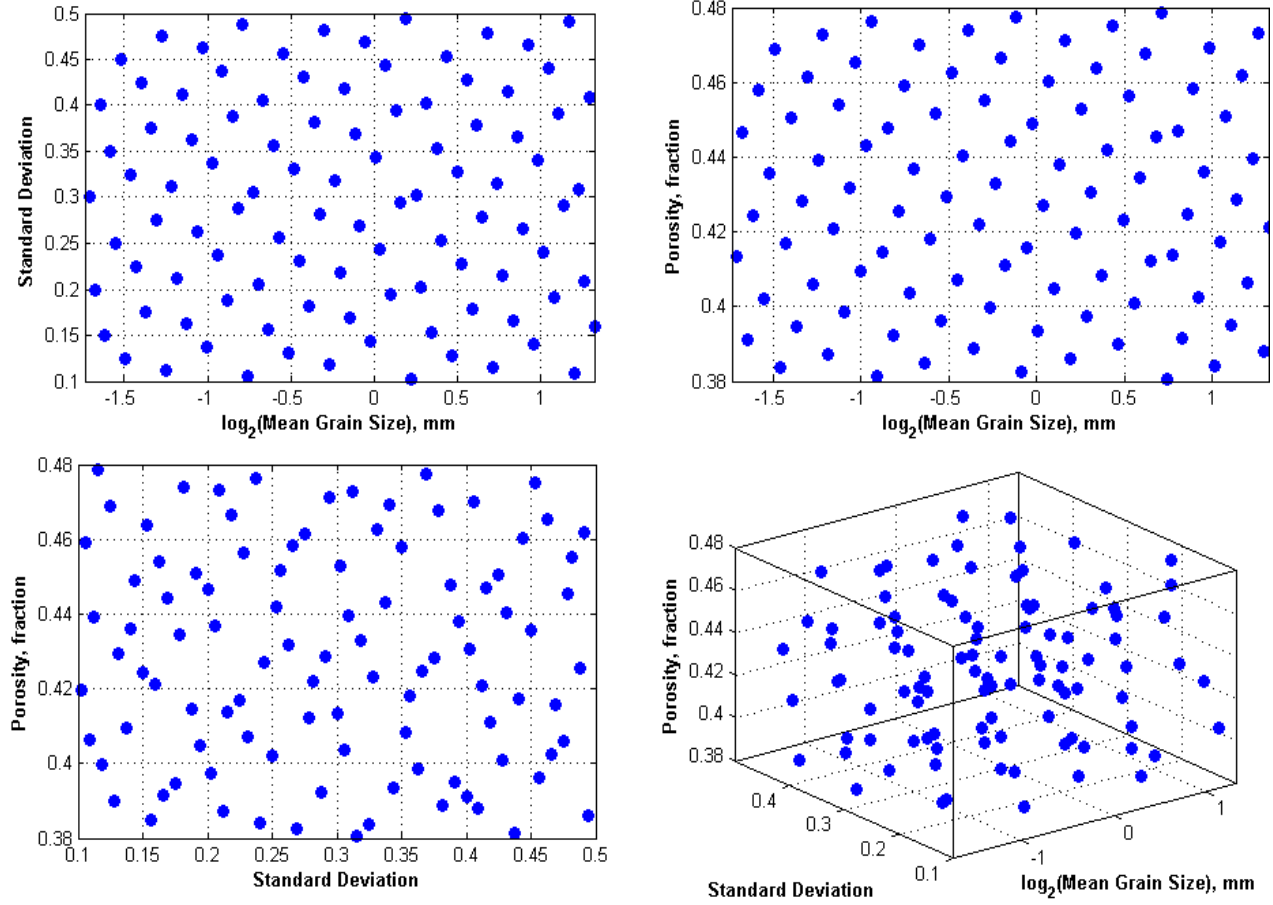


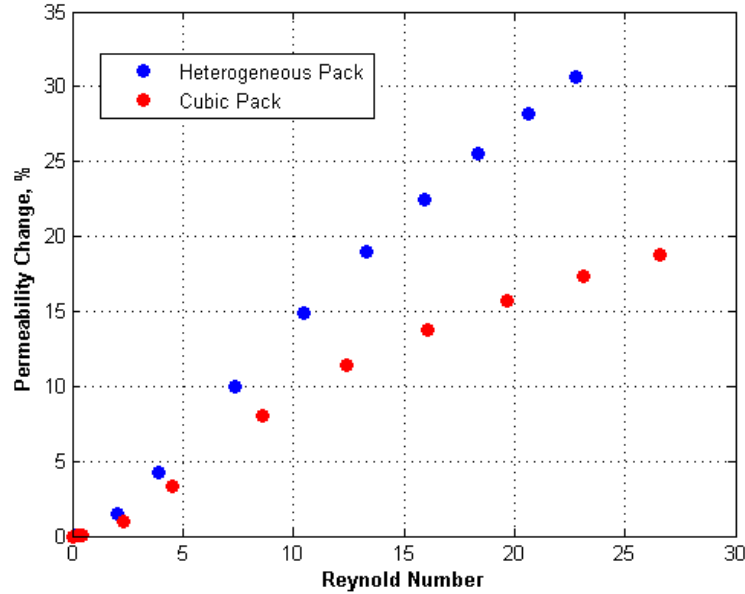
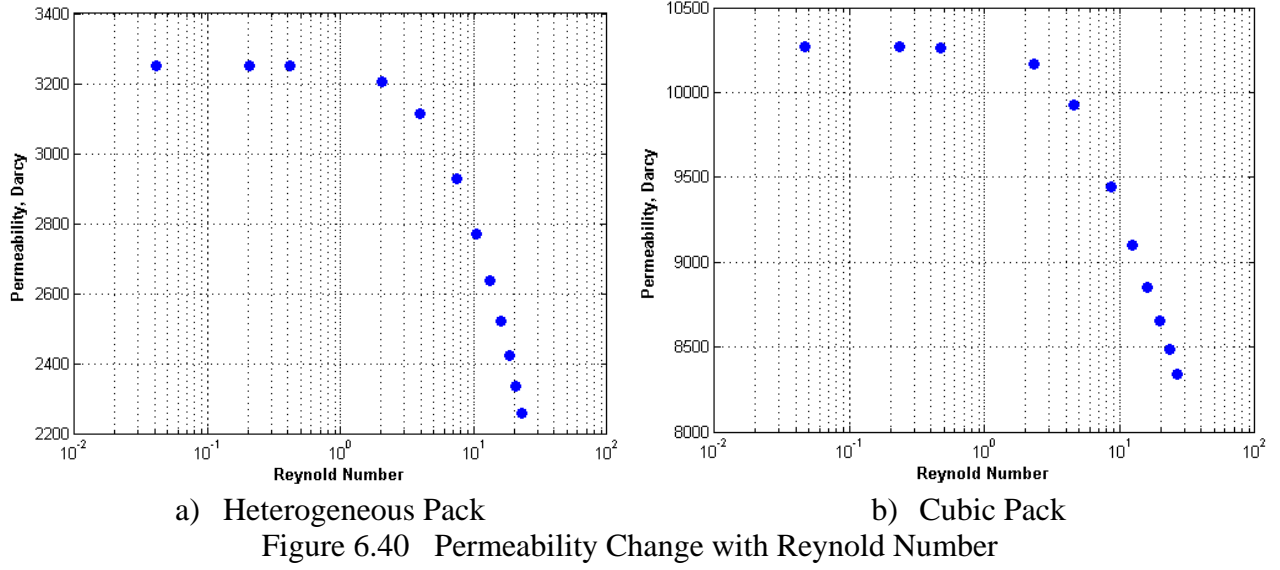
Figure 6.39 Hamersley Design of Experiment for Gravel Packs

### 6.5.2 Non-Darcy Coefficient and Tortuosity Calculations from LBM Simulations

Permeability at high Reynold numbers cannot be calculated from LBM with pressure difference boundary conditions because of compressibility errors; therefore, body force (e.g. gravity) is used. Permeability is calculated for heterogeneous pack (resolution of 0.015 mm) and cubic pack (resolution of 0.025 mm) from Darcy equation.

Apparent permeabilities do not change up to Reynold number 1 then they decrease with the increase in Reynold number (Figure 6.40) for both packs. Permeability of heterogeneous pack decreases from  $3.25 \times 10^3$  Darcy to  $2.26 \times 10^3$  Darcy (30.6% decrease) with the increase in Reynold number to 22.78. Permeability of cubic pack decreases from  $1.03 \times 10^4$  Darcy to  $8.34 \times 10^3$  Darcy (18.79%) with the increase in Reynold number to 26.55. Change of permeability

of heterogeneous pack is more compared to cubic pack permeability change (Figure 6.41) because heterogeneous pack pore structure is more complicated.



Eqn.6.24 is used to estimate the non-Darcy coefficient and the liquid permeability.

Plotting groups are:  $x \text{ axis} = \frac{\beta \rho v}{\mu}$  and  $y \text{ axis} = \frac{1}{k_{app}}$ . The liquid permeability and the non-Darcy

coefficient are obtained from the intercept ( $= 1/k$ ) and the slope ( $\beta$ ), respectively. To calculate

the permeability and non-Darcy coefficient, the lattice units are used. Figure 6.42 shows the non-Darcy plot for the heterogeneous and cubic packs. The non-Darcy coefficient and permeability for heterogeneous pack are 0.1157 1/voxel (7.71x10<sup>3</sup> 1/m) and 14.81 voxel<sup>2</sup> (3.38x10<sup>3</sup> Darcy), respectively. The non-Darcy coefficient and permeability for cubic pack are 0.0547 1/voxel (2.19x10<sup>3</sup> 1/m) and 16.44 voxel<sup>2</sup> (1.10x10<sup>4</sup> Darcy), respectively. In Forchheimer plot of cubic pack, the last data points are deviates from linear line, after Reynold number of 20. This is the only pack that deviates from the Forchheimer equation in this study. Similar observations are also given in the literature (Barree & Conway, 2004; Lai, Miskimins, & Wu, 2012).

$$\frac{1}{k_{app}} = \frac{1}{k_{liq}} + \frac{\beta \rho u}{\mu} \quad (6.24)$$

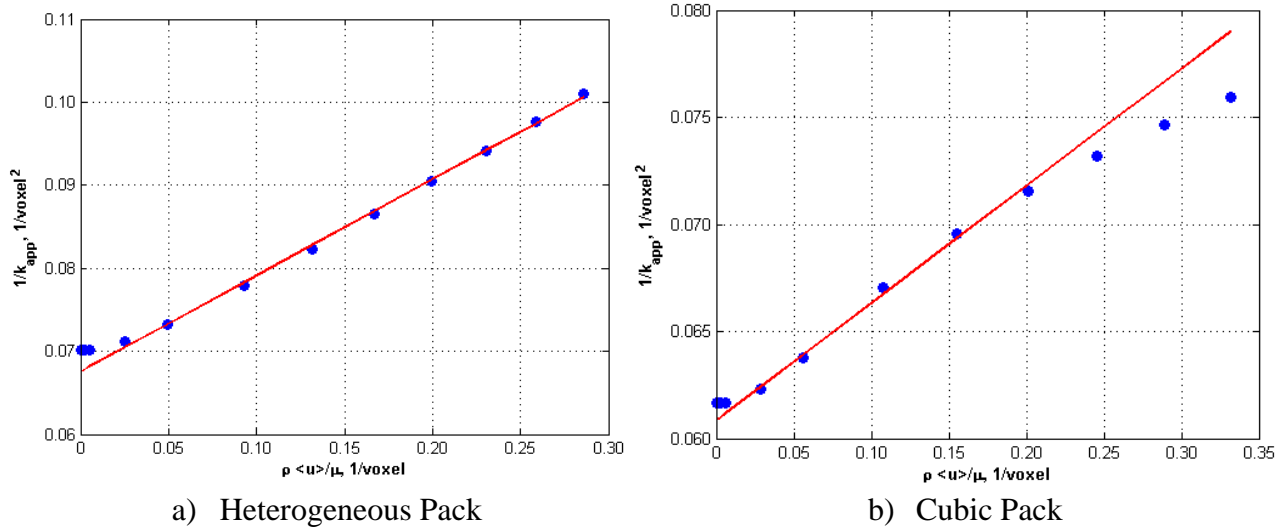


Figure 6.42 Forchheimer Plot for non-Darcy Coefficient and Permeability

Tortuosity change with Reynold number is calculated volume averaged velocities given in Eqn.6.25 (Nabovati & Sousa, 2009). For both packs, tortuosity decreases then increases with Reynold number (Figure 6.43). Cubic pack tortuosities are close to one and they are lower than to heterogeneous pack tortuosities. Comparing the streamlines of velocity fields indicated by red

points in the cubic pack tortuosities, streamlines of higher velocity becomes straighter with the increase in Reynold number; therefore, initially tortuosities decrease with Reynold number. After that the vortices increase, therefore, the tortuosities increase (Figure 6.44).

$$\tau_i = \frac{\sum u_{mag}(x, y, z)}{\sum |u_i(x, y, z)|} \text{ for } i = x, y, z \quad (6.25)$$

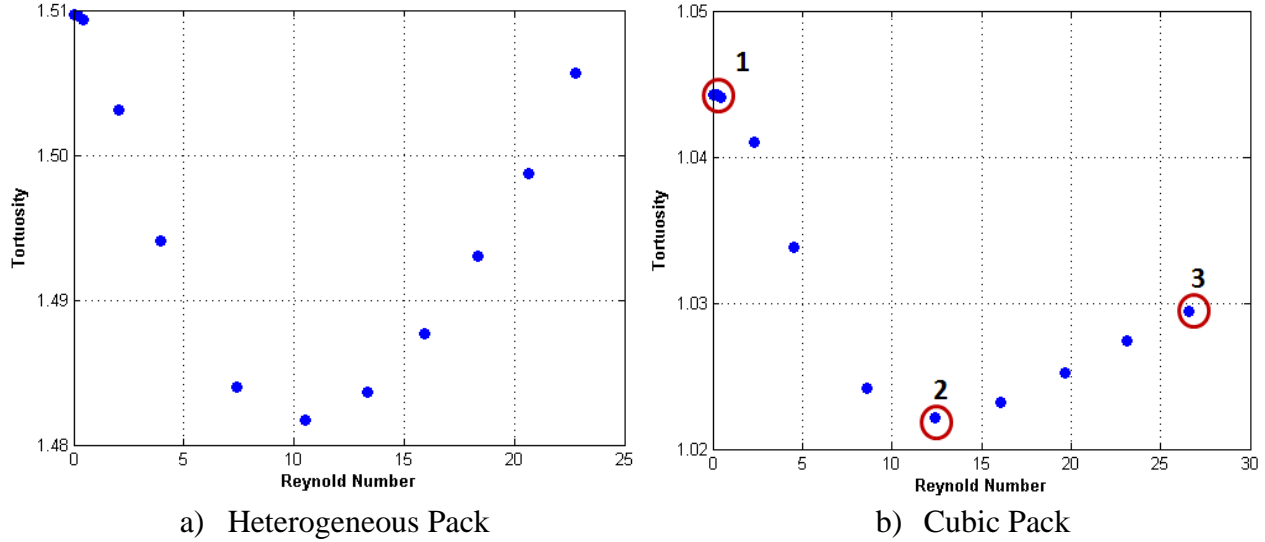


Figure 6.43 Tortuosity Change with Reynold Number

### 6.5.3 Flow Parameters Comparison with Literature Data

100 packs are constructed with Hammersley design (Figure 6.39). For each design case, the domain is voxelized by 800x800x800. For the most heterogeneous case, the minimum and maximum particle diameters are represented with 55 and 224 voxels, respectively. Permeabilities are calculated from LBM with low pressure difference method and network modeling (Figure 6.45), and both methods give similar permeabilities. Permeabilities calculated from network modeling are slightly higher than the ones calculated from LBM. Network modeling divides pore-space with spheres (pore body) and cylinder (pore throat); therefore, permeability obtained from network modeling is just approximation to the true permeability since pore space is not

smooth to be represented with spheres and cylinders. For further analysis, permeabilities obtained from LBM are used.

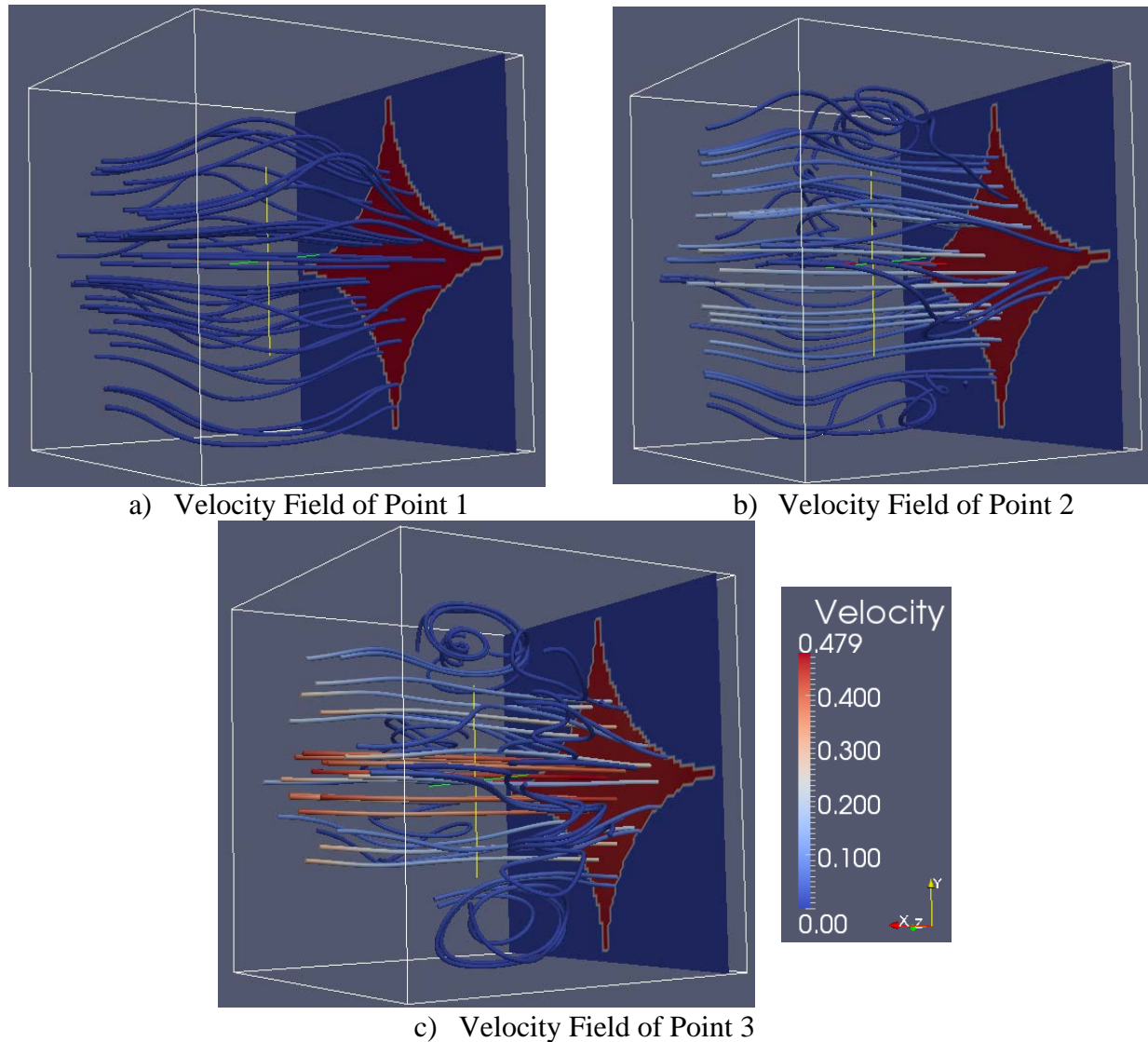


Figure 6.44 Velocity Field Change with Tortuosity

Non-Darcy coefficients, permeabilities and tortuosities calculated from LBM are compared with the ones calculated from correlations found from literature. Non-Darcy coefficients calculated from theoretically developed correlation for parallel and series representation of porous media (Eqn.6.26 and Eqn.6.27) (Li & Engler, 2001) are compared the ones calculated from LBM (Figure 6.46). The coefficients for parallel and serial models,  $c$  and



$c''$ , are  $10^{5.1354}$  and  $10^{6.6524}$ , respectively. Non-Darcy coefficients are consistent with the ones obtained from parallel model; however, estimated non-Darcy coefficients are inconsistent with the ones obtained from serial model, and also correlation for serial model representation of porous media is dimensionally inconsistent.

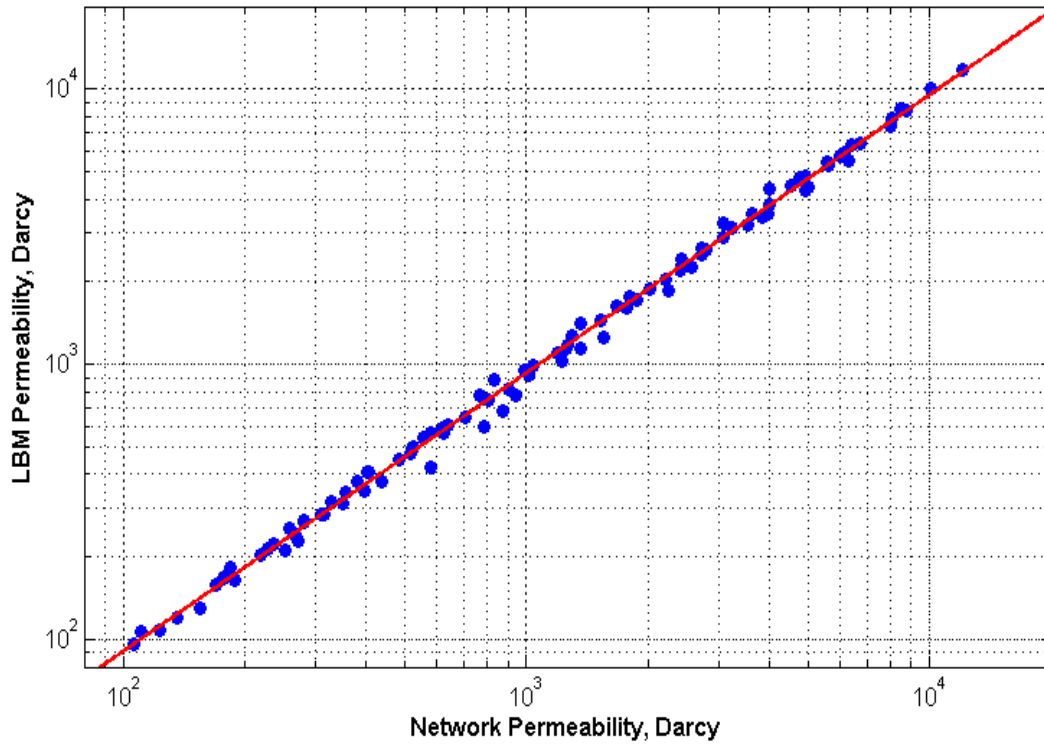


Figure 6.45 Comparison of Permeability Calculated from LBM and Network Model

$$\beta(1/m) = \frac{c}{k(D)^{0.5}\phi^{1.5}} \quad (6.26)$$

$$\beta(1/m) = \frac{c''\tau}{k(D)\phi} \quad (6.27)$$

Figure 6.47 gives the cross plot of non-Darcy coefficients calculated from the equation developed from Ergun equation (Eqn.6.28) (Bird et al., 1965) and the ones calculated from LBM. Non-Darcy coefficients calculated from Eqn.6.28 are slightly higher; if coefficient is lowered to 0.0106, the non-Darcy coefficients calculated from Eqn.6.28 matches the ones calculated from LBM.

$$\beta(1/m) = \frac{0.0117 D_p(m)}{k(m^2)(1 - \phi)} \quad (6.28)$$

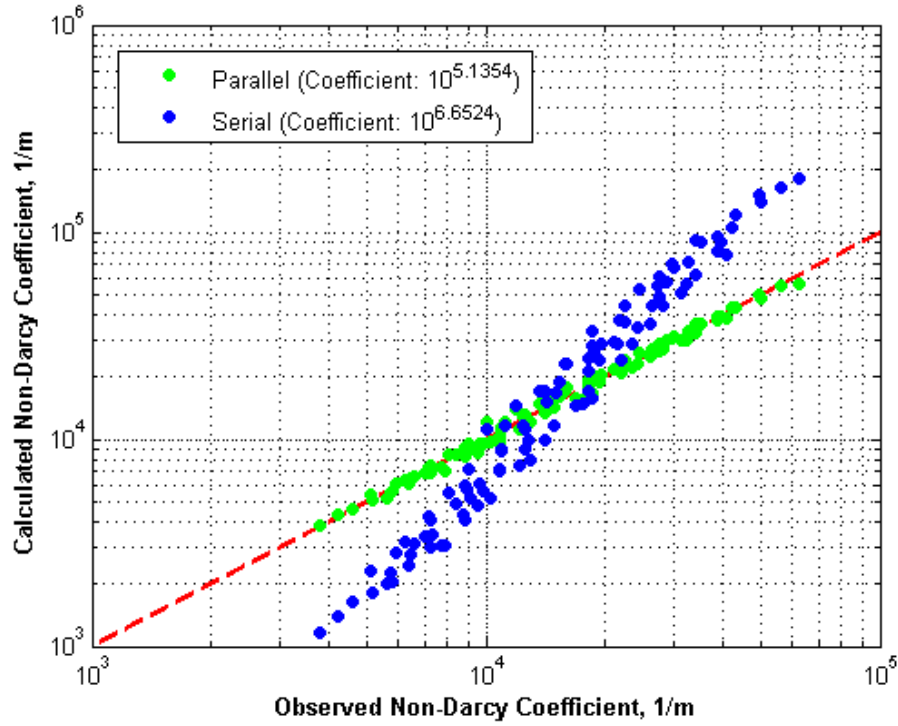


Figure 6.46 Comparison of Non-Darcy Coefficient with Theoretically Develop Correlations

The calculated non-Darcy coefficients are also compared with the correlations developed with linear regression by using experimental data found from literature. Figure 6.48 gives the cross plot of non-Darcy coefficients calculated from Geertsma correlation (Eqn.6.29) developed for unconsolidated and consolidated media and the ones calculated from LBM. Non-Darcy coefficients are underestimated and overestimated for low and high non-Darcy coefficients, respectively. Even though Geertsma correlation is dimensionally consistent, it gives rough estimation of non-Darcy coefficient.

$$\frac{\beta(1/m)}{\sqrt{1/k(m^2)}} \phi^{5.5} = 0.005 \quad (6.29)$$

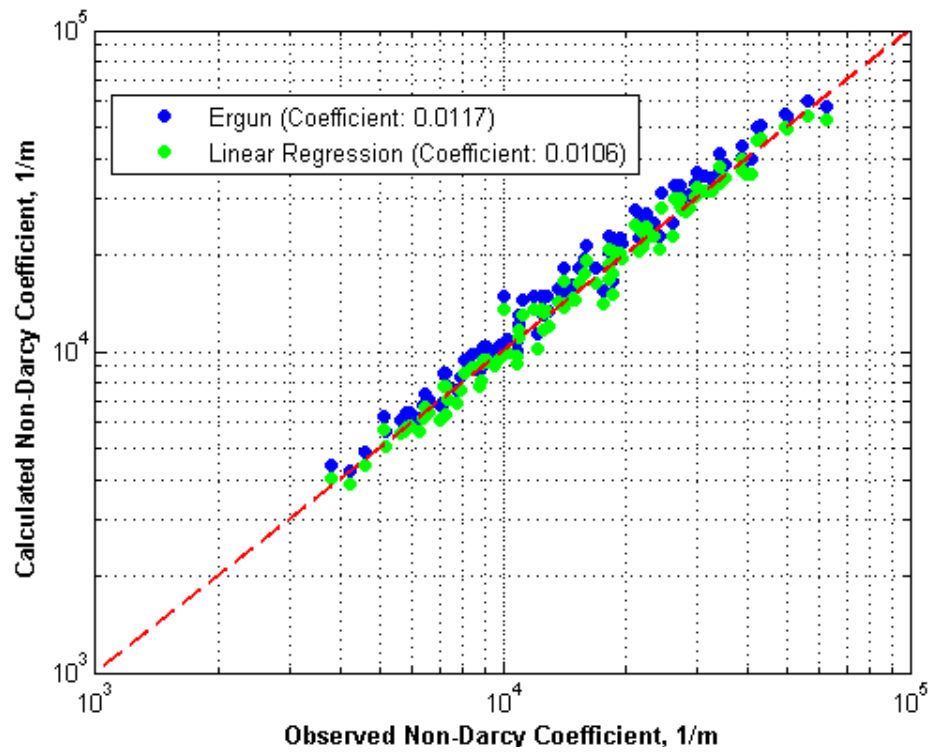


Figure 6.47 Comparison of Non-Darcy Coefficient with Theoretically Develop Correlations

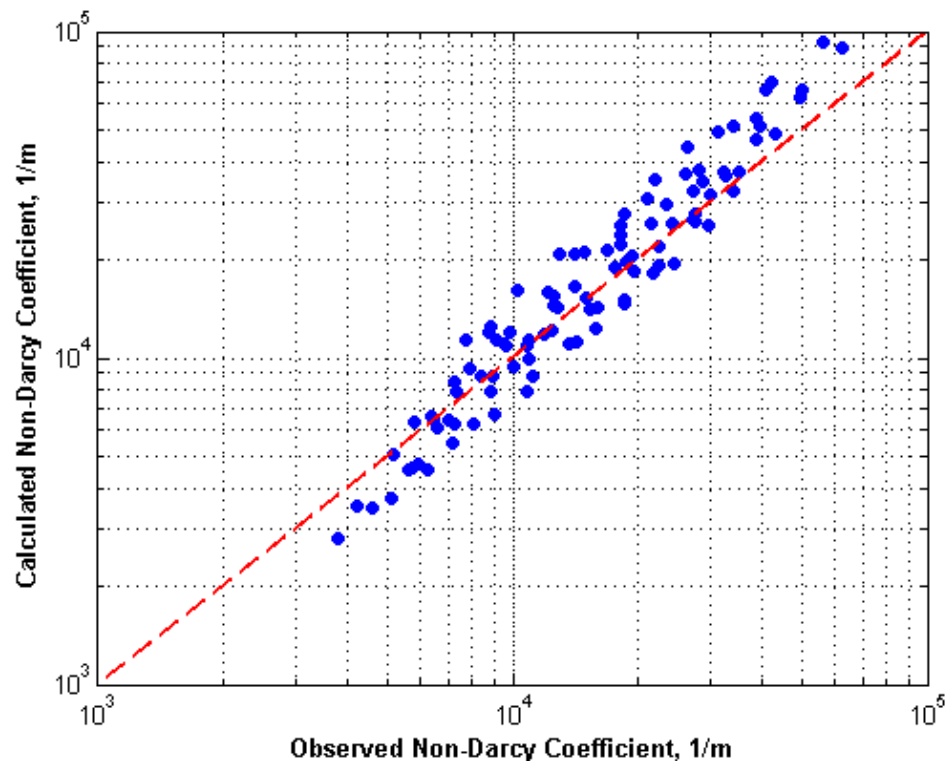


Figure 6.48 Comparison of Non-Darcy Coefficients with Geertsma Correlation

Jones developed two correlations using experimental data for 355 sandstone and 29 limestone media (Eqn.6.30 (C1) and Eqn.6.31 (C2)). He also developed two more correlations by modifying Geertsma correlation (Eqn.6.32 (C3) and Eqn.6.33 (C4)). Calculated non-Darcy coefficients from Eqn.6.30 through Eqn.6.33 are all inconsistent with the ones calculated from LBM (Figure 6.49). Calculated non-Darcy coefficients are also compared with other correlations developed for consolidated media such as Tek et al. (1962), Liu et al. (1995) and Coles et al. (1998); most of the correlations underestimate the non-Darcy coefficients.

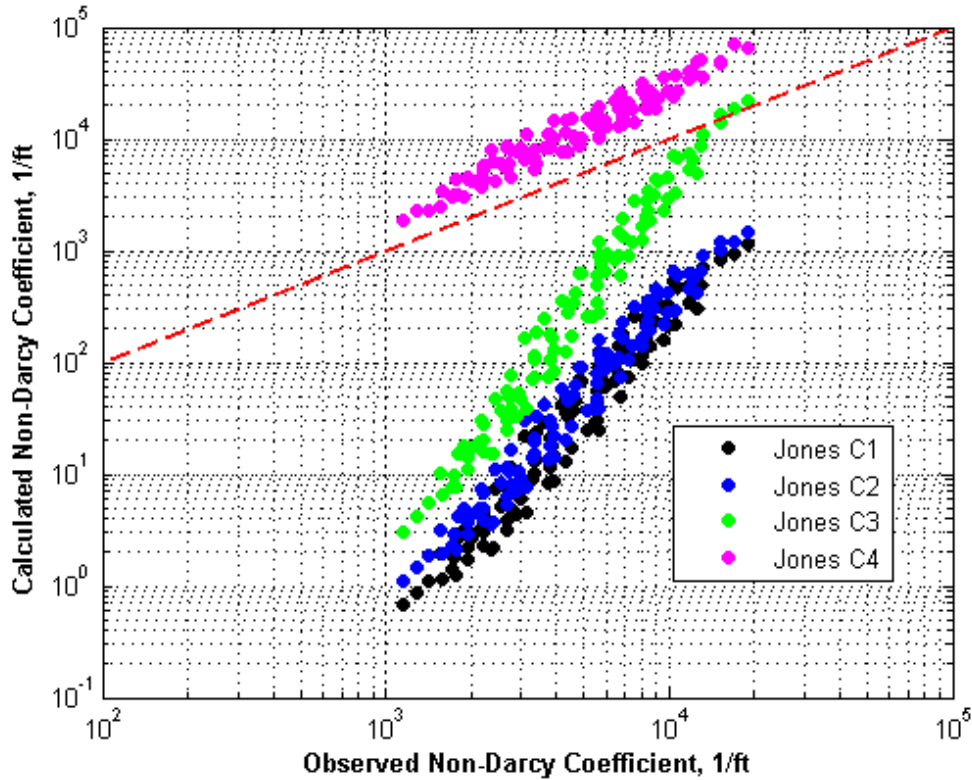


Figure 6.49 Comparison of Non-Darcy Coefficients with Jones Correlations

$$\beta = \frac{6.15 \times 10^{10}}{k^{1.55}} \quad (6.30)$$

$$\beta = \frac{1.88 \times 10^{10}}{k^{1.47} \phi^{0.53}} \quad (6.31)$$

$$\beta = \frac{3.13 \times 10^{12}}{k^{1.78} \phi^{1.78}} \quad (6.32)$$

$$\beta = \frac{1.27 \times 10^5}{k^{0.52} \phi^{5.68}} \quad (6.33)$$

Permeabilities calculated from LBM with low pressure difference method and permeabilities calculated from intercept of the Forchheimer equation (Eqn.6.24) are similar expect a few cases (Figure 6.50). Permeabilities calculated from Forchheimer equation are higher. Most of the differences are less than 5% and for seven cases the differences are high up to 30%. This may cause from unrepresentative of packing domains of these cases.

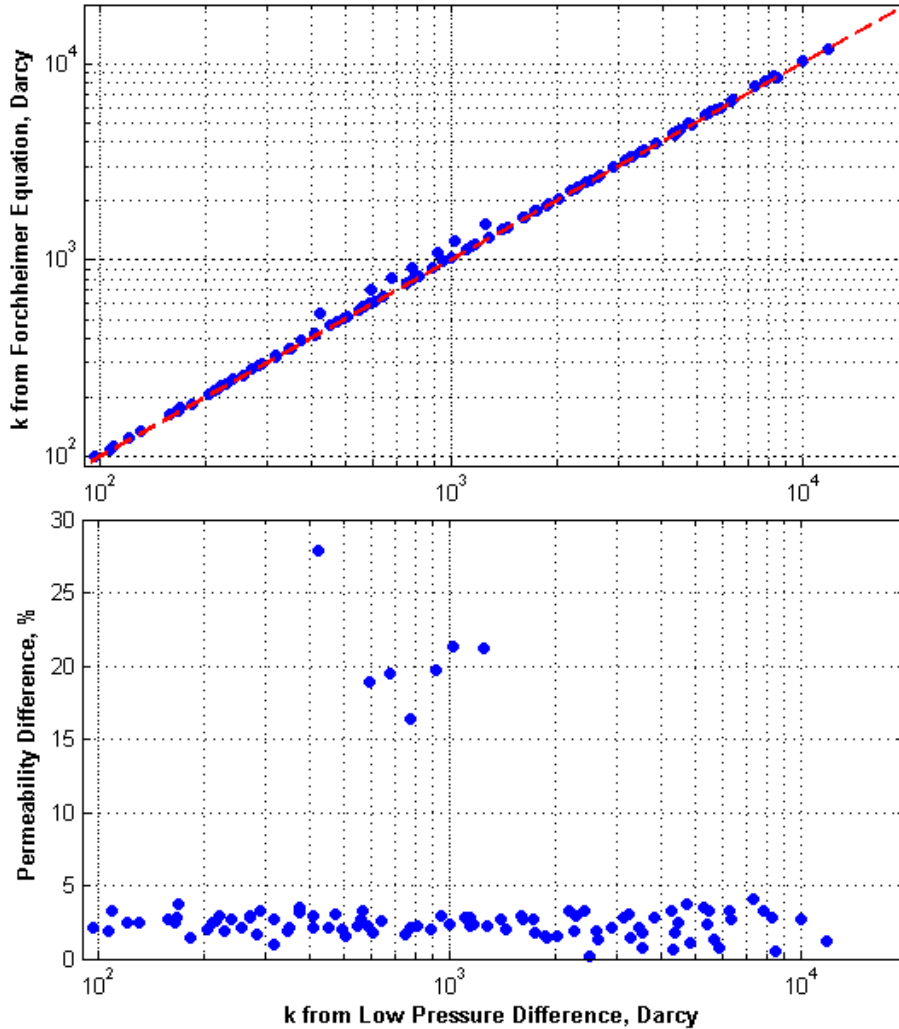


Figure 6.50 Comparison of Permeabilities from LBM with Low Pressure Difference Method and Forchheimer Equation

Permeabilities calculated from LBM with low pressure difference method are compared with the ones obtained from correlations found from the literature. Permeabilities calculated from Berg correlation (1970) (Eqn.6.34) are slightly lower than the ones calculated from LBM (Figure 6.51). If the coefficient is increased to 0.1229, calculated permeabilities are consistent with the ones obtained from LBM.

$$k(D) = 8.4 \times 10^{-2} D(\mu m)^2 \phi^{5.1} \quad (6.34)$$

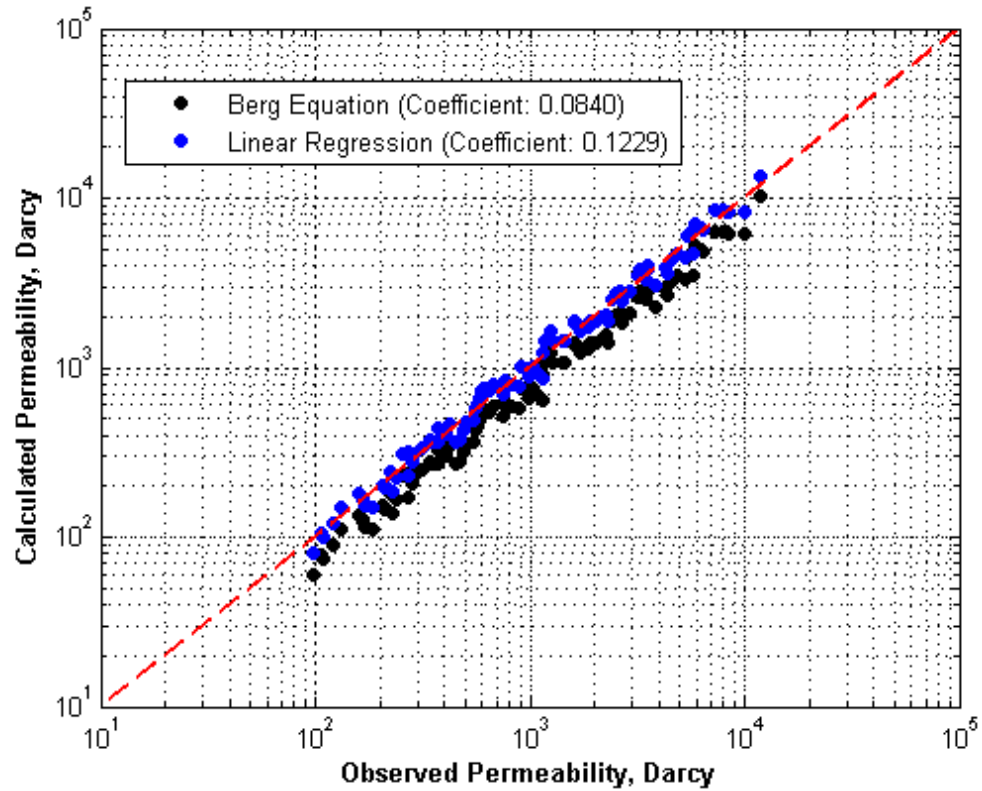


Figure 6.51 Comparison of Permeability with Berg Correlation

Permeabilities are also compared with the ones obtained from theoretically developed Kozeny correlation (Eqn.6.35).  $C$  is a shape factor that depends on the pore structure of media. The suggested values are 180 and 150 for Carman-Kozeny and Blake-Kozeny equations, respectively. Both coefficients give similar permeabilities; and best fit gives the coefficient of 164 between two suggested values (Figure 6.52).

$$k(m^2) = \frac{d(m)^2 \phi^3}{C (1 - \phi)^2} \quad (6.35)$$

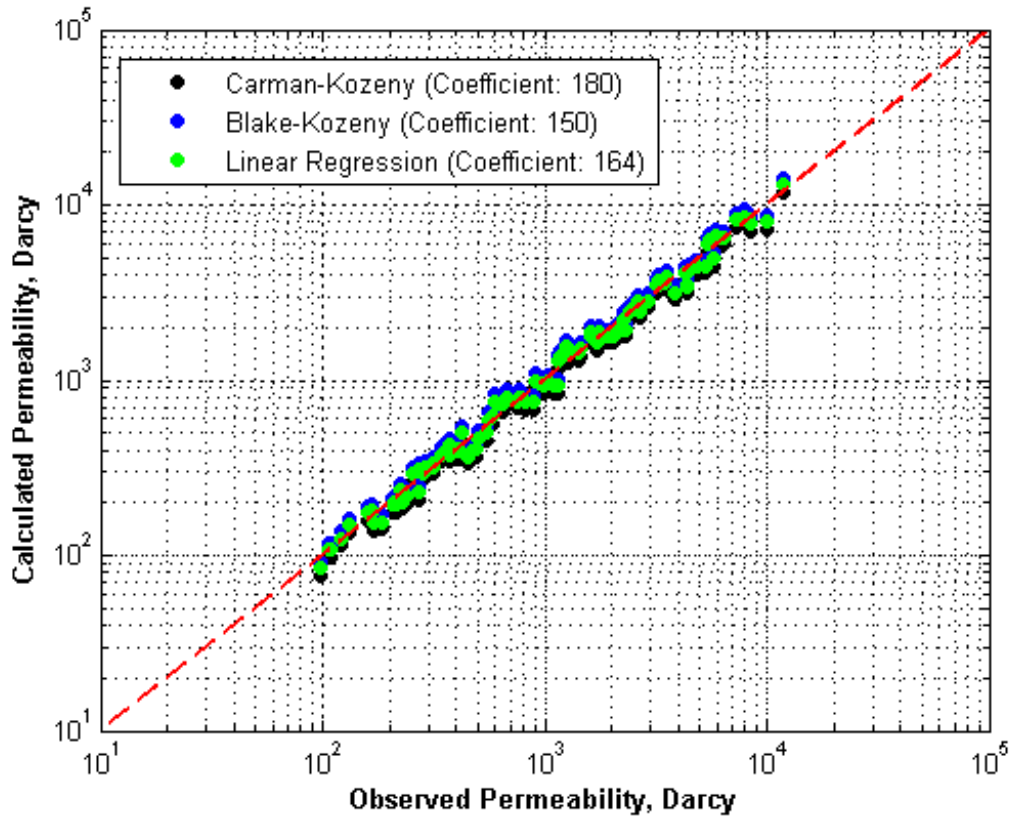


Figure 6.52 Comparison of Permeability with Kozeny Correlations

Tortuosities calculated from LBM are confirmed with correlations. Calculated tortuosities are fitted to logarithmic formula (Eqn.6.36) proposed by Comiti and Renaud (1989) with a  $p$  value is 0.2616 (Figure 6.53). Better fit can be obtained if the restriction 1 is removed.

$$\sqrt{\tau} = 1 - p \ln \phi \quad (6.36)$$

Tortuosities are fitted to the analytic equation (Eqn.6.37) proposed by Matyka et al. (2009) (Figure 6.54) with  $B$  of 1.0937.

$$\sqrt{\tau} = \sqrt{\frac{2\phi}{3[1 - B(1 - \phi)^{2/3}]}} + \frac{1}{3} \quad (6.37)$$

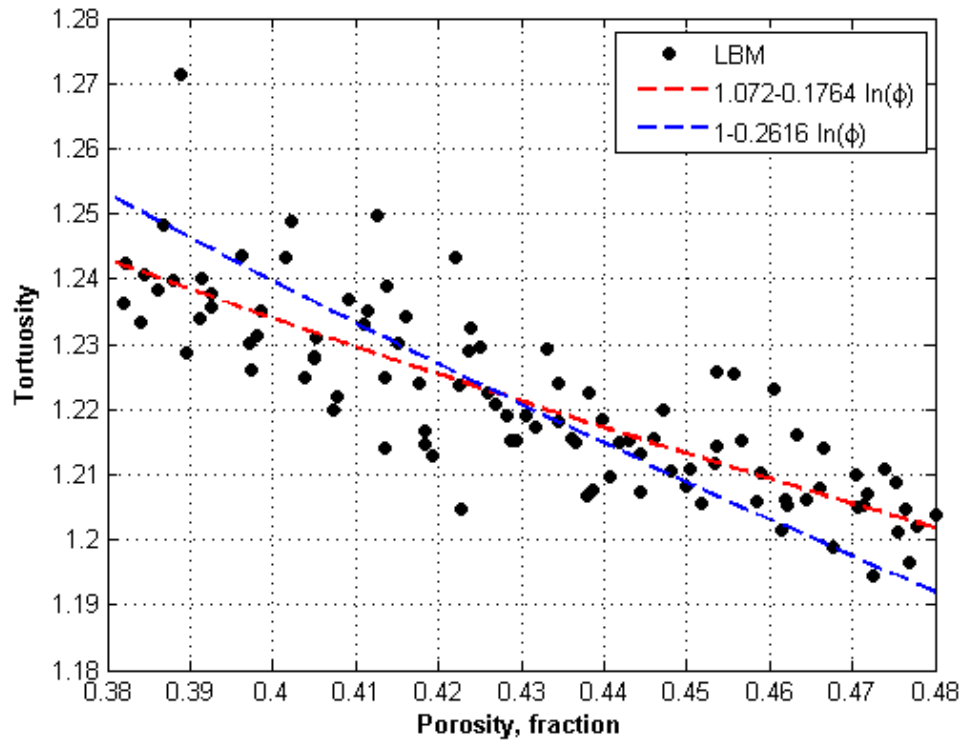


Figure 6.53 Tortuosity Comparison with Logarithmic Formula

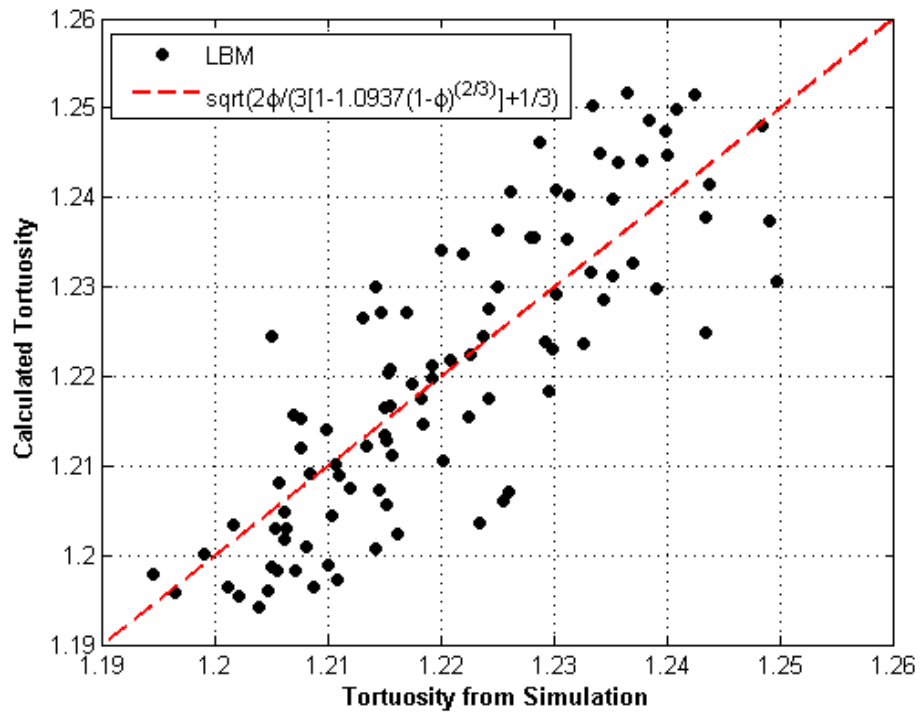


Figure 6.54 Tortuosity Comparison with Analytic Equation by Matyka et al. (2009)



There is a power law relation between electrical tortuosity and porosity given as Archie Law (Archie, 1942) (Eqn.6.38, Figure 6.55). For gravel packs, the coefficients  $a$  and  $n$  are 1.1690 and 2.2884, respectively.

$$\tau = a\phi^{-n} \quad (6.38)$$

All tortuosity fits are scattered compared with non-Darcy coefficient and permeability fits. Even though all tortuosities are calculated from flow path obtained from low pressure difference method, the small change of Reynold number leads to change in tortuosity because flow path changes even for small change in Reynold number.

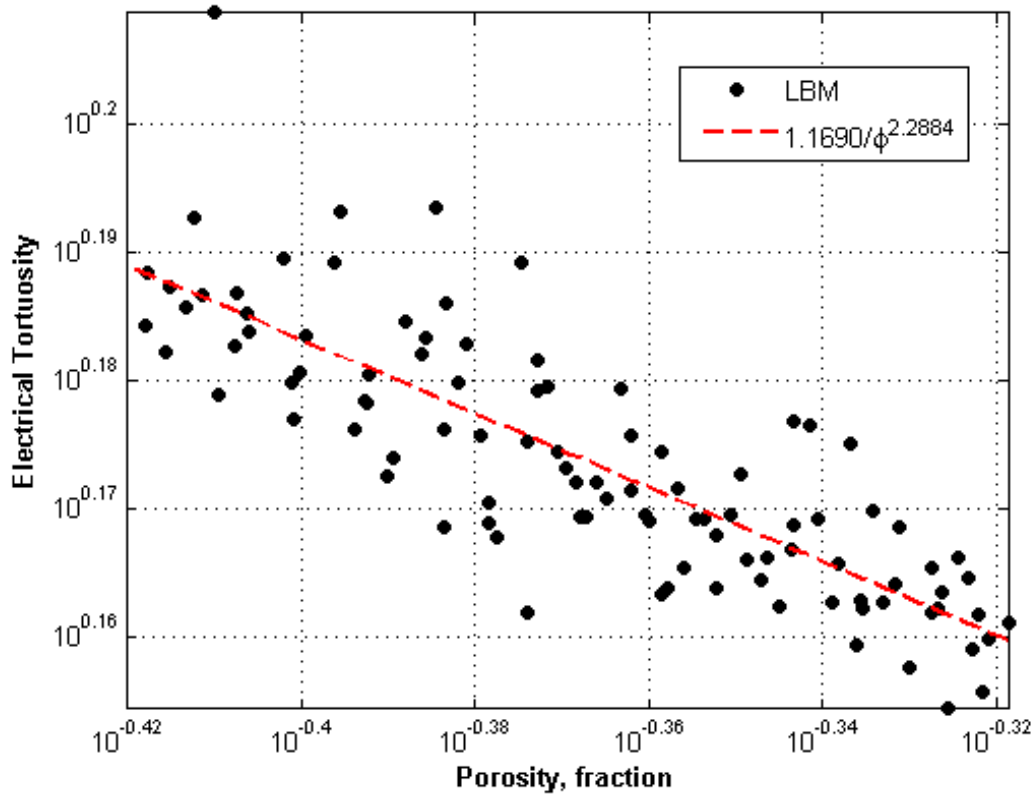


Figure 6.55 Tortuosity Porosity Relation – Archie Law

For gravel packs, it is proposed that the specific surface areas calculated by counting the grain voxels directly connected to the pore voxels are about 6 times of cross-sectional areas. Therefore, the ratio of the actual specific surface area to the specific surface area calculated from

voxel image is 1.5. To verify this, the specific surface areas are calculated from Minkowski functional (Legland, Kieu, & Devaux, 2007) and compared with the ones obtained from surface voxels count (Figure 6.56). Specific surface areas calculated by counting the grain voxels connected to the pore voxels are higher than the specific surface areas obtained from Minkowski functional and the difference increases as the specific surface area increases. A 1.5 correction factor perfectly adjusts the specific surface areas from voxel counts.

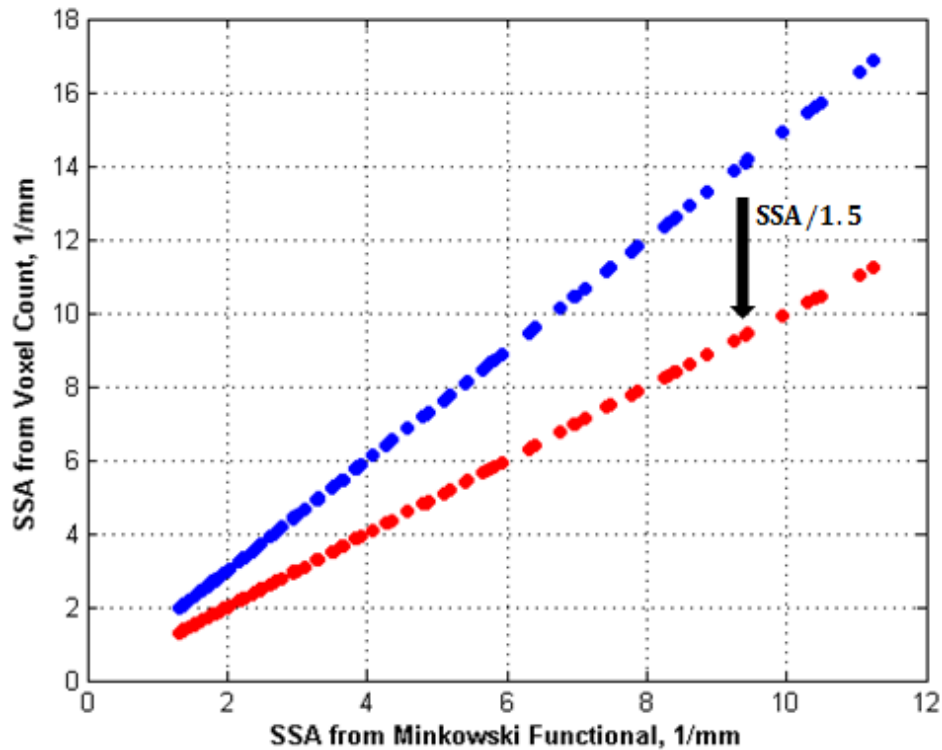


Figure 6.56 Specific Surface Area Comparison with Minkowski Functional

Swanson point is the tangent point of 45° line with logarithmic plot of mercury saturation according to bulk volume vs. capillary pressure. Capillary pressure is calculated from network modeling for each domain. The mercury saturation according to bulk volume,  $S_b$ , changes between 29.2% and 37.3%, and capillary pressure,  $P_c$ , changes between 0.38 psia and 3.86 psia. Swanson mercury saturation and capillary pressure are related with porosity and mean grain size, respectively (Figure 6.57). Increase in porosity leads to increase in saturation that makes the

porous media connected; increase in mean grain size leads to decrease in capillary pressure. Since the porosity and mean grain size are two parameters affecting permeability, Swanson point is directly related with permeability. The correlation between Swanson points and permeabilities calculated from LBM is given in Eqn.6.39 with a coefficient of determination is 0.9979 (Figure 6.58).

$$k = 1.4936 \left( \frac{S_b}{P_c} \right)^{1.9749} \quad (6.39)$$

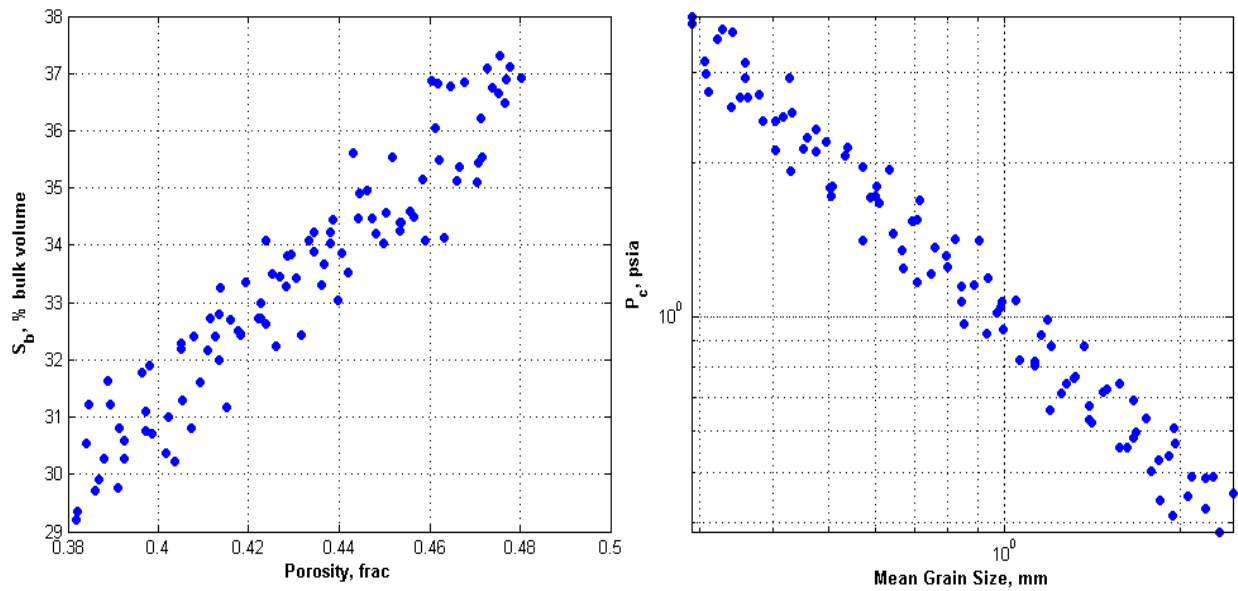


Figure 6.57 Swanson Point Relation with Porosity and Mean Grain Size

#### 6.5.4 Non-Darcy coefficient and Permeability Correlations Development

For reservoir simulation, accurate estimation of permeability and non-Darcy coefficient are important for correct prediction of production. Therefore, there are some correlations are developed to estimate these two parameters from other parameters calculated from LBM and network, and these correlations are evaluated statistically to emphasize the colinearity problem.

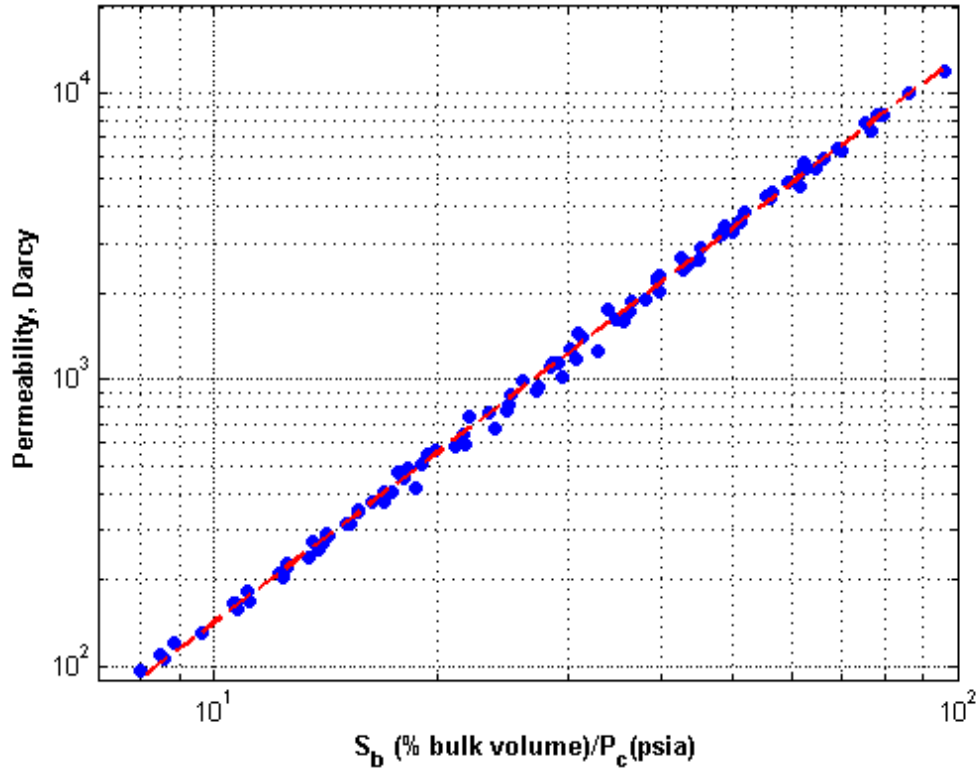


Figure 6.58 Swanson Point Correlation for Gravel Packs

Figure 6.59 summarizes the all parameters calculated from LBM and Network modeling. Some parameters such as permeability and non-Darcy coefficient are shown in logarithmic scale. There are high correlations between mean particle size ( $D_p$ ), specific surface area ( $SSA$ ), permeability ( $k$ ), non-Darcy coefficient ( $\beta$ ), mean pore radius ( $P_r$ ), mean throat radius ( $T_r$ ), and throat length ( $T_l$ ). As mean grain size increases, pores sizes, throat radius and their length increase. On the other hand, specific surface decreases. These lead to increase in permeability and decrease in non-Darcy coefficient. There is small correlation between porosity ( $\emptyset$ ), tortuosity ( $\tau$ ). Increase in porosity leads to less tortuous flow path. Even though porosity does not seem to be correlated with mean pore and throat radii, it is correlated with the ratio of mean pore radius to throat radius ( $P_r/T_r$ ). As porosity increases, increase in pore radius is more than increase in throat radius. There is also small correlation between ratio of mean pore radius to throat radius

and throat aspect ratio ( $2 T_r/T_l$ ). Median corrected coordination number is not correlated with any parameter. Coordination number change is not significant. Pore space of gravel pack is highly connected with a median coordination number is 3 or 4. For one of the points indicated with red circle in Figure 6.59, Case45, calculated tortuosity is very high. This point corresponds to the highest difference of permeability calculated from low body force and the one obtained from Forchheimer equation, 27.92% (Figure 6.50). This point can be considered as an outlier. However, this point is kept for correlation development so that other parameters of that point can be used.

For illustration, developments of some non-Darcy coefficient correlations from other parameters are given. Four parameters are used: permeability, porosity, tortuosity and specific surface area. In the first correlation (Eqn.6.40) permeability and porosity are used to estimate the non-Darcy coefficient,  $\beta = f(k, \phi)$ . Figure 6.60 gives the cross plot of the non-Darcy coefficients calculated from correlation (predicted) and the ones obtained from LBM simulations (actual). In this plot, red and blue lines give the  $45^\circ$  line to evaluate fit and mean value of non-Darcy coefficient. Table 6.8 and Table 6.9 give summary fit and parameter estimates. The coefficient of determination,  $R^2$ , is high, 0.9962, and both regression parameters are significant, absolute  $t$  values are greater than 2. The power of permeability is close to 0.5 that indicates the dimension match; dimension of permeability and non-Darcy coefficient are  $[L^2]$  and  $[1/L]$ , respectively. In addition, leverage plots (Figure 6.61) and  $p$  values confirm that both parameters are significant, and there is no trend in the residuals (Figure 6.62).

$$\beta(1/m) = \frac{10^{4.8674}}{k(D)^{0.4852} \phi^{2.1089}} \quad (6.40)$$

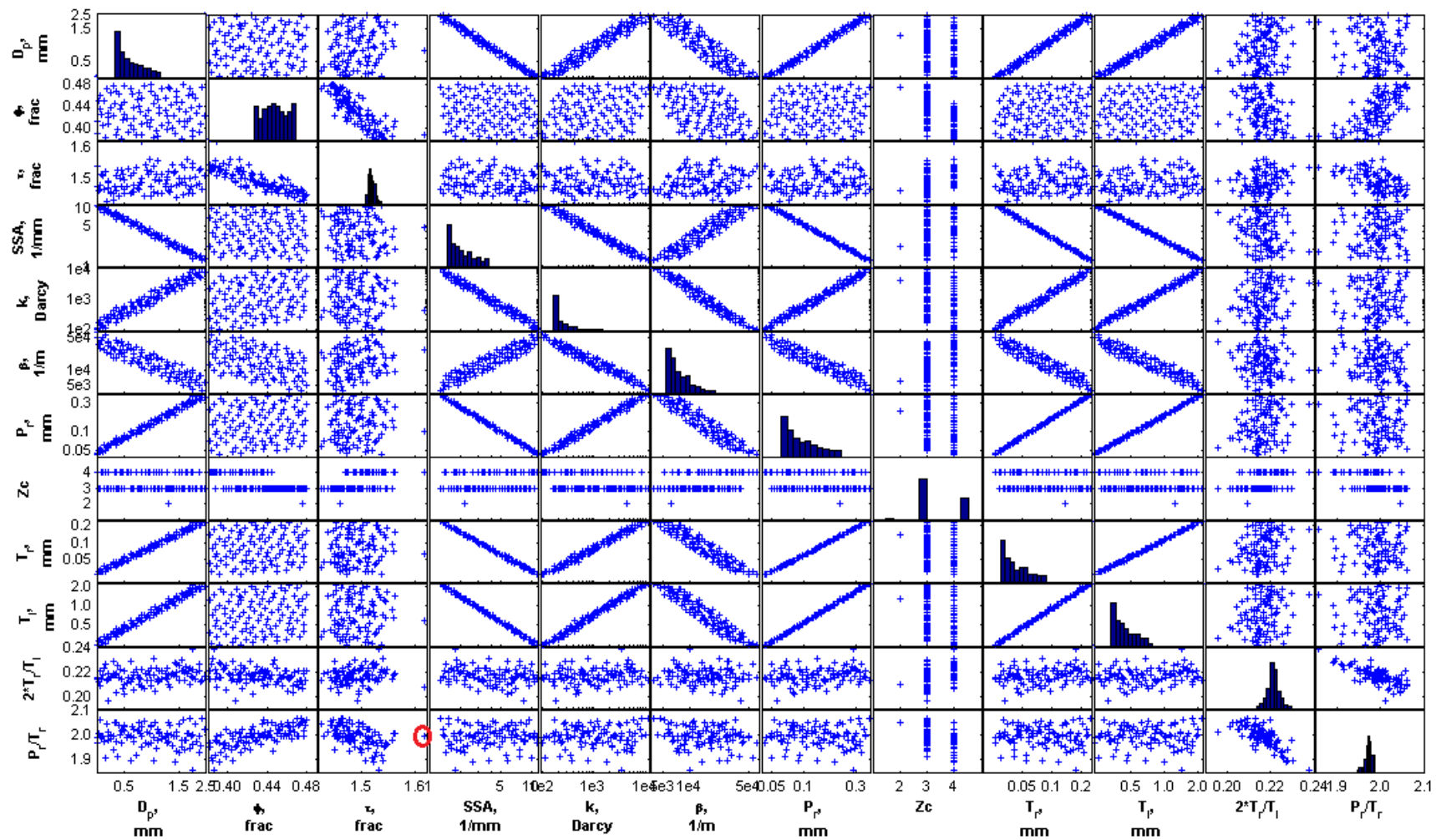


Figure 6.59 Scatter Plot of Flow Parameters and Network Parameters for Gravel Packs

Table 6.8 Fit Summary of  $\beta = f(k, \phi)$

Coefficient of Determination, $R^2$	0.9962
Adjusted $R^2$	0.9961
Root Mean Square Error, RMSE	0.0180
Mean of Response	4.1779

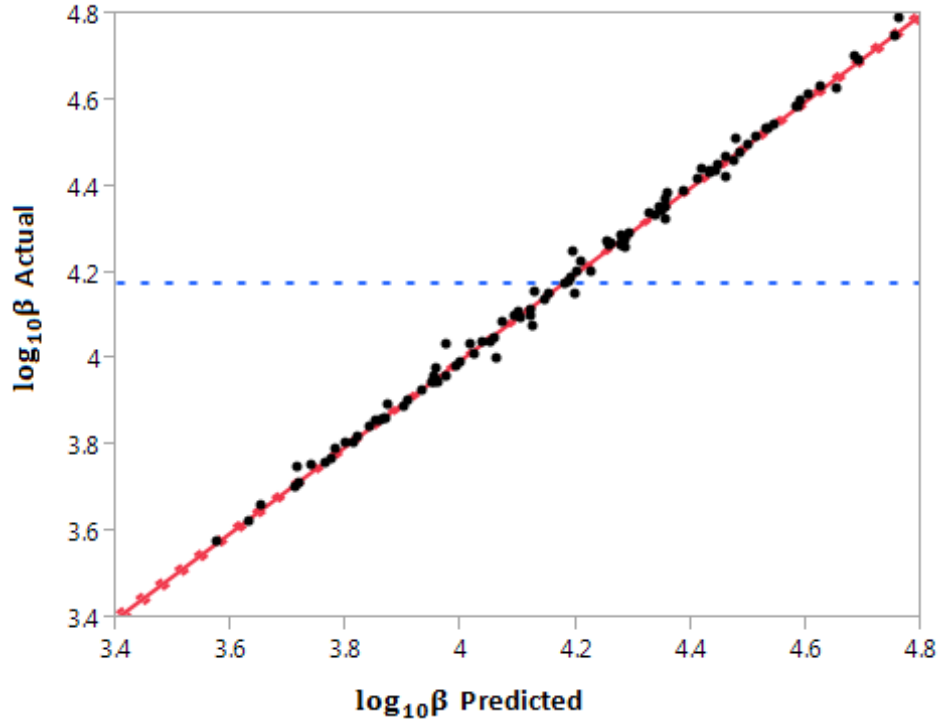


Figure 6.60 Actual by Predicted Plot of Non-Darcy Coefficient for  $\beta = f(k, \phi)$

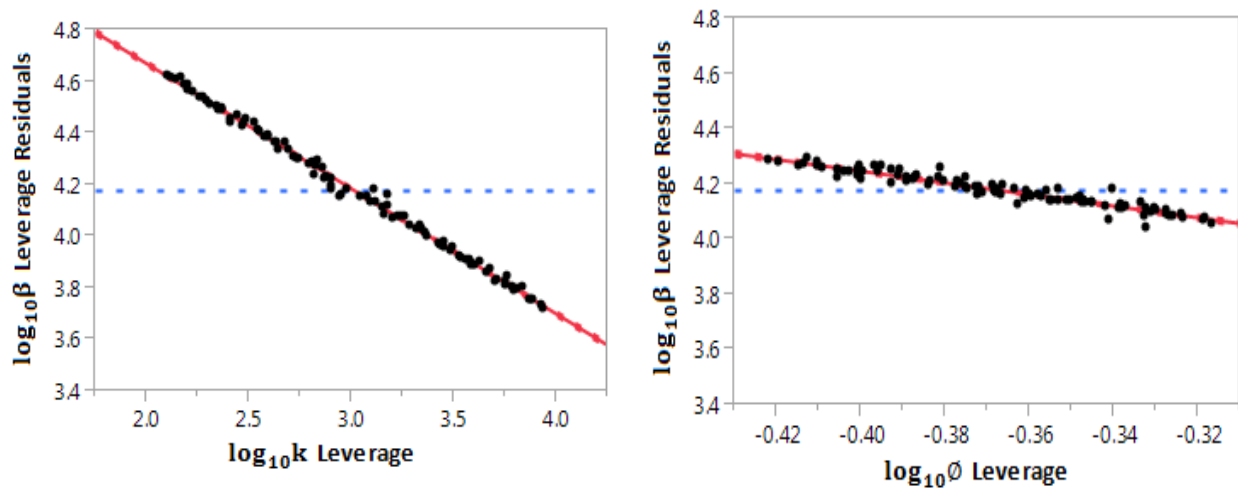
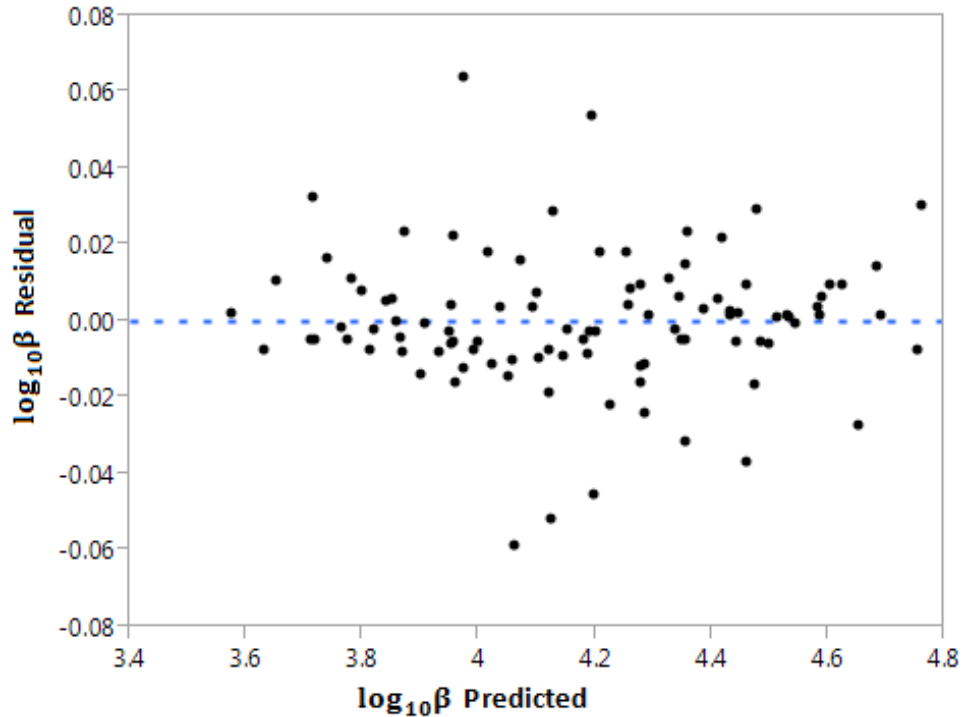


Figure 6.61 Leverage Plots of Correlation Parameters for  $\beta = f(k, \phi)$

Table 6.9 Parameters Estimate of  $\beta = f(k, \emptyset)$ 

Term	Estimate	Std. Error	t Ratio	Prob> t	Lower 95% CI	Upper 95% CI
Intercept	4.8674	0.0280	173.99	<.0001	4.8119	4.9230
$\log_{10}k$	-0.4852	0.0034	-143.96	<.0001	-0.4918	-0.4785
$\log_{10}\emptyset$	-2.1089	0.0648	-32.52	<.0001	-2.2376	-1.9802

Figure 6.62 Residual by Predicted Plot for  $\beta = f(k, \emptyset)$ 

In the second correlation (Eqn.6.41), tortuosity is used instead of porosity,  $\beta = f(k, \tau)$ .  $R^2$  decreases slightly (Table 6.10) and permeability power and correlation constant change little (Table 6.11). Both permeability and tortuosity are significant based on  $t$  and  $p$  values. Even though the coefficient of determination is high, 0.9841, the actual by predicted plot of the non-Darcy coefficient (Figure 6.63) and leverage plots (Figure 6.64) become more scatter compared the ones obtained from previous correlation,  $\beta = f(k, \emptyset)$ . Similar to previous correlation, there is no trend in residuals of fit (Figure 6.65); however, compared with residuals of  $\beta = f(k, \emptyset)$  (Figure 6.62), the porosity is better to estimate the non-Darcy coefficient.



$$\beta(1/m) = \frac{10^{4.8468} \tau^{4.9673}}{k(D)^{0.5078}} \quad (6.41)$$

Table 6.10 Fit Summary of  $\beta = f(k, \tau)$

Coefficient of Determination, $R^2$	0.9841
Adjusted $R^2$	0.9838
Root Mean Square Error, RMSE	0.0366
Mean of Response	4.1779

Table 6.11 Parameters Estimate of  $\beta = f(k, \tau)$

Term	Estimate	Std. Error	t Ratio	Prob> t	Lower 95% CI	Upper 95% CI
Intercept	4.8468	0.0677	71.55	<.0001	4.7124	4.9813
$\log_{10} k$	-0.5078	0.0067	-76.00	<.0001	-0.5211	-0.4946
$\log_{10} \tau$	4.9673	0.3688	13.47	<.0001	4.2353	5.6993

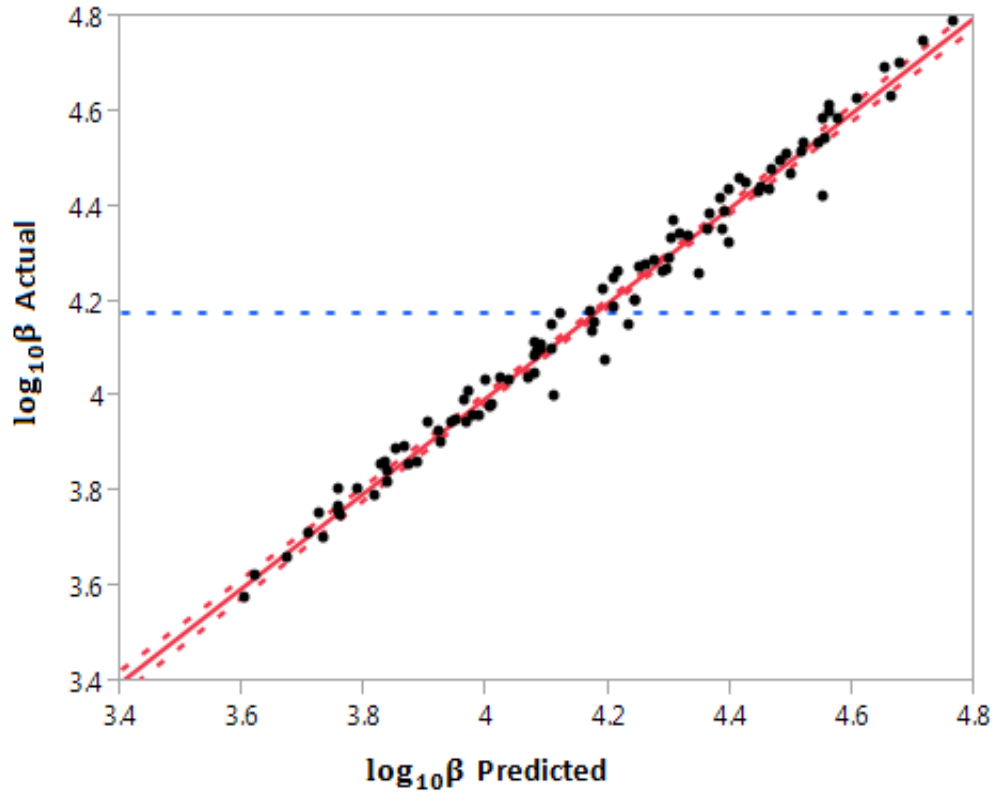


Figure 6.63 Actual by Predicted Plot of Non-Darcy Coefficient for  $\beta = f(k, \tau)$

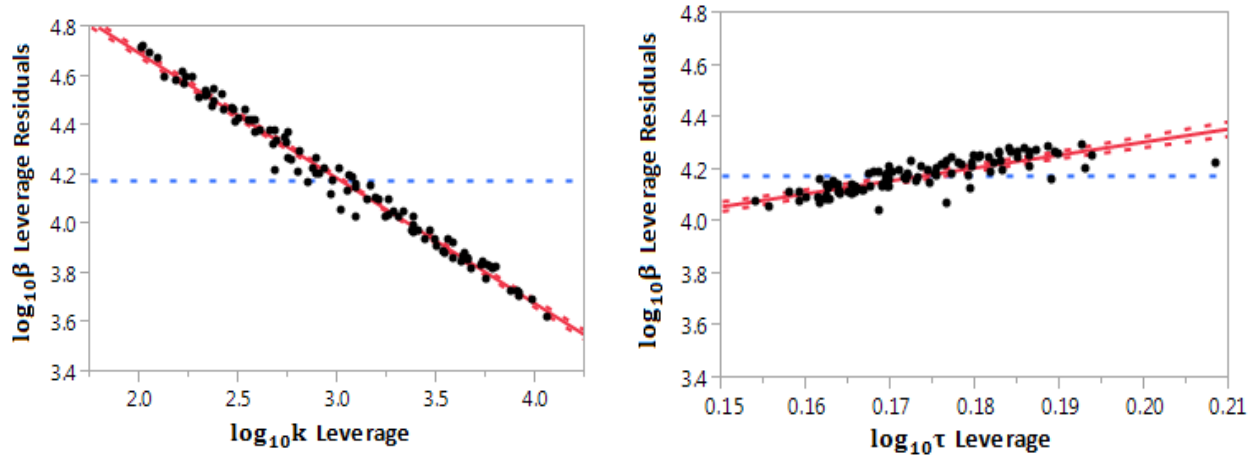


Figure 6.64 Leverage Plots of Correlation Parameters for  $\beta = f(k, \tau)$

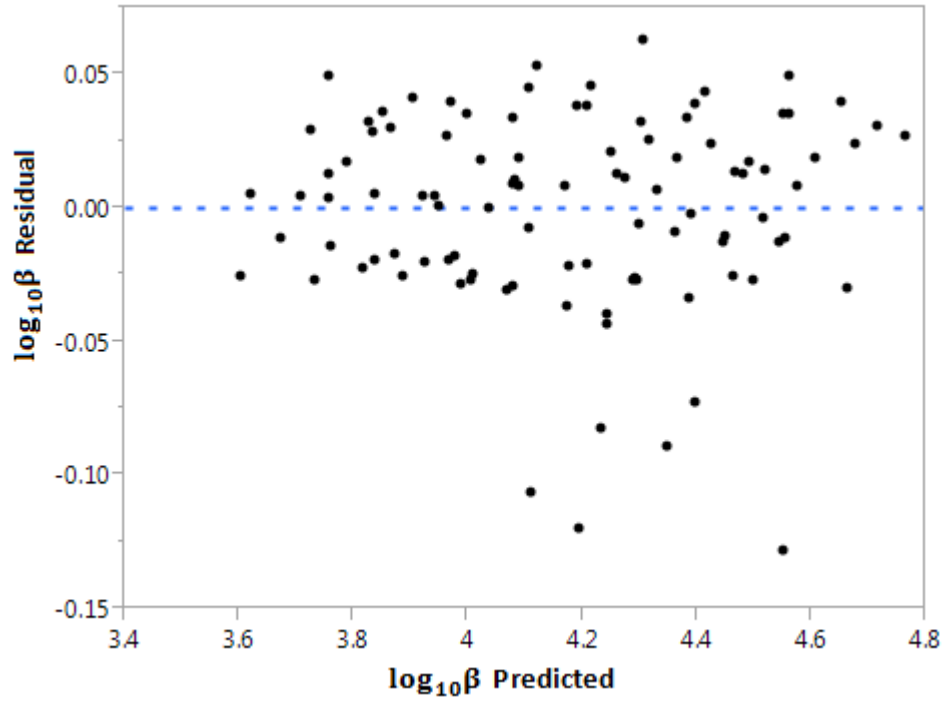


Figure 6.65 Residual by Predicted Plot for  $\beta = f(k, \tau)$

If both porosity and tortuosity are used in the correlation,  $\beta = f(k, \phi, \tau)$ , the actual by predicted plot of the non-Darcy coefficient (Figure 6.66) and the fit statistics (Table 6.12) do not change compared with the ones of  $\beta = f(k, \phi)$ . However, use of both porosity and tortuosity causes misestimation of the tortuosity effect. Tortuosity is at the denominator (Eqn.6.42), which

means an increase in tortuosity leads to a decrease in the non-Darcy coefficient. Parameter estimates also indicate that tortuosity is insignificant (Table 6.13).  $t$  value of tortuosity is less than 2 and the confidence interval contains 0. In addition, leverage plots show that porosity effect is distorted because of a correlation between porosity and tortuosity (Figure 6.67). Similar to actual by predicted plot, residual by predicted plot (Figure 6.68) is similar to the obtained from correlation of  $\beta = f(k, \phi)$ .

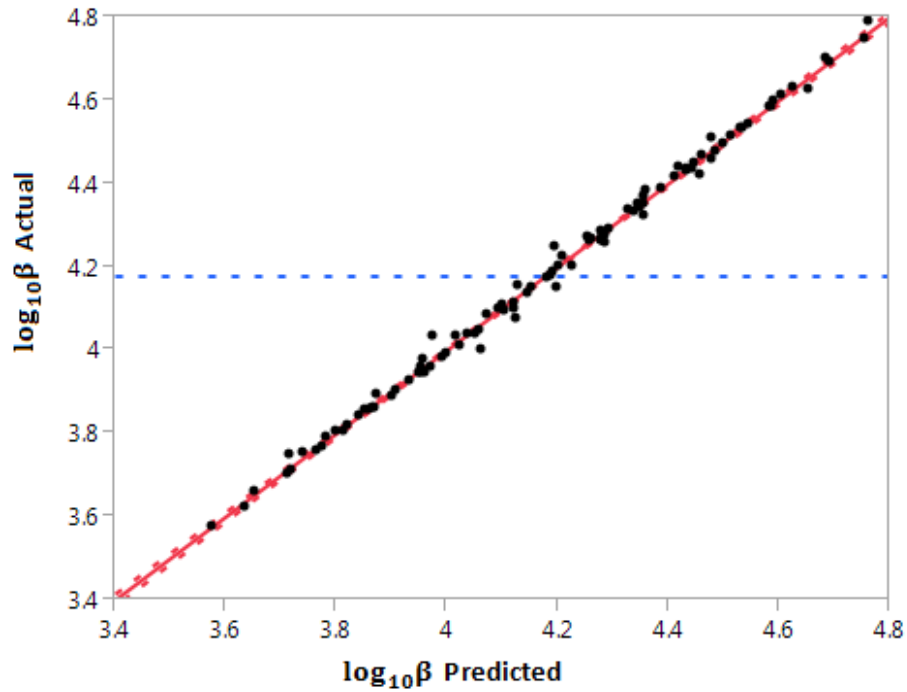


Figure 6.66 Actual by Predicted Plot of Non-Darcy Coefficient for  $\beta = f(k, \phi, \tau)$

$$\beta(1/m) = \frac{10^{4.8679}}{k(D)^{0.4851} \phi^{2.1115} \tau^{0.0086}} \quad (6.42)$$

Table 6.12 Fit Summary of  $\beta = f(k, \phi, \tau)$

Coefficient of Determination, $R^2$	0.9962
Adjusted $R^2$	0.9961
Root Mean Square Error, RMSE	0.0181
Mean of Response	4.1779

Table 6.13 Parameters Estimate of  $\beta = f(k, \phi, \tau)$

Term	Estimate	Std. Error	t Ratio	Prob> t	Lower 95% CI	Upper 95% CI
Intercept	4.8679	0.0335	145.50	<.0001	4.8015	4.9343
$\log_{10}k$	-0.4851	0.0035	-136.77	<.0001	-0.4922	-0.4781
$\log_{10}\phi$	-2.1115	0.1215	-17.38	<.0001	-2.3526	-1.8704
$\log_{10}\tau$	-0.0086	0.3392	-0.03	0.9798	-0.6820	0.6648

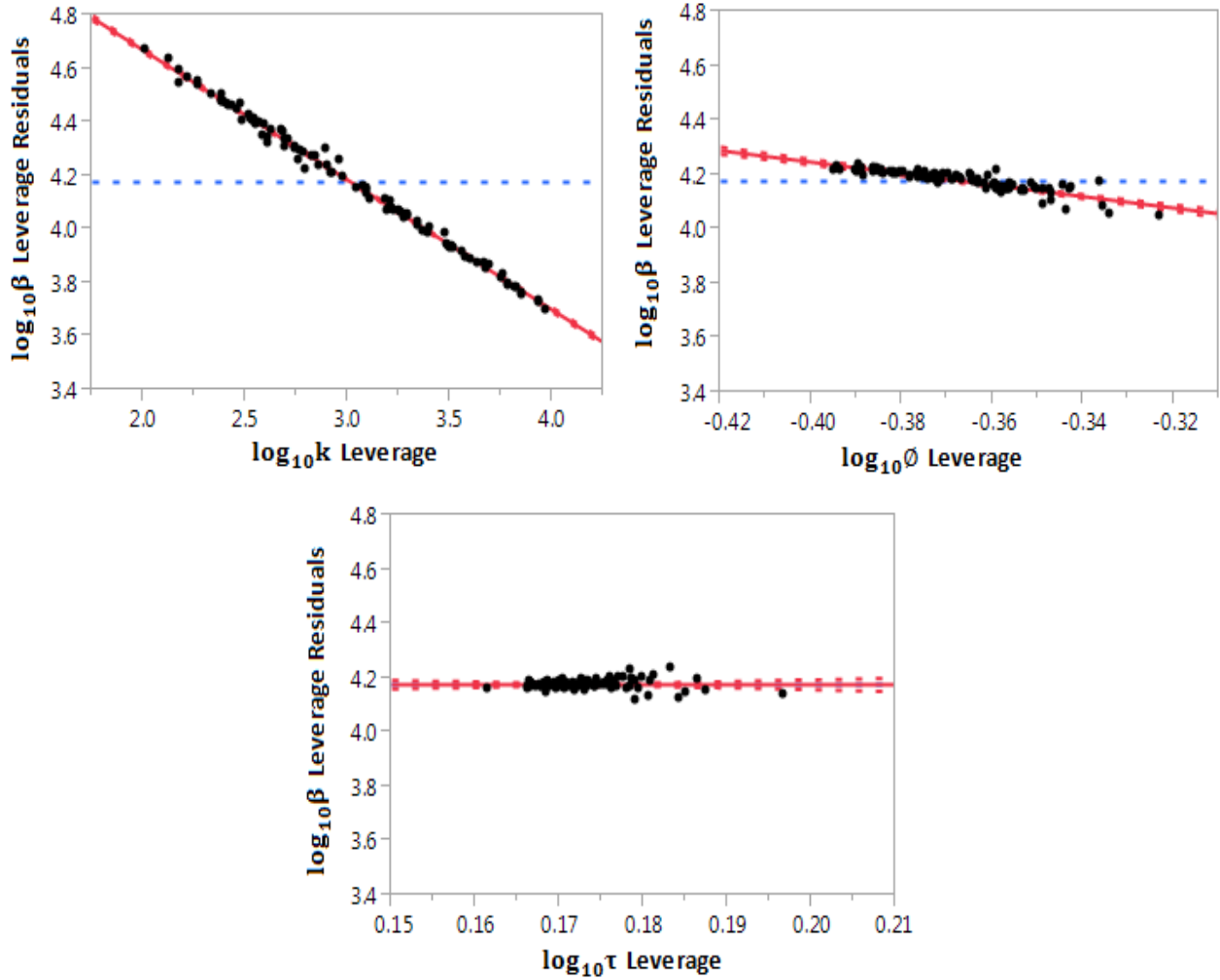


Figure 6.67 Leverage Plots of Correlation Parameters for  $\beta = f(k, \phi, \tau)$

If all variables are used to estimate the non-Darcy coefficient,  $\beta = f(k, \phi, \tau, SSA)$ ,  $R^2$  is highest compared previous correlations, 0.9974 (Table 6.14). However, permeability power changes sign and according to this correlation (Eqn.6.43), an increase in permeability leads to an

increase in the non-Darcy coefficient that is the opposite trend observed in scatter plot (Figure 6.59). Permeability is also insignificant based on  $t$  value (Table 6.15). Even though, the errors are less compared to the other fits (Figure 6.70), all parameters lose their significance and their leverage plots are completely distorted (Figure 6.71). This shows the importance of colinearity problem.

$$\beta(1/m) = \frac{10^{1.3188} k(D)^{0.1672} \tau^{1.6516} SSA(1/mm)^{1.3216}}{\phi^{3.5470}} \quad (6.43)$$

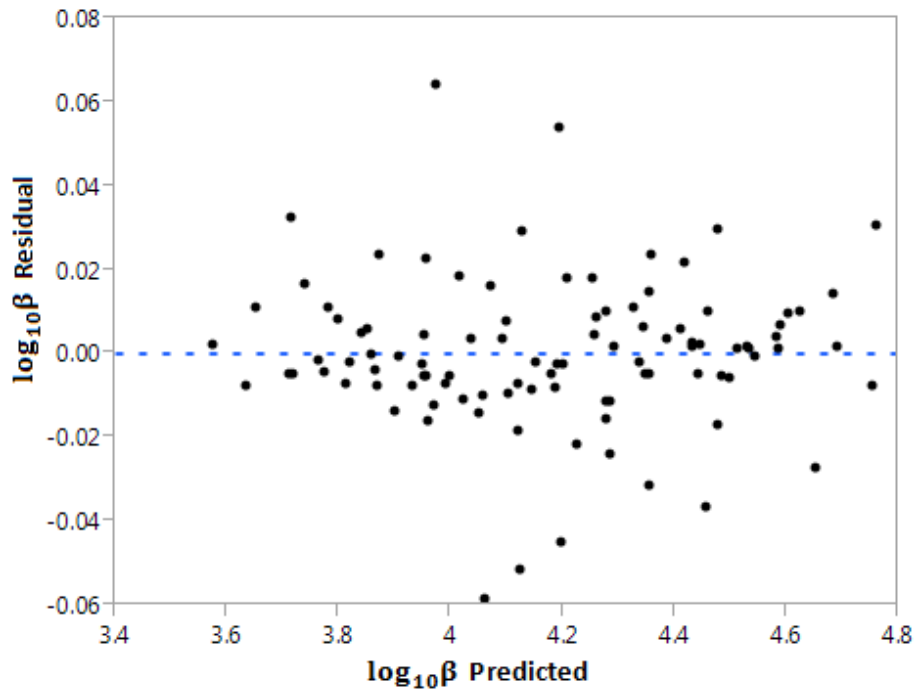


Figure 6.68 Residual by Predicted Plot for  $\beta = f(k, \phi, \tau)$

Table 6.14 Fit Summary of  $\beta = f(k, \phi, \tau, SSA)$

Coefficient of Determination, $R^2$	0.9974
Adjusted $R^2$	0.9973
Root Mean Square Error, RMSE	0.0149
Mean of Response	4.1779

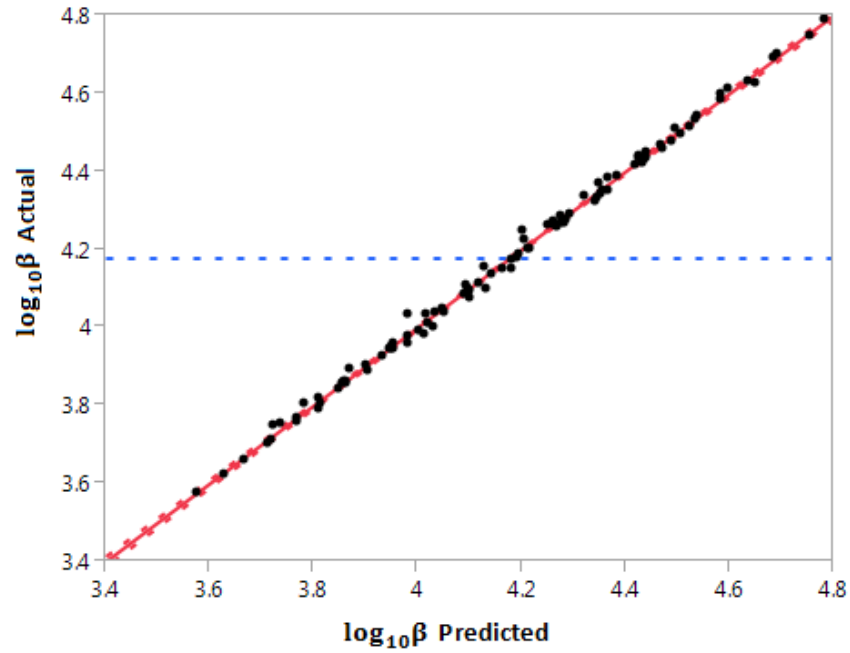


Figure 6.69 Actual by Predicted Plot of Non-Darcy Coefficient for  $\beta = f(k, \phi, \tau, SSA)$

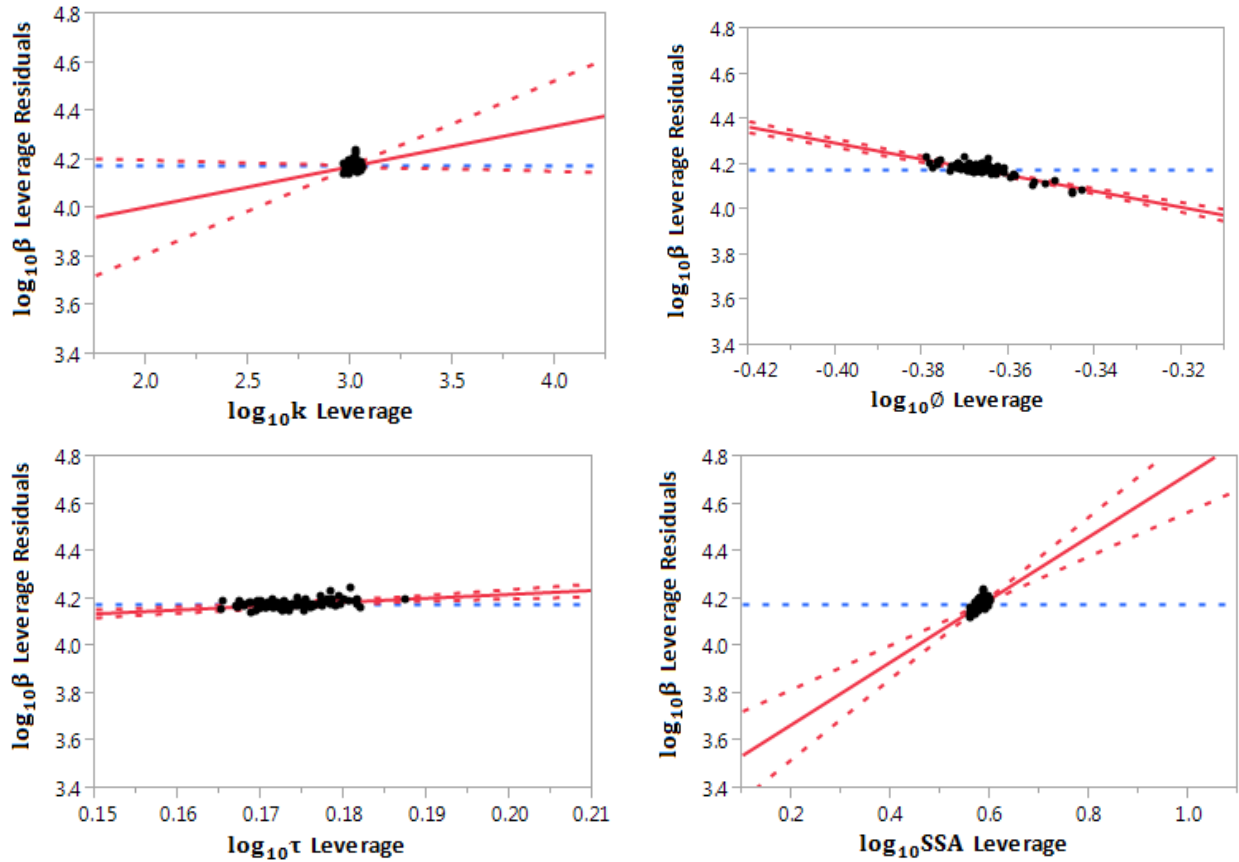


Figure 6.70 Leverage Plots of Correlation Parameters for  $\beta = f(k, \phi, \tau, SSA)$

Table 6.15 Parameters Estimate of  $\beta = f(k, \phi, \tau, SSA)$

Term	Estimate	Std. Error	t Ratio	Prob> t	Lower 95% CI	Upper 95% CI
Intercept	1.3188	0.5218	2.53	0.0131	0.2828	2.3547
$\log_{10}k$	0.1672	0.0958	1.74	0.0843	-0.0230	0.3574
$\log_{10}\phi$	-3.5470	0.2333	-15.20	<.0001	-4.0103	-3.0838
$\log_{10}\tau$	1.6516	0.3709	4.45	<.0001	0.9153	2.3879
$\log_{10}SSA$	1.3216	0.1940	6.81	<.0001	0.9364	1.7069

Table 6.16 summarizes the all statistically significant non-Darcy coefficient correlations. All equations are in the form of Eqn.6.44. Similar correlations are developed to estimate permeability from the parameters calculated from LBM and network modeling. Table 6.17 gives all statistically significant permeability correlations, their coefficient of determinations and parameter estimates. All non-Darcy coefficient and permeability correlations are consistent with respect to units.

$$\beta = 10^{a_0} x_1^{a_1} x_2^{a_2} \quad (6.44)$$

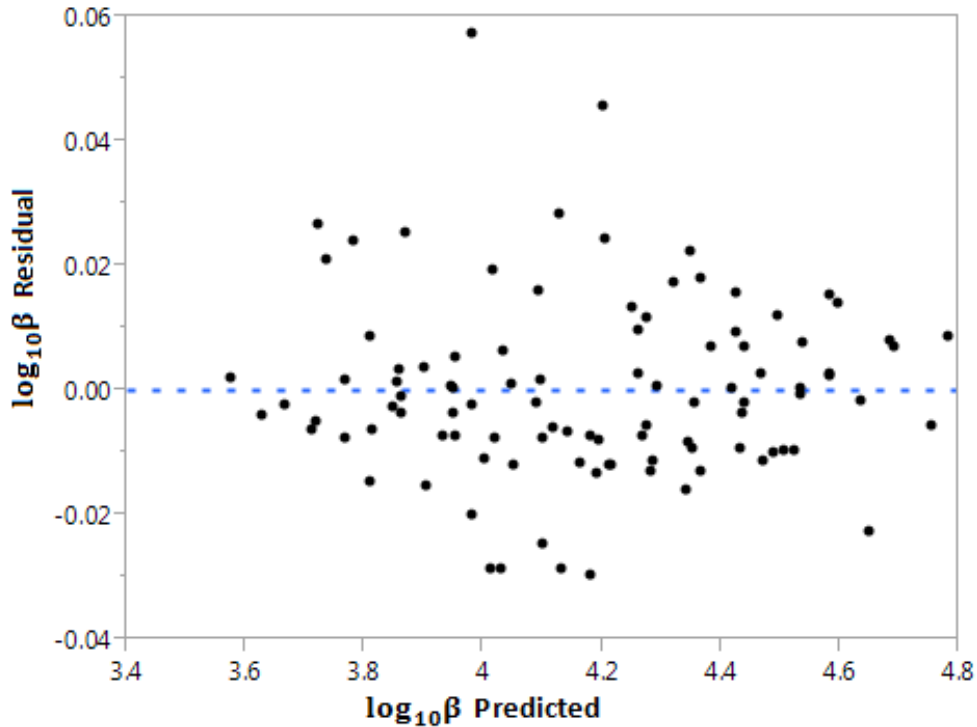


Figure 6.71 Residual by Predicted Plot for  $\beta = f(k, \phi, \tau, SSA)$

Table 6.16 Non-Darcy Coefficient Correlations of Gravel Packs

Equation	Power Term	Estimate	Std Error	t Ratio	Lower 95% CI	Upper 95% CI	R <sup>2</sup>
1	$a_0$	4.8674	0.0280	173.99	4.8119	4.9230	0.9962
	$\log_{10}k$	-0.4852	0.0034	-143.96	-0.4918	-0.4785	
	$\log_{10}\emptyset$	-2.1089	0.0648	-32.52	-2.2376	-1.9802	
2	$a_0$	4.8468	0.0677	71.55	4.7124	4.9813	0.9841
	$\log_{10}k$	-0.5078	0.0067	-76.00	-0.5211	-0.4946	
	$\log_{10}\tau$	4.9673	0.3688	13.47	4.2353	5.6993	
3	$a_0$	6.9850	0.1612	43.34	6.6651	7.3049	0.9725
	$\log_{10}k$	-0.5065	0.0088	-57.53	-0.5240	-0.4890	
	$\log_{10}PTR$	-4.2803	0.5362	-7.98	-5.3445	-3.2161	
4	$a_0$	2.5467	0.0334	76.31	2.4805	2.6130	0.9921
	$\log_{10}D_p$	-0.9712	0.0097	-99.86	-0.9905	-0.9519	
	$\log_{10}\emptyset$	-4.2267	0.0908	-46.57	-4.4068	-4.0466	
5	$a_0$	2.2542	0.1206	18.69	2.0149	2.4936	0.9459
	$\log_{10}D_p$	-1.0411	0.0258	-40.30	-1.0924	-0.9898	
	$\log_{10}\tau$	10.5801	0.6916	15.30	9.2075	11.9526	
6	$a_0$	6.7263	0.3201	21.01	6.0909	7.3616	0.8911
	$\log_{10}D_p$	-1.0011	0.0363	-27.61	-1.0731	-0.9292	
	$\log_{10}PTR$	-8.8024	1.0708	-8.22	-10.9277	-6.6771	
7	$a_0$	2.3140	0.0212	109.12	2.2719	2.3560	0.9968
	$\log_{10}SSA$	0.9750	0.0062	158.24	0.9627	0.9872	
	$\log_{10}\emptyset$	-3.5386	0.0576	-61.42	-3.6530	-3.4243	
8	$a_0$	2.0176	0.0924	21.84	1.8342	2.2009	0.9689
	$\log_{10}SSA$	1.0429	0.0194	53.80	1.0044	1.0814	
	$\log_{10}\tau$	8.9552	0.5201	17.22	7.9230	9.9874	
9	$a_0$	5.7835	0.2615	22.11	5.2645	6.3026	0.9268
	$\log_{10}SSA$	1.0160	0.0296	34.38	0.9573	1.0746	
	$\log_{10}PTR$	-7.3434	0.8747	-8.39	-9.0795	-5.6072	
10	$a_0$	2.0847	0.0232	89.98	2.0387	2.1307	0.9963
	$\log_{10}P_r$	-0.9721	0.0067	-146.02	-0.9853	-0.9589	
	$\log_{10}\emptyset$	-3.3812	0.0625	-54.09	-3.5053	-3.2572	
11	$a_0$	1.8067	0.0937	19.29	1.6207	1.9926	0.9686
	$\log_{10}P_r$	-1.0364	0.0193	-53.60	-1.0748	-0.9980	
	$\log_{10}\tau$	8.4191	0.5208	16.17	7.3855	9.4528	
12	$a_0$	5.4536	0.2449	22.27	4.9675	5.9396	0.9360
	$\log_{10}P_r$	-1.0169	0.0275	-36.95	-1.0715	-0.9622	
	$\log_{10}PTR$	-7.2512	0.8179	-8.87	-8.8744	-5.6280	
13	$a_0$	1.8938	0.0223	84.94	1.8496	1.9381	0.9966
	$\log_{10}T_r$	-0.9711	0.0063	-153.34	-0.9837	-0.9586	
	$\log_{10}\emptyset$	-3.3342	0.0596	-55.97	-3.4524	-3.2160	
14	$a_0$	1.6080	0.0932	17.26	1.4231	1.7930	0.9697
	$\log_{10}T_r$	-1.0348	0.0190	-54.54	-1.0724	-0.9971	
	$\log_{10}\tau$	8.2889	0.5119	16.19	7.2729	9.3050	
15	$a_0$	5.2554	0.2363	22.24	4.7864	5.7244	0.9406
	$\log_{10}T_r$	-1.0178	0.0265	-38.45	-1.0703	-0.9653	
	$\log_{10}PTR$	-7.3237	0.7881	-9.29	-8.8878	-5.7595	



Table 6.17 Permeability Correlations of Gravel Packs

Equation	Power Term	Estimate	Std Error	t Ratio	Lower 95% CI	Upper 95% CI	R <sup>2</sup>
1	$a_0$	4.7831	0.0640	74.71	4.6561	4.9102	0.9921
	$\log_{10} D_p$	1.9985	0.0187	107.12	1.9615	2.0355	
	$\log_{10} \emptyset$	4.3654	0.1741	25.08	4.0199	4.7109	
2	$a_0$	5.1248	0.1396	36.71	4.8477	5.4019	0.9802
	$\log_{10} D_p$	2.0721	0.0299	69.28	2.0128	2.1315	
	$\log_{10} \tau$	-11.1545	0.8006	-13.93	-12.7435	-9.5655	
3	$a_0$	0.4708	0.3592	1.31	-0.2421	1.1836	0.9626
	$\log_{10} D_p$	2.0293	0.0407	49.89	1.9486	2.1101	
	$\log_{10} PTR$	9.0769	1.2014	7.56	6.6924	11.4614	
4	$a_0$	5.2625	0.0269	195.53	5.2091	5.3159	0.9986
	$\log_{10} SSA$	-2.0073	0.0078	-256.69	-2.0228	-1.9918	
	$\log_{10} \emptyset$	2.9487	0.0731	40.32	2.8036	3.0939	
5	$a_0$	5.5847	0.0677	82.49	5.4504	5.7191	0.9954
	$\log_{10} SSA$	-2.0657	0.0142	-145.36	-2.0940	-2.0375	
	$\log_{10} \tau$	-7.8899	0.3812	-20.70	-8.6465	-7.1333	
6	$a_0$	2.3784	0.2247	10.59	1.9325	2.8243	0.9853
	$\log_{10} SSA$	-2.0415	0.0254	-80.41	-2.0918	-1.9911	
	$\log_{10} PTR$	6.0953	0.7515	8.11	4.6039	7.5867	
7	$a_0$	5.7339	0.0404	141.84	5.6536	5.8141	0.9969
	$\log_{10} P_r$	2.0003	0.0116	172.19	1.9772	2.0233	
	$\log_{10} \emptyset$	2.6257	0.1091	24.07	2.4092	2.8422	
8	$a_0$	6.0003	0.0810	74.10	5.8396	6.1610	0.9936
	$\log_{10} P_r$	2.0512	0.0167	122.73	2.0180	2.0844	
	$\log_{10} \tau$	-6.8238	0.4502	-15.16	-7.7173	-5.9303	
9	$a_0$	3.0375	0.2045	14.86	2.6317	3.4433	0.9878
	$\log_{10} P_r$	2.0354	0.0230	88.60	1.9898	2.0810	
	$\log_{10} PTR$	5.9004	0.6828	8.64	4.5452	7.2555	
10	$a_0$	6.1266	0.0386	158.60	6.0499	6.2032	0.9972
	$\log_{10} T_r$	1.9982	0.0110	182.11	1.9764	2.0200	
	$\log_{10} \emptyset$	2.5290	0.1032	24.50	2.3241	2.7338	
11	$a_0$	6.3926	0.0782	81.72	6.2373	6.5478	0.9942
	$\log_{10} T_r$	2.0474	0.0159	128.55	2.0158	2.0790	
	$\log_{10} \tau$	-6.5648	0.4298	-15.28	-7.4178	-5.7119	
12	$a_0$	3.4321	0.1860	18.45	3.0630	3.8012	0.9900
	$\log_{10} PTR$	2.0343	0.0208	97.65	1.9930	2.0757	
		6.0415	0.6202	9.74	4.8105	7.2725	

#### 6.5.4.2 Path Analysis of Petrophysical Variables

Structural Equation Modeling (SEM) is a statistical method used to analyze multivariate data to depict the relation among the observed variables and theoretical construct, latent variables, based on existing or proposed theories. This method is combination of Factor Analysis and Multiple Regression.

The main advantages of the SEM are (Iacobucci, 2009);

1. It provides a way to test all relationships as a whole.
2. It allows theory testing with the comparison of base model with constrained models.
3. It takes into account of the measurement errors of the observed and unobserved variables while regression analysis assumes that observations are perfect and without error.
4. Total effect, both direct and indirect effects, can be studied in SEM.
5. Group difference can be assessed with multi-group analysis.

Path analysis is a special kind of SEM, focusing on the relationship between observed variables only. SEM process can be grouped into 5 parts (Schumacker & Lomax, 2004):

- 1) Model Specification: Model to be tested is developed according to theory. In this stage, every relationship and parameters of interest are determined.
- 2) Model Identification: In this stage, model should be checked whether there is unique solution or not. Unknown model parameters can be uniquely estimated from sample variance-covariance matrix. In other words, data does not fit more than one implied theoretical models equally well. The problem arises when imposed constrained are not sufficient. To avoid identification problem, the number of free parameters to be estimated should be less than or equal to the number of distinct values in the sample covariance matrix.
- 3) Estimation Process: This stage aim is to find the model covariance,  $\Sigma_M$ , which is as close as sample covariance,  $\Sigma_s$  by minimizing the discrepancy function,  $f(\Sigma_M, \Sigma_s)$ .  $f(\Sigma_M, \Sigma_s)$  is positive scalar valued function and it is continuous in  $\Sigma_M$  and  $\Sigma_s$ .  $f(\Sigma_M, \Sigma_s)$  is 0 only when  $\Sigma_M = \Sigma_s$ . Every estimation method has different assumptions of distributional  $f(\Sigma_M, \Sigma_s)$ . Estimation process can be classified into five categories

according to  $f(\boldsymbol{\Sigma}_M, \boldsymbol{\Sigma}_s)$  definition given below. (Arbuckle, 2008; Schermelleh-Engel, Moosbrugger, & Müller, 2003; Widaman & Thompson, 2003).

- a. Maximum likelihood (ML) estimation:

$$f_{ML}(\boldsymbol{\Sigma}_M, \boldsymbol{\Sigma}_s) = \log|\boldsymbol{\Sigma}_M| + tr(\boldsymbol{\Sigma}_s \boldsymbol{\Sigma}_M^{-1}) - \log|\boldsymbol{\Sigma}_s| - p \quad (6.45)$$

$tr$  is the trace of the matrix which is the sum of element on the diagonals and  $p$  is the number of observed variables. ML estimation is generally preferred because overall model fit parameters can be calculated if the model is overidentified. In addition, ML estimation does not depend on the model variable scales; therefore, there is no need to normalize the data. The main assumption of maximum likelihood estimation is that data is multivariate normal distribution that implies that  $\boldsymbol{\Sigma}_s$  has a Wishart distribution. Even though ML is robust against the distribution assumption, if the distributional assumption does not hold, misleading results can be obtained, because fit statistics strongly depend on the normality assumption. Therefore, before SEM, distributions of variables in the model should be checked. If they are not normal, necessary transformations should be done. For ML estimation,  $\boldsymbol{\Sigma}_M$ ,  $\boldsymbol{\Sigma}_s$  should be positive definite that means both of them are nonsingular. The other advantages of ML estimators are consistent, asymptotically efficient and asymptotically normal distributed.

- b. Generalized least square (GLS):

$$f_{GLS}(\boldsymbol{\Sigma}_M, \boldsymbol{\Sigma}_s) = \frac{1}{2} tr[\boldsymbol{\Sigma}_s^{-1}(\boldsymbol{\Sigma}_s - \boldsymbol{\Sigma}_M)]^2 \quad (6.46)$$

It is special kind of ADF. When the data is multivariate normal distribution,  $f_{ADF}$  turns out to  $f_{GLS}$ . Underlying assumptions of GLS is less restrictive compared with ML. Kurtosis (fourth moment) of data should be close to zero. Like ML, GLS

estimates are consistent, asymptotically efficient and asymptotically normal distributed. Also,  $f_{GLS}$  is scale invariant. However, it performs less well compared with ML when sample size is small.

- c. Asymptotically distribution-free (ADF) estimation:

$$f_{ADF}(\boldsymbol{\Sigma}_M, \boldsymbol{\Sigma}_s) = [\mathbf{s} - \boldsymbol{\sigma}]' \mathbf{U}^{-1} [\mathbf{s} - \boldsymbol{\sigma}] \quad (6.47)$$

$\mathbf{s}$  and  $\boldsymbol{\sigma}$  are column vector of distinct elements of sample covariance and model covariance, respectively.  $\mathbf{U}$  is defined as;

$$U_{ij,kl} = w_{ij,kl} - w_{ij}w_{kl} \quad (6.48)$$

$$w_{ij,kl} = \frac{1}{N} \sum_{r=1}^N (x_{ir} - \bar{x}_i)(x_{jr} - \bar{x}_j)(x_{kr} - \bar{x}_k)(x_{lr} - \bar{x}_l) \quad (6.49)$$

$$w_{ij} = \frac{1}{N} \sum_{r=1}^N (x_{ir} - \bar{x}_i)(x_{jr} - \bar{x}_j) \quad (6.50)$$

$$\bar{x}_i = \frac{1}{N} \sum_{r=1}^N x_{ir} \quad (6.51)$$

$x_{ir}$  shows the  $r^{th}$  observation of the  $i^{th}$  variable. For this estimation method, raw data should be used because  $f_{ADF}$  depends on measurements. When the data is continuous and not normal, ADF is recommended. Also, if the variables are ordinal or dichotomous, ADF may be used. The main disadvantage of this method is that matrix size of  $\mathbf{U}$  increases rapidly with the number of observed variables. For consistent and efficient estimates, large number of observations is needed. When the model is complex and number of observation is small, ADF is not recommended.

- d. Scale-free least square (SLS):

$$f_{SLS}(\boldsymbol{\Sigma}_M, \boldsymbol{\Sigma}_s) = \frac{1}{2} \text{tr}[\mathbf{D}^{-1}(\boldsymbol{\Sigma}_s - \boldsymbol{\Sigma}_M)]^2 \quad (6.52)$$

where  $\mathbf{D}$  is,

$$\mathbf{D} = \text{diag}(\boldsymbol{\Sigma}_s) \quad (6.53)$$

e. Unweighted least square (ULS):

$$f_{ULS}(\boldsymbol{\Sigma}_M, \boldsymbol{\Sigma}_s) = \frac{1}{2} \text{tr}[\boldsymbol{\Sigma}_s - \boldsymbol{\Sigma}_M]^2 \quad (6.54)$$

$f_{ULS}$  minimizes the half of the sum of squared residuals between  $\boldsymbol{\Sigma}_M$  and  $\boldsymbol{\Sigma}_s$ . Like  $f_{GLS}$ ,  $f_{ULS}$  is special case of  $f_{ADF}$ . Distribution of data is not important. Although it produces consistent estimates, it is neither scale free nor asymptotically efficient.

Table 6.18 summarizes the 5 methods based on observed variable properties based on normality and their scale, and sample size (Backhaus, Erichson, Plinke, & Weiber, 2006).

Table 6.18 Decision Criteria for Different Discrepancy Functions

Decision Criterion	ML	GLS	ADF	SLS	ULS
Multivariate Normality of Observed Variables	yes	yes	–	–	–
Scale Invariance	yes	yes	yes	yes	–
Sample size	>100	>100	>100	>100	>100
Inferential Statistics	yes	yes	yes	–	–

4) Model Testing: In this stage, model fit parameters are checked. With some statistical measures, importance of the each path is determined. According to these tests, necessary modifications are made.

- 5) **Model Modification:** Modifications indices give the decrease in Chi-square ( $\chi^2$ ) when the implied changes are implied. If the required changes do not conflict with theory, suggested modification can be used to improve the model.

There are two specific extreme models: saturated model and independent model. In the saturated model, the unknown model parameters are equals to variance-covariance elements of the measurements. In other words, there is no constraint applied to the model. The other extreme case is independent model (null model) in which it is assumed that all observed variables are independent. These two models are used in fit statistics to evaluate the model.

In SEM, the main interest is that finding the model that does not conflict with the data. This means the aim is not rejecting the null hypothesis. Not rejecting the null hypothesis ever means that the proposed model is correct. Also, there may be many models that fit the measurements equally well. Therefore, subjective decisions are important. Researcher who uses SEM should know the theory behind the model so that he can evaluate whether the sign and magnitude of prediction are expected by available theory or not. Furthermore, replication can be used to validate the model. Data can be divided into two set randomly. First data set is used model development while the second data set is used for validation.

Evaluation of estimate is based on many statistics. Fit indices are used to evaluate model fit. There are two main types of fit indices: overall fit and local fit of individual parameters. Overall fit evaluates the how well the model is explained with measured data; whereas, local fit evaluates how well individual parameters are estimated. For individual parameters, significance of each estimate should be checked from  $t$  value that is the ratio of estimate to its standard error. As a rule of thumb,  $t$  value (critical value) should be greater than 2. The fit indices quantifies the how well the proposed model fits the sample data. There are many fit indices in the literature. All

fit indices have some advantages and disadvantages; therefore, to evaluate the model, fit indices should be used simultaneously. Below some basic concept are given used in the fit statistics (Arbuckle, 2008; Raykov & Marcoulides, 2006; Schumacker & Lomax, 2004; Smith & McMillan, 2001).

Degree of freedom ( $df$ ): The number of degree of freedom is defined as difference between the number of distinct parameters of variance-covariance matrix of sample measurement ( $p$ ) and number of model parameters to be estimated ( $q$ ).

$$df = p - q \quad (6.55)$$

Chi-square ( $\chi^2$ ): It is most commonly used overall fit indices. It gives the magnitude of discrepancy between the sample and the fitted covariance matrices. The null hypothesis is:

$$H_0: \Sigma_M - \Sigma_s = 0 \quad (6.56)$$

If null hypothesis is correct, minimum fit function times 1 minus number of observation gives  $\chi^2$  distribution with degree of freedom  $df$ .

$$\chi^2(df) = (N - 1)f_{ML}(\Sigma_M, \Sigma_s) \quad (6.57)$$

If the  $p$  value associated with  $\chi^2$  is greater than 0.05, the null hypothesis accepted. Value of  $\chi^2$  changes from 0 for saturated model to maximum value for the independence model.  $\chi^2$  value of 0 indicates a perfect fit since there is no difference between sample variance-covariance matrix and structural variance-covariance matrix.  $\chi^2$  has some shortcomings. If the data distribution is not normal, model  $\chi^2$  is higher or lower; therefore, model fit appears worse or better. Also,  $\chi^2$  is sensitive to correlation size between observed variables. If the correlation is high, higher  $\chi^2$  is obtained for incorrect models.  $\chi^2$  is strongly depends on sample size. With the increased in sample size, the model  $\chi^2$  increases and the  $\chi^2$  test failed even if the difference between sample covariance matrix and model covariance matrix is low. Therefore, some

researchers suggest the use of adjusted  $\chi^2$  to evaluate the goodness of the fit. The adjusted  $\chi^2$  is defined as;

$$\chi_{adj}^2 = \frac{\chi^2}{df} \quad (6.58)$$

$df$  is the number of degree of freedom. For good fit,  $\chi_{adj}^2$  should be as low as 2.

Akaike Information Criterion (AIC): The maximum likelihood method favors the overfitting; therefore, comparison of likelihood function alone always favors the more complex model. AIC is a criterion for selection of nested models. It considers both goodness of the fit and model complexity. It imposes a penalty with the increase in parameters to be estimated. The lower AIC is, the better the model is.

$$AIC = \chi^2 + 2q \quad (6.59)$$

Browne-Cudeck Criterion (BCC): BCC imposes slightly greater penalty compared with AIC.

$$BCC = \chi^2 + \frac{2q(N-1)}{(N-p-1)} \quad (6.60)$$

$N$  is number of observations.

Bayesian Information Criterion (BIC): It is similar to AIC in that it takes model complexity into account. However, it penalizes more for model complexity.

$$BIC = \chi^2 + q \ln(N) \quad (6.61)$$

Consistent Akaike Information Criteria (CAIC): CAIC assigns greater penalty due to model complexity than AIC and BCC; but not as much as BIC.

$$CAIC = \chi^2 + q(1 + \ln(N)) \quad (6.62)$$

Expected Cross Validation Index (ECVI): ECVI is similar to AIC except a constant scale factor.



$$ECVI = \frac{1}{N-1} (ACI) = \frac{\chi^2}{N-1} + \frac{2q}{N-1} \quad (6.63)$$

Modified Expected Cross Validation Index (MECVI): MECVI is similar to BCC except a constant scale factor.

$$MECVI = \frac{1}{N-1} (BCC) = \frac{\chi^2}{N-1} + \frac{2q}{(N-p-1)} \quad (6.64)$$

Root Mean Square Error of Approximation (RMSEA): RMSEA is badness of fit index. Its value of 0 indicates a perfect fit. It gives the average difference between model covariance and measured covariance. As it appears in Eqn.6.65, RMSEA depends on sample size and model degree of freedom. RMSEA decreases with the increase in sample size or degree of freedom. However, compared with  $\chi^2$ , it is less sensitive to sample size. For be good fit, RMSEA should less than 0.05.

$$RMSEA = \sqrt{\frac{\chi_{model}^2 - df_{model}}{(N-1)df_{model}}} \quad (6.65)$$

Root Mean Square Residual (RMR): It is an indication of badness of fit. It is the square root of the mean of the squared fitted residuals.

$$RMR = \sqrt{\frac{\sum_{i=1}^p \sum_{j=1}^i (s_{ij} - \sigma_{ij})}{p(p+1)/2}} \quad (6.66)$$

$s_{ij}$  and  $\sigma_{ij}$  are elements of sample and model implied covariance matrix elements, respectively. For good fit, RMR is close to 0. Since the elements of  $\Sigma_M$  and  $\Sigma_S$  are scale dependent, the value of RMR strongly depends on sizes of variance and covariance of the observed variables; therefore its value is ambiguous.

Standardized Root Mean Square Error (SRMR): To eliminate the scale dependency, RMR is scaled by dividing the standard deviation of sample measurement ( $s_i = \sqrt{s_{ii}}$ ). For good fit, SRMR should be less than 0.05.

$$SRMR = \sqrt{\frac{\sum_{i=1}^p \sum_{j=1}^i \frac{(s_{ij} - \sigma_{ij})}{s_i s_j}}{p(p+1)/2}} \quad (6.67)$$

Goodness of Fit Index (GFI): It is similar to a squared multiple correlation. Its value changes from 0 to 1. 1 indicates the perfect fit. It is very sensitive to sample size. As the sample size increases, GFI value goes up even for poor models; therefore, it is not reliable. In addition, as the model parameters increase, it goes up because more variance is explained; therefore, GFI always favors more complex models.

$$GFI = 1 - \left( \frac{\chi_{model}^2}{\chi_{null}^2} \right) \quad (6.68)$$

Adjusted Goodness of Fit Index (AGFI): To adjust the biased resulted from model complexity, GFI is modified as;

$$AGFI = 1 - \frac{df_{null}}{df_{model}} (GFI) = 1 - \left( \frac{\chi_{model}^2/df_{model}}{\chi_{null}^2/df_{null}} \right) \quad (6.69)$$

Parsimony Goodness of Fit Index (PGFI): It is modification of GFI. It ranges from 0 to 1. Higher PGFI values indicates more parsimonious model.

$$PGFI = \frac{df_{model}}{df_{null}} (GFI) \quad (6.70)$$

Normed Fit Index (NFI): It is as an alternative fit index to CFI. Its value changes from 0 to 1. Rule of thumb, it should be greater than 0.90. It compares the proposed model with null model and shows that how proposed model improves the fit compared with null model. Its shortcoming is that it is sensitive to sample size.

$$NFI = \frac{(\chi_{null}^2 - \chi_{model}^2)}{\chi_{null}^2} \quad (6.71)$$

Parsimony Normed Fit Index (PNFI): It is modification of NFI for model complexity.

$$PNFI = \frac{df_{model}}{df_{null}}(NFI) \quad (6.72)$$

Comparative Fit Index (CFI): It is also known as the Bentler Comparative Fit Index. It compares the existing model with null model. CFI value changes between 0 and 1. CFI value gives the fraction of sample covariance matrix explained with the proposed model. CFI should be greater than 0.90. It is similar to NFI but it is less sensitive to sample size. The shortcoming of CFI is that when the correlation of variables are low, CFI is low and not reliable.

$$CFI = 1 - \frac{\chi_{model}^2 - df_{model}}{\chi_{null}^2 - df_{null}} \quad (6.73)$$

Parsimony Comparative Fit Index (PCFI): It is modification of CFI.

$$PCFI = \frac{df_{model}}{df_{null}}(CFI) \quad (6.74)$$

Tucker-Lewis Index (TLI): It is also known as Nonnormed Fit Index (NNFI). It is less sensitive to the sample size. However, it is sensitive to correlation between the measured variables like CFI. This means if correlations are not high, TFI value becomes low. Its value changes from 0 to 1. However, it can be lower than 0 and higher than 1 in some cases. The recommended lower limit for TLI is 0.95.

$$TLI = \frac{(\chi_{null}^2/df_{null}) - (\chi_{model}^2/df_{model})}{(\chi_{null}^2/df_{null}) - 1} \quad (6.75)$$

Incremental Fit Index (IFI): Its value changes from 0 to 1, but sometimes it can be greater than 1. Rule of thumb, it should be greater than 0.90. It is not sensitive to sample size.

$$IFI = \frac{\chi_{null}^2 - \chi_{model}^2}{\chi_{null}^2 - df_{model}} \quad (6.76)$$

Relative Fit Index (RFI): Its value changes from 0 to 1, but sometimes it can be lower than 0 or greater than 1. It is recommended that RFI should be close to 1.

$$RFI = 1 - \frac{(\chi_{model}^2/df_{model})}{(\chi_{null}^2/df_{null})} \quad (6.77)$$

High correlation coefficient between permeability and the non-Darcy coefficient implies that the main factor for the non-Darcy coefficient estimation is permeability. It is proposed that permeability does not determine the non-Darcy coefficient, and the high correlation between them results from dependence on the same factors. Path Analysis is used to find the relations between design variables (mean gravel size, porosity) and calculated petrophysical properties (Figure 6.72). In the model, there are four observed endogenous variables: permeability, non-Darcy coefficient, specific surface area and tortuosity, two observed exogenous variables: mean gravel size and porosity, and four unobserved exogenous variables, error terms of endogenous variables. The path diagram can be represented with four regression equations (Eqn.6.78):

$$\begin{aligned} V_3 &= \gamma_{31}V_1 + \gamma_{32}V_2 + \gamma_{36}V_6 + \varepsilon_3 \\ V_4 &= \gamma_{41}V_1 + \gamma_{42}V_2 + \gamma_{46}V_6 + \varepsilon_4 \\ V_5 &= \gamma_{51}V_1 + \gamma_{52}V_2 + \varepsilon_5 \\ V_6 &= \gamma_{62}V_2 + \gamma_{65}V_5 + \varepsilon_6 \end{aligned} \quad (6.78)$$

As a matrix notation it can be represented as;

$$\mathbf{V} = \boldsymbol{\gamma}\mathbf{V} + \boldsymbol{\varepsilon} \quad (6.79)$$

$\mathbf{V}$  and  $\boldsymbol{\varepsilon}$  are the  $p \times 1$  vectors of observed variables and error matrix ( $p = 6$ ),  $\boldsymbol{\gamma}$  is  $p \times p$  regression coefficient matrix. The extended form of matrix notation is:

$$\begin{bmatrix} V_1 \\ V_2 \\ V_3 \\ V_4 \\ V_5 \\ V_6 \end{bmatrix} = \begin{bmatrix} 0 & 0 & 0 & 0 & 0 & 0 \\ 0 & 0 & 0 & 0 & 0 & 0 \\ \gamma_{31} & \gamma_{32} & 0 & 0 & 0 & \gamma_{36} \\ \gamma_{41} & \gamma_{42} & 0 & 0 & 0 & \gamma_{46} \\ \gamma_{51} & \gamma_{52} & 0 & 0 & 0 & 0 \\ 0 & \gamma_{62} & 0 & 0 & \gamma_{65} & 0 \end{bmatrix} \begin{bmatrix} V_1 \\ V_2 \\ V_3 \\ V_4 \\ V_5 \\ V_6 \end{bmatrix} + \begin{bmatrix} 0 \\ 0 \\ \varepsilon_3 \\ \varepsilon_4 \\ \varepsilon_5 \\ \varepsilon_6 \end{bmatrix} \quad (6.80)$$

The covariance matrices of observed variables,  $\Sigma_V$ , and error terms related with observed variables,  $\Sigma_\varepsilon$  are given matrix notation as;

$$\Sigma_V = \begin{bmatrix} \hat{\sigma}_{V_{11}} & & & & & \\ 0 & \hat{\sigma}_{V_{22}} & & & & \\ \hat{\sigma}_{V_{31}} & \hat{\sigma}_{V_{32}} & \hat{\sigma}_{V_{33}} & & & \\ \hat{\sigma}_{V_{41}} & \hat{\sigma}_{V_{42}} & \hat{\sigma}_{V_{43}} & \hat{\sigma}_{V_{44}} & & \\ \hat{\sigma}_{V_{51}} & \hat{\sigma}_{V_{52}} & \hat{\sigma}_{V_{53}} & \hat{\sigma}_{V_{54}} & \hat{\sigma}_{V_{55}} & \\ \hat{\sigma}_{V_{61}} & \hat{\sigma}_{V_{62}} & \hat{\sigma}_{V_{63}} & \hat{\sigma}_{V_{64}} & \hat{\sigma}_{V_{65}} & \hat{\sigma}_{V_{66}} \end{bmatrix} \quad (6.81)$$

$$\Sigma_\varepsilon = \begin{bmatrix} 0 & & & & & \\ 0 & 0 & & & & \\ 0 & 0 & \hat{\sigma}_{\varepsilon_{33}} & & & \\ 0 & 0 & \hat{\sigma}_{\varepsilon_{43}} & \hat{\sigma}_{\varepsilon_{44}} & & \\ 0 & 0 & \hat{\sigma}_{\varepsilon_{53}} & \hat{\sigma}_{\varepsilon_{54}} & \hat{\sigma}_{\varepsilon_{55}} & \\ 0 & 0 & 0 & 0 & 0 & 0 \end{bmatrix} \quad (6.82)$$

Variance of each variable ( $\hat{\sigma}_{ii}$ ) is given on the diagonal and its covariances ( $\hat{\sigma}_{ij} i \neq j$ ) are given below the diagonal. Due to the symmetry ( $\hat{\sigma}_{ij} = \hat{\sigma}_{ji}$ ), only the lower part of the matrices are given above. Exogenous variables are design variables and their values are assigned with Hammersley design; therefore, there is no correlation between them ( $\hat{\sigma}_{V_{21}}=0$ ).

Sample size is 100, point suspected as outlier (Case45) is not removed from the analysis. In this model, base 10 logarithms of the variables are used since some variables; e.g. permeability and non-Darcy coefficient, have lognormal distribution and correlations indicate that the trend of one variable effect to the other is based on a power of independent variable. Instead of design mean gravel size (based on base 2 logarithm of gravel size), calculated mean

gravel size is used to eliminate the standard deviation of base 2 logarithm of gravel size distribution.

The proposed model is recursive; no variable in the model has an effect on itself. Path model specifies that both permeability and non-Darcy coefficient depend on same parameters: gravel size, porosity and tortuosity. Specific surface area is highly correlated with permeability and non-Darcy coefficient because it also depends on gravel size and porosity, and also it has indirect effect to them via tortuosity. This explains the high correlation between permeability and the non-Darcy coefficient. Error terms of the permeability, the non-Darcy coefficient and the specific surface area are all related because they depend on the same factors.

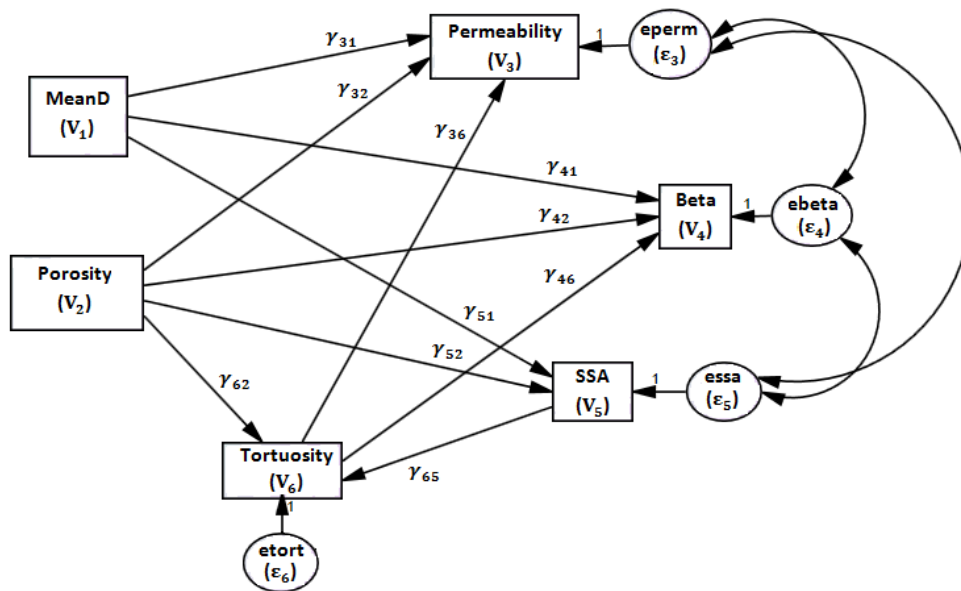


Figure 6.72 Path Model Analysis of Petrophysical Properties and Design Variables Notation

Based on the six observed variables, there are 21 distinct covariance matrix elements. The number of estimated parameters are 19, 10 regression weights between observed variables, 3 covariance between unobserved variables and 6 variance of observed variables. Therefore, the number of degree of freedom ( $df$ ) is 2 (21-19). SPSS Amos is used to fit the model with sample data with maximum likelihood (ML) estimation method.

In Figure 6.73, numbers on the single headed arrows give the standardized estimates of regression weight. For example, when mean gravel size goes up by one standard deviation, permeability goes up by 0.978 standard deviations (Table 6.19). The numbers above the endogenous variables give the Squared Multiple Correlations ( $R^2$ ). For example,  $R^2$  of permeability is 0.992 (Table 6.20). All observed endogenous variables have a high coefficient of determination. The numbers on the two-headed arrow give the correlation between the unobserved exogenous variables. For example, the correlation between error terms of permeability and specific surface area is -0.947 (Table 6.21). Table 6.22, Table 6.23 and Table 6.24 give the estimate of the regression weights, variances of the exogenous variables and covariances of error terms with their standard error of estimate, S.E. and  $t$  values, C.R. If absolute  $t$  value of estimate is greater than 2, the estimate is significantly different from zero at the .05 significance level. All regression weights, variances and covariances are significant. The covariance between error terms are all close to 0 (Table 6.24); however, all of them significant and they cannot be eliminated.

Table 6.19 Standardized Regression Weights between Observed Petrophysical Variables

Regression Path			Estimate
SSA	<---	MeanD	-.994
SSA	<---	Porosity	-.075
Tortuosity	<---	Porosity	-.841
Tortuosity	<---	SSA	-.180
Permeability	<---	MeanD	.978
Beta	<---	MeanD	-.910
Permeability	<---	Porosity	.189
Beta	<---	Porosity	-.386
Beta	<---	Tortuosity	.042
Permeability	<---	Tortuosity	-.046

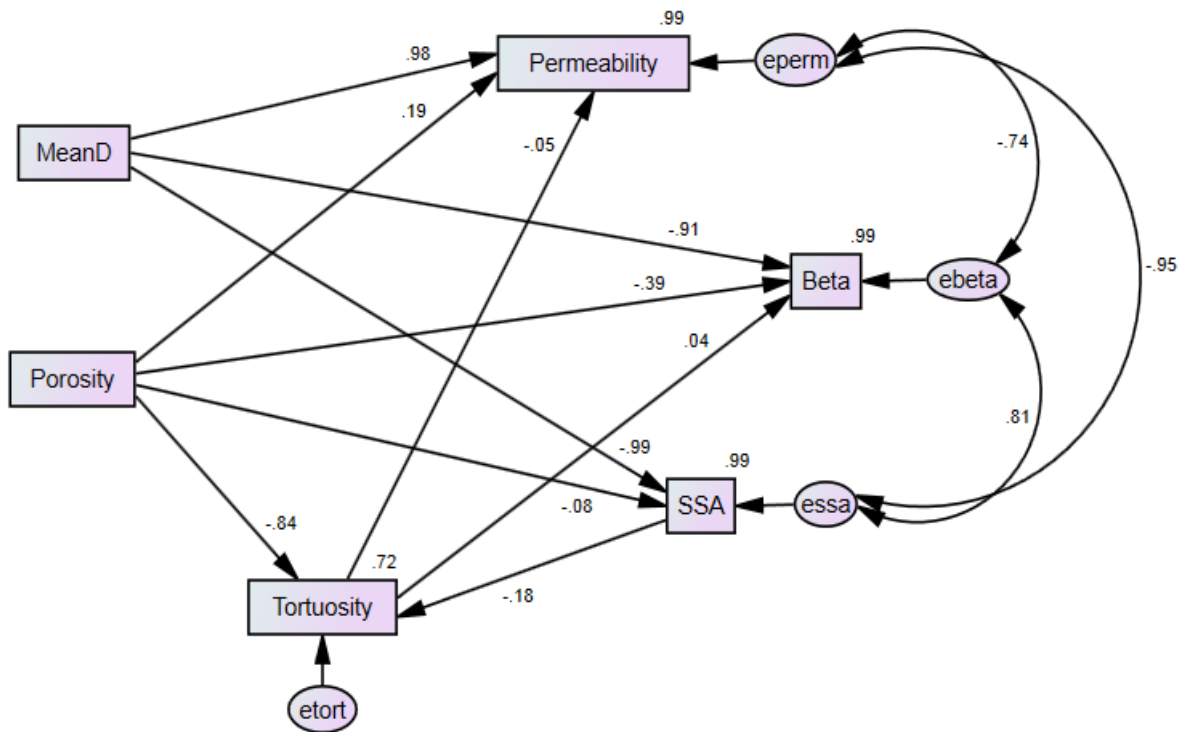


Figure 6.73 Path Model Analysis of Petrophysical Properties and Design Variables

Table 6.20 Squared Multiple Correlations of Predicted Observed Petrophysical Variables

Variable	Estimate
SSA	.993
Tortuosity	.717
Beta	.992
Permeability	.992

Table 6.21 Correlations between Error Terms

Correlation Path	Estimate
eperm <--> essa	-.947
ebeta <--> essa	.814
eperm <--> ebeta	-.738

In regression analysis, two correlated variables cannot be used to estimate a variable (colinearity problem). For the non-Darcy coefficient and permeability correlations development, tortuosity effect becomes insignificant when porosity is used in the correlation. However,



tortuosity is significant in the path diagram because the correlation between porosity and tortuosity is given as an indirect effect (Table 6.25), which gives the one observed variable effect to another through a mediator variable. Indirect effects are computed as the product of paths linking the variables, and total effect is the sum of the direct and indirect effects. For example, direct effect of porosity on permeability is 3.638. Porosity has two indirect effects on permeability via tortuosity, and specific surface area and tortuosity. The indirect effect of porosity via tortuosity is 0.739, multiplication of regression coefficients between porosity and tortuosity (-0.293), and tortuosity and permeability (-2.519). The indirect effect on porosity via specific surface area and tortuosity is -0.012, multiplication of regression weights between porosity and specific surface area (-0.706), specific surface area and tortuosity (-0.007), and tortuosity and permeability (-2.519). Total indirect effect of porosity on permeability is 0.727, sum of all indirect effects. Total effect of porosity on permeability is 4.366, sum of direct effect (3.638) and indirect effect (0.727).

Table 6.22 Regression Weights between Observed Petrophysical Variables

Regression Path			Estimate	S.E.	C.R.
SSA	<---	MeanD	-.995	.009	-116.857
SSA	<---	Porosity	-.706	.079	-8.880
Tortuosity	<---	Porosity	-.293	.019	-15.692
Tortuosity	<---	SSA	-.007	.002	-3.366
Permeability	<---	MeanD	2.015	.018	109.554
Beta	<---	MeanD	-.979	.010	-100.798
Permeability	<---	Porosity	3.638	.191	19.073
Beta	<---	Porosity	-3.879	.120	-32.340
Beta	<---	Tortuosity	1.206	.279	4.328
Permeability	<---	Tortuosity	-2.519	.296	-8.523

Table 6.23 Variances of Exogenous Variables

Variable	Estimate	S.E.	C.R.
MeanD	.071	.010	7.036
Porosity	.001	.000	7.036
essa	.001	.000	7.036
etort	.000	.000	7.036
eperm	.002	.000	7.035
ebeta	.001	.000	7.034

Table 6.24 Covariance between Error Terms

Covariance Path	Estimate	S.E.	C.R.
eperm <--> essa	-.001	.000	-6.841
ebeta <--> essa	.000	.000	6.280
eperm <--> ebeta	-.001	.000	-5.906

Table 6.25 Direct, Indirect and Total Effects

Effect	Parameter	Porosity	MeanD	SSA	Tortuosity
Direct	SSA	-0.706	-0.995	0.000	0.000
	Tortuosity	-0.293	0.000	-0.007	0.000
	Beta	-3.879	-0.979	0.000	1.206
	Permeability	3.638	2.015	0.000	-2.519
Indirect	SSA	0.000	0.000	0.000	0.000
	Tortuosity	0.005	0.007	0.000	0.000
	Beta	-0.348	0.008	-0.008	0.000
	Permeability	0.727	-0.017	0.017	0.000
Total	SSA	-0.706	-0.995	0.000	0.000
	Tortuosity	-0.289	0.007	-0.007	0.000
	Beta	-4.227	-0.971	-0.008	1.206
	Permeability	4.366	1.998	0.017	-2.519

NPAR, CMIN and DF in Table 6.26 represent the number of distinct parameters, the minimum value of discrepancy (chi-square statistic,  $\chi^2$ ) and the degree of freedom, respectively. In the saturated model, no constraints are placed on the population moments. Therefore, the degree of freedom is 0. Saturated model can fit any data set perfectly; however, it is not possible

to calculate any fit statistics due to 0 degree of freedom. In the independence model, observed variables are assumed to be uncorrelated with each other. Unlike saturated model, it gives the worst fit to any data set. These two models are used to calculate the comparative fit statistics to evaluate models. Path Model is assumed to be correct, the probability of getting a discrepancy,  $\chi^2$  as large as 0.627 is 0.731.  $\chi^2$  strongly depends on a sample size. With the increased in a sample size, the model  $\chi^2$  increases and the  $\chi^2$  test failed even if the difference between sample covariance matrix and model covariance matrix is low. Therefore, some researchers suggest the use of the adjusted  $\chi^2$  to evaluate the goodness of the fit, CMIN/DF ( $\chi^2/df$ ) . For adequate fit, CMIN/DF should be less than 2. HOELTER gives the largest sample size for which a model is accepted for specified significance level, chi-square statistic, degrees of freedom. For Path Model, the numbers of largest sample sizes are 947 and 1455 for significance level 0.05 and 0.01, respectively (Table 6.27). In this analysis, 100 samples are used. Therefore; CMIN/DF should be less than 2; otherwise, model should be rejected.

Table 6.26 Chi-square Statistics of Path Model

Model	NPAR	CMIN	DF	P	CMIN/DF
Path Model	19	0.627	2	0.731	0.313
Saturated model	21	0.000	0		
Independence model	6	1911.816	15	0.000	127.454

Table 6.27 HOELTER Critical N

Model	HOELTER 0.05	HOELTER 0.01
Path Model	947	1455
Independence model	2	2

RMR (root mean square residual) is an indication of the badness of the fit. The smaller RMR means a better fit; the Path Model RMR is small, 0.0, compared to the Independence Model RMR, 0.061.

The other model evaluation criterion is Standardized Residual Covariances (Table 6.28); each residual covariance has been divided by an estimate of its standard error. If a model is correct, the absolute value of the standardized residual should be less than 2. For this model, the maximum absolute value of the standardized residual is 0.061.

Table 6.28 Standardized Residual Covariances of Path Model

	Porosity	MeanD	SSA	Tortuosity	Beta	Permeability
Porosity	0.000					
MeanD	0.032	0.000				
SSA	-0.032	-0.020	0.003			
Tortuosity	0.004	-0.061	0.026	-0.007		
Beta	-0.027	-0.011	0.011	0.023	0.017	
Permeability	0.030	0.006	-0.007	-0.024	-0.014	0.010

Table 6.29 summarizes the fit indices based on model complexity: AIC (Akaike Information Criterion), BCC (Browne-Cudeck Criterion), BIC (Bayesian Information Criterion), CAIC (Consistent Akaike Information Criteria), ECVI (Expected Cross Validation Index) and MECVI (Modified Expected Cross Validation Index). Lower fit index value indicates the better fit. The path model is compared with saturated model and independence model. As expected, the fit index values highest for independence model since independent model represents the worst fit. Path model fit index values are smaller than best fit model, saturated model since the proposed model is less complex.

Table 6.30 gives the fit indices based on model comparison: GFI (Goodness of Fit Index), AGFI (Adjusted Goodness of Fit Index), NFI (The Bentler-Bonett Normed Fit Index), RFI

(Bollen's Relative Fit Index), IFI (Bollen's Incremental Fit Index), TLI (Tucker-Lewis Index) and CFI (Comparative Fit Index). All fit indices are close to one, which indicates that the model supports the sample data.

Table 6.29 Fit Statistics Based on Model Parsimony

Model	AIC	BCC	BIC	CAIC	ECVI	MECVI
Path Model	38.627	41.518	88.125	107.125	0.390	0.419
Saturated Model	42.000	45.196	96.709	117.709	0.424	0.457
Independence Model	1923.816	1924.729	1939.447	1945.447	19.432	19.442

Table 6.30 Fit Statistics Based on Model Comparison

Model	GFI	AGFI	NFI	RFI	IFI	TLI	CFI
Path Model	0.998	0.978	1.000	0.998	1.001	1.005	1.000
Saturated Model	1.000		1.000		1.000		1.000
Independence Model	0.314	0.040	0.000	0.000	0.000	0.000	0.000

After model validation with fit statistics, the model is used for missing data estimation. Instead of separating the data two and using the half part as a validation data, half of the hard estimated parameters: permeability, tortuosity and non-Darcy coefficient and specific surface area are randomly deleted and estimated. Figure 6.74 gives the part of the deleted data file. Missing values are represented with 'NaN', and for each case, the number of missing data is given in the last column. In some cases; there is no missing data; for example Case 2 and Case 4; in some cases all variables are missing; for example Case 12 and Case 22.

Missing values are estimated 100 times with a stochastic regression. In these imputations, model parameters such as regression weights and error variances are estimated from the complete cases with maximum likelihood. Then regression equations are used to estimate the

missing values and random error are added to restore the variability in the data. Figure 6.75 gives the scatter plots of actual vs. predicted values for estimated parameters. While estimation intervals are small for permeability, non-Darcy coefficient and specific surface area, estimation interval is very large for tortuosity. Mean tortuosity estimation is consisted with real tortuosity; however, for each case estimated tortuosities are very different. In the other word, uncertainty in tortuosity estimation is high. This result is expected because the  $R^2$  of tortuosity is lower, 0.72 compared to other petrophysical parameters.

Case Number	Mean Diameter (mm)	Porosity (fraction)	Permeability (Darcy)	Tortuosity	Beta (1/m)	SSA (1/mm)	Missing Number
1	0.2903	0.4134	NaN	1.474	49439.362	NaN	2
2	0.3056	0.4498	158.964	1.460	34085.251	10.402	0
3	0.2903	0.3914	97.220	NaN	NaN	NaN	3
4	0.3222	0.4251	130.651	1.512	43066.325	10.483	0
5	0.3098	0.4589	NaN	1.465	29541.311	NaN	2
6	0.3281	0.4049	120.662	NaN	NaN	10.305	2
7	0.3080	0.4360	170.051	1.477	35058.337	9.411	0
8	0.3521	0.4726	NaN	NaN	24527.391	8.858	2
9	0.3407	0.3840	NaN	1.521	55895.673	NaN	2
10	0.3597	0.4192	167.320	NaN	38575.726	NaN	2
11	0.3397	0.4505	NaN	NaN	27403.695	NaN	3
12	0.3799	0.4380	NaN	NaN	NaN	NaN	4
13	0.3631	0.4283	215.555	NaN	NaN	NaN	3
14	0.3857	0.4645	NaN	1.455	22466.321	7.785	1
15	0.3598	0.4079	183.232	1.493	39579.054	8.319	0
16	0.4180	0.4443	270.063	NaN	NaN	NaN	3
17	0.4056	0.4769	407.756	1.431	NaN	7.130	1
18	0.4276	0.3894	166.389	NaN	42275.723	NaN	2
19	0.4051	0.4227	NaN	NaN	NaN	7.435	3
20	0.4512	0.4613	NaN	NaN	21754.059	NaN	3
21	0.4326	0.3985	211.753	1.526	38495.454	7.482	0
22	0.4589	0.4345	NaN	NaN	NaN	NaN	4
23	0.4294	0.4661	NaN	NaN	NaN	6.315	3

Figure 6.74 Sample Data File used in the Data Imputation

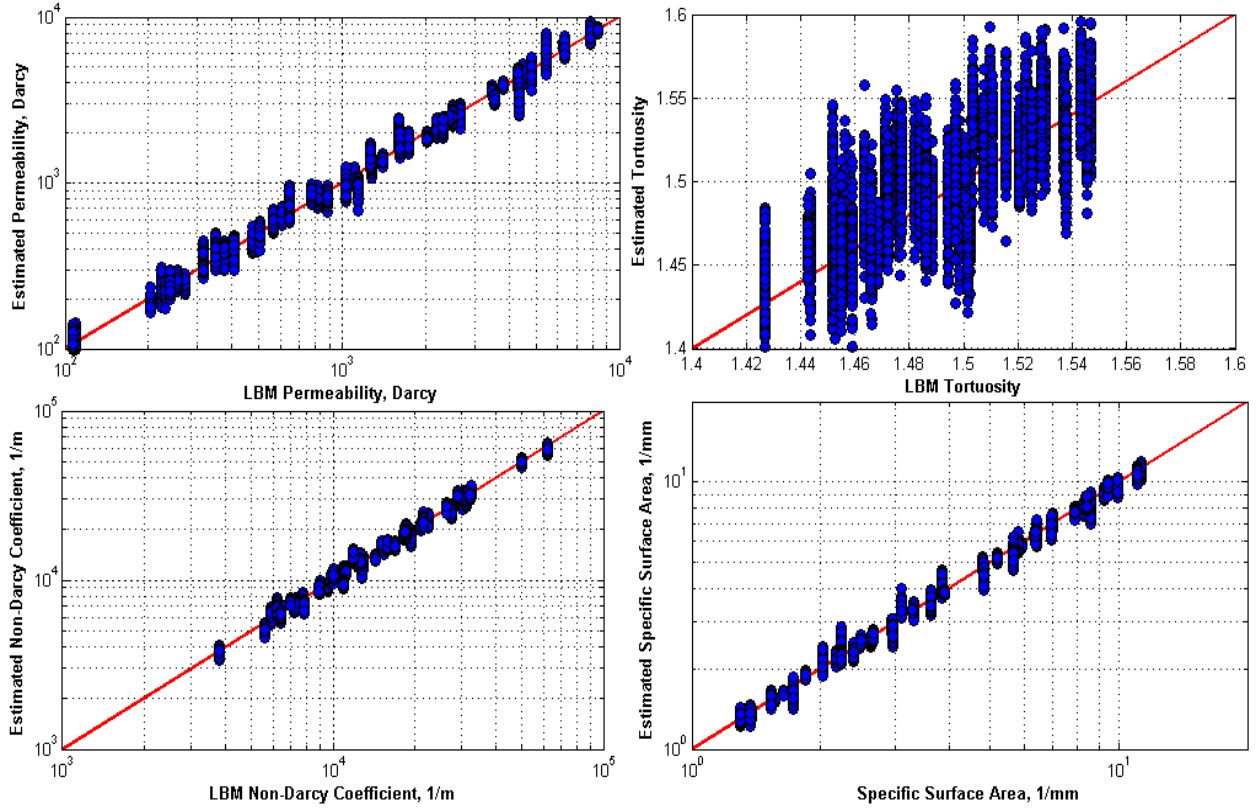


Figure 6.75 Actual by Predicted Data Comparison of Petrophysical Parameters

#### 6.5.5 Compaction Effect on Flow Properties

Pressure decrease in reservoir leads to sand grain expansion and reservoir volume reduction which lead to decrease in porosity and permeability, increase in non-Darcy coefficient. Permeability decrease due to porosity reduction is related with Kozeny-Carman equation. However, there is no study related with non-Darcy coefficient increase due to compaction in literature. Therefore, compaction effect is investigated for the most heterogeneous domain used representative elementary volume. The domain is voxelized 1200x1200x1200 voxels with a resolution 0.0075 mm in order to accurately resolve small expansion of sand volume. In the domain, minimum and maximum particle diameters are represented with 88 voxels and 352 voxels, respectively. Compaction is modelled by increasing the grain radius with different fractions. Figure 5.76 gives the increase in grain sizes with different percent. In this figure red

and blue colors represents the grain and pore voxels, respectively. As the grains expand, contact points of grains increase and pores become more disconnected.

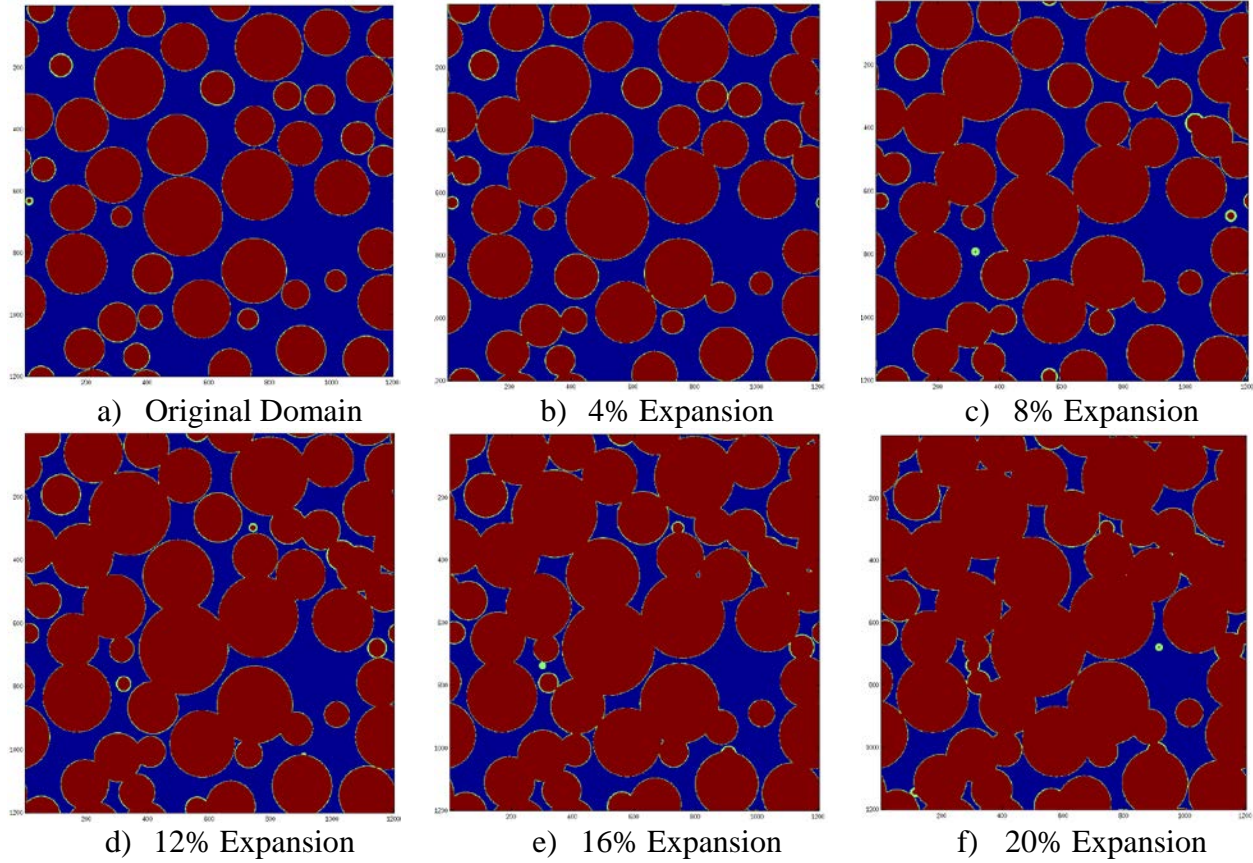


Figure 6.76 Grain Expansion of Heterogeneous Domain

Even if it is unrealistic, grain diameters are increased up to 26% in order to find a correlation between porosity and permeability. Permeabilities are calculated in three directions from Network modeling and in  $x$  direction from LBM with low pressure difference method (Figure 6.77). Calculated permeabilities are similar all directions that indicates the domain is isotropic and compaction does not affect the domain isotropy. Porosity decreases from initial value 44.77% to 9.82% with a 26% increase of grain radius. This leads to permeability decreases from  $3.26 \times 10^3$  Darcy to 19 Darcy. Network modelling is approximation of pore volume; therefore, permeability calculated from LBM is more accurate and it is used for further studies.



Kozeny-Carman relation is found between porosity and permeability. In Figure 6.78, blue dots and line give calculated permeabilities from LBM, and Kozeny-Carman fit (Eqn.6.83), respectively. Coefficient and exponent are close to 1 and 3; respectively.

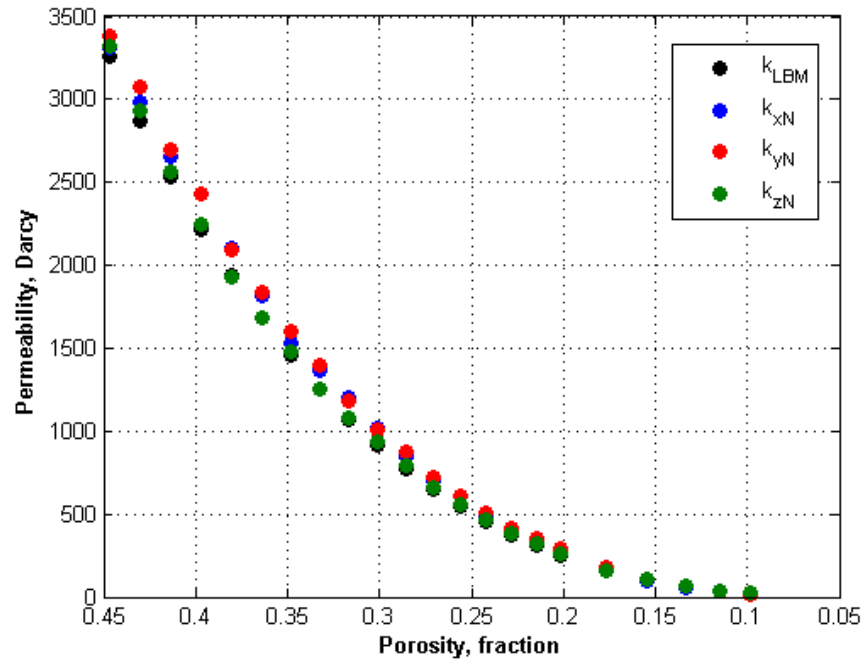


Figure 6.77 Compaction Effect on Porosity and Permeability

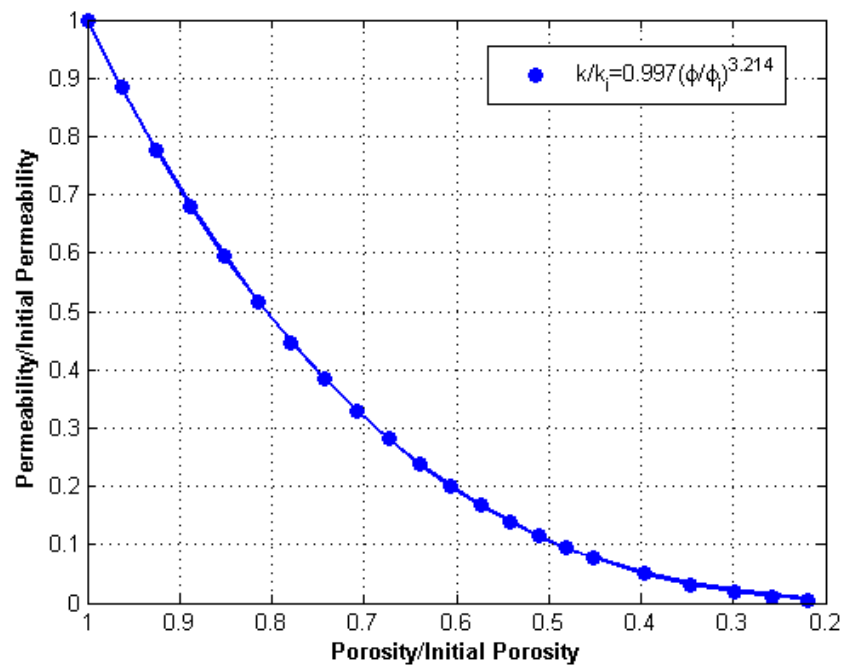
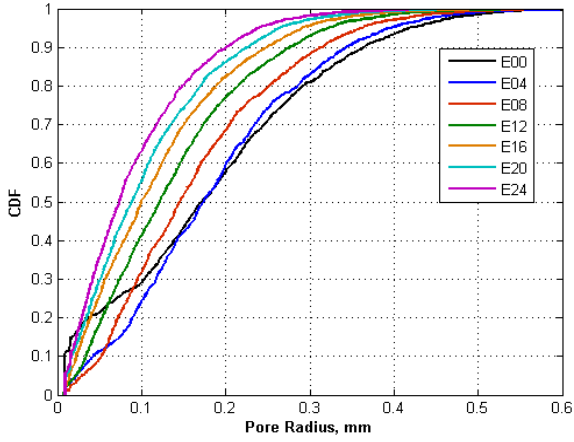


Figure 6.78 Kozeny-Carman Relation of Porosity and Permeability

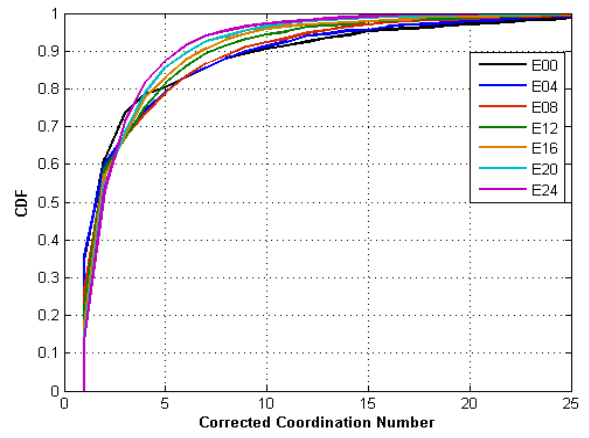
$$\frac{k_x}{k_{xi}} = 0.997 \left( \frac{\phi}{\phi_i} \right)^{3.214} \quad (6.83)$$

Permeability decrease can be figure out with Network parameters (Figure 6.79). In Figure 6.79, label represents the expansion amount; for example, E00 and E24 represent the original domain and the domain constructed with the increase in radius with 24%. Figure 6.80 gives four domains, E00, E08, E16 and E24, to illustrate the pore and throat properties change. Pore radius decreases with compaction. Median pore radius of original domain is 0.1714 mm and it decreases to 0.0737 mm as grain radius increases to 24%. Median corrected coordination numbers is almost not change (between 1.22 and 1.88). However, high values of corrected coordination number decreases with grain expansion. Throat radius decreases from 0.121 mm to 0.048 mm and throat length decreases from 1.1432 mm to 0.5691 mm; however, the throat aspect ratio almost does not change much with compaction (between 0.191 and 0.217). With compaction, pore space becomes more disconnected; therefore, pores become smaller and number of pores increases. For example, there are 1368 and 1783 pores in the domain E00 and E24, respectively. Therefore, pore-throat radius ratio decreases with compaction and this decrease is significant for high pore-throat radius ratio up to 5% increase in grain radius. Decrease in pore and throat radius, and coordination number leads to decrease in permeability.

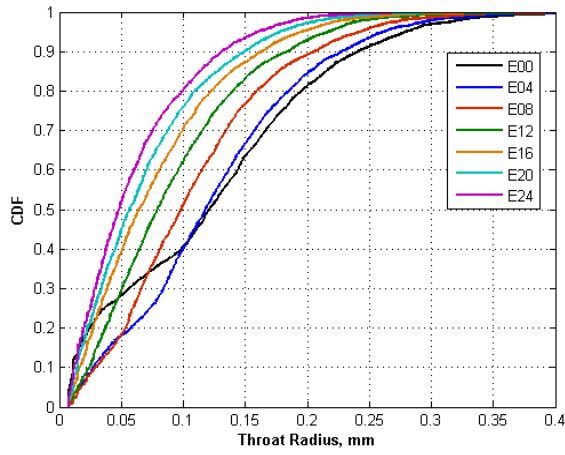
Permeability and non-Darcy coefficient are calculated from intercept and slope of Forchheimer equation (Eqn.6.24). Figure 6.81 gives the Forchheimer plot of expanded domains up to 13%. In this figure, blue dots and red lines give plotting variables ( $1/k_{app}$  and  $\rho u/\mu$ ) obtained from LBM simulations and linear fits of data, respectively. With compaction, permeability decreases (reciprocal of apparent permeability increases) and non-Darcy coefficient increases (slope of line increases).



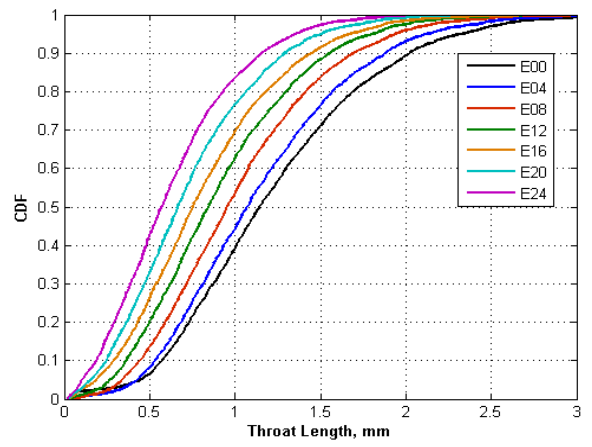
Pore Radius Distribution



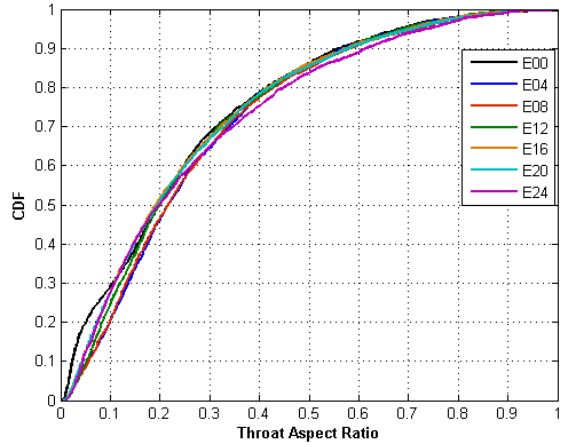
Corrected Coordination Number Distribution



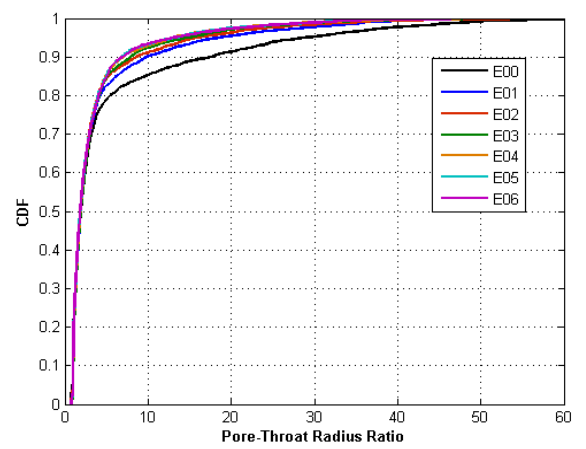
Throat Radius Distribution



Throat Length Distribution



Throat Aspect Ratio Distribution

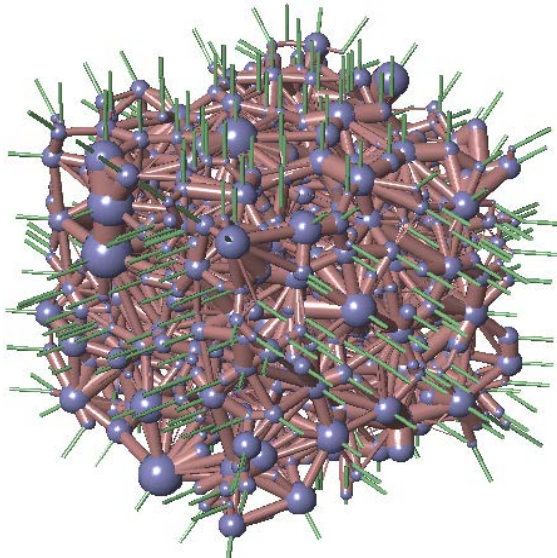


Pore-Throat Radius Ratio Distribution

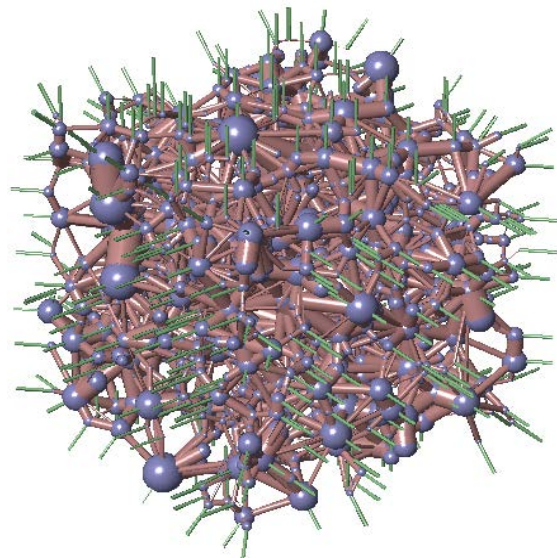
Figure 6.79 Compaction Effect on Network Parameters

Figure 6.82 gives the comparison of permeabilities calculated from LBM with low pressure difference method and the ones obtained from intercept of Forchheimer equation for domains up

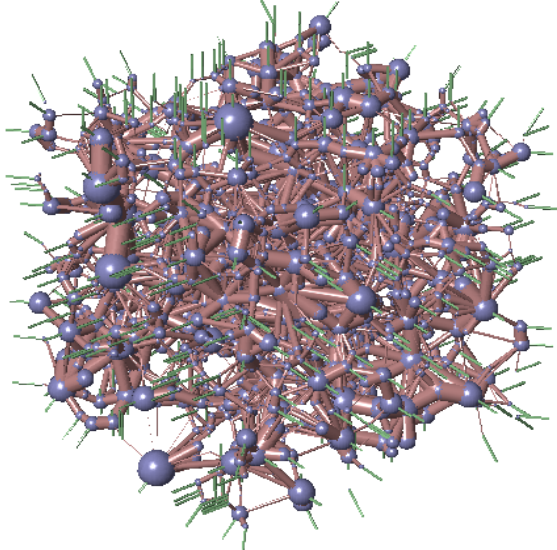
to 14% increase of particle radius. The maximum difference is about 5% and the difference decreases as the compaction increases since the Reynolds number at which inertial effect become significant decreases. Non-Darcy coefficient increases exponentially with permeability decrease (Figure 6.83). Permeability decreases from  $3.26 \times 10^3$  Darcy to 377 Darcy (88.43% decrease) and non-Darcy coefficient is increases from  $7.51 \times 10^3$  1/m to  $1.12 \times 10^5$  1/m (1467.56% increase) with a 14% increase of particle diameter.



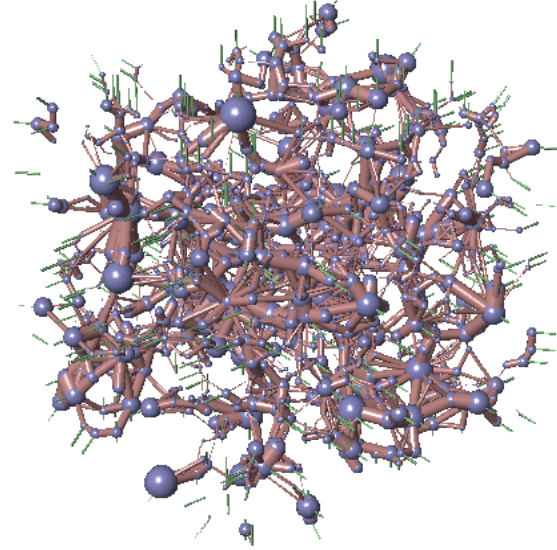
Network Model of E00



Network Model of E08



Network Model of E16



Network Model of E24

Figure 6.80 Compaction Effect on Network Model

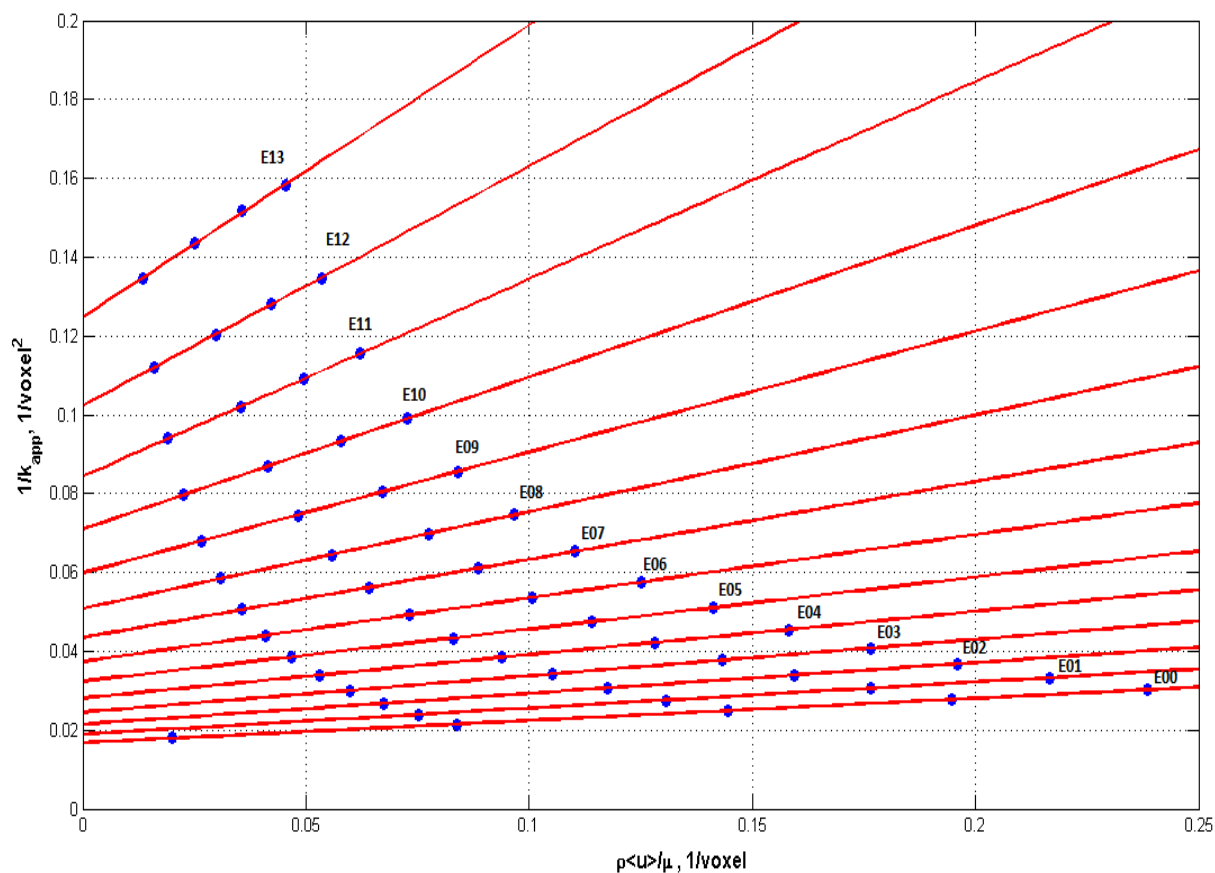


Figure 6.81 Compaction Effect on Forchheimer Plot

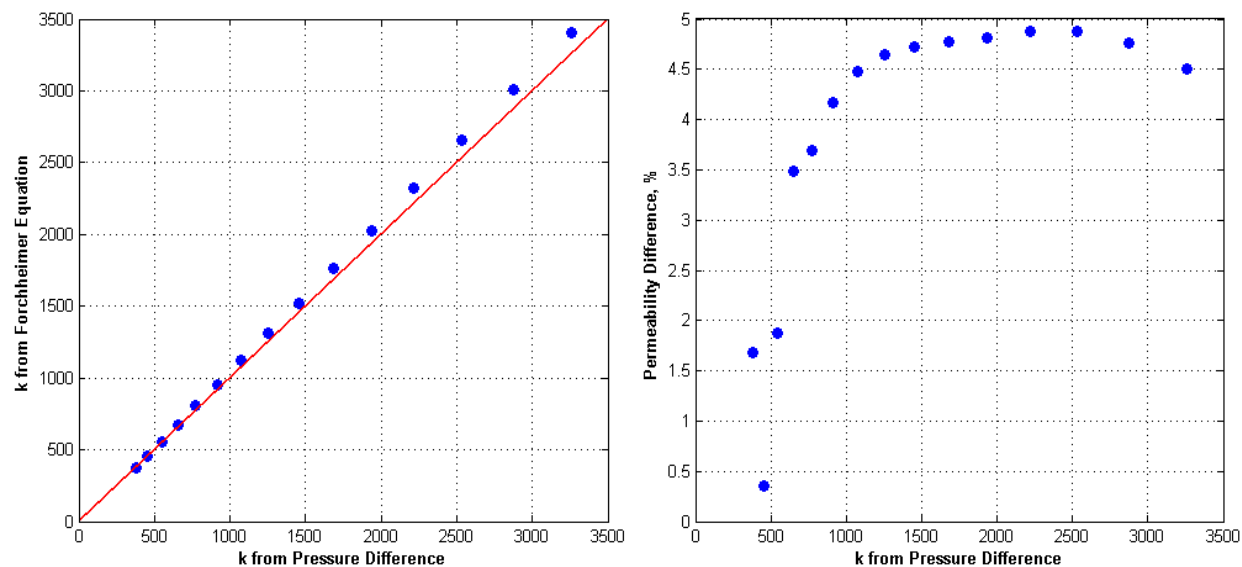


Figure 6.82 Permeability Comparison of Low Body Force Method and Low Pressure Difference Method

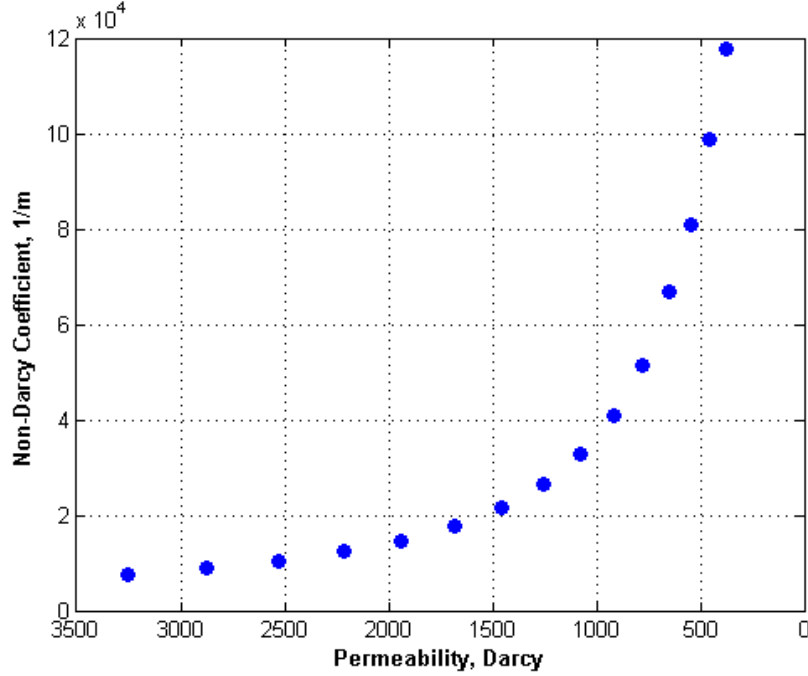


Figure 6.83 Non-Darcy Coefficient Change with Permeability Change due to Compaction

Permeability and non-Darcy coefficient are normalized based on their initial values and Kozeny-Carman type relation of permeability and non-Darcy coefficient is found (Figure 6.84 and Eqn.6.84).

$$\frac{\beta}{\beta_i} = 1.038 \left( \frac{k}{k_i} \right)^{-1.303} \quad (6.84)$$

In simulators, non-Darcy coefficient is updated with permeability and porosity. Figure 6.85 compares the non-Darcy coefficients calculated from LBM simulations with the ones estimated from developed correlation (Eqn.6.40). For high permeability domains, or for lower non-Darcy coefficients, calculated and estimated non-Darcy coefficients are close. However, the differences between calculated and estimated non-Darcy coefficients increase up to 25% with compaction (or permeability decrease). Non-Darcy coefficients estimated from the correlation are lower than the ones calculated from LBM. This indicates that for tight formation, developed correlation can be used safely. However, for loosely or unconsolidated formations, using

developed correlation to estimate non-Darcy coefficient change with compaction cause underestimation of inertial effects and unreliable production estimation.

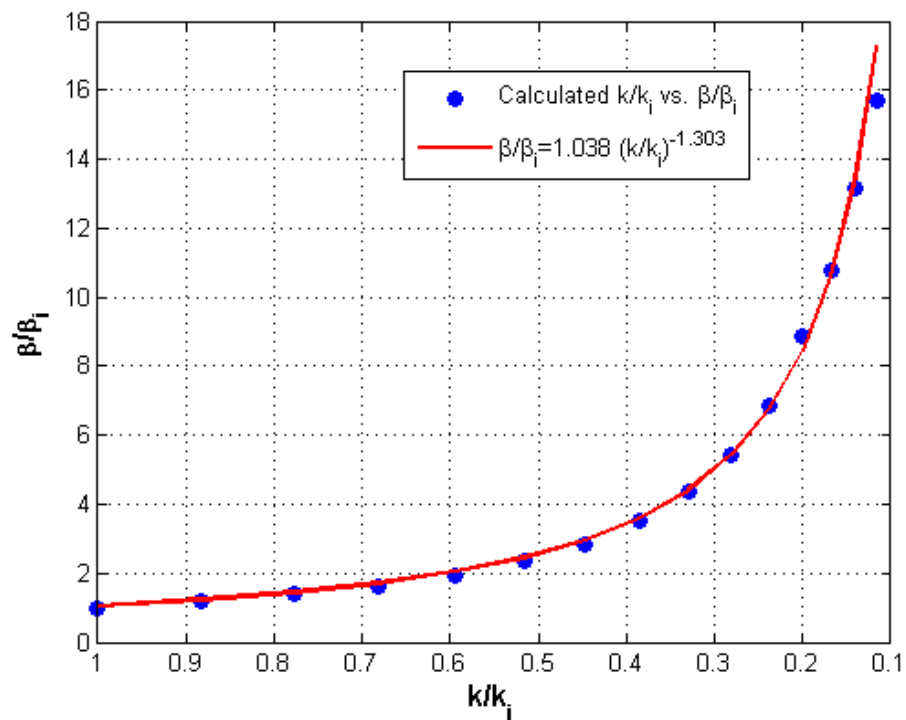


Figure 6.84 Kozeny-Carman Relation of Permeability and Non-Darcy Coefficient

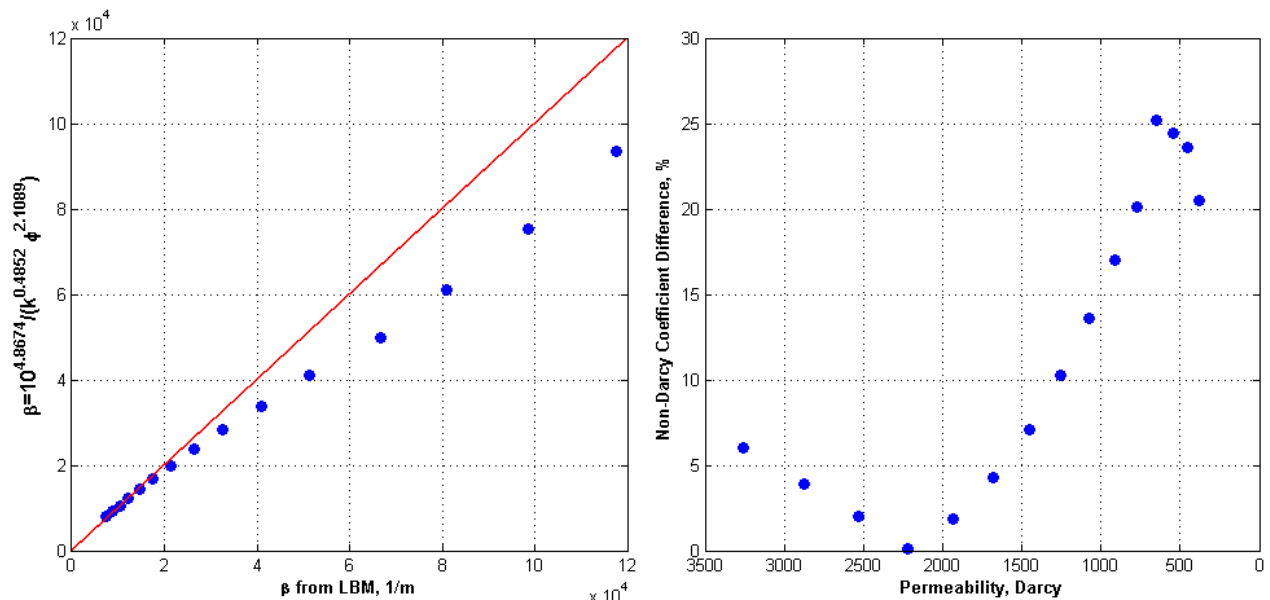


Figure 6.85 Comparison of Non-Darcy Coefficients Calculated from LBM and Estimated from Correlation

## 6.6 Sand Migration Effect on Flow Properties

Sand migration effects on porosity, permeability and the non-Darcy coefficient are investigated using pore-scale analysis. In this study, the locations of sand particles in the gravel pack are found using network simulations, and then permeability and the non-Darcy coefficient are calculated using LBM.

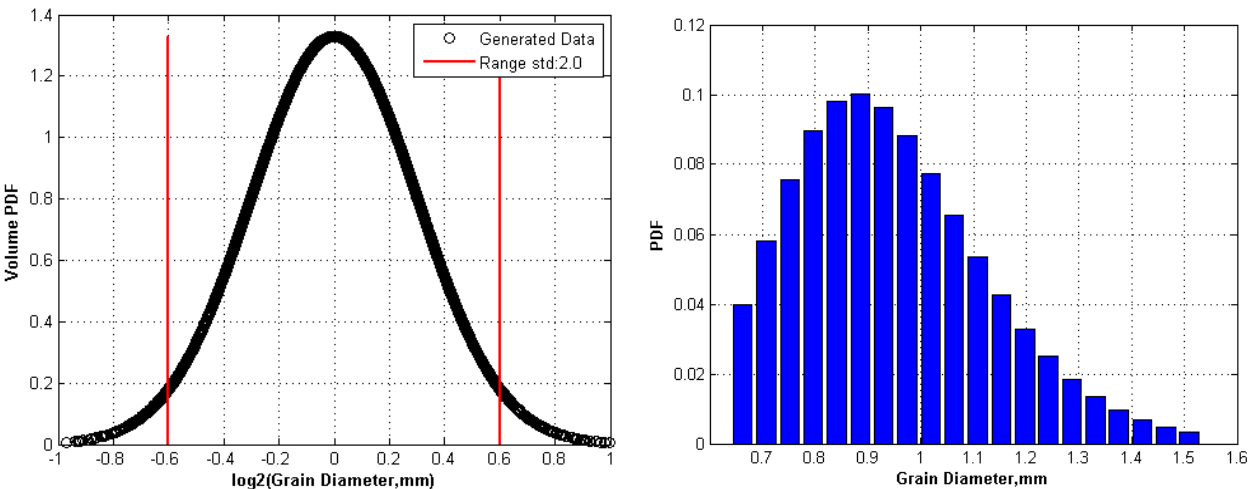
Gravel distribution data found from literature indicates that the base 2 logarithm of the grain volume is normally distributed with a standard deviation between 0.1 and 0.5. For the sand migration study, a mean and standard deviation of base 2 logarithm of gravel volume 0 and 0.3 are used to construct a simulated gravel pack (Figure 6.86a). The  $\pm 2$  standard deviation range is used to generate a gravel size distribution that contains 95.45% of the generated volume distribution data (Figure 6.86b). The domain size and target porosity are chosen as 6 mm and 0.44 respectively (Figure 6.86c). The minimum and maximum gravel sizes in the generated domain are 0.6402 mm and 1.4985 mm, respectively.

Five network simulations were conducted by a colleague (Dongxing Liu) with the amount of injected solids between 0.2% and 1.0% pore volumes. Sand particles were selected from a log-normal distribution with mean and standard deviation of 0.16 mm and 1 mm, respectively. Figure 6.87 gives the sand particle locations in the gravel pack for 1.0% pore volume plugging. The sand particles are almost uniformly distributed in the interior of the domain. There are no particles in the 1 mm outer edge of the domain, where pore throats are connected to the outside. Therefore, the simulation domain is chosen between 1 mm and 5 mm.

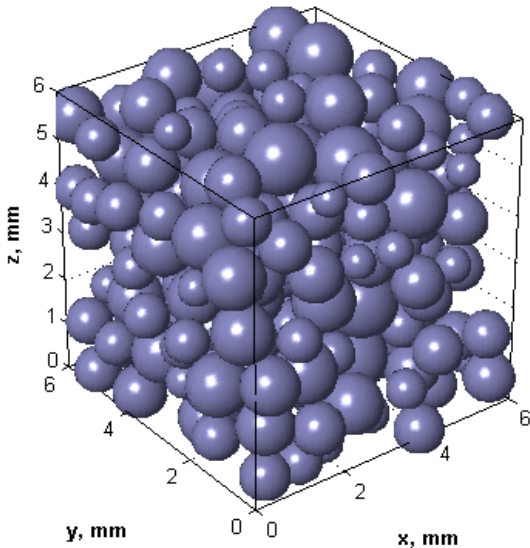
The original domain contains 245 gravel particles and the simulation domain contains 69 gravel particles. Both of the domains have similar gravel size distribution (Figure 6.88); therefore, trimming of the domain edges has no effect on gravel size distribution. The median gravel size of original domain and interior domain are 0.9344 mm and 0.9068 mm, respectively.



However, the interior domain may not be representative for permeability and non-Darcy coefficient. The representative elementary volume (REV) for most heterogeneous gravel pack domains (standard deviation of base 2 logarithm of the domain is 0.5) contains 334 particles.



a) Volume Distribution of Gravel Size                      b) Grain Size Distribution



c) Gravel Pack for Sand Migration

Figure 6.86 Gravel Pack Generation for Pore Scale Analysis of Sand Migration

Table 6.31 summarizes the domain name and minimum, maximum and median sizes of sand particles and the ratio of median gravel particle diameter to sand particle diameter. The domain F00 represents the gravel pack with no sand particle in the domain, while domain F10

represents the gravel pack with 1% of pore volume plugging. For the F10 domain, the minimum and maximum sand particle sizes are 0.1323 mm and 0.3069 mm. The median gravel particle diameter to sand particle diameter ratio is 5.1481.

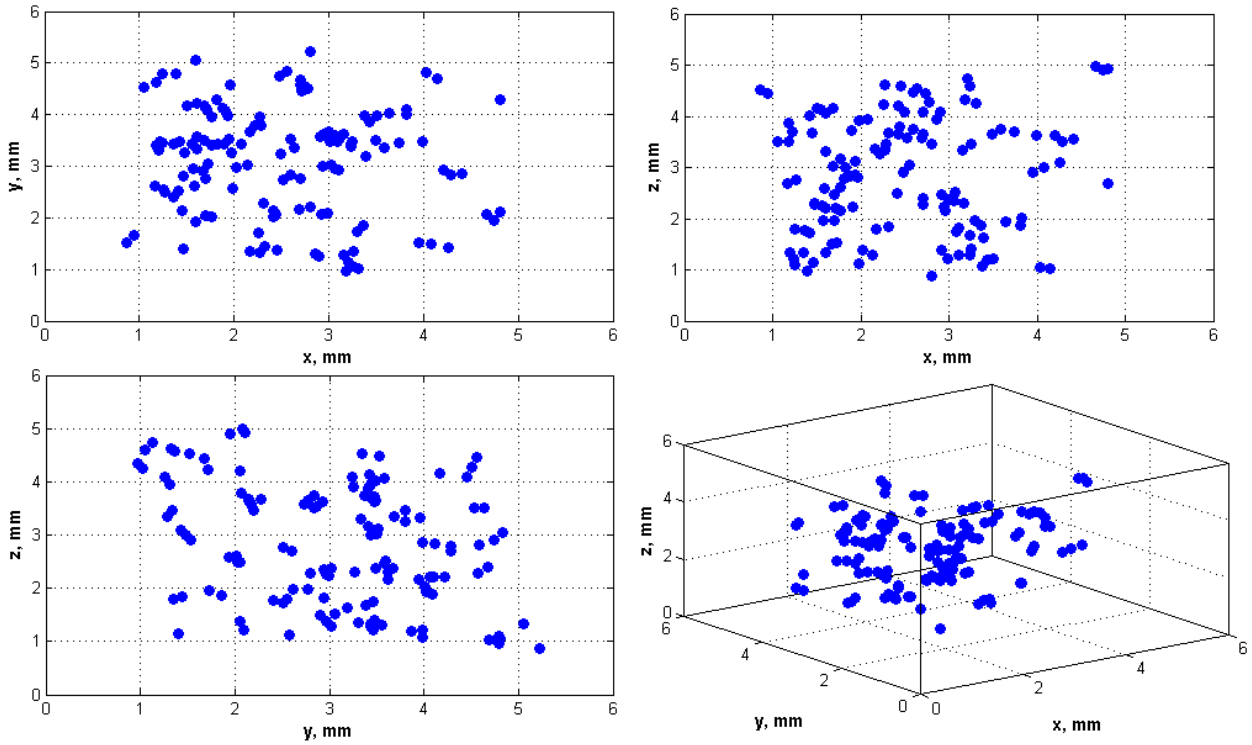


Figure 6.87 Sand Particle Location for 1% Pore Volume Plugging

Table 6.31 Sand Migration Domains and Sand Particle Range

Domain	$D_{p,min}$ (mm)	$D_{p,max}$ (mm)	$D_{p,median}$ (mm)	$D_{p,gravel}/D_{p,sand}$
F00	0.6402	1.4985	0.9344	—
F02	0.1547	0.2621	0.1733	5.2324
F04	0.1455	0.3430	0.1675	5.4122
F06	0.1269	0.3183	0.1696	5.3458
F08	0.1323	0.2994	0.1720	5.2712
F10	0.1323	0.3069	0.1761	5.1481

Figure 6.89 gives the sand particle distribution of domains F02 through F10. In the legend, the sand particle numbers are given. For example, the number of sand particles in the F02 domain (0.2% pore volume plugging) and F10 domain (1% pore volume plugging) contain

33 and 133 particles, respectively. Since the particles are chosen from same distribution, the particles plugged in the domains have similar distributions. For all domains, minimum and maximum particles sizes are 0.1323 mm and 1.4985 mm, respectively (Table 6.31). Voxel resolution is chosen as 0.005 mm where minimum particle and maximum particle diameters are represented by 26 voxels and 300 voxels, respectively. The simulation domain (1 mm – 5 mm) is represented by 800 x 800 x 800 voxels.

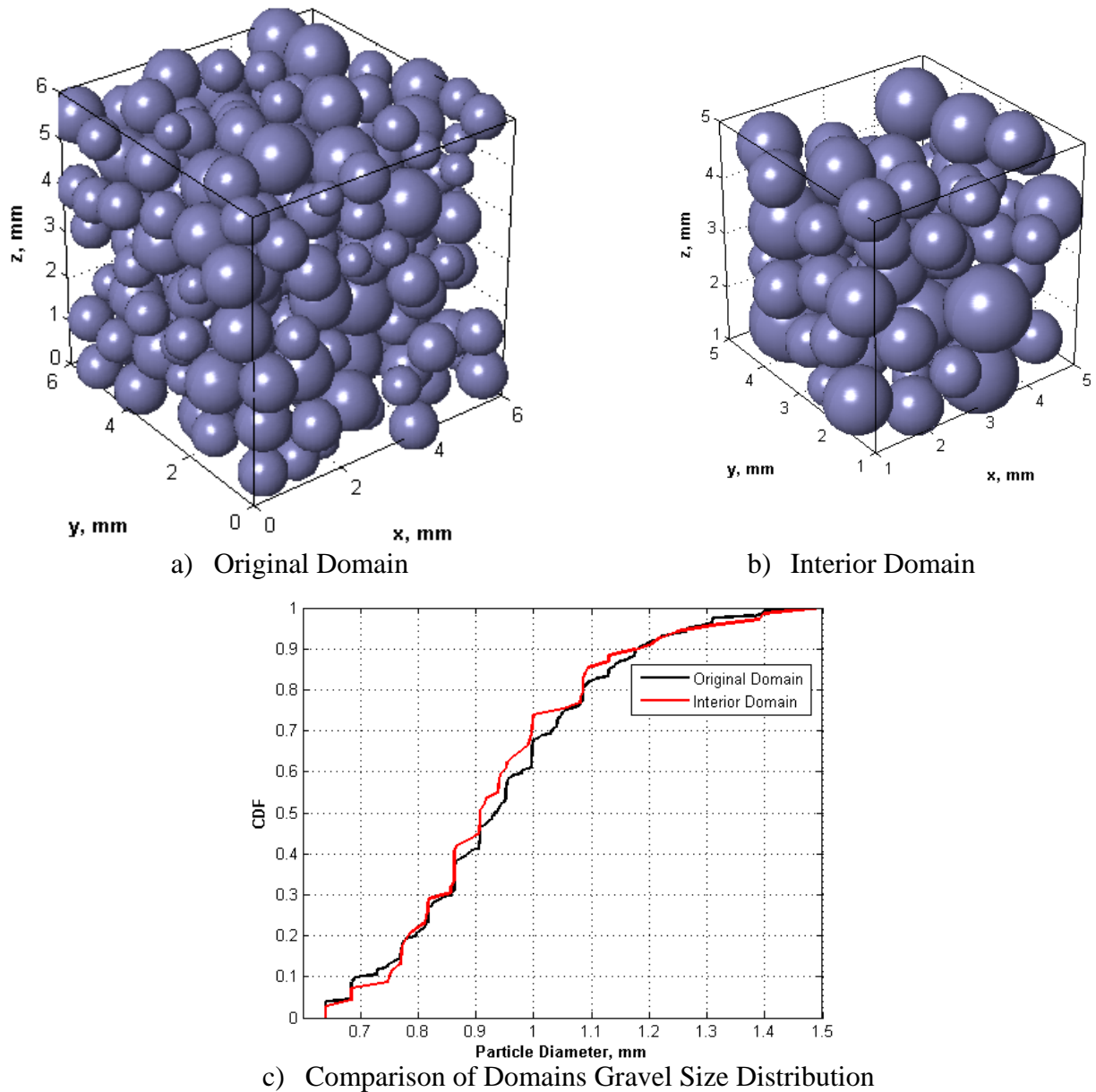


Figure 6.88 Edge Trimming Effect on Gravel Size Distribution

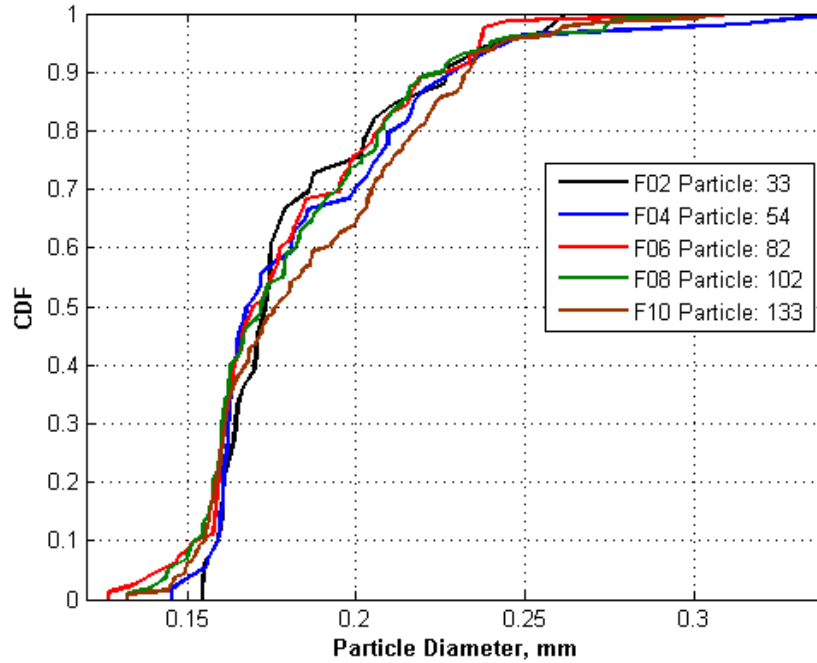
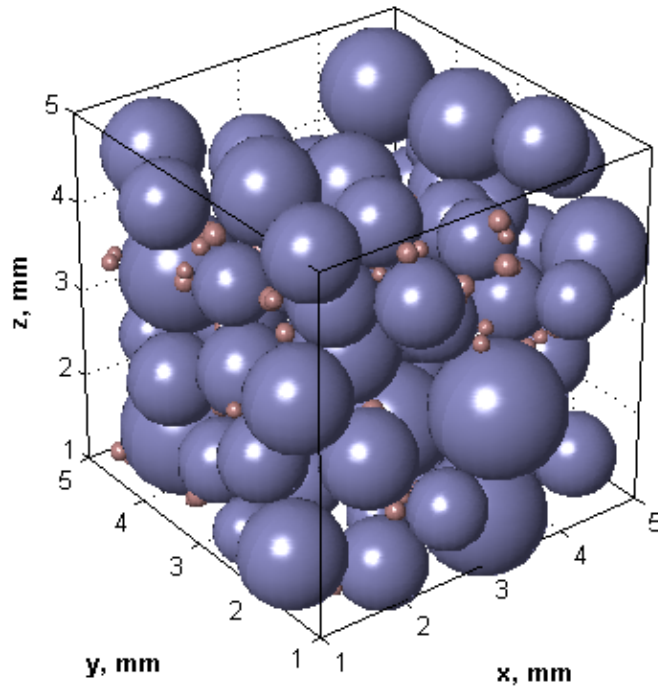


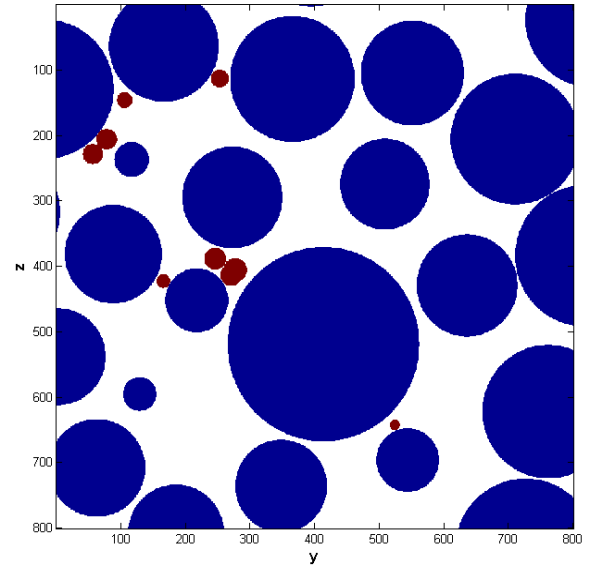
Figure 6.89 Sand Particle Distributions

Figure 6.90 gives the sand particle locations in the gravel pack for the F10 domain and three cross-sectional images taken from center of the domain. Blue and red particles represent the gravel and sand particles, respectively. Sand particles are generally located at the pore throat constraint since in network simulations mechanical straining is the exclusive mechanism for sand plugging.

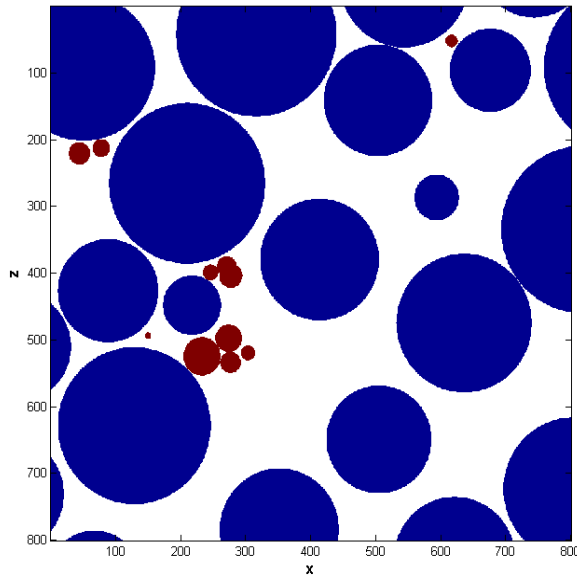
Permeability of each domain is calculated from LBM with two different methods: low pressure difference method and low body force method. Figure 6.91 gives the permeability comparison calculated from the two different methods. The original domain is anisotropic. Permeability is calculated from low body force in  $x$ ,  $y$  and  $z$  directions are  $1.14 \times 10^3$  Darcy,  $1.10 \times 10^3$  Darcy and  $1.28 \times 10^3$  Darcy, respectively. Permeability calculated from the pressure difference method is higher than the value calculated from the body force method. Permeability in the  $x$ ,  $y$  and  $z$  directions are  $1.44 \times 10^3$  Darcy,  $1.44 \times 10^3$  Darcy and  $1.60 \times 10^3$  Darcy, respectively. The permeability difference is up to 34%.



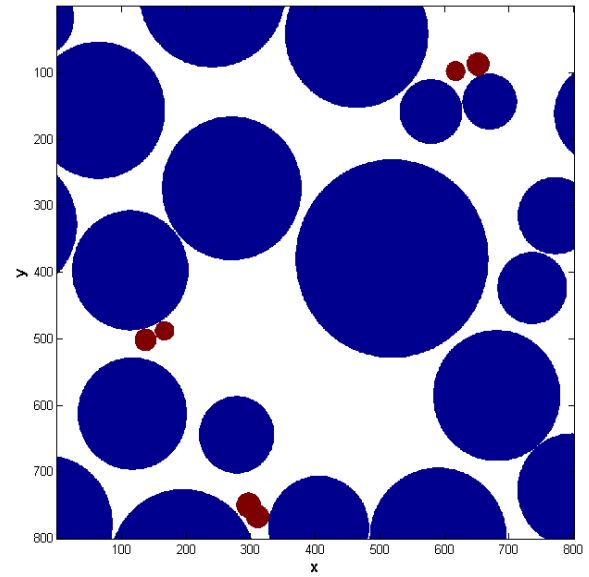
a) Sand Particles in Gravel Pack Domain of F10



b) Y-Z Cross-section Image  
(X= 400 voxel)



c) X-Z Cross-Section Image  
(Y = 400 voxel)



d) X-Y Cross-Section Image  
(Z = 400 voxel)

Figure 6.90 Sand Particle Location in the Domain F10

The calculated permeabilities from two methods have similar trends in each direction. To figure out this difference, the effect of the layer(s) used to create periodicity for low body force method is investigated. The permeability and non-Darcy coefficients calculated for varying layer

numbers between one and five layers are compared (Figure 6.92). The permeability and non-Darcy coefficient are calculated from the intercept and slope of a fit to the Forchheimer equation, respectively. The permeability calculated for one layer is  $1.12 \times 10^3$  Darcy ( $44.36 \text{ voxel}^2$ ), and for five layers is  $1.19 \times 10^3$  Darcy ( $46.89 \text{ voxel}^2$ ). The permeability difference is only 5.38%. Similarly, the difference is not significant comparing permeabilities calculated from the low body force method ( $1.14 \times 10^3$  Darcy), and from the intercept of the Forchheimer equation ( $1.18 \times 10^3$  Darcy), 4.05%. However, there is a significant difference between calculated non-Darcy coefficients. For the one-layer domain, the calculated non-Darcy coefficient is  $2.21 \times 10^4$  1/m ( $0.1107 \text{ 1/voxel}$ ) while for the five-layer domain the calculated non-Darcy coefficient is  $1.69 \times 10^4$  1/m ( $0.0846 \text{ 1/voxel}$ ). The difference between non-Darcy coefficients is 30.82%. For further calculations, five layers are used since few layers are suggested to make the domain periodic for flow to stabilize before flow enters the domain.

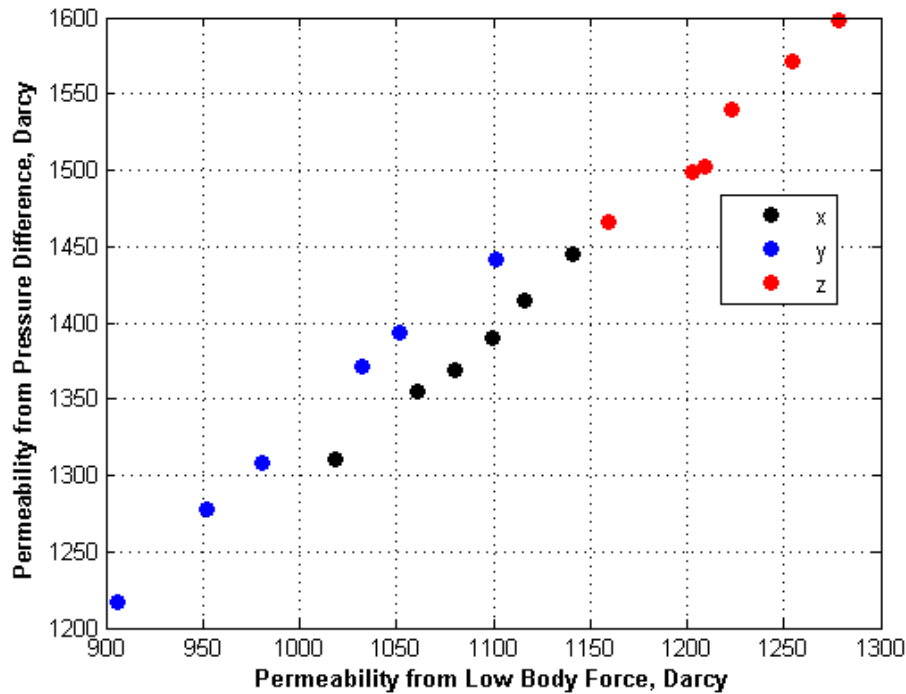


Figure 6.91 Permeability Comparison of Low Body Force Method and Low Pressure Difference Method

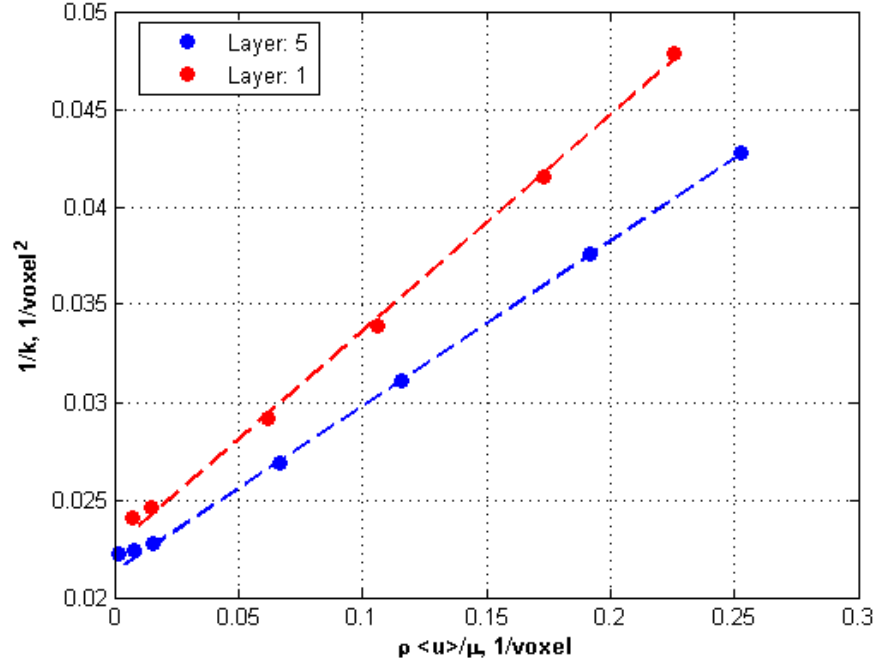
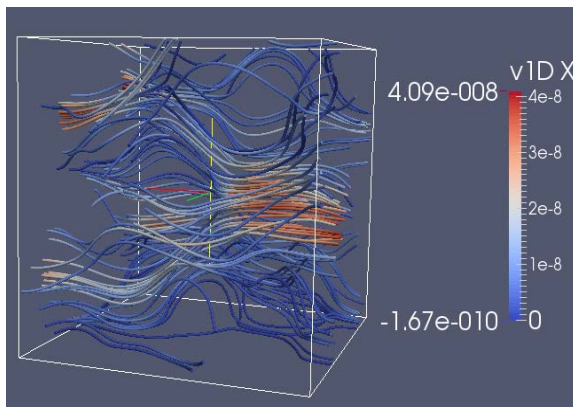


Figure 6.92 Forchheimer Plot for Periodic Domains with 1 Layer and 5 Layers

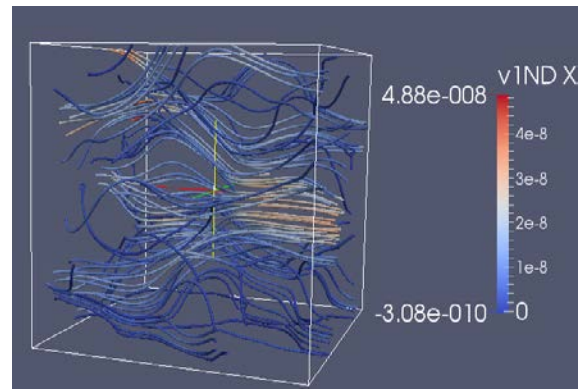
Velocity fields obtained from two methods are compared. To compare the velocity fields, the same input parameters are used; the relaxation parameter and pressure gradient in the  $x$  direction for both methods are 1.0 and  $1.25 \times 10^{-11}$  lu/ts<sup>2</sup>, respectively. Figure 6.93a and Figure 6.93b give streamlines of velocities obtained from the two different methods for the 400x400x400 part of the domain. Velocities are high in the pore throats and low in the pore bodies. Streamlines obtained from two methods are similar. Figure 6.93c gives the velocity difference. Generally, velocities obtained from the low pressure method are higher.

Velocities at different cross-sections are compared to visualize the main differences. Figure 6.94a and Figure 6.94b give the velocity difference between two methods for layer 200 and 300 layers and difference increases pore surface to pore centers. The lines AA' and BB' give the places where velocities in each direction and velocity magnitudes are compared. Solid lines and dashed lines give the velocities obtained from the low pressure difference method and low body force method, respectively. Red, blue, green and magenta colors give the velocities in the

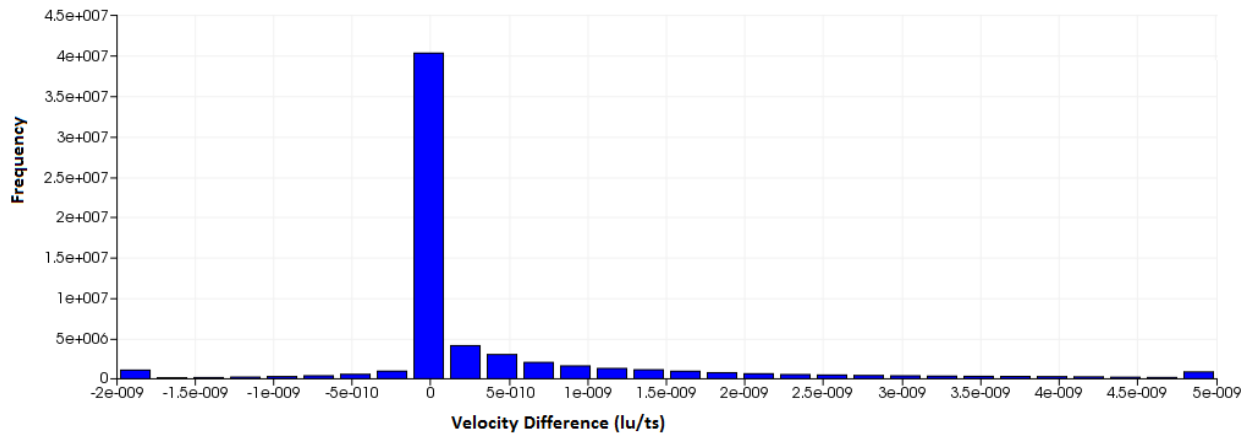
$x$ ,  $y$  and  $z$  directions and velocity magnitude, respectively. Since flow is in the  $x$  direction, the velocity magnitude in the  $x$  direction is greater than in the  $y$  and  $z$  directions. Velocities are zero inside the gravels and they are increases from gravel surface to pore centers. The velocity magnitude from the low pressure difference method is greater than velocities obtained from the low body force method and the difference increases toward pore centers. The velocity differences from two cross-sections indicate that the velocity difference is not random but systematic. This may results from using an unrepresentative domain. For further analysis, the permeability calculated from the low body force method is used because in this method, the pressure in the domain is constant meaning there is no compressibility error.



a) Velocity Field from Low Pressure Difference Method



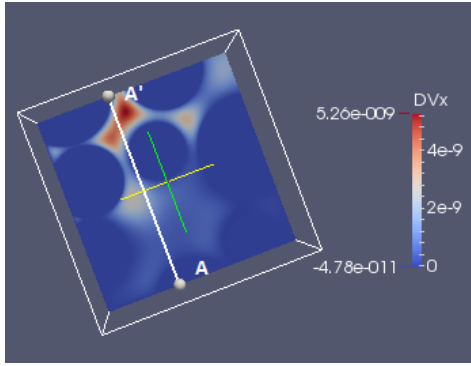
b) Velocity Field from Low Body Force Method



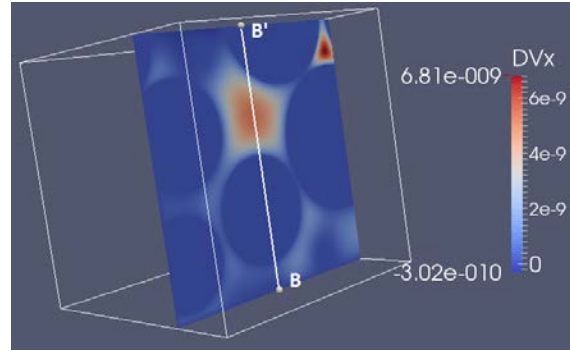
c) Velocity Difference between Two Methods

Figure 6.93 Velocity Field Comparison of Low Body Force Method and Low Pressure Difference Method

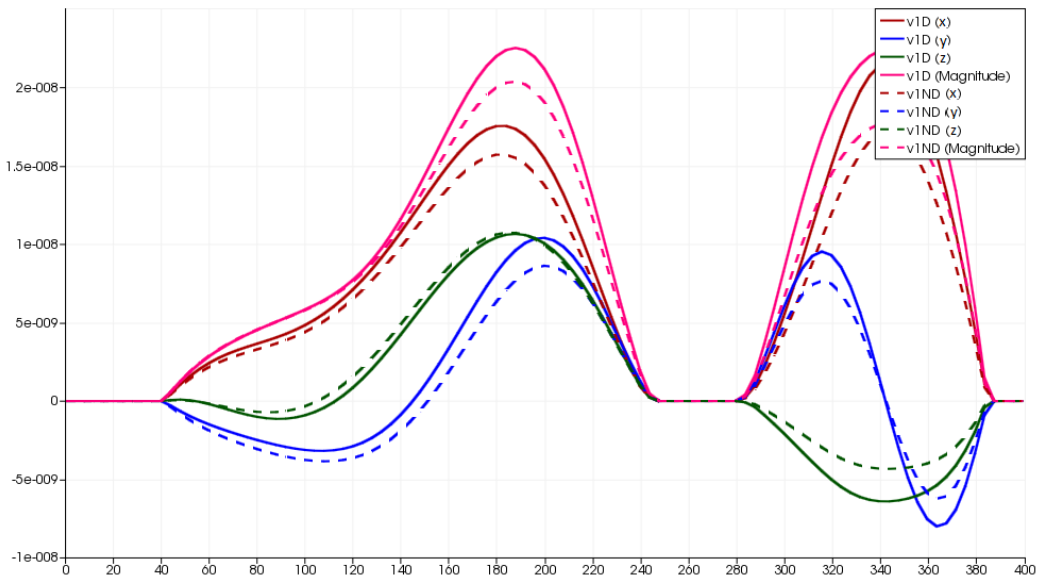




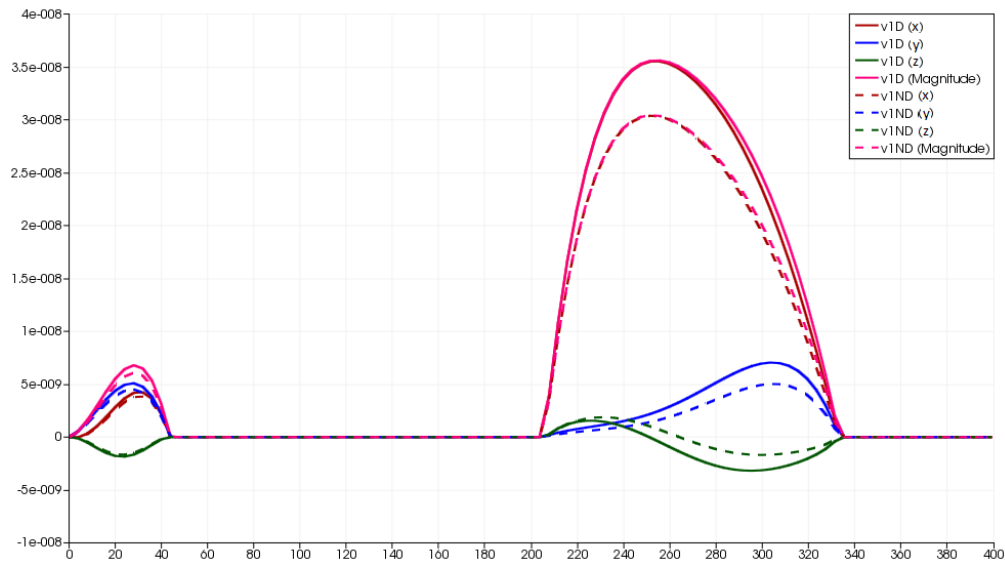
a) Velocity Difference at Layer 200 voxel



b) Velocity Difference at layer 300



c) Velocity Profile along the line AA'



d) Velocity Profile along the line BB'

Figure 6.94 Velocity Comparison of Low Body Force Method and Low Pressure Difference Method

Sand migration simulations are conducted in the  $y$  direction. Permeability changes from  $1.14 \times 10^3$  Darcy for the F00 domain to  $1.02 \times 10^3$  Darcy for the F10 domain (10.76% decrease) in the  $x$  direction. Permeability changes from  $1.10 \times 10^3$  Darcy for domain F00 to 906 Darcy for domain F10 (17.81% decrease) in  $y$  direction. Permeability changes from  $1.28 \times 10^3$  Darcy for domain F00 to  $1.16 \times 10^3$  Darcy for domain F10 (9.28% decrease) in  $z$  direction (Figure 6.91). Permeability decrease in  $y$  direction is about two times more compared to  $x$  and  $z$  directions since sand migration simulations are conducted in  $y$  direction; therefore, pore throats in  $y$  directions are plugged more.

A Kozeny-Carman type relationship is investigated between porosity and permeability for the simulated sand plugging. Results are normalized based on their initial values. Figure 6.95 gives the normalized porosity and permeability in three directions. Black, blue and red dots give the LBM simulation results in  $x$ ,  $y$  and  $z$  directions, respectively. Dashed lines give the curve fits of the Kozeny-Carman type relation (Eqn.6.85). All coefficients are close to one and exponents are 6.512, 11.690 and 5.364 in the  $x$ ,  $y$  and  $z$  directions. The Kozeny-Carman exponent is double the other values in the flow direction,  $y$ , because pore throats were plugged during flow in to that direction are plugged. All Kozeny-Carman exponents are significantly greater than the Kozeny-Carman exponent related with porosity loss due to compaction (3) because in these simulations the domain porosity is decreased due to pore throat plugging where the permeability is much more affected while with compaction, porosity decreases both in pore throat and pore bodies.

$$\begin{aligned} \frac{k_x}{k_{xi}} &= 1.003 \left( \frac{\phi}{\phi_i} \right)^{6.512} \\ \frac{k_y}{k_{yi}} &= 1.001 \left( \frac{\phi}{\phi_i} \right)^{11.690} \end{aligned} \tag{6.85}$$

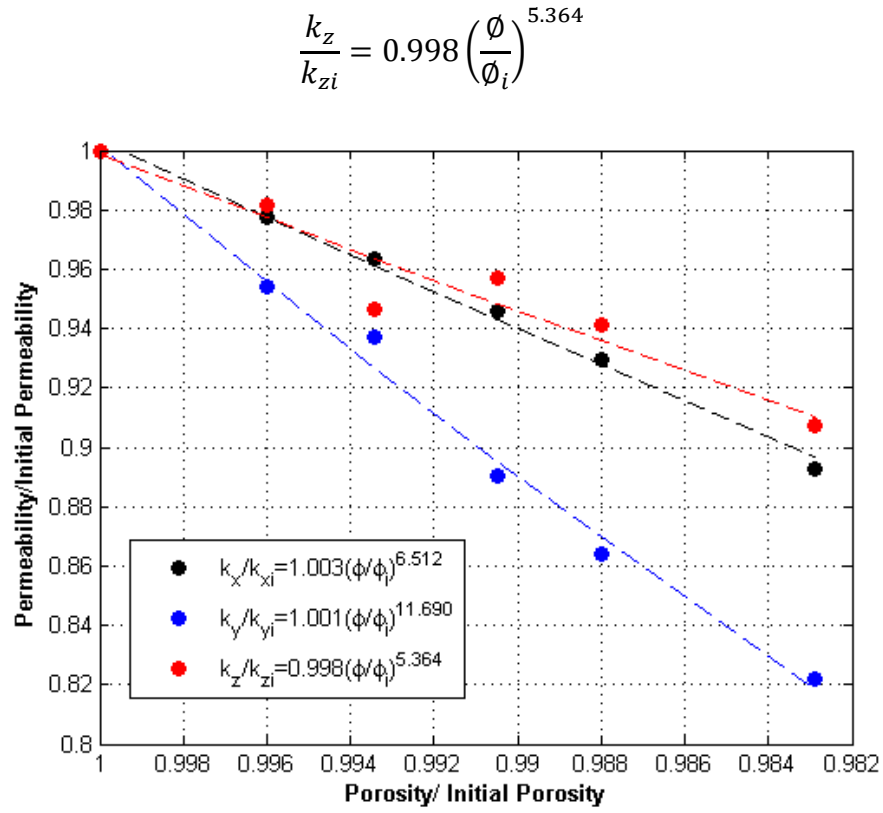


Figure 6.95 Kozeny-Carman Relation of Porosity and Permeability

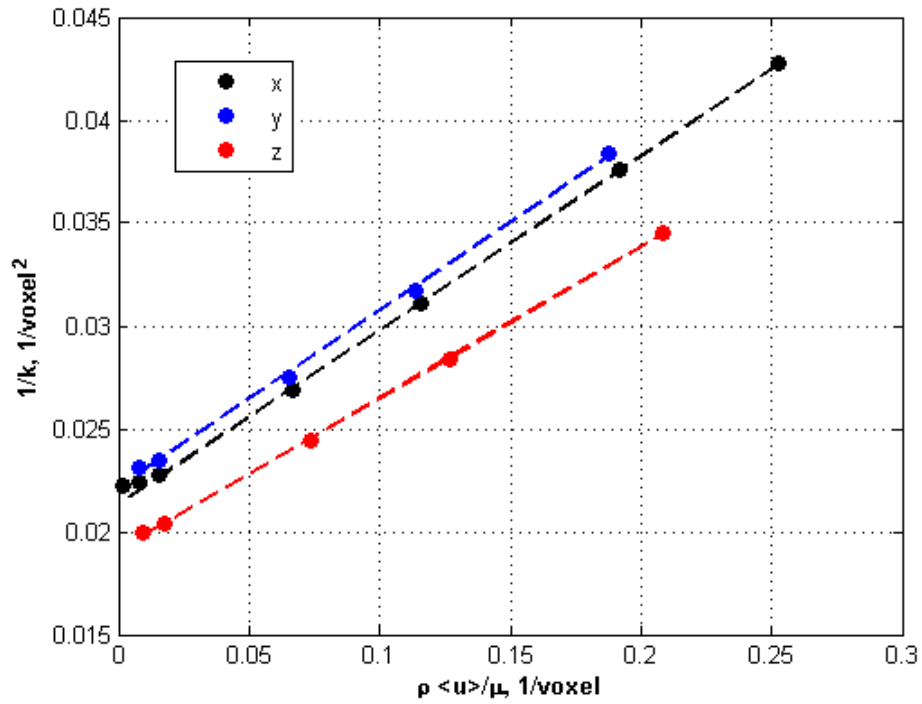


Figure 6.96 Non-Darcy Coefficient of Domain F00

Non-Darcy coefficients in the F00 domain are different in each direction due to anisotropy (Figure 6.96). The non-Darcy coefficient is higher in the  $y$  direction,  $1.71 \times 10^4$  1/m (0.0854 1/voxel) than in the  $x$  direction,  $1.66 \times 10^4$  1/m (0.0829 1/voxel) and  $z$  direction,  $1.47 \times 10^4$  1/m (0.0734 1/voxel).

Figure 6.97 gives the non-Darcy coefficient change with permeability due to sand plugging. Non-Darcy coefficients increase from  $1.66 \times 10^4$  1/m to  $2.02 \times 10^4$  1/m in the  $x$  direction (17.93%), from  $1.71 \times 10^4$  1/m to  $2.42 \times 10^4$  1/m (29.41%) in  $y$  direction, from  $1.47 \times 10^4$  1/m to  $1.74 \times 10^4$  1/m (15.66%) in  $z$  direction. The non-Darcy coefficient increase is twice as large in the  $y$  direction compared to  $x$  and  $z$  directions since the permeability decrease is more in that direction.

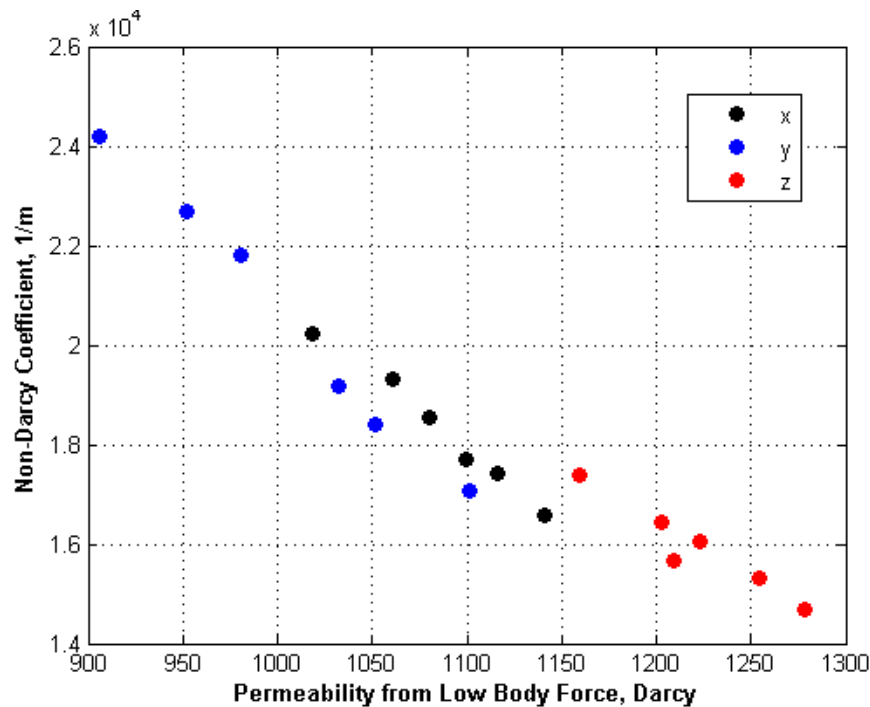


Figure 6.97 Non-Darcy Coefficient Change with Permeability

Similar correlations are developed for porosity and the non-Darcy coefficient. Non-Darcy coefficients are normalized based on their initial values. Figure 6.98 gives the non-Darcy

coefficient ratio change with porosity change in three directions. Black, blue and red dots give the LBM simulations results and dashed lines give the Kozeny-Carman fits. The Kozeny-Carman coefficients are close to one and exponents are -11.71, -21.23 and -9.644 in the  $x$ ,  $y$  and  $z$  directions, respectively (Eqn.6.86). Similar to the porosity-permeability relations, the exponent of the porosity-non-Darcy coefficient is twice in the  $y$  directions relative to the other two directions. The ratios of exponent of porosity – non-Darcy coefficient to exponent of porosity – permeability coefficient are similar; -1.808, -1.816 and -1.798 in  $x$ ,  $y$  and  $z$  directions, respectively. One correlation can be developed based on permeability and non-Darcy coefficient.

$$\begin{aligned}\frac{\beta_x}{\beta_{xi}} &= 0.999 \left( \frac{\phi}{\phi_i} \right)^{-11.77} \\ \frac{\beta_y}{\beta_{yi}} &= 1.003 \left( \frac{\phi}{\phi_i} \right)^{-21.23} \\ \frac{\beta_z}{\beta_{zi}} &= 1.001 \left( \frac{\phi}{\phi_i} \right)^{-9.644}\end{aligned}\tag{6.86}$$

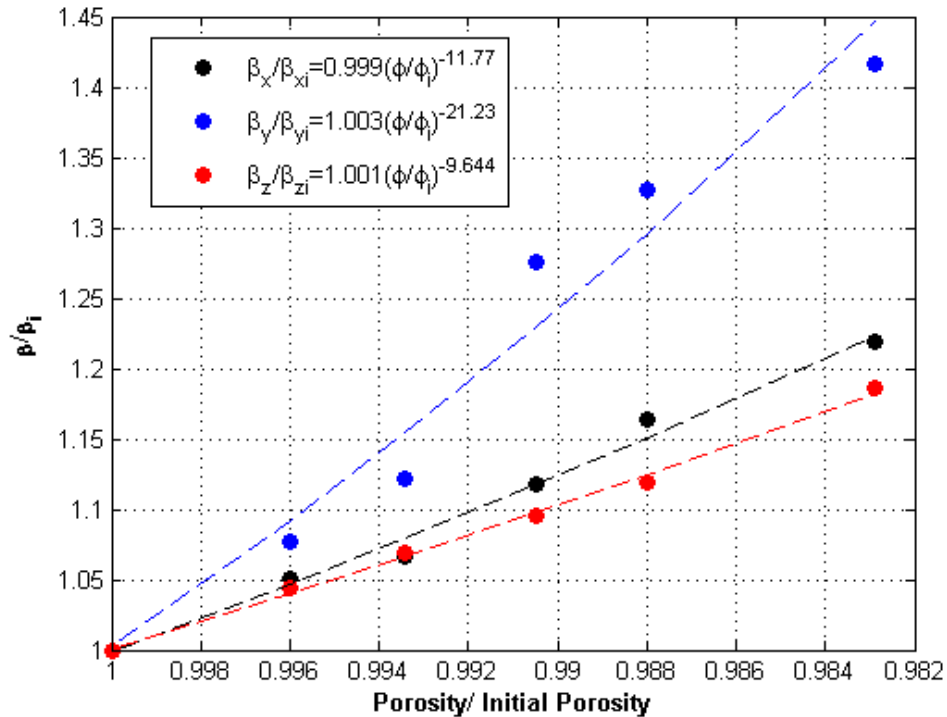


Figure 6.98 Kozeny-Carman Relation of Porosity and Non-Darcy Coefficient

Figure 6.99 gives the non-Darcy coefficient change with permeability change. The trend is similar in all directions; therefore, all data are fitted instead of relying on directional fits (Eqn.6.87). The exponent of permeability - non-Darcy coefficient Kozeny-Carman type relation for sand plugging is higher, -1.830 than the exponent of the one obtained for compaction, -1.303.

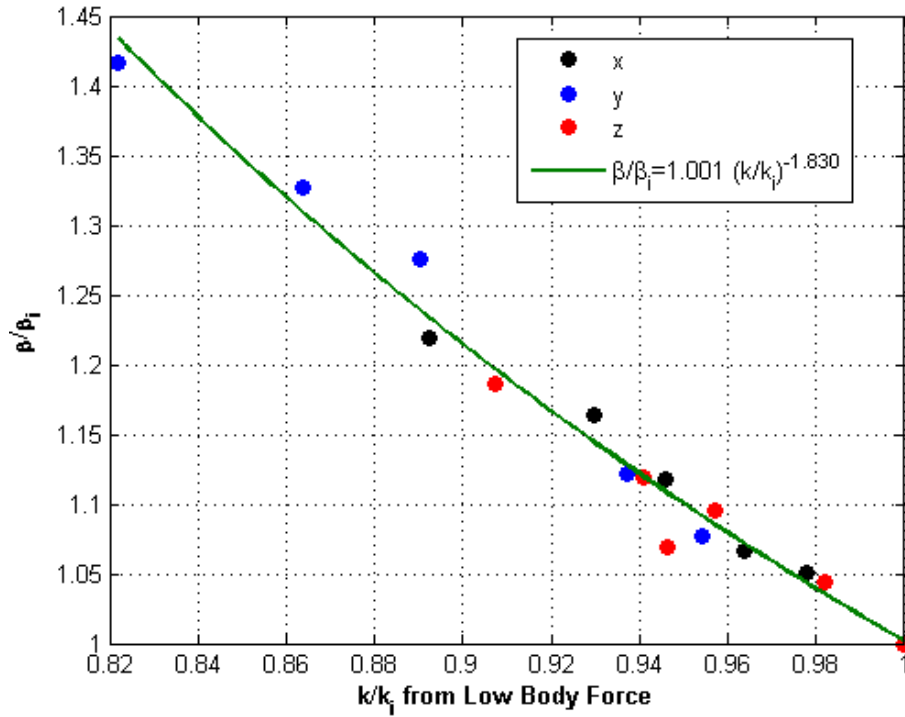


Figure 6.99 Kozeny-Carman Relation of Permeability and Non-Darcy Coefficient

$$\frac{\beta}{\beta_i} = 1.001 \left( \frac{k}{k_i} \right)^{-1.830} \quad (6.87)$$

The non-Darcy coefficients calculated from LBM are compared with non-Darcy coefficients calculated from correlation (Eqn.6.40). For the F00 domain, the differences between non-Darcy coefficients from LBM and the ones calculated from Eqn.6.40 are 16.54%, 17.55% and 10.67% in the  $x$ ,  $y$  and  $z$  directions, respectively. The main problem is that the domain may be unrepresentative. The difference increases up to 33.62% (Figure 6.100). In sand migration, estimation of non-Darcy coefficient from permeability and porosity leads to underestimation.

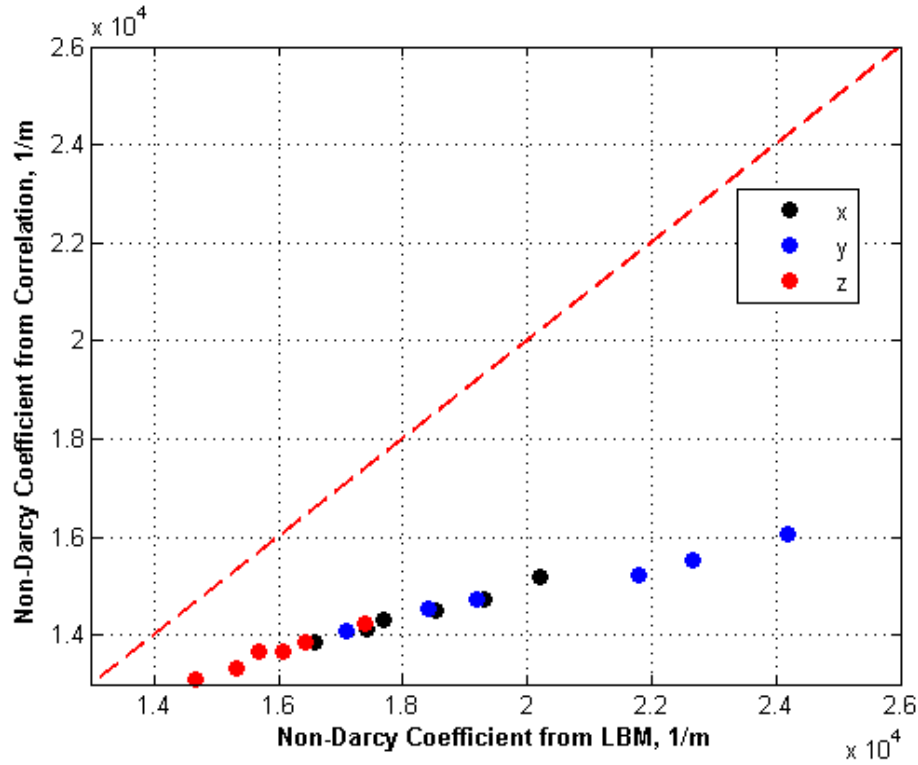


Figure 6.100 Non-Darcy Coefficient Comparison

In reservoir simulations, porosity decrease results from not only pore throat plugging but also pore surface deposition. Based on Kozeny-Carman exponents due to compaction and pore throat plugging, the permeability decrease is more in cases of pore-throat plugging. Therefore, permeability is related to sand concentration. The sand density is chosen as 2670 kg/m<sup>3</sup>. Figure 6.101 gives the permeability ratio change in three directions due to increases in sand concentration at pore throats. Instead of permeability ratio, one minus the permeability ratio is used to find power relation. The exponent of sand concentration is close to unity, which means the permeability ratio decreases almost linearly with increases in sand concentration in each direction (Eqn.6.88).

$$\left(1 - \frac{k_x}{k_{xi}}\right) = 0.00358\sigma_s^{1.134} \quad (6.88)$$

$$\left(1 - \frac{k_y}{k_{yi}}\right) = 0.01028\sigma_s^{0.960}$$

$$\left(1 - \frac{k_z}{k_{zi}}\right) = 0.00571\sigma_s^{0.917}$$

Similar correlations are found between sand concentration and the non-Darcy coefficient.

Figure 6.102 gives the non-Darcy coefficient ratio change in each direction with sand concentration. Similar to the permeability ratio change, the non-Darcy coefficient ratio change is almost linear and direction dependent (Eqn.6.89).

$$\left(\frac{\beta_x}{\beta_{xi}} - 1\right) = 0.00846\sigma_s^{1.093}$$

$$\left(\frac{\beta_y}{\beta_{yi}} - 1\right) = 0.01869\sigma_s^{1.054} \quad (6.89)$$

$$\left(\frac{\beta_z}{\beta_{zi}} - 1\right) = 0.00771\sigma_s^{1.056}$$

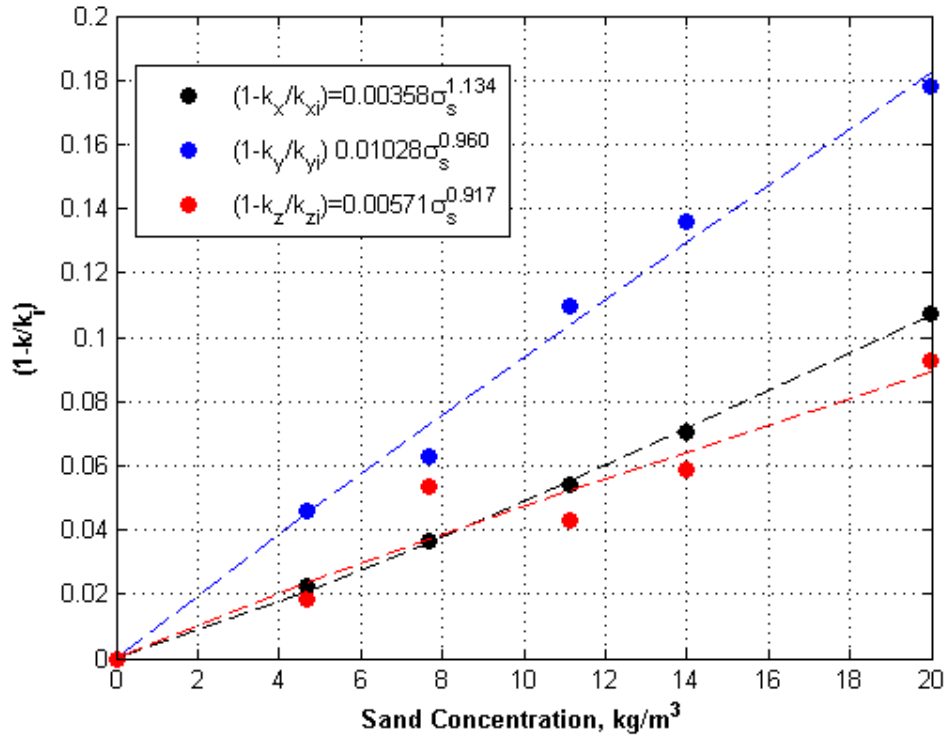


Figure 6.101 Kozeny-Carman Relation of Sand Concentration and Permeability



In literature, permeability changes due to sand migration are updated with a Kozeny-Carman type relation with an exponent equal to three based on porosity reduction (Eqn.6.90) and the non-Darcy coefficient is calculated from correlations (Bouhroum, Liu, & Civan, 1994). This can cause overestimation of permeability and underestimation of inertial effects. Therefore, in reservoir simulation, the sand concentration is used for permeability update (Eqn.6.88) and the non-Darcy coefficient is updated based on permeability reduction (Eqn.6.87).

$$k = k_{initial} \left[ (1 - f)k_p + f \frac{\phi^{n+1}}{\phi_{initial}} \right]^3 \quad (6.90)$$

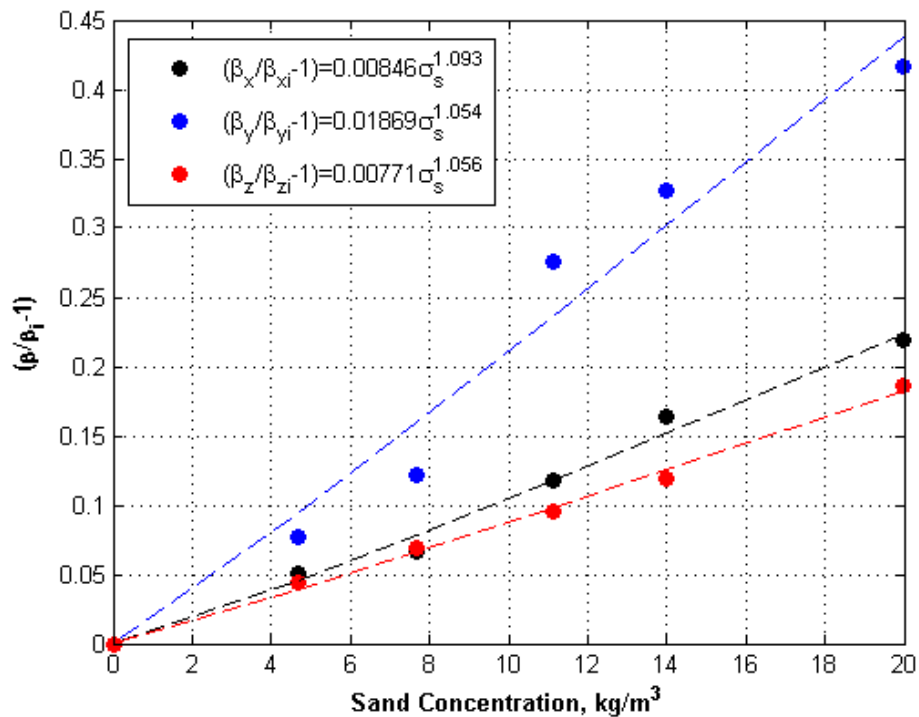


Figure 6.102 Kozeny-Carman Relation of Sand Concentration and Non-Darcy Coefficient

## CHAPTER 7: RESERVOIR-SCALE ANALYSIS

In last two chapters, it is described how reliable flow properties data for reservoir and proppant used in the frac-pack completion can be obtained from lab experiments and correlations. In this part of the study, the findings from the core-scale and pore-scale analyses integrated to reservoir simulator for reliable well productivity estimation. By using the developed simulator, sand migration problem for loosely or unconsolidated reservoirs are investigated with parametric study. Some case studies are illustrated to show how frac-pack completion can mitigate the sand production and how fracture properties such as its dimensions and conductivity affect the sand production.

### 7.1 Simulation Algorithm for Single Phase Flow with Sand Migration

To develop a simulator, flow equation and sand migration equations are coupled and solved implicitly. The detail of equation, how discretize with finite difference method are given below.

The continuity equation for flow of liquid is written as;

$$-\frac{\partial(\rho_l u_{lx})}{\partial x} - \frac{\partial(\rho_l u_{ly})}{\partial y} + \frac{q_{ml}}{V_b} = \frac{\partial(\rho_l \phi S_l)}{\partial t} \quad (7.1)$$

$\rho_l$  and  $S_l$  are fluid density and saturation.  $q_{ml}$  is sink/source term; it is positive for injection and it is negative for production.  $u_{l\alpha}$  and  $\delta_{l\alpha}$  are fluid velocity and controlling parameter.  $\alpha$  indicates the direction of  $x$  or  $y$ . They are defined as;

$$u_{lx} = -\delta_{lx} \frac{k_{apx}}{\mu_l} \frac{\partial P}{\partial x} \quad u_{ly} = -\delta_{ly} \frac{k_{apy}}{\mu_l} \frac{\partial P}{\partial y} \quad (7.2)$$

$$\delta_{lx} = \frac{1}{1 + \frac{\beta_x \rho_l k_{apx}}{\mu_l} |u_{lx}|} \quad \delta_{ly} = \frac{1}{1 + \frac{\beta_y \rho_l k_{apy}}{\mu_l} |u_{ly}|} \quad (7.3)$$

$k_{ap}$  is apparent permeability obtained from Klinkenberg equation.

$$k_{ap} = k \left( 1 + \frac{b}{P_{av}} \right) \quad (7.4)$$

$b$  and  $P_{av}$  are Klinkenberg coefficient and average pressure, respectively.  $\beta$  is non-Darcy coefficient and it is function of permeability. Jones correlation is used for reservoir and developed correlation based on permeability and porosity is used for gravel pack in fracture.

Density and viscosity of the fluid is adjusted for sand concentration as;

$$\rho_l = \rho_l^o + \left( 1 - \frac{\rho_l^o}{\rho_s} \right) C_l \quad (7.5)$$

$$\mu_l = \mu_l^o \left( 1 + 2.5 \frac{C_l}{\rho_s} \right) \quad (7.6)$$

$\rho_l^o$  and  $\mu_l^o$  are pure fluid density and viscosity, respectively.  $C_l$  is concentration of sand particles in fluid  $l$ .  $\rho_s$  is density of sand particle.

Putting Eqn.7.2 into Eqn.7.1;

$$\frac{\partial}{\partial x} \left( \delta_{lx} \frac{k_{apx}}{\mu_l} \rho_l \frac{\partial P}{\partial x} \right) + \frac{\partial}{\partial y} \left( \delta_{ly} \frac{k_{apy}}{\mu_l} \rho_l \frac{\partial P}{\partial y} \right) + \frac{q_{ml}}{V_b} = \frac{\partial(\rho_l \phi S_l)}{\partial t} \quad (7.7)$$

Multiplying Eqn.7.7 with bulk volume,  $V_b = \Delta x \Delta y \Delta z$  and using the definition of area,  $A_x = \Delta y \Delta z$  and  $A_y = \Delta x \Delta z$ , Eqn.7.7 can be written as;

$$\frac{\partial}{\partial x} \left( \delta_{lx} \frac{k_{apx}}{\mu_l} A_x \rho_l \frac{\partial P}{\partial x} \right) \Delta x + \frac{\partial}{\partial y} \left( \delta_{ly} \frac{k_{apy}}{\mu_l} A_y \rho_l \frac{\partial P}{\partial y} \right) \Delta y + q_{ml} = V_b \frac{\partial(\rho_l \phi S_l)}{\partial t} \quad (7.8)$$

The first term of Eqn.7.8 is discretized as;

$$\begin{aligned} & \frac{\partial}{\partial x} \left( \delta_{lx} \frac{k_{apx}}{\mu_l} A_x \rho_l \frac{\partial P}{\partial x} \right) \Delta x \\ &= \frac{1}{\Delta x} \left[ \left( \delta_{lx} \frac{k_{apx}}{\mu_l} A_x \rho_l \frac{\partial P}{\partial x} \right)_{i+\frac{1}{2},j} - \left( \delta_{lx} \frac{k_{apx}}{\mu_l} A_x \rho_l \frac{\partial P}{\partial x} \right)_{i-\frac{1}{2},j} \right] \Delta x \\ &= \left( \delta_{lx} \frac{k_{apx}}{\mu_l} \frac{A_x}{\Delta x} \rho_l \right)_{i+\frac{1}{2},j} (P_{i+1,j} - P_{i,j}) - \left( \delta_{lx} \frac{k_{apx}}{\mu_l} \frac{A_x}{\Delta x} \rho_l \right)_{i-\frac{1}{2},j} (P_{i,j} - P_{i-1,j}) \end{aligned} \quad (7.9)$$

Similarly second term of Eqn.7.8 is discretized as;

$$\begin{aligned} & \frac{\partial}{\partial y} \left( \delta_{ly} \frac{k_{ap y}}{\mu_l} A_y \rho_l \frac{\partial P}{\partial y} \right) \Delta y \\ &= \left( \delta_{ly} \frac{k_{ap y}}{\mu_l} \frac{A_y}{\Delta y} \rho_l \right)_{i,j+\frac{1}{2}} (P_{i,j+1} - P_{i,j}) - \left( \delta_{ly} \frac{k_{ap y}}{\mu_l} \frac{A_y}{\Delta y} \rho_l \right)_{i,j-\frac{1}{2}} (P_{i,j} - P_{i,j-1}) \end{aligned} \quad (7.10)$$

Defining the transmissibility terms as;

$$T_{l i \pm \frac{1}{2}, j} = \left( \delta_{lx} \frac{k_{ap x}}{\mu_l} \frac{A_x}{\Delta x} \rho_l \right)_{i \pm \frac{1}{2}, j} \quad T_{l i, j \pm \frac{1}{2}} = \left( \delta_{ly} \frac{k_{ap y}}{\mu_l} \frac{A_y}{\Delta y} \rho_l \right)_{i, j \pm \frac{1}{2}} \quad (7.11)$$

Using the transmissibility definition, the Eqn.7.9 and Eqn.7.10 can be written in short notation as;

$$\frac{\partial}{\partial x} \left( \delta_{lx} \frac{k_{ap x}}{\mu_l} A_x \rho_l \frac{\partial P}{\partial x} \right) \Delta x = T_{l i+\frac{1}{2}, j} (P_{i+1, j} - P_{i, j}) - T_{l i-\frac{1}{2}, j} (P_{i, j} - P_{i-1, j}) \quad (7.12)$$

$$\frac{\partial}{\partial y} \left( \delta_{ly} \frac{k_{ap y}}{\mu_l} A_y \rho_l \frac{\partial P}{\partial y} \right) \Delta y = T_{l i, j+\frac{1}{2}} (P_{i, j+1} - P_{i, j}) - T_{l i, j-\frac{1}{2}} (P_{i, j} - P_{i, j-1}) \quad (7.13)$$

Time derivative of Eqn.7.8 is discretized with conservative expansion;

$$\frac{\partial(\rho_l \emptyset)}{\partial t} = \emptyset^n \frac{\partial \rho_l}{\partial t} + \rho_l^{n+1} \frac{\partial \emptyset}{\partial t} \quad (7.14)$$

Density derivative is calculated from Eqn.7.5, density is function of concentration and pressure,

$\rho_l = f(C_l, P)$ . Using the chain rule, density derivative is extended as;

$$\frac{\partial \rho_l}{\partial t} = \frac{\partial \rho_l}{\partial C_l} \frac{\partial C_l}{\partial t} + \frac{\partial \rho_l}{\partial P} \frac{\partial P}{\partial t} \quad (7.15)$$

$$\frac{\partial \rho_l}{\partial C_l} = \left( 1 - \frac{\rho_l^o}{\rho_s} \right) \quad (7.16)$$

$$\frac{\partial \rho_l}{\partial P} = \frac{\partial \rho_l^o}{\partial t} - \frac{C_l}{\rho_s} \frac{\partial \rho_l^o}{\partial t} \quad (7.17)$$

Using the definition of liquid compressibility,  $c_l$ , pressure derivative of pure liquid density can be written as;

$$\frac{\partial \rho_l^o}{\partial P} = \rho_l^o c_l \quad (7.18)$$

Using Eqn.7.16 through Eqn.7.18, Eqn.7.15 is written as;

$$\frac{\partial \rho_l}{\partial t} = \left(1 - \frac{\rho_l^o}{\rho_s}\right) \frac{\partial C_l}{\partial t} + \left(1 - \frac{C_l}{\rho_s}\right) \rho_l^o c_l \frac{\partial P}{\partial t} \quad (7.19)$$

For porosity derivative, porosity is defined as a sum of fluid porosity and solid porosity;

$$\emptyset = \emptyset_f + \emptyset_s \quad (7.20)$$

It is assumed that pressure only has an effect on the pore space filled with liquid,  $\emptyset_f$  and sand particles are assumed to be incompressible. Therefore, fluid porosity is updated based on pressure change based on reference pressure,  $P^o$

$$\emptyset_f = (\emptyset^o - \emptyset_s)[1 + c_\emptyset(P - P^o)] \quad (7.21)$$

$c_\emptyset$  and  $\emptyset^o$  are pore volume compressibility and porosity at reference pressure. Solid porosity is calculated from fluid solid concentration,  $C_l$ , and sand particle density,  $\rho_s$ , as;

$$\emptyset_s = \frac{C_l + C_f}{\rho_s} \quad (7.22)$$

In Eqn.7.22, subscript,  $f$ , indicates irreducible fluid. Using Eqn.7.21 and Eqn.7.22, Eqn.7.20 is written as;

$$\emptyset = \left(\emptyset^o - \frac{C_l + C_f}{\rho_s}\right)[1 + c_\emptyset(P - P^o)] + \frac{C_l + C_f}{\rho_s} \quad (7.23)$$

Porosity is function of sand concentration and pressure,  $\emptyset = f(C_l, C_f, P)$ . Time derivative of porosity is extended from chain rule as;

$$\frac{\partial \emptyset}{\partial t} = \frac{\partial \emptyset}{\partial C_l} \frac{\partial C_l}{\partial t} + \frac{\partial \emptyset}{\partial C_f} \frac{\partial C_f}{\partial t} + \frac{\partial \emptyset}{\partial P} \frac{\partial P}{\partial t} \quad (7.24)$$

$$\frac{\partial \emptyset}{\partial C_l} = -\frac{1}{\rho_s} [1 + c_\emptyset(P - P^o)] + \frac{1}{\rho_s} = -\frac{1}{\rho_s} c_\emptyset(P - P^o) \quad (7.25)$$

For the irreducible phase,  $\partial C_f / \partial t$  is 0.

$$\frac{\partial \phi}{\partial P} = \left( \phi^o - \frac{C_l + C_f}{\rho_s} \right) c_\phi \quad (7.26)$$

Using the Eqn.7.25 and Eqn.7.26, Eqn.7.24 is written as;

$$\frac{\partial \phi}{\partial t} = \frac{\partial \phi}{\partial C_l} \frac{\partial C_l}{\partial t} + \frac{\partial \phi}{\partial P} \frac{\partial P}{\partial t} = -\frac{1}{\rho_s} c_\phi (P - P^o) \frac{\partial C_l}{\partial t} + \left( \phi^o - \frac{C_l + C_f}{\rho_s} \right) c_\phi \frac{\partial P}{\partial t} \quad (7.27)$$

Combining density and porosity derivatives, time derivative, Eqn.7.14, becomes;

$$\begin{aligned} \frac{\partial(\rho_l \phi)}{\partial t} &= \phi^n \left[ \left( 1 - \frac{\rho_{lav}^o}{\rho_s} \right) \frac{\partial C_l}{\partial t} + \left( 1 - \frac{C_{lav}}{\rho_s} \right) \rho_{lav}^o c_{lav} \frac{\partial P}{\partial t} \right] \\ &\quad + \rho_l^{n+1} \left[ -\frac{1}{\rho_s} c_\phi (P_{av} - P^o) \frac{\partial C_l}{\partial t} + \left( \phi_{av}^o - \frac{C_{lav} + C_{fav}}{\rho_s} \right) c_\phi \frac{\partial P}{\partial t} \right] \\ &= \left[ \phi^n \left( 1 - \frac{\rho_{lav}^o}{\rho_s} \right) - \frac{\rho_l^{n+1}}{\rho_s} c_\phi (P_{av} - P^o) \right] \frac{\partial C_l}{\partial t} \\ &\quad + \left[ \phi^n \left( 1 - \frac{C_{lav}}{\rho_s} \right) \rho_{lav}^o c_{lav} + \rho_l^{n+1} \left( \phi_{av}^o - \frac{C_{lav} + C_{fav}}{\rho_s} \right) c_\phi \right] \frac{\partial P}{\partial t} \end{aligned} \quad (7.28)$$

Left hand side of the Eqn.7.8 is discretized as;

$$\begin{aligned} V_b S_l \frac{\partial(\rho_l \phi)}{\partial t} &= (V_b S_l)_{i,j} \left[ \phi^n \left( 1 - \frac{\rho_{lav}^o}{\rho_s} \right) - \frac{\rho_l^{n+1}}{\rho_s} c_\phi (P_{av} - P^o) \right]_{i,j} \frac{C_{l,i,j}^{n+1} - C_{l,i,j}^n}{\Delta t} \\ &\quad + (V_b S_l)_{i,j} \left[ \phi^n \left( 1 - \frac{C_{lav}}{\rho_s} \right) \rho_{lav}^o c_{lav} \right. \\ &\quad \left. + \rho_l^{n+1} \left( \phi_{av}^o - \frac{C_{lav} + C_{fav}}{\rho_s} \right) c_\phi \right]_{i,j} \frac{P_{i,j}^{n+1} - P_{i,j}^n}{\Delta t} \end{aligned} \quad (7.29)$$

Defining the concentration,  $T_{lc}$ , and pressure terms,  $T_{lp}$ , as;

$$T_{lc} = \frac{V_b S_l}{\Delta t} \left[ \phi^n \left( 1 - \frac{\rho_{lav}^o}{\rho_s} \right) - \frac{\rho_l^{n+1}}{\rho_s} c_\phi (P_{av} - P^o) \right] \quad (7.30)$$

$$T_{lp} = \frac{V_b S_l}{\Delta t} \left[ \phi^n \left( 1 - \frac{C_{lav}}{\rho_s} \right) \rho_{lav}^o c_{lav} + \rho_l^{n+1} \left( \phi_{av}^o - \frac{C_{lav} + C_{fav}}{\rho_s} \right) c_\phi \right] \quad (7.31)$$

Eqn.7.8 is written in compact form as;

$$\begin{aligned}
& T_{l\ i+\frac{1}{2},j}(P_{i+1,j} - P_{i,j}) - T_{l\ i-\frac{1}{2},j}(P_{i,j} - P_{i-1,j}) + T_{l\ i,j+\frac{1}{2}}(P_{i,j+1} - P_{i,j}) \\
& - T_{l\ i,j-\frac{1}{2}}(P_{i,j} - P_{i,j-1}) + q_{ml\ i,j} \\
& = T_{lc\ i,j}(C_{l\ i,j}^{n+1} - C_{l\ i,j}^n) + T_{lp\ i,j}(P_{i,j}^{n+1} - P_{i,j}^n)
\end{aligned} \tag{7.32}$$

Arranging the equations for unknown pressures to solve implicitly, Eqn.7.32 can be written as for gas flow;

$$\begin{aligned}
& (P_{g\ i+1,j})^{v+1} \left( T_{g\ i+\frac{1}{2},j} \right)^v \left( T_{g\ i+\frac{1}{2},j} \right)^{n+1} + (P_{g\ i-1,j})^{v+1} \left( T_{g\ i-\frac{1}{2},j} \right)^v \left( T_{g\ i-\frac{1}{2},j} \right)^{n+1} \\
& + (P_{g\ i,j+1})^{v+1} \left( T_{g\ i,j+\frac{1}{2}} \right)^v \left( T_{g\ i,j+\frac{1}{2}} \right)^{n+1} + (P_{g\ i,j-1})^{v+1} \left( T_{g\ i,j-\frac{1}{2}} \right)^v \left( T_{g\ i,j-\frac{1}{2}} \right)^{n+1} \\
& + (P_{g\ i,j})^{v+1} \left[ - \left( T_{g\ i+\frac{1}{2},j} \right)^v \left( T_{g\ i+\frac{1}{2},j} \right)^{n+1} - \left( T_{g\ i-\frac{1}{2},j} \right)^v \left( T_{g\ i-\frac{1}{2},j} \right)^{n+1} - \left( T_{g\ i,j+\frac{1}{2}} \right)^v \left( T_{g\ i,j+\frac{1}{2}} \right)^{n+1} \right. \\
& \left. - \left( T_{g\ i,j-\frac{1}{2}} \right)^v \left( T_{g\ i,j-\frac{1}{2}} \right)^{n+1} - (T_{gp\ i,j})^v \right] \\
& = -q_{ml\ i,j} + (T_{gc\ i,j})^v \left[ (C_{g\ i,j})^{n+1} - (C_{g\ i,j})^n \right] \\
& - (T_{gp\ i,j})^v (P_{g\ i,j})^n
\end{aligned} \tag{7.33}$$

$n$  and  $n + 1$  are the old and new time steps.  $v$  and  $v + 1$  are old and new iterations.

Sand migration equation is given as;

$$- \frac{\partial(u_{lx}C_l)}{\partial x} - \frac{\partial(u_{ly}C_l)}{\partial y} + \frac{q_{cl}}{V_b} = S_l \frac{\partial(\phi C_l)}{\partial t} + R_l \tag{7.34}$$

Multiply Eqn.7.34 with bulk volume,  $V_b = \Delta x \Delta y \Delta z$  and use the area definitions,  $A_x = \Delta y \Delta z$  and  $A_y = \Delta x \Delta z$ , Eqn.7.34 is written as;

$$- \frac{\partial(u_{lx}C_l A_x)}{\partial x} \Delta x - \frac{\partial(u_{ly}C_l A_y)}{\partial y} \Delta y + q_{cl} = V_b S_l \frac{\partial(\phi C_l)}{\partial t} + V_b R_l \tag{7.35}$$

The space dependent terms are extended with central difference formula as;

$$\begin{aligned} \frac{\partial(u_{lx}C_lA_x)}{\partial x}\Delta x &= \frac{1}{\Delta x}\left[(u_{lx}C_lA_x)_{i+\frac{1}{2},j} - (u_{lx}C_lA_x)_{i-\frac{1}{2},j}\right]\Delta x \\ &= (u_{lx}A_x)_{i+\frac{1}{2},j}C_{l\ i+\frac{1}{2},j} - (u_{lx}A_x)_{i-\frac{1}{2},j}C_{l\ i+\frac{1}{2},j} \end{aligned} \quad (7.36)$$

Similarly, in y direction space dependent term is expanded as;

$$\frac{\partial(u_{ly}C_lA_y)}{\partial y}\Delta y = (u_{ly}A_y)_{i,j+\frac{1}{2}}C_{l\ i,j+\frac{1}{2}} - (u_{ly}A_y)_{i,j-\frac{1}{2}}C_{l\ i,j-\frac{1}{2}} \quad (7.37)$$

Velocities at block boundaries are obtained from pressure equations. The concentrations at block boundaries are estimated from upwinding as;

$$\begin{aligned} C_{l\ i\pm\frac{1}{2},j} &= C_{l\ i,j} \quad \text{if} \quad P_{i,j} > P_{i\pm 1,j} \\ C_{l\ i\pm\frac{1}{2},j} &= C_{l\ i\pm 1,j} \quad \text{if} \quad P_{i\pm 1,j} > P_{i,j} \\ C_{l\ i,j\pm\frac{1}{2}} &= C_{l\ i,j} \quad \text{if} \quad P_{i,j} > P_{i,j\pm 1} \\ C_{l\ i,j\pm\frac{1}{2}} &= C_{l\ i,j\pm 1} \quad \text{if} \quad P_{i,j\pm 1} > P_{i,j} \end{aligned} \quad (7.38)$$

Time derivative of Eqn.7.34 is expanded with chain rule and similar to time derivative of pressure equation, conservative expansion is use.

$$\frac{\partial(\phi C_l)}{\partial t} = C_l^n \frac{\partial \phi}{\partial t} + \phi^{n+1} \frac{\partial C_l}{\partial t} \quad (7.39)$$

For porosity derivative with respect to time, Eqn.7.27 is used.

$$\begin{aligned} \frac{\partial(\phi C_l)}{\partial t} &= C_l^n \left[ -\frac{1}{\rho_s} c_\phi (P_{av} - P^o) \frac{\partial C_l}{\partial t} + \left( \phi_{av}^o - \frac{C_{lav} + C_{fav}}{\rho_s} \right) c_\phi \frac{\partial P}{\partial t} \right] + \phi^{n+1} \frac{\partial C_l}{\partial t} \\ &= \left[ \phi^{n+1} - \frac{C_l^n}{\rho_s} c_\phi (P_{av} - P^o) \right] \frac{\partial C_l}{\partial t} + C_l^n \left( \phi_{av}^o - \frac{C_{lav} + C_{fav}}{\rho_s} \right) c_\phi \frac{\partial P}{\partial t} \end{aligned} \quad (7.40)$$

Time derivative term of Eqn.7.35 is discretized as;



$$\begin{aligned}
V_b S_l \frac{\partial(\phi C_l)}{\partial t} = & [V_b S_l]_{i,j} \left[ \phi^{n+1} - \frac{C_l^n}{\rho_s} c_\phi (P_{av} - P^o) \right]_{i,j} \frac{C_{l,i,j}^{n+1} - C_{l,i,j}^n}{\Delta t} \\
& + [V_b S_l]_{i,j} \left[ C_l^n \left( \phi_{av}^o - \frac{C_{lav} + C_{fav}}{\rho_s} \right) c_\phi \right]_{i,j} \frac{P_{i,j}^{n+1} - P_{i,j}^n}{\Delta t}
\end{aligned} \quad (7.41)$$

Defining the concentration,  $R_{cl}$ , and pressure,  $R_{pl}$ , dependent terms as;

$$R_{cl} = \frac{V_b S_l}{\Delta t} \left[ \phi^{n+1} - \frac{C_l^n}{\rho_s} c_\phi (P_{av} - P^o) \right] \quad (7.42)$$

$$R_{pl} = \frac{V_b S_l C_l^n}{\Delta t} \left( \phi_{av}^o - \frac{C_{lav} + C_{fav}}{\rho_s} \right) c_\phi \quad (7.43)$$

The term  $R_l$  in Eqn.7.35 is the net rate loss of solid particles and it is defined as;

$$R_l = \frac{\partial \sigma_l}{\partial t} + \frac{\partial \sigma_l^*}{\partial t} \quad (7.44)$$

$\sigma_l$  is the mass of solid particles available in the pore bodies in contact with fluid  $l$  per unit bulk volume of porous media.  $\sigma_l^*$  is the mass solid particles captured by plugging or bridging at pore throats from fluid  $l$  per unit bulk volume of porous media. The terms in  $R_l$  are calculated with rate equations (Xinghui Liu & Civan, 1993).

Retention and entrainment of particles in pore bodies is defined with rate equation as;

$$\frac{\partial \sigma_l}{\partial t} = k_{dl} \|u_{lav}\| C_{lav} - k_{el} \sigma_{lav} (\|u_{lav}\| - u_{lc}) \quad (7.45)$$

$k_{dl}$  and  $k_{el}$  are rate coefficients for the surface retention and entrainment of solid particles in fluid  $l$ .  $u_{lc}$  is critical velocity for fluid  $l$ . If fluid velocity,  $u_l$ , is less than the critical velocity,  $k_{el}$  is 0 since there is no entrainment of solid particles. In order to calculate the surface retention and entrainment, the velocities at the block centers should be known. Block center velocities are calculated by averaging the boundary velocities as;

$$u_{lx\ i,j} = \frac{u_{lx\ i+\frac{1}{2},j} + u_{lx\ i-\frac{1}{2},j}}{2} \quad u_{ly\ i,j} = \frac{u_{ly\ i,j+\frac{1}{2}} + u_{ly\ i,j-\frac{1}{2}}}{2} \quad (7.46)$$

Then velocity magnitude is calculated as;

$$\|u_l\|_{i,j} = \sqrt{(u_{lx\ i,j})^2 + (u_{ly\ i,j})^2} \quad (7.47)$$

Eqn.7.45 is discretized as;

$$\frac{\sigma_{l\ i,j}^{n+1} - \sigma_{l\ i,j}^n}{\Delta t} = k_{dl}(\|u_{l\ av}\| C_{l\ av})_{i,j}^{n+1} - k_{el} \sigma_{l\ av\ i,j}^{n+1} \left( \|u_{l\ av}\|^{n+1} - u_{lc} \right) \quad (7.48)$$

Retention of solid particles in pore throats is defined as;

$$\frac{\partial \sigma_l^*}{\partial t} = k_{ptl} \|u_{l\ av}\| C_{l\ av} \quad (7.49)$$

$k_{ptl}$  is rate constant for pore throats plugged by solid particles in fluid  $l$ . If flow efficiency factor,  $f$ , is less than minimum flow efficiency factor,  $f_{min}$ , then  $k_{ptl}$  is 0.  $f$  gives the fraction of pore throat that are not plugged with solid particles (Eqn.7.50). Fraction of pore throats never plugged with solid particles is represented with  $f_{min}$ .

$$f = 1 - k_{fe} \sigma_l^* \quad (7.50)$$

$k_{fe}$  is characteristic constant reflecting the properties of pore throats and solid particles. Eqn.7.49 is discretized as;

$$\frac{\sigma_{l\ i,j}^{*n+1} - \sigma_{l\ i,j}^{*n}}{\Delta t} = k_{ptl} (\|u_{l\ av}\| C_{l\ av})_{i,j}^{n+1} \quad (7.51)$$

Eqn.7.35 is written as;

$$\begin{aligned} & -(u_{lx} A_x)_{i+\frac{1}{2},j} C_{l\ i+\frac{1}{2},j} + (u_{lx} A_x)_{i-\frac{1}{2},j} C_{l\ i-\frac{1}{2},j} - (u_{ly} A_y)_{i,j+\frac{1}{2}} C_{l\ i,j+\frac{1}{2}} \\ & + (u_{ly} A_y)_{i,j-\frac{1}{2}} C_{l\ i,j-\frac{1}{2}} + q_{cl\ i,j} \\ & = R_{cl\ i,j} (C_{l\ i,j}^{n+1} - C_{l\ i,j}^n) + R_{pl\ i,j} (P_{i,j}^{n+1} - P_{i,j}^n) + V_{b\ i,j} R_{l\ i,j} \end{aligned} \quad (7.52)$$

Source and sink term,  $q_c$  is function of volumetric flow rate at reservoir condition and well block concentration as;

$$q_{cl\ i,j} = q_{ml\ i,j} C_{l\ i,j} \quad (7.53)$$

For implicit solution, Eqn.7.52 is written for gas flow as;

$$\begin{aligned}
& - \left( u_{gx \ i+\frac{1}{2},j} \right)^v A_{x \ i+\frac{1}{2},j} \left( C_{g \ i+\frac{1}{2},j} \right)^{v+1} + \left( u_{gx \ i-\frac{1}{2},j} \right)^v A_{x \ i-\frac{1}{2},j} \left( C_{g \ i-\frac{1}{2},j} \right)^{v+1} \\
& - \left( u_{gy \ i,j+\frac{1}{2}} \right)^v A_{y \ i,j+\frac{1}{2}} \left( C_{g \ i,j+\frac{1}{2}} \right)^{v+1} \\
& + \left( u_{gy \ i,j-\frac{1}{2}} \right)^v A_{y \ i,j-\frac{1}{2}} \left( C_{g \ i,j-\frac{1}{2}} \right)^{v+1} - (R_{cg \ i,j})^v (C_{g \ i,j})^{v+1} \quad (7.54) \\
& = - (q_{cg \ i,j})^v - (R_{cg \ i,j})^{v+1} (C_{g \ i,j})^v \\
& + (R_{pg \ i,j})^{v+1} \left[ (P_{g \ i,j})^{v+1} - (P_{g \ i,j})^v \right] + V_{b \ i,j} (R_{g \ i,j})^{v+1}
\end{aligned}$$

After solving the resulted system of equations for sand concentration of gas (Eqn.7.54), porosity is updated as;

$$(\phi^o)^{n+1} = (\phi^o)^n - \Delta t \left( \frac{\partial \sigma_l}{\partial t} + \frac{\partial \sigma_l^*}{\partial t} \right) \frac{1}{\rho_s} \quad (7.55)$$

$$(\phi_s)^{n+1} = \frac{C_g^{n+1}}{\rho_s} + \frac{C_w}{\rho_s} \quad (7.56)$$

$$\phi^{n+1} = ((\phi^o)^{n+1} - (\phi_s)^{n+1})[1 + c_\phi(P - P^o)] + (\phi_s)^{n+1} \quad (7.57)$$

Permeability and non-Darcy coefficient are updated based on the pore throat solid concentration with the correlation developed by using the pore-scale simulations.

$$\left( 1 - \frac{k}{k_i} \right) = 0.01028 \sigma_s^{*0.960} \quad (7.58)$$

$$\frac{\beta}{\beta_i} = 1.001 \left( \frac{k}{k_i} \right)^{-1.830} \quad (7.59)$$

If there is no pore throat plugging, the Kozeny-Carman relations are used to update permeability and non-Darcy coefficient.

$$\frac{k}{k_i} = 0.997 \left( \frac{\phi}{\phi_i} \right)^{3.214} \quad (7.60)$$

$$\frac{\beta}{\beta_i} = 1.038 \left( \frac{k}{k_i} \right)^{-1.303} \quad (7.61)$$

## 7.2 Reservoir Simulation Algorithm Validation

Developed reservoir simulator is validated into two parts. In the first part, pressure algorithm is validated with material balance and the second part the algorithm is validated with sand migration experiments data found from the literature.

For volumetric gas reservoirs without water influx, the material balance equation is given as (W. J. Lee & Wattenbarger, 1996);

$$G(B_g - B_{gi}) = G_p B_g \quad (7.62)$$

$G$  and  $G_p$  are original gas in place (OGIP) and cumulative gas production.  $B_g$  and  $B_{gi}$  are gas formation factor after cumulative production  $G_p$  and gas formation factor at initial reservoir production. Gas formation factor is defined in terms of gas density as;

$$B_g = \frac{\rho_{gsc}}{\rho_g} \quad (7.63)$$

Gas density is calculated from the real gas law as;

$$\rho = \frac{P MW}{zRT} \quad (7.64)$$

$P$  and  $T$  are pressure and temperature.  $z$  is gas compressibility factor and it is calculated from correlation developed by Dranchuk and Abou-Kassem (1975).  $MW$  and  $R$  are molecular weight and universal gas constant. Using Eqn.7.64, gas formation factor is written as;

$$B_g = \frac{P_{sc} z T}{T_{sc} P} \quad (7.65)$$

Subscript  $sc$  refers to standard conditions and standard conditions are chosen as 14.65 psia and 60 °F. Using Eqn.7.65, Eqn.7.62 can be written as;

$$\frac{P}{z} = \frac{P_i}{z_i} \left( 1 - \frac{G_p}{G} \right) \quad (7.66)$$

Index  $i$  refers to initial condition. Plotting  $P/z$  and  $G_p$  gives a straight line with intercept OGIP.

2D reservoir simulation is conducted for the gas composition given in Table 7.1. Gas density is calculated from real gas law (Eqn.7.64) and gas viscosity is calculated from correlation developed by Lee et al. (1966). To calculate the  $z$  factor mixture critical properties are calculated from Steward et al. mixing rules (1959). Reservoir length is 4800 m in  $x$  and  $y$  directions. Grid number in  $x$  and  $y$  directions are 47 and refined grids are used near the wellbore. The wellblock is located at the center and its dimension is 0.5 m. Reservoir porosity, permeability and irreducible water saturation are 0.25, 0.25 mD and 0.12, respectively. Initial reservoir pressure is 25 MPa. Simulation is conducted for 5 years production with a specified flow rate,  $10^6$  m<sup>3</sup>/day/m. The estimated OGIP from the Eqn.7.66 (Figure 7.1) and volumetric calculation are  $1.138 \times 10^9$  m<sup>3</sup>/m and  $1.133 \times 10^9$  m<sup>3</sup>/m, respectively. The difference between OGIP obtained from volumetric calculation and OGIP obtained from material balance is about 0.38%.

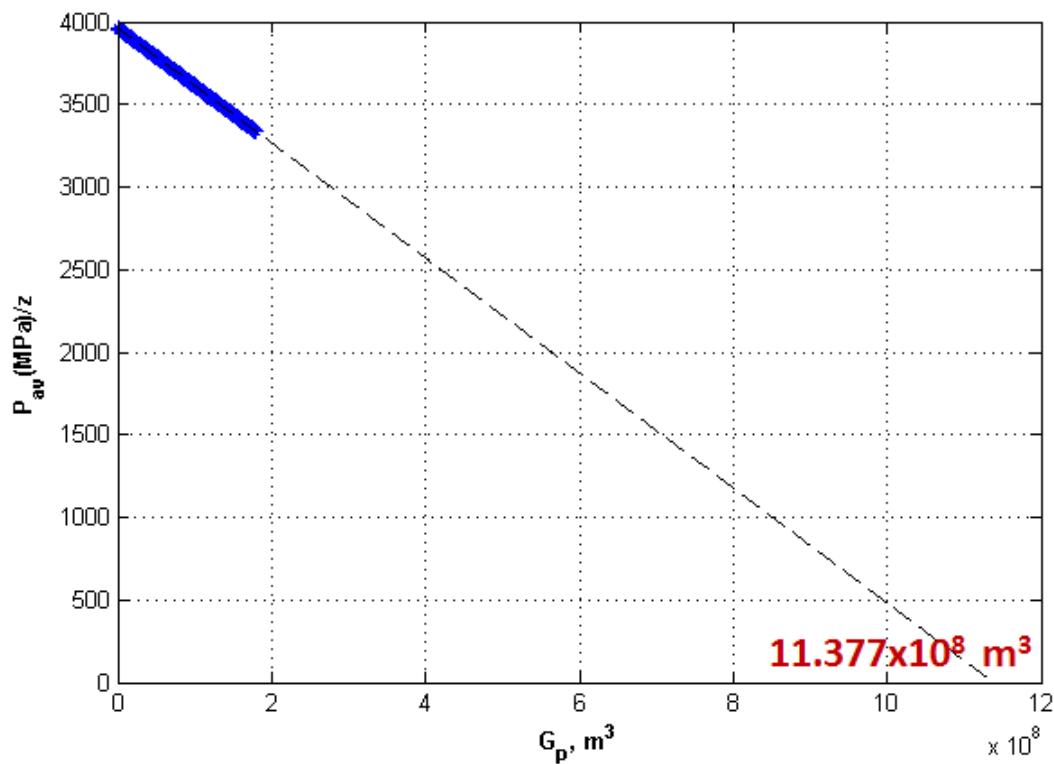


Figure 7.1 Material Balance Plot of Volumetric Dry Gas Reservoir

Table 7.1 Gas Composition used in Reservoir Simulation (W. J. Lee & Wattenbarger, 1996)

Component	Mole Fraction (fraction)	Molecular Weight	Critical Temperature, $T_c$	Critical Pressure, $P_c$
N <sub>2</sub>	0.0138	28.013	227.16	493.1
CH <sub>4</sub>	0.9302	16.043	343.00	666.4
C <sub>2</sub> H <sub>6</sub>	0.0329	30.070	549.59	706.5
C <sub>3</sub> H <sub>8</sub>	0.0136	44.097	665.73	616.0
iC <sub>4</sub> H <sub>10</sub>	0.0023	58.123	734.13	527.9
nC <sub>4</sub> H <sub>10</sub>	0.0037	58.123	765.29	550.6
iC <sub>5</sub> H <sub>12</sub>	0.0012	72.150	828.77	490.4
nC <sub>5</sub> H <sub>12</sub>	0.0010	72.150	845.47	488.6
C <sub>6</sub> H <sub>14</sub>	0.0008	86.177	913.27	436.9
C <sub>7+</sub>	0.0005	114.23	1005.3	375.5

To confirm the sand migration codes, the experiments data from literature (X. Liu, 1994) is used. The experiment set-up is 46 cm long consisting of 23 cm long sand pack and gravel pack (Figure 7.2). The first set of experiments are conducted for glass beads size for sand pack and gravel pack of 400  $\mu\text{m}$  and 2000-4000  $\mu\text{m}$ , respectively. The median gravel size to sand size ratio is 7.5. Second set of experiments are conducted for glass beads size for sand pack and gravel pack of 250  $\mu\text{m}$  and 1000-2000  $\mu\text{m}$ , respectively. The median gravel size to sand size ratio is 6.3. For both gravel to sand size ratios, two experiments are conducted with different inlet water velocity.

Mobile sand concentration and critical velocity are determined from experiments and deposition and entrainment rate constants are determined from fitting the simulation sand concentration to measured sand concentration. Sand concentrations are measured after flow stabilization. Table 7.2 and Table 7.3 give the input data used in the simulations for gravel-sand ratio of 7.5 and 6.3, respectively. For gravel-sand ratio of 7.5, experiments are conducted for two different inlet water velocities; 0.00285 and 0.002 m/sec. The main difference between these experiments is mobile sand concentration. Mobile sand concentrations are 92 and 28 kg/m<sup>3</sup> for

high flow rate (HFR) and low flow rate (LFR) experiments, respectively. For gravel-sand ratio of 6.3, experiments are conducted for inlet water velocities 0.00285 and 0.00136 m/sec. Similarly, the main difference is mobile sand concentration, 500 and 55 kg/m<sup>3</sup> for HFR and LFR experiments, respectively.

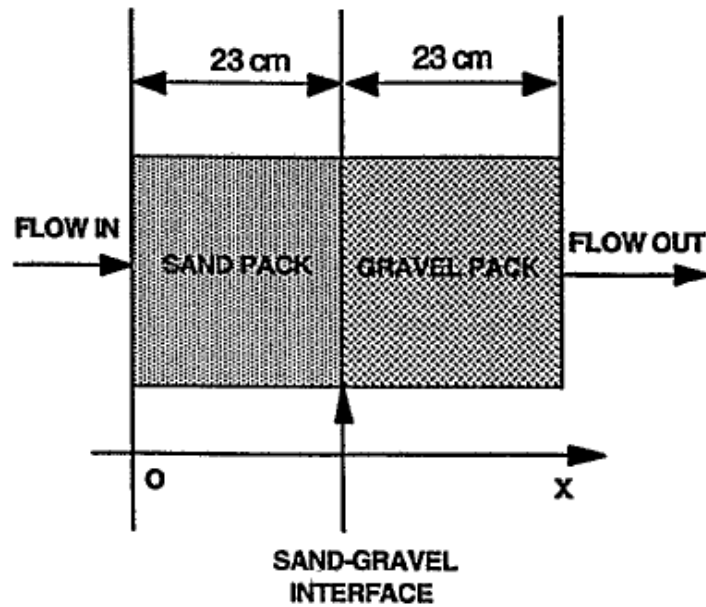


Figure 7.2 Sand Migration Experiment Set-Up

Table 7.2 Input Data for Sand-Gravel with G-S Ratio of 7.5

Data	High Flow Rate (0.00285 m/sec)	Low Flow Rate (0.002 m/sec)
Mobile Sands $\sigma_o$ (kg/m <sup>3</sup> )	92	28
Mobile Sands (Weight %)	5.70	1.71
$u_c$ (m/sec)	0.001	0.001
$k_e$ (1/m)	10	10
$k_d$ (1/m)	30	30

Figure 7.3 gives the sand concentration along the core for HFR and LFR experiments for gravel-sand ratio of 7.5. Blue and red solid lines give the sand concentrations obtained from HFR and LFR simulations, respectively. Blue and red dots give the measured sand concentrations. For

both experiments, sand concentrations increase sharply at the sand-gravel interface and decreases exponentially away from the interface. The simulated sand concentration closely matched with experiment data near the interface; however, away from the interface simulated sand concentration is little higher. The reason is that deposition of sand particles is approximated as rate equation.

Table 7.3 Input Data for Sand-Gravel with G-S Ratio of 6.3

<b>Data</b>	<b>High Flow Rate</b> (0.00285 m/sec)	<b>Low Flow Rate</b> (0.00136 m/sec)
Mobile Sand $\sigma_o$ (kg/m <sup>3</sup> )	500	55
Mobile Sands (Weight %)	30.9	3.40
$u_c$ (m/sec)	0.001	0.001
$k_e$ (1/m)	10	10
$k_d$ (1/m)	4.5	30

There are no permeability and porosity measurements during the end of experiment. Figure 7.4 gives the porosity along the core at the end of experiment obtained from simulations. Initial porosity of sand and gravel pack is 0.40. Due to sand migration, porosity increases in the sand pack. Increase in porosity in HFR experiment is higher than LFR experiment because mobile sand concentration is higher, 92 kg/m<sup>3</sup>. Porosity decreases sharply at the sand-gravel interface. Since sand concentration is high for HFR experiment, decrease in porosity much more severe. Sand pack and gravel pack permeabilities before the experiments are not specified. Sand pack and gravel pack permeabilities before the experiments are determined from the developed correlation at pore-scale analysis based on particle diameter and porosity (Eqn.7.67). Sand particle diameter and porosity are 400  $\mu\text{m}$  and 0.4; sand pack permeability is 178 Darcy. Mean gravel particle diameter and porosity are 3000  $\mu\text{m}$  and 0.4, gravel pack permeability is 9987



Darcy. Permeability change due to sand migration is estimated from Kozeny-Carman relation with a coefficient 3. Figure 7.5 gives permeability along the core at the end of experiment obtained from simulations. Sand pack part, permeability increases due to porosity increase. At the sand-gravel interface permeability decreases suddenly due to porosity decrease caused by sand migration.

$$k = 10^{4.7831} D_p^{1.9985} \phi^{4.3654} \quad (7.67)$$

Cumulative sand production is calculated from integration of outlet water sand concentration with time (Figure 7.6). Glass beads density is  $2700 \text{ kg/m}^3$ . Total sand productions are negligible,  $4.29 \times 10^{-8} \text{ m}^3$  ( $1.16 \times 10^{-4} \text{ kg}$ ) and  $1.32 \times 10^{-8} \text{ m}^3$  ( $3.56 \times 10^{-5} \text{ kg}$ ) for HFR and LFR experiments, respectively.

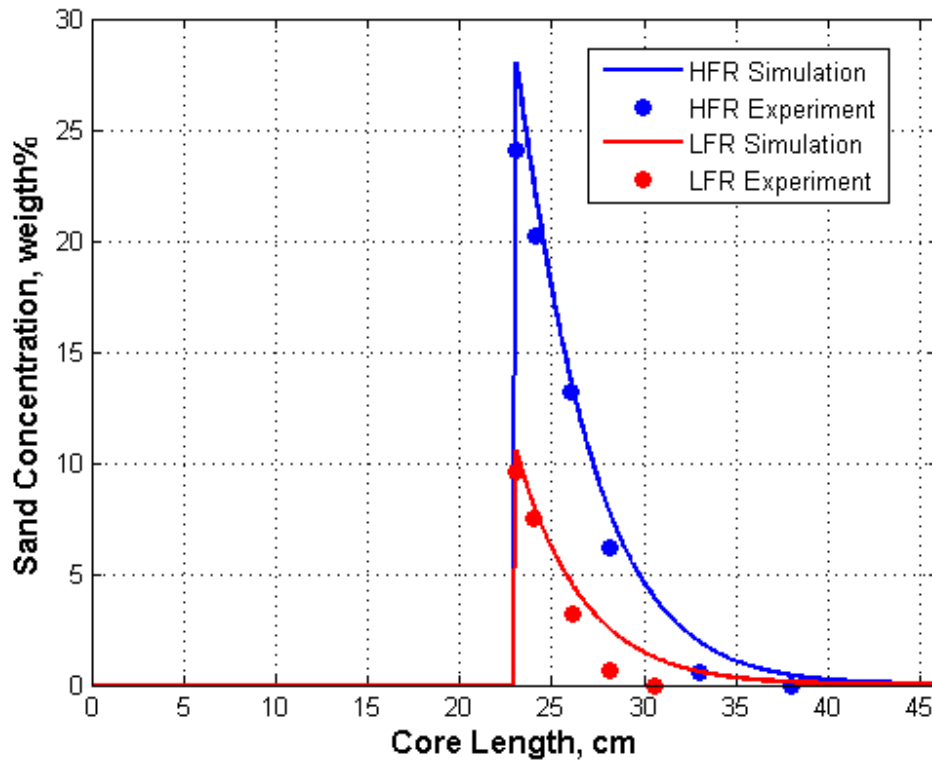


Figure 7.3 Sand Concentration along the Core for Gravel-Sand Ratio of 7.5

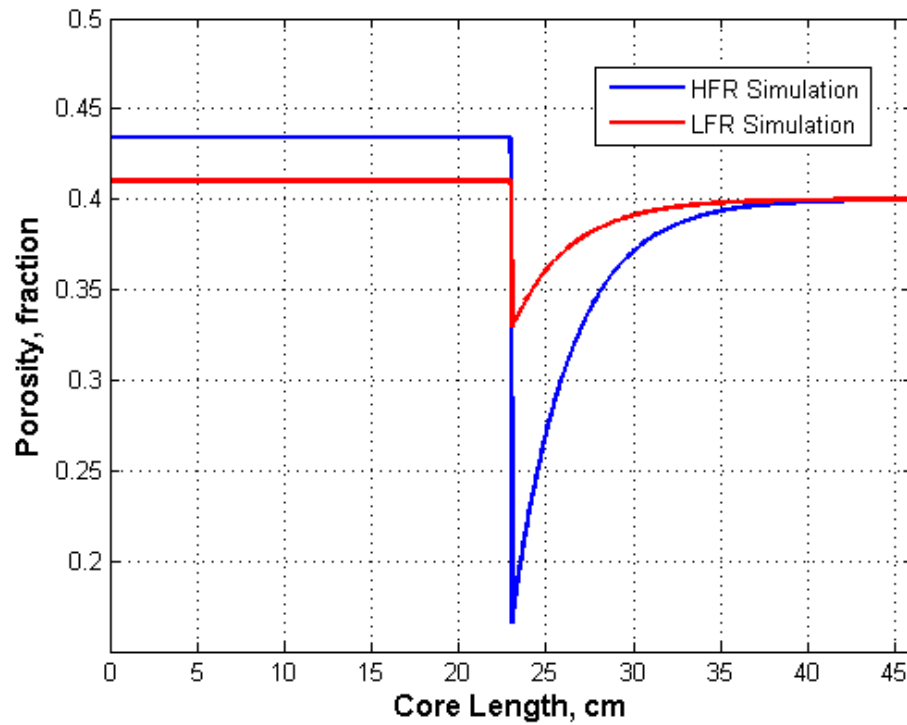


Figure 7.4 Porosity along the Core after Experiment for Gravel-Sand Ratio of 7.5

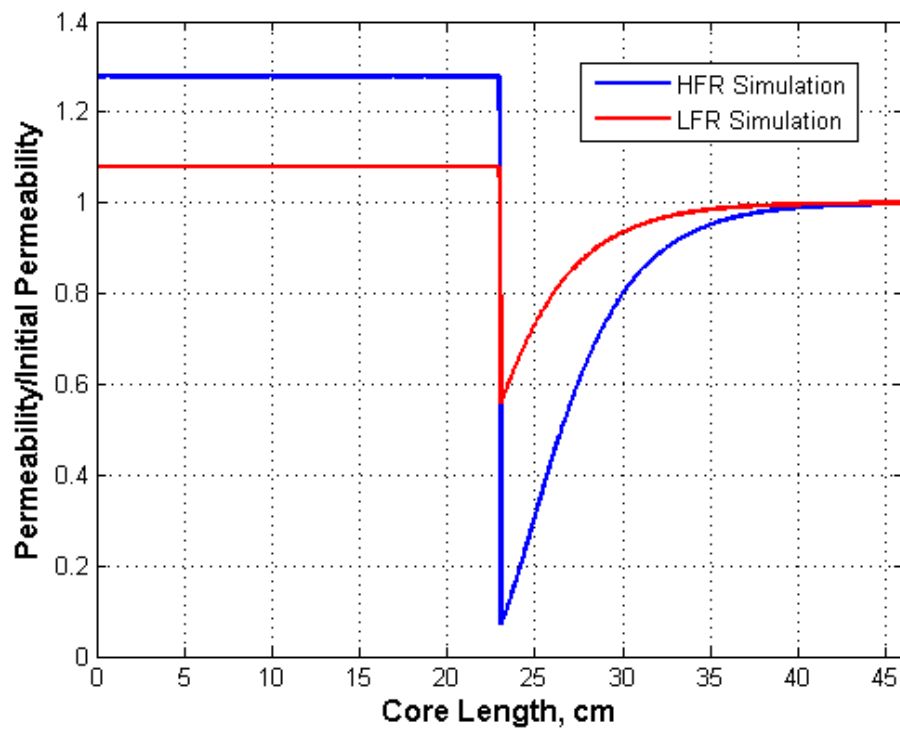


Figure 7.5 Permeability along the Core after Experiment for Sand-Gravel Ratio of 7.5

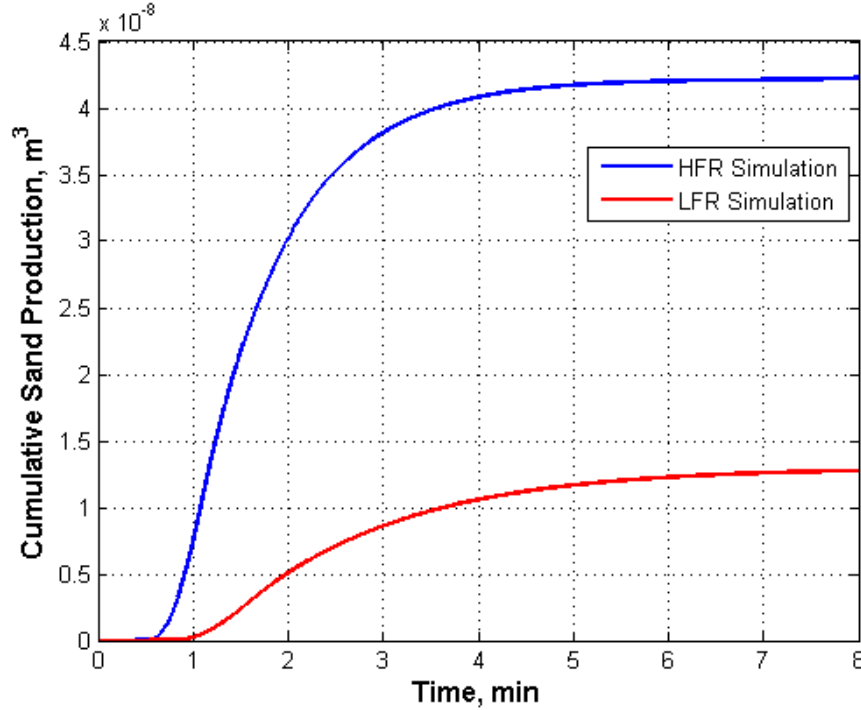


Figure 7.6 Cumulative Sand Production for Sand-Gravel Ratio of 7.5

Figure 7.7 gives the sand concentration along the core for gravel-sand ratio of 6.3. Compared with experiments of gravel-sand ratio of 7.5, similar trends are observed. Sand concentration increase at the sand-gravel interface and decreases along the gravel pack. For HFR experiment, mobile sand concentration is high,  $500 \text{ kg/m}^3$ ; therefore, sand concentration near gravel pack outlet is as high as 10% weight.

Figure 7.8 gives the porosity along the core at the end of experiment obtained from simulations. In the sand pack part, porosity increases; especially for HFR experiment. Porosity increases up to 0.585 and decrease to 0.198 at the sand-gravel interface. Permeability of sand pack and gravel pack before the experiments are calculated from the correlation (Eqn.7.67). Sand mean diameter and porosity are  $250 \mu\text{m}$  and 0.4, and corresponding permeability is 70 Darcy. Mean gravel diameter and porosity are  $1575 \mu\text{m}$  and 0.4, and corresponding permeability is 2755 Darcy. Figure 7.9 gives the permeability along the core at the end of experiment obtained from

Kozeny-Carman relation. Change of permeability shows similar trend with porosity change. Total sand production is negligible  $2.57 \times 10^{-8} \text{ m}^3$  ( $6.93 \times 10^{-5} \text{ kg}$ ) for LFR experiment; however, total sand production is significant,  $7.56 \times 10^{-5} \text{ m}^3$  (0.204 kg), for HFR experiment (Figure 7.10).

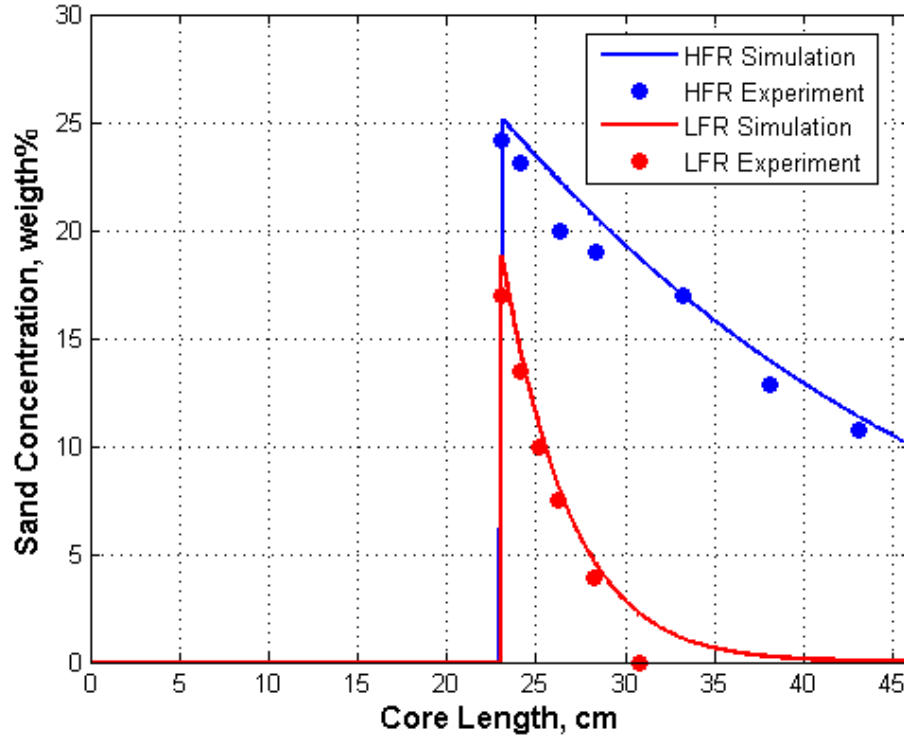


Figure 7.7 Sand Concentration along the Core for Sand-Gravel Ratio of 6.3

Sensitivity analysis is conducted for parameters determined from experiments (initial mobile sand,  $\sigma_o$ , and critical velocity,  $u_c$ ) and parameters obtained from fitting the experiment data and simulation (surface retention rate coefficient,  $k_d$ , and surface entrainment rate coefficient,  $k_e$ ) and inlet water velocity ( $u$ ) to investigate the effect of each estimated parameters on cumulative sand production and sand concentration along the gravel pack. For sensitivity analysis, high flow rate experiment of gravel-sand ratio of 7.5 is used.

Surface retention rate coefficient reflects the sand particle attachment on the pore surface. Increase in surface retention rate coefficient means more sand particles attached the pores in gravels; therefore, sand production significantly decreases and sand concentration near the

interface increases slightly (Figure 7.11). For accurate estimation of retention coefficient, cumulative sand production should also be known.

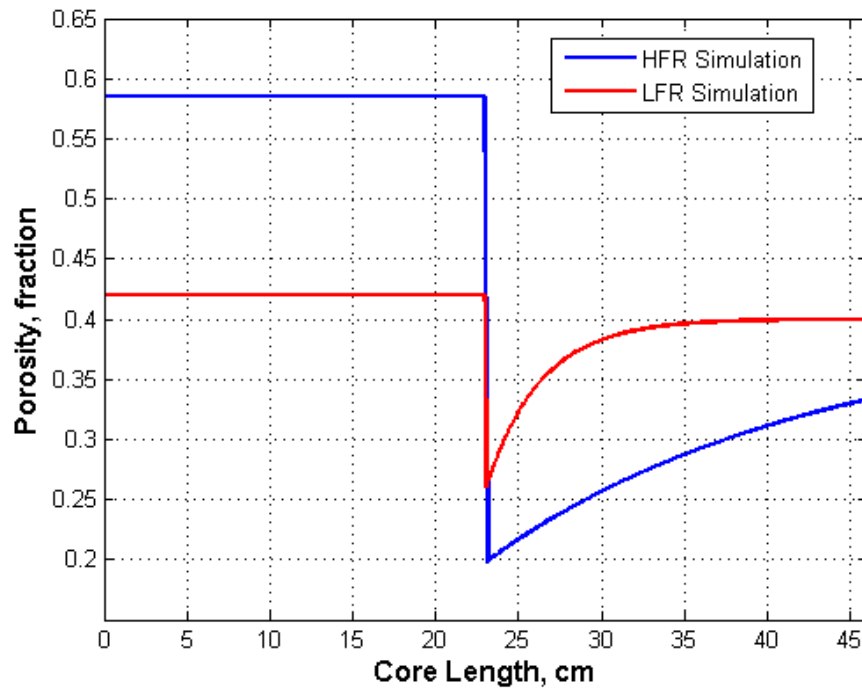


Figure 7.8 Porosity along the Core after Experiment for Sand-Gravel Ratio of 6.3

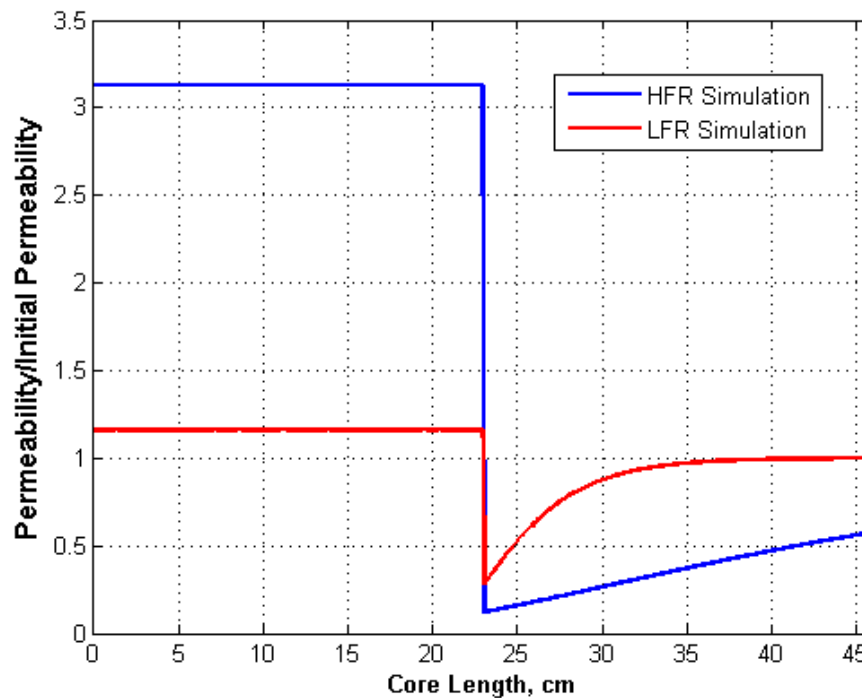


Figure 7.9 Permeability along the Core after Experiment for Sand-Gravel Ratio of 6.3

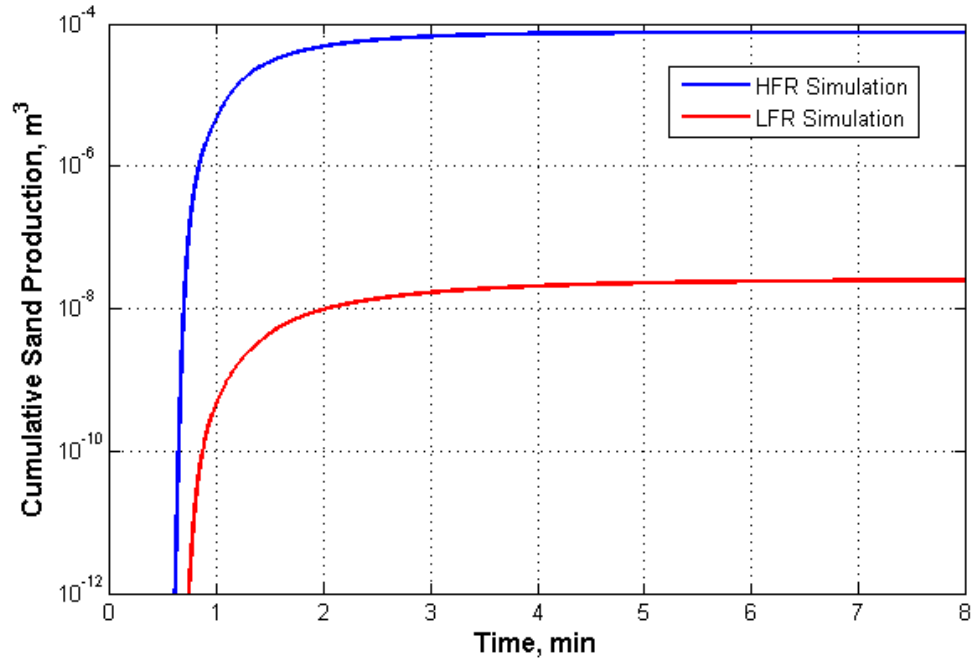


Figure 7.10 Cumulative Sand Production for Sand-Gravel Ratio of 6.3

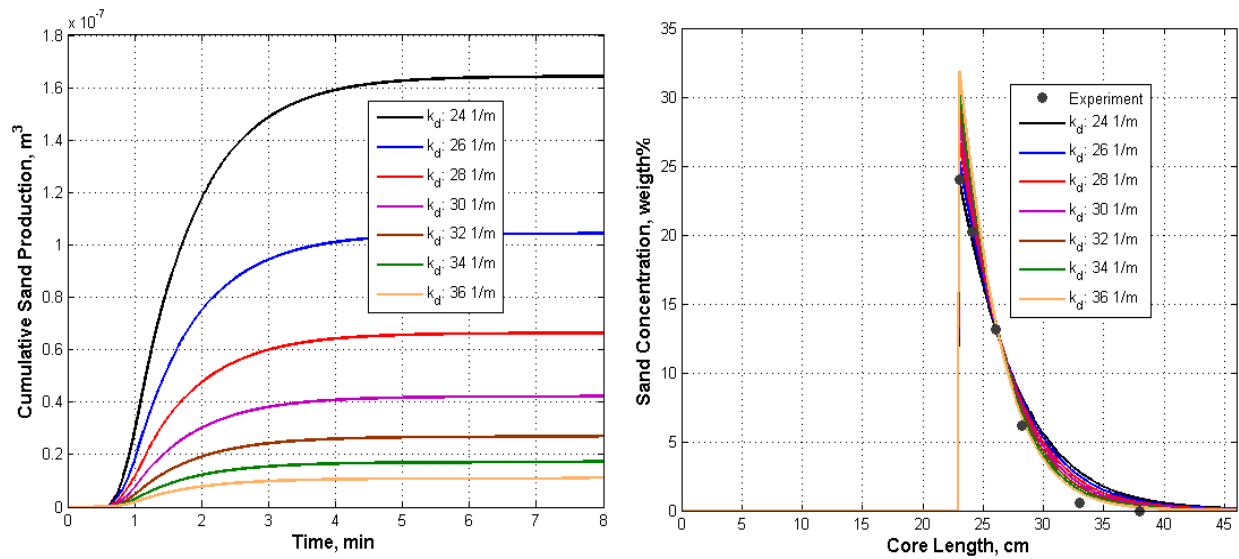


Figure 7.11 Sensitivity Analysis of Surface Retention Rate Coefficient

Surface entrainment rate coefficient reflects the sand particle leaving the pore surface. Increase in the surface entrainment rate coefficient leads to increase in early sand production; however, both the total produced sand and equilibrium sand concentration along the gravel pack are not affected (Figure 7.12).

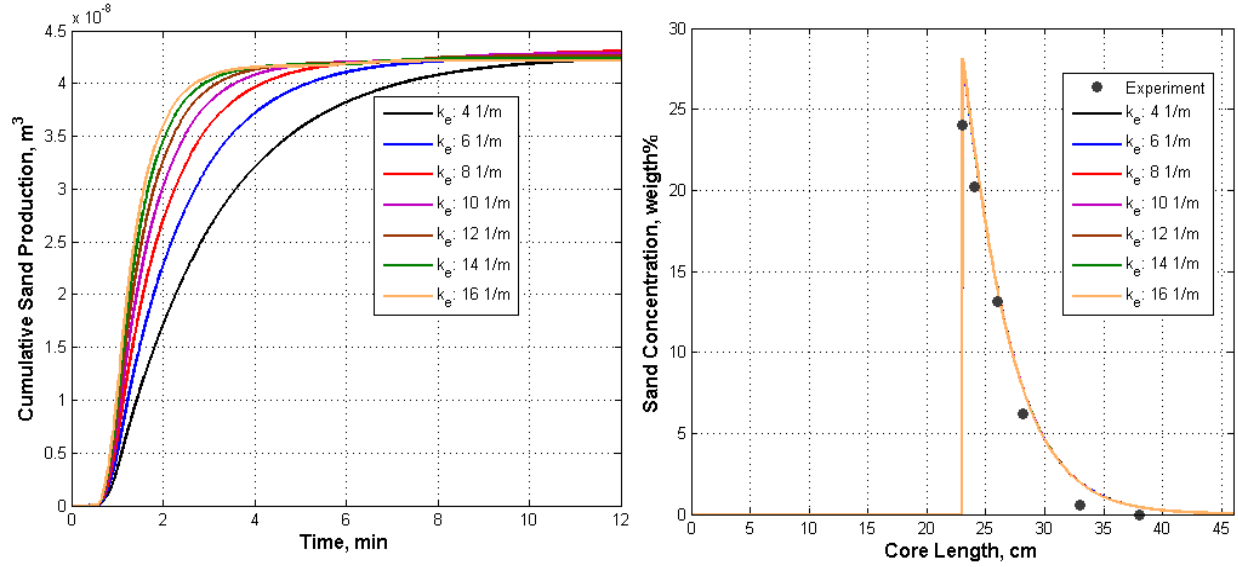


Figure 7.12 Sensitivity Analysis of Surface Entrainment Rate Coefficient

Increase in mobile sand concentration ( $\sigma_0$ ) leads to increase in total sand production; however, the sand concentration along the gravel pack is little affected with mobile sand (Figure 7.13). Comparing the initial mobile sand concentration effect with surface retention rate coefficient effect, decrease in surface retention coefficient leads more sand production and less sand particle trapping in gravel part. However, increase in initial mobile sand leads increase in both sand production and more sand particle trapping.

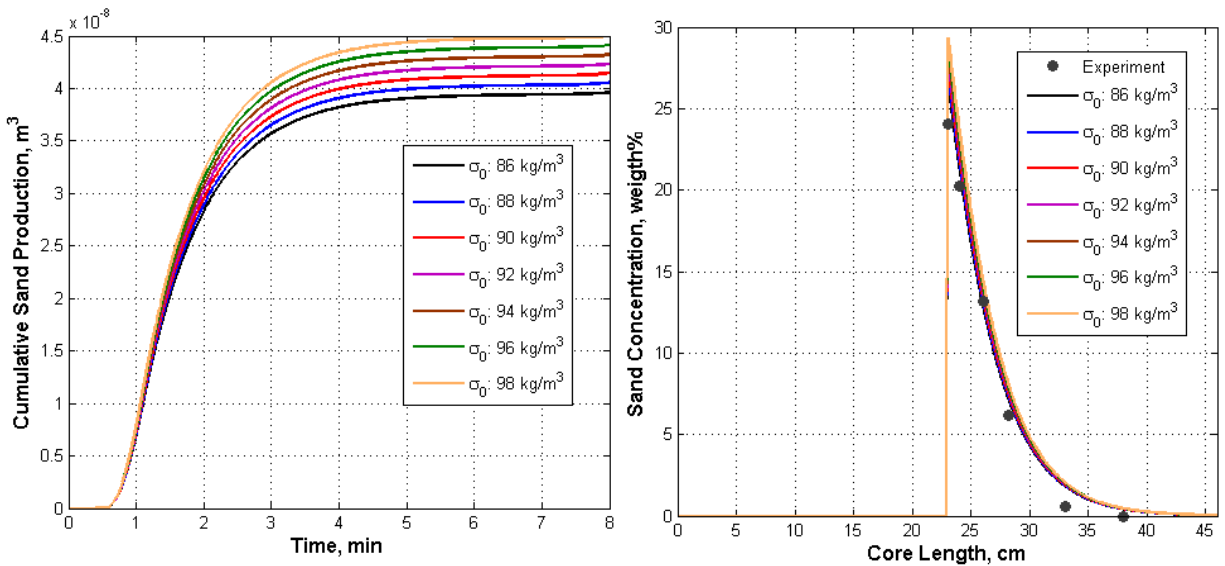


Figure 7.13 Sensitivity Analysis of Initial Mobile Sand Concentration

Increase in critical velocity leads to increase in time in which cumulative sand production stabilizes. Critical velocity has no effect on total sand production and sand concentration along the gravel pack (Figure 7.14).

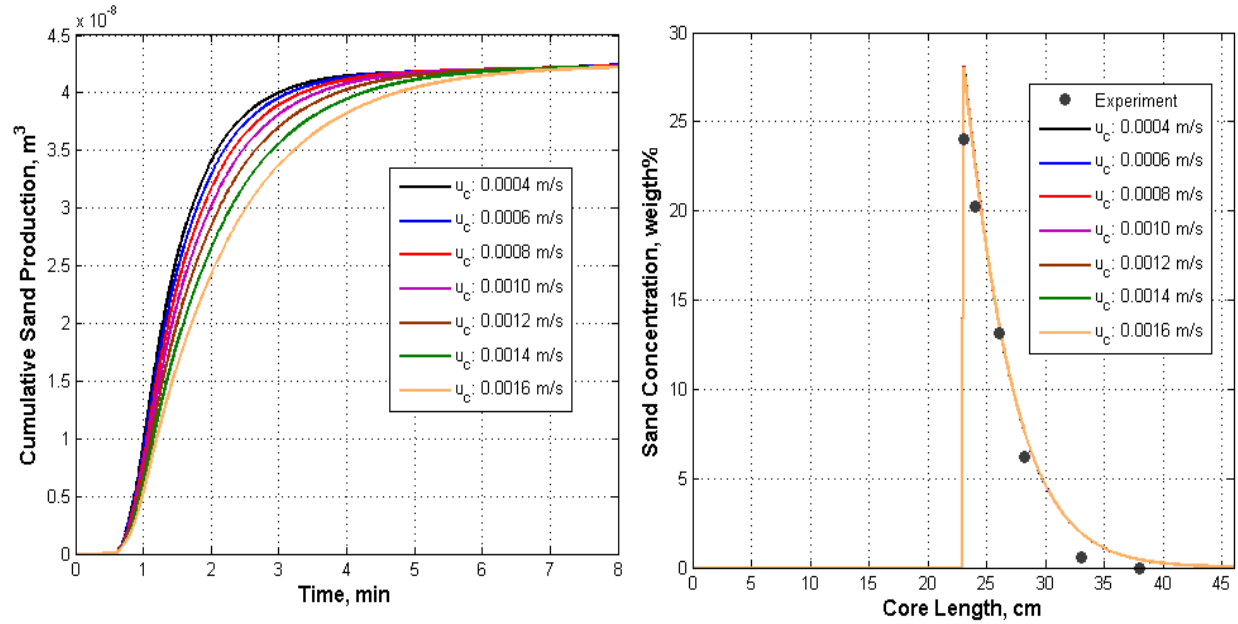


Figure 7.14 Sensitivity Analysis of Critical Velocity

Increase in inlet velocity leads to decrease in time in which cumulative sand production stabilizes since the difference between velocity and critical velocity (driving mechanism for sand entrainment) increases. Similar to critical velocity, both total sand production and sand concentration along the gravel pack are not affected with inlet velocity (Figure 7.15).

Permeability and pressure measurements are not stated. Therefore, permeability effect is investigated. For the validation part of the experiment and sensitivity analysis, sand pack and gravel pack permeabilities calculated from mean grain size and porosity (Eqn.7.67); and non-Darcy coefficients are calculated from permeability and porosity (Eqn.7.68). To figure out the permeability effect, calculated permeabilities are decreased and increased by 10% and 20%. Outlet fluid sand concentrations and cumulative sand productions are same since the experiments



are conducted constant inlet velocity, 0.00285 m/sec. However, pressure along the core changes with the permeability (Figure 7.16).

$$\beta = \frac{10^{4.8674}}{k^{0.4852} \phi^{2.1089}} \quad (7.68)$$

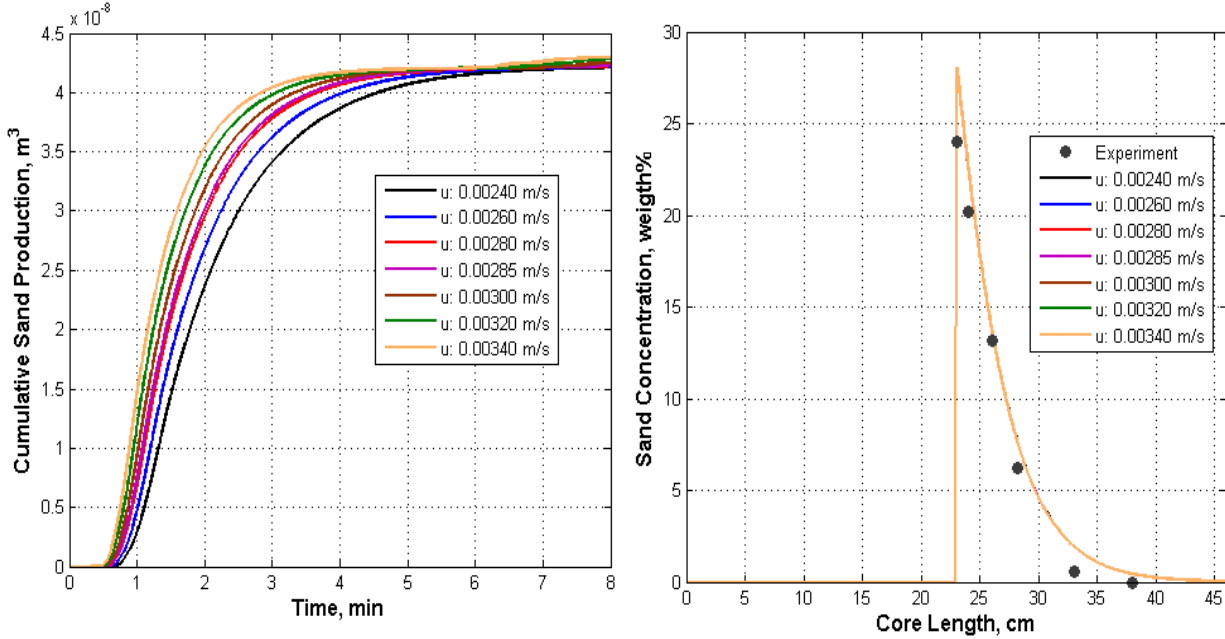


Figure 7.15 Sensitivity Analysis of Inlet Velocity

Even though permeability and non-Darcy coefficient change seem to be different with sand migration, the ratios of them to initial values are same (Figure 7.17 – Figure 7.18). Therefore, correct estimation of permeability depends on pressure measurement. If the experiments would be conducted at a constant inlet pressure, permeability would have significant effect on sand migration since velocity will change with permeability and would not be constant during the experiment.

During these experiments, moveable sand concentration, critical velocity and sand concentration along the gravel pack are measured. Sand migration rate coefficients are found by fitting the sand concentration obtained from simulation to the measured sand concentrations. Sensitivity analysis indicates that for correct estimation of sand migration parameters, sand

production with time should also be known for correct parameter estimation. If pressure measurements are available, permeability change with time due to sand migration could be estimated.

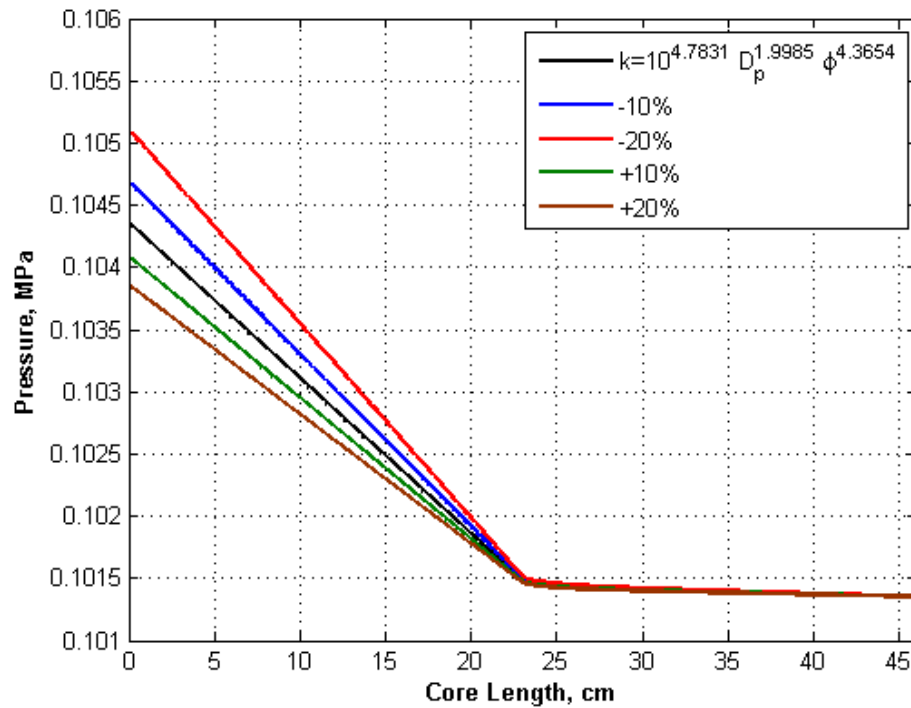


Figure 7.16 Sand Pack and Gravel Pack Permeabilities Effect on Pressure

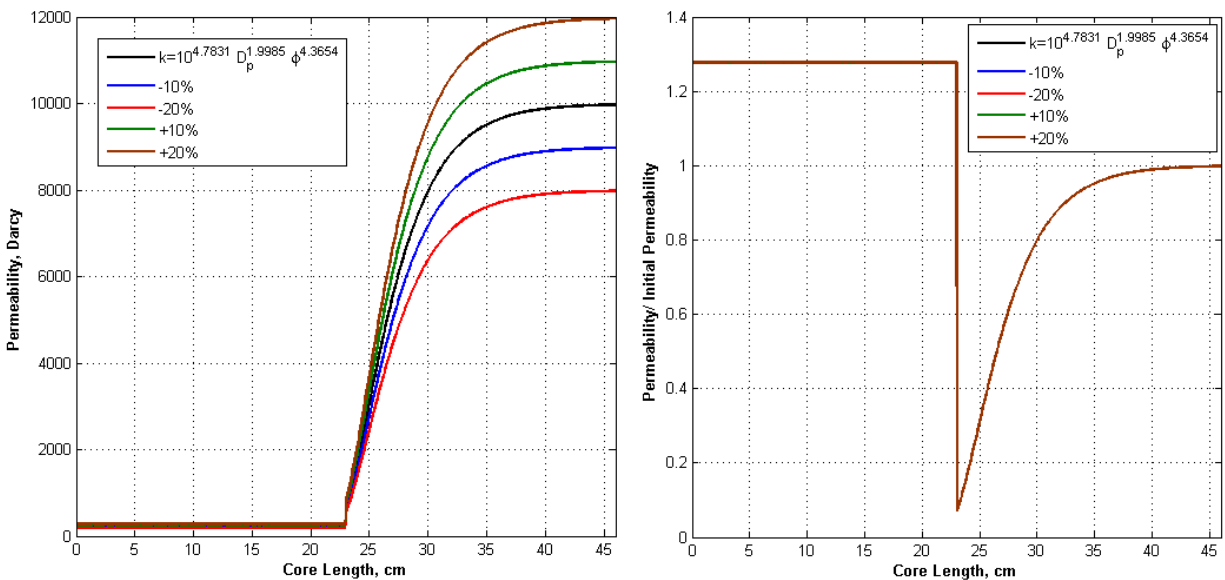


Figure 7.17 Sand Pack and Gravel Pack Permeability along the Core

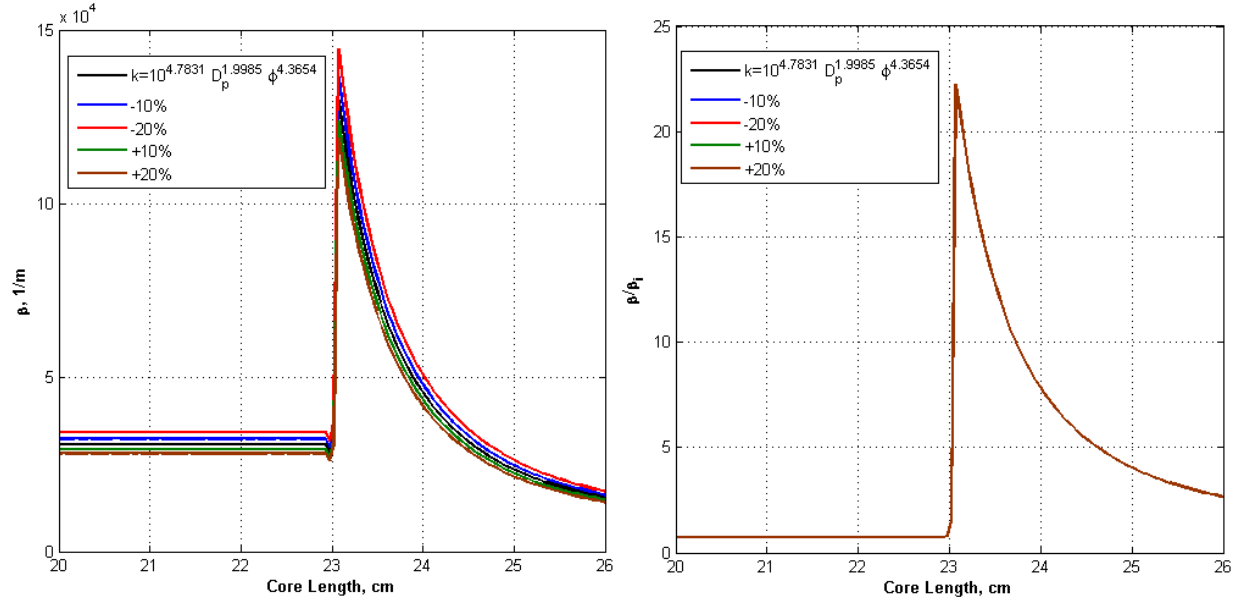


Figure 7.18 Sand Pack and Gravel Pack Non-Darcy Coefficient along the Core

### 7.3 Parametric Study of Sand Migration

2D reservoir simulations are conducted to emphasize the sand migration problem, there cases are compared. In Case 1, there is no sand production and reservoir produced with a constant rate  $1.6 \text{ MMm}^3/\text{day}/\text{m}$ . In Case 2, due to high flow rate, the sand migration is considered; however, the produced sand particles moves through the wellbore without redeposition on pore surface or at pore throat. In the Case 3, the potentials of produced sand deposition on pore surface and at pore throat are considered. Using the symmetry, a quarter of the reservoir is simulated. Table 7.4 gives the reservoir properties and sand migration rates constants. The gas composition given in Table 7.1 is used for all reservoir simulations.

Figure 7.19 gives the wellblock pressure change with time and pressure profiles along the reservoir after 100 days production. If there is no sand migration in the reservoir, the wellbore block pressure decreases to 11.03 MPa after 100 days production. Sand migration enhances the production if produced sand does not redeposit in the reservoir. Compared to production without sand production, decrease in wellblock pressure is lower, 12.36 MPa. Sand migration has a little

effect on pressure profile and wellblock pressure for the case of small sand deposition constants compared Case 1. In that case, the wellblock pressure decreases to 10.55 MPa.

Table 7.4 2D Reservoir Simulation Input Parameters

Reservoir Dimension (m)	1000 x 1000
Number of Grid	48 x 48
$\phi$ (fraction)	0.25
k (mD)	25
$S_{wi}$ (fraction)	0.12
Initial Reservoir Pressure (MPa)	25
Flow Rate ( $Mm^3/day$ )	40
$\sigma_o$ ( $kg/m^3$ )	30
$u_c$ (m/sec)	0.0001
$k_e$ (1/m)	0.01
$k_d$ (1/m)	0.005
$k_{pt}$ (1/m)	0.001
$k_{fe}$ ( $m^3/kg$ )	0.025
$f_{min}$ (fraction)	0.2

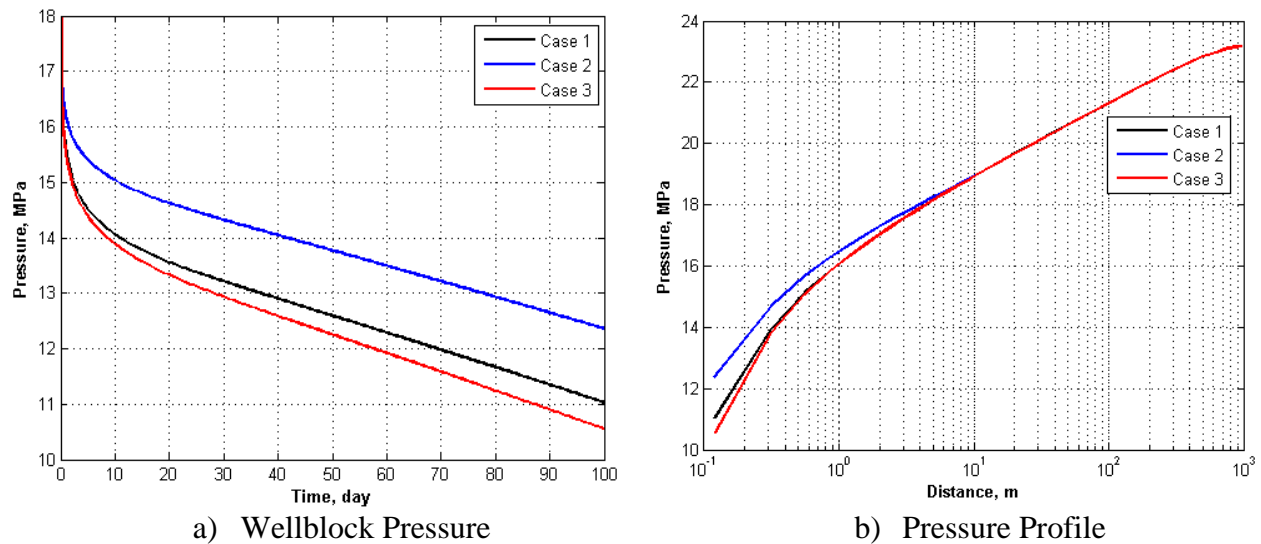


Figure 7.19 Sand Migration Effect on Wellblock Pressure and Reservoir Pressure Profile after 100 days Production

The differences between pressures profiles can be explained with changes of porosity (Figure 7.20), permeability (Figure 7.21) and non-Darcy coefficient (Figure 7.22) after 100 days

production. For Case 1, porosity decrease a little due to compaction. The small decrease of porosity leads to small decrease in permeability and increase in non-Darcy coefficient. In Case 2, sand production leads to increase in porosity from 0.25 to 0.261 due to sand production. Porosity starts to increase at a distance about 14.09 m where velocity, 0.00012 m/sec, is greater than critical velocity, 0.0001 m/sec. Porosity is almost constant after 7.5 m due to pore surface sand concentration is 0 (Figure 7.23). Since there is no sand deposition, permeability and porosity are related with Kozeny-Carman relation. Porosity increase leads to increase in permeability up to 28.44 mD and decrease in non-Darcy coefficient up to  $1.164 \times 10^9$  1/m. In Case 3, pore surface retention or pore throat plugging occur during the sand migration, porosity slightly decreases to 0.259. Surface retention and pore throat plugging cause decrease in sand concentration in gas phase and the difference in sand concentration with and without sand particle deposition increases along the wellbore up to  $0.0039 \text{ kg/m}^3$  (Figure 7.24). Even though this has a slight effect on wellblock sand concentration and cumulative sand production (Figure 7.25), pore throat plugging has influence on permeability and non-Darcy coefficient. Therefore, wellblock pressures and pressure profiles along the reservoirs are different. Increase in pore throat sand concentration up to  $6.54 \text{ kg/m}^3$  (Figure 7.26) leads to decrease in permeability up to 23.44 mD and increase in non-Darcy coefficient up to  $1.54 \times 10^9$  1/m.

The non-Darcy coefficient calculated at the wellblock grid boundary is out of trend. The main reason is that velocity cannot be estimated in the wellblock. Therefore, erosion and deposition of sand particles cannot be calculated. As a result, the wellblock porosity and permeability are slightly overestimated, and the non-Darcy coefficient is underestimated. The wellbore model should be integrated for more reliable estimations. From near wellbore studies,

the sand migration near the wellbore should be modeled as a function of sand concentration in gas phase and flow rate. This part left as a future work of this research.

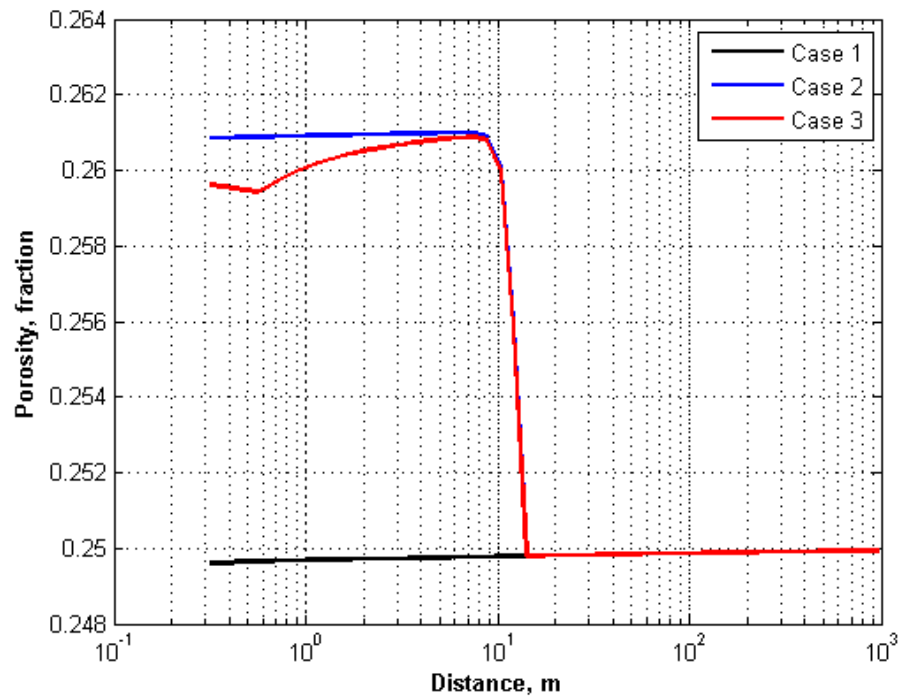


Figure 7.20 Porosity Profile after 100 days Production

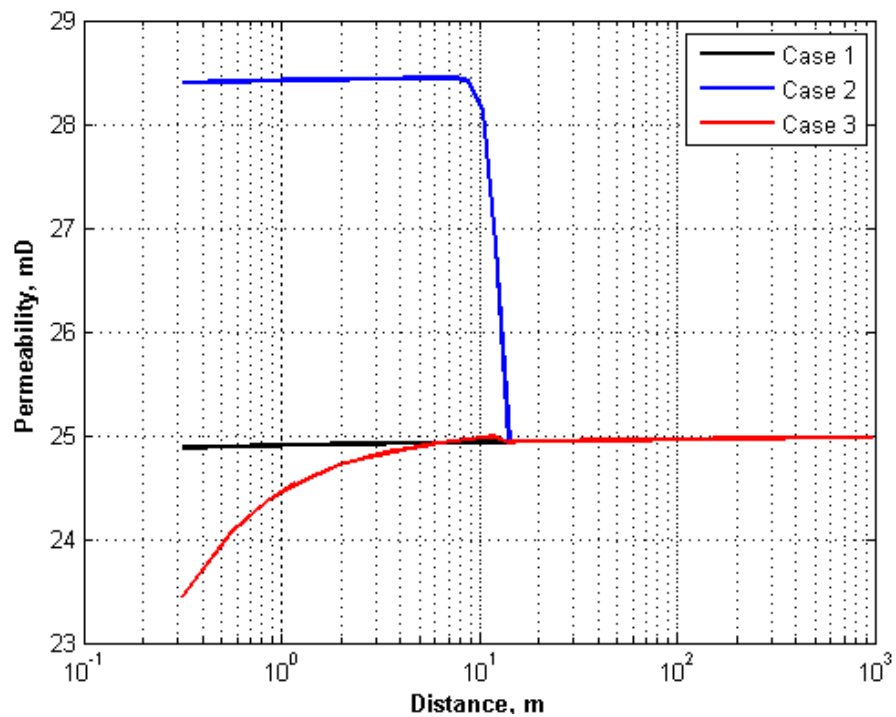


Figure 7.21 Permeability Profile after 100 days Production

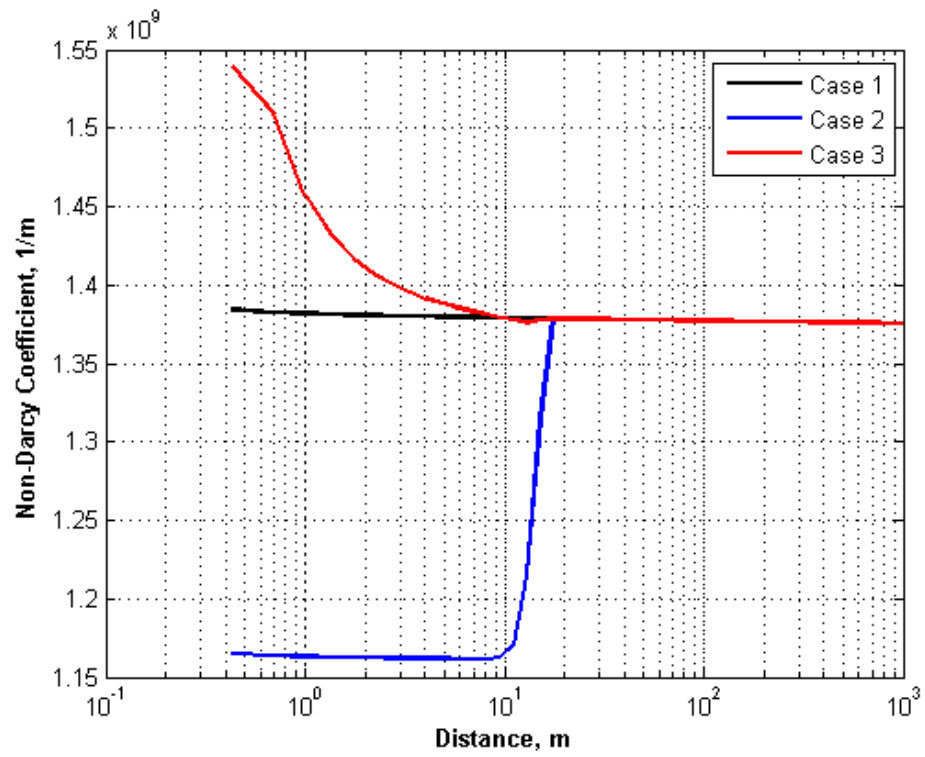


Figure 7.22 Non-Darcy Coefficient Profile after 100 days Production

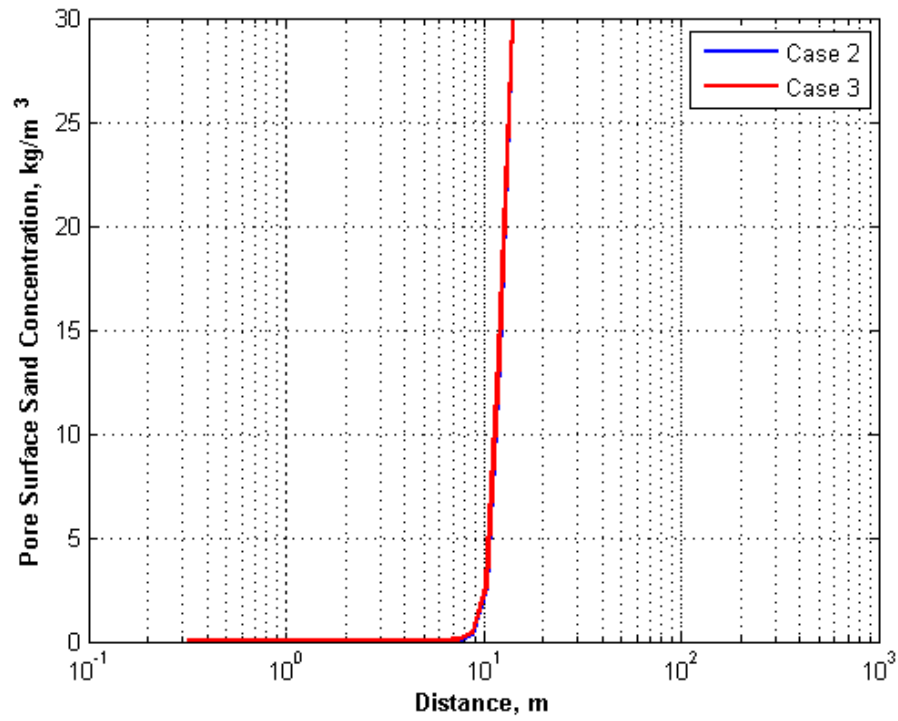


Figure 7.23 Pore Surface Sand Concentration Profile after 100 days Production

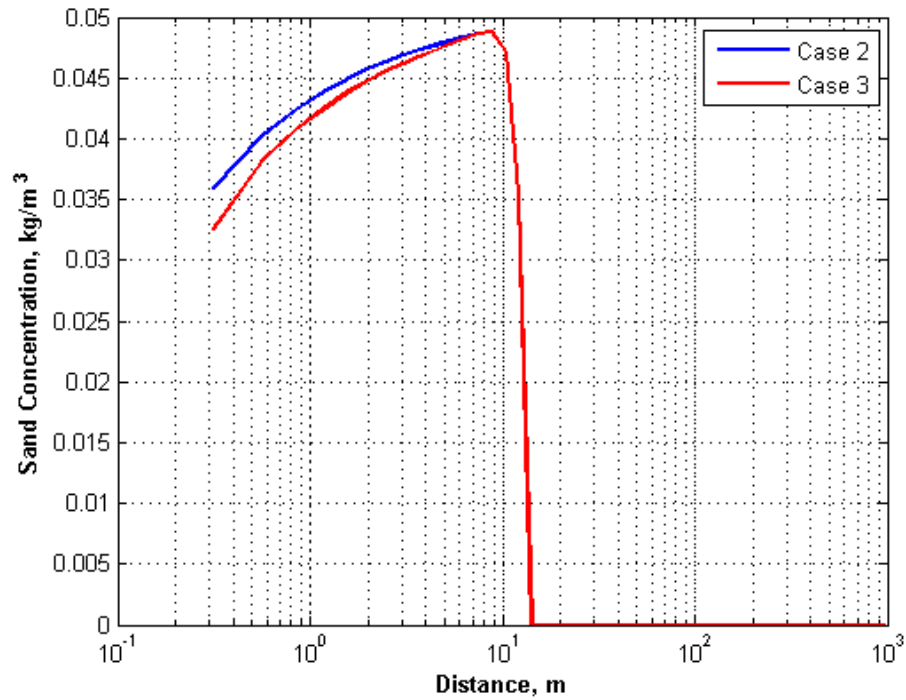


Figure 7.24 Sand Concentration in Gas Phase Profile after 100 days Production

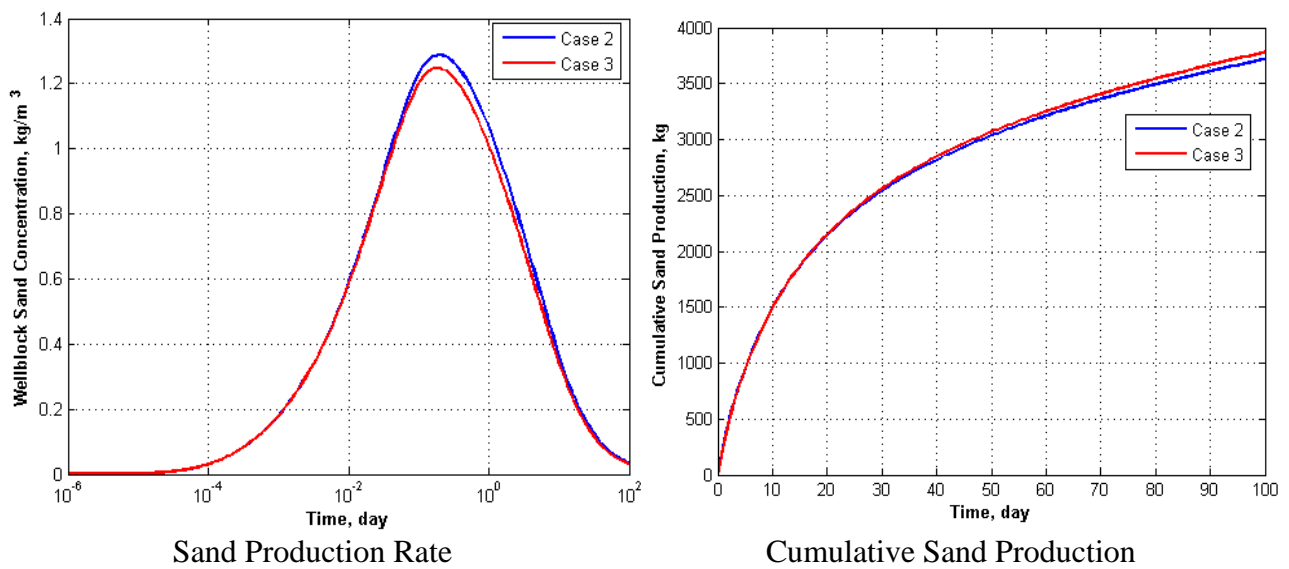


Figure 7.25 Sand Production Change with Time

Initial movable sand concentration, critical velocity, flow rate and rate coefficients related to erosion and deposition of sand particles have effect on production. Parametric study is



conducted to investigate the change of reservoir properties and sand production by using the base case as Case3.

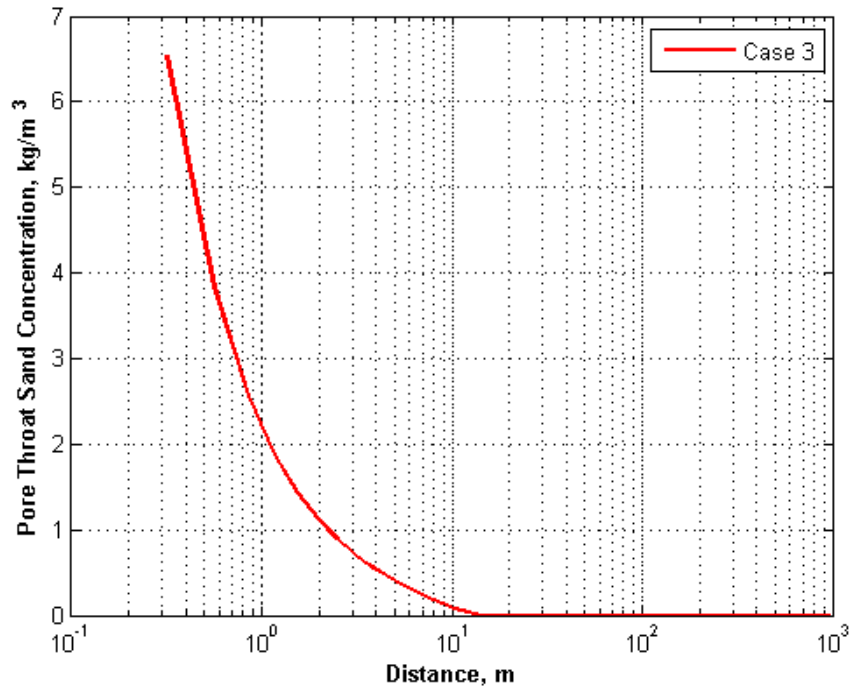


Figure 7.26 Pore Throat Sand Concentration Profile after 100 days Production

### 7.3.1. Initial Movable Sand Concentration Effect on Sand Production

Initial moveable sand concentration range is chosen between 10 and 100 kg/m<sup>3</sup>. Increase in movable sand concentration leads to decrease in wellblock pressure. Figure 7.27 gives the wellblock pressure change with movable sand concentration for 100 days production. Change of wellblock pressure is almost linearly decreases from 10.90 MPa to 8.96 MPa with the increase in sand concentration from 10 kg/m<sup>3</sup> to 100 kg/m<sup>3</sup>. Increase in movable sand concentration leads to increase in wellblock sand concentration especially early times (Figure 7.28). Maximum sand concentration increases from 0.41 kg/m<sup>3</sup> to 4.27 kg/m<sup>3</sup> at 0.18 day of production, after that sand concentrations decreases. Increase in sand concentration in gas phase leads to increase in gas viscosity. This causes increase in pressure difference and lower wellblock pressure. Similar to wellblock pressure change, the increase in cumulative sand production is almost linearly changes

with increase in movable sand concentration (Figure 7.29). Increase in initial mobile sand concentration leads to increase in maximum production rate and cumulative sand production from 89 kg/d to 941 kg/d and from 1251 kg to 12974 kg, respectively.

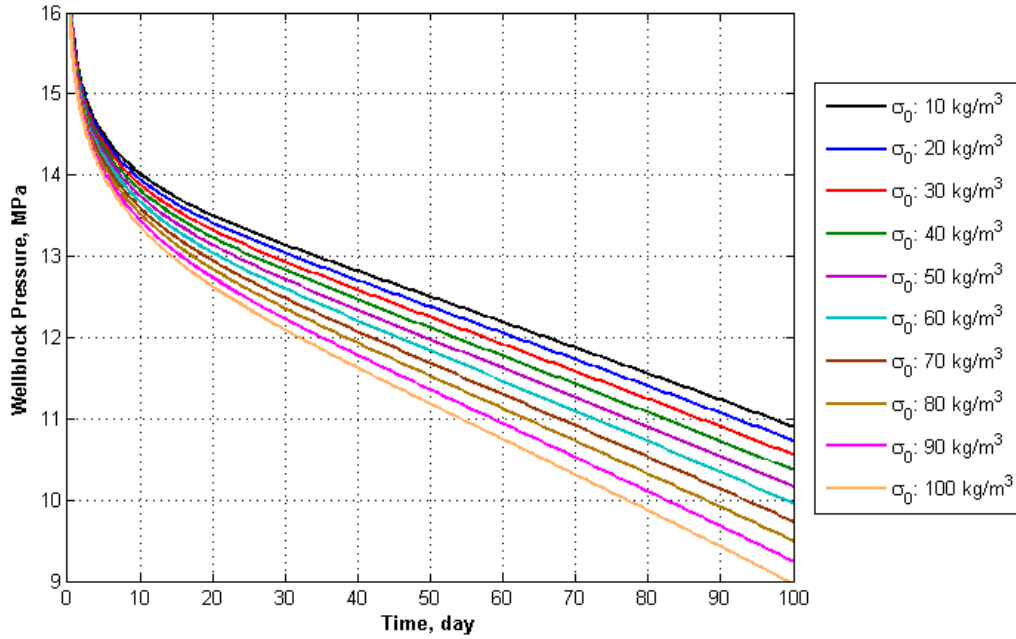


Figure 7.27 Wellblock Pressure Change with Initial Movable Sand Concentration

Pore surface sand concentration decreases from initial mobile sand concentration to 0 between distance 14.09 m and 7.49 m (Figure 7.30). Sand concentration in gas phase increases from 0.016 kg/m³ to 0.158 kg/m³ between the distances where pore surface concentration decreases to 0 (Figure 7.31). Sand production and sand particle plugging at pore throats lead to decrease in gas sand concentration near the wellbore.

Pore throat sand concentration increases from 2.18 kg/m³ to 21.78 kg/m³ with the increase in movable sand concentration from 10 and 100 kg/m³ (Figure 7.32). Increase in pore throat sand concentration leads to decrease in permeability up to 24.46 mD and 20.08 mD (Figure 7.33) and increase in non-Darcy coefficient up to  $1.428 \times 10^9$  1/m and  $2.023 \times 10^9$  1/m (Figure 7.34). Increase in sand production leads to increase in porosity near wellbore. At the

distance, 12.10 m away from the wellbore, porosity suddenly increases up to 0.253 and 0.287 with the increase in movable sand concentration due to erosion, and slight decrease due to sand particle deposition (Figure 7.35). Increase in porosity does not affect the permeability since permeability is much more affected from pore throat plugging.

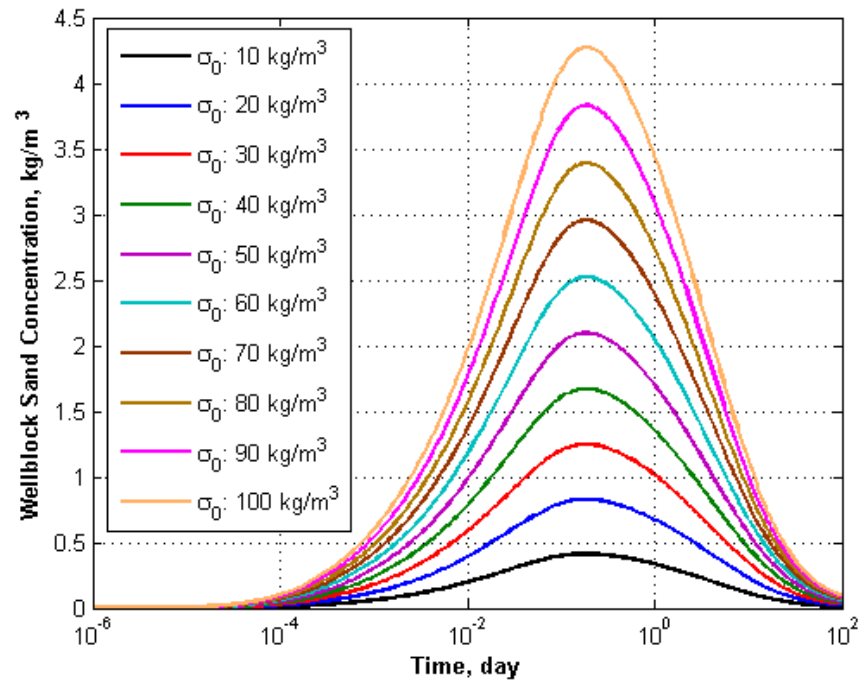
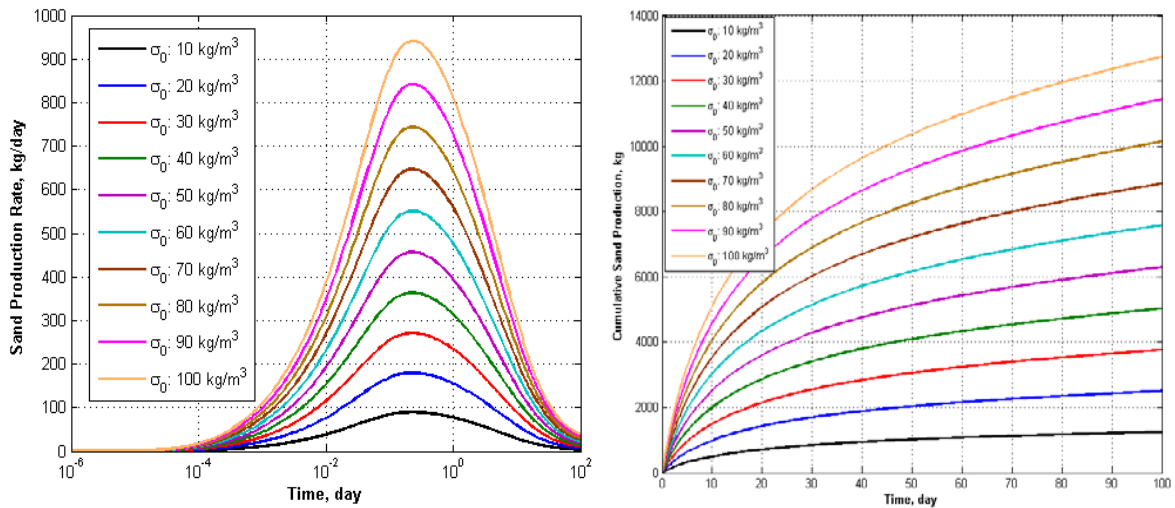


Figure 7.28 Wellblock Sand Concentration Change with Initial Movable Sand Concentration



Sand Production Rate Cumulative Sand Production  
Figure 7.29 Sand Production Change with Initial Movable Sand Concentration

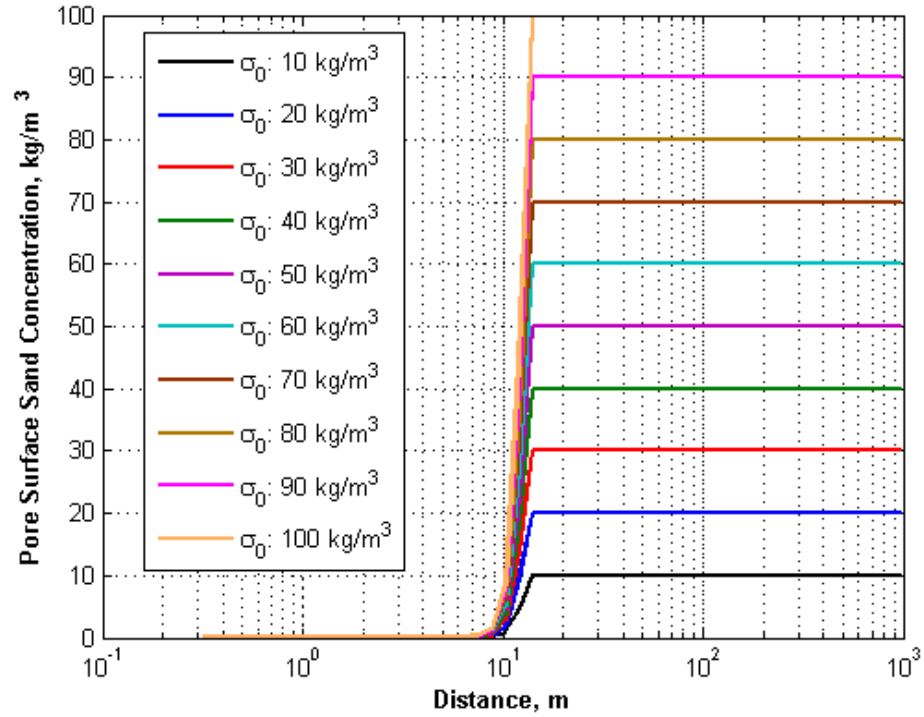


Figure 7.30 Pore Surface Sand Concentration Profile after 100 days Production with Initial Movable Sand Concentration

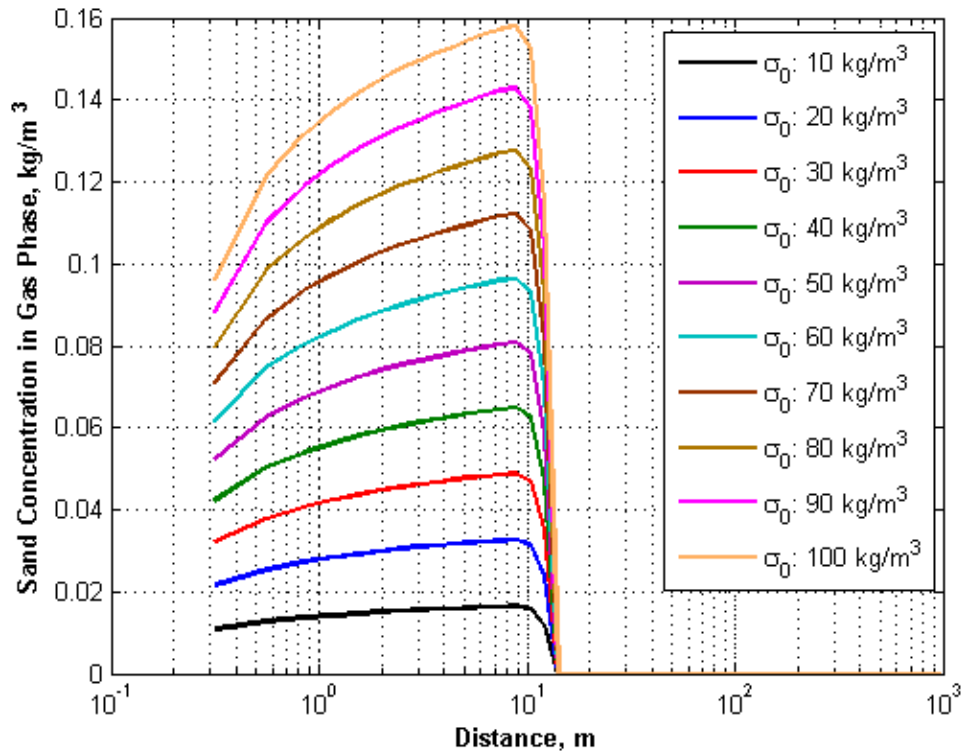


Figure 7.31 Sand Concentration Profile Change after 100 days Production with Initial Movable Sand Concentration

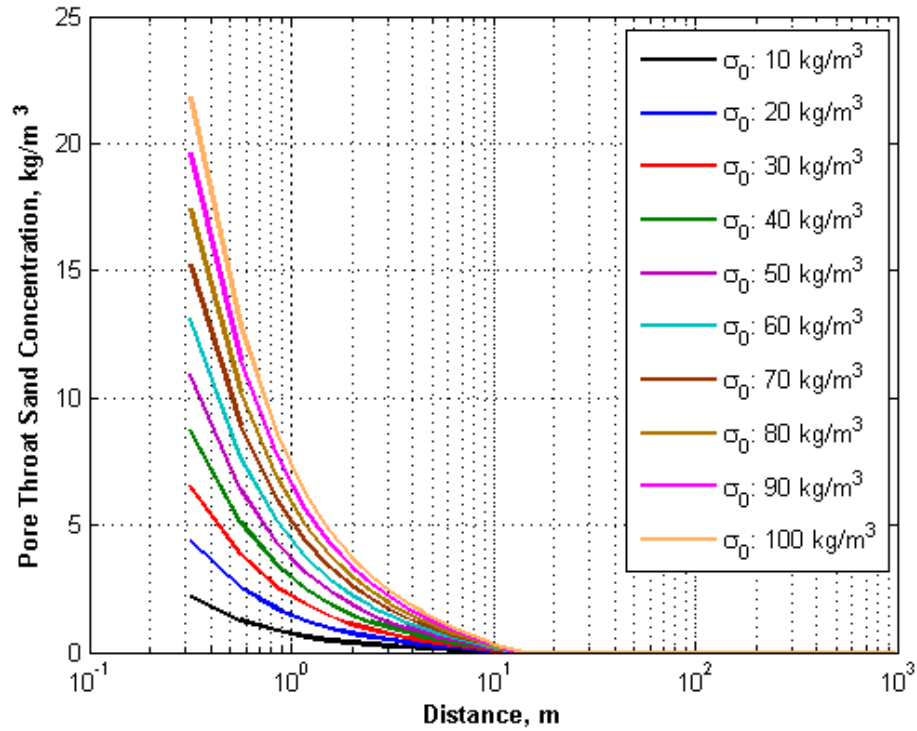


Figure 7.32 Pore Throat Sand Concentration Profile Change after 100 days Production with Initial Movable Sand Concentration

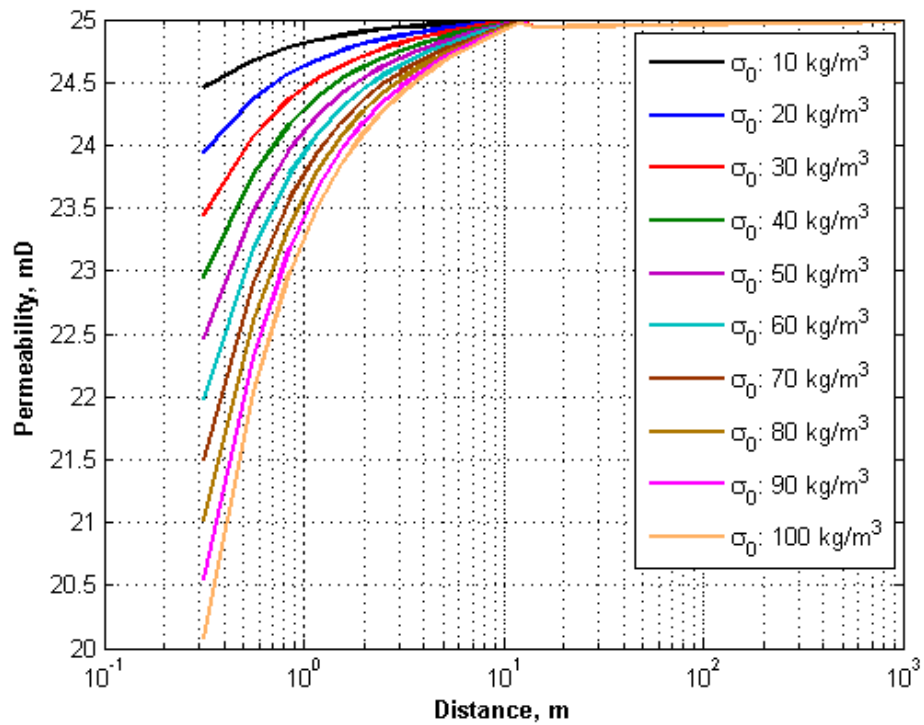


Figure 7.33 Permeability Profile Change after 100 days Production with Initial Movable Sand Concentration

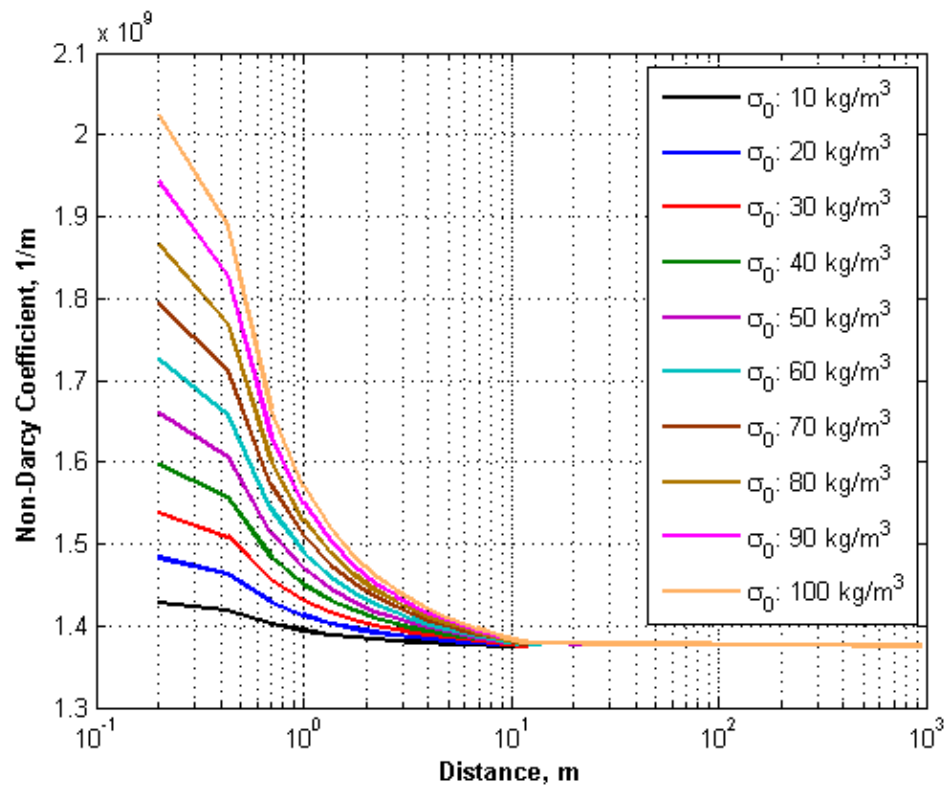


Figure 7.34 Non-Darcy Coefficient Profile Change after 100 days Production with Initial Movable Sand Concentration

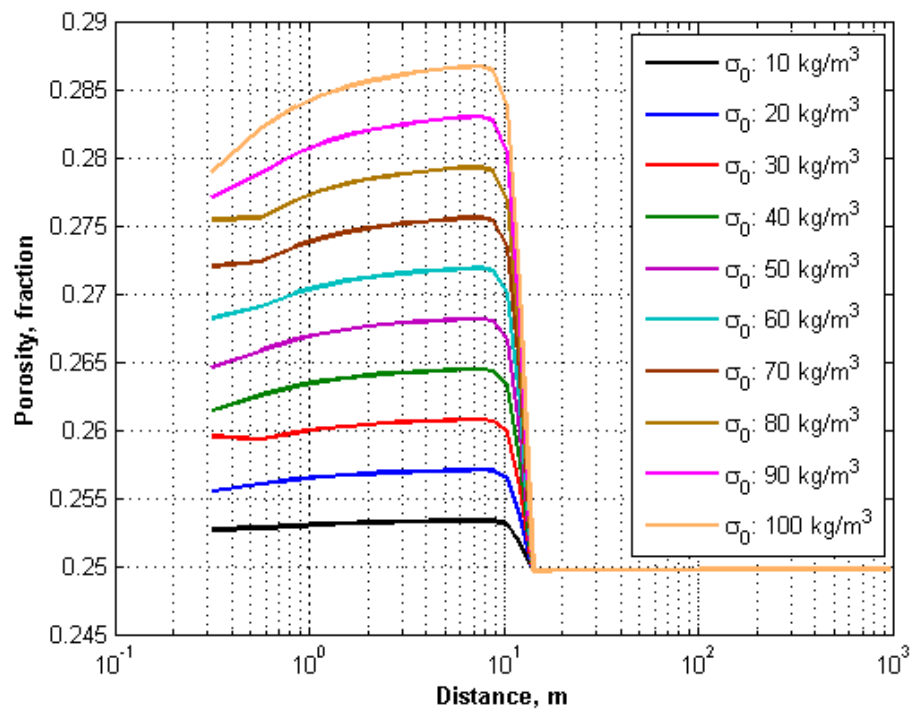


Figure 7.35 Porosity Profile Change after 100 days Production with Initial Movable Sand Concentration

### 7.3.2. Critical Velocity Effect on Sand Production

Erosion of sand particle occurs if the fluid velocity is greater than the critical velocity; therefore, critical velocity has great impact on sand production and reservoir properties. Figure 7.36 gives the wellblock pressure change with critical velocity between 0.00002 m/sec to 0.001 m/sec. Small critical velocities has great effect on wellblock pressure; for example, increase in critical velocity from 0.00002 m/sec to 0.00003 m/sec leads to increase in wellblock pressure from 4.50 MPa to 6.29 MPa. On the other hand, increase in critical velocity from 0.0002 m/sec to 0.001 m/sec leads to increase in wellblock pressure from 10.93 MPa to 11.06 MPa.

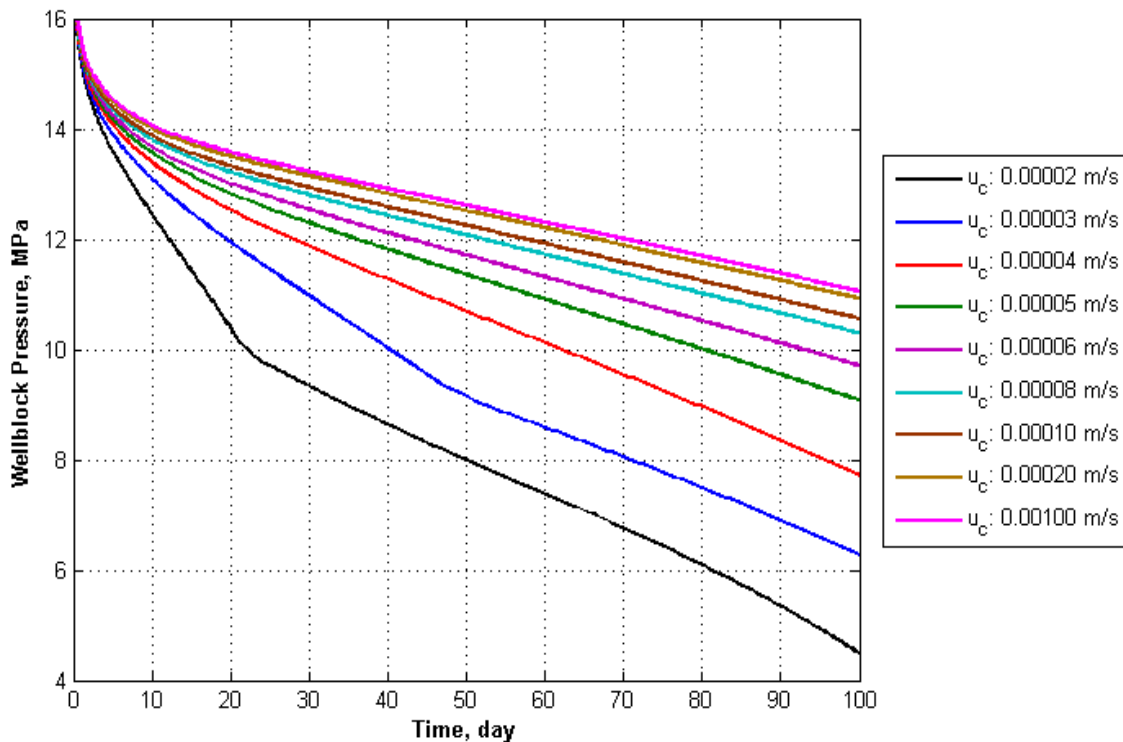


Figure 7.36 Wellblock Pressure Change with Critical Velocity

With the decrease in critical velocity, both the wellblock sand concentration and the time at which maximum sand concentration appears increase (Figure 7.37). For example, maximum sand concentrations and the corresponding times are 0.061 kg/m<sup>3</sup> and 0.67 days, and 4.355 kg/m<sup>3</sup> and 2.51 days for the critical velocities of 0.00002 m/sec and 0.00002 m/sec. This significant

increase in wellblock sand concentration leads to increase in sand production (Figure 7.38). Cumulative sand production increases from 55 kg to 60581 kg with the decrease in critical velocity.

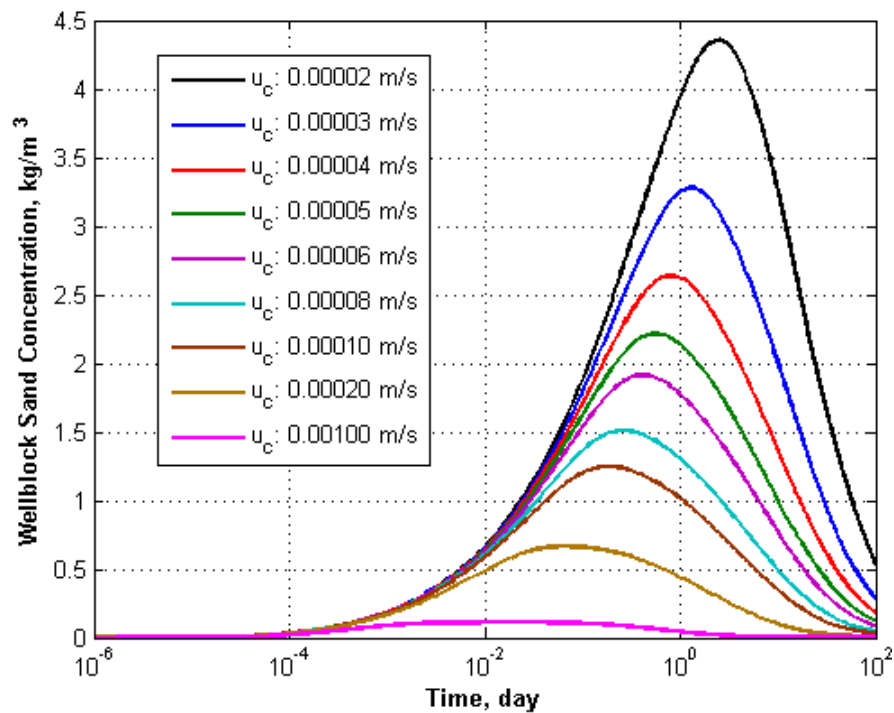
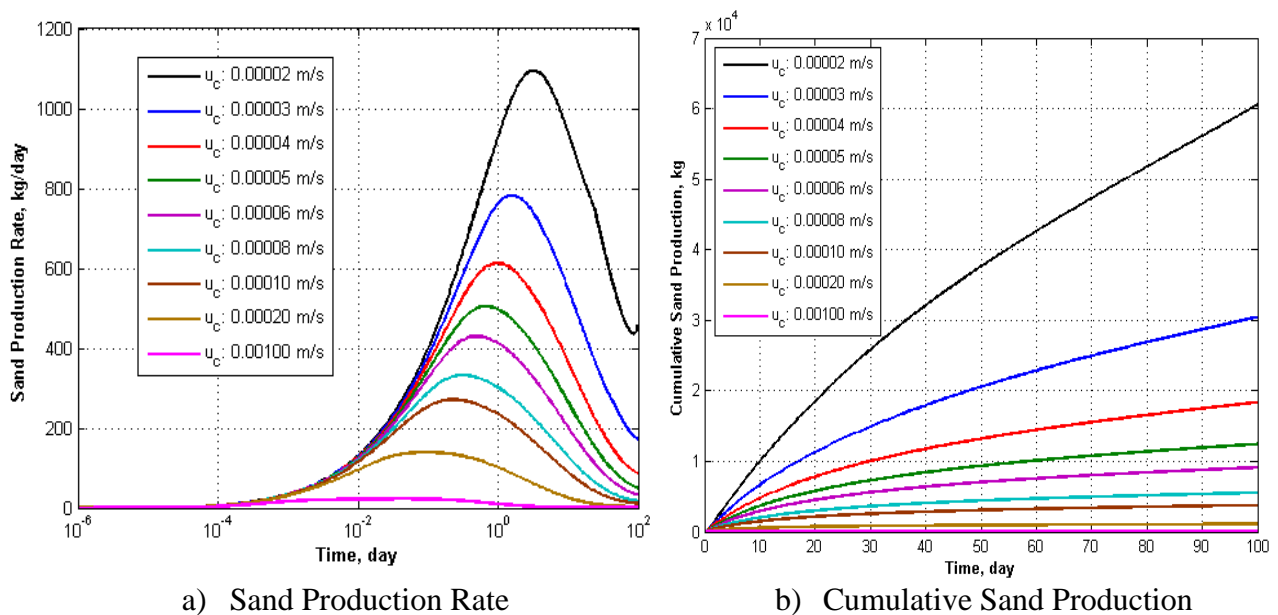


Figure 7.37 Wellblock Sand Concentration Change with Critical Velocity



a) Sand Production Rate

b) Cumulative Sand Production

Figure 7.38 Sand Production Change with Critical Velocity



As the critical velocity decrease, the region suspected to sand migration increases. Decrease in critical velocity from 0.001 m/sec to 0.00002 m/sec leads to increase in sand migration region away from the wellbore from 2 m to 70.43 m, respectively (Figure 7.39 and Figure 7.40). Therefore, while pore surface sand concentration decreases, sand concentration in gas phase increases with decrease in critical velocity.

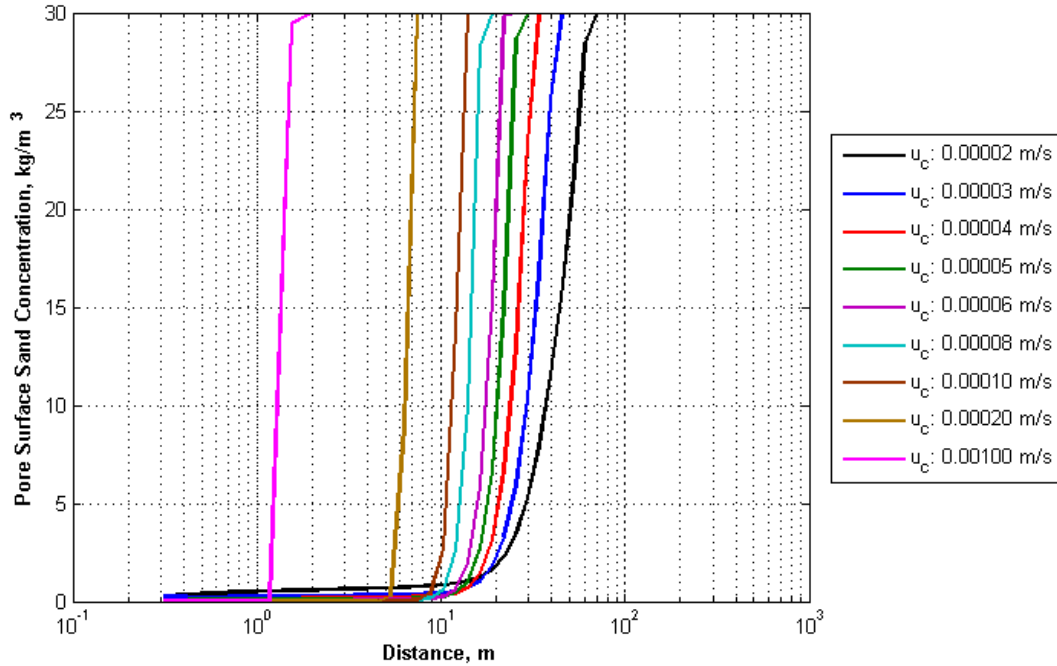


Figure 7.39 Pore Surface Sand Concentration Profile after 100 days Production with Critical Velocity

Increase in gas sand concentration leads to increase in sand concentration at pore throats (Figure 7.41). Critical velocity higher than 0.0003 m/sec, the increase in sand concentration at pore throat is smooth. For lower critical velocities, sand concentration increases approaching the wellbore, then it stabilizes to 32 kg/m³. This is the limiting value of sand concentration at pore throats and it depends on the fraction of pore throat never plugged,  $f_{min}$ , and the characteristic constant of pore throat plugging,  $k_{fe}$ .  $f_{min}$  and  $k_{fe}$  are 0.2 and 0.025 m³/kg, respectively. Similar effects appear in permeability and non-Darcy coefficient. With the increase in sand

concentration at pore throat leads to decrease in permeability and increase in non-Darcy coefficient with a limiting values of 17.83 mD and  $2.548 \times 10^9$  1/m, respectively (Figure 7.42 and Figure 7.43).

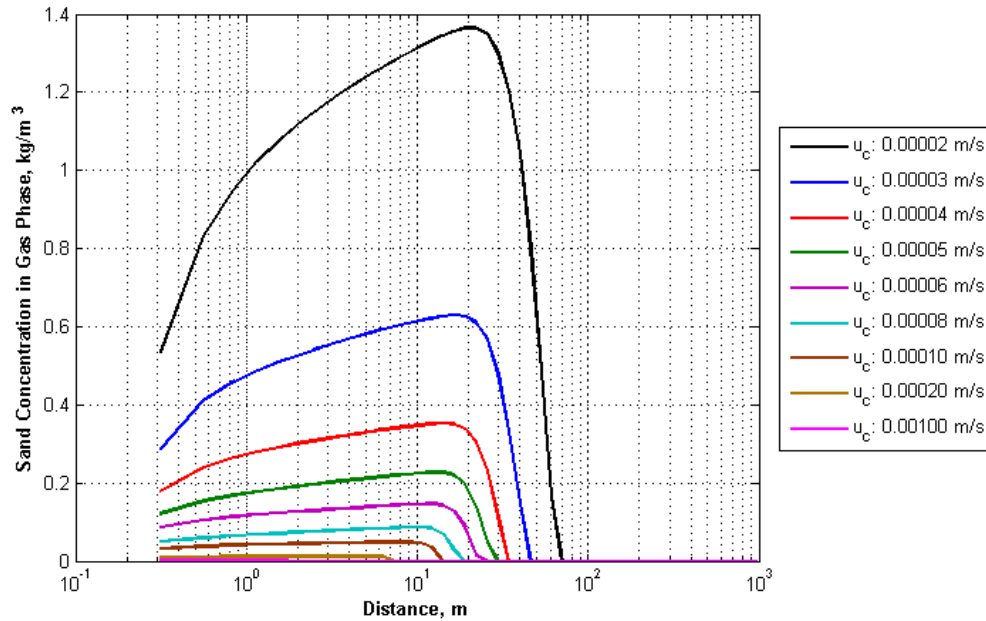


Figure 7.40 Sand Concentration Profile Change after 100 days Production with Critical Velocity

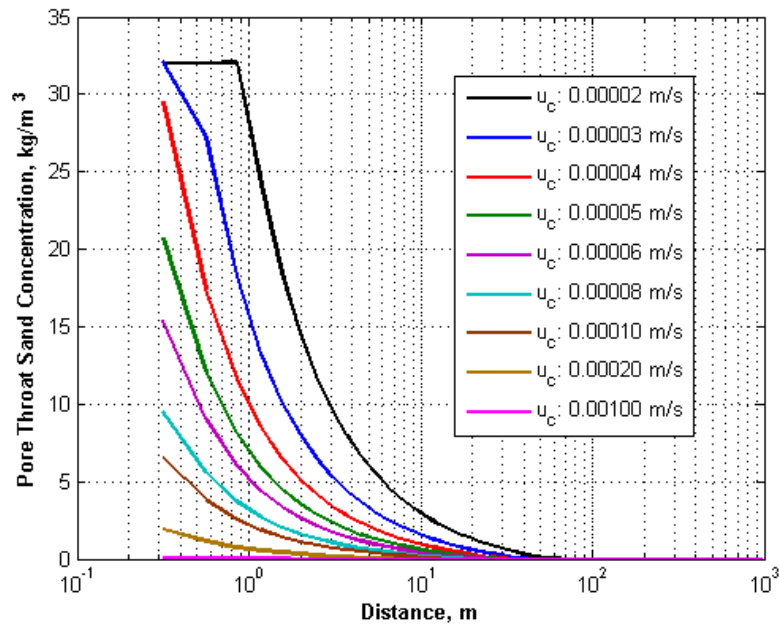


Figure 7.41 Pore Throat Sand Concentration Profile Change after 100 days Production with Critical Velocity

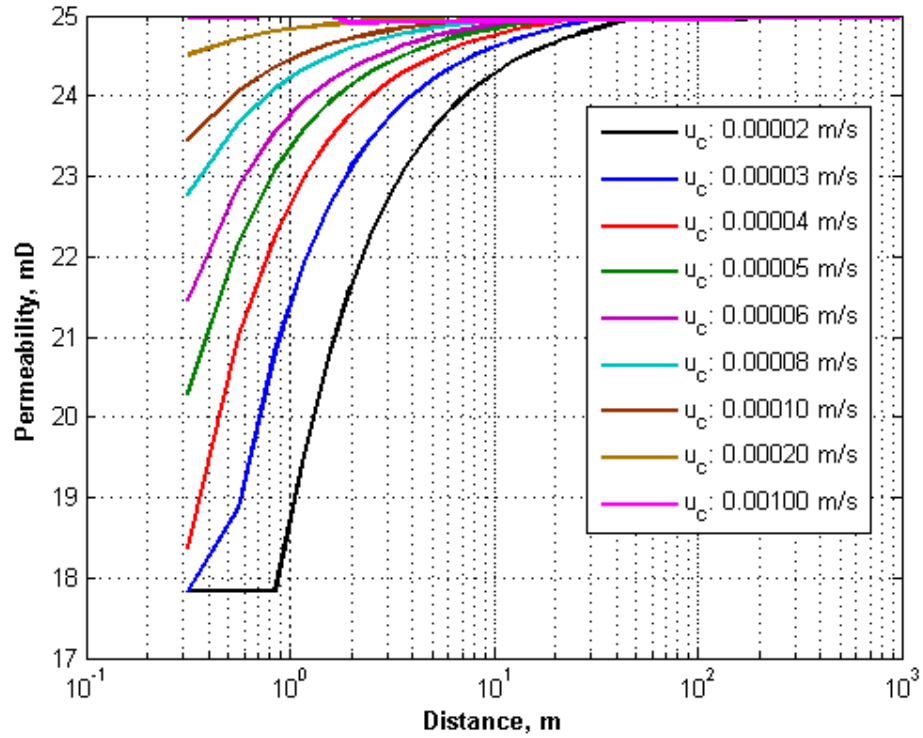


Figure 7.42 Permeability Profile Change after 100 days Production with Critical Velocity

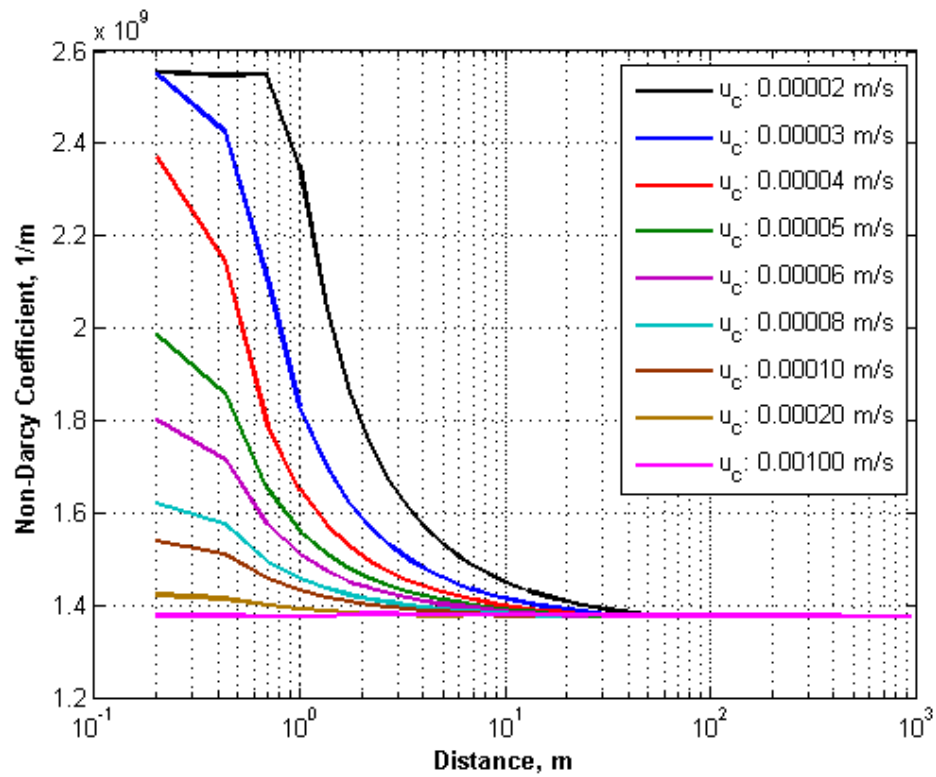


Figure 7.43 Non-Darcy Coefficient Profile Change after 100 days Production with Critical Velocity

For lower critical velocities, porosity away from the wellbore increases since deposition of sand particles cannot compensate the erosion due to low sand concentration in gas phase. Approaching the wellbore, porosity starts to decrease and reach minimum value (Figure 7.44). Unlike permeability and non-Darcy coefficient, the minimum value of porosity depends on both pore throat plugging and surface deposition. Since the maximum pore throat sand concentration is greater than initial movable sand concentration, the limiting porosity, 0.249, is less than initial porosity, 0.25. The porosity decrease after maximum value becomes less as the critical velocity increase due to low sand concentration in gas phase. Porosity decrease is negligible for critical velocities of 0.002 m/sec and 0.001 m/sec.

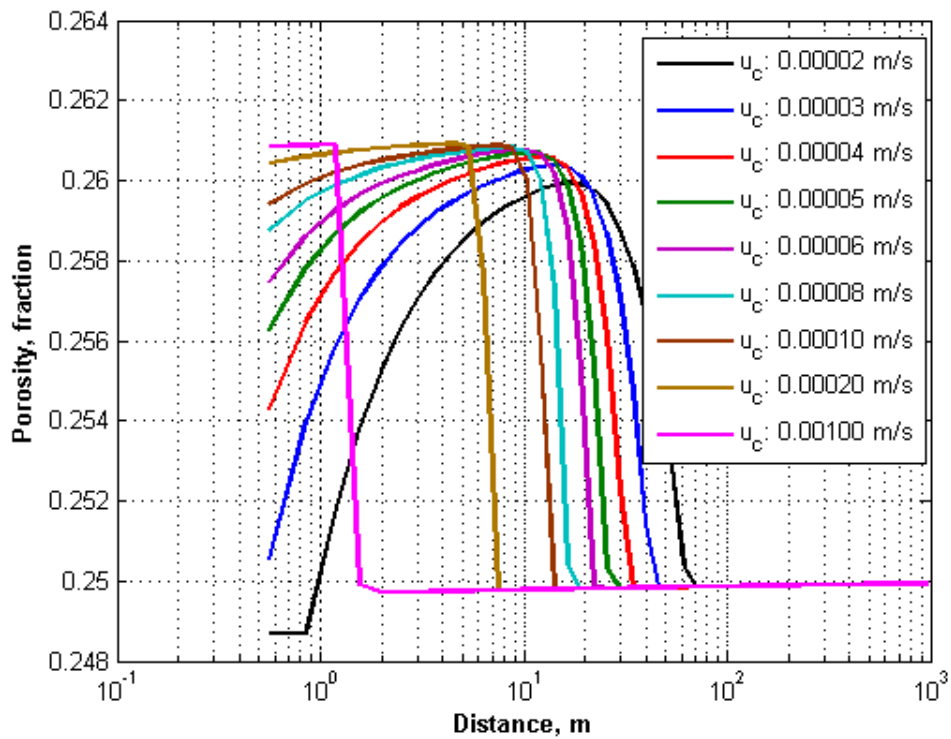


Figure 7.44 Porosity Profile Change after 100 days Production with Critical Velocity

### 7.3.3. Flow Rate Effect on Sand Production

Flow rate has a great effect on wellblock pressure. Wellblock pressure decreases from 22.37 MPa to 9.15 MPa with production increase from 10 Mm<sup>3</sup>/day/m to 42 Mm<sup>3</sup>/day/m (Figure

7.45). The increase in flow rates effect on sand production is similar to effect of critical velocity decrease. Increase in flow rates leads to increase in wellblock sand concentration (Figure 7.46) and sand production (Figure 7.47). Maximum wellblock sand concentration increases from  $0.3416 \text{ kg/m}^3$  to  $1.277 \text{ kg/m}^3$  with the increase from  $10 \text{ Mm}^3/\text{day/m}$  to  $42 \text{ Mm}^3/\text{day/m}$ . Unlike critical velocity effect, the time at which maximum sand concentration appear is constant, 0.181 days. With the increase in wellblock sand concentration, maximum sand production rate and cumulative sand production increases from  $13 \text{ kg/d}$  to  $303 \text{ kg/d}$  and from  $165 \text{ kg}$  to  $4322 \text{ kg}$ , respectively.

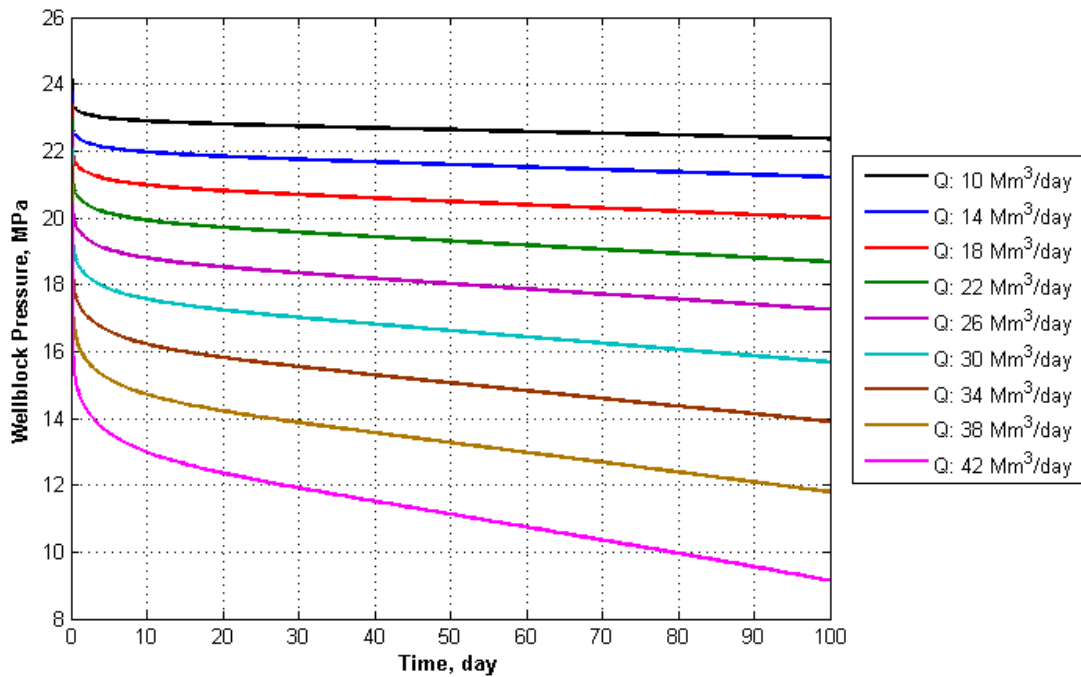


Figure 7.45 Wellblock Pressure Change with Flow Rate

Similar to critical velocity effect, the region effected from sand migration increases with the increase in flow rate since velocities are greater than critical velocity away from the wellbore for high flow rates. For flow rate of  $10 \text{ Mm}^3/\text{day/m}$ , the effected region is  $3.05 \text{ m}$ ; on the other hand, the effected region is  $16.4 \text{ m}$  for the flow rate of  $42 \text{ Mm}^3/\text{day/m}$  (Figure 7.48). Sand

concentration in gas phase increases from 0.007 kg/m<sup>3</sup> to 0.059 kg/m<sup>3</sup> as the flow rate increases and through the wellbore sand concentration decreases due to sand production (Figure 7.49).

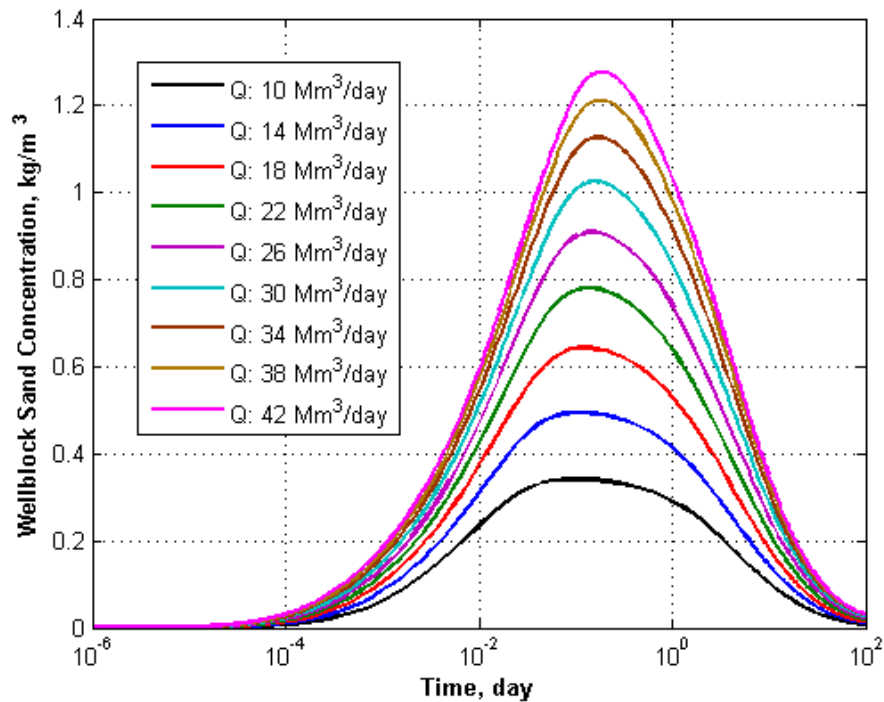
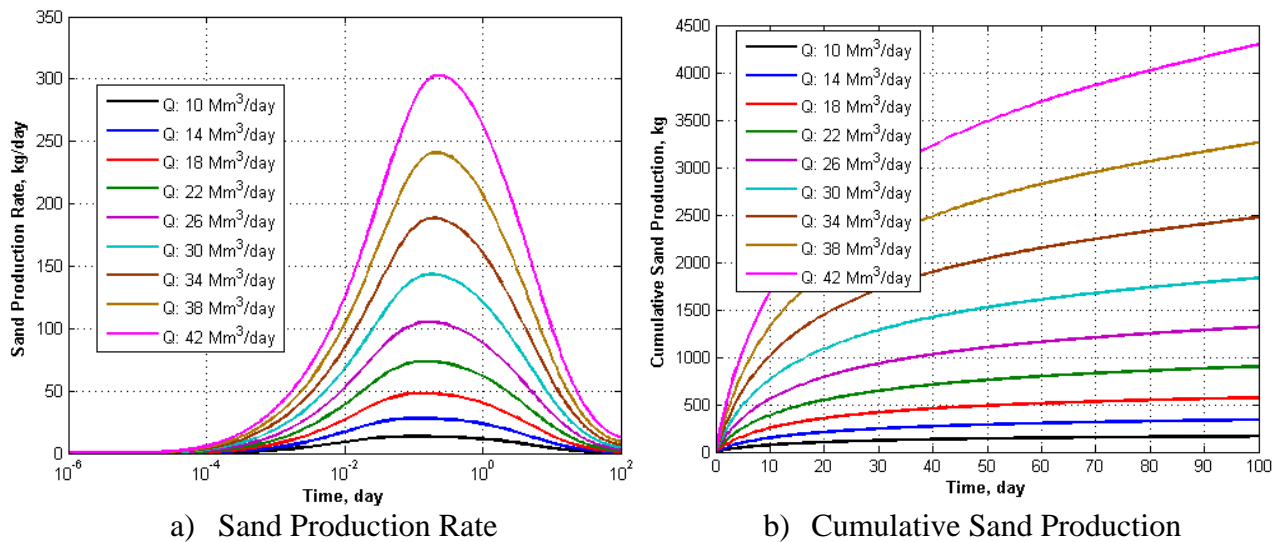


Figure 7.46 Wellblock Sand Concentration Change with Flow Rate



a) Sand Production Rate

b) Cumulative Sand Production

Figure 7.47 Sand Production Change with Flow Rate

Sand concentration at pore throat increases up to 7.22 kg/m<sup>3</sup> due to increase in sand concentration in gas phase (Figure 7.50). Increase in sand concentration at pore throat leads to

decrease in permeability up to 23.29 (Figure 7.51) and increase in non-Darcy coefficient up to  $1.56 \times 10^9$  1/m (Figure 7.52). The change of permeability and non-Darcy coefficient seems to be insignificant. The changes of them are limited with the initial movable sand concentration.

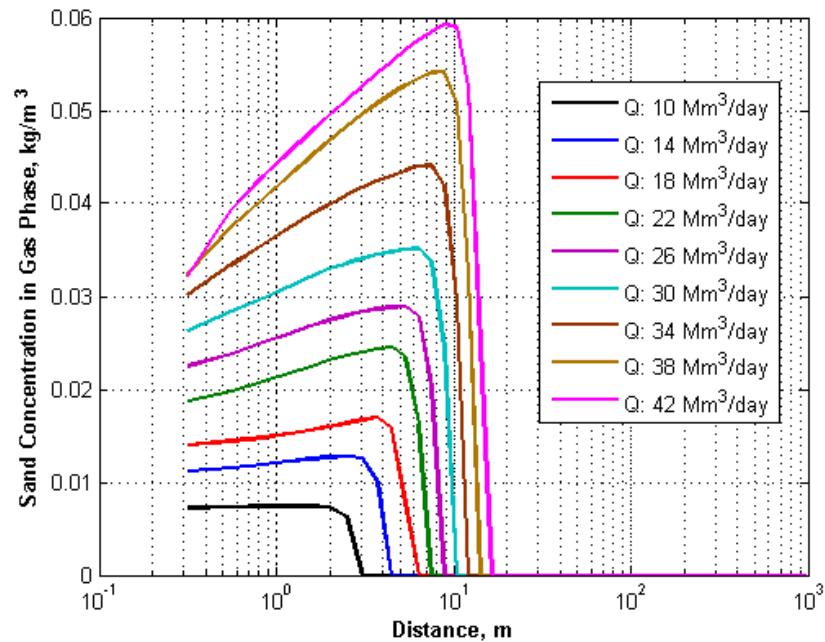


Figure 7.48 Sand Concentration Profile Change after 100 days Production with Flow Rate

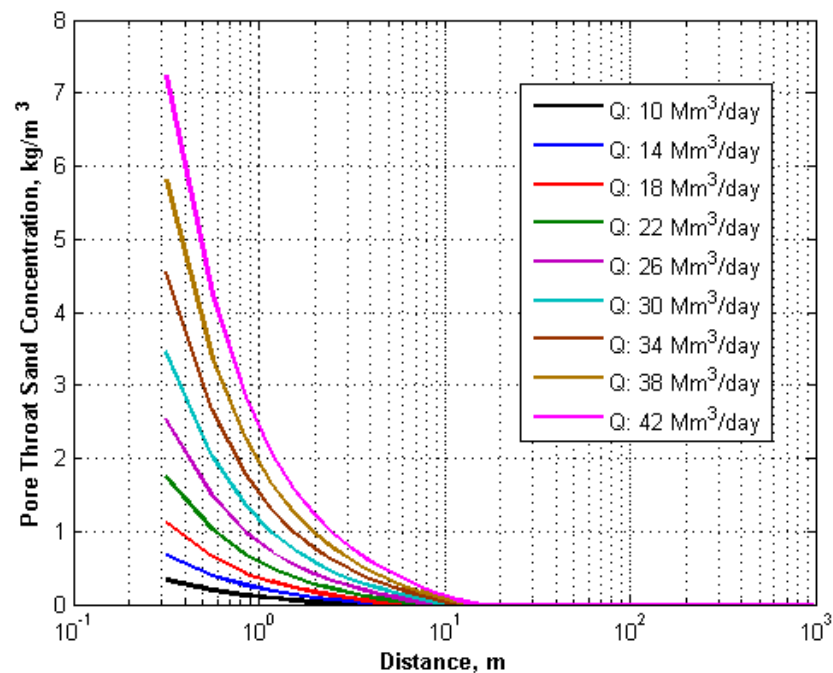


Figure 7.49 Pore Throat Sand Concentration Profile Change after 100 days Production with Flow Rate

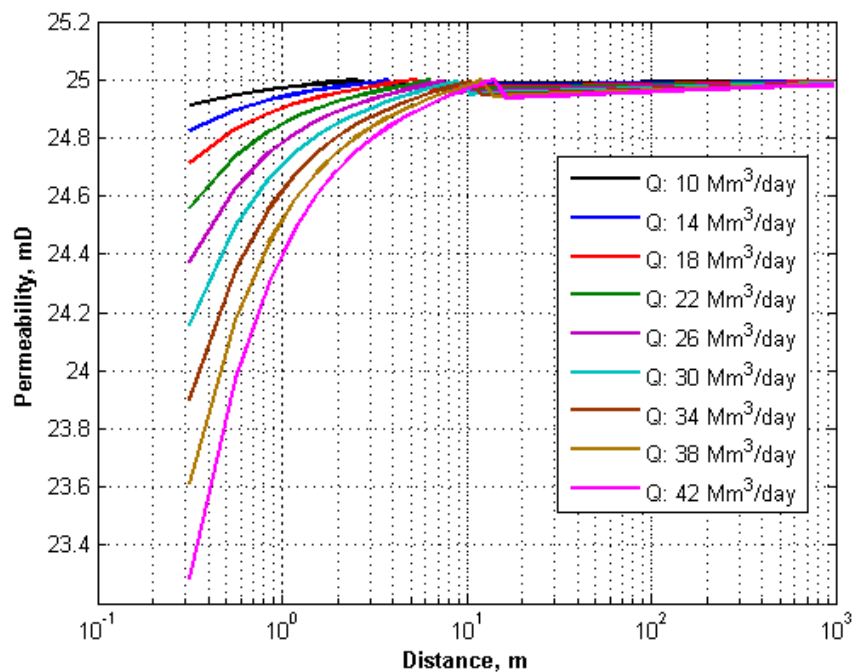


Figure 7.50 Permeability Profile Change after 100 days Production with Flow Rate

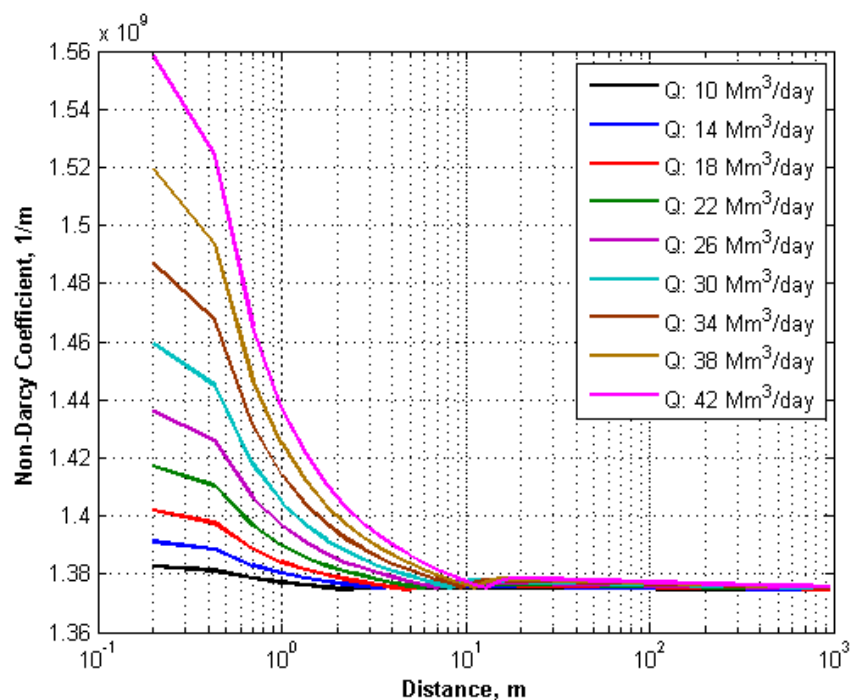


Figure 7.51 Non-Darcy Coefficient Profile Change after 100 days Production with Flow Rate

Porosity increases up to 0.2611 that equals to sum of initial porosity, 0.25, and initial movable sand concentration over sand density,  $30 \text{ kg/m}^3 / 2670 \text{ kg/m}^3$  (Figure 7.53). Porosity



decreases slightly near the wellbore for the high flow rates since the possibility of sand particle capture at the pore throat or on the pore surface increases with the increase in region affected by sand migration.

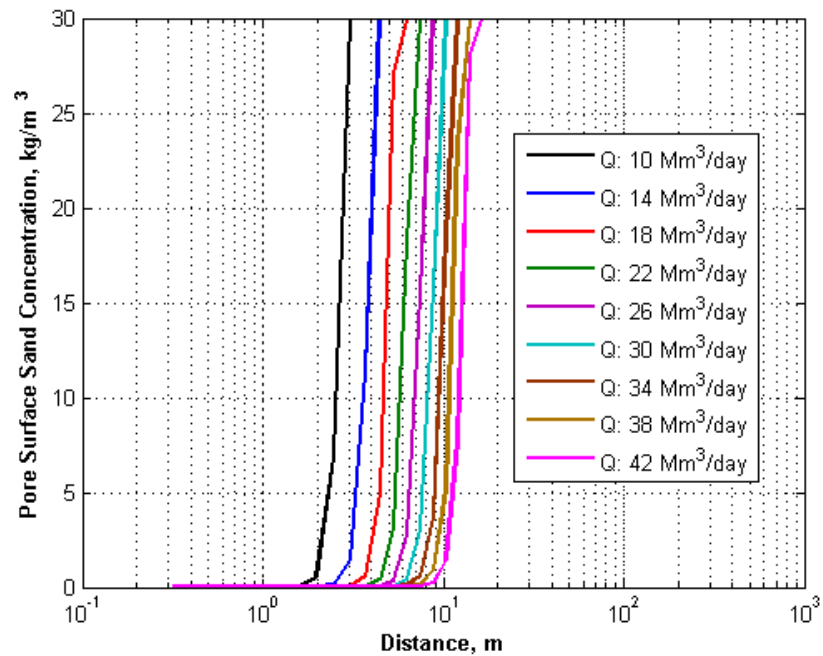


Figure 7.52 Pore Surface Sand Concentration Profile after 100 days Production with Flow Rate

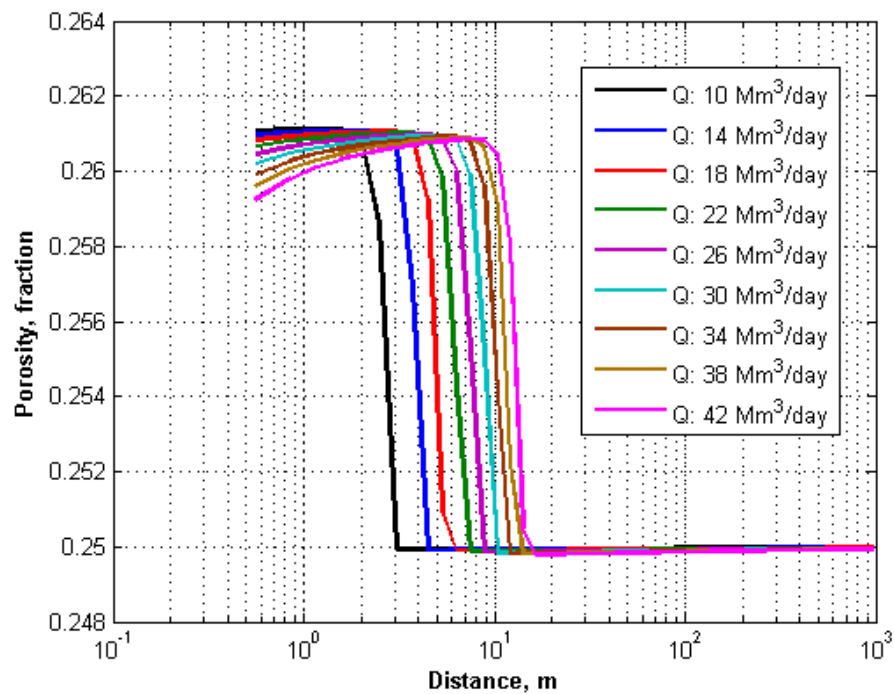


Figure 7.53 Porosity Profile Change after 100 days Production with Flow Rate

#### 7.3.4. Pore Throat Plugging Rate Constant Effect on Sand Production

Increase in pore throat plugging rate constant has great effect on wellblock pressure. Wellblock pressure changes from 11.02 MPa to 4.50 MPa as pore plugging rate constant increases from 0.0001 1/m to 0.03 1/m (Figure 7.54). However, for small pore throat plugging constants, between 0.0001 1/m and 0.001 1/m, the change of wellblock pressure is negligible, 0.46 MPa.

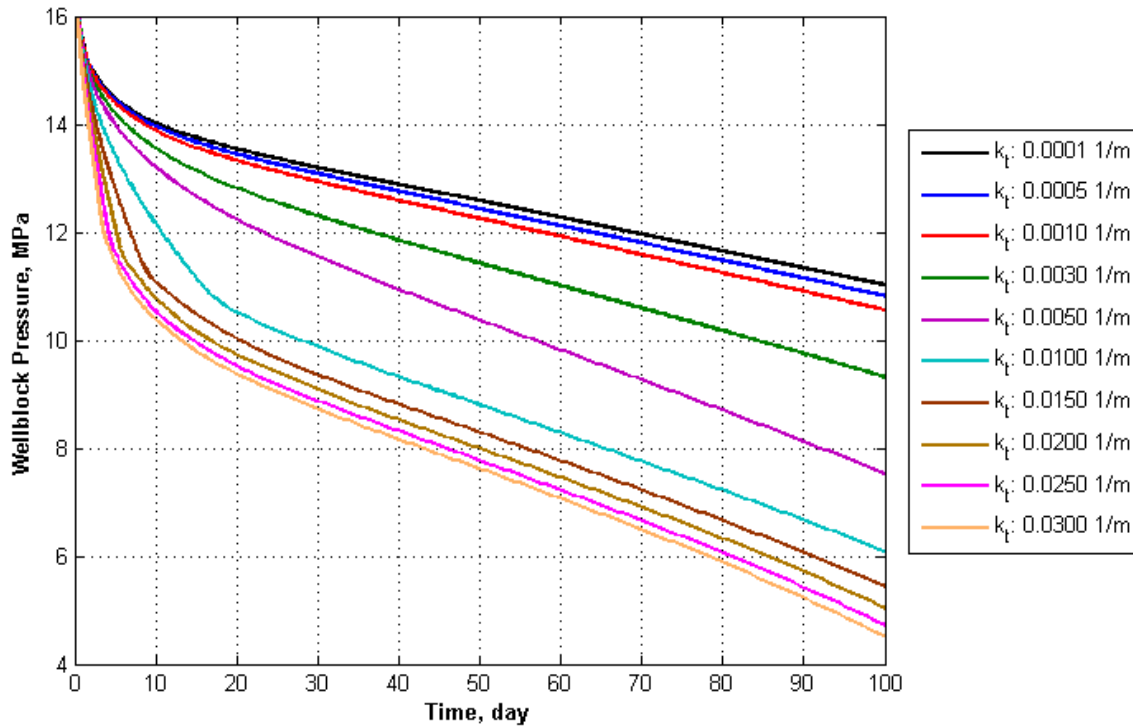


Figure 7.54 Wellblock Pressure Change with Pore Throat Plugging Constant

Wellblock sand concentration (Figure 7.55) and sand production (Figure 7.56) are slightly affected from pore throat plugging rate constant. Maximum wellblock sand concentration decreases from 1.247 kg/ m<sup>3</sup> to 1.114 kg/ m<sup>3</sup> with the increase in pore throat plugging constant from 0.0001 1/m to 0.03 1/m. Cumulative sand production changes from 3885 kg to 3570 kg. Sand concentration in gas phase is affected with pore throat plugging constant (Figure 7.57). The maximum value of sand concentration decreases from 0.0489 kg/ m<sup>3</sup> to

0.0431 kg/m<sup>3</sup> due to sand deposition at pore throat. After reaching maximum value at a distance of 8.81 m, sand concentration start to decreases approaching the wellbore.

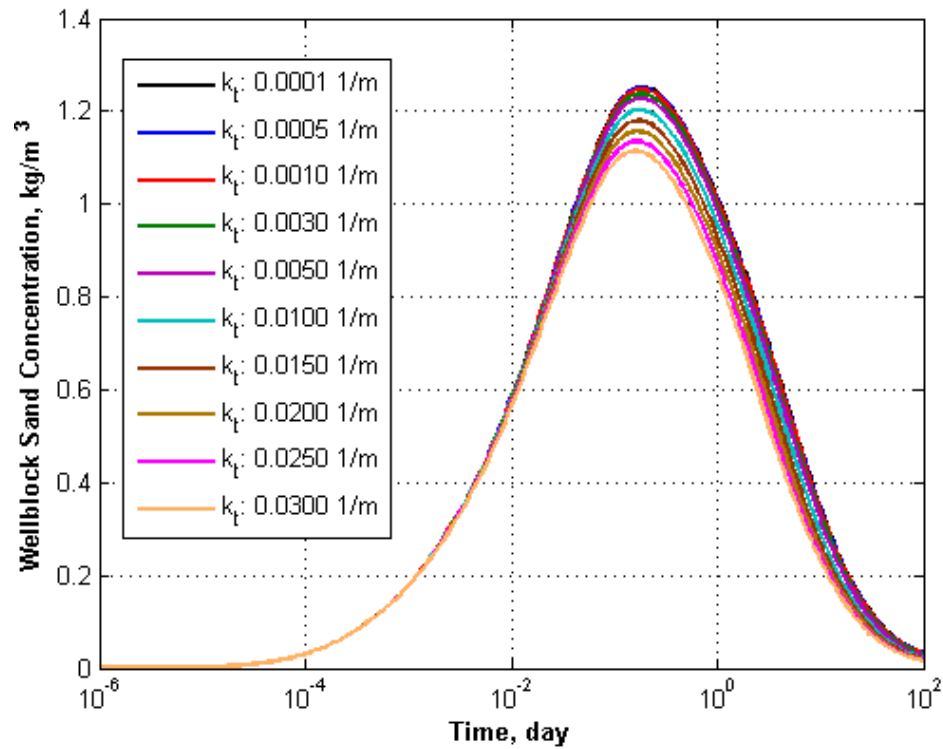
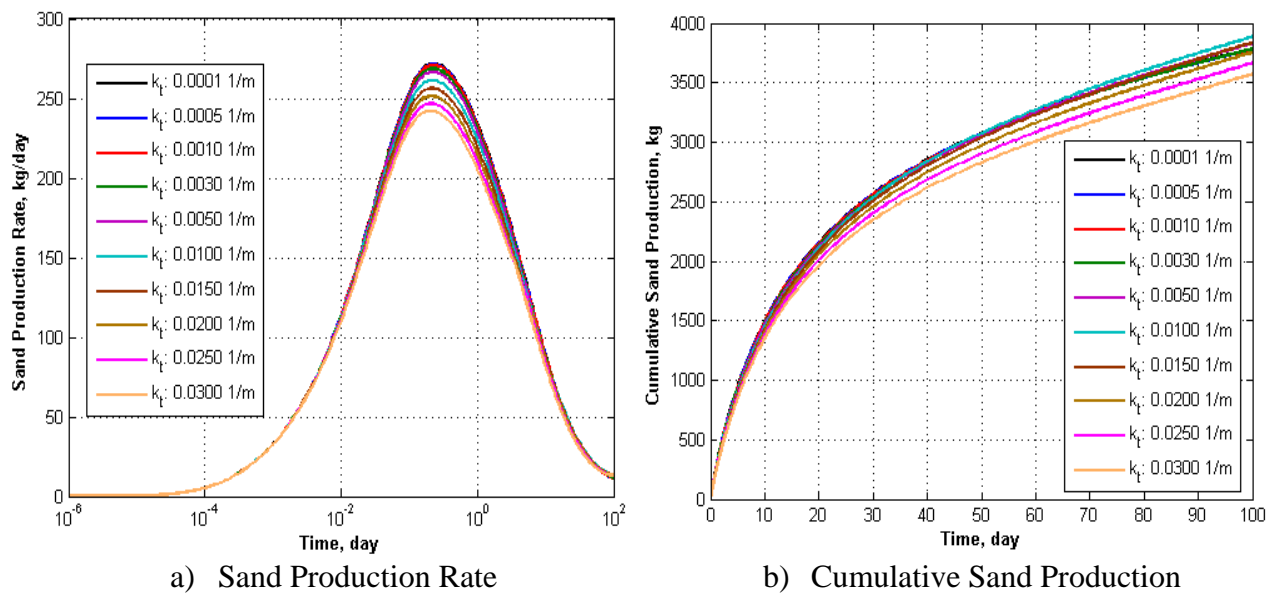


Figure 7.55 Wellblock Sand Concentration Change with Pore Throat Plugging Constant



a) Sand Production Rate  
b) Cumulative Sand Production  
Figure 7.56 Sand Production Change with Pore Throat Plugging Constant

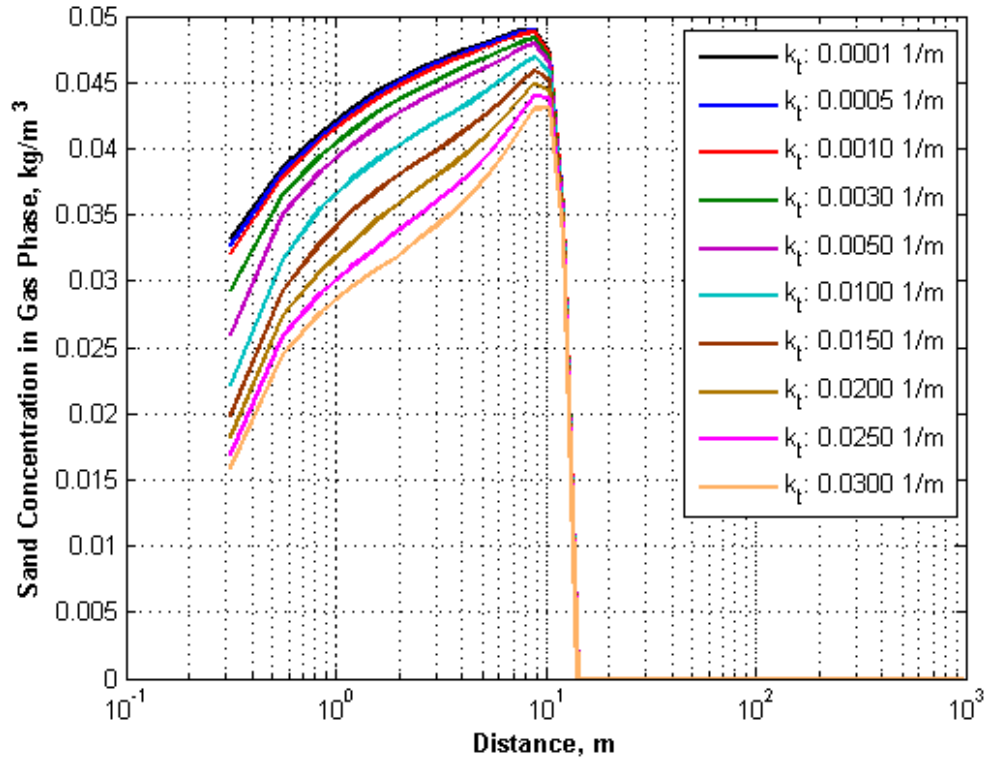


Figure 7.57 Sand Concentration Profile Change after 100 days Production with Pore Throat Plugging Constant

Erosion is much more affected than sand deposition near wellbore; therefore, pore surface sand concentration is 0 up to a distance 7.49 m and it does not depend on pore throat plugging rate constant (Figure 7.58). This indicates that difference in sand concentration in gas phase is only related with sand deposition at pore throats. Sand concentration at pore throat increases from 0.66 kg/ m<sup>3</sup> to limiting value of 32 kg/ m<sup>3</sup> (Figure 7.59). After reaching the limiting value of pore throat sand concentration, maximum pore throat plugging region extents to 1.55 m.

Even though pore throat plugging constant has little effect on sand production, permeability and non-Darcy coefficient change strongly as a function of sand concentration at pore throat. These strongly affect the wellblock pressures. Increase in sand concentration up to

limited value leads to decrease in permeability (Figure 7.60) and increase in non-Darcy coefficient (Figure 7.61) with limiting values of 17.81 mD and  $2.552 \times 10^9$  1/m, respectively.

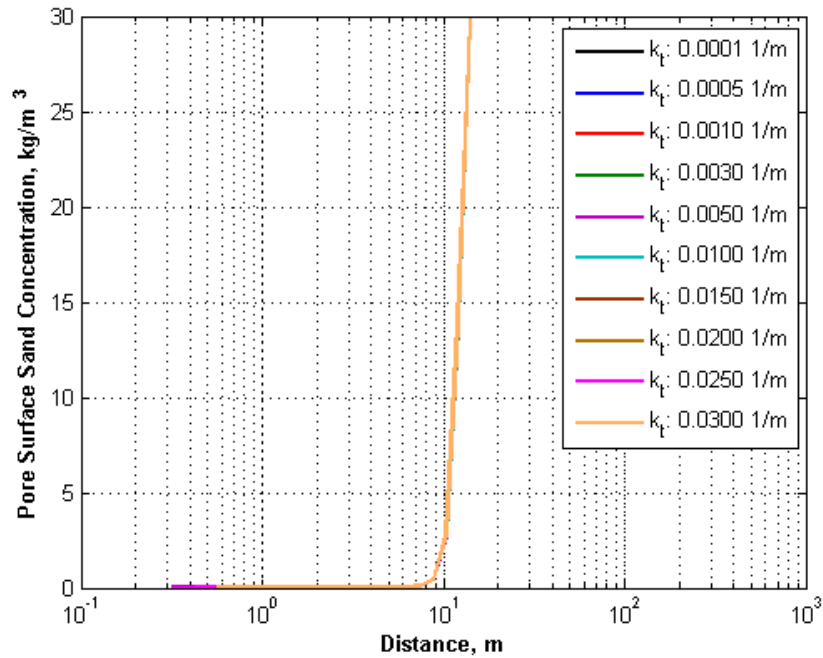


Figure 7.58 Pore Surface Sand Concentration Profile after 100 days Production with Pore Throat Plugging Constant

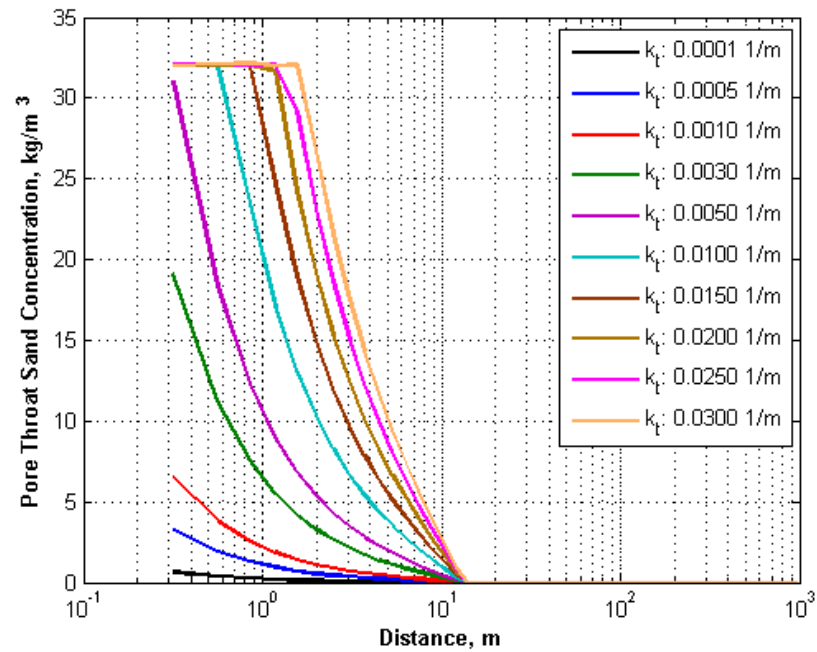


Figure 7.59 Pore Throat Sand Concentration Profile Change after 100 days Production with Pore Throat Plugging Constant

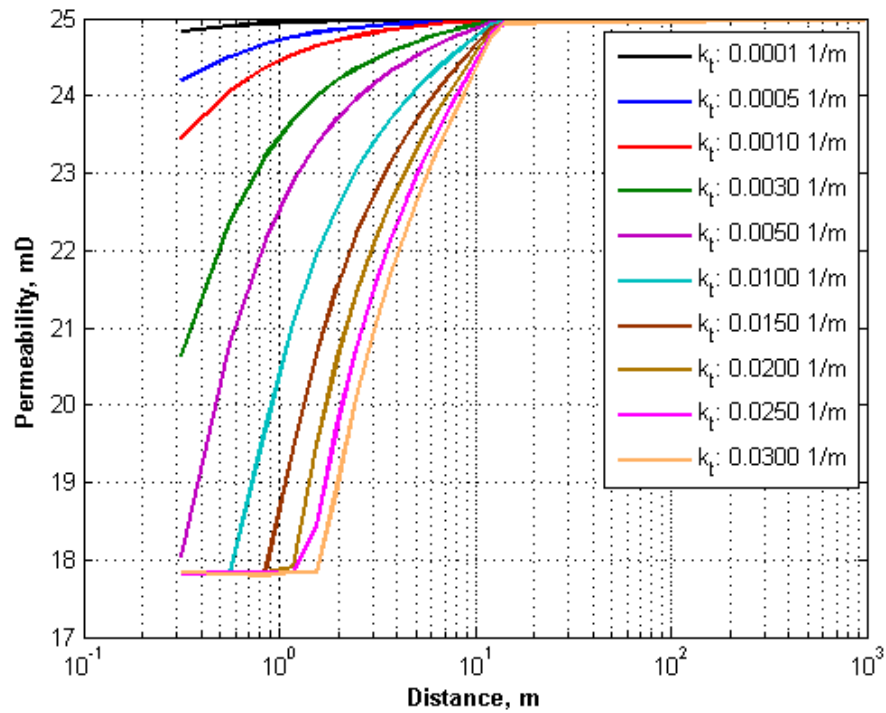


Figure 7.60 Permeability Profile Change after 100 days Production with Pore Throat Plugging Constant

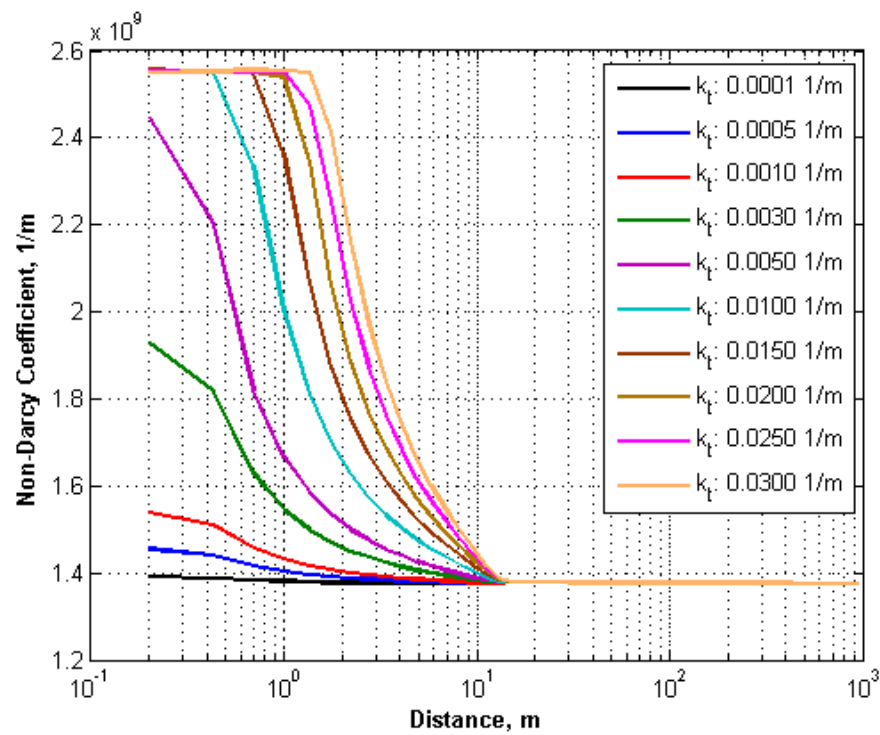


Figure 7.61 Non-Darcy Coefficient Profile Change after 100 days Production with Pore Throat Plugging Constant

Increase in sand concentration at pore throat leads to decrease in porosity, limited value of porosity is constant, 0.249 (Figure 7.62). This is the related with initial moveable sand concentration,  $30 \text{ kg/ m}^3$ , and maximum limited pore throat sand concentration,  $32 \text{ kg/ m}^3$ . The difference is  $2 \text{ kg/ m}^3$  and its cause only porosity decrease of 0.001.

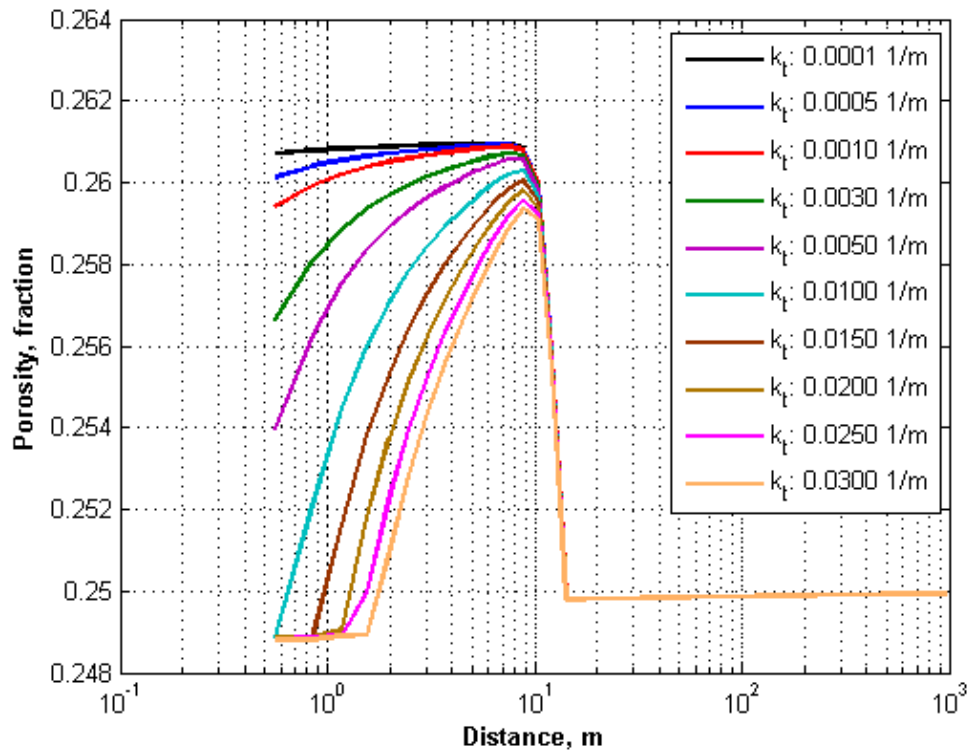


Figure 7.62 Porosity Profile Change after 100 days Production with Pore Throat Plugging Constant

#### 7.3.5. Pore Surface Retention Rate Constant Effect on Sand Production

Surface retention of solid particles has almost no effect on wellblock pressure and its changes is similar with the base case (Figure 7.19 – Case 3) even though increase in surface retention cause slight decrease in wellblock sand concentration (Figure 7.63) and cumulative sand production (Figure 7.64). The maximum wellblock sand concentration decreases from  $1.266 \text{ kg/ m}^3$  to  $1.104 \text{ kg/ m}^3$  at about 0.17 days. The wellblock sand concentration difference negligible after 8 days production. Small difference in wellblock sand production leads to

decrease in cumulative sand production from 3787 kg to 3671 kg (Figure 7.64). In addition to negligible sand production change, the sand concentration in gas phase change is negligible (Figure 7.65) and pore surface sand concentrations are same (Figure 7.66).

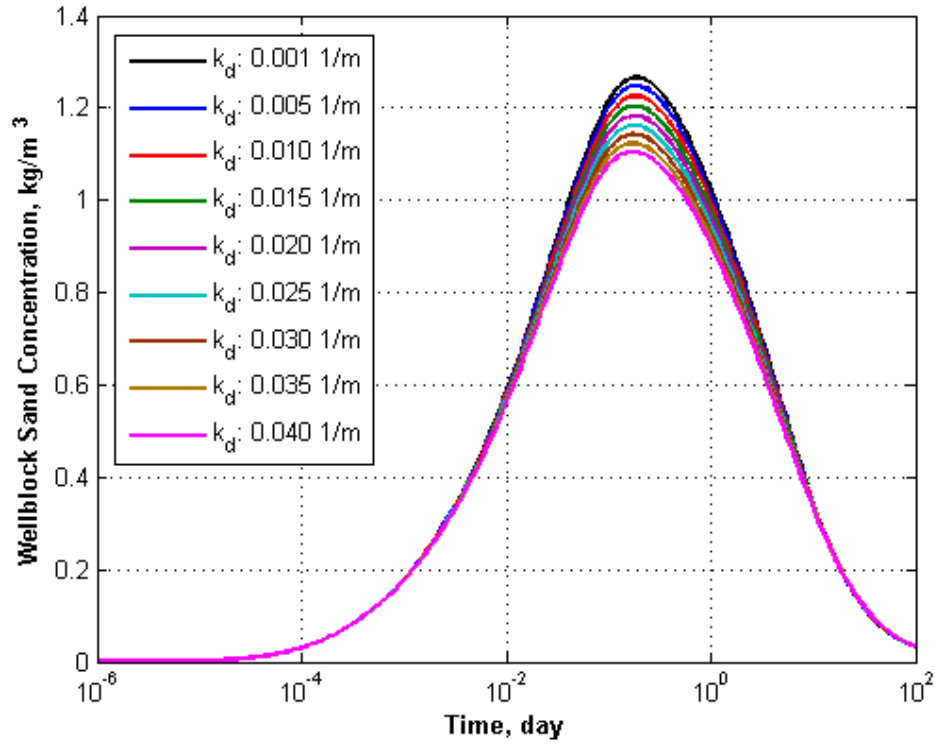


Figure 7.63 Wellblock Sand Concentration Change with Pore Surface Retention Rate Constant

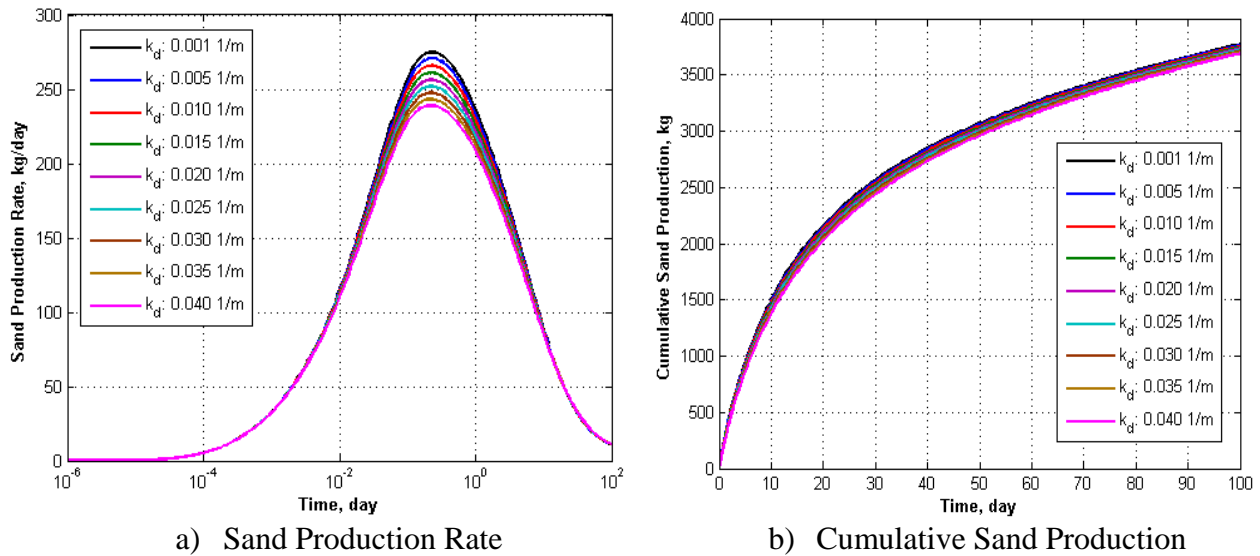


Figure 7.64 Sand Production Change with Pore Surface Retention Rate Constant



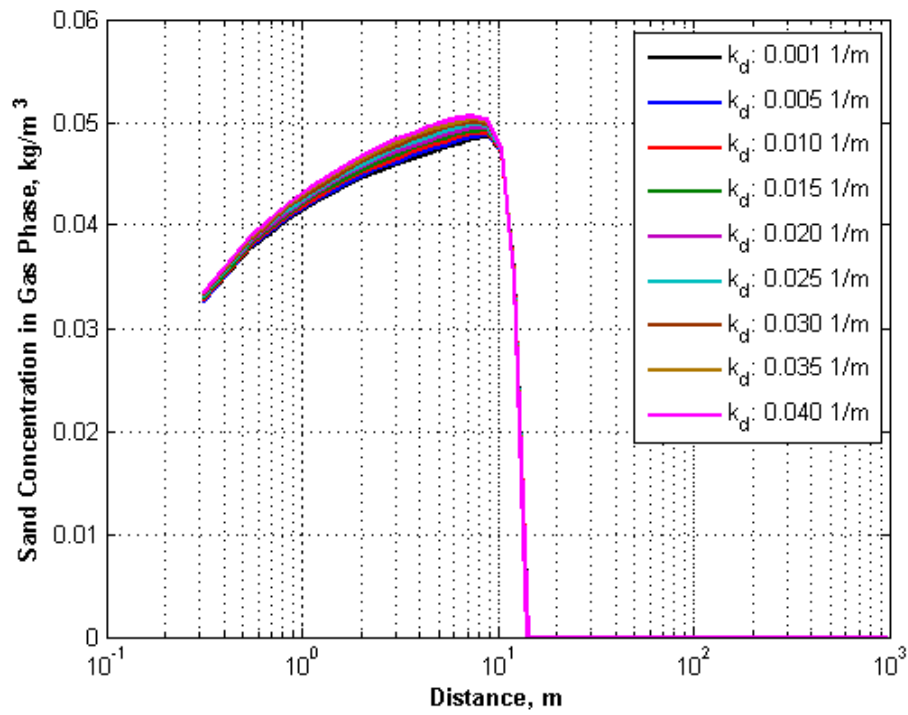


Figure 7.65 Sand Concentration Profile after 100 days Production with Pore Surface Retention Rate Constant

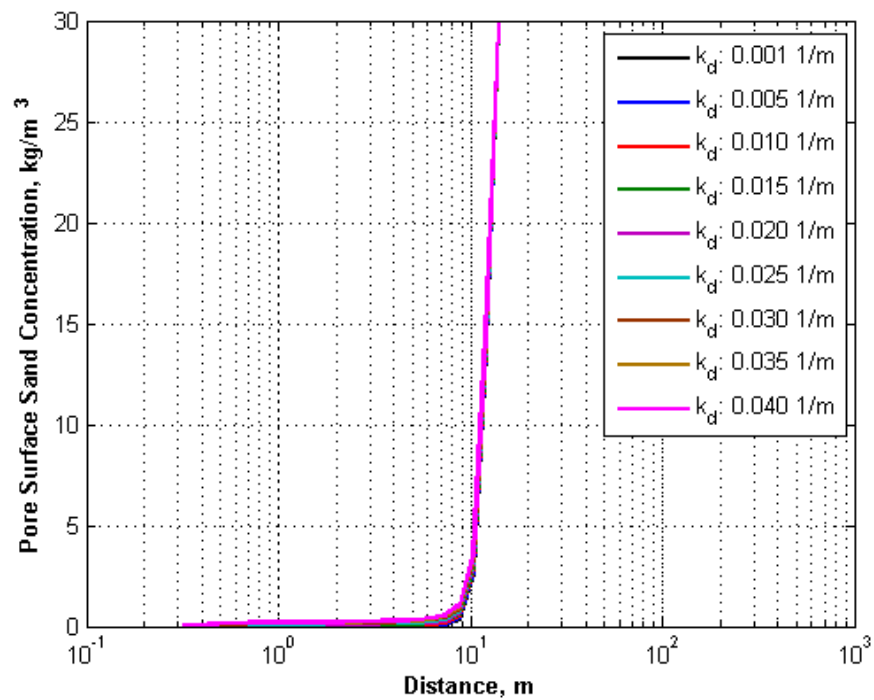


Figure 7.66 Pore Surface Sand Concentration Profile after 100 days Production with Pore Surface Retention Rate Constant

Permeability and non-Darcy coefficient do not function of solid particle deposition on pore surface but pore throat solid concentration. Sand concentrations at pore throat are same compared to base case (Figure 7.26); therefore permeability and non-Darcy coefficient profiles do not change compared to base case (Figure 7.21, Figure 7.22).

### 7.3.6. Pore Surface Entrainment Rate Constant Effect on Sand Production

Pore surface entrainment rate coefficient has little effect on wellblock pressure (Figure 7.67). Wellblock pressure decreases from 10.84 MPa to 10.44 MPa as pore surface entrainment rate increase from 0.001 1/m to 0.08 1/m. With the increase in pore surface entrainment coefficient from 0.001 1/m to 0.080 1/m, maximum wellblock sand concentration and cumulative sand production increase from 0.13 kg/ m<sup>3</sup> to 8.0 kg/ m<sup>3</sup> (Figure 7.68) and from 1714 kg to 4500 kg (Figure 7.69), respectively. Increase in cumulative sand production is insignificant for the entrainment coefficient greater than 0.030 1/m.

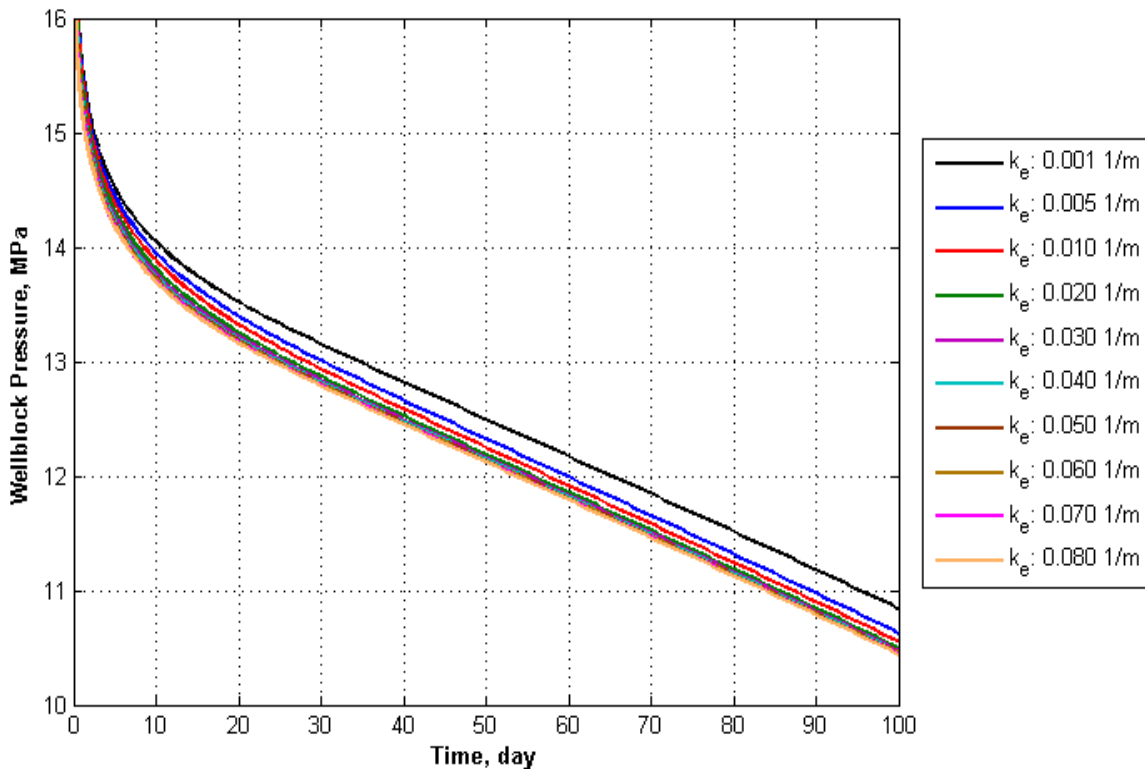


Figure 7.67 Wellblock Pressure Change with Pore Surface Entrainment Rate Constant

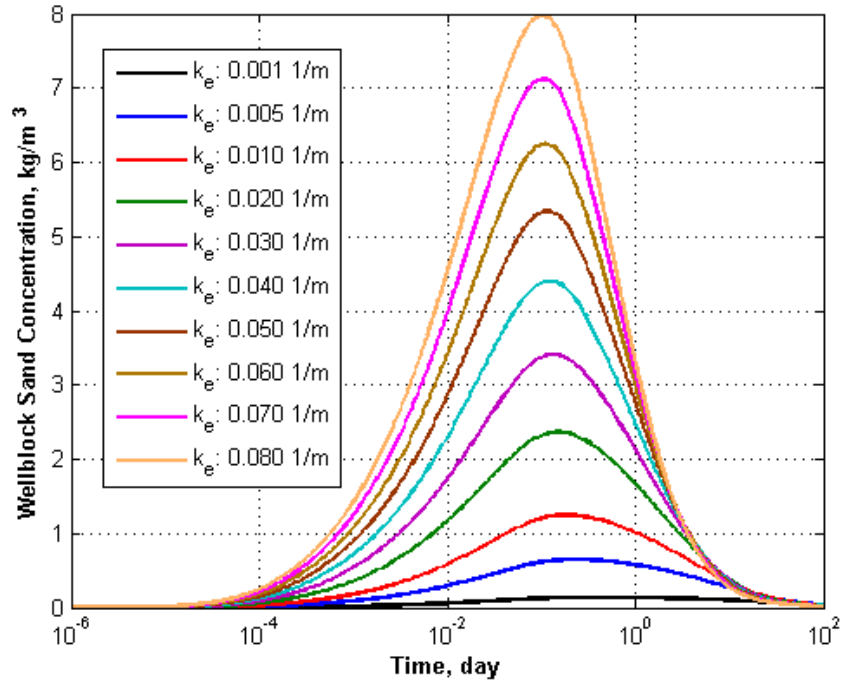
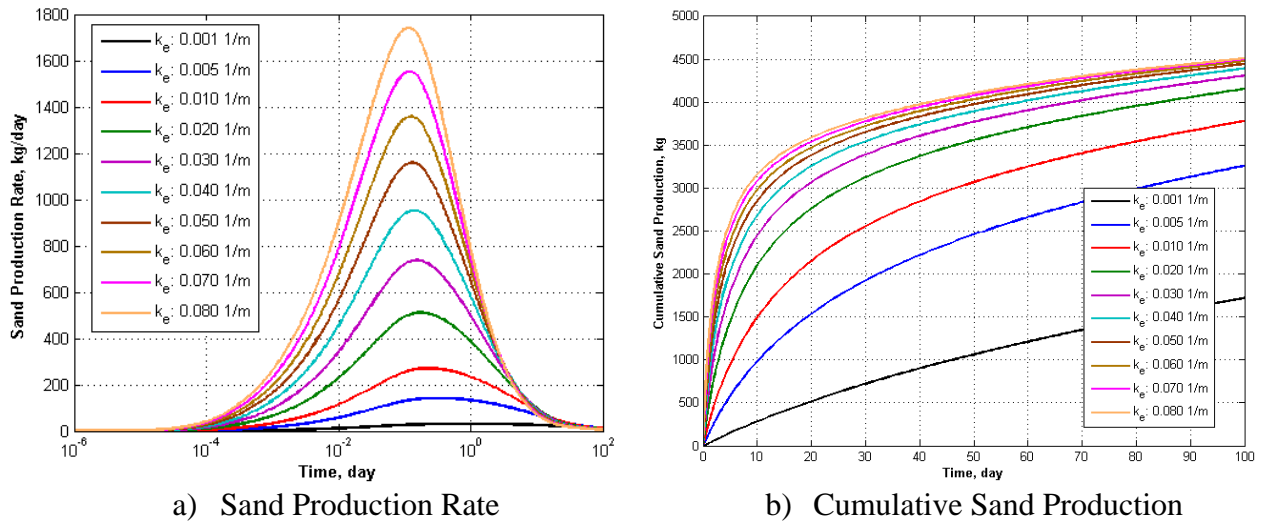


Figure 7.68 Wellblock Sand Concentration Change with Pore Surface Entrainment Rate Constant



a) Sand Production Rate  
b) Cumulative Sand Production  
Figure 7.69 Sand Production Change with Pore Surface Entrainment Rate Constant

Sand concentration in gas phase seems to decrease with the increase in pore surface entrainment rate coefficient (Figure 7.70). With the increase in pore surface entrainment rate, sand production rate increase to maximum value and decrease are sharp. Therefore, sand production rate after 100 days lower for higher entrainment rate coefficient. Therefore, this trend

is related with pore surface sand concentration after 100 days of production. The surface sand concentration is less for high entrainment rate coefficient (Figure 7.71).

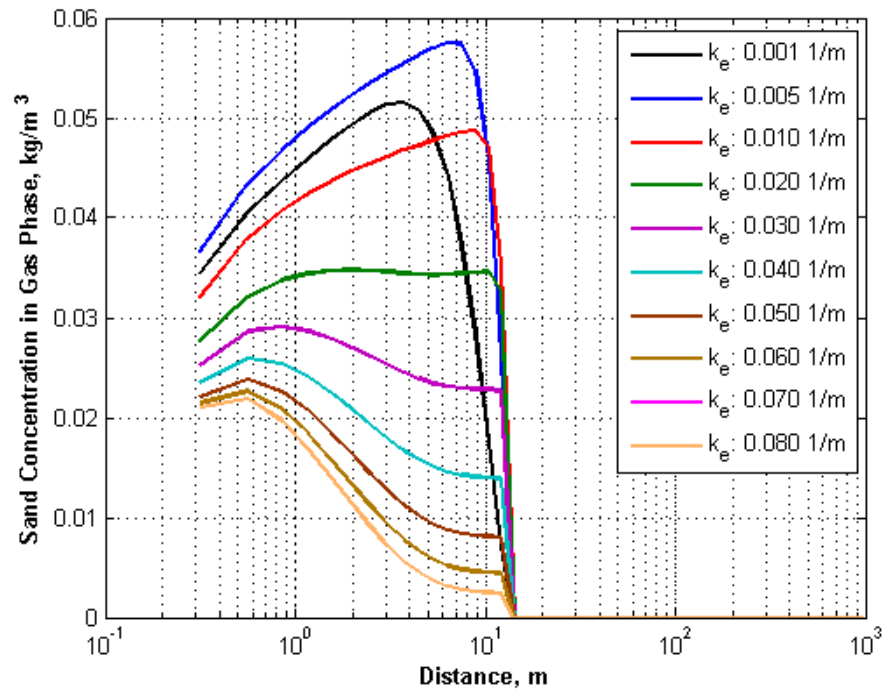


Figure 7.70 Sand Concentration Profile after 100 days Production with Pore Surface Entrainment Rate Constant

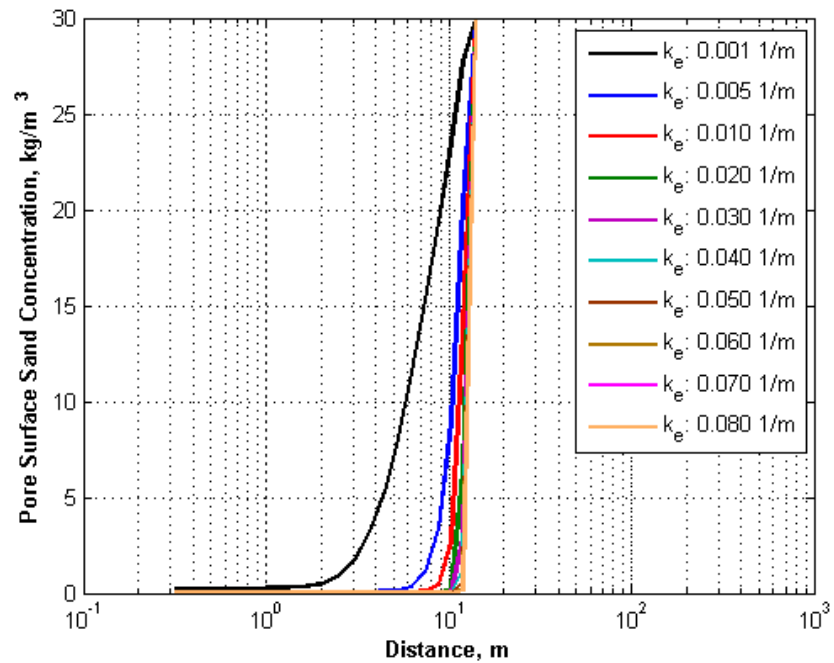


Figure 7.71 Pore Surface Sand Concentration Profile after 100 days Production with Pore Surface Entrainment Rate Constant

Pore throat sand concentration increases from 2.95 kg/ m<sup>3</sup> to 7.91 kg/ m<sup>3</sup> with the increase in pore surface entrainment rate constant; however, the change of sand concentration at pore throat is negligible after entrainment rate constant of 0.020 1/m (Figure 7.72). Permeability and non-Darcy coefficient changes show similar trend with sand concentration at pore throat. Permeability decreases from 24.27 mD to 23.14 mD (Figure 7.73), and non-Darcy coefficient increases from 1.447 x10<sup>9</sup> 1/m to 1.574 x10<sup>9</sup> 1/m (Figure 7.74). For pore surface entrainment rate coefficients greater than 0.020 1/m, porosity increases to 0.2612 and shows similar trends due to similar pore throat sand concentration (Figure 7.75).

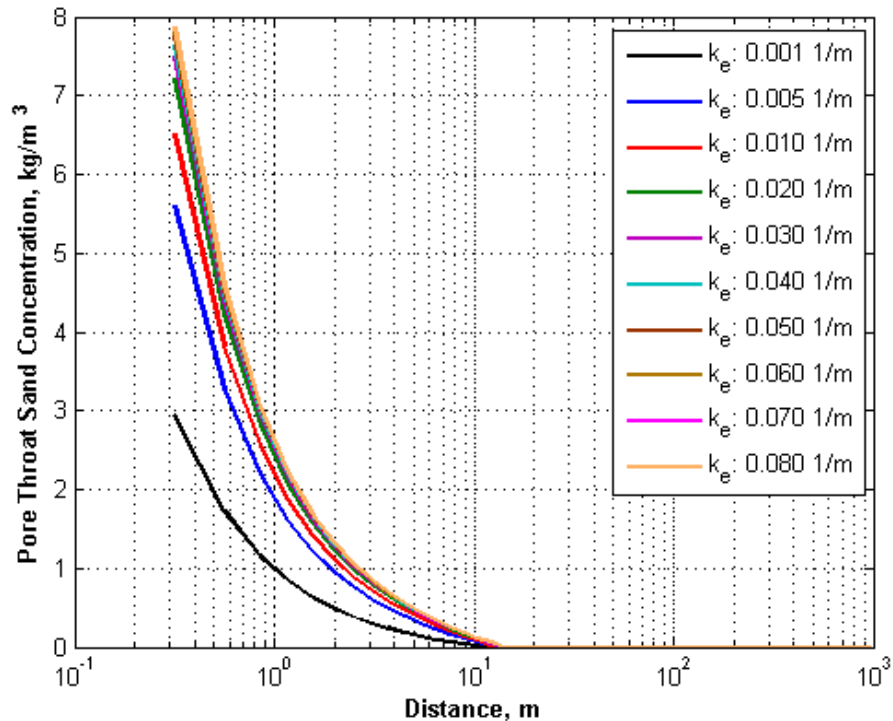


Figure 7.72 Pore Throat Sand Concentration Profile Change after 100 days Production with Pore Surface Entrainment Rate Constant

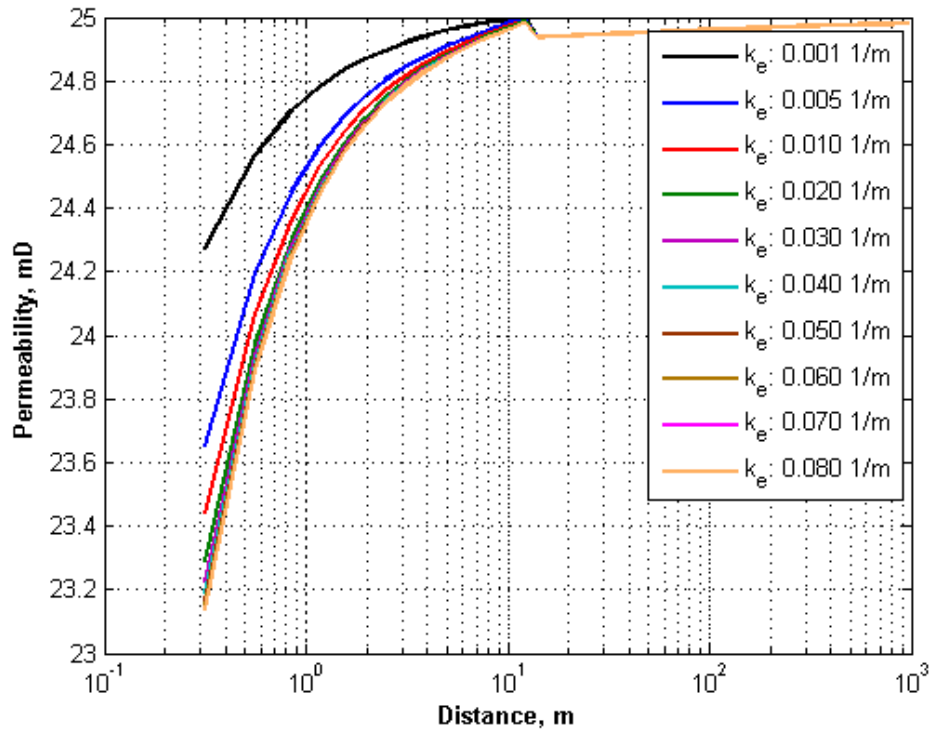


Figure 7.73 Permeability Profile Change after 100 days Production with Pore Surface Entrainment Rate Constant

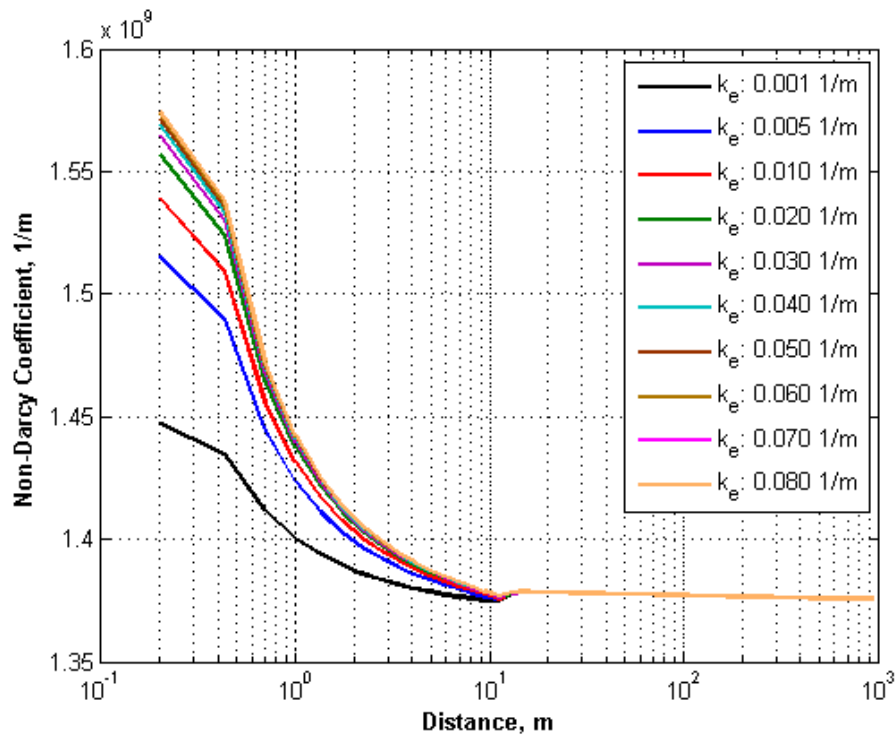


Figure 7.74 Non-Darcy Coefficient Profile Change after 100 days Production with Pore Surface Entrainment Rate Constant

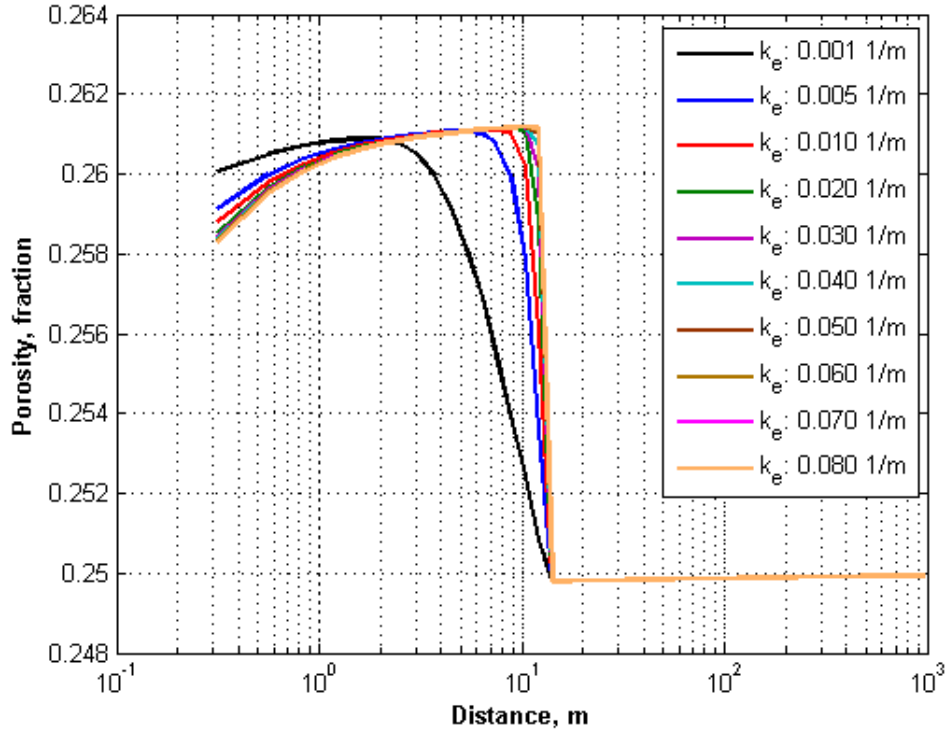


Figure 7.75 Porosity Profile Change after 100 days Production with Pore Surface Entrainment Rate Constant

#### 7.4 Fracture Effect on Sand Migration

Frac-pack completion is general technique to prevent sand migration for loosely or unconsolidated reservoirs. Frac-pack completion effect on sand production and flow properties of reservoir and fracture is investigated with reservoir simulations. Refined grid is used in near the wellbore to simulate fracture (Figure 7.76). Different rock indexes are used to differentiate the reservoir, fracture, casing and wellbore. Different rock properties are assigned for each rock type. Reservoir dimensions, rock and fluid properties are same with the Case 3 used as a base case (Table 7.4). Table 7.5 gives the fracture properties, sand migration parameters, and rate constants. Initially no movable sand is available in the fracture. Sand deposition in the pores occurs due to pore plugging and deposited particles are assumed immobile afterwards. Fracture pore space is much more connected, and pores and pore throats sizes are greater than the ones in

the reservoir. Therefore, the rate constants of deposition,  $k_d$ , and pore throat plugging,  $k_{pt}$ , are chosen less compared the sand migration rate constants of reservoir, and fraction of pore throat never plugged,  $f_{min}$ , is greater than the one for the reservoir. A sand particle can plug the pore throat of reservoir rock. Generally, few particles are necessary for plugging of proppant pack pore throat; therefore, characteristic constant of pore throat plugging,  $k_{fe}$ , is chosen less compared the one for reservoir. For casing, permeability, porosity and pore volume compressibility are assigned as 0. Since wellbore is filled with proppant, flow properties of wellbore are similar with fracture. The flow direction in fracture is in the x-y plane; on the other hand, the flow direction in the wellbore is in z direction. Therefore, sand migration rate constants are 0.

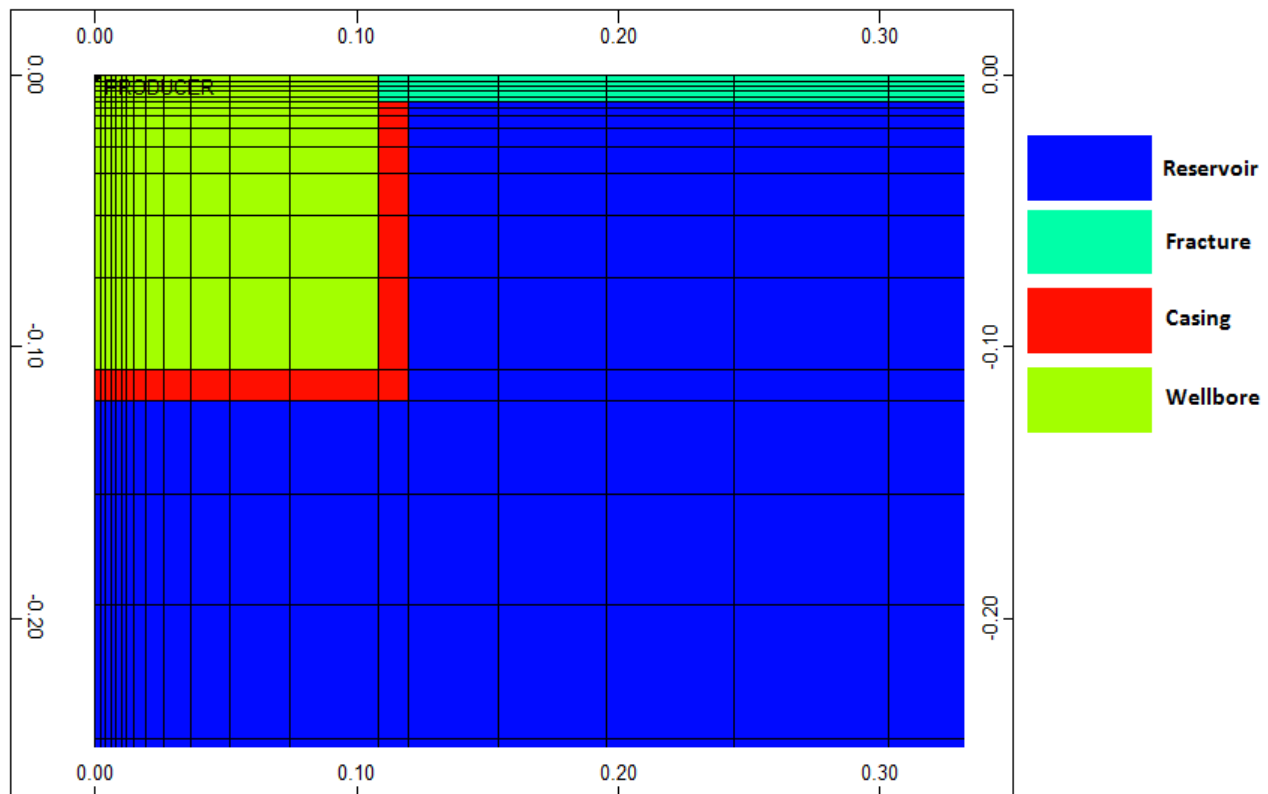


Figure 7.76 Rock Index of Frac-pack Completed Reservoir



Small high conductivity region near wellbore has a great effect on wellblock pressure compared the Base Case (Case 3) (Figure 7.77). Wellblock pressure increases from 10.60 to 18.15. Pressure field of fractured reservoir is not symmetric; pressure change is elongated around the fracture (Figure 7.78).

Table 7.5 2D Frac-pack Completed Reservoir Simulation Input Parameters

Number of Grid	65 x 65
Fracture Half Length (m)	30
Fracture Width (m)	0.02
$\phi$ (fraction)	0.40
k (D)	400
$S_{wi}$ (fraction)	0.0
$\sigma_o$ (kg/m <sup>3</sup> )	0.0
$k_d$ (1/m)	0.003
$k_{pt}$ (1/m)	0.0006
$k_{fe}$ (m <sup>3</sup> /kg)	0.02
$f_{min}$ (fraction)	0.3

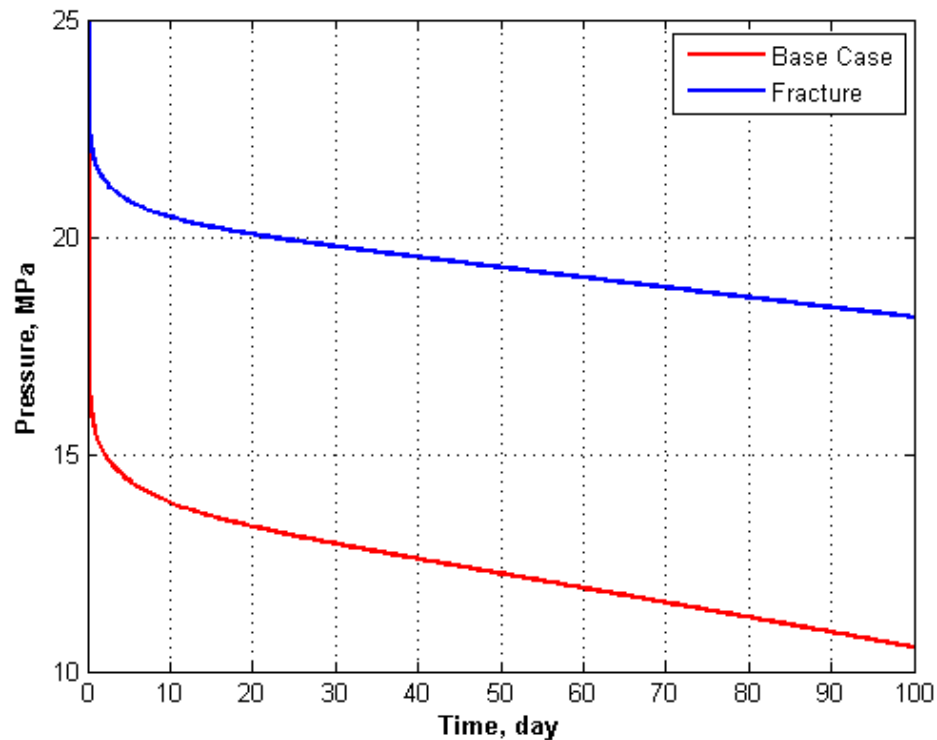


Figure 7.77 Frac-pack Completion Effect on Wellblock Pressure

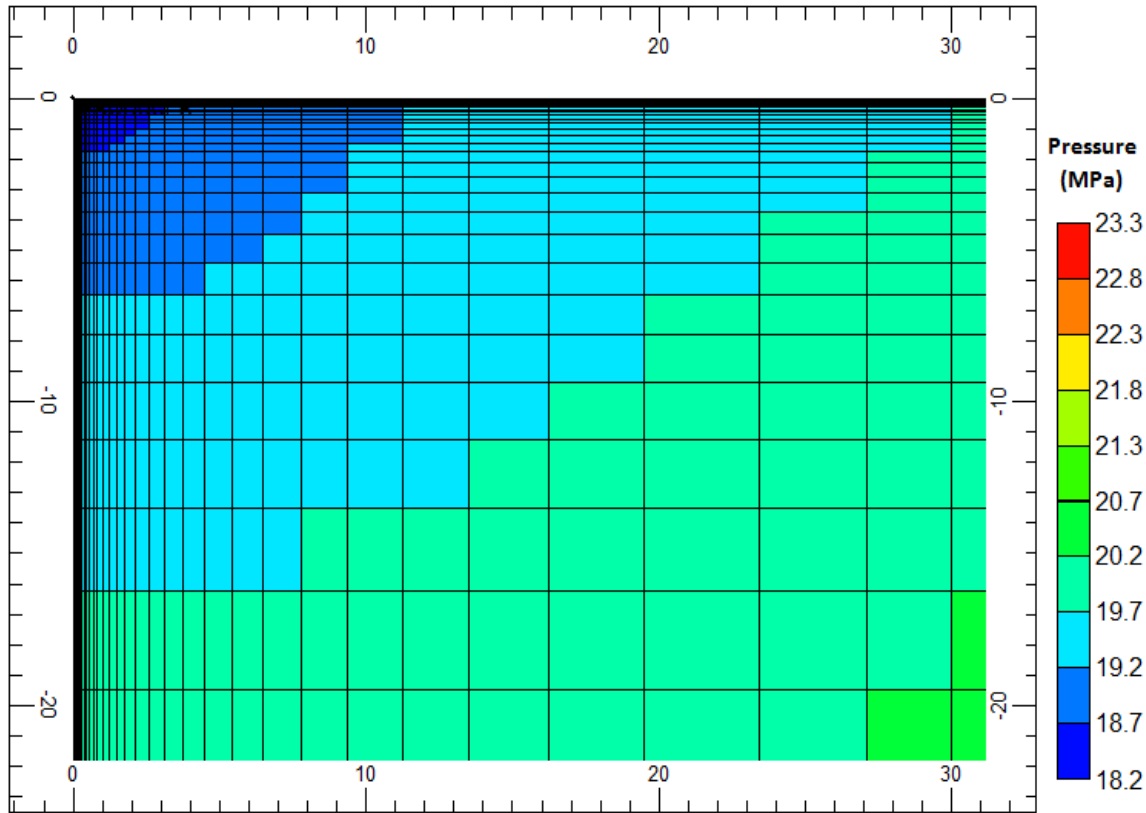
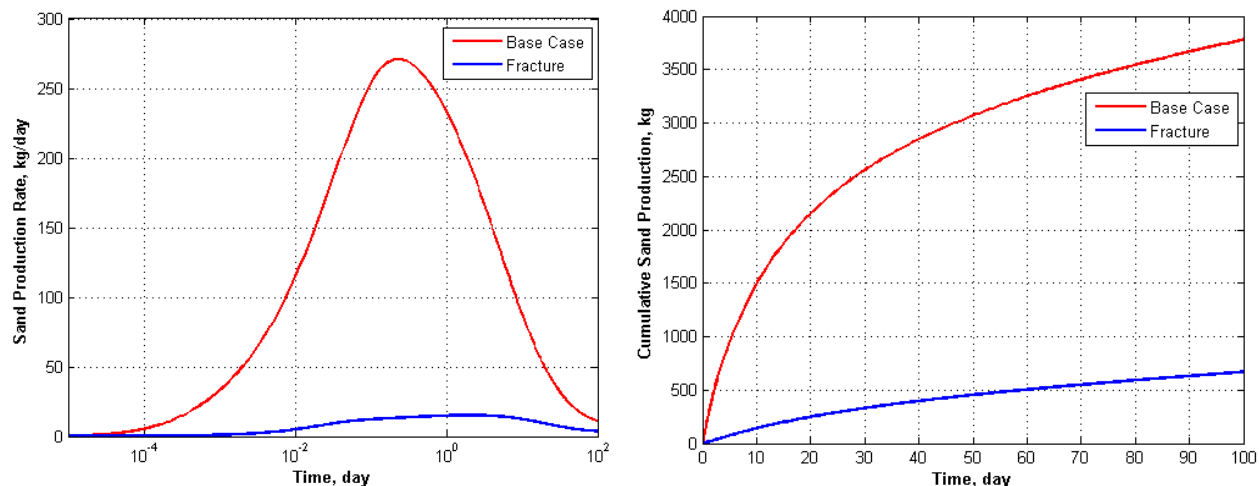


Figure 7.78 Pressure Profile of Frac-pack Completed Reservoir after 100 days Production

Sand production is significantly decreases due to decrease in pressure difference or velocity (Figure 7.79). Cumulative sand production decreases from 3776 kg to 669 kg. In the Base Case, the production is conducted from open-hole completion; therefore, pressure profile, permeability and porosity change and sand concentrations in gas phase, on pore surface and at pore throats are symmetric. Changes of these parameters are visualized with a profile taken from the  $x$  or  $y$ -axis in the sand production parametric study. However, in fractured reservoir, the flow is from reservoir to fracture and wellbore. Therefore, none of the stated properties is symmetric. Figure 7.80 gives distribution of the sand concentration in gas phase. Sand concentration in gas phase increases up to  $0.047 \text{ kg/m}^3$ . High sand concentration region is located behind the casing due to no direct flow into the wellbore.



a) Sand Production Rate  
b) Cumulative Sand Production  
Figure 7.79 Frac-pack Completion Effect on Sand Production Change

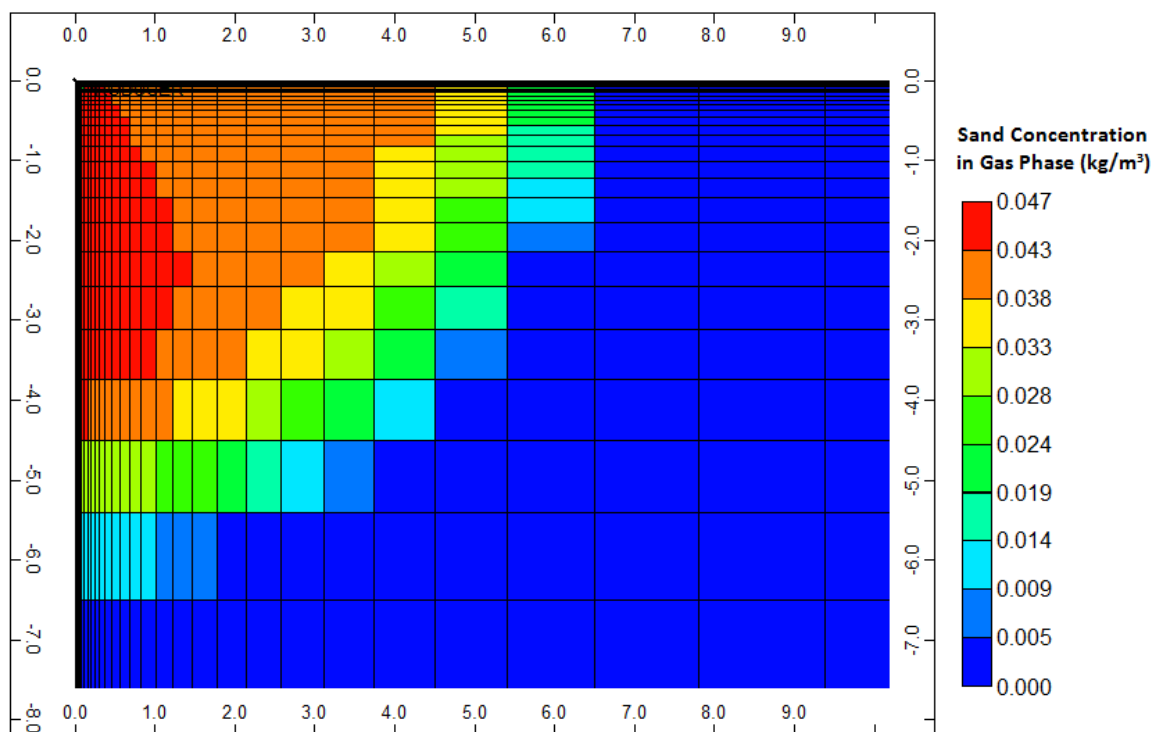


Figure 7.80 Frac-Pack Completion Effect on Sand Concentration in Gas Phase

Most of the sand particle deposition on pore surface and at pore throat occurs at the fracture reservoir interface near the wellbore (Figure 7.81 and Figure 7.82) since all flow enters the fracture and goes to the wellbore. Sand concentrations of pore surface and pore throat increase up to  $440 \text{ kg/m}^3$  and  $35 \text{ kg/m}^3$  at the reservoir fracture interface and decreases along the

fracture inside. Sand particle deposition inside the reservoir is negligible. Maximum sand concentration of pore surface and pore throat are  $0.025 \text{ kg/m}^3$  and  $0.912 \text{ kg/m}^3$ , respectively.

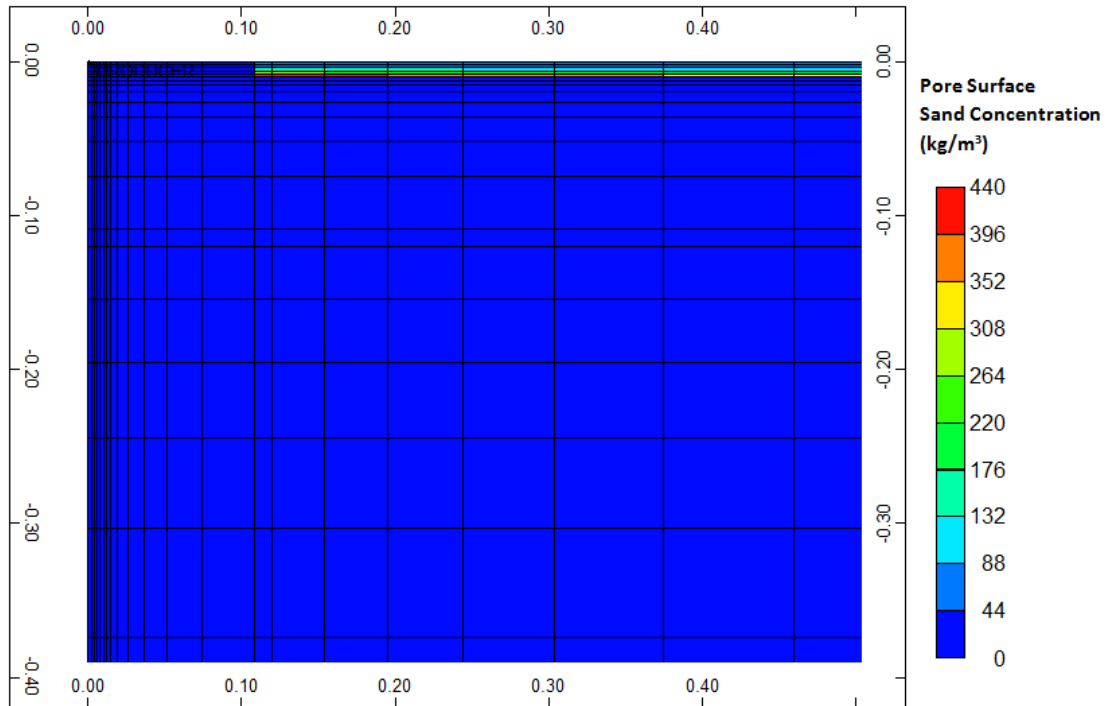


Figure 7.81 Frac-Pack Completion Effect on Pore Surface Sand Concentration

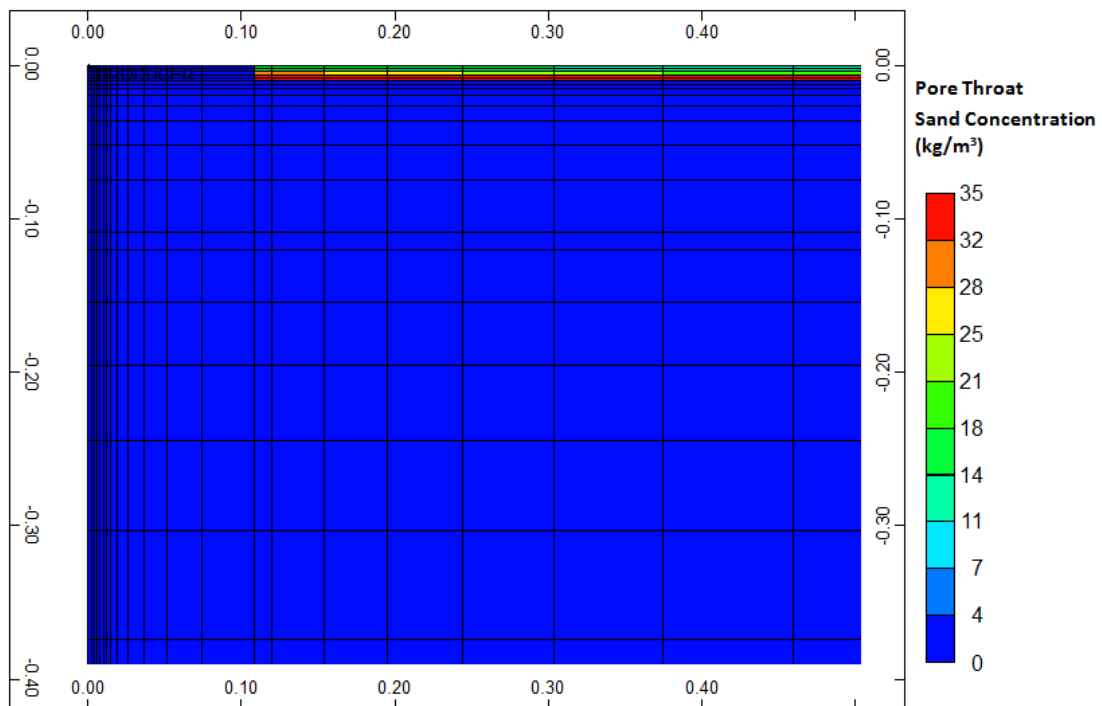


Figure 7.82 Frac-Pack Completion Effect on Pore Throat Sand Concentration

Sand production leads to slight increase in porosity in the reservoir. Figure 7.83 gives the ratio of porosity after 100 days of production to initial porosity. Porosity ratio increases up to 1.04 inside the reservoir. However, permeability inside the reservoir does not affected from porosity increase due to small sand throat plugging (Figure 7.84). Porosity at the fracture decreases significantly due to sand deposition. Near the reservoir and fracture interface, porosity and permeability ratio decrease to 0.55 and 0.68, respectively. Permeability decrease near the interface leads to increase in non-Darcy coefficient up to 2.0 (Figure 7.85). Even though non-Darcy coefficient of proppant,  $2.780 \times 10^4$  1/m, is small compared to non-Darcy coefficient of reservoir rock,  $1.374 \times 10^9$  1/m, the inertial effects in the fracture cannot be ignored due to high velocity (Figure 7.86). While maximum velocity in the reservoir is 106 m/d, maximum velocity in the fracture is 17720 m/d.

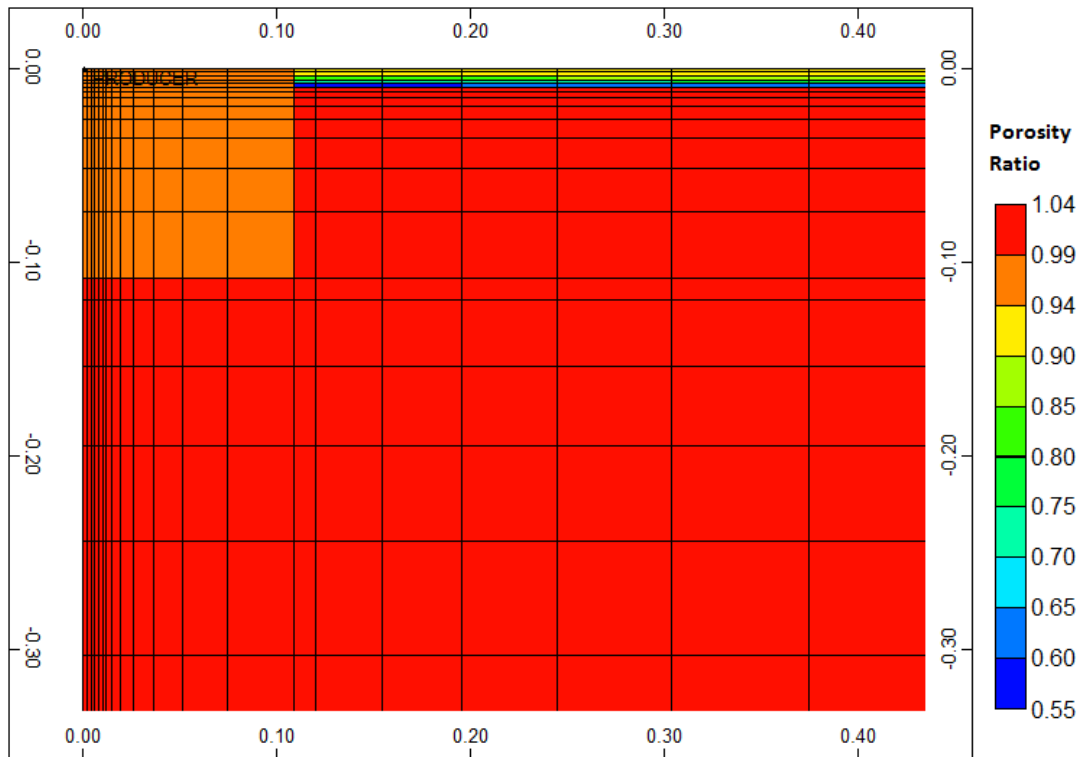


Figure 7.83 Frac-Pack Completion Effect on Porosity

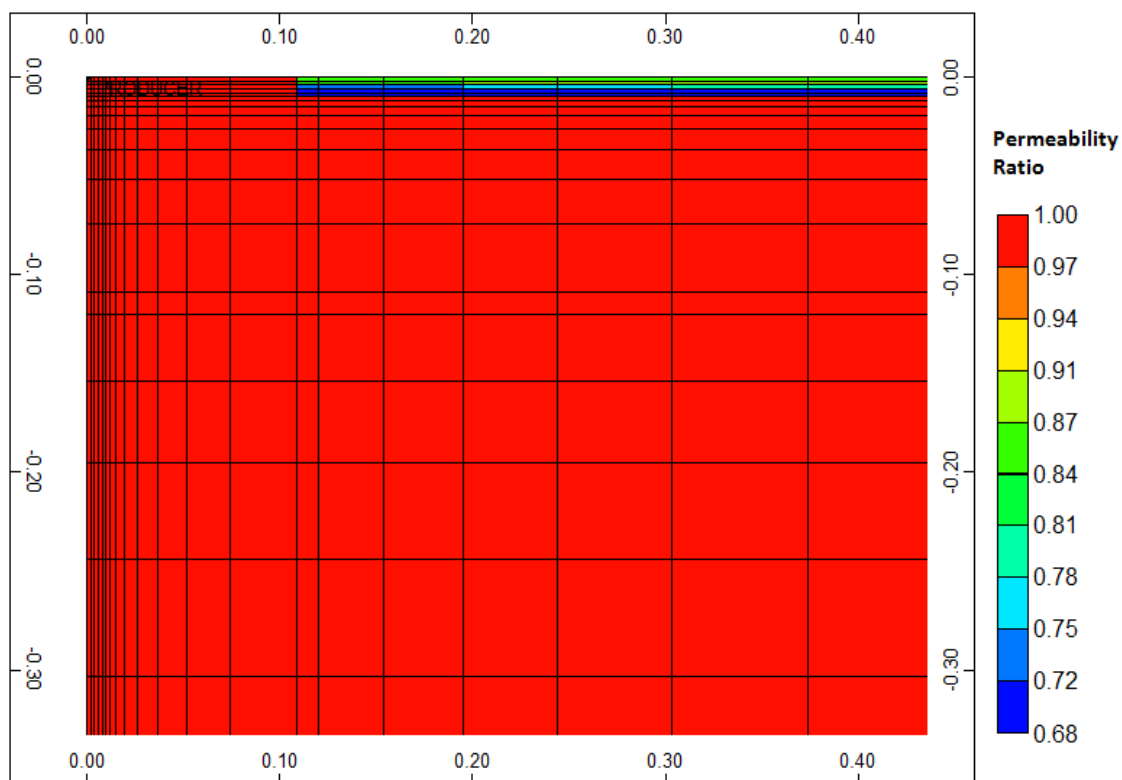


Figure 7.84 Frac-Pack Completion Effect on Permeability

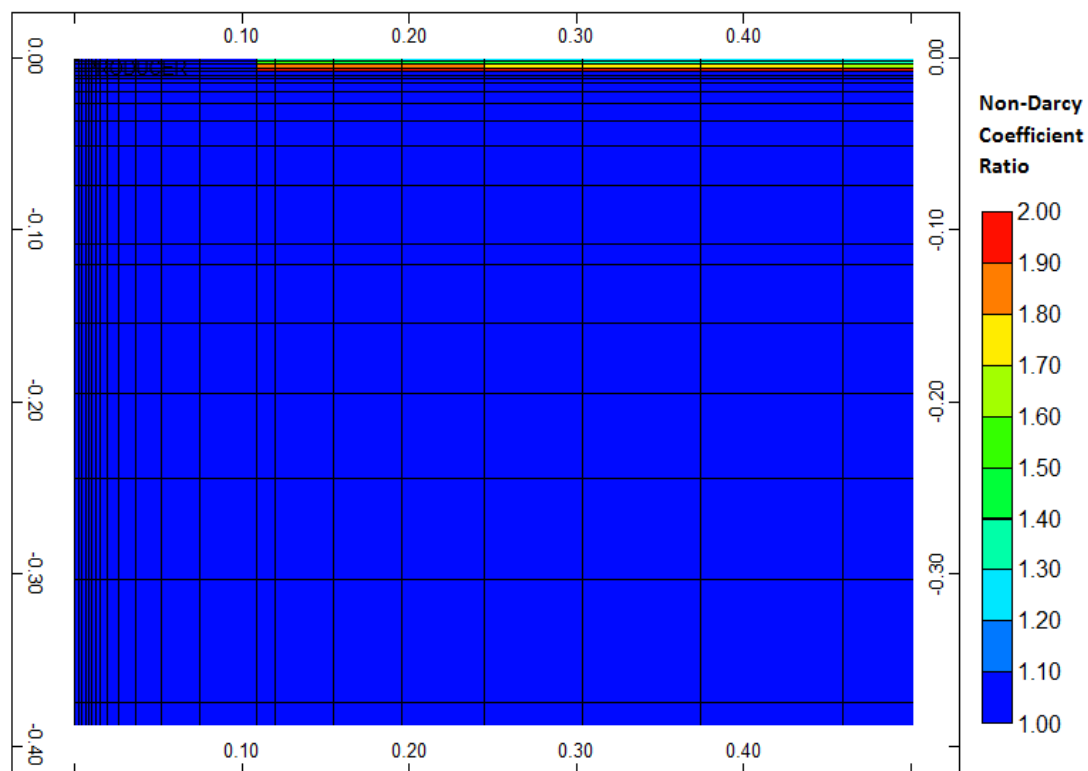


Figure 7.85 Frac-Pack Completion Effect on Non-Darcy Coefficient

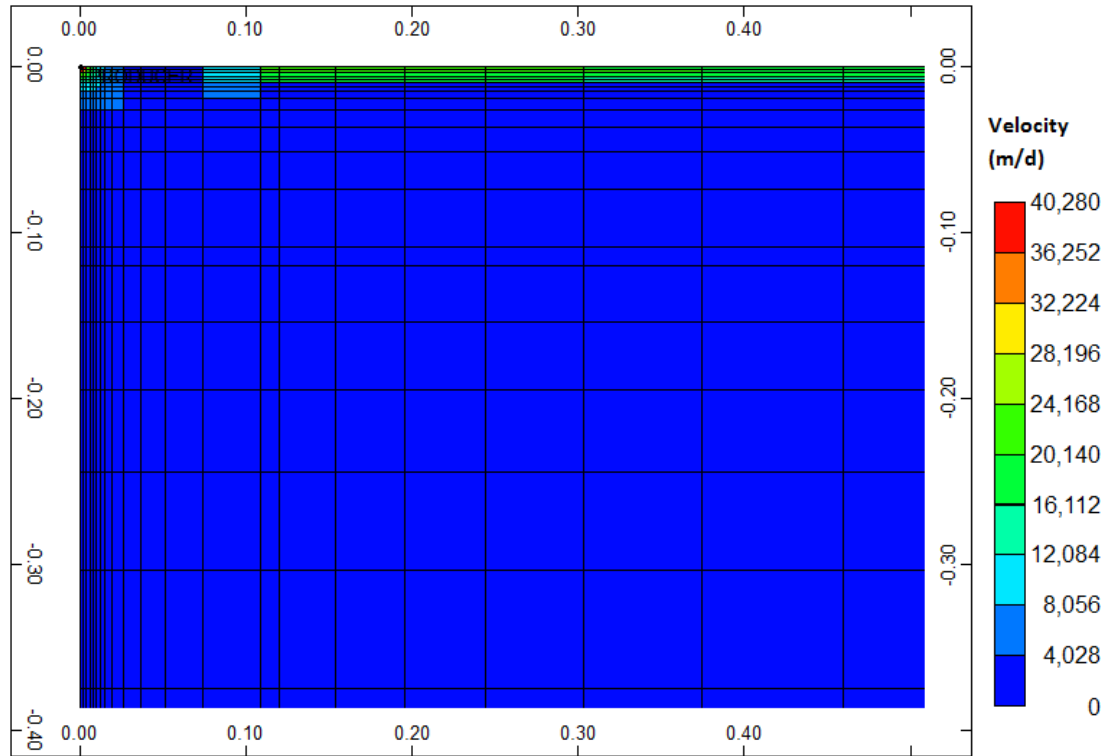


Figure 7.86 Velocity Field of Frac-Pack Completed Reservoir

#### 7.4.1 Fracture Half-Length Effect on Sand Production

The fracture half-length is chosen between 2 m and 50 m. Increase in fracture length leads to increase in wellblock pressure (Figure 7.87). Increase in fracture half-length from 2 m to 6 m significantly affects the well block pressure. Well block pressure increases from 15.73 MPa to 16.90 MPa. As the fracture half-length increases, the effect on well block pressure decreases. For example, increase in fracture half-length from 40 m to 50 m leads to increase in well block pressure about 0.09 MPa.

Well block sand concentration decreases with increase in fracture half-length (Figure 7.88). Maximum well block sand concentration changes between  $1.293 \text{ kg/m}^3$  and  $0.076 \text{ kg/m}^3$ . Fracture half-lengths greater than 18 m have insignificant effect on wellblock sand concentration. Wellblock sand concentration decreases  $0.085 \text{ kg/m}^3$  as the fracture half-length increases from 18 m to 50 m.

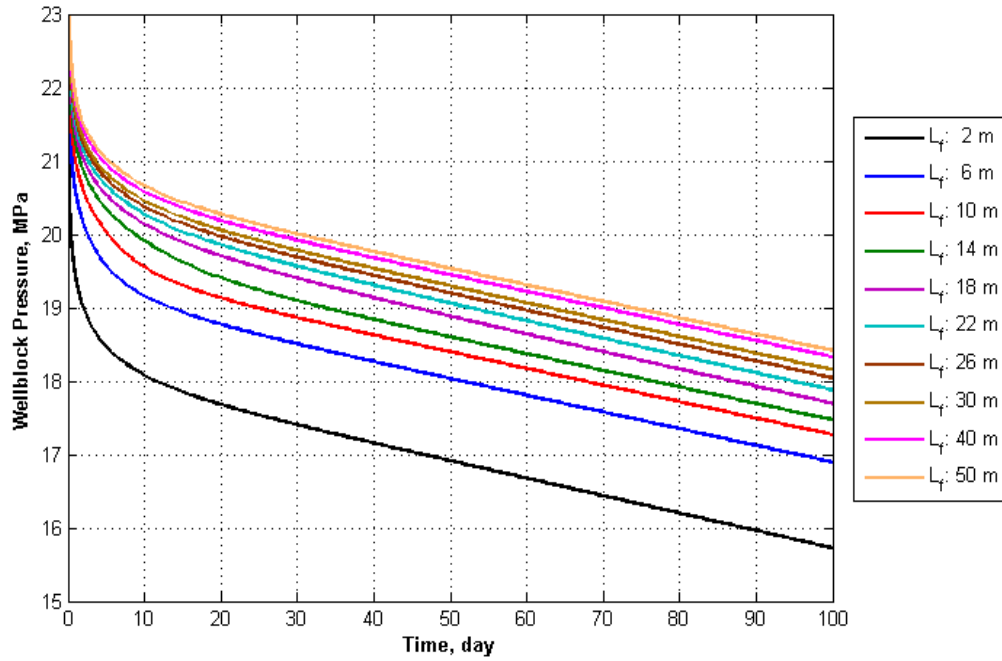


Figure 7.87 Wellblock Pressure Change with Fracture Half-Length

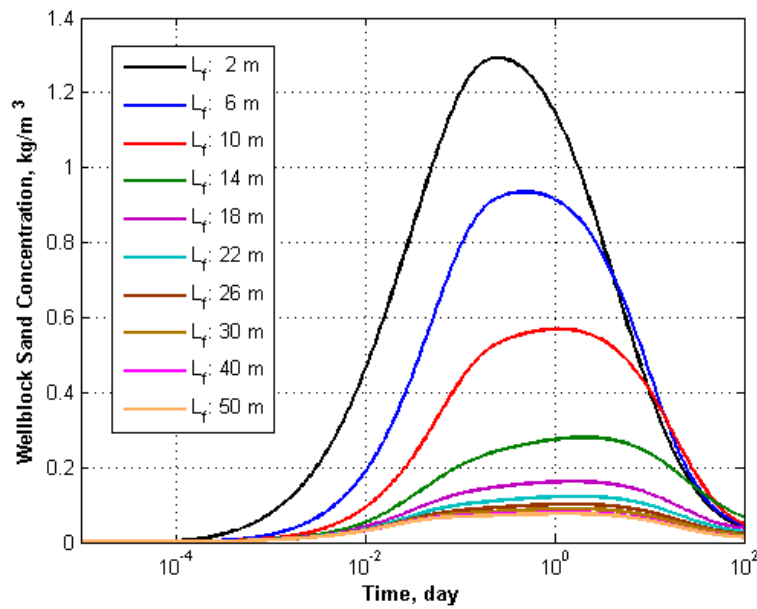


Figure 7.88 Wellblock Sand Concentration Change with Fracture Half-Length

Sand production decreases with the increase in fracture half-length (Figure 7.89). Maximum sand production rate and cumulative sand production decreases from 232.4 kg/d to 12.63 kg/d and from 3368 kg to 510 kg, respectively. For small fracture half-length, decrease in



cumulative sand production decrease is small. Fracture half-length between 10 m and 28 m, decrease in cumulative sand production is significant, 2475 kg. Cumulative sand production almost does not change between 34 m and 50 m. Fracture half-length parametric study indicates that medium length fractures are effective to prevent sand migration.

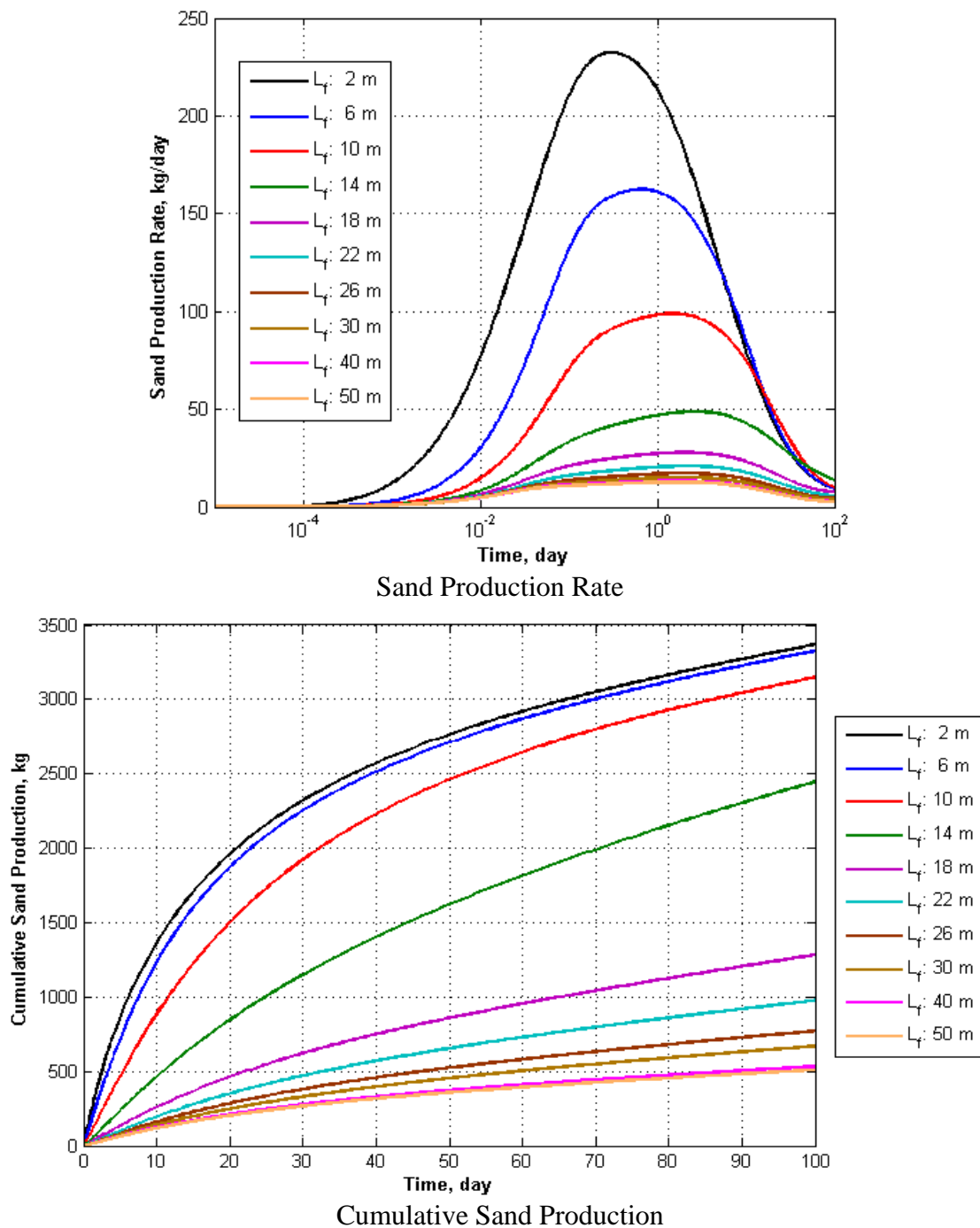


Figure 7.89 Sand Production Change with Fracture Half-Length

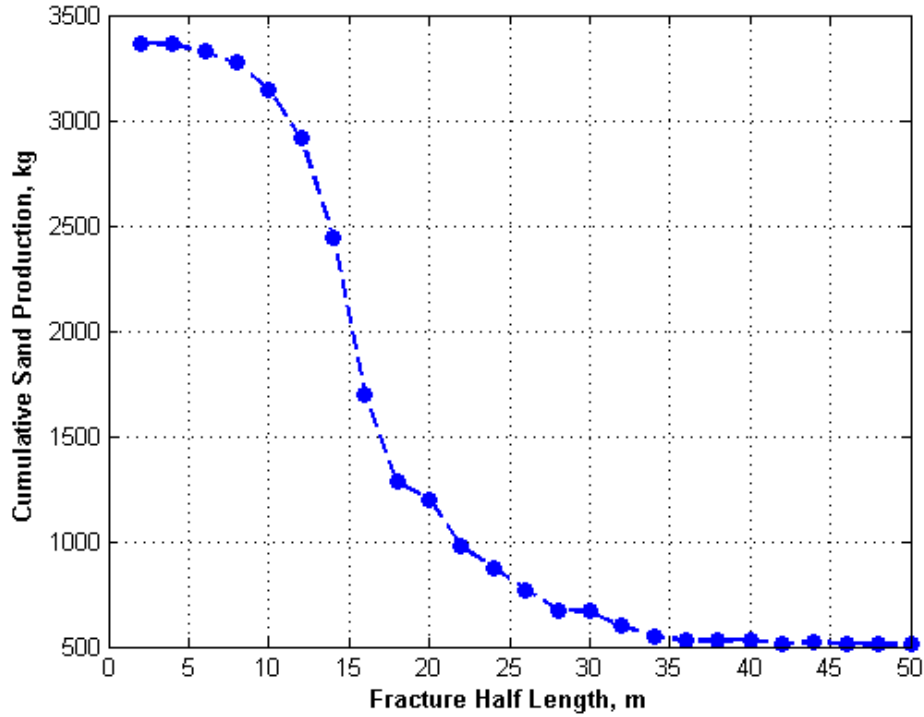


Figure 7.90 Cumulative Sand Production after 100 days Change with Fracture Half Length

#### 7.4.2 Fracture Width Effect on Sand Production

Fracture width range is chosen between 0.012 m and 0.032 m. Wellblock pressure changes between 17.22 MPa and 18.71 MPa (Figure 7.91). Similar to fracture half-length, high fracture widths effect on wellblock pressure are negligible. For example, increase in wellblock pressure is only 0.055 MPa with the increase in fracture width from 0.030 m to 0.032 m. Wellblock sand concentration decreases with the increase in fracture width (Figure 7.92). Maximum wellblock sand concentration changes between  $0.283 \text{ kg/m}^3$  and  $0.023 \text{ kg/m}^3$ .

Decrease in wellblock sand concentration with the increase in fracture width leads to decrease in sand production rate and cumulative sand production. Maximum sand production rate and cumulative sand production decrease from 48.4 kg/d to 3.41 kg/d and from 1301 kg to 271 kg, respectively (Figure 7.93). Cumulative sand production does not change for fracture width greater than 0.028 m (Figure 7.94).

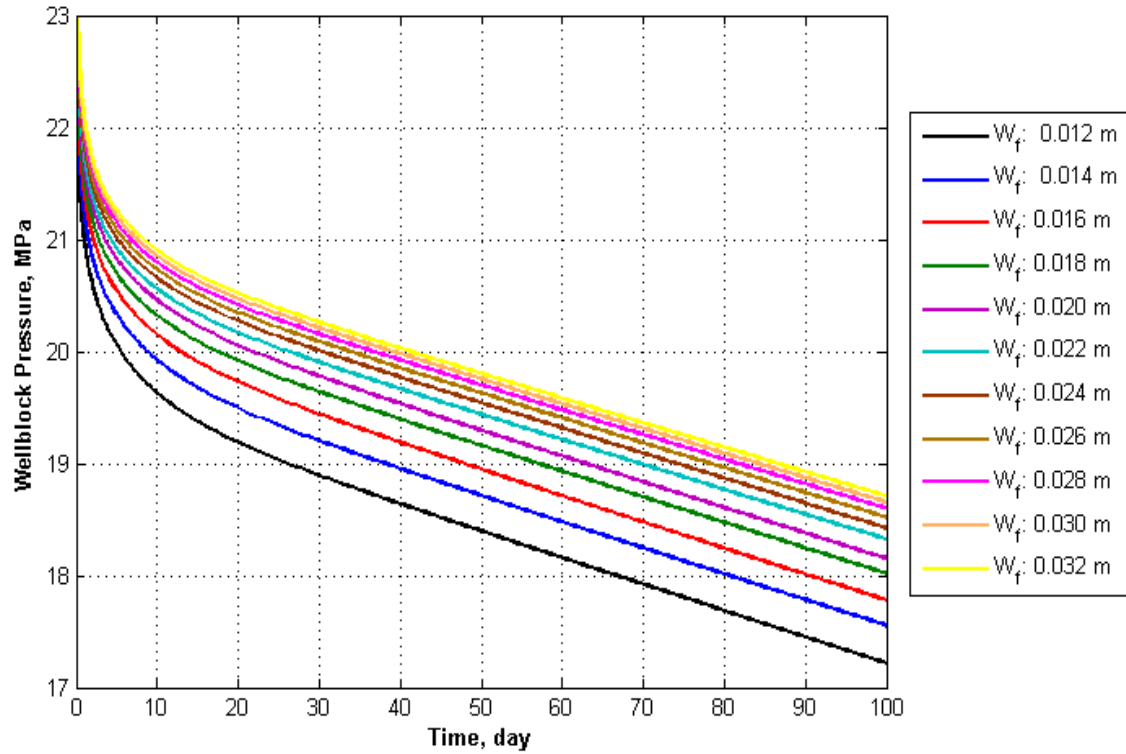


Figure 7.91 Wellblock Pressure Change with Fracture Width

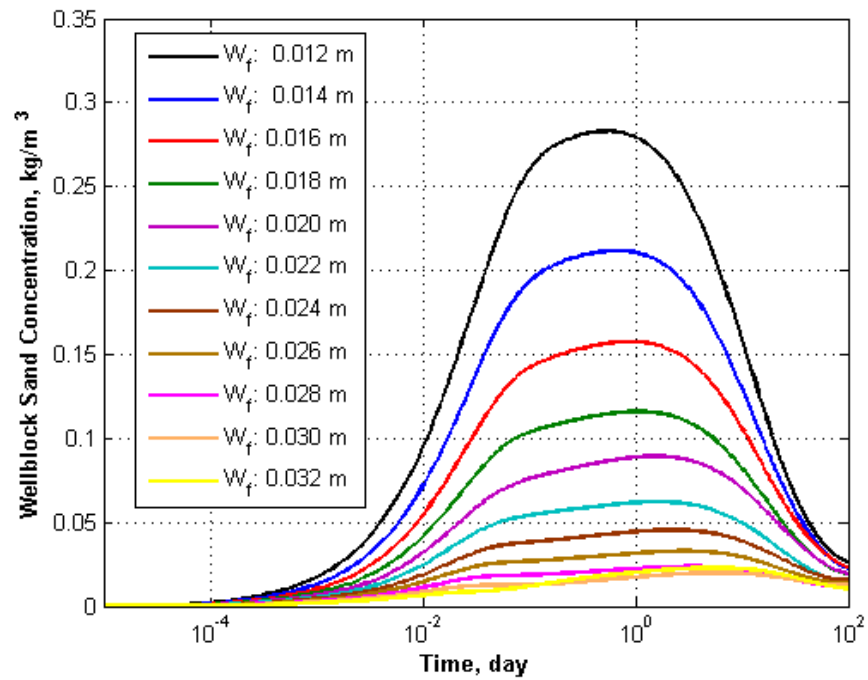


Figure 7.92 Wellblock Sand Concentration Change with Fracture Width

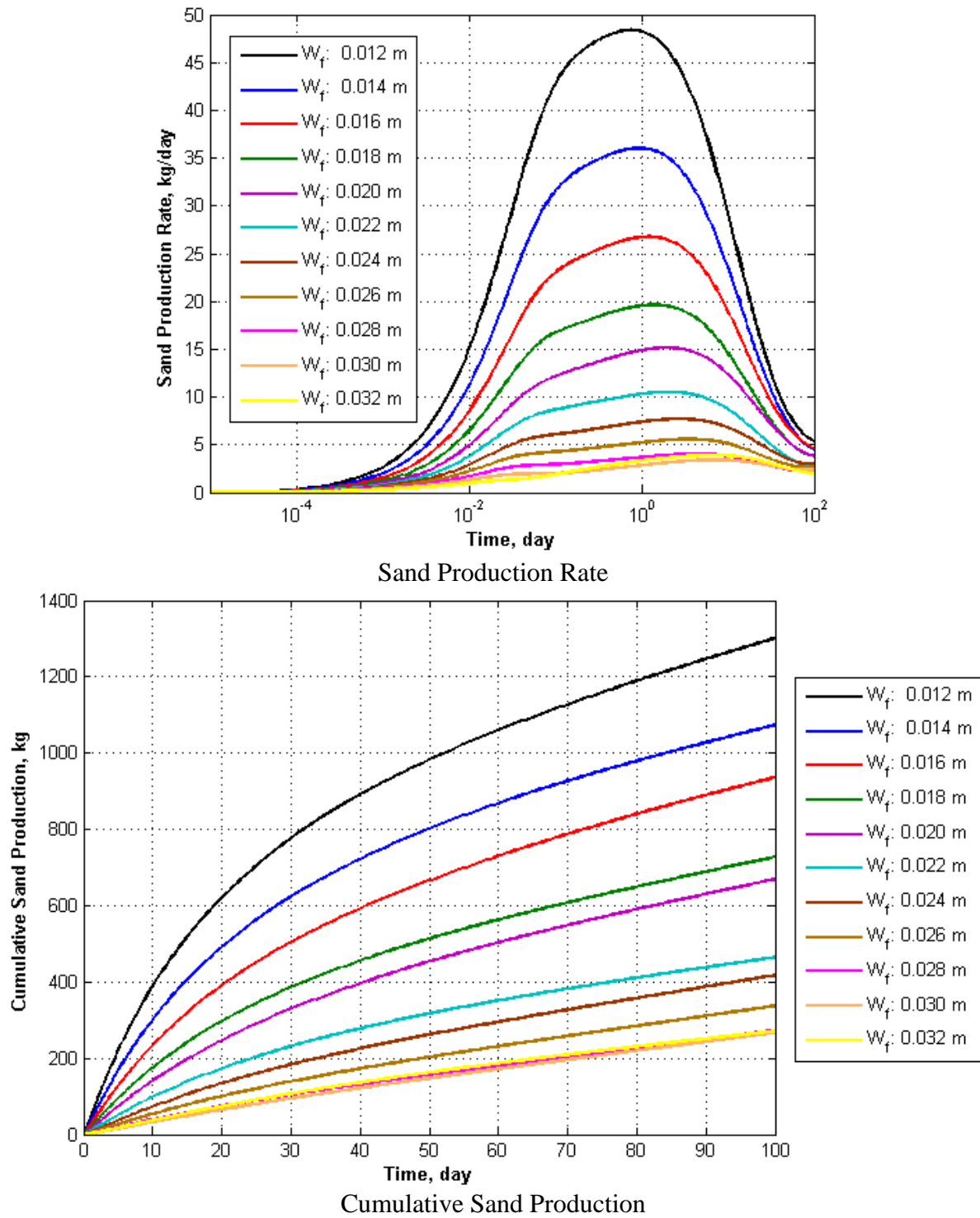


Figure 7.93 Sand Production Change with Fracture Width

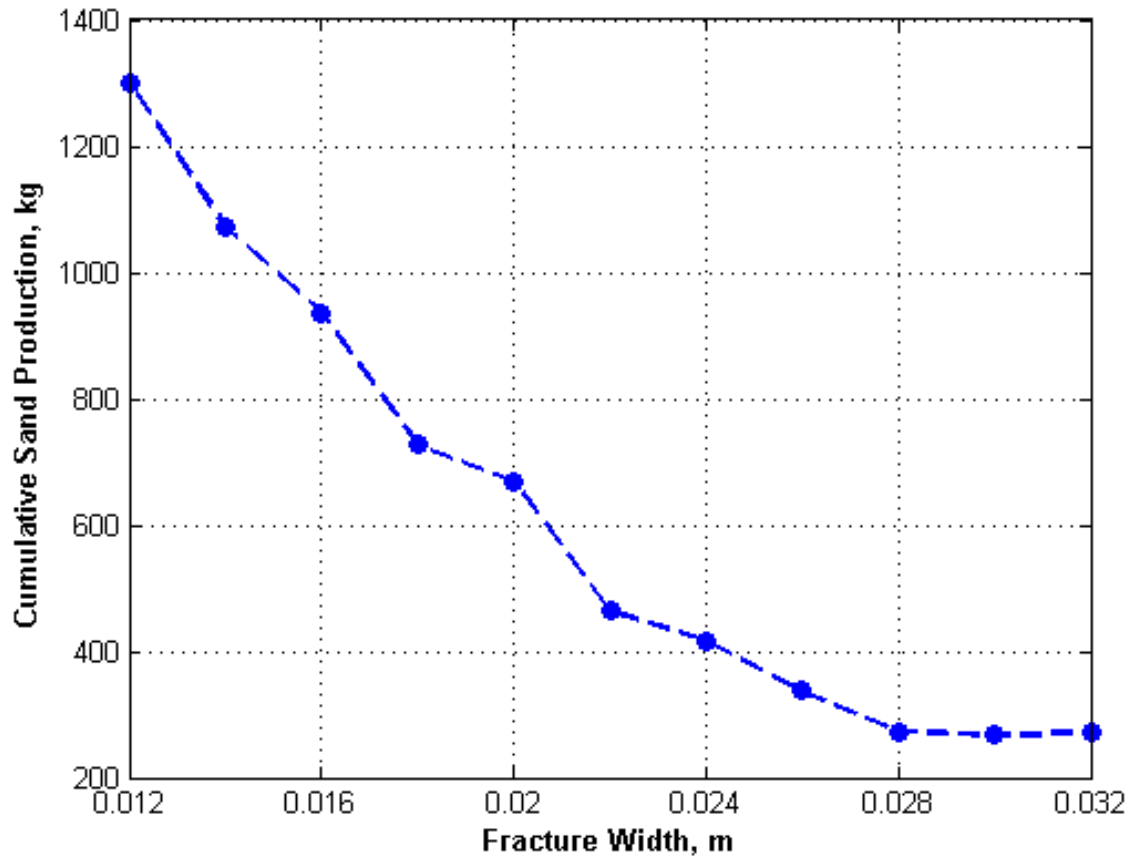


Figure 7.94 Cumulative Sand Production after 100 days Change with Fracture Width

#### 7.4.3 Fracture Permeability Effect on Sand Production

Fracture permeability range is changed between 50 Darcy 700 Darcy. Increase in fracture permeability leads to increase in well block pressure 17.3 MPa 18.37 MPa (Figure 7.95). Similar to fracture length and width effects, fracture well block pressure changes becomes less for higher fracture permeabilities. Increase in fracture permeability leads to decrease in maximum well block sand concentration from 0.351 kg/m<sup>3</sup> to 0.057 kg/m<sup>3</sup> (Figure 7.96), maximum sand production rate from 60.35 kg/d to 9.72 kg/d and cumulative sand production from 1530 kg to 510 kg (Figure 7.97). Cumulative sand production decreases exponentially with fracture permeability (Figure 7.98).

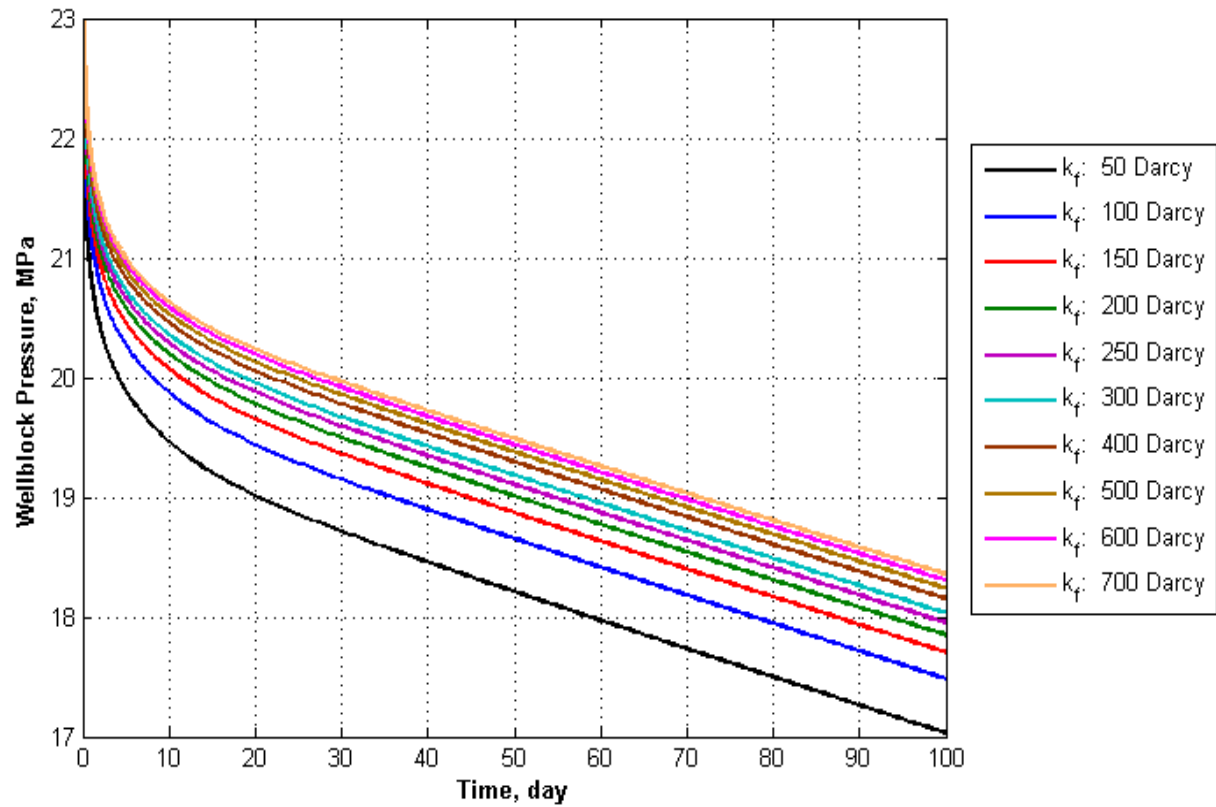


Figure 7.95 Wellblock Pressure Change with Fracture Permeability

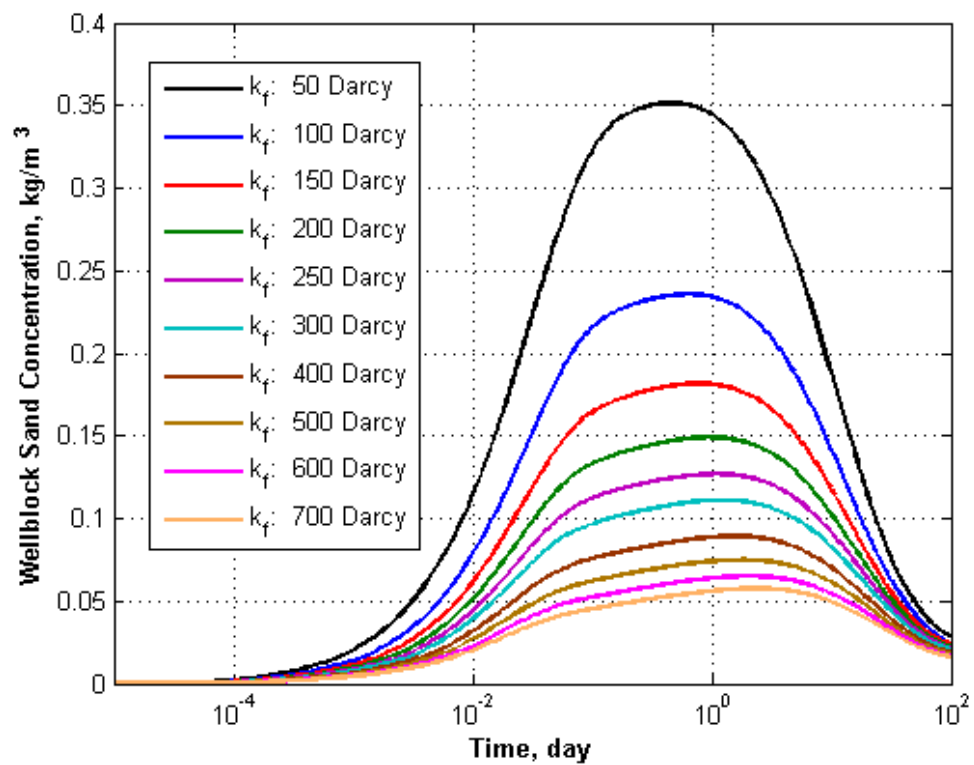
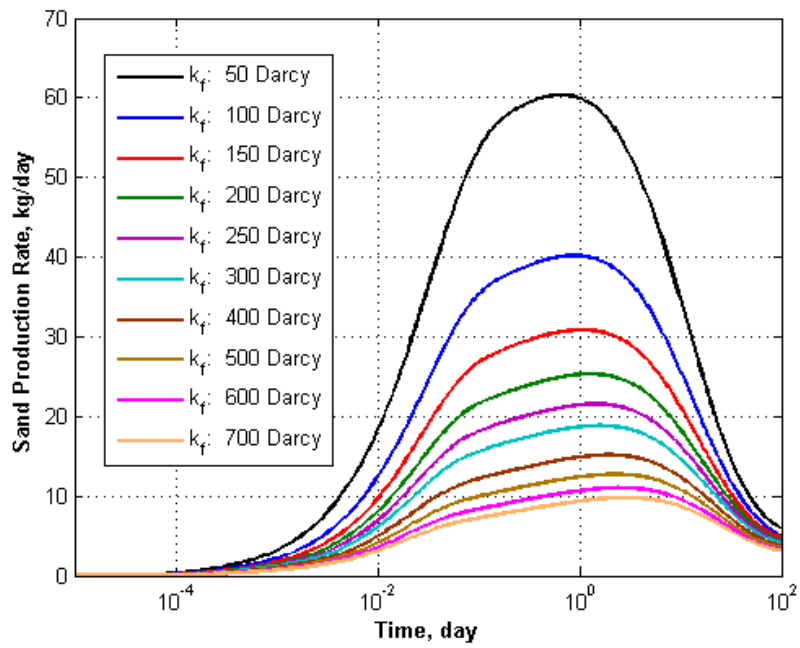
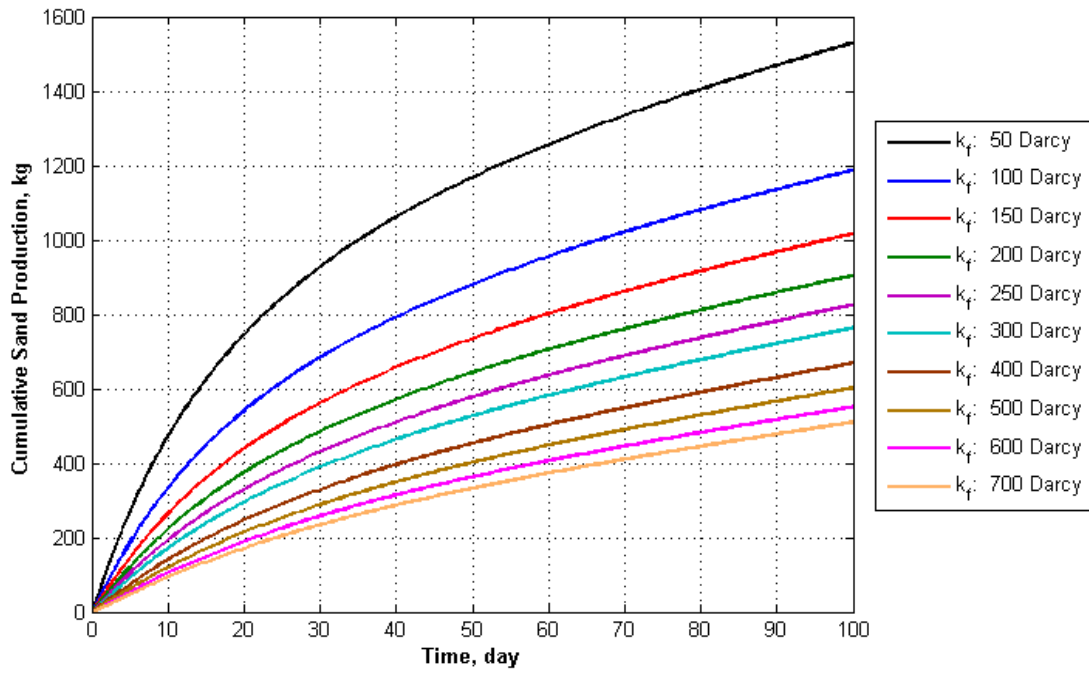


Figure 7.96 Wellblock Sand Concentration Change with Fracture Permeability



a) Sand Production Rate



b) Cumulative Sand Production

Figure 7.97 Sand Production Change with Fracture Permeability

However, the analyses of fracture dimensions and conductivity effects on sand productions are the only sensitivity analyses results. The fracture width and fracture permeability

are not independent parameters. For example, for small fracture widths, the parallel plate model should be considered (Eqn.7.69). This model indicates that the fracture width is directly related with the fracture permeability. On the other hand, for large fracture width, the packing parameters should be considered. Kozeny-Carman relation gives the permeability change with porosity and mean grain size (Eqn.7.70). As the porosity or grain size increases, not only permeability increases but also the pore structure changes. The pores and pore throats get larger and this pore structure change affects the rate constants of sand migration equations. Therefore, the pore structure effects on sand migration constants should be investigated with pore-scale simulations for reliable estimation of fracture properties effect on sand productions.

$$k = \frac{w_f^2}{12} \quad (7.69)$$

$$k = \frac{c D_p^2 \phi^3}{(1 - \phi)^2} \quad (7.70)$$

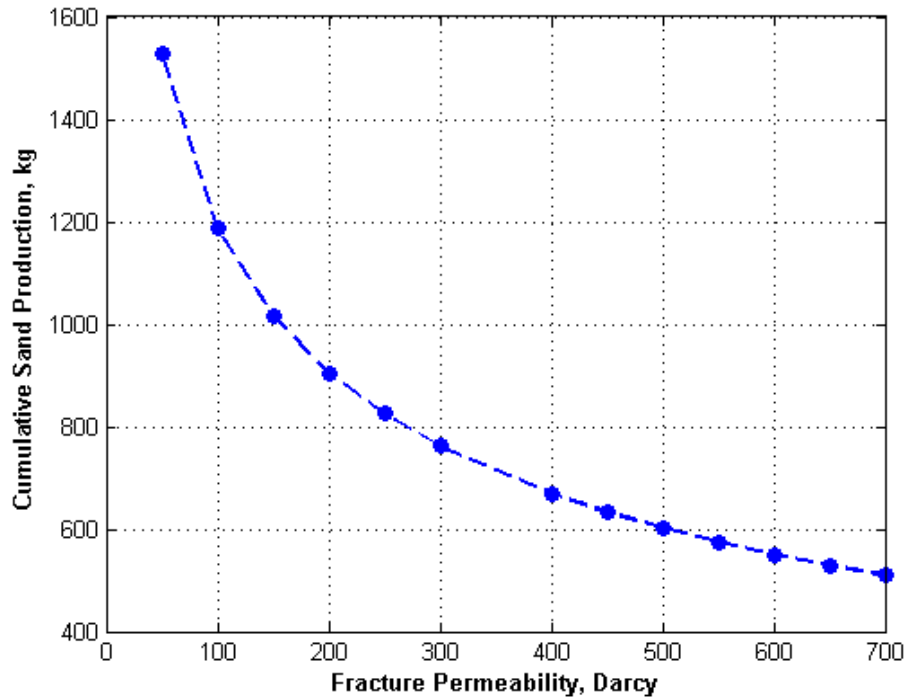


Figure 7.98 Cumulative Sand Production after 100 days Change with Fracture Permeability



## CHAPTER 8: RESULTS AND DISCUSSIONS

For reliable production estimation of a high rate frac-pack completed gas reservoirs, the flow properties of reservoir and frac-pack completion, and compaction and sand migration effect on flow properties should be accurately estimated. The literature review shows that there are many non-Darcy coefficient correlations. The pore structure of consolidated media is complex; therefore, estimation of non-Darcy coefficient from correlations is unreliable. In addition, non-Darcy correlations are mainly developed with linear regression even though petrophysical properties such as permeability and specific surface area, porosity and tortuosity are correlated highly correlated. Due to the multicollinearity problem, non-Darcy correlations are unreliable; therefore, non-Darcy coefficients should be determined from lab experiments such as steady-state experiments and pulse decay experiments.

For the steady-state flow experiments, simultaneous estimation of permeability, Klinkenberg coefficient and non-Darcy coefficient are essential because neglecting the inertial effects in the Klinkenberg analysis or neglecting the slippage effect in the Forchheimer analysis leads to misestimation of the flow properties. For simultaneous estimation, an optimization algorithm is developed and this algorithm is verified with synthetic steady-state data. None of the measurement is perfect; therefore, the pressure and the flow rate measurement errors (up to  $\pm 0.5\%$ ) effect on permeability and non-Darcy coefficient estimations are investigated. While estimations of mean flow parameters are little affected with pressure measurement errors, the confidence intervals of estimations increase. On the other hand, the flow rate measurement errors have more effect on estimations of mean flow parameters.

The recommended steady-state experiment analysis starts with outlier detection from  $T^2$  or Jackknife distance methods. After removing the outliers, flow properties are estimated from steady-state experiment optimization algorithm and their confidence intervals are found from

bootstrap method. The experiment data provided by Exxon-Mobil is used for this analysis procedure. The Forchheimer and Klinkenberg plots obtained from the optimization algorithm are scattered because of the measurement errors. 1-D single-phase flow simulations are conducted by using the estimated permeability, non-Darcy and Klinkenberg coefficients to calculate flow rate measurement errors. The flow rate errors are as high as 8%.

In the steady-state flow experiments, both pressure and flow rates are recorded, and flow rates errors are high and inevitable; therefore, today's trend is pulse-decay experiments. There are many studies in the literature about pulse-decay experiments; however, there is no recommended procedure. Pulse-decay procedure may result in unreliable estimations if experiment duration is short. Pulse decay analyses are conducted by using 2C and 3C core experiments data provided by Schlumberger. This analysis reveals that there is not only one combination of permeability, Klinkenberg coefficient and non-Darcy coefficient for a given pulse-decay experiment. For reliable estimations of the flow properties, a Bootstrap method should be used to determine the estimation confidence interval.

Selection of pulse-decay analysis methodology has great effect on estimation of the flow properties. 2C and 3C pulse-decay core experiments indicate that ignoring the inertial effects by Kaczmarek method leads to misestimation of permeability and Klinkenberg coefficient. Pulse-decay experiment duration has significant effect on the confidence intervals of the estimated flow parameters. As the experiment duration decreases, the confidence intervals of estimated flow parameters increase. If the pulse-decay experiment duration is short, the estimated Klinkenberg coefficient is lower and estimated permeability and non-Darcy coefficient are higher. Increase in the confidence interval of estimated flow properties leads to increase in uncertainty in production estimation.

The pulse-decay simulation is written with a finite difference method and confirmed with an analytical solution. Sensitivity analysis is conducted to find the experimental set-up and core dimensions and properties effects on pulse-decay experiment duration. The most and the least sensitive parameters are core permeability and porosity, and experiment duration changes smoothly with each sensitivity parameter. After sensitivity analysis, 300 pulse-decay simulations are prepared with Hamersley design by using experimental set-up data such as tank volumes and pressures, and core properties such as permeability and porosity for 1 tank and 2 tank experiment set-ups. Non-Darcy coefficient and Klinkenberg coefficient are calculated from correlations developed by Jones (1982) and random variations are added to the calculated values to replicate the experimentally measured variability. Using the design variables and experiment duration obtained from pulse-decay simulations, correlations are developed to estimate the experiment duration. Compared to pulse-decay sensitivity analyses, similar trends are observed from the profiler plot of the design variables obtained from developed correlations such as an insignificant porosity effect on the experiment duration. The developed correlations are tested with 2C core pulse-decay experiment by estimating the experiment duration with Monte-Carlo method and inverse permeability prediction. The question left for the pulse-decay analysis part, what is the minimum required pulse-decay experiment duration for reliable estimation of flow parameters. This requires pulse-decay experiments for cores with different permeabilities and this question is left as a future work.

Experimental determination of the gravel packs flow properties is hard due to high porosity and permeability of gravel packs. Therefore, their flow properties are estimated from flow simulations. For flow simulations, a computer generated packing algorithm is used for domain construction. Packing algorithm used in domain generation produces statistically similar

packs for the same input parameters: domain size, grain size distribution and porosity. Due to high-resolution requirement, the volume of the domain used in LBM simulations is limited. Therefore, the representative elementary volume is found for the most heterogeneous gravel pack, 0.5 standard deviation of the base 2 logarithm of the grain size distribution. Representative elementary volumes of porosity and permeability are same, 6 mm, and domain contains about 334 particles.

For pore-scale modeling, LBM and network modeling are compared with respect to a resolution and a grain shape or a pore geometry effects. Permeability calculated from LBM depends on the resolution and the relaxation time. For reliable estimation, a minimum particle diameter should be represented with 30 voxels; then, the relaxation time has a little effect on permeability. For a highly resolved domain, permeabilities calculated from single (BGK) and multi-relaxation (MRT) LBMs give similar results and less dependent of the relaxation time.

Permeability calculated from the network modeling does not depend on the resolution but the merging condition. Permeability calculated from the network prepared with the overlapping merge condition is higher than the one calculated from the network prepared with the touching merge condition. Permeability calculated from the network prepared with the touching merge condition is close to permeability calculated from LBM. Resolution has an effect on the pore structure obtained from the network modeling. Increase in resolution leads to increase in the pore and pore throat numbers, decrease in average pore throat length and pore coordination number due to appearance of new pores similar to pore throat size. However, change in the pore structure does not affect the capillary pressure. If the grain geometry is elongated, there is a difference between the permeabilities calculated from LBM and network modeling, especially for the

symmetric arrangement of grains since the number of pores and pore throats do not change; therefore, LBM is more reliable for permeability estimation.

To develop permeability and non-Darcy coefficient, all possible packs should be considered. Therefore, range of mean and standard deviation of the proppant size distribution and porosity are found in the literature, and 100 packs are prepared with Hamersley design. For each domain, permeabilities calculated from LBM and network modeling are similar. For each pack, a capillary pressure curve is calculated from the network modeling, and Swanson correlation is extended for gravel packs. Calculated permeabilities, non-Darcy coefficients and tortuosities of all domains are compared with the ones calculated from correlations found from the literature. Calculated permeabilities are similar to ones obtained from correlations. Most of the non-Darcy correlations developed from lab experiments underestimates the non-Darcy coefficient. Calculated tortuosities are consistent with the trends obtained from correlations; however, the correlations give rough estimations.

The colinearity problem is emphasized for some of the non-Darcy coefficient correlations by using the correlated parameters. If permeability and specific surface area or porosity and tortuosity are used simultaneously, each variable effect is distorted due to colinearity. All statistically significant correlations are given for permeability and non-Darcy coefficient by using the mean grain size, and calculated porosity, tortuosity and specific surface area and network parameters; mean pore throat radius, throat length and pore to throat radius ratio. All developed correlations are dimensionally consistent.

A path model is developed for the petrophysical parameters. There is a strong correlation between permeability and the non-Darcy coefficient since both parameters depend on the same parameters and each parameter effect on these parameters is same except porosity. With path

analysis, indirect effects can be included which cannot modeled with linear regression due to colinearity problem. Porosity and specific surface area have indirect effects on permeability and the non-Darcy coefficient through tortuosity. Proposed path model is used for the missing data estimation. Half of the permeability, non-Darcy coefficient, tortuosity and specific surface area data is deleted and estimated 100 times with stochastic regression by using the path model. Estimated permeability, non-Darcy coefficient and specific surface area are close to the actual values while estimated tortuosity is very uncertain due to low coefficient of determination.

Compaction effects on permeability and non-Darcy coefficient are investigated from pore-scale simulations. Decrease in porosity due to compaction leads to decrease in permeability and increase in inertial effects. The exponent of Kozeny-Carman relation of porosity and permeability is 3.2, it is close to literature value, 3. With network modeling, compaction effect on pore structure is investigated. With compaction, pore and throat radii and throat length decrease and pore space becomes less connected. The developed correlations underestimate the non-Darcy coefficient change due to compaction. The exponent of Kozeny-Carman relation of permeability and non-Darcy coefficient is -1.303.

Sand migration effects on permeability and non-Darcy coefficients are investigated. The sand particle locations in gravel pack are found from network simulations and permeability and non-Darcy coefficient are calculated from LBM. Sand migration effects on permeability and non-Darcy coefficient are more significant than the compaction effects due to pore constraint plugging. The exponent of Kozeny-Carman relation of porosity and permeability is about 11 and 6 for the flow direction and the other directions. Since porosity can be changed due to sand deposition to pore body, sand concentration at pore throat is used for correlation development and the developed correlation is used in the reservoir simulation. The trend of permeability and

non-Darcy coefficient changes are similar in all directions and the exponent of Kozeny-Carman relation of permeability and non-Darcy coefficient is -1.830.

Reservoir simulation is developed with finite difference method and flow equation and sand migration equations are coupled and solved implicitly. A sand migration phenomenon is modelled with rate equations that can be determined experimentally. The simulation is validated for gas reservoir without sand migration with material balance. Sand migration part is validated with core experiments found from the literature. Sensitivity analysis of sand migration experiment is conducted for initial movable sand concentration, rate coefficients, critical velocity, inlet velocity and permeability. Even though the entrainment rate, critical velocity, inlet velocity and permeability have no effect on equilibrium sand concentration plugged in the pore throats, the cumulative sand production profiles change. Therefore, for correct estimation of rate coefficients both the pressures and cumulative sand production profile should be known.

Parametric study is conducted to investigate the initial movable sand concentration, critical velocity, flow rate, pore throat plugging rate constant, and surface retention and entrainment rate coefficient constants. The wellblock pressure is more affected from flow rates and the parameters affecting the pore throat plugging since the permeability and non-Darcy coefficient is direct function of sand concentration at pore throat. Pore throat plugging increases significantly with the increase in initial movable sand concentration and pore throat plugging rate coefficient. However, the maximum sand concentration at pore throats is limited because some pore throats are large and never plugged. Therefore, both permeability reduction and non-Darcy coefficient increase are up to a specific value determined from characteristic constant reflecting the properties of pore throats and solid particles.

Sand production increases with the increase in movable sand concentration, flow rate and pore surface entrainment rate constant and decrease in critical velocity. In addition, both flow rates and critical velocity have effect on the region suspected to sand migration. Increase in flow rate or decrease in critical velocity leads to increase in radius of the region suspected to sand migration. Even though pore throat plugging rate constant have an impact on wellblock pressure, the sand production is slightly decreased with the increase in this constant. Pore surface deposition rate constant almost has no effect on production since redeposited particles due to high sand influx becomes mobile during the production.

Frac-pack completion is common method to prevent the sand migration. Frac-pack completion leads to significant increase in wellblock pressure and decrease in sand production. Changes of permeability and non-Darcy coefficient in the reservoir are negligible. Pore surface deposition and pore throat plugging occurs near the interface of the reservoir and fracture. Therefore, permeability decrease and non-Darcy coefficient increase are observed at the reservoir-fracture interface.

The fracture dimension and its conductivity effects on sand production are investigated. Increase in fracture length, width and permeability result in decrease in pressure drop and sand production. However, the decrease in cumulative sand production is not linearly related with the increase in fracture dimensions and permeability. For example, increase in fracture half-length and width over the 30 m and 0.028 m almost has no effect on sand production. Sand production decreases exponentially with fracture permeability. During the sensitivity analysis, the each parameter is assumed to be independent from the other parameters. For example, sand migration rate constants are assumed to be remain same during the change of fracture dimensions or fracture permeability. However, fracture width is related with fracture permeability and fracture



permeability depends on both porosity and proppant properties used in the frac-pack. Therefore, change of fracture dimensions or permeability lead to change in pore structure of frac-pack. This affects the sand migration rate constants. Therefore, these constant should be determined from experiments or pore-scale simulations.

The whole study is related to reliable production estimation of the loosely or unconsolidated frac-pack completed gas reservoirs. Reliable estimation requires four main steps. Firstly, the reservoir flow properties should be simultaneously estimated from the steady-state or the pulse-decay lab experiments. Secondly, the proppants flow properties should be estimated from the developed correlations or the path model. Thirdly, sand migration rate constants should be determined from the experiments or the pore-scale simulations. Finally, the developed reservoir simulator should be used to estimate the productivity of gas well by using the estimated flow properties of reservoir and the proppants, and the sand migration rate constants.

## CHAPTER 9: CONCLUSION

The primary objective of this study is accurate production estimation for frac-pack completed gas reservoirs. For accurate production estimation, reservoir and proppant flow properties and compaction and sand migration effects on the flow properties are investigated. The following items summarize the findings of this study.

1. Flow properties of reservoir rock should be determined from steady-state or pulse-decay experiments. A new optimization algorithm is proposed for simultaneous estimation of flow properties from steady-state lab experiments. Pressure and flow rate measurement errors may cause a misestimation of flow properties. Therefore, measurement points containing large errors should be detected with the Jackknife method and removed from the analysis. Then, flow properties and their confidence intervals can be found from the proposed optimization algorithm using Bootstrap method.
2. Two pulse-decay experiments from cores labeled 2C and 3C were analyzed. Results indicate that the duration of the experiments is critical for accurate estimation of the flow properties. Short pulse-decay duration leads to lower estimates of the Klinkenberg coefficient and higher estimates of permeability and non-Darcy coefficient. Correlations are developed for the experiment duration as a function of experimental set-up parameters and core properties using linear regression, for 1-tank and 2-tank experimental set-ups. The correlation is validated with core 2C pulse-decay data by estimating the durations and performing inverse prediction of permeability.
3. Estimated permeability from LBM depends on both grid resolution and relaxation time. For reliable estimation of permeability from LBM with single-relaxation or multi-relaxation methods, the minimum particle diameter should be represented by at least 30 voxels. Estimated permeability from network modeling does not depend on resolution but

does depend on network parameters, including pore merging conditions for the algorithm used here. Permeabilities obtained from network modeling with an overlapping merge condition are larger than than what is obtained with a touching merge condition. Estimated permeability from network modeling with a touching merge condition is close to the one obtained from LBM.

4. Statistically significant correlations are developed to estimate permeability and non-Darcy coefficients from other petrophysical and network model parameters. A path analysis is conducted to relate all petrophysical properties. The path model is validated with missing data estimation for permeability, non-Darcy coefficient, tortuosity and specific surface area using stochastic regression.
5. Permeability decrease associated with compaction can be estimated from the Kozeny-Carman relation. Permeability decrease associated with pore-throat plugging (e.g., sand migration) can be estimated from correlations that were developed for sand concentration at pore throats. Changes in the non-Darcy coefficients with compaction and sand migration are underestimated if standard non-Darcy correlations are used. Therefore, the equation developed here to relate permeability-non-Darcy coefficient Kozeny-Carman type relations should be used to estimate inertial effects.
6. A simulation algorithm is developed by coupling the continuity and sand migration equations, and using the finite difference method. The change in permeability and non-Darcy coefficient due to compaction and sand migration are estimated from Kozeny-Carman type relations found from pore-scale analysis.
7. A parametric study is conducted for initial mobile sand concentration, rate constants for sand migration equations, critical velocity, and flow rate. Cumulative sand production

increases with an increase in initial mobile sand concentration, flow rate, pore surface entrainment rate constant, and decreasing critical velocity. The region affected by sand migration increases with the increasing flow rate and decreasing critical velocity. Reservoir rock properties are significantly affected by pore throat sand concentration. Permeability decreases and inertial effects increase with the pore-throat-plugging rate constant. Pressure near the wellbore decreases with increasing pore-throat rate constant and flow rate.

8. Frac-pack completions lead to decreasing pressure drop and velocity in the reservoir. As a result, sand production decreases significantly. The most significant changes occur at the reservoir-fracture interface. Increasing sand concentration on pore surfaces and at pore throats leads to decreases in porosity and permeability but larger inertial effects. The effects of fracture length, width, and conductivity on sand migration are investigated with sensitivity analysis. Cumulative sand production does not decrease linearly with an increase in fracture dimensions or permeability; therefore, fracture properties can be optimized to mitigate sand production.

## REFERENCES

- Al-Rumhy, M. H., & Kalam, M. Z. (1993). Relationship of Core-Scale Heterogeneity With Non-Darcy Flow Coefficients. doi: 10.2118/25649-PA
- Alvarez, C. H., Holditch, S. A., & McVay, D. A. (2002). *Effects of Non-Darcy Flow on Pressure Transient Analysis of Hydraulically Fractured Gas Wells*.
- Amao, A. M. (2007). *Mathematical Model for Darcy Forchheimer Flow with Applications to Well Performance Analysis*. (Msc), Texas Tech University.
- Andrade, J. A., Costa, U. M. S., Almeida, M. P., Makse, H. A., & Stanley, H. E. (1998). Inertial effects on fluid flow through disordered porous media. *Phys. Rev. Lett.*, 82(26), 5249–5252.
- Arbuckle, J. L. (2008). *Amos 17.0 User's Guide*: SPSS Inc.
- Archie, G. E. (1942). The electrical resistivity log as an aid in determining some reservoir characteristics. *Trans. AMIE*, 146, 54-62.
- Armenta, M., & Wojtanowicz, A. K. (2003). *Rediscovering Non-Darcy Flow Effect In Gas Reservoir*.
- Avila, C. E., & Evans, R. D. (1986). *The Effect Of Temperature And Overburden Pressure Upon The Non-Darcy Flow Coefficient In Porous Media*. Paper presented at the The 27th U.S. Symposium on Rock Mechanics (USRMS), Tuscaloosa, AL. <http://www.onepetro.org/mslib/app/Preview.do?paperNumber=ARMA-86-0623&societyCode=ARMA>
- Backhaus, K., Erichson, B., Plinke, W., & Weiber, R. (2006). *Multivariate Analysemethoden: eine anwendungsorientierte Einführung*: Springer.
- Balhoff, M. T., & Wheeler, M. F. (2009). A Predictive Pore-Scale Model for Non-Darcy Flow in Porous Media. doi: 10.2118/110838-PA
- Barree, R. D., & Conway, M. W. (2004). *Beyond Beta Factors: A Complete Model for Darcy, Forchheimer, and Trans-Forchheimer Flow in Porous Media*.
- Basak, P. (1977). Non-Darcy flow and its implications to seepage problems. *Journal of the irrigation and drainage division*, 103(4), 459-473.
- Bear, J. (1972). *Dynamics of fluids in porous media*: American Elsevier Pub. Co.
- Beard, D. C., & Weyl, P. K. (1973). Influence of Texture on Porosity and Permeability of Unconsolidated Sand. *AAPG Bulletin*, 57(2), 349-369.
- Belhaj, H. A., Agha, K. R., Nouri, A. M., Butt, S. D., & Islam, M. R. (2003). *Numerical and Experimental Modeling of Non-Darcy Flow in Porous Media*.

- Belhaj, H. A., Agha, K. R., Nouri, A. M., Butt, S. D., Vaziri, H. F., & Islam, M. R. (2003). *Numerical Simulation of Non-Darcy Flow Utilizing the New Forchheimer's Diffusivity Equation*.
- Berg, R. R. (1970). Method for Determining Permeability from Reservoir Rock Properties. *Transaction, Gulf Coasts Association of Geological Societies*(20), 303-317.
- Bhatnagar, P. L., Gross, E. P., & Krook, M. (1954). A Model for Collision Processes in Gases. I. Small Amplitude Processes in Charged and Neutral One-Component Systems. *Physical Review*, 94(3), 511-525.
- Bird, R. B., Stewart, W. E., & Lightfoot, E. N. (1965). *Transport phenomena [by] R. Byron Bird, Warren E. Stewart [and] Edwin N. Lightfoot*. New York,: Wiley.
- Borujeni, A. T. (2013). Multi-scale Modeling of Inertial Flows through Propped Fractures. *Doctoral dissertation, etd-07072013-222509*.
- Bouhroum, A., Liu, X., & Civan, F. (1994). *Predictive Model and Verification for Sand Particulates Migration in Gravel Packs*.
- Brace, W. F., Walsh, J. B., & Frangos, W. T. (1968). Permeability of Granite under High Pressure. *J. Geophys. Res.*, 73(6), 2225-2236. doi: 10.1029/JB073i006p02225
- Brar, G. S., & Aziz, K. (1978). Analysis of Modified Isochronal Tests To Predict The Stabilized Deliverability Potential of Gas Wells Without Using Stabilized Flow Data (includes associated papers 12933, 16320 and 16391 ). doi: 10.2118/6134-PA
- Chen, T., & Stagg, P. W. (1984). Semilog Analysis of the Pulse-Decay Technique of Permeability Measurement. *Society of Petroleum Engineers Journal*, 24(6), 639-642. doi: 10.2118/11818-pa
- Chen, T., & Stagg, P. W. (1984). Semilog Analysis of the Pulse-Decay Technique of Permeability Measurement. doi: 10.2118/11818-PA
- Chilton, T. H., & Colburn, A. P. (1931). II—Pressure Drop in Packed Tubes1. *Industrial & Engineering Chemistry*, 23(8), 913-919. doi: 10.1021/ie50260a016
- Chukwudozie, C. P. (2011). *Pore-Scale Lattice Boltzmann Simulations of Inertial Flows in Realistic Porous Media: A First Principle Analysis of the Forchheimer Relationship*. (Master of Science), Louisiana State University.
- Civan, F., & Evans, R. D. (1991). *Non-Darcy Flow Coefficients and Relative Permeabilities for Gas/Brine Systems*.
- CMG. (2013). *User's Guide-GEM: Advanced Compositional Reservoir Simulator*: Computer Modelling Group Ltd.,Calgary, AB, Canada.

- Coles, M. E., & Hartman, K. J. (1998). *Non-Darcy Measurements in Dry Core and the Effect of Immobile Liquid*. Paper presented at the SPE Gas Technology Symposium, Calgary, Alberta, Canada.  
<http://www.onepetro.org/mslib/app/Preview.do?paperNumber=00039977&societyCode=SPE>
- Comiti, J., & Renaud, M. (1989). A new model for determining mean structure of fixed beds from pressure drop measurements: application to beds parallelipipedal particles. *Chem. Eng. Sci.*, 44(7), 1539-1545.
- Cooper, J. W., Wang, X., & Mohanty, K. K. (1999). Non-Darcy-Flow Studies in Anisotropic Porous Media. doi: 10.2118/57755-PA
- Cornell, D., & Katz, D. L. (1953). Flow of Gases through Consolidated Porous Media. *Industrial & Engineering Chemistry*, 45(10), 2145-2152. doi: 10.1021/ie50526a021
- d'Humieres, D., Ginzburg, I., Krafczyk, M., Lallemand, P., & Luo, L. S. (2002). Multiple-relaxation-time lattice Boltzmann models in three dimensions. *Philosophical Transactions of the Royal Society of London Series a-Mathematical Physical and Engineering Sciences*, 360(1792), 437-451. doi: 10.1098/rsta.2001.0955
- Darcy, H. (1856). *Les Fontaines Publiques de la Ville de Dijon*, Victor Dalmont, Paris.
- de Hoog, F., Knight, J., & Stokes, A. (1982). An Improved Method for Numerical Inversion of Laplace Transforms. *SIAM Journal on Scientific and Statistical Computing*, 3(3), 357-366. doi: 10.1137/0903022
- Dong, H. (2007). *Micro CT Imaging and Pore Network Extraction*. (PhD), Imperial College, London.
- Dranchuk, P. M., & Abou-Kassem, J. H. (1975). Calculation of Z factors for natural gases using equation of state. *Canadian Petroleum Technology*, 14, 34 - 36.
- Dybbs, A., & Edwards, R. V. (1984). A New Look at Porous Media Fluid Mechanics — Darcy to Turbulent. In J. Bear & M. Y. Corapcioglu (Eds.), *Fundamentals of Transport Phenomena in Porous Media* (Vol. 82, pp. 199-256): Springer Netherlands.
- Ergun, S. (1952). Fluid flow through packed columns. *Chem. Engng. Prog.*, 48(2), 89-94.
- Evans, R. D., Hudson, C. S., & Greenlee, J. E. (1987). The Effect of an Immobile Liquid Saturation on the Non-Darcy Flow Coefficient in Porous Media. *SPE Production Engineering*(11). doi: 10.2118/14206-pa
- Ezeudembah, A. S., & Dranchuk, P. M. (1982). *Flow Mechanism of Forchheimer's Cubic Equation in High-Velocity Radial Gas Flow Through Porous Media*.

- Fancher, G. H., Lewis, J. A., & Barnes, K. B. (1933). Some physical characteristics of oil sands. [Porosity, permeability, and screen analysis]. *Journal Name: Penn. State Coll., Mineral Ind. Expt. Sta., Bull.*; *Journal Volume: 12*, Medium: X; Size: Pages: 65-171.
- Firoozabadi, A., & Katz, D. L. (1979). An Analysis of High-Velocity Gas Flow Through Porous Media. doi: 10.2118/6827-PA
- Forchheimer, P. (1901). Wasserbewegung Durch Boden. *1781*, 45.
- Frederick Jr., D. C., & Graves, R. M. (1994). *New Correlations To Predict Non-Darcy Flow Coefficients at Immobile and Mobile Water Saturation*. Paper presented at the SPE Annual Technical Conference and Exhibition, New Orleans, Louisiana. <http://www.onepetro.org/mslib/app/Preview.do?paperNumber=00028451&societyCode=SPE>
- Geertsma, J. (1974). Estimating the Coefficient of Inertial Resistance in Fluid Flow Through Porous Media. (10). doi: 10.2118/4706-pa
- Gewers, C. W. W., & Nichol, L. R. (1969). *Gas Turbulence Factor in a Microvugular Carbonate*.
- Green, L. J., & Duwez, P. (1951). Fluid flow through porous metals. *j. Appl. Mech.*, 39-45.
- Hampton, D. R., & Heuvelhorst, H. G. (1990). Designing gravel packs to improve separate-phase hydrocarbon recovery: Laboratory experiments. *In: Proc. NWWA/API Conf. on Petroleum Hydrocarbons and Organic Chemicals in Ground Water*, 195-209.
- Hampton, D. R., Smith, M. M., & Shank, S. J. (1991). Further Laboratory Studies of Gravel Pack Design for Hydrocarbon Recovery Wells. *In: Proc. NWWA/API Conf. on Petroleum Hydrocarbons and Organic Chemicals in Ground Water*, 615-629.
- Hubbert, M. K. (1956). Darcy's Law and the Field Equations of the Flow of Underground Fluids: Society of Petroleum Engineers.
- Iacobucci, D. (2009). Everything you always wanted to know about SEM (structural equations modeling) but were afraid to ask. *Journal of Consumer Psychology*, 19(4), 673-680. doi: <http://dx.doi.org/10.1016/j.jcps.2009.09.002>
- Irmay, S. (1958). On the Theoretical Derivation of Darcy and Forchheimer Formulas. *Trans. Amer. Geophys. Union*, 39(4), 702 - 707.
- Jones, S. C. (1972). A Rapid Accurate Unsteady-State Klinkenberg Permeameter. (10). doi: 10.2118/3535-pa
- Jones, S. C. (1987). *Using the Inertial Coefficient, B, To Characterize Heterogeneity in Reservoir Rock*. Paper presented at the SPE Annual Technical Conference and Exhibition, Dallas, Texas.



<http://www.onepetro.org/mslib/app/Preview.do?paperNumber=00016949&societyCode=SPE>

- Jones, S. C. (1997). A Technique for Faster Pulse-Decay Permeability Measurements in Tight Rocks. *SPE Formation Evaluation*(03). doi: 10.2118/28450-pa
- Kaczmarek, M. (2008). Approximate Solutions for Non-stationary Gas Permeability Tests. *Transport in Porous Media*, 75(2), 151-165. doi: 10.1007/s11242-008-9216-x
- Kamath, J., Boyer, R. E., & Nakagawa, F. M. (1992). Characterization of Core Scale Heterogeneities Using Laboratory Pressure Transients. *SPE Formation Evaluation*(09). doi: 10.2118/20575-pa
- Katz, D. L. V. (1959). *Handbook of natural gas engineering*: McGraw-Hill.
- Khaniaminjan, & Goudarzi. (2008). Non-Darcy Fluid Flow through Porous Media: Society of Petroleum Engineers.
- Kim, B. Y. K. (1985). The Resistance to Flow in Simple and Complex Porous Media Whose Matrices are Composed of Spheres. *MSc thesis, University of Hawaii at Manoa, Honolulu, Hawaii*.
- Klinkenberg, L. J. (1941). *The Permeability Of Porous Media To Liquids And Gases*. Paper presented at the Drilling and Production Practice. <http://www.onepetro.org/mslib/app/Preview.do?paperNumber=API-41-200&societyCode=API>
- Koza, Z., & Matyka, M. K., A. (2009). Finite-size anisotropy in statistically uniform porous media. *Phys. Rev. E*, 79, 066306.
- Lai, B., Miskimins, J. L., & Wu, Y.-S. (2012). Non-Darcy Porous-Media Flow According to the Barree and Conway Model: Laboratory and Numerical-Modeling Studies. doi: 10.2118/122611-PA
- Lee, A. L., Gonzalez, M. H., & Eakin, B. E. (1966). The Viscosity of Natural Gases. doi: 10.2118/1340-PA
- Lee, W. J., & Wattenbarger, R. A. (1996). *Gas Reservoir Engineering*: Soc. of Petroleum Engineers.
- Legland, D., Kieu, K., & Devaux, M. F. (2007). Computation of Minkowski measures on 2D and 3D binary images. *Image Analysis and Stereology*, 27(2).
- Lemmon, E. W., & Jacobsen, R. T. (2004). Viscosity and Thermal Conductivity Equations for Nitrogen, Oxygen, Argon and Air. *International Journal of Thermophysics*, 25(1), 21 - 69.

- Li, D., & Engler, T. W. (2001). *Literature Review on Correlations of the Non-Darcy Coefficient*. Paper presented at the SPE Permian Basin Oil and Gas Recovery Conference, Midland, Texas.  
<http://www.onepetro.org/mslib/app/Preview.do?paperNumber=00070015&societyCode=SPE>
- Li, D., & Engler, T. W. (2002). *Modeling and Simulation of Non-Darcy Flow in Porous Media*.
- Li, D., Svec, R. K., Engler, T. W., & Grigg, R. B. (2001). *Modeling and Simulation of the Wafer Non-Darcy Flow Experiments*. Paper presented at the SPE Western Regional Meeting, Bakersfield, California.  
<http://www.onepetro.org/mslib/app/Preview.do?paperNumber=00068822&societyCode=SPE>
- Liu, X. (1994). *Modelling of Formation Damage due to Particulate Processes in Two-Phase Flow Systems*. (Doctoral), The University of Oklahoma, Oklahoma.
- Liu, X., & Civan, F. (1993). *Characterization and Prediction of Formation Damage in Two-Phase Flow Systems*.
- Liu, X., Civan, F., & Evans, R. D. (1995). Correlation of the Non-Darcy Flow Coefficient. doi: 10.2118/95-10-05
- Llewellyn, E. W. (2010). LBflow: An extensible lattice Boltzmann framework for the simulation of geophysical flows. Part I: theory and implementation. *Computers & Geosciences*, 36(2), 115-122. doi: <http://dx.doi.org/10.1016/j.cageo.2009.08.004>
- Lolon, E. P., Chipperfield, S. T., McVay, D. A., & Schubarth, S. K. (2004). *The Significance of Non-Darcy and Multiphase Flow Effects in High-Rate, Frac-Pack Gas Completions*.
- Lombard, J. M., Longeron, D., & Kalaydjian, F. (1999). *Influence of Connate Water and Condensate Saturation on Inertial Effects in Gas-Condensate Fields*.
- Ma, H., & Ruth, D. W. (1993). The microscopic analysis of high forchheimer number flow in porous media. *Transport in Porous Media*, 13(2), 139-160. doi: 10.1007/BF00654407
- Ma, H., & Ruth, D. W. (1997). Physical Explanations of Non-Darcy Effects for Fluid Flow in Porous Media. doi: 10.2118/26150-PA
- Mathworks. <http://www.mathworks.com/>. from <http://www.mathworks.com/>
- Mohan, J., Pope, G. A., & Sharma, M. M. (2006). *Effect of Non-Darcy Flow on Well Productivity in a Hydraulically Fractured Gas/Condensate Well*.
- Morrison, S. J., & Dugan, T. P. (1991). A Practical Approach. *Advances in Core Evaluation Evaluation: Accuracy and Precision in Reserves Estimation*, 447 - 462.

- Muskat, M. (1937). The Flow of Homogeneous Fluids through Porous Media. *International Series in Physics, Mcgraw Hill Book Company, Incorporated.*
- Nabovati, A., & Sousa, A. C. M. (2009). Fluid Flow Simulation in Random Porous Media at Pore Level Using Lattice Boltzmann Method. In F. G. Zhuang & J. C. Li (Eds.), *New Trends in Fluid Mechanics Research* (pp. 518-521): Springer Berlin Heidelberg.
- Narayanaswamy, G., Sharma, M. M., & Pope, G. A. (1999). Effect of Heterogeneity on the Non-Darcy Flow Coefficient. doi: 10.2118/56881-PA
- Noman, R., Shrimanker, N., & Archer, J. S. (1985). *Estimation of the Coefficient of Inertial Resistance in High-Rate Gas Wells*. Paper presented at the SPE Annual Technical Conference and Exhibition, Las Vegas, Nevada. <http://www.onepetro.org/mslib/app/Preview.do?paperNumber=00014207&societyCode=SPE>
- Pascal, H., & Quillian, R. G. (1980). *ANALYSIS OF VERTICAL FRACTURE LENGTH AND NON-DARCY FLOW COEFFICIENT USING VARIABLE RATE TESTS*. Paper presented at the SPE Annual Technical Conference and Exhibition, Dallas, Texas. <http://www.onepetro.org/mslib/app/Preview.do?paperNumber=00009348&societyCode=SPE>
- Qian, Y. H., D'Humières, D., & Lallemand, P. (1992). Lattice BGK Models for Navier-Stokes Equation. *EPL (Europhysics Letters)*, 17(6), 479.
- Raykov, T., & Marcoulides, G. (2006). *A First Course in Structural Equation Modeling*: Lawrence Erlbaum Associates.
- Ruth, D., & Ma, H. (1992). On the derivation of the Forchheimer equation by means of the averaging theorem. *Transport in Porous Media*, 7(3), 255-264. doi: 10.1007/BF01063962
- SAS. (2014). *JMP 11 Fitting Linear Models*: Cary, NC: SAS Institute Inc. .
- Scheidegger, A. E. (1974). *The physics of flow through porous media* (3d ed.). Toronto: University of Toronto Press.
- Schermelleh-Engel, K., Moosbrugger, H., & Müller, H. (2003). Evaluating the fit of structural equation models: Tests of significance and descriptive goodness-of-fit measures. *Methods of Psychological Research-Online*, 8, 23-74. doi: citeulike-article-id:7222182
- Schumacker, R., & Lomax, R. (2004). *A Beginner's Guide to Structural Equation Modeling (The Inquiry and Pedagogy Across Diverse Contexts Series)*: Psychology Press.
- Silin, D. B., Jin, G., & Patzek, T. W. (2003). *Robust Determination of the Pore Space Morphology in Sedimentary Rocks*. Paper presented at the SPE Annual Technical Conference and Exhibition, Denver, Colorado. <http://www.onepetro.org/mslib/app/Preview.do?paperNumber=00084296&societyCode=SPE>

- Smith, T. D., & McMillan, B. F. (2001). A Primer of Model Fit Indices in Structural Equation Modeling. *Annual Meeting of the Southwest Educational Research Association*.
- Span, R., Lemmon, E. W., Jacobsen, R. T., & Wagner, W. (1998). A Reference Quality Equation of State for Nitrogen. *International Journal of Thermophysics*, 19(4), 1121 - 1132.
- Stewart, W. F., Burkhardt, S. F., & Voo, D. (1959). Prediction of Pseudo-critical Parameters for Mixtures. *Presented at the AIChE Meeting, Kansas City, Missouri, USA, 18 May 1959*.
- Sukop, M. C., & Thorne, D. T. J. (2007). *Lattice Boltzmann Modeling: An Introduction for Geoscientists and Engineers*: Springer Publishing Company, Incorporated.
- Tek, M. R., Coats, K. H., & Katz, D. L. (1962). *The Effect of Turbulence on Flow of Natural Gas Through Porous Reservoirs*.
- Thauvin, F., & Mohanty, K. K. (1998). Network Modeling of Non-Darcy Flow Through Porous Media. *Transport in Porous Media*, 31(1), 19-37. doi: 10.1023/A:1006558926606
- Torrest, R. S. (1974). Gravel Packs: Their Placement, Impairment And Effect On Well Productivity: Society of Petroleum Engineers.
- W.F. Brace, J. B. W., W.T. Frangos. (1968). Permeability of Granite Under High Pressure. *Geophys. Res.*, 73(6), 2225 - 2236.
- Web1. (N.d.). Proppant and Gravel Pack Sands. from <http://www.premiersilica.com/>
- Widaman, K. F., & Thompson, J. S. (2003). On Specifying the Null Model for Incremental Fit Indices in Structural Equation Modeling. *Psychological Methods*, 8, 16-37.
- Wong, S. W. (1970). *Effect of Liquid Saturation On Turbulence Factors For Gas-Liquid Systems*.
- Zeng, Z., & Grigg, R. (2003). A Criterion for Non-Darcy Flow in Porous Media. *Transport in Porous Media*, 63(1), 57-69. doi: 10.1007/s11242-005-2720-3

## **VITA**

Sultan Anbar was born in 1982, in Corum, Turkey. She attended Baskent high school and received her diploma in 2000. She went to Middle East Technical University (METU) and graduated with degrees in Bachelor of Petroleum and Natural Gas Engineering and minor of Geographic Information Systems and Remote Sensing in 2007. She got MSc degree in Petroleum Engineering focusing on CO<sub>2</sub> Sequestration in METU in 2009. She is currently a candidate for the PhD in Petroleum Engineering, to be awarded in December 2014.